

**VIII International Conference  
on Textile Composites and  
Inflatable Structures**

# **STRUCTURAL MEMBRANES 2017**

9-11 october 2017, Munich, Germany

**K. Bletzinger , E. Oñate and B. Kröplin (Eds.)**





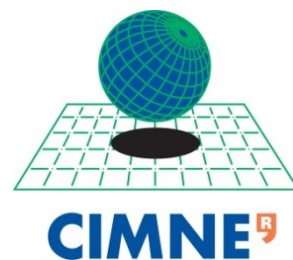
**VIII International Conference on  
Textile Composites and Inflatable  
STRUCTURAL MEMBRANES 2017**



**9 – 11 October 2017  
Munich, Germany**

A publication of:

**International Center for Numerical  
Methods in Engineering (CIMNE)**  
Barcelona, Spain



Printed by: Artes Gráficas Torres S.L., Huelva 9, 08940 Cornellà de Llobregat, Spain

ISBN: 978-84-946909-9-0

## TABLE OF CONTENTS

Preface .....	7
Acknowledgements .....	9
SUMMARY.....	11
Contents .....	13
Plenary Lectures .....	17
Invited Sessions .....	29
Contributed Sessions.....	415
Authors Index.....	503



## PREFACE

This volume contains the full papers presented at the **VIII International Conference on Textile Composites and Inflatable Structures – Structural Membranes 2017**, held in Munich, Germany, on October 9-11, 2017.

Previous editions of the conference were held in Barcelona (2003), Stuttgart (2005), Barcelona (2007), Stuttgart (2009) and Barcelona (2011) and Munich (2013). Structural Membranes is one of the Thematic Conference of the European Community in Computational Methods in Applied Science (ECCOMAS) and is also a Special Interest Conference of the International Association for Computational Mechanics (IACM).

Textile composites and inflatable structures have become increasingly popular for a variety of applications in – among many other fields - civil engineering, architecture and aerospace engineering. Typical examples include membrane roofs and covers, sails, inflatable buildings and pavilions, airships, inflatable furniture, airspace structures, bio-membranes, clothes, etc.

The objectives of **Structural Membranes 2017** are to collect and disseminate state-of-the-art research and technology for design, analysis, construction and maintenance of textile and inflatable structures.

Contributions to the **Structural Membranes 2017** deal with the presentation of the challenging tasks in the individual design steps of pre-stressed and inflatable structures made from textiles, foils and composite materials. The topics vary from geometrical modelling in the design and construction process, advanced simulation technologies for structural analysis of lightweight structures under various load conditions (e.g. coupled aero-elastic analysis), the description and validation of new materials and suitable constitutive laws, methodologies for form finding and patterning, adaptive membrane structures, energetic aspects, testing procedures, maintenance techniques up to manufacturing. **Structural Membranes 2017** addresses the full scope from the theoretical bases for structural analysis and constitutive modelling, through the numerical algorithms necessary for efficient and robust computer implementation to the impact of practical experience and experimental testing.

The collection of full papers includes contributions sent directly from the authors and the editors cannot accept responsibility for any inaccuracies, comments and opinions contained in the text.

The organizers would like to take this opportunity to thank all authors for submitting their contributions.

Munich, October 2017

**Kai-Uwe Bletzinger**  
Technical University of Munich (TUM)  
Munich, Germany

**Bernd Kröplin**  
Tao GmbH  
Stuttgart, Germany

**Eugenio Oñate**  
CIMNE and Technical University of Catalonia (UPC)  
Barcelona, Spain



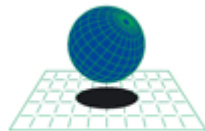
# ACKNOWLEDGEMENTS

The conference organizers acknowledge the support of the following organizations:



Technische Universität München

Technische Universität München (TUM),  
Germany



CIMNE

International Center for Numerical  
Methods in Engineering (CIMNE),  
Barcelona, Spain



Universitat Politècnica de Catalunya,  
BarcelonaTech, Spain



European Community on  
Computational Methods in Applied  
Sciences (ECCOMAS)



International Association for  
Computational Mechanics (IACM)



International Association for Shell and  
Spatial Structures (IASS)



TAO GmbH, Stuttgart, Germany



Dlubal Software GmbH, Germany



## SUMMARY

<b>PLENARY LECTURES</b> .....	17
<b>INVITED SESSIONS</b> .....	29
ADAPTIVE LIGHTWEIGHT STRUCTURES .....	29
ADVANCES ON INFLATABLE STRUCTURES IN ENGINEERING AND ARCHITECTURE .....	41
DETAILED CASE STUDIES .....	51
DURABILITY OF LIGHT WEIGHT STRUCTURES .....	93
ENERGETIC ASPECTS .....	133
NEW DEVELOPMENTS IN MEMBRANE BUILDING .....	147
NEW MATERIAL.....	198
NUMERICAL METHODS AND MODELLING OF TENSILE STRUCTURES .....	265
RETRACTABLE MEMBRANE STRUCTURES .....	323

TRANSPARENT BUILDING SKINS - CHALLENGES AND SOLUTIONS.....	331
WIND ENGINEERING AND FLUID-STRUCTURE INTERACTION ....	360
<b>CONTRIBUTED SESSIONS</b> .....	<b>415</b>
CASE STUDIES .....	415
DESIGN METHODS.....	427
STRUCTURAL ANALYSIS .....	455
AUTHORS INDEX.....	503

# CONTENTS

## PLENARY LECTURES

- Modern pressure measurement technology and structural design for wind: a new collaborative paradigm for wind and structural engineers** ..... 17  
*E. Simiu*

## INVITED SESSIONS

### ADAPTIVE LIGHTWEIGHT STRUCTURES

*Organized by Knut Göppertand and Christoph Paech*

- Wimbledon no.1 court retractable roof - a case study** ..... 29  
*M Roberts*

### ADVANCES ON INFLATABLE STRUCTURES IN ENGINEERING AND ARCHITECTURE

*Organized by Javier Marcipar and Eugenio Oñate*

- Dynamics Testing and Simulation of Inflatable Deployable Membrane Antennas** ..... 41  
*J. Wei, L. Yu, J. Yu and H. Tan*

### DETAILED CASE STUDIES

*Organized by Josep Ignasi Llorens and Günther H. Filz*

- Architectural membranes for high-performance building skins, Latest material developments, Case study: façade in Ecuador** ..... 51  
*K. Bernert*

- Detailed Design and Construction of the St. Louis Park Ice Rink** ..... 57  
*C. Huntington and J. Carpenter*

- Detailing for refurbishment with structural membranes** ..... 69  
*J.I. De Llorens*

- Membrane concept for The Nuvola for the New Centro Congressi in Rome** ..... 81  
*B. Stimpfle*

## DURABILITY OF LIGHT WEIGHT STRUCTURES

*Organized by Heidrun Bögner-Balz*

<b>Experimental method for biaxial tensile strength of fabrics and preliminary investigations</b> .....	93
<i>W. Chen, T. Shi, C. Gao, J. Hu and B. Zhao</i>	
<b>Mechanical properties of technical coated fabrics under axial and off-axial tensile tests</b> .....	100
<i>A. Kustov, N. Mokin and A. Ibragimov</i>	
<b>Tearing fracture properties for PVDF coated bi-axial warp knitted fabrics</b> .....	112
<i>J. W. Chen, W. J. Chen, M. Y. Wang, B. Yao, H. Zhou, B. Zhao and JH. Hu</i>	
<b>Test and mesoscopic finite element analysis on mechanical properties degradation of aged coated fabrics</b> .....	125
<i>Q.L. Zhang and Y.T. Li</i>	

## ENERGETIC ASPECTS

*Organized by Jianhui Hu, Karsten Moritz and Wujun Chen*

<b>Improved Daylight Comfort by a New 3D-Foil That Allows to Trade off Solar Gains and Light Individually.</b> .....	133
<i>J. Cremers and H. Marx</i>	
<b>Performance of curved organic photovoltaics modules for membranes integration: solar simulation tests</b> .....	141
<i>H. Ibrahim Ali and P. Beccarelli</i>	

## NEW DEVELOPMENTS IN MEMBRANE BUILDING

*Organized by Lars Schiemann and Karsten Moritz*

<b>Common problems in the design and construction of membrane structures</b> .....	147
<i>F. Weller</i>	
<b>Design and Construction of the Asymptotic Pavilion</b> .....	178
<i>E. Schling, D. Hitrec, J. Schickore and R. Barthel</i>	
<b>Importance of the Context for the design of the membrane structures</b> .....	190
<i>S. Toso, M. Chivante and K. Moritz</i>	

## NEW MATERIAL

*Organized by Thomas Stegmaier and Andreas Kunze*

<b>A multiscale non-orthogonal model for tensile properties of uncoated and coated F-12 aramid fabric</b> .....	198
<i>H.F. Tan, X.L. Luo and G.C. Lin</i>	
<b>Investigation of the structure and properties of flexible polymeric materials for integration with thin heat conductors.</b> .....	210
<i>I. Cherunova, M. Stenkina and P. Cherunov</i>	

<b>Investigations into the Long-term Behaviour of Fabrics.....</b>	217
<i>H. Asadi, J. Uhlemann, T. Stegmaier, V. von Arnim and N. Stranghöner</i>	
<b>Saturation behaviour and load-induced thickness change of woven glass fibre fabrics. ....</b>	229
<i>J. Uhlemann, D. Balzani, N. Stranghöner and M. Motevalli</i>	
<b>Stretch controlled shading capabilities of special elastomeric silicone films .....</b>	241
<i>T. Stegmaier, V. Arnim, A. Kunze, B. Ewert, G. Gresser, A. Teixeira and F. Weininger</i>	
<b>Viscous characteristics of ETFE film sheet under temperature change .....</b>	253
<i>T. Yoshino and S. Kato</i>	

## **NUMERICAL METHODS AND MODELLING OF TENSILE STRUCTURES**

*Organized by Benedikt Philipp, Falko Dieringer and Kai-Uwe Bletzinger*

<b>Active bending starting on curved architectural shape .....</b>	265
<i>J. Bellmann</i>	
<b>Advanced approaches for analysis and formfinding of membrane structures with finite elements I .....</b>	275
<i>R. Kemmler, M. Bischoff and J. Gade</i>	
<b>Challenges of the implementation of Membrane Structures into BIM .....</b>	294
<i>G. Grunwald and A. Ihde</i>	
<b>Form finding of shell and membrane structures .....</b>	303
<i>R. Lang and I. Němec</i>	
<b>Isogeometric Analysis for Staged Construction within Lightweight Design .....</b>	311
<i>A. M. Bauer, R. Wüchner and K-U. Bletzinger</i>	

## **RETRACTABLE MEMBRANE STRUCTURES**

*Organized by Alfred Rein and Mike Sieder*

<b>Khan Shatyr Entertainment Centre cable net supply, engineering and installation .....</b>	323
<i>S. Geyer, D. Lombardini and S. Lenk</i>	

## **TRANSPARENT BUILDING SKINS - CHALLENGES AND SOLUTIONS**

*Organized by Karsten Moritz, Simone Toso and Lars Schiemann*

<b>Acoustic performance test assessment on sound generated by rainfall on multilayer ETFE Cushion Systems .....</b>	331
<i>M. Chivante, S. Toso and K. Moritz</i>	
<b>Engineering and fabrication of the "Off The Cuff" pavilion, FuoriSalone 2017, Milan .....</b>	338
<i>P. Beccarelli and R. Maffei</i>	
<b>ETFE-Foil-Cushion technology for cruise ships .....</b>	347
<i>G. Müller, F. Goecke and K. Moritz</i>	

# WIND ENGINEERING AND FLUID-STRUCTURE INTERACTION

Organized by Roland Wächner and Kai-Uwe Bletzinger

<b>Aerodynamic damping of membranes in still air</b> .....	360
<i>M. Zschke and J. Wacker</i>	
<b>An integrated framework for the reliability and validity assessment of numerical wind engineering simulations</b> .....	371
<i>A. Abodonya, J. Cotela, R. Wüchner and K-U. Bletzinger</i>	
<b>Numerical simulation of an air-supported structure in the air flow</b> .....	383
<i>N. Mokin, A. Kustov and S. Trushin</i>	
<b>Research on wind pressure and wind-induced vibration characteristics of Expo Axis cable-membrane structure by field measurement</b> .....	394
<i>Q.L. Zhang and Z.Y. Li</i>	
<b>The effect of gravity in transient fluid-structure interaction simulations of a large horizontal axis wind turbine with composite blades</b> .....	403
<i>G. Santo, M. Peeters, W. Van Paepegem and J. Degroote</i>	

## CONTRIBUTED SESSIONS

### CASE STUDIES

<b>Tangent developable surfaces elements in thin-walled structures</b> .....	514
<i>Z. Belyaeva, S. Berestova and E. Mityushov</i>	

### DESIGN METHODS

<b>Bending-Active Dome-Shaped Structure</b> .....	427
<i>A.V. Chesnokov, V.V. Mikhaylov and I.V. Dolmatov</i>	
<b>Cable roof structure with flexible fabric covering</b> .....	436
<i>V.V. Mikhaylov and A.V. Chesnokov</i>	
<b>Design of a cost effective small span tensile roof</b> .....	448
<i>H. Ibrahim Ali, P. Beccarelli, V. Reed and R. Carpenter</i>	

### STRUCTURAL ANALYSIS

<b>Analysis of cable structures by means of trigonometric series</b> .....	455
<i>A.V. Chesnokov and V.V. Mikhaylov</i>	
<b>High speed design and analysis of cable-membrane structures on graphics cards</b> .....	467
<i>P. Iványi</i>	
<b>Membrane roof structures</b> .....	478
<i>C. Corte</i>	

# MODERN PRESSURE MEASUREMENT TECHNOLOGY AND STRUCTURAL DESIGN FOR WIND: A NEW COLLABORATIVE PARADIGM FOR WIND AND STRUCTURAL ENGINEERS

EMIL SIMIU\*

\*Engineering Laboratory  
National Institute of Standards and Technology (NIST)  
100 Bureau Drive, Gaithersburg MD 20899, USA  
e-mail: [emil.simiu@nist.gov](mailto:emil.simiu@nist.gov)

**Key words:** Aerodynamic Pressures, Database-assisted Design, Wind Load Factors.

**Summary.** Against a brief historical overview, this paper presents the Database-assisted Design (DAD) approach, a conceptually simple, transparent, and rigorous approach to structural design for wind, which fully exploits the potential of modern computational capabilities and pressure measurement technology. A novel collaborative framework between wind and structural engineers assures the effectiveness of this approach and establishes clear lines of responsibility for their respective contributions to the design process. Wind effects with design mean recurrence intervals are determined by DAD more accurately than is possible by using conventional methods for estimating aerodynamic loads, dynamic effects, and wind directionality effects. The DAD approach is consistent with Building Information Modeling (BIM) requirements, and is in principle applicable to most structures for which wind pressures are determined by aerodynamic testing or CFD methods.

## 1 INTRODUCTION

The recent development of simultaneous pressure measurement technology, and the availability of powerful computational capabilities, have offered the potential for achieving significantly improved structural designs. To fully realize this potential, a novel, computer-intensive (“big data”) time-domain approach has been developed, known as database-assisted design (DAD).

In DAD the wind engineering laboratory’s task consists of providing the structural engineer with the requisite wind climatological and aerodynamic pressure coefficient data. The structural engineer’s task is to use those data as input to specialized software, the output of which consists of member demand-to-capacity indexes (DCIs) and appropriate measures of the structure’s motions. The software performs the following operations: (i) using the aerodynamic pressure data to determine the time histories of the stochastic aerodynamic loads acting on the structure; (ii) determining stiffness matrices by accounting for secondary effects due to moments induced by gravity loads on the deformed structure (iii) performing the dynamic analyses that yield the time histories of the inertial loads; (iv) rigorously combining,

via simple summations, time histories of simultaneous wind effects induced by the wind-induced forces; (v) rigorously accounting for wind directionality, and (vi) determining DCIs, displacements and accelerations with the respective requisite MRIs. It follows from this division of tasks that once the requisite wind climatological and aerodynamic data are available, the structural designer is in full control of the design process. This approach parallels the aseismic design process wherein, once the basic information required to define the seismic loads is available, the design process is controlled by the structural engineer. The conceptual simplicity and transparency of the DAD approach allow the clear and effective scrutiny of the design by owners, building officials, and insurers, and make it possible to achieve the requisite accountability of the entities responsible for contributions to the design for wind. A rare public analysis of the wind engineering contributions has clearly shown that opacity effectively thwarts accountability.<sup>1</sup>

Section 2 is devoted to a brief historical overview. Section 3 presents a review of the DAD approach and notes that, as CFD methods evolve, they may be expected to be a valid substitute for wind tunnel simulations. Section 4 briefly discusses the extent to which elements of the DAD approach may be applicable to tension structures. Section 5 presents the conclusions of this work.

## **2 BRIEF HISTORICAL OVERVIEW**

Procedures used during the past half-century to design structures for wind are rooted in advances achieved in the modeling of turbulent atmospheric boundary layer flow, the probabilistic modeling of the extreme wind speeds, and the dynamic along-wind response produced by atmospheric flow normal to a building face. The increase of wind speeds with height above ground was first reported by Helmann in 1916.<sup>2</sup> Extreme value probabilistic models for geophysical applications were developed by Gumbel in the 1940s.<sup>3</sup> Aerodynamic effects of turbulent flows were first researched by Flachsbart in 1932<sup>4</sup> (Fig. 1).<sup>1</sup> A pioneering approach to the estimation of the dynamic response of bodies immersed in turbulent flow was developed by Liepmann in 1951<sup>7</sup>. However, a synthesis of these developments was first achieved in the 1960s by Davenport<sup>8, 9</sup>, a University of Bristol student of the eminent British engineer Sir Alfred Pugsley. That synthesis was not capable of accounting for wind effects induced by vorticity shed in the wake of the structure, for winds skewed with respect to a building face or affected by the presence of neighboring buildings, or for aeroelastic behavior. Specialized wind tunnels were therefore developed in 1960s with a view to simulating the atmospheric boundary layer flow and its aerodynamic, dynamic and aeroelastic effects on structures.

During the 1970s wind tunnel techniques were not sufficiently developed to allow accurate measurements of wind effects for structural design purposes. Information on wind effects was based in large part on non-simultaneous pressures measured at typically small numbers of taps, with unavoidable and, in many instances, significant errors.

---

<sup>1</sup> Flachsbart was dismissed by the Nazi authorities for refusing to divorce his Jewish wife and could not complete his wind engineering research.<sup>5</sup> Some of his results were re-discovered independently by Jensen in the 1960s.<sup>6</sup>

An improvement in the capability to determine wind effects was achieved in the early 1980s with the development of the high frequency force balance (HFFB).<sup>10</sup> The HFFB approach is applied to tall buildings designed to experience no aeroelastic response under extreme wind speeds attainable in practice. HFFB provides time histories of the effective (aerodynamic plus dynamic) base moments induced by the wind loads. Its chief drawback is that it provides no data on the distribution of the wind loading with height, since there is no unique

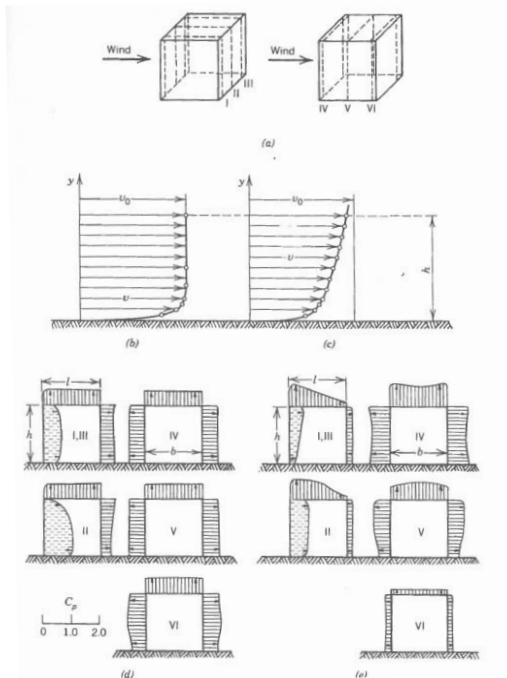


Figure 1. Results of model tests in smooth and boundary-layer flow. From *Ergebnisse der aerodyn. Versuchsanstalt zu Goettingen*, IV Lieferung, L. Prandtl and A. Betz (eds.) (1932).

correspondence between that distribution and the base moments or shears. The loading information needed to calculate the DCIs (i.e., the quantities required for the sizing of the structural members) therefore depends largely on guesswork, especially for buildings influenced aerodynamically by neighboring structures. In addition, HFFB estimates of dynamic response are based on the assumption that the fundamental sway modal shapes are linear and that higher modes of vibration are negligible. The HFFB approach is nevertheless useful in the preliminary phase of the design process, as it allows the rapid, qualitative aerodynamic assessment of building configurations, orientations and facade features such as balconies; it is, however, unsatisfactory for final design purposes.

The wind load distribution problema was solved in the 1990s through the use of large numbers of pressure taps on the building facades. Nevertheless, wind engineering laboratories still use the HFFB for the estimation of dynamic effects. Such use is no longer necessary, since the structural engineer has the ready capability – not available to the wind engineer -- of accounting effectively for the actual fundamental modal shapes in sway and torsion, as well as for higher modes of vibration. In addition, should changes in the structural features occur during the design process, the structural engineer can easily update the

estimates of the dynamic effects with no need for unwieldy interactions with the wind engineering laboratory.

### 3 DATABASE-ASSISTED DESIGN

The DAD technique relies on a natural and effective division of tasks between wind engineers and structural engineers.

#### 3.1 Wind Engineering Tasks

Following the preliminary design phase, the wind engineer's role is to provide, in formats suitable for use by the structural designer and for Building Information Modeling<sup>11</sup> (BIM) purposes, (i) the requisite wind speed data as affected by the micrometeorological features of the building site, and (ii) the aerodynamic pressure coefficient time series measured in the wind tunnel at a sufficient number of pressure taps. The wind engineer must also provide estimates of the uncertainties in the data. As CFD methods evolve and progress occurs toward gaining acceptance of such methods by the structural engineering community, numerical simulations of wind loading will increasingly be used in lieu of measurements. CFD may be especially advantageous for estimating the aeroelastic response of certain types of tension structures in which wind effects change the structures' shape, thus affecting the aerodynamic load.<sup>12</sup>

#### 3.2 Structural Engineering Tasks

The structural designer's first task is to perform a preliminary design of the structure's main wind force resisting system, using simplified wind loads specified in conventional standard provisions. The preliminary, conventional design is denoted by  $D_0$ . The structural designer's subsequent tasks are automated – see <sup>13</sup>. These tasks include determining the system's mechanical properties for the design  $D_0$ , i.e., (i) the effective stiffness matrix that accounts for  $P$ - $\Delta$  and  $P$ - $\delta$  effects, (ii) the requisite influence coefficients, and (iii) modal shapes and frequencies. Time histories of directional applied aerodynamic forces are then calculated from directional pressure coefficient records by apportioning to each floor or group of floors pressures weighted by the respective taps' tributary areas. This operation is performed for mean wind speeds ranging from, say, 20 m/s to 70 m/s in increments of, say, 10 m/s, with directions ranging from, say,  $0 \leq \theta < 360^\circ$  in increments of, say,  $15^\circ$ . Dynamic analyses are performed for each of those wind speeds and directions to obtain the respective time histories of the inertial forces induced by the aerodynamic loads. The time histories of the effective wind-induced loads acting on the structure consist of the sums of the aerodynamic and inertial force time histories.

Checking the adequacy of the preliminary design  $D_0$  requires determining the structural members' peak demand-to-capacity indexes (DCIs) corresponding to the specified design mean recurrence interval  $\bar{N}$ . This phase of the design process is performed as follows:<sup>14</sup>

1. DCI time histories are determined for each of the wind speeds and directions for which the dynamic analyses have been performed. For example, for DCIs of steel members subjected to flexure and axial forces, the following design criteria for strength are specified in:<sup>15</sup>

$$\text{tarIf } \frac{P_r}{\phi P_n} \geq 0.2, \frac{P_r}{\phi P_n} + \frac{8}{9} \left( \frac{M_{rx}}{\phi_b M_{nx}} + \frac{M_{ry}}{\phi_b M_{ny}} \right) \leq 1.0 \quad (1a)$$

$$\text{If } \frac{P_r}{\phi P_n} < 0.2, \frac{P_r}{2\phi P_n} + \left( \frac{M_{rx}}{\phi_b M_{nx}} + \frac{M_{ry}}{\phi_b M_{ny}} \right) \leq 1.0 \quad (1b)$$

Equations 1 are called *design interaction equations*; their left-hand sides are called *demand-to-capacity indexes* (DCIs). In Eqs. 1 the required strengths are based on Load and Resistance Factors Design (LRFD) load combinations that include gravity loads;  $P_r$  and  $P_n$  are the required and available tensile or compressive strength;  $M_{rx}$  and  $M_{nx}$  the required and available flexural strength about the strong axis;  $M_{ry}$  and  $M_{ny}$  the required and available flexural strength about the weak axis;  $\phi$ ,  $\phi_b$  are resistance factors. In the ASCE 7-16 Standard<sup>16</sup> no wind load factor is specified. To compensate for its absence, the design mean recurrence interval is augmented commensurately, for example from 50 to 700 years.

In Eqs. 1 the time histories of the internal forces are sums of the time histories of the effective aerodynamic forces  $W_k$  acting on the structure at locations identified by the index  $k$ , times the respective applicable influence coefficients  $r_{mk}$ . The coefficient  $r_{mk}$  represents the effect being considered (e.g., a bending moment induced in the cross section  $m$  by a unit force normal to the structure's surface acting at point  $k$ ;  $m = 1, 2, \dots, m_{max}$  and  $k = 1, 2, \dots, k_{max}$ ). All wind load combinations are automatically performed via these summations.

For each of the  $m_{max}$  cross sections of interest and for each wind speed and direction for which dynamic analyses have been performed, the peaks of the DCI time series,  $\max_t(\text{DCI}_m) \equiv \text{DCI}_m^{pk}$ , are obtained using standard procedures (see, for example,<sup>17</sup>). The results of the computations are represented as peak DCI response surfaces (Fig. 2).

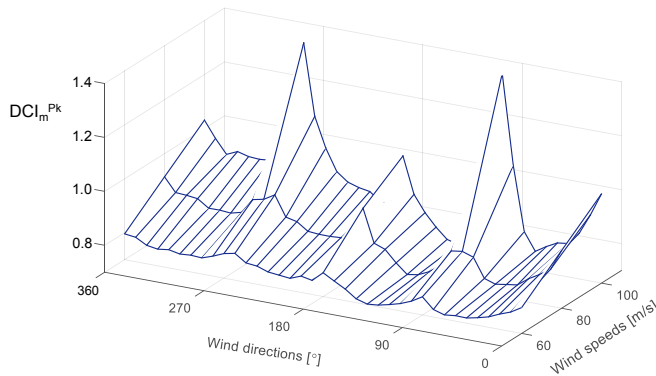


Figure 2. Response Surface for, peak DCI of member subjected to bending and axial force.

2. In the wind speed matrix  $[U_{ij}]$  provided by the wind engineering laboratory, where  $i$  and  $j$  identify the storm event and wind direction, respectively, the entries  $U_{ij}$  are replaced by the

quantities  $DCI_m^{pk}(U_{ij})$  taken from the response surface for  $DCI_m^{pk}$ .

3. The matrix  $[DCI_m^{pk}(U_{ij})]$  is transformed into a vector  $\{\max_j(DCI_m^{pk}(U_{ij}))\}^T \equiv \{DCI_m^{pk}(U_i)\}^T$ , (T denotes transpose) by disregarding in each row  $i$  all DCIs lower than  $DCI_m^{pk}(U_i)$ , since only the largest DCI occurring in each of the storm events is of interest from a design viewpoint.

4. The quantities  $DCI_m^{pk}(U_i)$  are rank-ordered, and non-parametric statistics are typically used in conjunction with the mean annual rate of storm arrival  $\lambda$  to obtain the quantities  $DCI_m^{pk}(\bar{N})$ .

If the peak  $DCI_m^{pk}(\bar{N})$  so determined is approximately equal to unity, the design for strength is acceptable. Inter-story drift and top floor accelerations are similarly checked. Typically, the preliminary design  $D_0$  does not satisfy the strength and/or serviceability design criteria. The structural members are then re-sized to produce a modified structural design  $D_1$ . This iterative process continues until the final design is satisfactory; convergence is generally rapid. A deliberately simple illustration of the process just described follows.

*Directional Wind Speed Matrix.* Consider the 3 x 4 matrix of wind speeds (in m/s):

$$[U_{ij}] = \begin{bmatrix} 34 & \mathbf{45} & 32 & 44 \\ 37 & 39 & 36 & \mathbf{51} \\ 42 & 44 & 35 & \mathbf{46} \end{bmatrix} \quad (2)$$

at the site of the structure. Under the convention inherent in the notation  $U_{ij}$  this matrix corresponds to three storm events and four wind directions, that is,  $i = 1, 2, 3$  and  $j = 1, 2, 3$ . For example, the wind speed that occurs in the second storm event from the third direction is  $U_{23} = 36$  m/s. (The entries in the wind speed matrix could, for example, be mean hourly speeds at the top of the structure, with direction  $j$  over terrain with suburban exposure.) In the matrix of Eq. 2 the largest wind speeds in each of the three storms are indicated in bold type.

*Transformation of Matrix  $[U_{ij}]$  into Matrix  $[DCI_m^{pk}(U_{ij})]$  of peak DCIs.* The matrix  $[U_{ij}]$  is transformed into the matrix  $[DCI_m^{pk}(U_{ij})]$  by substituting the quantities  $DCI_m^{pk}(U_{ij})$  for the quantities  $U_{ij}$ . Assume that the result of this operation is the matrix

$$[DCI_m^{pk}(U_{ij})] = \begin{bmatrix} 0.70 & \mathbf{1.02} & 0.80 & 0.68 \\ 0.83 & 0.77 & \mathbf{1.01} & 0.91 \\ \mathbf{1.07} & 0.98 & 0.96 & 0.74 \end{bmatrix} \quad (3)$$

*Transformation of Matrices of Peak Wind Effects  $[DCI_m^{pk}(U_{ij})]$  Into Vectors  $\{DCI_m^{pk}(U_i)\}^T$ .* The peak wind effects induced by the wind speeds occurring in storm event  $i$  depend upon the wind direction  $j$ . It is only the largest of those wind effects, that is,  $DCI_m^{pk}(U_i)$ , ( $i = 1, 2, 3$ ), that are of interest from a design viewpoint. These largest DCIs, shown in bold type in Eq. 3, form a vector  $\{1.02, 1.01, 1.07\}^T$ . Note that  $DCI_m^{pk}(U_3)$  is not necessarily induced by the speed  $\max_j(U_{3j})$ . For example,  $DCI_m^{pk}(U_3) = \max_j(DCI_m^{pk}(U_{3j})) = 1.07$  is not induced by the speed  $U_3 = \max_j(U_{3j}) = U_{34} = 46$  m/s, but rather by the speed  $U_{31} = 42$  m/s. The components of the

vector  $\{\text{DCI}_m^{pk}(U_i)\}^T$  constitute the sample of the largest DCIs that occur in each of the  $i$  storm events (in this example  $i = 1, 2, 3$ ) at the cross section  $m$  being considered.

*Estimation of Wind Effects with Specified MRIs.* The variate  $\text{DCI}_m^{pk}$  with an MRI  $N_f$ , where  $N_f$  is the number of average time intervals between successive storms, corresponds to a CDF ordinate  $P = 1 - 1/N_f$ . However, the designer is interested in the variate  $\text{DCI}_m^{pk}$  with an MRI  $\bar{N}$  in years. Since the mean annual rate of storm arrival is  $\lambda$ ,  $\bar{N} = N_f/\lambda$ . For example, if the storms being considered are tropical cyclones, it is typically the case that  $\lambda < 1$  storm/year, so  $\bar{N} > N_f$ . Therefore, the variate  $\text{DCI}_m^{pk}$  with an MRI  $\bar{N}$ ,  $\text{DCI}_m^{pk}(\bar{N})$ , corresponds to the ordinate  $P = 1 - 1/(\lambda\bar{N})$  of the CDF fitted to the data sample  $\max_j(\text{DCI}_{m,ij}^{pk})$  ( $i = 1, 2, \dots, n$ ). For a detailed example of the application of non-parametric statistical approach see.<sup>18</sup>

If the specified design MRIs are much longer than the wind speed record length, the application of non-parametric statistics may require the development by the wind engineering laboratory of large synthetic directional wind speed data sets. The development entails three steps. First, the measured directional wind speeds are processed by the wind engineer so that they are consistent with the micrometeorological features of the structure's site. Second, the directional wind speed data so obtained are fitted to Extreme Value Type I distributions, which are widely accepted as appropriate for the probabilistic description of extreme wind speeds. A probability distribution is fitted to the wind speeds from each direction  $j$ . Third, the Extreme Value Type I distributions are used to develop by Monte Carlo simulation the requisite sets of directional extreme wind speed data.<sup>19</sup> These sets are then provided by the wind engineering laboratory to the structural designer.

The analysis and design process briefly described so far is represented in the flow chart of Fig. 3. The aerodynamics and wind climatological data provided by the wind engineering laboratory must be fully documented and recorded. This allows the development of Building Information Modeling (BIM), and enables full traceability and scrutiny of the project by its stakeholders – the structural engineer, the owner, the insurer, and the building official.

The DAD approach is designed to be transparent and fully understandable to project stakeholders. The wind engineering laboratory performs wind engineering tasks, for which it is fully equipped, and the structural engineering office performs structural engineering tasks, for which it has the structural engineering and computational wherewithal. This division of tasks between the wind and the structural engineer is efficient, and establishes clear lines of responsibility. The interface between the wind engineering and structural engineering phases of the design is smooth and entails no loss of information. In particular, as noted earlier, wind effects, including DCIs induced simultaneously by loads acting on all building facades, are determined objectively via simple weighted summations of contributions to those effects, with no need for subjective combination factors. Higher modes of vibration and any modal shape are readily accounted for. Wind effects with specified MRIs obtained by accounting for wind directionality are determined transparently, are consistent with the structural properties inherent in the final structural design, and are determined more accurately than is possible by using conventional methods for determining aerodynamic loads, dynamic effects, wind directionality effects, and mean recurrence intervals of wind effects.

The DAD approach was successfully applied to the structure depicted in Fig. 4. This case study showed that only one or two iterations are needed to satisfy the requisite design criteria,

and that the computing times required for the design of as many as thousands of different members are fully compatible with typical structural engineering office capabilities.

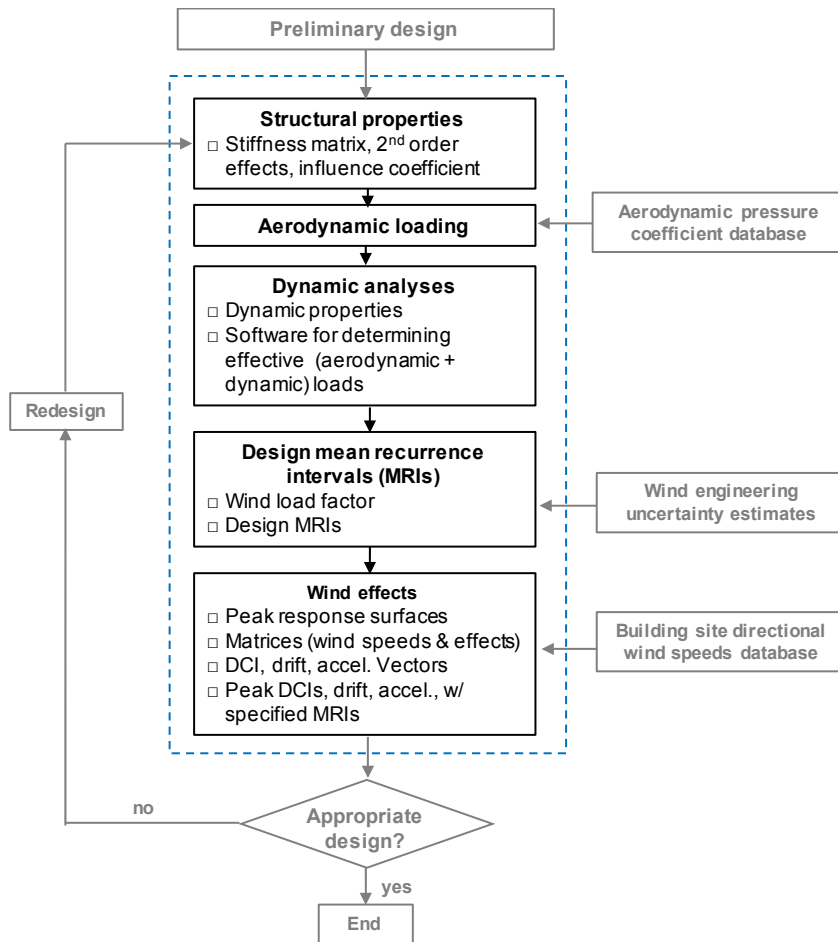


Figure 3. Flow chart representing DAD approach to structural design for wind.

#### 4 MEMBRANE STRUCTURES

A vast literature is available on capabilities for the estimation of stresses and deformations in membrane structures as functions of their loading (see, for example<sup>20</sup>), -- in particular of their wind loading. The use of those capabilities requires an accurate definition of the wind loads and their variation in space and time.

For enclosed membrane structures for which aeroelastic oscillations of the membrane are not acceptable (e.g., structures similar in this respect to the Denver airport), wind pressures can be obtained by measurement. Whenever possible, the measurements should be conducted in large-scale aerodynamic facilities allowing the use of relatively large models. Examples are the large-scale boundary-layer aerodynamic facilities at the Florida International University<sup>21</sup>

and the Insurance Institute of Business and Home Safety,<sup>22</sup> which allow portions of the structure and/or the entire structure to be tested at Reynolds numbers larger than  $10^6$ , with detailed modeling of relatively small features of the structure that may influence its

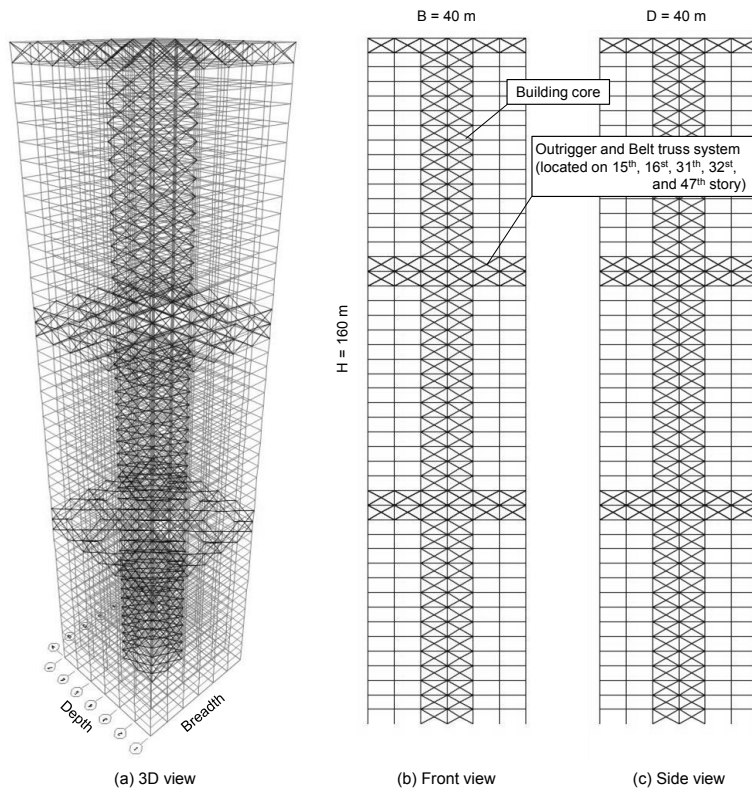


Figure 4. Schematic views of structural system for the building prototype.

aerodynamics. Simple experimental techniques are available that can be used to identify zones of high pressures (“hot spots”).<sup>23</sup> Pressure time histories can then be measured simultaneously at and around those zones using the pressure scanner, thus allowing the estimation of wind loads over small areas and over the tributary areas of the various members and member assemblies of the supporting structure. For open membrane structures for which no aeroelastic effects are permitted, the wind tunnel model would have to make allowance for the presence between the upper and lower roof surface of the plastic tubes that connect the taps to the pressure scanner, meaning that the scale of the prototype roof thickness would differ from the overall model scale. The extent to which this causes unacceptable aerodynamic distortions would need to be checked. The pressure coefficient time histories and the wind climatological data can be used to obtain the requisite information on the structure’s state given the specified MRIs, which can be estimated by accounting for wind directionality as shown in Section 2.

An alternative to the measurement of pressures in aerodynamic facilities is the use of CFD methods. Such methods can be applied to study the behavior of structures that may be assumed to be rigid, as well as of structures experiencing aeroelastic effects – see, e.g.,<sup>12, 24</sup>.

One well-known drawback of CFD methods applied to civil engineering structures is the lack of confidence in results obtained in the absence of ad-hoc validation. However, in view of the weight of other types of uncertainty, including the dominant weight of uncertainties in the wind speeds, coefficients of variation of pressure coefficient uncertainties as large as 15 % result in an increase of the design wind load by less than approximately 10 %.<sup>25</sup>

## 5 CONCLUSIONS

The brief historical review of structural design for wind presented in this paper notes the progressively improved modeling of the effects of wind on structures and the decreasing role of subjective estimates as measurement techniques have evolved. It was noted that the High Frequency Force Balance approach provides no information on the distribution of the wind loads with height, rendering impossible an accurate estimation of the structural members' demand-to-capacity indexes. The need to eliminate or reduce shortcomings of current conventional practices has given rise to the development of a time-domain, computer-intensive, iterative database-assisted design (DAD) approach that fully exploits the potential of simultaneous measurements of aerodynamic pressures acting on the structure. For any specified mean recurrence interval DAD determines peak demand-to-capacity indexes used for member sizing, peak inter-story drift values, and peak top-floor accelerations. The DAD approach accounts rigorously for wind directionality effects and for elaborate combinations of multiple time histories of wind effects.

DAD entails a natural and effective division of tasks between the wind engineering laboratory and the structural design office, thus establishing clear lines of responsibility. The role of the wind engineer in the final design process is to produce the requisite micrometeorological, wind climatological, and aerodynamic information in formats suitable for effective use by the structural engineer and for incorporation into building information modeling (BIM). In the interest of accuracy, dynamic analyses are performed by the structural engineer. This practice has the added advantage of avoiding impractical back-and-forth between wind and structural engineers as the structural design undergoes successive changes during the course of the design process. The wind engineering laboratory thus performs wind engineering tasks, for which it is fully equipped, and the structural designer performs structural engineering tasks, for which it has the structural engineering and computational wherewithal. The interface between the wind engineering and structural engineering phases of the design is natural, smooth, and entails no loss of information. Finally, DAD makes it possible to achieve, to the extent permitted by constructability and serviceability constraints, the differentiated and risk-consistent design of the structural members. Whether applied by using measured or numerically simulated aerodynamic pressure data, DAD results in transparent designs and safer, more economical structures than can be achieved by earlier practices.

## REFERENCES

- [1] Skidmore Owings and Merrill LLP, *Report on Estimation of Wind Effects on the World Trade Center Towers*, NCSTAR1-2, Appendix D dated 13 April 2004 (<http://wtc.nist.gov/NCSTAR1/NCSTAR1-2index.htm>).
- [2] G. Hellman, "Ueber die Bewegung der Luft in den tiefsten Schichten der Atmosphaere," *Meteorologische Z.*, **34** (1916) 273.
- [3] E. Gumbel, *Statistics of Extremes*, Columbia Univ. Press, New York (1958).
- [4] O. Flachsbar, "Winddruck auf offene und geschlossene Gebäude," *Ergebnisse der aerodynamischen Versuchsanstalt zu Göttingen*, IV Lieferung, L. Prandtl and A. Betz (eds.) Oldenburg, Munich and Berlin (1932).
- [5] E. Plate, Personal communication (1995).
- [6] M. Jensen and N. Franck (1965). *Model-scale Tests in Turbulent Wind*, Danish Technical Press.
- [7] H.W. Liepmann, "On the application of statistical concepts to the buffeting problem," *J. Atmosph. Sci.* **19** (Dec. 1952), 793-800, 822.
- [8] A.G. Davenport, "The application of statistical concepts to the wind loading of structures," *Proc. Inst. Civ. Eng.*, **19** (1961), 449-472.
- [9] A.G. Davenport, "Gust Loading Factors," *J. Struct. Div*, ASCE, **93** (1967), 11-349.
- [10] T. Tchantz (1982). "Measurement of Total Dynamic Loads Using Elastic Models with High Natural Frequencies," *Wind Tunnel Modeling for Civil Engineering Applications*, T.A. Reinhold, ed. Cambridge University Press, pp. 296-312.
- [11] *Building Information Modelling*. [http://www.arup.com/services/building\\_modeling](http://www.arup.com/services/building_modeling), last access April 12, 2017.
- [12] M. Heil, L. H. Andrew, and B. Jonathan (2008), "Solvers for large-displacement fluid-structure interaction problems: segregated versus monolithic approaches," *Comp. Mech.* **43** (1) 91-101.
- [13] S. Park and D. Yeo, *Database-Assisted Design of Steel and Reinforced Concrete Structures for Wind: Concepts, Software, and User's Manual*, NIST Technical Note, National Inst. of Standards and Technology, in review (July 2017).
- [14] E. Simiu and D. Yeo (2015). "Advances in the design of high-rise structures by the wind tunnel procedure: Conceptual framework." *Wind and Structures* **21** (5) 489-503.
- [15] ANSI/AISC. *Specification for Structural Steel Buildings*. Chicago, Illinois: American Institute of Steel Construction (2010).
- [16] ASCE/SEI 7-16. *Minimum Design Loads for Buildings and Other Structures*. Reston, VA: American Society of Civil Engineers, 2016.
- [17] A. L. Pintar, D. Duthinh, and E. Simiu, "Estimating peaks of stationary random processes: a peaks-over-threshold approach," *J. Risk and Uncertainty in Eng. Systems* (in press).
- [18] E. Simiu, *Design of Structures for Wind*, Hoboken: Wiley (2011), p. 158.
- [19] D. Yeo, "Generation of Large Directional Wind Speed Data Sets for Estimation of Wind Effects with Long Return Periods," *J. Struct. Eng.*, **140**, p. 04014073, 2014.
- [20] Oñate E. and Zárata F., "Rotation-free triangular plate and shell elements," *Int. J. Num. Meth. in Eng.*, **47** 557-603 (2000).

- [21] Florida International University, <https://fiu.designsafe-ci.org/> (July 2017)
- [22] Insurance Institute of Business and Home Safety <https://disastersafety.org/> (July 2017).
- [23] E. Simiu and R. H. Scanlan *Wind Effects on Structures* (3<sup>rd</sup> ed.), Hoboken: Wiley, pp. 533-534 (1996).
- [24] A. Michalski, P.D. Kermel, E. Haug, R. Loehner, R. Wuechner, K.-U. Bletzinger  
“Validation of the computational fluid-structure interaction simulation at real-scale tests of a flexible 29 m umbrella in natural wind flow. *J. Wind Eng. Ind. Aerod.* **99** 400-412 (2011).
- [25] E. Simiu, A. L. Pintar, D. Duthinh and D. Yeo, “Wind Load Factors for Use in the Wind Tunnel Procedure,” *J. Risk and Uncertainty in Eng. Systems* (in press).

## WIMBLEDON NO.1 COURT RETRACTABLE ROOF – A CASE STUDY

**Michael J. Roberts CEng MICE**

Thornton Tomasetti  
Exmouth House, 3-11 Pine Street  
London, EC1R 0JH, UK

e-mail: [mroberts@thorntontomasetti.com](mailto:mroberts@thorntontomasetti.com) web page: [www.thorntontomasetti.com](http://www.thorntontomasetti.com)

**Key Words:** Retractable, Adaptable, Long span, Lightweight, Movement, Tolerance.

**Summary:** This paper presents the design of the new retractable roof for No.1 Court, AELTC, Wimbledon. Specifically, the engineering response, and the challenges of designing for movements, deflections and tolerances of the moveable long span structures supported on new and existing structure.

### 1 INTRODUCTION

Wimbledon No.1 Court retractable roof is a lightweight structure comprising concertinaed, tensioned fabric fields spanning between long span prismatic steel trusses. These prismatic trusses are supported on flexible long span primary steel trusses, which in turn are supported on new and existing structures of varying stiffness. Movement and relative deflection at interfaces were key to the design, construction and performance of this project.

The All England Lawn Tennis Club (AELTC) is a world class, high profile venue that has a global news access audience estimated at over 1 billion people<sup>1</sup>. The retractable roof is a structure that must work first time, every time. The engineering response must be robust and carefully considered to ensure all the relative movements of the various components, under varying loading conditions, work within the operational requirements of the roof.

This paper will present aspects of the design for No.1 Court operable roof, focusing on some of the key engineering challenges associated with supporting a long span operable roof on a long span flexible structure, supported on a combination of new and existing structure, using mechanisation components with very small tolerance to movement.

## 2 OVERVIEW OF NO.1 COURT

### 2.1 Retractable roof

The new roof structure for No.1 Court covers a total area of approximately 12,000m<sup>2</sup>.



Figure 1: Render showing final No.1 Court retractable roof (Image courtesy AELTC)

The retractable component, which makes up just over half of this area, traverses a distance of 84 metres and takes the form of 6.7m wide tensioned fabric fields spanning between eleven prismatic trusses, 75m in length, which deploy and retract in a concertina fashion.

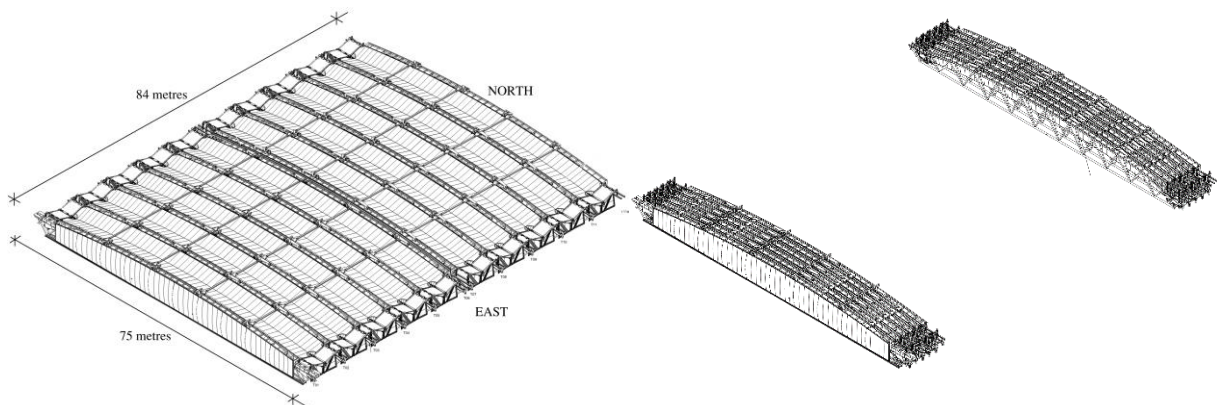


Figure 2: Image of retractable roof – deployed and retracted (image courtesy Tong Hogg Design)

The moveable roof structure is divided into 2 groups; the south group comprising 6 trusses and 5 fabric fields, and the north group comprising 5 trusses and 5 fabric fields. The roof takes up 3 primary positions: deployed, retracted and parked north. This parked north position is to

maximise the amount of photosynthetically active radiation (PAR) reaching the grass playing surface when the roof is not in use. The transitions between these three states induce varying amounts of movement in the supporting structure that must be accommodated at the interfaces with the operable roof.

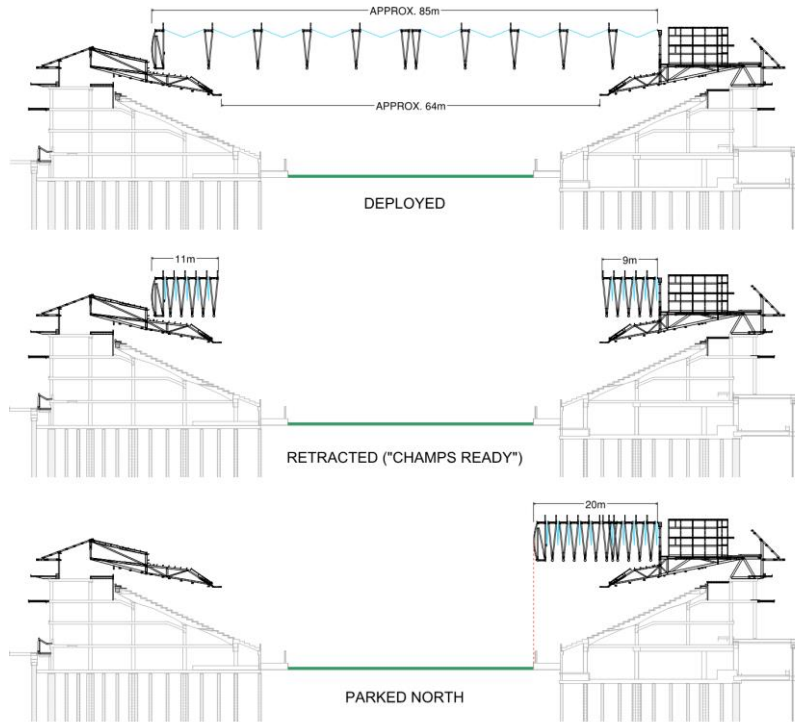


Figure 3: Retractable roof positions

The main structure for the retractable roof utilises eleven trusses. Ten prismatic Warren trusses and one box truss, all 74m long, formed from tubular steel, and symmetrical about both axis on plan. The main trusses have a single horizontal bottom chord, with the top chords curved to a constant radius to ensure that water is channelled to either side. The trusses are 1.5m in width and 6.6m deep in the middle. The prismatic shape allows for a minimal visual appearance when viewed from below, but provides the necessary width at the top to provide lateral stiffness to the truss and to provide sufficient area to mount the mechanisation equipment.

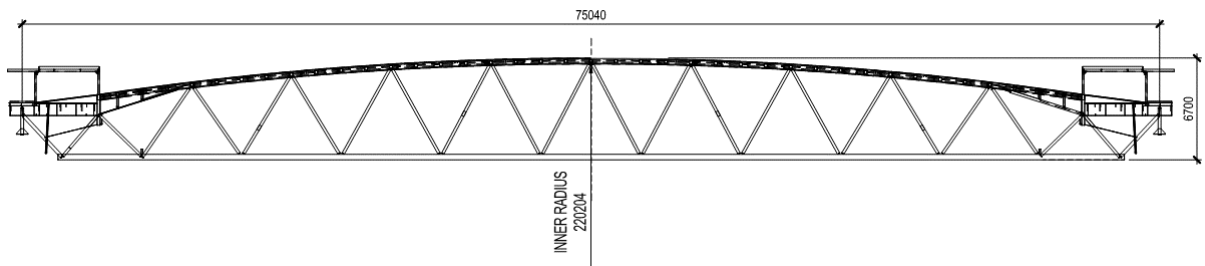


Figure 4: Elevation of steel truss

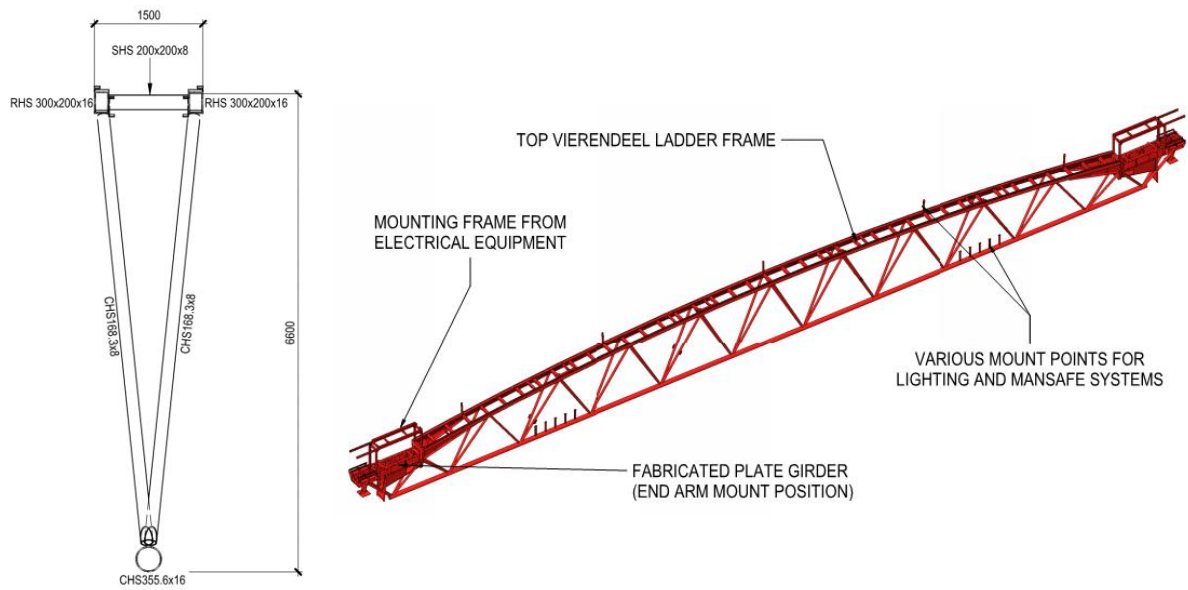


Figure 5: Typical truss elevation, section and isometric

One of the three principle mechanised systems are the bogeys which support each end of the trusses. These run on rails supported by the primary fixed roof structure. The detailing of this interface must accommodate the varying displacements of the supporting structure, the expansion and contraction of the moving trusses, and the fabrication and erection tolerances of the various components. This is discussed further in Section 3.

At the ends of each truss, mounted on the fabricated plate girder elements, are the mechanised end arms. These are hinged structures driven by 4 actuators arranged around a pivot. This arrangement provides fixity between the end arm and the truss, forming a portal structure that stabilises the trusses.

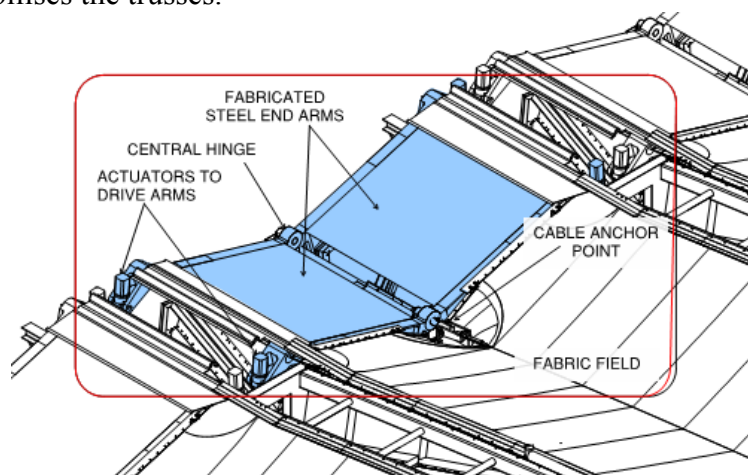


Figure 6: End arm arrangement (base image courtesy Tong Hogg Design)

Four sets of actuator driven restraint arms, equally spaced across the width of the trusses, ensure the trusses remain restrained at all stages of deployment.

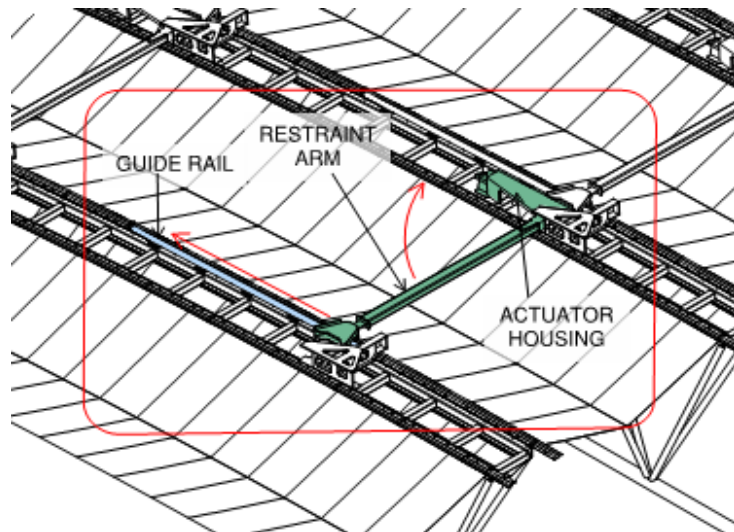


Figure 7: End arm assembly (base image courtesy Tony Hogg Design)

The forces induced in the restraint arms are resolved back along the roof in a north-south direction to points of connectivity with the fixed roof structure. In the north there is a direct connection to the fixed roof, whilst in the south, connectivity is achieved via a deployable locking mechanism. Both of these are key interfaces with the fixed roof, and the detailing must accommodate the differential movements between the moveable and fixed roof structures.

Both the end arms and the restraint arms are fabricated to tighter tolerances than the main truss steelwork, to ensure the mechanised components function correctly. They must also be aligned accurately across the length of the roof. Section 3 discusses the careful detailing and erection methodology required at the interfaces.

The main roof covering comprises ten primary fabric fields, tensioned with a steel valley cable, and formed from Sefar Tenara fabric. Tenara uses a base fabric of woven high strength expanded PTFE fibres with additional coatings for waterproofing. This particular fabric was chosen over more traditional PTFE/glass or PTFE/fibreglass fabrics because of its ability to flex and fold repeatedly without cracking or losing strength. Its other properties of reflectivity, and light transmittance were also key to ensure the playing environment feels as natural as possible. The fabric has interfaces with the moving trusses, the mechanised components, and the static roof structure. This not only generates varying load conditions as the roof deploys, but adds further parameters to be considered as part of the overall movement and tolerance strategy.

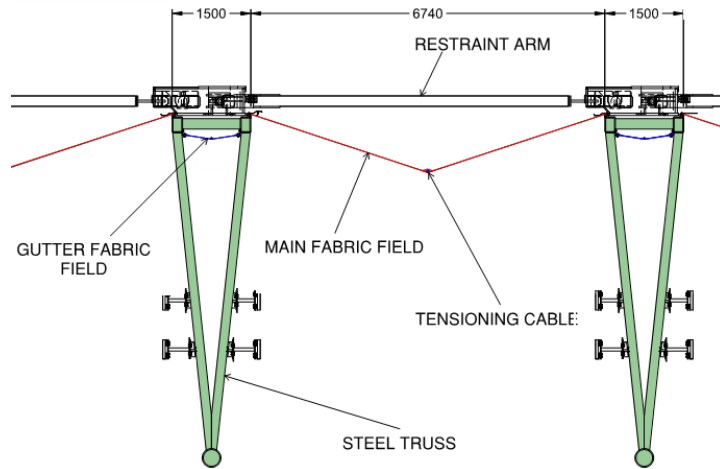


Figure 8: Fabric field arrangement

## 2.2 The Static Roof

The static roof provides support for the moving roof, provides the necessary cover to the seating bowl, and houses the mechanical and electrical equipment necessary to both condition the bowl space when the roof deploys, and service the hospitality spaces below. The structure comprises a series of 80m span prismatic trusses in the east and west, and a series of long span planar trusses up to 77m in length in the north and south. The inner section of the roof is comprised of simple cantilever planar trusses, supported from the main long span trusses. The static roof structure is supported on the 8 existing concrete cores, and also 3 new “super” columns carefully integrated into three corners of the existing building.

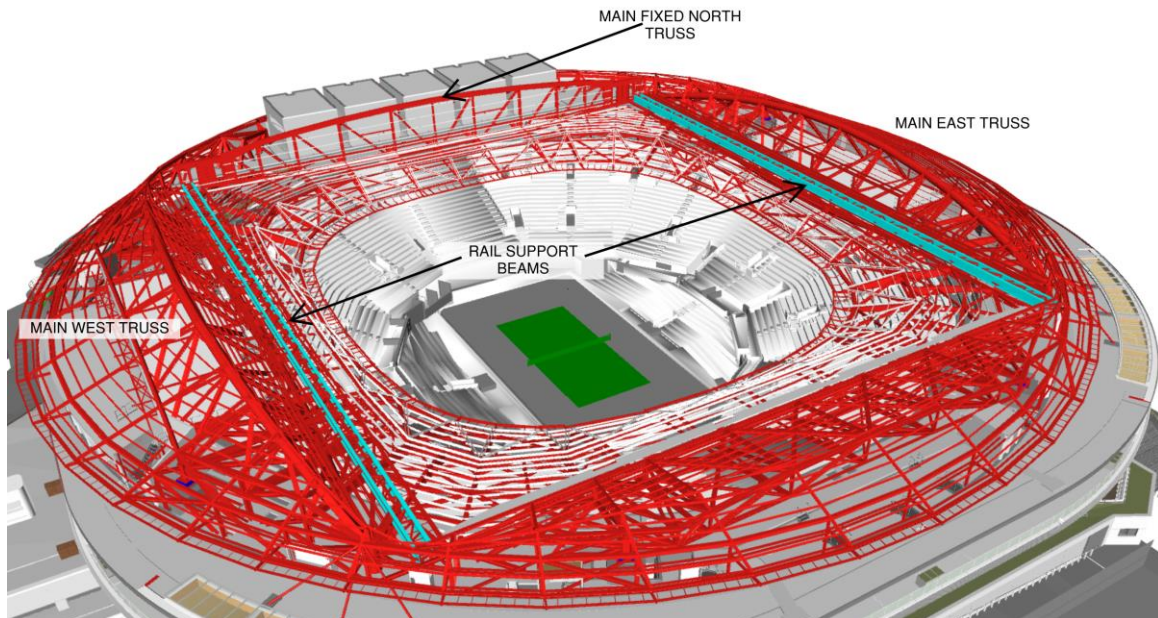


Figure 9: Overview of roof structure

The main east and west trusses support a pair of deep beams that sit eccentrically to the centroid of the truss. These deep beams form the main rail supports upon which the retractable roof bogeys travel.

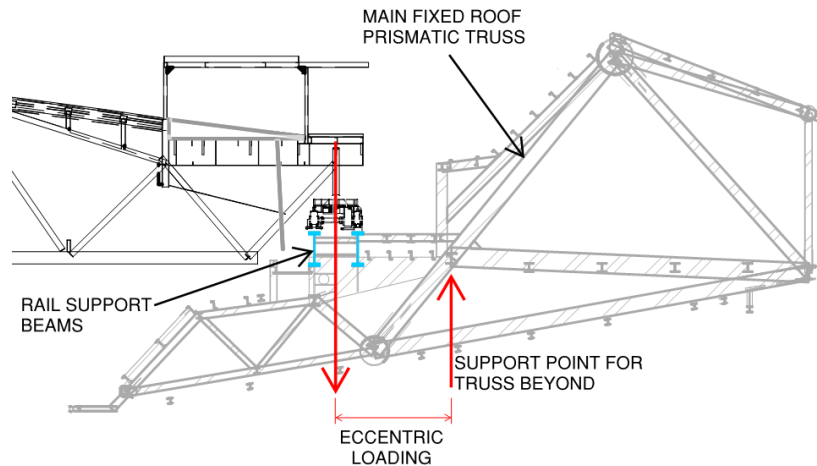


Figure 10: Section through main east support truss

The long span nature of the trusses, the eccentricity of the moving roof support, the transfer elements, the mix of new and existing support structure are significant factors influencing movement and tolerances.

### 3 MOVEMENTS AND TOLERANCES

All buildings move, the degree of which is governed by stiffness and applied force. It is generally not feasible to completely prevent the movement, it's about understanding how the structure moves, to what degree, and then designing for it.

In the case of the No.1 Court development, the challenge of understanding the movement is compounded by the fact that there is moving structure that can take up multiple positions, applying forces in different ways, inducing a varying response in the supporting structure. For the moving roof, it is also important to ensure that there is a direct load path back through the structure that can be resolved back the main stability elements with the building. The mechanised components also need to be fabricated, installed and operated to much tighter tolerances than standard steelwork.

#### 3.1 Primary Support Structure

The moving roof is supported on the long span east and west trusses. These undergo varying degrees of movement as the roof is deployed and retracted. When designing the long span trusses it was important to consider overall magnitude of vertical and horizontal deflection, deflection profile – in particular the gradient that the moving roof must traverse, relative movements between adjacent rails, and relative movements between the east and west rails.

Survey data for the Centre Court retractable roof shows that the supporting structure for moving roof deflects approximately 116mm vertically (span/630) at the rail locations. The spacing between the east rails and west rails increased by up to 69mm during deployment due to rotation of the supporting structure. Discussions with the mechanisation consultant agreed that the No.1 Court supporting structure should achieve at least the equivalent of span/630 for the vertical deflection, and should not exceed the lateral displacements observed at Centre Court. It was also agreed that the supporting structure should be pre-cambered such that when the roof is deployed, the entire structure is “level” and achieves the theoretical design position.

The design of the long span support trusses evolved to minimise the eccentricity of the rail support beams from the bottom chord of the truss to control the lateral deflections. The stiffness of the truss was then tuned to ensure the vertical deflection criteria was achieved.

The following graphs, normalised against the deployed case, show the deflection performance of the supporting structure measured at the rail locations.

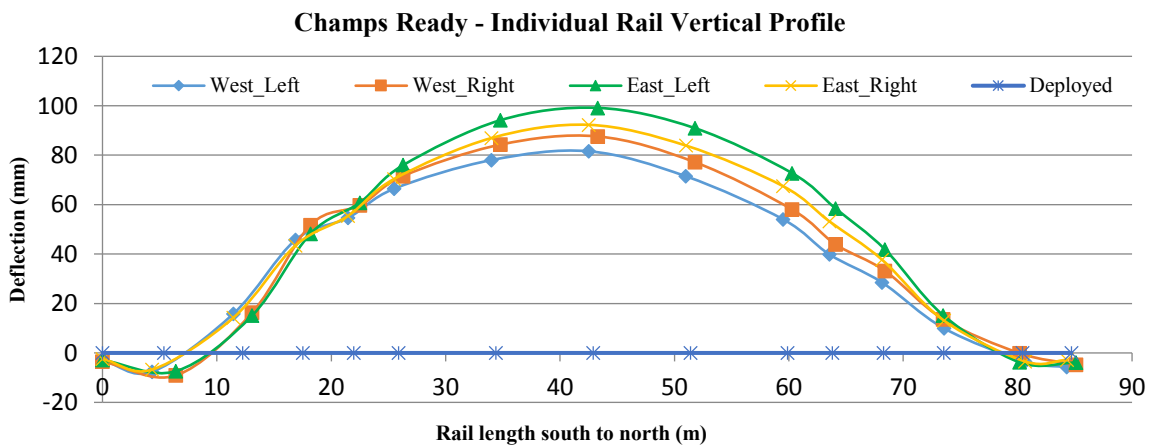


Figure 11: Vertical Rail profile in “Champs ready” position

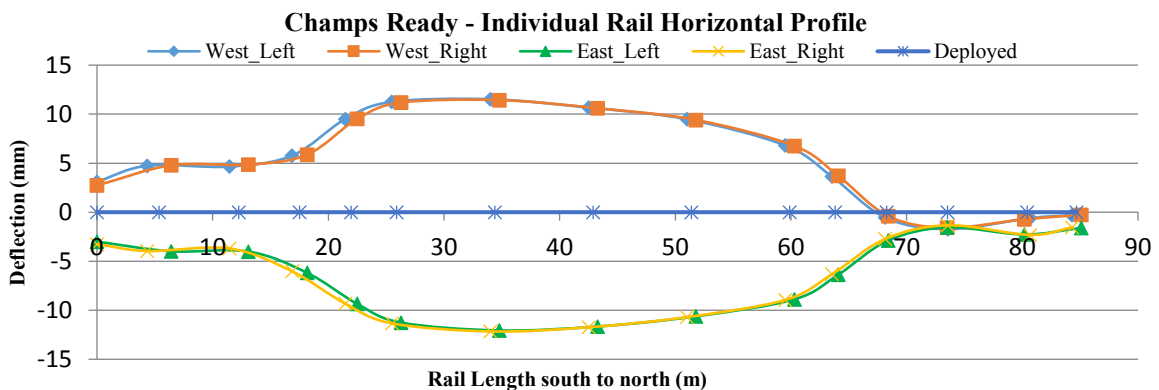


Figure 12: Horizontal rail profile in "champs ready" position

The predicted deflections also account for the varying differential settlements and displacements of the supporting structure. Since the aim is to achieve a level rail structure when the roof is deployed, the rail support structure hogs in the retracted and parked-north cases. The peak vertical deflection of the rail support structure when the roof is deployed is 100mm which is the equivalent of approximately span/850. It can also be seen that that change in distance between the east and west rails peaks at 25mm, well within the agreed criteria.

This movement must be accommodated at the interface with the moving roof, otherwise there is the risk of either the bogey guidance rollers being damaged, or the moving roof structure acting as a prop to the fixed roof. The solution to this is to use bearings between the bogeys and the moving roof trusses. No.1 court uses bearings that allow a displacement of up to 150mm on the west side, and 50mm on the east side. As well as accounting for the change in rail spacing, these bearing also permit the moving roof trusses to expand and contract freely under thermal loading without imposing lateral forces onto the bogeys.

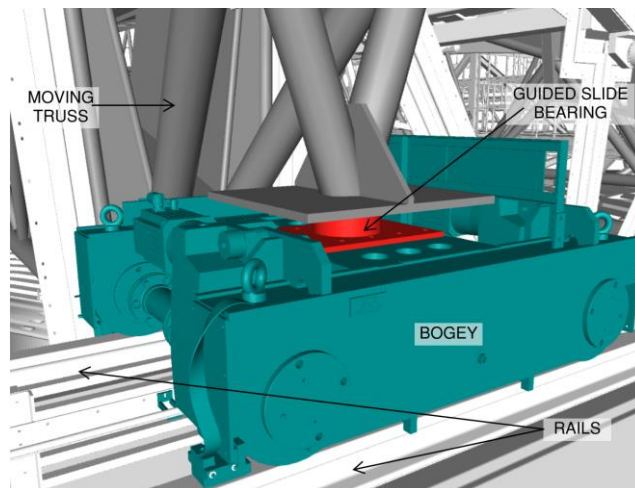


Figure 13: Bearing detail

The bearing arrangement requires some consideration though, as there is still a requirement to achieve some restraint in certain locations to ensure the moving roof structure remains stable. The following diagram illustrates the bearing release strategy:

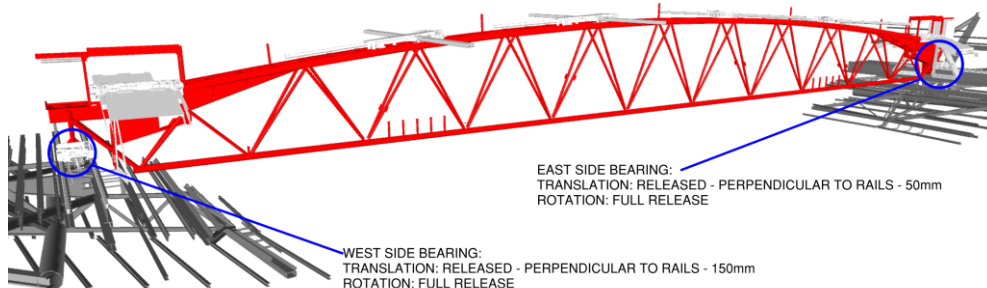


Figure 14: Typical bearing release strategy

The east side bearings on the leading trusses of the south group (truss 1 and truss 6), and the leading truss of the north group (truss 7) have full restraint in an east-west direction to provide a plan rotational restraint to the truss group.

### 3.2 Primary interface at north end

The connection of the moving roof structure to the fixed roof structure in the north forms a critical interface. At this junction, the engineering solution must deal with differential movements of the fixed and moving roof structure, the interfaces of the mechanisation equipment, the fabric connection, and water tightness.

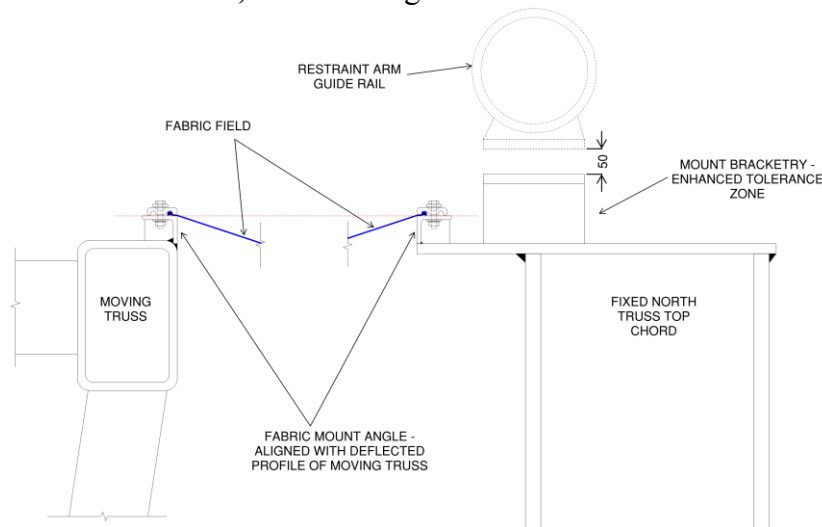


Figure 15: North Truss interface

The moving roof trusses are not pre-cambered so the profile of the fixed structure (the fixed north truss) was profiled to match the deflected geometry of the moving roof trusses. This was important to ensure a consistent fabric interface detail on both the fixed roof and the moving roof. This also ensures that the cutting pattern for the fabric remains consistent for each fabric field. The mechanisation mounting points were lowered an additional 50mm to provide an enhanced tolerance zone for mounting the mechanisation equipment. Differential movements are accommodated in the rotation of the restraint arm, and the general flexibility of the fabric.

Since the moving roof trusses utilise bearings at the interface with the bogeys, they are free to expand and contract under thermal loads. There is then the potential for the end arms mechanisms, which are fixed onto both the moving truss and the fixed roof structure, to act as a restraint to the thermal loads, which may lead to potential over stress. A simple solution of using a bearing detail at the interface of the end arms with the fixed roof structure was not feasible due to the tension forces in the main fabric field cable. The fixed north truss was also not easily divorced from the supporting structure to integrate a bearing either. The final solution was to expose the fixed north truss to same environmental conditions as the moving truss to minimise the potential differential thermal expansion. Whilst there is still some differential,

the forces this induces in the both the structure and the mechanisation equipment are within the acceptable limits.

### 3.3 Tolerances

Understanding the tolerances has been a key part of the design process. The steel fabricator, who is responsible for fabricating and erecting both the fixed roof steelwork and the moving roof steelwork is typically working to National Structural Steelwork Specification recommended tolerances. The mechanisation consultant who is responsible for fabricating and installing the mechanisation components is working to a much tighter set of tolerances. The fabric consultant who is responsible for the final design of the interface connection and the installation of the fabric is working to another set of tolerances. Ensuring these are compatible at the interfaces has been one of the key challenges.

The mechanisation consultant uses “BS ISO 12488-1:2012 – Cranes – Tolerance for wheels and travel and traversing tracks” as the basis for the permissible movement and tolerances for the rails and the supporting structure. The moving roof mechanisation has been defined as Class 2 installation. This code puts very tight controls on the positioning and profile of the rails. The entire supporting long span truss structure is being pre-cambered to ensure that once constructed, and the moving roof is deployed, the entire structure is in the theoretical designed “level” position. When dealing with long span structures and pre-sets, there are many factors that can influence how the deflection response of the structure will manifest. Variation in connection fixity between the theoretical design and actual performance, variations in calculated loadings, thermal effects, and connection “slip” are just some of the factors. By considering each of these and generating a potential movement envelope, the deflection performance of the supporting structure could be estimated. Using this envelope informs how much permissible adjustment needs to be designed into certain connections to allow adjustment to meet the required tolerance. In the case of the main bogey rails, the primary support beams had full lateral and vertical adjustment to ensure they could be positioned correctly. The rail connections then had further adjustment for fine tuning.

For the mounting of the mechanisation equipment, the interfaces were dealt with primarily by providing oversize or slotted holes, together with adequate shim zones. In certain locations, for instance the fixed north truss, enhanced shim zones were provided to provide for potential lack of pre-set “drop-out”.

For the mechanised end arms, the alignment is critical to ensure the smooth deployment of the roof. Lack of alignment has the potential to cause the end arms to lock up, potentially generating high stresses in both the structure and the equipment. The ends arms must be consistently spaced between the east and west ends, and be aligned on an axis parallel to the rails. As the moving trusses are sequentially erected on the supporting structure, along with the end arms, the supporting structure deflects both vertically and laterally. Providing oversize or slotted holes for the mounting does not give sufficient adjustment. In this case, the mount

positions on the moving roof trusses are drilled off site for the east side, but are site drilled in the west once the alignment has been set. Where the end arms mount onto the fixed north truss, direct site drilling is not feasible into the fabricated box girder which forms the top chord. In this instance an interface plate has been utilised which can fixed directly to the top chord, and be site drilled and tapped to suit the end arm position.

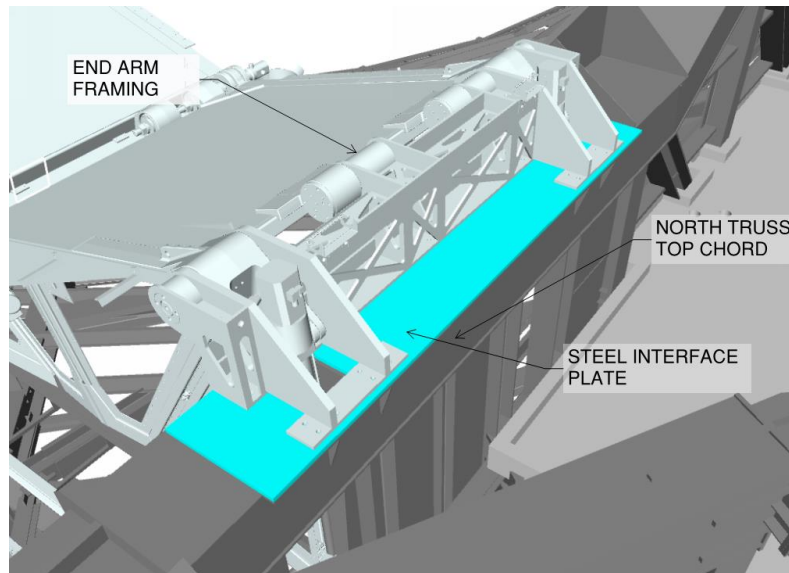


Figure 16: North truss interface plate

The fabric fields have interfaces with both the primary steelwork and mechanisation equipment. The fixing detail comprises a clamp plate detail with bolt fixings at regular centres. For these interfaces, the steel fabricator has ensured that the fabrication tolerances match the requirements of the fabric consultant.

#### 4 CONCLUSIONS

Whilst there are many different moving roof typologies that are a response to a specific brief and constraints, there are many common engineering challenges. Movement, relative deflection and tolerance are one of the most important aspects to understand, and correctly design for. The varying load cases induced by a deployable structure adds further complexity and misalignments and lack of tolerance to movement have the possibility of causing the moving roof structure to “lock-up”. For No.1 Court roof and Centre Court roof, which are the only significant moving roof structures in the UK that can be operated during stadium occupation, a deployment failure is unacceptable.

---

<sup>1</sup> Facts and Figures / FAQ,  
[http://www.wimbledon.com/en\\_GB/atoz/faq\\_and\\_facts\\_and\\_figures.html](http://www.wimbledon.com/en_GB/atoz/faq_and_facts_and_figures.html), 12<sup>th</sup> April 2017

# Dynamics Testing and Simulation of Inflatable Deployable Membrane Antennas

Wei Jianzheng<sup>1\*</sup>, Yu Lin<sup>1</sup>, Jiang Yu<sup>2</sup>, Tan Huifeng<sup>1</sup>, zhang Jinxiu<sup>2</sup>

(1 Center for Composite Materials, Harbin Institute of Technology, Harbin, R.P. China, 150080,

\*weijz@hit.edu.cn)

(2 School of Astronautics, Harbin Institute of Technology, Harbin, R.P. China, 150080)

**Abstract:** The inflatable deployable membrane antenna structures have many advantages such as small folding size, high reliability and low cost. The structure mainly consists of its center hub, thin-plate ribs, inflatable thermo-curing torus, reflected membrane and inflation control system. This paper establishes a deployable system to simulate zero-gravity based on the parabolic membrane antenna with inflatable torus and tests the deployable process. The shell-membranes finite element model of the antenna structures is modeled to simulate of the dynamics characters of the structure. After that the effects of the different inflatable pressure inside its support torus, the temperature of thermos-curing on the dynamic characteristics are also discussed. Finally, the dynamic characters of the inflatable antenna was tested on the condition of the horizontal suspension system with 12 elastic strings and the fully structural vibrational frequency were given, and the mode of vibration and damping ratio was verified to the correctness of the simulation method. These results provide the reference for the design of inflatable deployment antenna structures.

Keyword: Dynamics Testing, Membrane antenna, Inflatable, Deployment

## 1 Introduction

It is a development tendency to develop reflector with large apertures and high accuracy [1,2] which have the potential to offer an ideal solution for large apertures reflector[3]. Reflectors with large aperture radiate more energy than smaller ones and reflectors accuracy determines whether an antenna is capable of the scheduled requirements. Although inflatable antennas have been considered since In the 1960s, inflatable antennas was successful deployed for L and S band applications[4], now interest is turning to such antennas shorter wavelength bands. After data transmission rates of communication in near-Earth-orbit and deep-space missions reach hundreds of megabits per second, the diameter of the aperture may need to reach 10 m or more to support that rates [5]. However, larger reflectors typically means heavier weight, the less folded efficiency, so it is difficult to design a large reflector that can be folded and deployed several times after which the surface accuracy is still competent. Puig et al. conduct a preliminary FE(Finite Element) analysis using Nastran/Patran on a typical deployable truss structure in an astrophysics mission requiring a focal length extension.[3] Hu et al. develop a Fully-Cartesian-coordinate (FCC) method using Cartesian coordinates of points and Cartesian components of unitary vector to describe three-dimension mechanism large deployable structures. Guan et al. [6] analyze the static deformation of the synchronism deployable antenna consists of tetrahedral elements from central element.[7] Wang et al. analyzed the wrinkling of membrane with a new modified displacement

component method and made an influence parameter analysis and wrinkling control for inflatable reflectors. In this paper[8], an inflatable deployable paraboloid reflector(IDPR)was fabricated[9] which compromise the advantages of three kinds reflector: the truss reflector[10], the rib reflector [11, 12], and the inflatable reflector[13]. As far as structure dynamics concerned, in 2011, Pazhooch employed a non-contacting electromagnetic exciter and two laser displacement sensors[14]. The identified frequencies of the present study were higher than the measured frequencies by Ruggiero et al.[15], which indicated that the modal experiment of the SRT proved that dynamic testing of this structure was very challenging. In 2013, tan used hammer and tri-axial accelerometers for experimental modal test on inflatable membrane torus, and extracted the former 8 in-plane modes and the former 6 out-of-plane modes[16]. Compared to noncontact method in Pazhooch, Song and Ruggiero, impact hammer provided more energy for higher modes. As the inflatable deployable reflector antenna is much larger than inflatable torus, more energy is needed for global vibration. In conclusion, modal test on space membrane structure is still very challenging. A scale model in vacuum condition with a scanning laser Doppler vibrometer is good way to minimize the effect of air during testing, but it will be problematic for a large-scale full size antenna as the total cost increase sharply.

## 2 Structure of the inflatable deployable membrane antenna

The main part of the inflatable deplorable membrane antenna is the deployable reflector, which is the key component that makes the antenna suitable for the scheduled requirements. Also, the antenna contains other component such as inflate system, packing system and sub-reflector supporting system. The deployable reflector is supported by the supporting system consisting of a central hub, the supporting ribs, an inflatable torus and the tension system. (Fig 1)

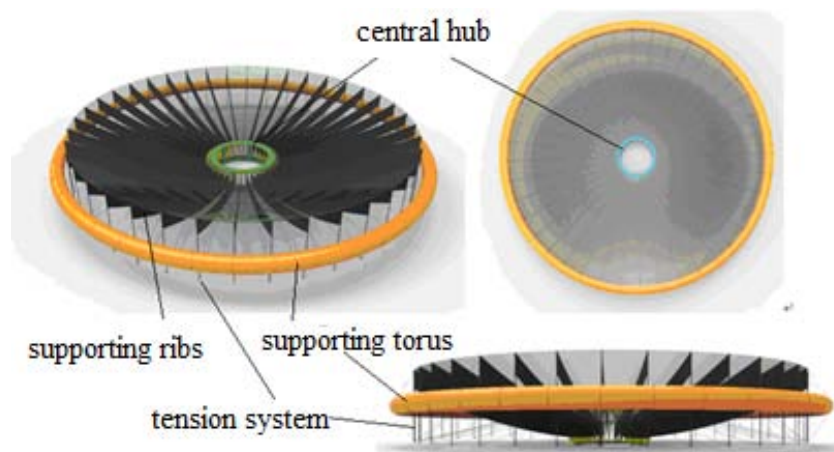


Figure 1 Design diagram of the inflatable deployable membrane antenna

The reflector is the main functional part which can send and receive the electrical signal. To achieve a better working condition, the material of the reflector should be flexible and have the property of resilience after folding. Here, the desired material is the mesh knitted by the gold-coated molybdenum wires, which may almost achieve all functions of the reflector.

The central hub (Fig. 2) is located in the center of the reflector, around which the support ribs are extended. The outermost component of reflector is the support torus (Fig. 3), which is connected with support ribs by the tension system. The reflecting surface is biaxial tensioned and hung on the ribs (Fig. 4).With the aid of the central hub, the ribs can be located and oriented in the supporting system. As the foundation of the inflatable reflector, the precision of the central hub have effect on

the other components and the final RMS of the reflector. The number of the supporting rib is chosen as 24 and the angle between the neighbor ribs is 15 degree. Here, the desired material of the rib is the carbon-fiber laminate. The shape of the rib, which directly influences surface accuracy, is maintained and controlled by the tension of the torus. The morphing of the rib has different performances in different tensions. To avoid the out plane buckling of the rib, the tension system is introduced. The location of the tension system is chosen base on the method proposed by Wang [9]. The tension system transfer tension between the ribs and torus and control the shape of the rib. In the working status, the shape of rib, which is in the pretension state, should be the assigned shape. Based on the structure aforementioned, an inflatable deployable paraboloid reflector with aperture of 3m and a $\Phi$ 3.2m torus was fabricated to validate the foldability and the ability to deploy experimentally.



Figure 2 The central hub's design diagram



1) folded

2) deployed

Figure 3 The supporting torus in folded and deployed configurations

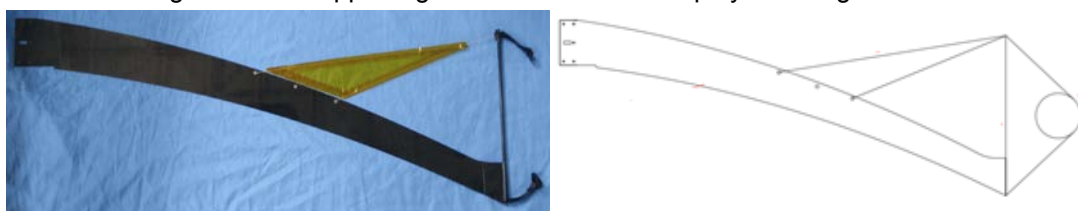


Figure 4 The supporting rib and its design diagram

### 3 Testing of folding and deployment of the membrane antenna

In order to save the cost of launching, the size of the antenna after packing should be minimized. The presented inflatable reflector achieve the foldability form the flexibility of its component, while the deploy process is driven by the inner pressure in the torus.

The experiments of fold and deploy of the inflatable deployable paraboloid reflector conducted on the ground utilizing the gravity-free simulating system (Fig. 5) confirm that the inflatable reflector can endure tens of times of folding and deploying. The main part of the gravity-free simulating

system is a rigid frame fixed to the ground, and a bunch of elastic ropes was dropped from the sliding groove on the frame. While the lower end of the elastic rope were attached to the ribs and the torus. The stiffness of the elastic rope was chosen in advance to reduce the deflection of the ribs while folding.

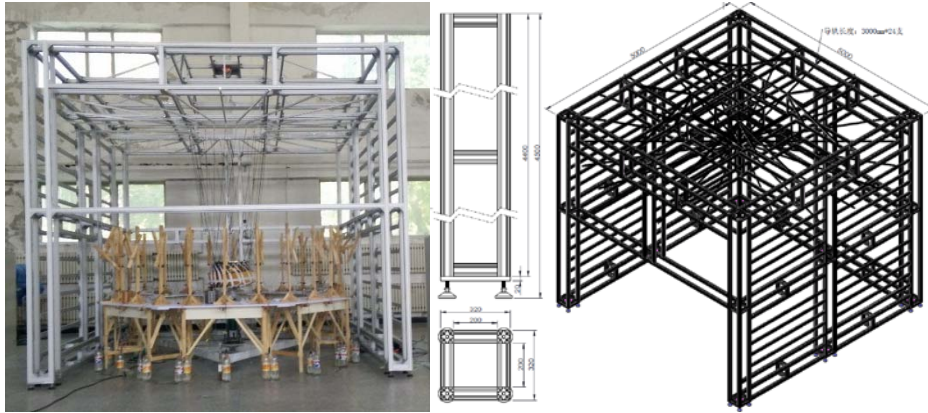


Figure 5 The gravity-free simulating system and its design diagram

### 3.1 Folding

To minimize the volume the inflatable reflector, ribs are wrapped around the central hub during folding process. In this process, the evenly distribution and the neatness of the ribs are the difficult points. A pump is used to pump the air out of the torus from two air taps on the opposite position of the supporting torus. And the torus was folded in a zigzag pattern. Due to the limitation of the gas speed of the inflating, the process of folding start at the center of two air taps. The asynchrony of the ribs and torus folding will cause the uneven intervals between two ribs. So the monitor of the ribs' shapes in the folding process is necessary and adjustments of the ribs' shape should be made while pumping. (Fig. 6) In the folding process the ribs were bended to the outer boundary of the central hub in which a certain amount of strain energy was gathered and stored in the ribs. So a woven ribbon was used to packing the folded inflatable reflector. (Fig. 7)



Figure 6 Adjusting the shape and the distribution of the ribs



1) top view

2) bottom view

Figure 7 Inflatable membrane antenna after folding

### 3.2 Inflatable deployment

According to the main driven force in the deployment, the process of deploying can be divided to two sub-process. The first sub-process is mainly driven by the strain energy stored in the ribs and torus, while in the second sub-process the inflatable reflector obtain the power from the inflating gas.

The first step to deploy the folded inflatable reflector was the release the woven ribbon. Upon release of the ribbon, the stored strain energy caused the wrapped ribs to spring to their stiff, deployed shape. But the volume of the initial inflating gas prevented the fully deployment of the torus, so the ribs were constrained by the half-deployed torus and a small portion of the stain energy was still left in the deformed ribs. This sub-process only took about 1s to release the large portion of the strain energy, so an impact load was exerted to the inflatable reflector. The impact load should be taken into consideration in the design procedure. Figure 8 shows the inflatable reflector at the start and the end of the sub-process.



1) At the start of the sub-process 2) At the end of the sub-process

Figure 8 Strain energy driven deploying sub-process

In the second sub-process, the torus was inflated and the tension of the torus drives these ribs to deploy further to reach the assigned shape. In this sub-process the remained strain energy was released thoroughly. And the driven force of the inflating changed to the inner gas pressure. The inner pressure was determined by the total gas volume in the torus. So we could manipulated the total deploying time by adjusting the speed of the inflating gas. In the fabrication of the torus, the

inner diameter of the air tap was chosen as 5mm to reduce the weight as the air tap is mainly made of copper. The speed of the inflating gas is limited by the cross section area of the air tap, so the total deploying time is mainly depended on the inflating speed.

At the beginning of the sub-process, the zigzag pattern near the air tap started to inflate because of the local higher pressure. As the inner pressure become higher and higher, the torus expanded to a round circle, and the inner volume of the torus formed a wholly connected space. In the meantime, the ribs followed the torus to realize the deployment.

At the end of the sub-process, the inflatable reflector was fully deployed and the final inner pressure reached 20kPa. The tension system transfer the force from the torus to the ribs, resulting an expected configuration and precision. The sub-process driven by the inner gas pressure is depicted in the Fig. 9.



Figure 9 Inner gas pressure driven deploying sub-process

The experiments of folding and deploying of the inflatable deployable paraboloid reflector were conducted 5 times, and the average time consuming is recorded and calculated. The main event in the sequence of the deployment is listed in the Table 1, so as the corresponding time nodes. The average time of fully deployment of the inflatable reflector is about 10 min. And the successive deployment of the inflatable reflector give evidence of the high-speed, the reliability and durability of the inflatable reflector fabricated.

Table 1 Sequence of the deployment and time nodes

No.	Time*	Event
-----	-------	-------

	(Initial as 0, min)	
1	0	Ribbon released, deployment begins
2	2	Zigzag pattern straightened
3	5	Inner volume of torus wholly connected
4	7	Torus fully deployed, inner pressure rises
4	10	Inner pressure reach 20kPa , deployment ends

\* Average time of 5 deployments

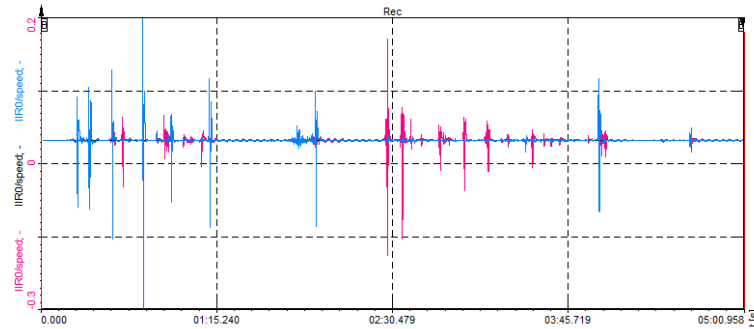


Figure 10 Curve of deployment velocity for the IDPR

The acceleration of one point on the torus was measured and the deploying speed of the torus was gathered by integrating and averaging the acceleration. The results show that the maximum speed in circumferential direction and normal direction is 0.2m/s and -0.3m/s, respectively. (Fig.10)

## 4 Dynamics testing

### 4.1 Testing methods

During the dynamic test, the IPDR is fully deployed and hung on the gravity-free simulating system. The hanging point is evenly distributed on the inflatable torus. The acceleration transducers are mounted on the middle and the outer border of the alternative ribs and corresponding point on the torus in the corresponding direction as shown in the Fig. 11. In the dynamics test, to avoid the frequency of the rigid body, two additional acceleration transducers are mounted the central hub. For each acceleration transducer, the acceleration in  $x$ ,  $y$ ,  $z$  directions are captured and the overall response in 114 channels describe the dynamics characteristic of the IDPR. The knocking points and the directions of the force hammer locate on the outer edge of the No. 1 rib in the vertical direction and on the outer edge of the central hub in the vertical, normal, tangential directions. The geometry, active point, transducer location, and the directions of the response point are depicted in the Fig. 11.

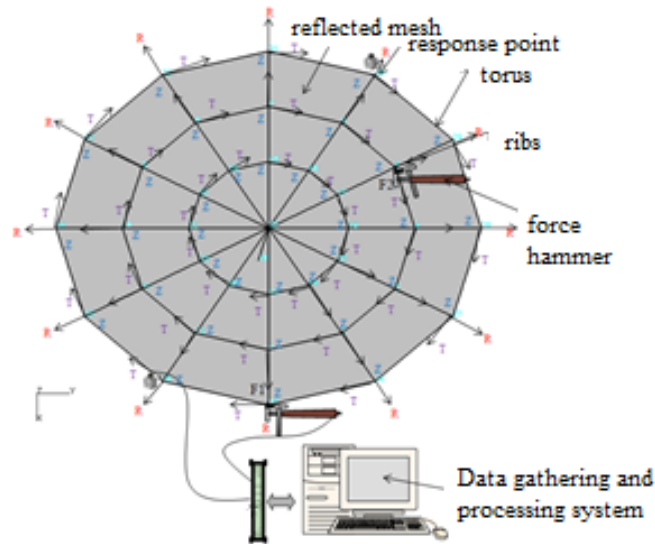


Figure 11 Model testing methods for the IDPA

## 4.2 Testing results

The dynamic response of the IDPR is tested under two circumstances. Figure 12 and Table 2 depict the response of the IDPR when the inflatable torus was heated up to and kept at the glass transition temperature ( $T_g$ ),  $70^\circ\text{C}$  and the inner pressure was kept at  $10.0\text{kPa}$  (circumstances I). When the temperature of the torus came to  $25^\circ\text{C}$  and got cured, and the pressure in the torus was  $0\text{Pa}$  meaning that the torus and the IDPR was totally self-supported (circumstances II), the response of the IDPR was shown in Fig. 13 and Table 3.

The first order frequency and damp ratio of the IDPR are  $6.81\text{Hz}$  and  $6.07\%$  respectively when the torus is kept at the  $T_g$  and inner pressure. The first order frequency and damp ratio of the IDPR are  $6.41\text{Hz}$  and  $6.93\%$  respectively after the torus got cured. The difference is so small that the torus satisfy the design requirements.

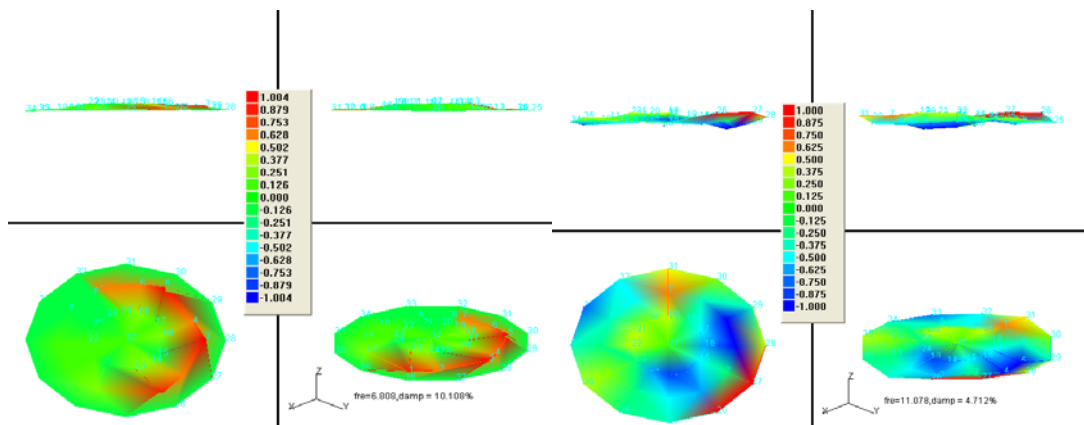


Figure 12 Mode of vibration: 1st order torsion and 1st order bend (circumstances I)

Table 2 Test result under circumstances I

Order	Frequency (Hz)	Damp ratio (%)	Mode of vibration
1	6.81	6.07	1st order torsion (average over the ribs, local modes between $4\text{Hz}$ and $8\text{Hz}$ exist)

2	11.08	4.71	1st order bend
3	24.84	3.64	2nd order torsion
4	29.20	2.86	3rd order torsion

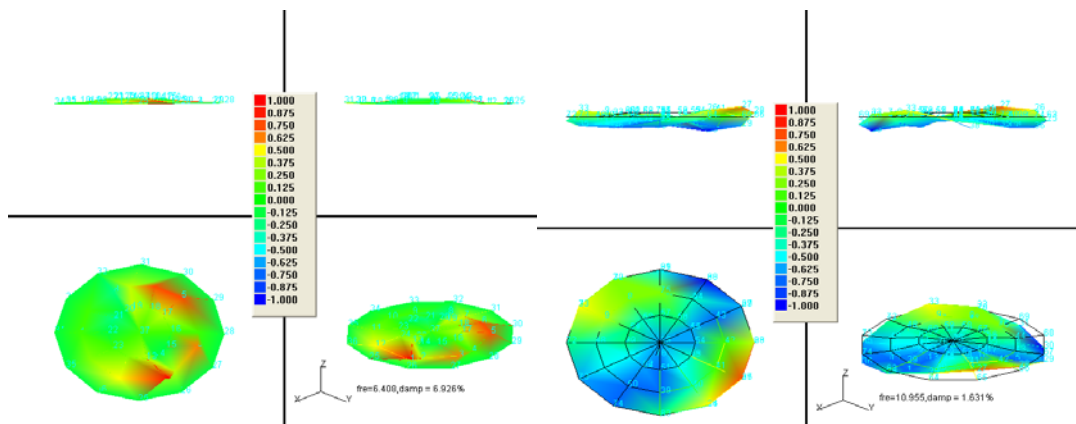


Figure 1314 Mode of vibration: 1st order torsion and 1st order bend (circumstances II)

Table 3 Test result under circumstances II

Order	Frequency (Hz)	Damp ratio (%)	mode of vibration
1	6.41	6.93	1st order torsion (average over the ribs, local modes between 3.75Hz and 8Hz exist)
2	10.96	1.63	1st order bend

## 5 Conclusions

An inflatable deployable membrane antenna was fabricated and the design method was testified. The experiments of folding and deploying of the inflatable reflector were conducted with the assistance of the gravity-free simulating system for multiple times. A series of successive experiments test and verify the reliability and durability of the inflatable membrane antenna. The average time to fully deploy the inflatable reflector is about 10min, which enable the fast deployment in the orbit. In the lower order, the mode of the IDPR is mainly displayed as torsion mode. And the difference in dynamic response between the circumstances (high temperature at  $T_g$  and with inner pressure vs. cured torus with 0 pressure) is not obvious, showing that the IDPR with the cured torus meet the design requirements.

## 6 Reference

1. Meguro, A., Harada, S., and Watanabe, M., "Key Technologies for High-Accuracy Large Mesh Antenna Reflectors," *Acta Astronautica*, Vol. 53, No. 11, 2003, pp. 899–908. doi:10.1016/S0094-5765(02)00211-4
2. Lane, S. A., Murphey, T. W., and Zatman, M., "Overview of the Innovative Space-Based Radar Antenna Technology Program," *Journal of Spacecraft and Rockets*, Vol. 48, No. 1, 2011, pp. 135–145.
3. L. Puig, A. Barton, N. Rando, A review on large deployable structures for astrophysics missions, *Acta Astronautica*, Volume 67, Issues 1–2, July–August 2010, Pages 12-26, ISSN 0094-5765.
4. Thomson, M. W., "Astromesh Deployable Reflectors for Ku and Ka Band Commercial Satellites,"

AIAA Paper 2002-2032, 2002.

5. Michael J. Coleman, Frank Baginski, and Robert R. Roman of sky. "Effect of Boundary Support and Reflector Dimensions on Inflatable Parabolic Antenna Performance", *Journal of Spacecraft and Rockets*, Vol. 49, No. 5 (2012), pp. 905-914.
6. Hu Qi-biao, Guan Fu-ling, Hou Peng-fei. *J. Zhejiang Univ. Sci. A* (2001) 2: 152. doi:10.1631/jzus.2001.0152
7. Guan F., Shou J., Hou G. et al. *J. Zhejiang Univ. - Sci. A* (2006) 7: 1365. doi:10.1631/jzus.2006.A1365
8. Wang C.G., Mao L.N., Du X.W., and He X. D., "Influence Parameter Analysis and Wrinkling Control of Space Membrane Structures," *Mechanics of Advanced Materials and Structures*, Vol. 17, No. 1, 2010, pp. 49–59.
9. Wang C. G., Xia Z. M., and Tan H. F. "Initial Shape Design and Stability Analysis of Rib for Inflatable Deployable Reflector", *AIAA Journal*, Vol. 53, No. 2 (2015), pp. 486-492.Xia
10. Xu, Y., Guan, F. L., Chen, J. J., and Zheng, Y., "Structural Design and Static Analysis of a Double-Ring Deployable Truss for Mesh Antennas," *Acta Astronautica*, Vol. 81, No. 2, 2011, pp. 545 – 554.
11. Tan, L. T., and Pellegrino, S., "Thin-Shell Deployable Reflectors with Collapsible Stiffeners: Experiments and Simulations," *AIAA Journal*, Vol. 50, No. 3, 2012, pp. 6
12. James Pearson, James Moore, and Houfei Fang. "Large and High Precision Inflatable Membrane Reflector", 51st AIAA/ASME/ASCE/AHS/ASC Structures, Structural Dynamics, and Materials Conference, Structures, Structural Dynamics, and Materials and Co-located Conferences, 2010.
13. Soykasap, O, and Tan, L. T., "High-Precision Offset Stiffened Springback Composite Reflectors," *AIAA Journal*, Vol. 49, No. 10, 2011, pp. 2144 – 2151.
14. M. D. Pazhooh, M.A. Dokainish, S. Ziada. Experimental modal analysis of an inflatable, self-rigidizing toroidal satellite component[C]. In T. Proulx (ed.), *Experimental and Applied Mechanics*, Volume 6, Conference Proceedings of the Society for Experimental Mechanics Series 9999, DOI 10.1007/978-1-4614-0222-0\_23.
15. E. J. Ruggiero, D.J. Inman. Gossamer spacecraft: recent trends in design, analysis, experimentation, and control [J]. *Journal of spacecraft and rockets*. 2006, 43(1): 10-24.
16. H. F. Tan, Y. L. Li, C. Q. Miao. Progress in dynamic analysis of space inflatable structure [J], *Chinese Journal of Advance in Mechanics*. 2007, 37(2): 214-224

## **Architectural membranes for high-performance building Skins Latest material developments Case study: façade in Ecuador**

**DIPL.-ING. ARCHITECT KATJA BERNERT\***

\* Textile Architecture  
Low & Bonar GmbH  
Rheinstr.11, 41836 Hueckelhoven, Germany  
e-mail: Katja.Bernert@lowandbonar.com, web page: <http://www.mehgies.com/mta/>

**Key words:** mesh fabrics, sun shading, wind shading, cinema projection, coating technology

**Summary.** This document provides information on a façade project in Ecuador. The office building in Esmeraldas was recently wrapped in Low & Bonar's TF400 mesh. Apart from creating a homogeneous layout for the whole building, the mesh membrane serves as a sun and wind screen.

### **1 INTRODUCTION**

The city of Esmeraldas on the west coast of Ecuador is mostly known for its port and the head office of Flopec, the national petrol company. When Flopec decided to build a new head office building, the local municipalities succeeded in combining this with a development of urban landscaping. In between the coastline and the city centre there is now not only the new office building but as well lots of recreation space, restaurants, little shops and an open air cinema. In order to give a unifying appearance to all these structures the designers used tensile structures as common element. There is the prominent wrap of the office building on the one hand and a prismatic roof above the restaurant and shop structures on the other.



Figure 1: Flopec Building in Esmeraldas with Low & Bonar screen, Photo by Preysi, Ecuador

The building is completely wrapped into a white mesh fabric. Therefore the façade smoothly integrates into the colour of the sky. Structurally the architect Marlon Guillén used a steel construction which was first filled with the primary façade. In front of this climatic envelope lies the secondary façade: a 16.000 sq. textile wrap.

The fabric serves as sun screen and wind shield. Being so close to the equator, Esmeralda is facing an extremely bright sun light. In order to avoid mechanical, individual sun shading systems the architect chose a universal wrap for the whole building. At the same time the mesh fabric reduces the wind loads significantly. Half of it is carried by the primary, the other by the secondary structure. It is the biggest tensile façade in Ecuador – maybe even in South America.

There is yet another side effect: during night time the façade serves as a cinema screen. Apart from the office building and the urban landscaping the architect designed a little projection hut. At night time people watch the cinema façade.

## **2 SETTING**

### **2.1 Light in Abundance**

Ecuador is literally one of the lightest countries in the world. Where you have sun light in abundance you need to care more about how to get the sun light *out* than the other way around – especially when it comes to office spaces. To provide homogeneously lit offices is one of the main tasks where glare is a significant problem.

### **2.2 Sea Side Setting**

Of course the pros and cons of an office building right on the beach are easily outlined: the view on the ocean is a merit for any office work place. Nonetheless being right next to one of the windiest spots in Ecuador means that you cannot easily open a window - unless you want to reorganize all loose paper on your desk. In all administrative areas it adds to the employees' well-being if they are able to open their windows individually.

## **3 FABRIC SOLUTION**

The Ecuadorian architects convinced the user of the office building that a fabric wind and sun screen was the optimal solution for the specific climatic conditions on Esmeralda's coastline. The permanent screen that wraps almost the whole building is made of a vinyl-coated polyester fabric. Low & Bonar GmbH provided the fabric "made in Germany", the Ecuadorian manufacturer Preysi prefabricated the membrane modules in Quito and installed them in Esmeraldas. For this Preysi used the prefabricated tensioning systems of Facid.



Figure 2: Facid65 – membrane tensioning system

#### 4 SUB CONSTRUCTION

Before the fabrics came to the building site the construction seemed to be an ordinary steelwork. In fact it is no complicated task to prepare a façade for a tensile wrap. Similar to other claddings there are only a couple of fixation points as links between façade and main building. What is important in tensile architecture is that the loads of the cladding material are significantly lower than that of aluminum panels for example – let alone that of stone claddings. Wind loads for example are shared between sub- and main-construction: As for the applied mesh TF400 for example there is an open area of around 30% which means that the loads on the building's steel construction are shared between primary and secondary structure.

The fixation of the fabric clipping system is easy enough: only about three of Preysi's installation experts were needed to get the aluminum profiles on the steel construction. Clipping the prefabricated mesh into these profiles happens within a couple of minutes so that huge triangular panels of the TF400 mesh were installed quickly.



Figure 3: aluminum clipping profiles on steel construction, Photo by Preysi



Figure 4: first steps of installation, Photo by Preysi

For everybody involved in tensile architecture it is the moment when the fabric comes to the site that is most important. The following picture gives a perfect impression of the actual *textile* character of the fabric. Of course fabrics in big scale architecture make only sense and are structurally only feasible when tensioned. But having the prefabricated fabric lying on the ground reveals the fact that we are still talking about a *woven* material – even if it is a technically highly sophisticated product.



Figure 5: Low and Bonar's TF400 Mesh Fabric as a cloth before installation, Photo by Preysi

## 5 THE FABRIC: VALMEX TF400 MESH FABRIC

The mesh is woven of high tenancy polyester yarns. Low & Bonar use a specific weaving technology that makes the mesh geometrically stable. The yarn went through a low-wick treatment first. That means that the polyester does not allow any wicking of humidity into the fabric. Together with the coating the fabric has a *no-wicking* property.

The company's weaving mill is situated in Fulda, Germany, right next to the coating lines. There the woven fabric is first equipped with an adhesion layer. This facilitates the bonding of the vinyl compound with the fabric. A proper connection is crucial for many functionalities which fabric and coating deliver as a joint venture. The top layer on the fabric is a lacquer which provides the final protection of the whole compound. Low & Bonar is market leader in providing a weldable pvdf lacquer: usually a high share of Fluor in the top coat means that this layer must be removed before welding. Fluor is important when it comes to cleanability and thus a long lasting performance of the material. Low & Bonar provides an extremely high Fluor content on the one hand while making abrasion for welding unnecessary on the other. This significantly lowers the risk of having damages during the manufacturing process and hence leads to an outstandingly long durability. Additionally Low & Bonar provides a Nano lacquer which enhances cleanability further by lowering down the material's surface energy – water droplets or dirt particles have minimised contact surfaces on the fabric and hence wash off easily – a property that is widely known as lotus effect.



Figure 6: installation of the prefabricated material almost finished, Photo by Preysi

Low & Bonar provides fabrics up to a width of five metres that means that welding seams

will not often disturb the homogeneous outlook of the façade. Preysi chose the panel size accordingly.

The colour of the fabric was a custom made bright white version of the mesh which is regularly done in colours like silver and black or equipped with a finish that allows long lasting prints on the fabric. In the case of the Flopec building the white wrap is used as a cinema screen by night.



Figure 7: cinema projection at night, Photo by Preysi

## 6 CONCLUSIONS

- A fabric mesh is a perfect solution for façades that are meant to have a homogenous appearance.
- Having a fabric sun and wind screen improves working conditions in the offices while simultaneously facilitating the load transfer between primary and secondary structure.
- The prefabricated membrane reduces significantly the installation time on site.

## REFERENCES

- [1] All pictures taken by the manufacturer Preysi, Quito, Ecuador

## DETAILED DESIGN AND CONSTRUCTION OF THE ST. LOUIS PARK ICE RINK

Craig G. Huntington\*, and Jeffrey A. Carpenter†

\*Huntington Design Associates, 6768 Thornhill Drive, Oakland, CA 94611USA  
e-mail: [craig@huntingtondesign.com](mailto:craig@huntingtondesign.com), web page: <http://www.huntingtondesign.com>

†Birdair Incorporated, 65 Lawrence Bell Drive, Amherst, NY 14221 USA  
e-mail: [jcarpenter@birdair.com](mailto:jcarpenter@birdair.com), web page <http://www.birdair.com>

**Key words:** Arch, Drainage, Fabric Reinforcement, Sectionalizing, Snow

### 1 INTRODUCTION

The structure is the cover of a new ice skating rink, owned by the City of St. Louis Park, MN. It has a PTFE-coated fiberglass fabric roof, supported on glu-laminated timber arches. The cover is 73m x 41m in plan, and supported by eight parallel arches bearing on concrete piers (Figures 1-3). The roof has a plan area of approximately 2,500 m<sup>2</sup>.

The original design of the structure was created by a project team that included the following:

RSP Architects; Minneapolis, Minnesota  
Blackwell Structural Engineers (roof structure); Toronto, Ontario, Canada  
Timber Systems (glu-laminated arch engineering); Lapeer, Michigan

The design created by this team addressed difficult challenges of snow loading, drainage, and constructability to create a beautiful structure that will be a major asset to the City of St. Louis Park for decades to come.

Construction of the membrane roof and associated cabling and anchorages was awarded to Birdair Inc. of Buffalo, New York in competitive bidding, and Birdair performed this work under subcontract to RJM Construction of Minneapolis, Minnesota. Birdair was responsible for fabrication and erection of these construction elements, as well as for the generation of final calculations and drawings that reflected their proposed fabrication and erection methods. The team assembled by Birdair for this work included the following:

Huntington Design Associates, Inc. (fabric engineering); Oakland, California  
IFS Consulting (fabric roof erector); Edmonton, Alberta, Canada

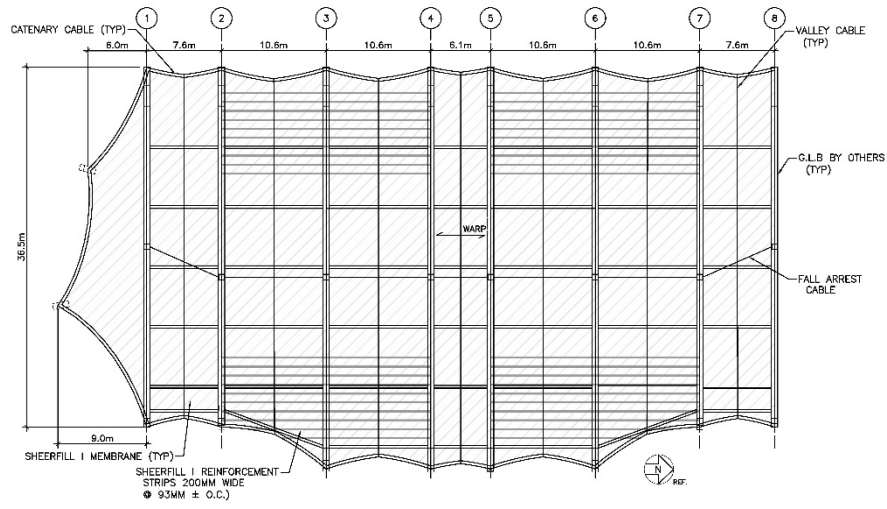


Figure 1: Roof plan



Figure 2: The roof structure nearing completion



Figure 3: Interior view, looking south, showing glu-lam arches, fabric reinforcement

## **2 DESIGN REQUIREMENTS**

### **2.1 Loading**

The structure's design is governed by the 2012 International Building Code<sup>1</sup>, which references American Institute of Civil Engineers Standard 7-10<sup>2</sup> for loading requirements. These requirements are summarized as follow:

- Live load: Nominally 1.0 kPa, but reducible to 0.6 kPa for member tributary area.
- Wind: Considered maximum wind speed of 51 m/sec., with open exposure conditions. Varying wind direction and upward and downward loading cases analyzed.
- Snow: Based on ground snow load of 2.5 kPa. Analysis considered unbalanced snow loads varying from 1.0 kPa at the arch peaks to 4.0 kPa at the eave, and from 1.0 kPa at the arch ridge lines to 4.0 kPa in the valleys midway between arches.

### **2.2 Ponding**

The arched roof form creates a flat area subject to ponding in the valleys between the apexes of adjacent arches. The potential ponding area extends well away from the centerline of the structure, due to the unbalanced snow load near the eaves. Blackwell considered ponding in their original design, and incorporated valley cables midway between the arches in order to force a drainage path towards the eaves. Our analytical work evaluated the deflected shape of the membrane under snow load to confirm if and where ponding might occur, following a criterion established by Birdair that dictates a positive drainage path for water, even when a reduced stiffness modulus is considered for the fabric. Membrane plate and other details were engineered to prevent ponding and coordinate with drainage requirements.

### **2.3 Drainage**

Visitors enter and exit the ice rink beneath the edges of the membrane roof, and it was therefore important to prevent rainwater runoff from the roof. The Blackwell design included a diverter system of upstanding 150mm tall aluminum plates, bent to conform to the membrane surface. The final design completed by Huntington Design considered alternative diverter systems comprising of a foam profile encased in PTFE-coated fiberglass membrane.

### **2.4 Services**

The design requires a path for electrical conduit along the top of each glu-laminated timber arch, as required to service lighting. The exposed timbers provide no ready location to

conceal the conduit, other than atop the arches. Detailing of the roof membrane needed to provide a clear path for the conduit beneath steel standoffs that support the membrane itself.

## **2.5 Aesthetics**

The RSP design had specific aesthetic goals, and RSP reviewed the final design documents prepared by Huntington Design in order to confirm that any revisions to details reflected these goals. This included the requirement that visual congruity be retained between connections of like kind (such as membrane plates of varying geometry and operability demands). RSP also emphasized the requirement for a distinct “rib” in the fabric profile at each arch line, and this is seen in the final details prepared by Huntington.

## **3 ERECTION CONSIDERATIONS**

### **3.1 Original Erection Scheme**

The Blackwell drawings indicated panels separated (“sectionalized”) at each arch (Lines 1-8). When Birdair began considering the installation process it was immediately clear that installation of a design matching the Design Drawings would be extremely difficult.

The issue under consideration is that during the installation, the four corners of each individual bay (28 corners in all) would need to be pulled diagonally in a connection that is designed for a pull parallel to the arch. Since there were concerns about putting the turnbuckle jaw in bending and ‘jumping’ the hardware over the hopper side plates, the alternative would be to first fasten the two membrane plates together with the slider plates and pull everything together. This is effectively the same procedure as having one membrane plate for the same connection and pulling it parallel to the arch.

Another concern with the Blackwell details was that sectionalizing is hard clamped to steel angles along each side of the arches. All of the fabric’s compensation on those edges needs to be pulled out before the edge clamping can be made, since the steel/aluminum clamping system obviously does not stretch like the fabric in the fill direction. Stretching the fabric to the corner/arch-end would be problematic and costly, since the process would not be utilizing the permanent materials to bring the fabric to that corner/arch end.

### **3.2 Birdair Erection Scheme**

The solution to these concerns was to have one fabric assembly cover all the arches (Lines 1-8), with a separate assembly for the sloped South panel. This allowed Birdair to stretch the

fabric in the fill direction on top of the arches utilizing the membrane plates and eliminated the need for diagonal pulls at the interior arches; which are the most difficult to execute.

By making this one large panel we reduced 28 corner pulls down to 4; and those 4 are over the full length and width of the large panel, giving much more leeway to stretch prior to achieving the final shape with valley and catenary cables. The membrane plates at the ends of the intermediate arches were changed from two plates to one in this scheme (Figures 4 & 5).

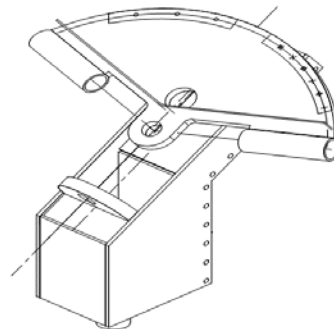


Figure 4: Blackwell membrane plate & drain scupper      Figure 5: Membrane plate & scupper as constructed

In order to solve the problem regarding pulling in the fill direction, Birdair used hard clamping at arches 1 and 8 instead of floating clamping so that there was a fixed position to pull to using pull frames. The membrane was fastened to the intermediate arches by means of a clamping “holddown” profile that is screwed in place in the field, making it possible to pull all the fill compensation out and allowing the membrane to find its equilibrium position prior to fastening it to the arches (Figures 6 & 7). Pulling such a large panel into place was difficult. It required a very long hard day for deployment in order to get all the necessary components rigged, attached, and secured for the night. However, this was seen as a more streamlined process to perform the installation efficiently, and led to a better end-product for the owner.

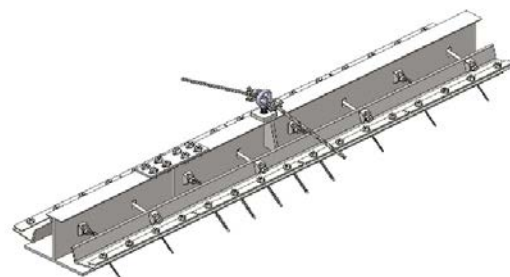
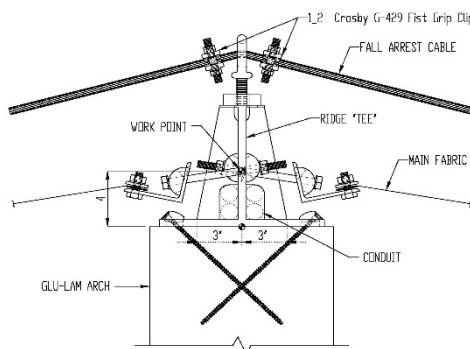


Figure 6: Blackwell top of arch detail (section & isometric)

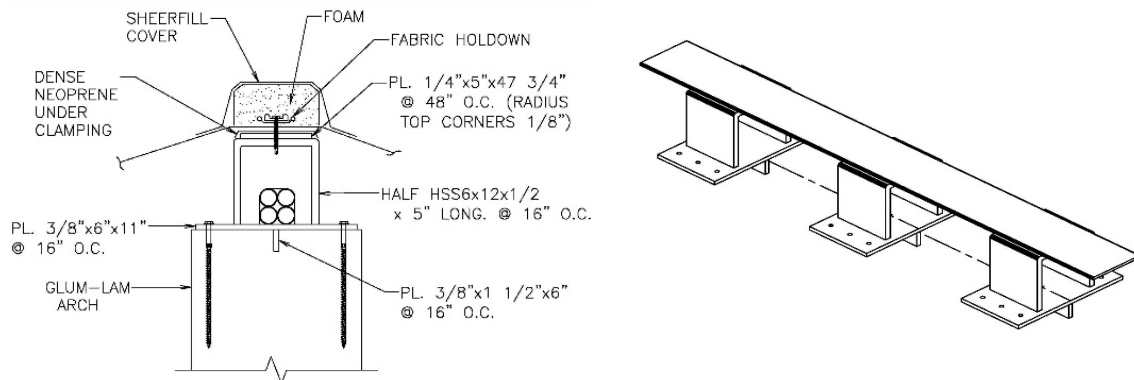


Figure 7: Top of arch detail as constructed (section & isometric)

## 4 DESIGN SOLUTIONS

### 4.1 Membrane Stresses

Governing downward load is generally created by snow load, rather than live load or combined partial live plus snow load. Warp fiber membrane stress as high as 2220 N/5cm occur near the roof eaves in the 10.7m wide bays under unbalanced snow loading. Using Sheerfill I fabric with a warp strip tensile strength of 8959 N/5cm provides a factor of safety of 4.0, less than the requirement of American Society of Civil Engineers Standard 55-10<sup>3</sup> for a factor of safety of 5.0 under snow load.

Several approaches were evaluated as solutions to the warp fiber overstress. First was the addition of “snow cables” beneath (and unsecured to) the fabric as a means of sharing some of the load carried by the warp fibers. In order to reduce the maximum warp stress to acceptable levels, three snow cables running generally perpendicular to the arches are required near the eaves on each side of the arch crown, with a seventh cable required at the crown in order to raise the fabric crown and avoid ponding in this area. The fabric lifts clear of the cables under wind uplift, and the snow cables are therefore deleted from the model under these load cases. This approach was rejected due to the architect’s aesthetic objection.

A second approach evaluated analytically was changing the uniform prestress field of 175 N/5cm in both warp and fill to an unbalanced field of 175 N/5cm in warp and 350 N/5cm in the fill. This increases the sag of the fabric between the arches, providing more efficient support of downward load. However, analysis showed that substantial areas of warp fiber

midway between the arches go slack under wind uplift loading while “popping through” into reversed curvature. The potential for the fabric to flap under such wind conditions argued against the unbalanced stress field as a ponding solution.

The final solution involved a combination of strategies. First, the fabric was laboratory tested for strip tensile strength, and the strongest material was strategically placed in high-stress areas during the patterning process. Second, the St. Gobain Sheerfill I fabric was reinforced with 200mm wide Sheerfill I reinforcement strips spaced 910mm on center in the remaining areas of overstress. The reinforcement strips are of course highly visible under certain lighting conditions, but their orderly pattern was considered visually acceptable.

#### **4.2 Ponding Avoidance**

Our initial analysis of the structure omitted the valley cables midway between arches that were a part of the Blackwell design, in order to test whether the design could be simplified in this manner. This analysis indicated areas of roof ponding under the unbalanced snow load. As with the warp fiber overstress, the area of ponding occurred only in the wider (10.7m) bays, and well away from the arch apexes, in the region closer to the eave where higher snow loads occur. Subsequent analysis indicated that valley cables provided an effective drainage path, and a reliable solution.

#### **4.3 Top of Arch Details**

Inverted U-shaped steel standoffs were provided atop each arch to accommodate the passage of electrical conduits between the arch tops and the membrane above (Figure 7). Analysis assumed complete membrane failure in alternate bays, resulting in large horizontal forces perpendicular to each supporting arch. Aluminum extrusions secure the membrane to the tops of the standoffs, and vertical steel shear tabs are welded to the standoff baseplates and fitted into slots cut into the top of each arch. These transmit the differential horizontal forces to the arches without using fasteners loaded in shear perpendicular to the grain of the timber.

#### **4.4 Drainage**

The design incorporates foam-filled fabric water diverters around the perimeter of the membrane to control water runoff (Figure 9). The diverters are positioned to assure positive slope to drainage holes in the membrane plates at the ends of each arch, where the water is gathered into scuppers and diverted to pipes passing to grade. Detailing of a transition closure at the intersection of the diverters and valley cable closures was done in the shop for efficiency, and provides continuous water flow over the intersection.

#### 4.5 Membrane Plate Details

Membrane plates at interior column Lines 2-7 and the two south piers provide adjustable anchorage for the membrane corners, with sleeved catenary cable terminations to each side (Figure 10). Water diverters to each side of the glu-lam arch terminate on the fabric just above the membrane plate, and the water that then passes onto the membrane plate is gathered by upstanding gutter plates and directed through a drain hole into a steel scupper assembly that is in turn bolted to the end of the glu-lam arch.

A rod and clevis mechanism provides adjustable anchorage of the membrane plate to a fixed plate welded to the scupper assembly. The design criteria assumed complete failure of the membrane to one side of each arch. This introduces large transverse forces to the membrane plates, which are secured against lateral displacement by guide plate assemblies that are in turn anchored to the glu-lams by pairs of 25mm diameter bolts that are drilled through the full depth of the glu-lams.

#### 4.6 Fabric Details

The structure employs conventional heat welding for seams and application of the reinforcement strips. Fabric is secured at the two ends (Lines 1 & 8) by cord edges secured by aluminum clamp bars. Fabric holdowns at the arch tops have the capacity to develop the full membrane strength, in order to provide a safe connection in the event of full membrane failure to one side of the arch.

Two bays of the structure (Lines 2-3 and 6-7) have large differences in the length of arch to either side, which results in the tendency of the valley cable to “wander” across the membrane under varying load conditions. At these locations, the cable is restrained by passing through a fabric cuff of the type normally employed to contain catenary edge cables. In the remaining bays, the valley cable is overlain by a simple cover strip (Figure 8).

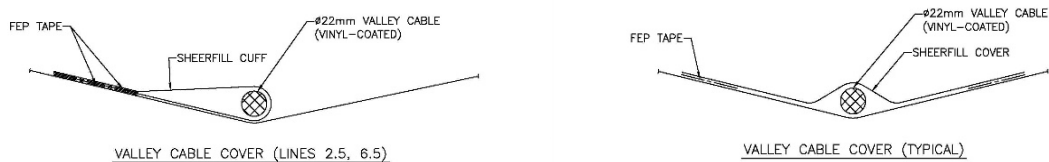


Figure 8: Valley cable lateral restraint cuff (Lines 2.5, 6.5) (left) and cover (other locations) (right)



Figure 9: Diverter detail at membrane edge



Figure 10: Typical “floating” membrane plate

## 5 PATTERNING & FABRICATION

### 5.1 Membrane Patterning and Fabrication

Patterning of the membrane was carried out in a special way to utilize stronger goods in areas of high stress, in order to minimize reinforcement strips and maximize capacity (see Figures 1, 3, 11 for fabric reinforcements). Rolled goods were tested both at the supplier and in Birdair’s quality lab to determine the actual strength of each roll. Rolls were then grouped by strength and by biaxial test results (compensations) to determine the most efficient layout of the material. Rolls with specific strengths and compensations were grouped together with similarly stressed areas within the assembly (i.e. higher strength goods with similar compensations were paired with the higher stressed areas and so on). Birdair was also careful to use reinforcing strips from the same rolled goods as the main membrane for more efficiency and integrity during fabrication and erection.

During the patterning and detailing process, Birdair carefully noted, in tabular format, the distance to pull each ridge and valley during the fabrication process so that these multi-layer areas would not be too stiff for the installer to pull out. Patterning of complicated details such as the interface of the valley cables and diverter cuffs were carried out by

mocking up first with paper, then with fabric in Birdair's quality lab, then sending those mock-ups to Birdair's fabrication plant for execution.

## **5.2 Steel Fabrication**

In order to meet fabrication schedule, two separate steel fabricators were used. The fabrication was broken up into separate lots to avoid compatibility issues. Arch-top weldments were done by one fabricator while the arch end weldments and membrane plates were performed by another. In this way, there would be no fit-up issues between the fabricators. The arch-top weldments were further broken up into two separate fabrication/shipment lots in order to provide materials to the site in a timely fashion to stage the work. Due to the slight curvature of the arches with respect to the weldments, some weldments were fabricated in a jig while others were fabricated flat and bent to shape in place. The bending was of the elastic type and tested out on a sample to prove it could be done by hand so that this would not pose any additional work for the installers.

## **6 ERECTION**

### **6.1 Steel Weldments and Preparation**

Prior to erection of the glu-lam arches, the glu-lam contractor needed to assemble the arches at the ground level. IFS took this opportunity to get many of the arch-top weldments in place before the glu-lam contractor erected the arches with their crane. This proved to be an efficient process both in terms of schedule and cost. While the arches were at ground level, IFS worked with the glu-lam contractor to drill thru-width holes in the glu-lam beams in order to attach the arch-end weldments. These would have been better bored in the shop, but project scheduling did not allow this. On the contrary, there were through-depth holes to be drilled for hold-down hardware related to the membrane plates and these were better done in the controlled shop environment due to their relatively higher complexity of execution than the through-width holes, so these were held to a higher priority in the design phase. Further preparation took place in the padding and protection of the weldments during this phase so that the membrane wouldn't tear when being unfurled along the arches.

### **6.2 Membrane Installation & Tensioning**

As previously mentioned, the initial spreading and securing of the large fabric panel made for a long hard day. Three cranes were used with spreader beams to position the fabric at the ridge (Figure 12). Next, the membrane was unfurled along the direction of the arches, cables were roughly installed, and everything was secured for the night with ropes, come-

alongs, and special clamps. The next few days were also challenging as the fabric was incrementally pulled to the arch ends and corners, mainly in the fill direction. As a result of these challenges, this is the range of time when the installers began calling the Engineering team to verify things were designed correctly. After incrementally pulling the membrane to the 4 corners the team found that the membrane actually fit quite well at those corners. At one point, the installers also surmised that the valley cables were designed too long but after careful investigation, it was found that they were correct and that the membrane simply hadn't been fully tensioned in the fill direction.

The smaller south fabric panel had its own set of challenges. Because it was smaller, there was less of a field of fabric to spread error. As a result, the installation team made some minor adjustments to the perimeter at the high corners in order to avoid wrinkles there.

Review of the completed installation supports the decision to erect a single large fabric panel. The challenges at the corners that presented themselves on the large and small panel would have likely occurred similarly on the 7 subpanels between the trusses had they been separate panels. This, combined with the enormous amount of hard clamping if separate panels were used in each bay would have been quite a time consuming and laborious task.



Figure 11: Fabric reinforcements during erection



Figure 12: Three cranes with spreader bars placing fabric

### **6.3 Coordination with Top of Arch Electrical, etc.**

Coordination of installation of the electrical systems with the arch-top weldments was handled on-site. The contractors worked out the sequencing amongst themselves with the

guidance of general contractor RJM Construction. One omission that occurred as a result of multiple versions of the shop drawings was that some holes for electrical wire pass-through were missed on the arch-end weldments, so these needed to be drilled in the field.

#### 6.4 Diverters & Closures

Diverters and Closures present a challenge on jobs of any size and complexity because they are done near the end of the job, they have relatively little to no tension in them. The ridge closures were specially patterned due to the ribbed-look condition atop the arches and this proved effective in getting the closures looking nice (Figure 13). Valley closure-to-diverter details were prepared in the shop, so this was not something the field team needed to spend as much time on (Figure 14). The diverters themselves are challenging to install on any job because the foam needs to be relatively tight in the diverter cuff to make them look nice, which creates difficult in sliding the foam into the cuff. However, the end result is functional and aesthetically pleasing.



Figure 13: Fabric closure at arch top



Figure 14: Valley closure / diverter intersection

#### REFERENCES

- [1] *International Building Code*, International Code Council, 2012.
- [2] *ASCE Standard 7-10 Minimum Design Loads for Buildings and Other Structures*, American Society of Civil Engineers, 2010
- [3] *ASCE Standard 55-10 Tensile Membrane Structures*, American Society of Civil Engineers, 2010

## DETAILING FOR REFURBISHMENT WITH STRUCTURAL MEMBRANES

JOSEP I. DE LLORENS

School of Architecture, Barcelona (ETSAB). Technical University of Catalunya, Spain

e-mail: [ignasi.llorens@upc.edu](mailto:ignasi.llorens@upc.edu)

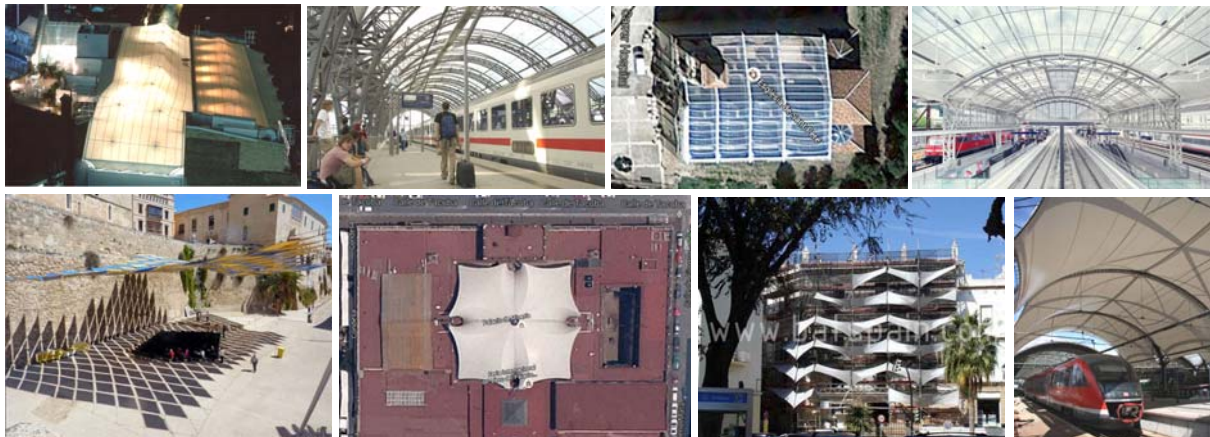
web page: <http://sites.upc.es/~www-cal/cat/recerca/tensilestruc/portada.html>

**Key words:** Textile Roofs, Structural Membranes, Refurbishment, Detailing.

**Summary.** The connections of new structural membranes to historic buildings are explored on the basis of traditional examples and recent experiences.

### 1 INTRODUCTION

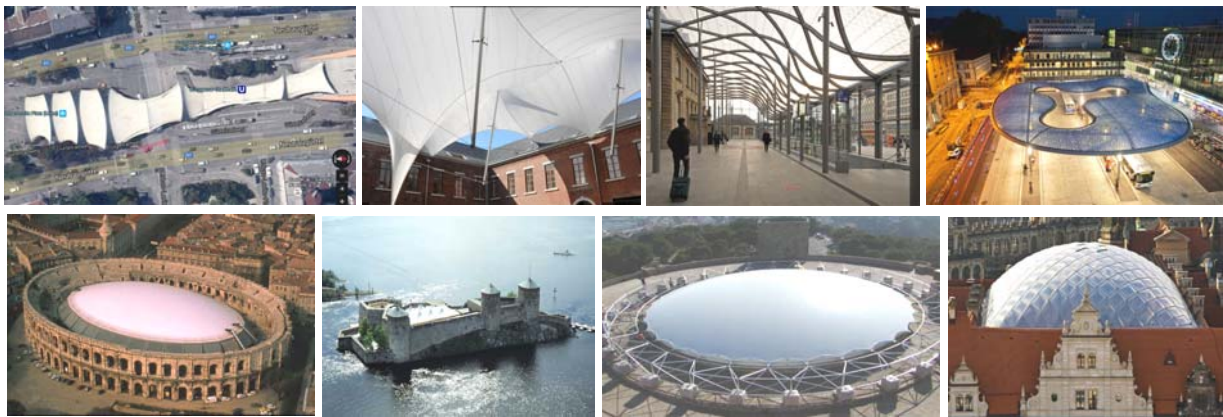
Structural membranes have been recognized as being suitable for the refurbishment of existing buildings. In a previous paper [1], 80 interventions in 24 countries were investigated to identify the design strategies together with the conformity of the solutions with the principles established by the International Council on Monuments and Sites. The research has continued, including more case studies and analysing the different ways of connecting new structural membranes to old existing buildings.



Left to right and top to bottom: Fig.1: Imagination Headquarters, London, 1989. Fig.2: Dresden Station Redevelopment, 2006. Fig.3: Corbera d'Ebre Church, 2013. Fig.4: Salzburg Central Station, 2013. Fig.5: Baluart de Ses Voltes, Palma de Mallorca, 1991. Fig.6: Roof for the central courtyard of the "Palacio de Minería", Mexico City 2002. Fig.7: Fachada andamio Puerta Tierra, Cádiz 2007. Fig.8: Wrocław railway station.

The strategy of integrating membranes into the building layout while preserving its architectural character and construction integrity is illustrated by the roofs added or replaced in the Imagination Headquarters of London, 1989 (fig.01), the Dresden Station Redevelopment, 2006 (fig.02), the Corbera d'Ebre Church, 2013 (fig.03) and the Salzburg Central Station, 2013 (fig.04).

Other options rely on independency, establishing a dialogue with the pre-existing elements such as the “Baluart de Ses Voltes“ in Palma de Mallorca, 1991 (fig.05), the roof for the central courtyard of the “Palacio de Minería” in Mexico City, 2002 (fig.06), the “Fachada andamio Puerta Tierra” in Cádiz, 2007 (fig.07) and the Wroclaw railway station, 2013 (fig.08). A third option is to introduce a totally new concept by juxtaposing an outstanding new shape, which could be an appropriate choice if the context lacks character or definition. Some outstanding examples have been identified: the Urban Loritz Platz in Vienna, 2000 (fig.09), the Julianus Shopping Centre in Tongeren, 2008 (fig.10), the Luxembourg Central Station, 2012 (fig.11) and the Bus Station of Aarau, 2014 (fig.12).



Left to right and top to bottom: Fig.9: Urban Loritz Platz, Vienna 2000. Fig.10: Julianus Shopping Centre, Tongeren, 2008. Fig.11: Luxembourg Central Station, 2012. Fig.12: Bus Station, Aarau, 2014. Fig.13: Arena, Nîmes 1988. Fig.14: Olavinlinna Castle, 2000. Fig.15: Bellver Castle, 2006. Fig.16: Kleiner Schlosshof, Dresden 2009.

On special occasions, the preservation of the external image of the building is added to the aforementioned principles. It is a requirement that considerably affects the design, as the case of the ancient Arena of Nîmes that was covered with a lens-shaped pneumatic form (fig.13). The roof is not visible from outside and no changes had been made to the classical structure of the Arena. Another example is that of the new roof of the Olavinlinna castle courtyard, scarcely visible from outside (fig.14). It had to harmonise with the historical building, new insertions to the old walls were not permitted and the whole structure had to be such that it could be erected and dismantled efficiently. A combination of both solutions is the short-term use roof for the Gothic Bellver castle in Mallorca to protect the yard during seasonal events (fig.15). Sand bag ballasts instead of anchors were used to support wind loads up to 100 km/h. The old walls remained untouched. More sophisticated is the roof of the Dresden Castle Kleiner Hof (fig.16). It hides behind the ridges and gables and had to take them into account while not being obtrusively visible from the outside.

It is also noticeable the suitability of membranes to cover large areas on existing stadiums and arenas. This capability is based on the lightness, translucency and compatibility of the intervention that does not alter the basic outlines and preserves the architectural character being easily differentiated and in some cases, easily removed. (figs.17 to 20).



Left to right and top to bottom: Fig.17: Vista Alegre - Bullfight Arena Roof, Madrid 2000. Fig.18: Berlin Olympic Stadium, 2004. Fig.19: Kiev Stadium, 2011. Fig.20: Poznan Stadium, 2012. Fig.21: Shelter for terrace house 2, Ephesos, 2000. Fig.22: Sachsenhausen Memorial, 2005. Fig.23: Nuestra Señora del Rosario, Antigua, 2005. Fig.24: Megalithic temples of Malta, 2009.

The same features are also convenient for the protection of ruins and archaeological areas that require minimal and reversible interventions. Their particularities have been previously exposed in Barozzi et al.[2], Beccarelli et al.[3], Lombardi & Canobbio [4] and Zanelli[5]. Some prominent examples are the shelter for the Terrace House 2, Ephesos, to preserve the ruins, fulfil the climatic requirements and make the monument accessible (fig.21), the protective shelter for the remains of the crematorium of the Sachsenhausen concentration camp in the form of a translucent envelope structure with a homogeneous surface (fig.22), the roof of Nuestra Señora del Rosario ruins in Antigua, Guatemala (fig.23) and the fast and reversible intervention on the megalithic temples of Malta (fig.24).

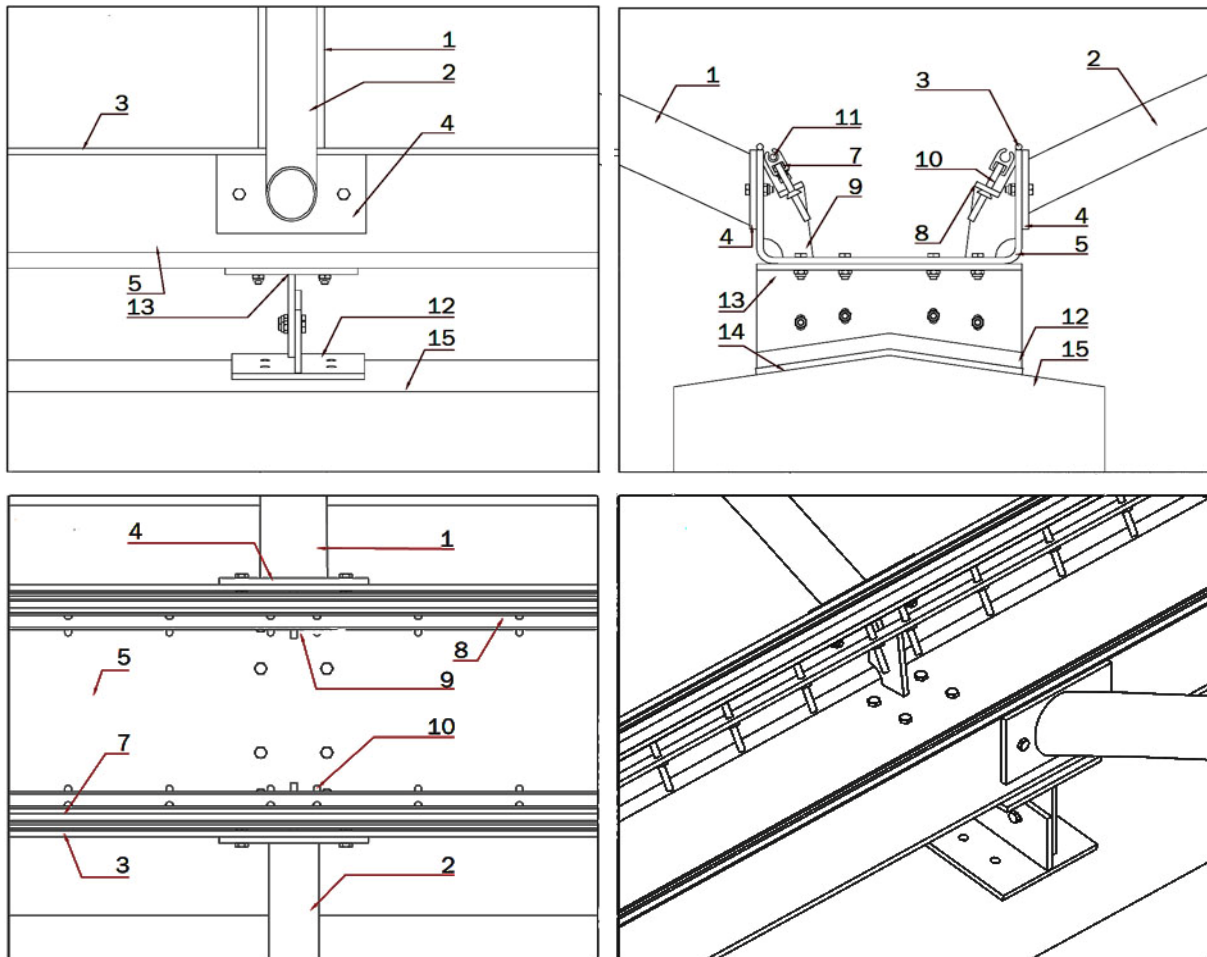
### 3 CASE STUDIES

**3.1 Corbera d'Ebre Church restoration.** F.Vizioso & N.Bordas, Architects, 2013. Manufactured and installed by IASO.

To recover the use of the church as a public space, preserving its character of ruin as a memorial of the devastation produced by the civil war (1936-1939), a transparent light roof made of ETFE was envisaged. Its connection to the stone walls was solved with a reinforced concrete ring on top of them to anchor the frames made of cold-formed U steel channels, painted in white to be clearly distinguished, subdivided by tubular arches and valley cables. A gap between the frames and the supporting frames prevent from confusions between the added parts and the old ones.



Fig.25: Axonometric view. Figs.26 and 27: The transparent roof. Fig.28: Reinforced concrete ring on top of the walls.



Figs.29 to 32: 1 CHS Ø 101,6 x 3,6 mm. 2 CHS Ø 76,1 x 3,25 mm. 3 CHS Ø 10 mm. 4 End plate. 5 Channel 400 x 180 x 6 mm. 7 Aluminium extruded section. 8 Longitudinal steel flat plate receiving threaded rods 10. 9 Gusset plate. 10 Threaded rod to tighten the ETFE foil. 11 Keder rail. 12 Plate anchored to the ring. 13 Plate screwed to 12. 14 Ø 12 mm threaded rods embedded into the ring. 15 Reinforced concrete ring (Courtesy of F.Vizoso).

**3.2 Awning in Palma de Mallorca.** J.A.Martínez Lapeña & E.Torres with J.Llorens & A.Soldevila, Architects, 1989.

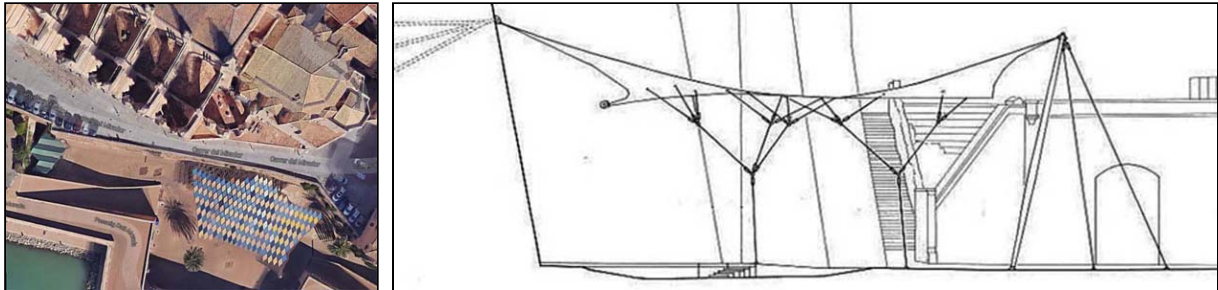


Fig.33: aerial view. Fig.34: Cross section. The main cables are anchored to the city walls.



Fig.35: Plan. Figs.36 and 37: Anchor to the city wall.

A small outdoor theatre in the former moat beneath the cathedral of Palma de Mallorca has been covered with a steel cable net filled with coloured lozenges made of polyester fabric. (figs 33 and 35). The main cables are anchored to the city walls and to two hinged masts held in position by cable stays. Complementary tree-like cable systems attach the net to the ground to keep the awning as rigid as possible (fig.34). Anchors to the wall are  $\varnothing$  28 mm steel bars grouted in 50 mm drilled holes. Their total length include at least an embedment of 2 m into the unaltered rock behind the superficial cladding (figs.36 and 37).

**3.3 Roof for the central courtyard of the "Palacio de Minería", Mexico City.** J.G.Oliva, M.Ontiveros, & I.Ortiz. Manufactured and installed by Carpas y Lonas El Carrusel SA.

The "Palacio de Minería" in old downtown Mexico City was designed by the Architect Manuel Tolsá and built between 1797 and 1813. It is considered a masterpiece of Latin American neoclassicism that has to be preserved. The schedule included the requirement of not altering neither the existing structure nor the external look, meaning that no structural elements of the roof might be seen from the streets (Figs.38 and 39). This requirement implied that the intervention had to be very light and the height of the masts limited. Also, to reduce the impact to a minimum, plates for anchoring and supporting masts were embedded in the concrete slab poured in 1973 during a restoration work to replace the former wooden beams and brick roof (figs.41 to 43). Therefore the intervention was limited to the screwed removable plates. In summary, the historic building has been enhanced by the functionality of

the membrane designed taking into account the formal guidelines of the Palacio to preserve its architectural configuration. The membrane is easy to erect and dismantle, light enough to rest on the existing structure without special reinforcements and flexible to admit the irregular sinking of the site (a former lagoon). In addition, if the roof is removed, all its elements would disappear and the courtyard would return to its original situation.

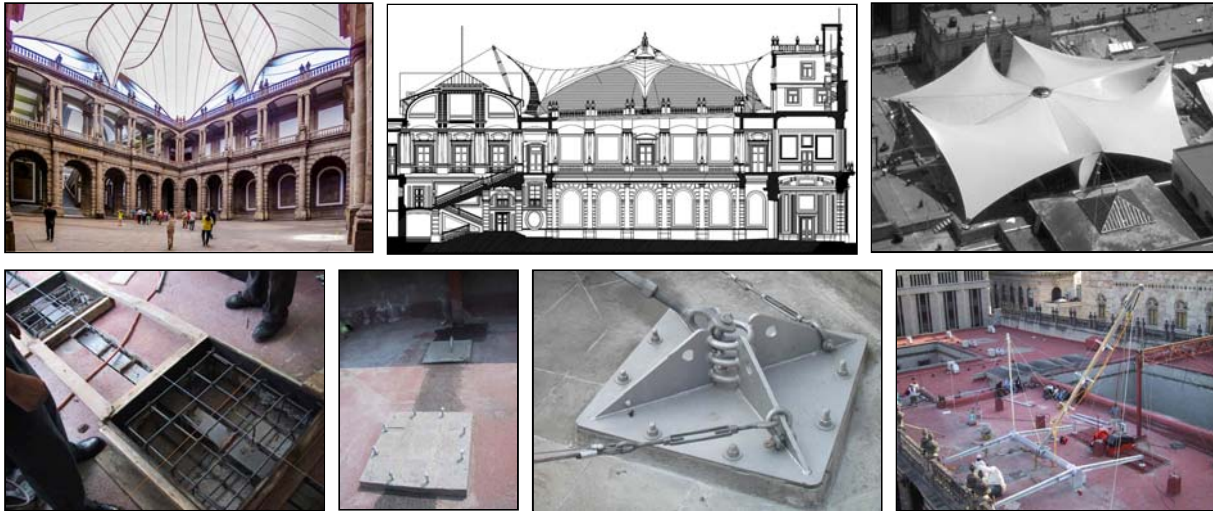
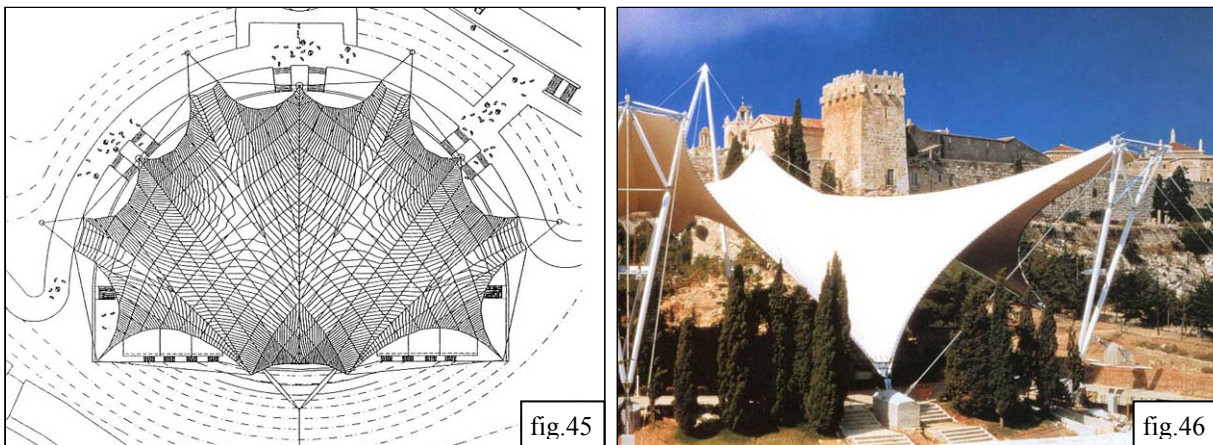


Fig.38: Palacio de Minería courtyard. Fig.39: Section. Fig.40: Aerial view. Fig.41 to 43: Plates anchored in the concrete slab of the roof (poured during a previous restoration). Fig.44: Installation.

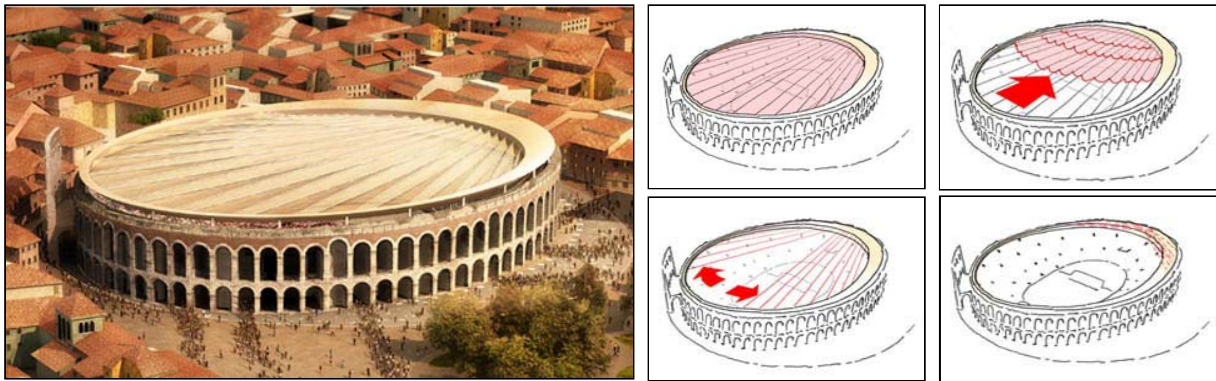
### 3.4 "Camp de Mart Auditorium", Tarragona. Tensoforma, S.Bertino, 1993.



The Camp de Mart auditorium in Tarragona is a 3000-seat open-air amphitheatre located close to the city's Roman walls (fig.45) [6]. The proximity of the historical enclosure was of great concern during the design and construction processes. Work was interrupted by the local historical/archaeological authorities, who were not able to accept such a combination of styles, materials and technologies. But they finally accepted a tensile roof due to its openness, light weight, translucency and the ease with which it could be dismantled and could (almost) disappear (fig.46) [7].

**3.5 Roofing the Roman amphitheatre of Verona.** gmp Architects with Schlaich, Bergermann Partner, 2017.

An international competition was launched to find ideas for a retractable roof over the Verona Roman amphitheatre. The brief required a structure fully reversible, visually coherent with the amphitheatre and its historical surroundings, cost-effective, structurally feasible, functionally and acoustically compatible with the live events and concerts which the Arena regularly accommodates, and at the same time it should include an artificial lighting system, being retractable, and have no negative impacts on the original building.



The controversial winner scheme is a 12.000 m<sup>2</sup> foldable membrane sliding through a radial set cables, hidden and stored beneath the compression ring, when not in use. The solution claims to be "a subtle intervention that will not take focus away from the architecture of the historical arena". But main unknowns are the compatibility between the structure required by such a roof and how its foundations would be executed without substantially affecting the existing building (figs 47 to 51) [8].

**3.6 Berlin Olympic Stadium new roof,** gmp Architects with Schlaich, Bergermann Partner, 2004.



Figures 52 to 55: The transformation of the Berlin Olympic Stadium into a modern arena has been reconciled in accordance with conservation constraints. The most importance change is the new lightweight roof that plays down the politically motivated heaviness of the stone. Some fans object to the slender columns in the upper tier of stands, but, as a result, the old stadium has been recycled and upgraded [9].

### 3.7 The shelter for Terrace House 2, Ephesus, O.Häuselmayr & W.Ziesel, 2000.

Recent contributions based on textile architecture for protecting excavations and ruins prove to be compatible with the general configuration of different sites and adaptable to particular requirements of functionality, geometry, structure and environmental impact. It is the case of the terrace houses of Ephesus.

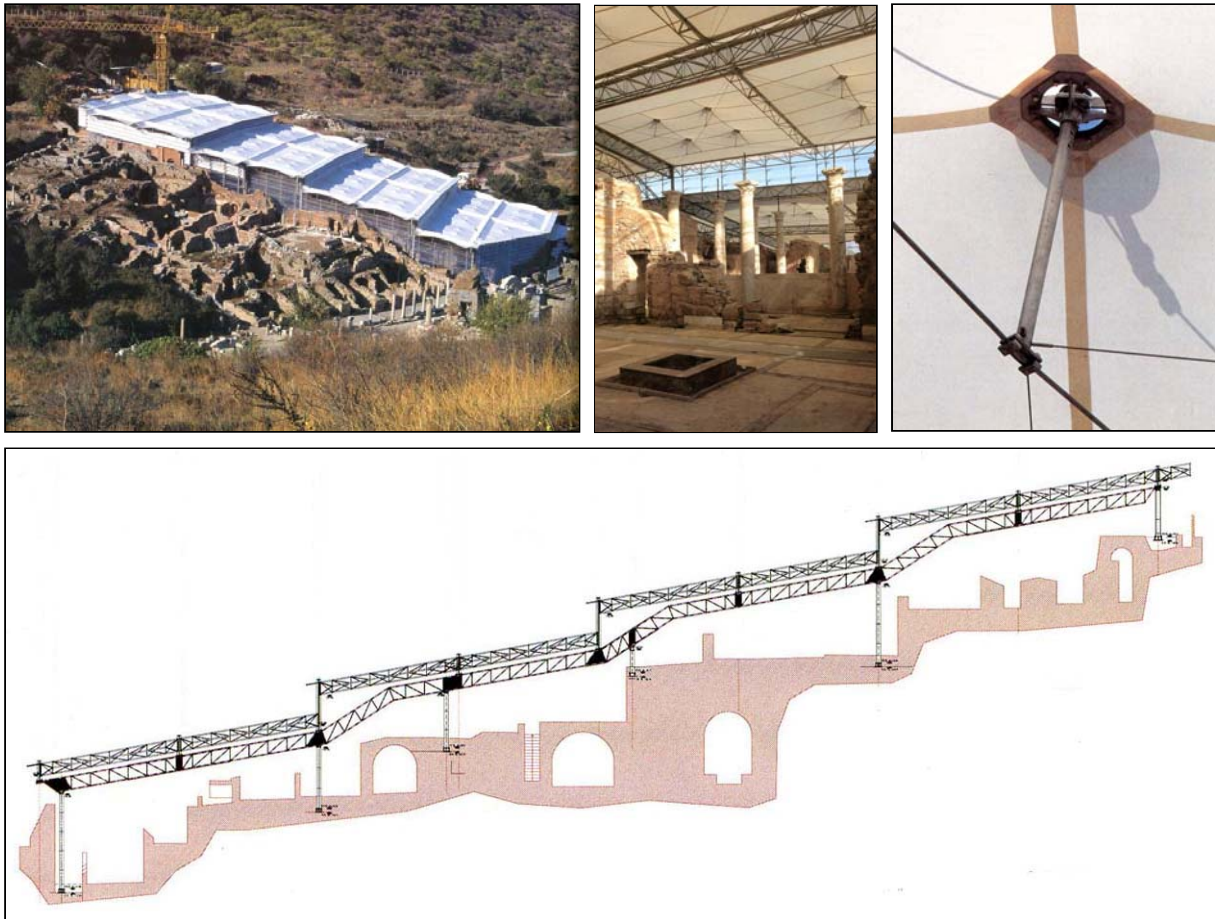


Fig.56: The shelter for Terrace House 2, Ephesus. Fig.57: Housing unit 6: Marble Hall (room 31) and peristyle courtyard (room 31a). Fig.58: Detail of flying mast. Fig.59: Longitudinal section.

After the discovery of the monuments in 1962, it became clear that the painting and mosaic decorations should be left on site. It was necessary, therefore, to protect the ruins with a roof for climatic protection and also make the monument accessible to the public. The entire Terrace House 2 has been covered by a roof with a bearing steel structure conforming to the gradient of the slope. The material of the light roof is a translucent textile Teflon coated fibreglass membrane. In this way, the protective structure conserves the monument and allows for the contemporary presentation of the remains. A year-round conservation season independent of the weather conditions, is ensured [10].

### 3.8 Covering the Amphitheatre House ruins in Mérida, J.Llorens, Ch.García-Diego & H.Pöppinghaus, 2003.

A competition was launched to find a solution for the preservation of the 4th century “Amphitheatre House” ruins of the Roman city of Emerita Augusta, modern-day Mérida, Spain. As the ruins of the “Amphitheatre House” were uncovered, they lied exposed to the rain and UV rays. A noticeable degradation process was observed over the course of the last 50 years. Moreover, excavations are slated to continue, more remains will need protection and the solution had to be capable of being extended according to what excavations and discoveries were made. Because the site is frequently visited, the routes of the visitors also had to be preserved.



Figs 60 to 62: The ruins of the Roman House have been protected with a conventional steel structure. F.Visedo, 2014 [11].

The proposal that was adopted is a conventional structure made of steel sections and metal sheets. It adversely affects the general perception of the site because it changes the natural conditions by interfering with and obstructing natural light.

Another proposal (not retained) based on tensegrity principles, was a modulated lightweight and translucent textile roof that would have been able to adapt to cover whichever areas needed to be protected. It would have been made up of a tensile membrane stretched across frames made of hollow sections supported by masts. Their position would have been able to vary so as to avoid interferences with mosaics and ruins. It was conceived as a uniform, translucent white plane that would have acted as a diffuser of the natural light yet not interfere with the general atmosphere, character and environment of the site [12].

The structural system would have been based on a series of frames made of tubular latticed box girders hung from masts forming a succession of 11.2-metre-wide strips that could be extended in any direction, so as to increase the spans, the number of supports or to add more strips. The spans in each frame would have been changed to fit the dimension of the ruins and bending in the span reduced by tie bars. The foundations would have not been made of heavy blocks of concrete but rather screw anchors or grouted bars according to the resistance of the soil. The roof itself would have been a prestressed structural membrane stretched across the trussed beams and extended by flying masts pushed up by adjustable cable nets. As the membrane is structural, neither purlins nor ties to the ground were necessary; the system was

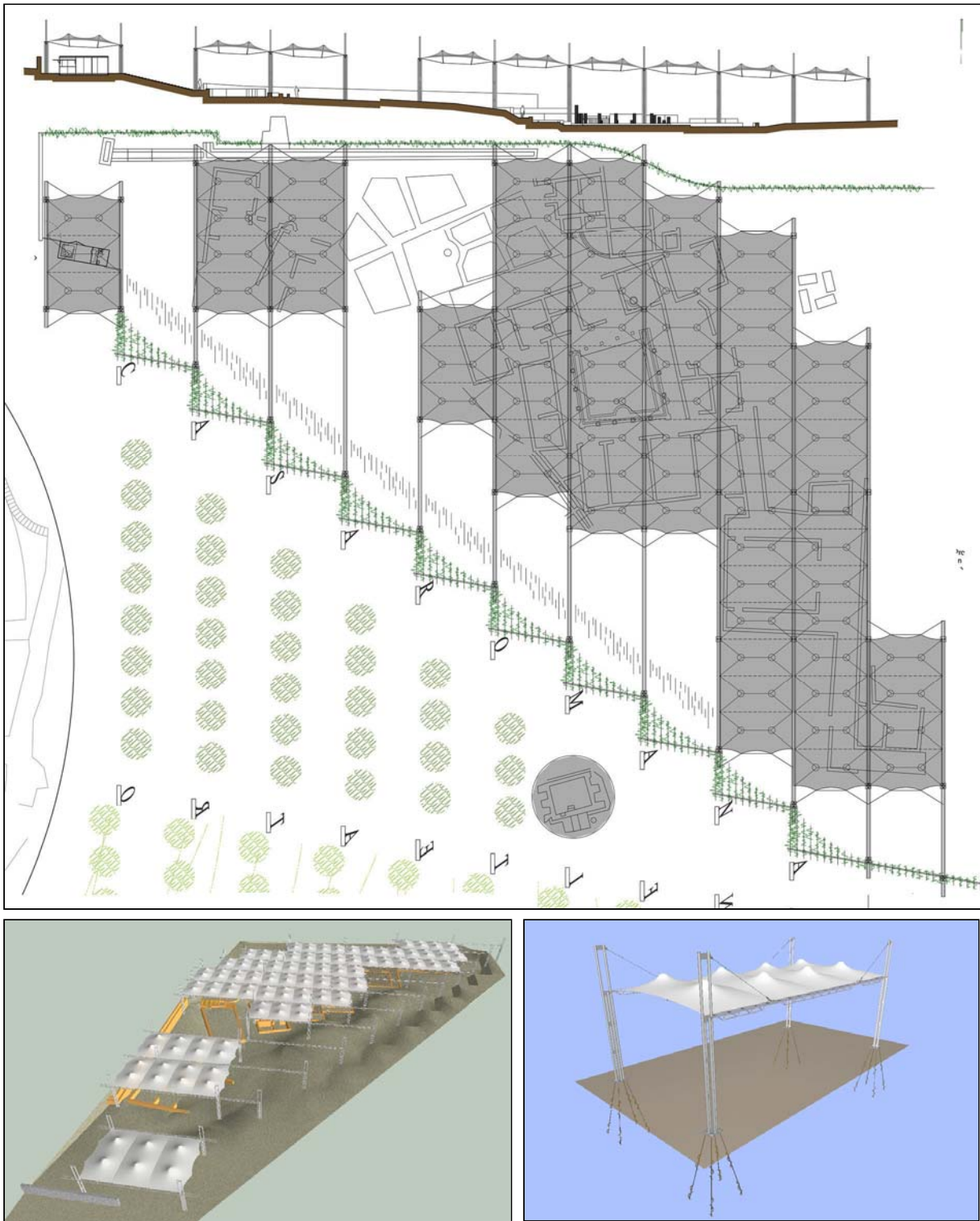


Fig.63: Plan of the modulated latticed frames adaptable to whichever areas needed to be protected. Fig.64: Axonometric view. Fig.65: Detail of the module.

self-stabilizing. The self-weight of the roof with its fittings would not have exceeded the range 50 to 100 N/m<sup>2</sup>. As the membrane is structural, neither purlins nor ties to the ground were necessary; the system was self-stabilizing. The self-weight of the roof with its fittings would not have exceeded the range 50 to 100 N/m<sup>2</sup>.

### 3.9 Juxtaposed roofs by N.Kugel & A.Rein, Architekten und Ingenieure.

The juxtaposed roofs designed by N.Kugel & A.Rein are mentioned as an illustration of the principles of the International Council on Monuments and Sites (ICOMOS) referring to "differentiating from the historic parts" and "reversibility"[13].



Fig.67: Kufstein fortress, 2006. Fig.68: Felsenreitschule Salzburg, 2008. Fig.69: Salzburg Residence courtyard, 2012. Fig.70: Castle ruins of Thierstein, 2013.

## 4 CONCLUSIONS

The review of 80 interventions on historic buildings has revealed the characteristics that make structural membranes suitable for the refurbishment according to the principles formulated by ICOMOS, the International Council on Monuments and Sites. Because they are light, translucent, non invasive, differentiated, reversible and compatible, they can be integrated into the building layout and preserve its historic character and architectural configuration. And, most important for the designer, they enable the difficult balance between conservation and creativity that arises in refurbishment operations.

Three design strategies have been observed. If the intervention has to be overlooked, an option would be the symbiotic integration that causes the ETFE foil. But if additions or replacements are needed, a tailored tensile surface specifically designed to fit in the place may dialogue with the pre-existences. More appealing would be the juxtaposition of an outstanding different shape despite the difficulties of integration and compatibility.

Several applications have been identified, specially the protection of ruins and archaeological sites and in recent years, structural membranes cover large existing open spaces such as stadiums and arenas promoting the updating and recycling of existing buildings.

## REFERENCES

- [1] J. Llorens & A. Zanelli, 2016: "Structural membranes for refurbishment of the architectural heritage" in *Procedia Engineering* 155 (2016) 18-27, doi:10.1016/j.proeng.2016.08.003
- [2] M.Barozzi et al. 2015: "Design of novel covering system for archaeological areas" in "Structural Membranes 2015 - VII International Conference on Textile Composites and Inflatable Structures", E.Oñate, B.Kröplin & U.Bletzinger (eds.), CIMNE, Barcelona, p.105-114.
- [3] P.Beccarelli et al. 2010: "Textile shelters for archaeological areas: a change in the preservation of cultural heritage" in H.Bögner-Balz & M.Mollaert, ed. "Tensile Architecture: Connecting past and future". TensiNet Symposium 2010, Sofia, p.165-175.
- [4] S.Lombardi & R.Canobbio, 2010: "Covering for archaeological sites (few examples)" in H.Bögner-Balz & M.Mollaert, ed. "Tensile Architecture: Connecting past and future". TensiNet Symposium 2010, Sofia, p.339-349.
- [5] A.Zanelli, 2015: "Architectural fabric structures in the refurbishment of archaeological and cultural heritage areas" in J.Llorens, ed. "Fabric Structures in Architecture", Woodhead Publishing, Cambridge, p.481-527.
- [6] H.J.Schock, 1997: "Soft shells. Design and technology of tensile architecture". Birkhauser, Basel.
- [7] J.Llorens, 2003: "Details in context. Case studies" in M.Mollaert et al.(ed) "TensiNet Symposium: Designing Tensile Architecture", Vrije Universiteit Brussel, p.84-94.
- [8] <http://www.designboom.com/architecture/gmp-arkitekten-verona-arena-roof-cover-italy-02-01-2017/> (visited 17/06/2017)
- [9] Von Gerkan, Marg & Partner, 2005: "Olympic Stadium in Berlin". *DETAIL* 9/2005, p.931-949.
- [10] F.Krinzinger, 2000: "A roof for Ephesos". Österreichisches Archäologisches Institut, Wien
- [11] <http://www.fernandovisedo.com/cubricion-casa-romana-del-anfiteatro-de-merida/> (visited 23/06/2017)
- [12] J.Llorens, Ch.García-Diego & H.Pöppinghaus, 2003: "Tensegrity structures for textile roofs" in E.Oñate & B.Kröplin (ed): "Textile composites and inflatable structures", CIMNE, Barcelona, p.64-72.
- [13] <http://www.kugel-architekten.de/> (visited 23/06/2017)

## THE NUVOLA FOR THE NEW CENTRO CONGRESSI IN ROME STRUCTURAL MEMBRANES 2017

BERND STIMPFLE\*

\* formTL ingenieure für tragwerk und leichtbau gmbh  
Kesselhaus, Güttinger Straße 37  
78345 Radolfzell, Germany  
e-mail: bernd.stimpfle@form-tl.de, web page: <http://www.form-tl.de>

**Key words:** membrane, mechanically tensioned, nurbs geometry, formfinding, analysis, silicone coated glass, cutting pattern, extrusion profiles, parametric process

**Summary:** In Rome's EUR district, a new congress centre has opened recently, designed by the Italian architect Massimiliano Fuksas. The project consists of three main elements, which the architect calls „Teca“ (theca), „Lama“ (blade) and „Nuvola“ (cloud).

The central element located inside the Teca is the Nuvola. Almost floating only with few points fixed to the floor and to the building, it dominates the huge glass box. The Nuvola is a membrane clad steel structure with a length of 126 m, a width of 65 m and a height of 29 m. It contains a café, foyers, meeting rooms and an auditorium for 2000 spectators.

The paper is about this central element, the Nuvola from the geometry driven design process to the installation. It describes the design process, especially the very complex formfinding process in order to achieve the defined geometry derived from a nurbs shape. The analysis process with mock-up installations is presented, as well as the detailing and the automated process for the workshop design and the cutting pattern.



Figure 1: Nurbs model of 2004

## 1. INTRODUCTION

In 1998 the city of Rome together with the future owner EUR launched an international architect competition, which was won by Massimiliano Fuksas. In 2004 we have received the first inquiries together with a 3D nurbs geometry. The surface was smooth all over the Nuvola.

We made first suggestions for the orientation of a supporting grid, for the details and we tested different seam layouts. We tried to convince the client to start with the membrane engineering and to do a large scale mockup of a critical zone in order to test the different ways to create the shape with a tensioned membrane.

The client decided to continue with a steel consultant, who developed in the following a concept that allowed an easier way to produce the steel, which was then basis of the tender documents. The concept was to cut the nurbs surface in slices in the yz, xz and xy plane.

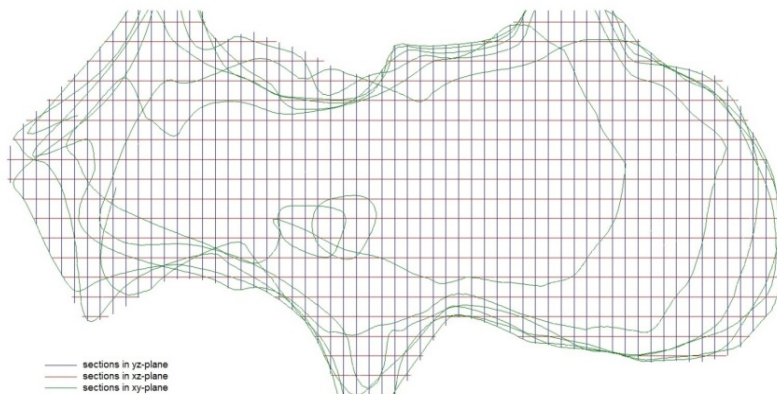


Figure 2: sections of the steel structure

In some areas this created reasonable slices which can easily be covered with membranes, but in many areas the geometry was not ideal and made the shape development of the membrane very difficult.

After a first try with another cladding supplier we have been involved in 2011 in the design of the membrane cladding. The interface to the steel had been defined with small studs made of rectangular hollow sections, where the initial contractor was supposed to attach his cladding.

The majority of the steel was already in place when we started our design, so that we had to find a detail that fits to the existing studs in the steel. The studs were oriented in the plane of the section, which led to geometry problems where one section joins the other. Different inclinations led to different levels which needed to be compensated with the attachment lines of the membrane.

## 2. ANALYSIS

Due to its location inside the building, the membrane is only loaded with internal overpressure. For the overall project a wind tunnel test has been performed by the University of Florence in their wind tunnel in Prato.

The static pressures on the inside and on the outside of the Nuvola membrane are equalizing one against the other, only due to fluctuation differential pressure it is acting on the membrane. The dynamic wind pressure used for the project is based on a 100 year return period. As the fabric cladding is not part of the primary structure and has a lower life expectancy, a return period of 20 years has been applied for the fabric.

With all these assumptions the wind load to be applied on the membrane has been determined with  $\pm 0.14 \text{ kN/m}^2$ .

The material used is a silicone coated glass fabric with an acoustic punch pattern, to improve the sound absorption. The raw material has a tensile strength of  $52 \text{ kN/m}$  in warp and  $40 \text{ kN/m}$  in weft. Due to the punched holes and the stitched seams the strength is reduced.

Based on tensile tests performed, admissible stresses in the service limit state had been determined for permanent load (prestress) and for wind load. The admissible stress for permanent load was determined with  $2.3 \text{ kN/m}$  in warp and with  $2 \text{ kN/m}$  in weft. For wind load the admissible stress has been determined with  $2.7 \text{ kN/m}$  in warp and  $2.4 \text{ kN/m}$  in weft.

The membrane shape has been defined with an initial prestress state of  $1.5 \text{ kN/m}$  in warp and  $0.5 \text{ kN/m}$  in weft direction. In areas with sharp edges this ratio has been changed to  $2.4 \text{ kN/m}$  in warp and  $0.4 \text{ kN/m}$  in weft.

For the stress analysis a relevant numerical model in Zone 2 has been analysed. The shape was determined as a tension surface in-between the rigid support lines of the Nuvola. The saddle of the membrane was in the sharp edges of the Nuvola rather deep, and in flat areas almost negligible.

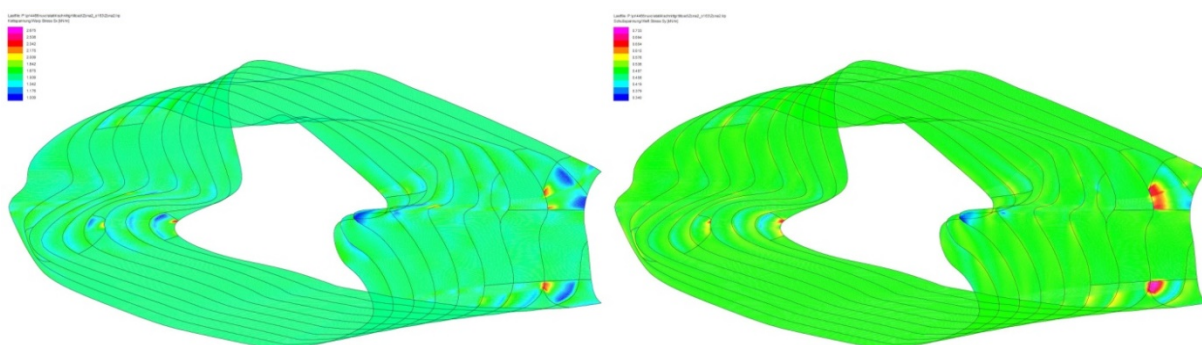


Figure 3: numerical model zone 2 - prestress state warp and weft stress

### 3. MOCK-UP

In order to test the details a mock-up of the most difficult area has been made. The seams should follow as much as possible the axes of the steel structure. Additional seams were necessary in areas with high curvature. In 2012 a third mock-up was introduced, which showed the minimized number of seams and represented the membrane shape with adopted stress ratio in heavy curved areas.



Figure 4 / Figure 5: First tensioned membrane mock-up / Second tensioned membrane mock-up

The conclusion of the mockup phase was that in no area of the project a distortion angle higher than  $5^\circ$  should be allowed, and that additional seams are needed to allow this. Furthermore a reasonable saddle should be kept even in sharp areas, so that the membrane is able to redistribute loads in both directions, and reduce stress peaks.

### 4. DETAILS

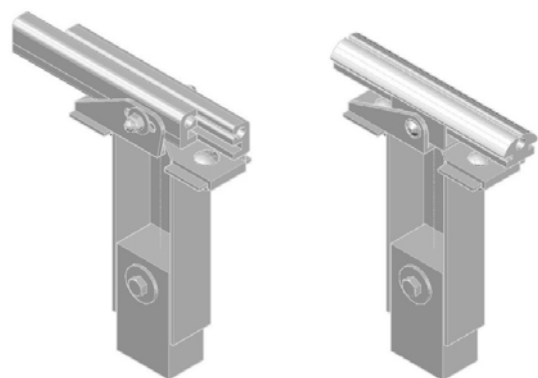


Figure 6 / Figure 7: stud detail of the steel structure / isometric view attachment and push up detail

As mentioned before, the steel structure has in a regular distance of typically 400 mm steel studs, where we had to fix the brackets for the secondary structure. We have developed a detail that consists of a channel section screwed laterally to the studs. A slotted hole allows the adjustment of the details. On the top, two extrusion profiles are attached to fix the membrane panels. The extrusions can be moved horizontally to compensate tolerances.

Where the membrane saddles come too close to the steel structure a push up profile has been inserted, this is a round extrusion profile which is redirecting the membrane around the steel structure. In some areas this push up profile is also used to pull the membrane, therefore the extrusion allows also to insert a keder.

The complex geometry of the project required to have these details with different heights and with different inclinations. All brackets are made with a reference line marking, and on the survey drawings for installation the level for all brackets differing from the standard are given. The brackets have been developed with a parametric design in the Inventor software, which allows an easy adaption to the different levels and inclinations.

For the detail development and the workshop process of the attachment lines an automatic process was developed. The input data were reference nodes on each stud in one section, which has been offset and splined. Along this spline, the bended extrusion profiles have been generated with machine ready dxf files to cut from the straight profiles and with all bending and drilling information. Where the brackets are inclined, the profiles needed to be bent in two axes.

In total approximately 6500 different pairs of clamping have been generated and approximately 180 different types of brackets.

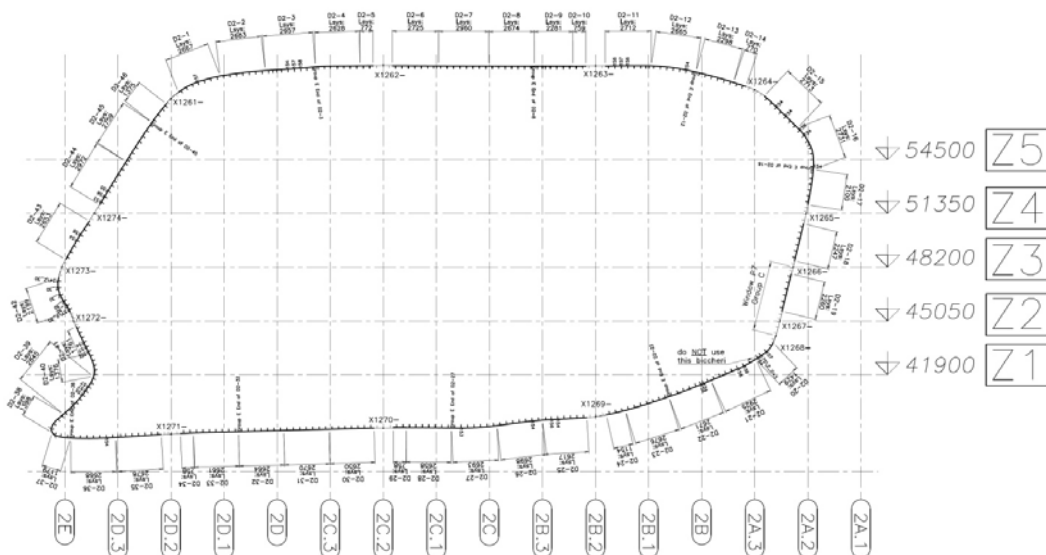


Figure 8: generated overview of clamping profiles in one section

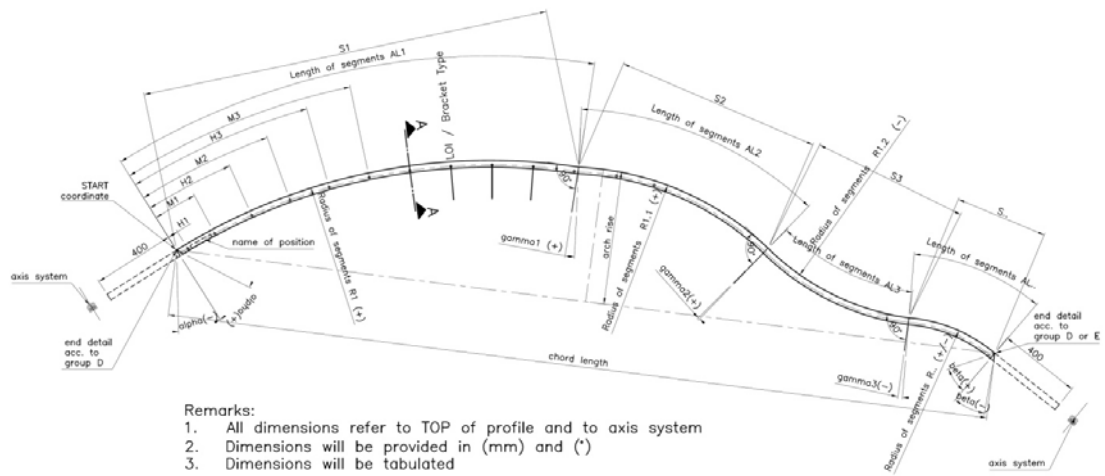


Figure 9: principle drawing for the generated clamping profiles

To avoid steps in the crossings, the attachment lines are joined with typically four sets of twisted twin profiles. The software generating the standard profiles left the space open and generated the input geometry and data for the software which generated the crossings. Also generated by this software generated are machine ready drawings for all profiles.

## 5. SEAM LAYOUT AND PATTERNING

Very important for the appearance of the Nuvola is the seam layout. The architects asked us to follow as much as possible the steel structure with the seam layout. As the curvature in many areas is rather high, it was necessary to add there additional seams in between the steel axes.

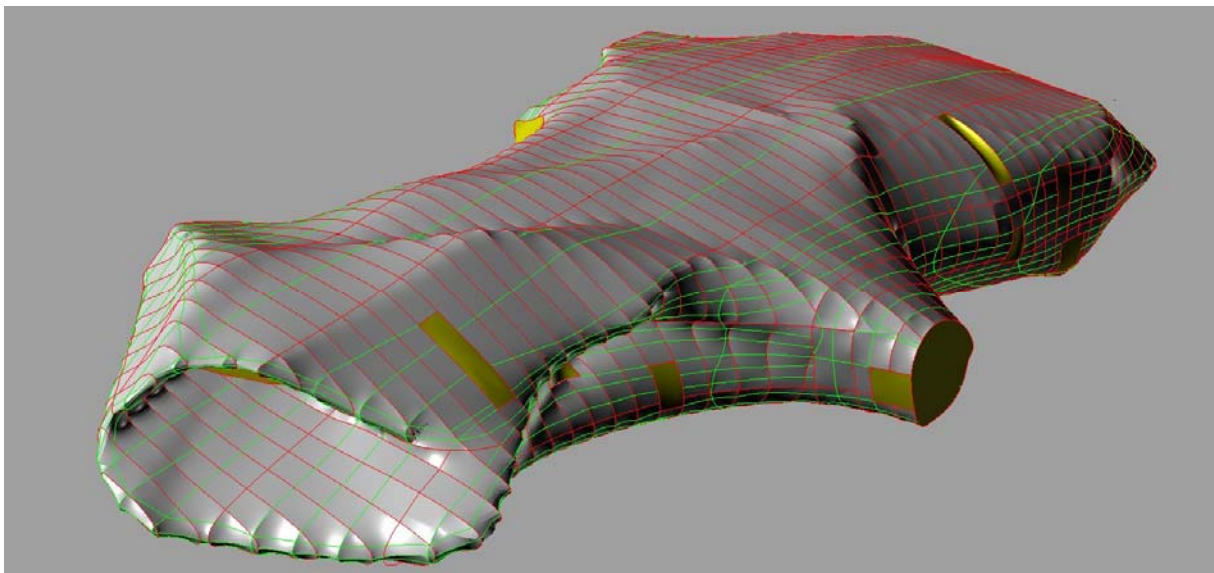


Figure 10: View on the "mouth" above the entrance

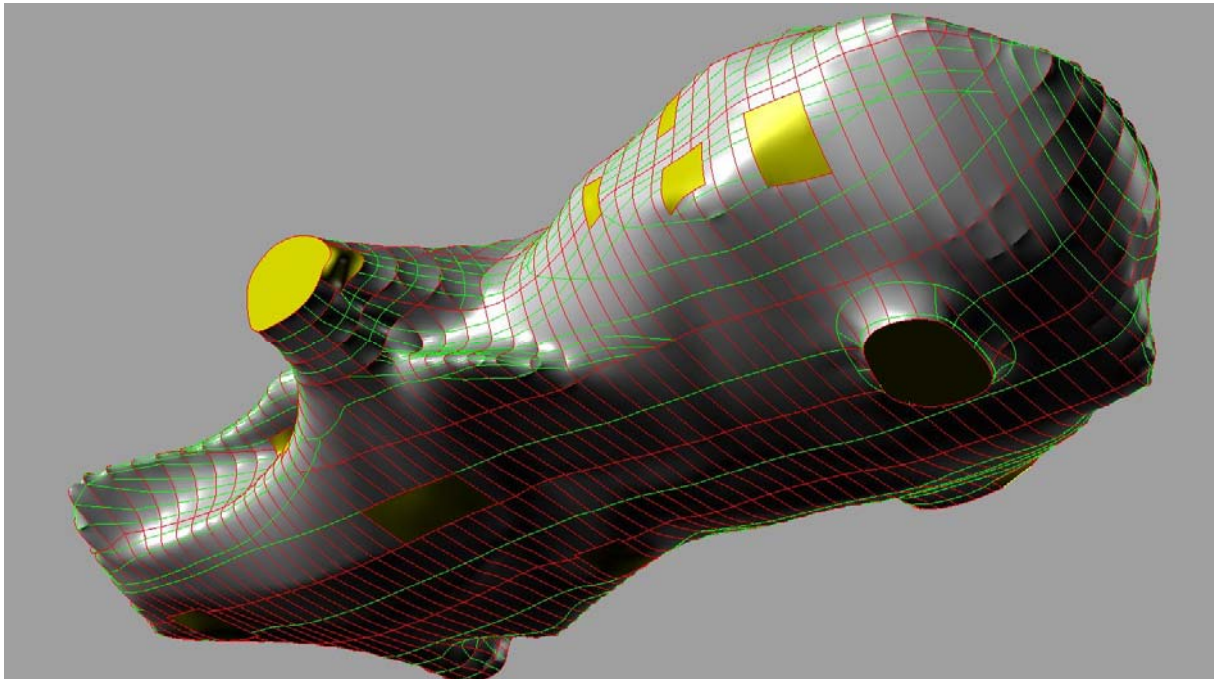


Figure 11: View form below

In a very long coordination process with the architect we determined the seam layout. In the following figure the version number 18 of this coordination process is shown, which was the finally agreed layout. The red lines show the panels borders, which are formed by the clamping lines, and the green lines show the stitched seams inside the panels.

This agreed seam layout was the basis of the patterning model. Many panels consist of only two patterns, some of only one, but all of the difficult ones consist of more patterns. The patterns are joined with stitched seams. The seam has been optimised with regard to the fabrication speed and to the resistance based on tests.

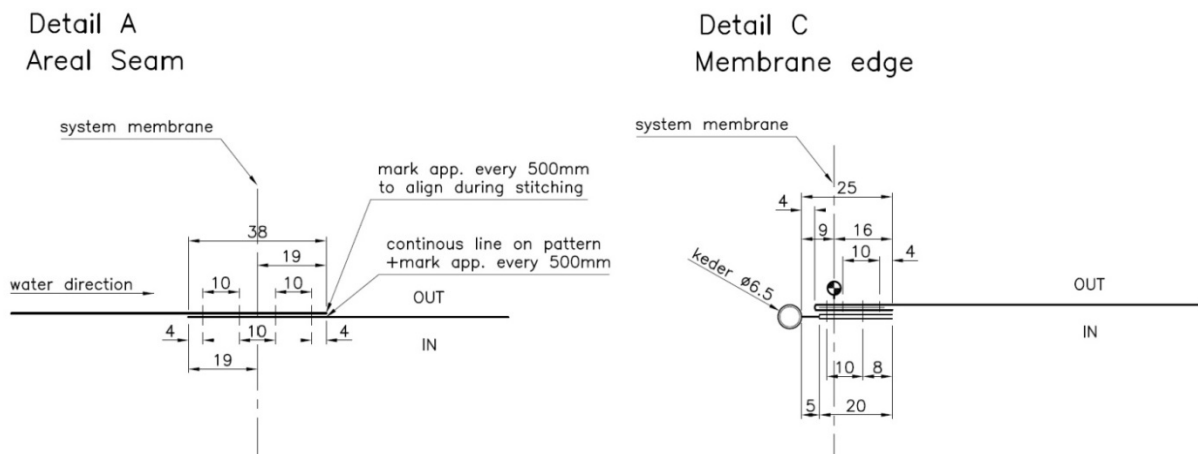


Figure 12: membrane details

## 6. REALISATION

The manufacturing of membrane clamping required highly specialized personal and methods to control the pre manufactured pieces.



Figure 13: work shop control template

The surface area of approximately 14000 m<sup>2</sup> has been realized with 607 panels which consist of 2763 individual cutting pattern. The panels have been joined with stitched seams.



Figure 14 / Figure 15: stitching process / packed panels

The logistic on site benefits from the workshop documentation, which provides information, which allows the site staff to organize their activity.

Prior to installation on site dimensions were taken to check, if as built dimensions of the primary steel match with the secondary structure.

The activity on site was divided in two lots. First all the clamping elements were installed. In this phase the accurate fit and functionality could be tested.



Figure 16: steel structure with installed secondary structure

The second step to install the membrane panels was launched at a later phase. The strategy was to install the visually highly relevant and most delicate membrane after a possible pollution from other trades is reduced. The membrane installation was executed with climbing personal, since traditional methods were not flexible enough. The membranes needed to be installed from the inside of the structure as façade parts, roof parts outside down and roof parts outside upwards.



Figure 17: installation from inside

The segmentation size of the membranes allowed to move the material in position and attach it to the secondary structure without heavy equipment. All the adjacent panels were installed to a reduced stress level. In this situation the joints between the membranes were slightly open. Finetuning like aligning the seams was possible at this time.



Figure 18: open joints during installation

In the final installation step the joints were closed by turning the bolts in the double clamping channel. No additional access from outside was necessary.



Figure 19: outside view zone 5

## 7. CONCLUSION

The Nuvola is a complex project, different from all other tensile projects. The panels are very small and the amount of attachment details is very high. The shape is difficult, and the constraints of the project are higher than usual. The design tools had to be improved as much as possible, so that the big quantities of drawings and fabrication documents could be finalised on time.



Figure 20: bottom view zone 3/4



Figure 21 / Figure 22: View through the “mouth” / inside appearance



Figure 23 / Figure 24: general view form outside / Nuvola zone 1a

## PROJECT DATA AND PARTICIPANTS

Name of the project: Nuvola del Nuovo Centro Congressi, Rome

Location address: Via Cristoforo Colombo, Rome

Function of building: Convention centre

Type of application of the membrane: mechanically tensioned

Year of construction: finished in 2016

Material: Atex 2000 with punch pattern WS 14

Membrane surface area: 14400 m<sup>2</sup>

Client (investor): E.U.R. S.p.A., Rome

Architect: Massimiliano Fuksas, Rome

Consulting engineer for the membrane: formTL, Radolfzell

Main contractor: Condotte S.p.A., Rome

Contractor for the membrane (Tensile membrane contractor): Canobbio, Castelnuovo-Scivia

Supplier of the membrane material: Valmiera Glass UK, Sherborne

Manufacture: Canobbio, Castelnuovo-Scivia

Installation: Condotte S.p.A., Rome

## PICTURE CREDITS

Figures 1 to 12 formTL and Canobbio, Figures 13 to 18 Studio Moreno Maggi

## REFERENCES

- [1] Stimpfle, B.: The Nuvola for the Nuovo Centro Congressi in Rome, *Steel Construction* 8 (2015), No. 4
- [2] Stimpfle, B.: Die Nuvola im neuen Centro Congressi in Rom - Höchste Anforderungen an die Formfindung, *Deutsches Ingenieurblatt* 04/2017
- [3] Stimpfle, B.: From NURBS to Textile Architecture, *Structural Membranes* 2013

## EXPERIMENTAL METHOD FOR BIAXIAL TENSILE STRENGTH OF FABRICS AND PRELIMINARY INVESTIGATIONS

W. J. CHEN<sup>\*†</sup>, T. B. SHI<sup>†</sup>, C. J. GAO<sup>†</sup>, J. H. HU<sup>†</sup> AND B. ZHAO<sup>†</sup>

<sup>\*</sup> School of Naval Architecture, Ocean and Civil Engineering  
Shanghai Jiao Tong University  
Dongchuan Road, Minghang District, 200030, Shanghai, China  
e-mail: cwj@sjtu.edu.cn, web page: <http://naoce.sjtu.edu.cn>

<sup>†</sup> Space Structures Research Center (SSRC)  
Shanghai Jiao Tong University  
Dongchuan Road, Minghang District, 200030, Shanghai, China  
Email: gcj.sjtu@sjtu.edu.cn - Web page: <http://www.ssrc.cn>

**Key words:** Fabrics, Biaxial tensile strength, novel cruciform specimen, numerical analysis.

**Summary.** This paper presents a novel experimental approach to determine the biaxial strength of fabrics. A double-layer cruciform specimen was proposed based on the improvement of previous test specimen. The design and manufacture process of the novel specimen was described in detail. Uniaxial and biaxial tests of a specific material were performed subsequently. Based on numerical simulation, the biaxial strength of the fabrics was preliminarily investigated. And the correlation between uniaxial and biaxial strength of the material was discussed. The proposed experiments could characterize the biaxial strength of fabrics, and the biaxial strength of the fabrics at 1:1 tension is higher than the weft strength and little lower than the warp strength.

### 1 INTRODUCTION

With its unique material features such as light weight, high strength, economical costing and extraordinary aesthetic expression [1,2], fabrics provides a widely applicative construction material. For more than 40 years, fabrics were employed in the fields of architecture and aerospace engineering. To analyse the structural load response and enhance the service reliability, the mechanical behaviour of fabric materials was desired.

According to previous research, the mechanical properties of fabrics differs significantly from the traditional construction materials [3,4]. Results from the special manufacture process, the mechanical performance of fabric materials showed prominent orthotropy [5]. Usually, the spinning process of fabrics was weft yarns going up and down through the straight warp yarns. Therefore, the warp direction of fabrics normally possesses a higher stiffness level and uniaxial strength. For the purpose of revealing the mechanical performance of fabrics, uniaxial and biaxial tensile tests have been widely used. Kang et al. [6] focused on the mechanical property characterization of film-fabric laminate for stratospheric airship envelope. They performed uniaxial tensile tests in thermal chamber at low, room and high temperatures to investigate the tensile property and temperature dependency. Blum and Balz [7] developed

a biaxial tension instrument for fabrics, and a linear stress-strain increment model was proposed for specific materials. Chen and Chen [3] performed the tearing analysis on laminate fabrics used in pneumatic structures. Uniaxial and biaxial tearing tests were conducted thoroughly. It was found that the tearing strength and failure performance were significantly related to the biaxial stress ratios.

Since the working condition of fabrics is generally under biaxial compound load. Biaxial parameters could give a better mechanical explanation of the material, which is close to the practical service state. However, previous research only focused on elastic constants determination and uniaxial strength measurement. The biaxial strength, one of the key parameters of fabrics, remained unsolved. Based on Japanese standard [9] and European design guidance [10], the current biaxial specimen of fabrics can only be applied in elastic constants tests, where the load level was usually limited under 30% of the uniaxial tensile strength. With a higher load value, the failure of specimen would occur at the arm of the cruciform, tear propagate at the end of slits or the corner of the arm due to stress concentration. Such failure performance cannot characterize the real biaxial strength of fabrics, and a new experimental approach is therefore needed.

This paper proposed a new cruciform specimen aiming to solve this problem. In order to obtain the authentic biaxial failure, the strength arrangement of the traditional cruciform specimen was optimized and a double-layer cruciform specimen was designed. Strength tests were fulfilled for specific laminate fabrics under both uniaxial and biaxial conditions. And preliminary analysis was performed utilizing numerical simulation.

## 2 METHODOLOGY

### 2.1 Material

To reach both mechanical requirements and the workability demands, fabrics are usually manufactured through multi layers laminated on a base cloth. The base cloth comprises warp and weft yarns interweaving, and the external load is mainly born by it. At the same time, various kinds of materials can be employed as the functional layers, which are utilized to enhance the workability. The typical composition of fabrics is illustrated in Figure 1.

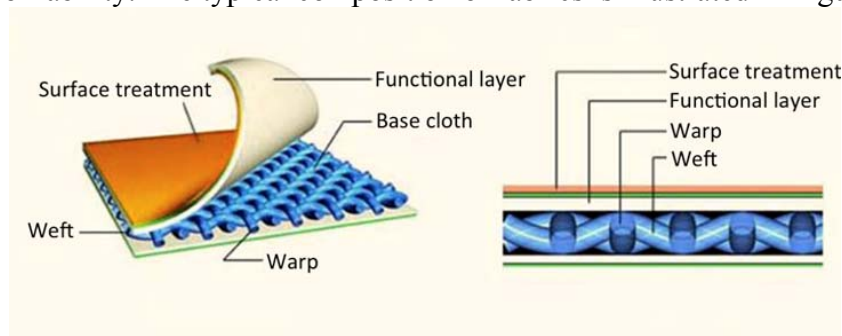


Figure 1: Typical composition of fabrics

In this study, a specific fabric was selected as the sampling material, and the basic

specification of the material are listed in Table 1. In accordance with the previous description, the fabrics possessed a high strength with light weight.

**Table 1:** Basic specification of the sampling material

Variable	Specification
Thickness	0.20mm
Areal density	250g/mm <sup>2</sup>
Weave Count	48*48 ends/5cm

## 2.2 Uniaxial specimen and tester

In line with the ISO testing standard, a stripe-shape specimen was employed in the uniaxial tensile test. The width of the specimen was 50mm and the length was 600mm. At each end of the specimen, a 200-mm-length clamping region was flattened for the clamping. On the other hand, a uniaxial tensile tester was utilized to fulfill the experimentation. Under the uniaxial tester, replaceable clamping provided stable load application. And a monitor system would record the test data for further analysis. The appearance of the uniaxial tester is demonstrated in Figure 2. Three uniaxial specimens were prepared for consistency.



Figure 2: Uniaxial tensile tester

## 2.3 Biaxial specimen and tester

As discussed previously, biaxial specimens suggested by current criteria only suits for elastic constant determination. The failure would occur at the loading arms when the biaxial load reaches a high level, however it cannot characterize the biaxial strength of fabrics yet. In order to obtain the authentic biaxial tensile failure, a novel double-layer specimen was

proposed and manufactured. Since the stress concentration was the main reason leading to the unsatisfactory test results, a direct optimization was to rearrange the strength layout. With relatively stronger loading arms, the biaxial failure would occur at the core region of the specimen.

To achieve the ideal strength configuration, the arms of the cruciform specimen were prolonged. With each arm folding back and gluing onto the top of the first layer, a double-layer specimen was created. The plane and sectional diagram of the novel biaxial specimen is displayed in Figure 3

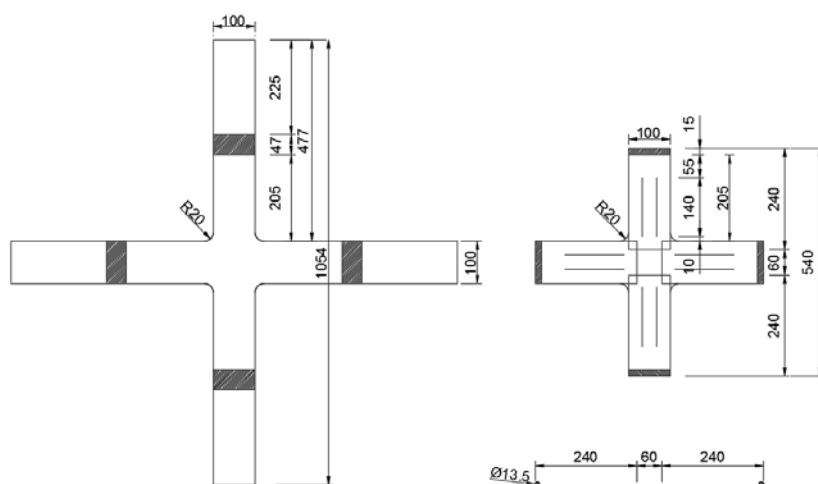


Figure 3: The novel biaxial cruciform specimen (unit: mm)

As shown in the figure 3, an ethylene propylene diene monomer(EPDM) bar was installed at each end of the cruciform arm. Three slits were cut at each loading arm every 33mm. when biaxial tensile load was applied to the specimen, these slits would ensure the stress uniformity at the core square.

Furthermore, an advanced biaxial tester was developed in our laboratory. The controllable biaxial load was applied through four high precision servo hydraulic cylinders at each end of the cruciform, the load and displacement value can be measured and recorded accurately with the computer monitor system. Two biaxial specimens were prepared for consistency.

## 2.4 Experiments

For both uniaxial and biaxial tensile tests, the specimens were clamped firmly onto the tester at first. A pre-load of 0.5N/mm was applied to ensure the flatness of the specimen. With the installation error less than 0.3%, the load was applied at a velocity of 0.1N/mm. The experimental process was performed at a temperature of  $19\pm 1$  °C and a  $41\pm 3$ % humidity.

### 3 RESULTS AND DISCUSSION

#### 3.1 Failure performance

At a certain loading rate, the specimen would rupture under tensile load. The typical failure performance biaxial specimen was illustrated in Figure 4.

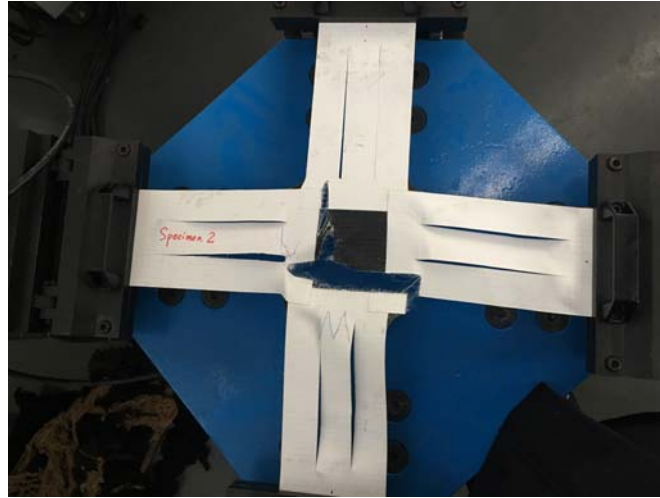


Figure 4: Typical failure appearance of novel biaxial specimen

As shown in the figure 4, a cross slits failure occurred at the center of the fabric specimen. Both warp and weft directions ruptured under a 1:1 biaxial loading condition, which may also justify the novel design. According to the straight fracture morphology and test observation, it can be concluded that the biaxial failure was brittle failure. In the future, a high-speed camera should be introduced to detect the failure process accurately.

#### 3.2 Numerical analysis

To reveal the authentic stress value at the core square of the specimen, a preliminary numerical analysis was fulfilled utilizing finite element software ABAQUS. The geometrical information was accurately built in the model. The specimen was defined as shell element of orthotropy. The elastic constants were determined based on the linear section of uniaxial test results. Since the biaxial load was applied in perpendicular directions, the plane principal stress should be considered as the representative results instead of Mises stress. The principal stress in warp direction ( $S_{11}$ ) was reported in Figure 5.

As shown in the figure, the maximal stress of the specimen appeared nearing the rim of the single-layer core square. The simulation results coincided with the experimental results properly. When the biaxial load continued to increase, the failure would occur at this position. Meanwhile, the stress uniformity of the specimen can also be justified.

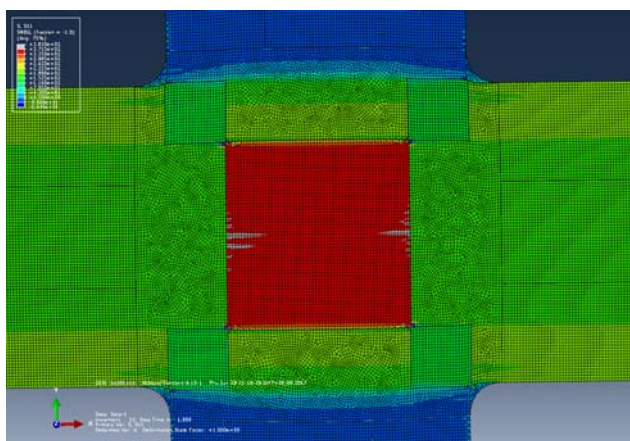


Figure 5: The principal stress in warp direction based on numerical simulation (unit: MPa)

### 3.3 Biaxial tensile strength determination

According to the experimental data and numerical simulation, preliminary analysis on the biaxial strength of fabrics was conducted. The specific results are listed in Table 2.

**Table 2:** Biaxial strength of fabrics

Uniaxial strength (warp)	88.61kN/m	Uniaxial strength (weft)	69.43kN/m
Biaxial strength		85.88kN/m	
Strength ratio (biaxial to warp)	0.969	Strength ratio (biaxial to weft)	1.23

As can be observed in Table 2, the biaxial strength of the fabric was between the warp and weft uniaxial strength under a 1:1 load ratio. Other than the traditional viewpoint, the authentic biaxial strength may be higher than the lower uniaxial strength. Future research should focus on a wider material range and failure process analysis.

## 4 CONCLUSIONS

- A novel biaxial cruciform specimen was firstly proposed for the biaxial strength determination of fabrics. Tensile tests were performed on both uniaxial and biaxial tests. It was obtained that a cross slits failure may appear at the biaxial failure in the center single layer of the cruciform.
- The preliminary analysis of the biaxial strength was fulfilled based on the numerical simulation. It was found that the biaxial strength was higher than the weft strength and lower than the warp strength. It is different from the published conclusions that the design strength of fabrics should consider a reduction factor about 0.85 due to biaxial tensile effects with respect to uniaxial tensile strength

- Future research may carry out extensive experiments with various tensile stress ratio, different fabrics, various loading rate, and formulate biaxial strength criteria, etc.

## ACKNOWLEDGEMENT

The authors gratefully acknowledge the financial support from the National Natural Science Foundation of China (Nos. 51478264, 51278299, 51608320), National Key R&D Program of China (Grant No.2016YFB1200200).

## REFERENCES

- [1] R. Kronenburg, 1-Introduction: the development of fabric structures in architecture A2 - LLORENS, JOSEP IGNASI DE. *Fabric structures in architecture*, WOODHEAD PUBLISHING, 2015.
- [2] A. C. Long, *Design and manufacture of textile composites*, CRC PRESS, 2005.
- [3] J. Chen and W. Chen, Central crack tearing testing of laminated fabric uretek3216lv under uniaxial and biaxial static tensile loads. *J. Mate. Civ. Eng.*, (2016) **28**:(7), 04016028
- [4] J. B. Pargana, D. Lloyd-smith and B. A. Izzuddin, Advanced material model for coated fabrics used in tensioned fabric structures. *Eng. Struct.*, (2007) **29**(7), 1323-1336.
- [5] Y. Li, Study and application on mechanical properties of membrane material and structures. *Tongji University*, 2007.
- [6] W. Kang, Y. Suh, K. Woo and I. Lee, Mechanical property characterization of film-fabric laminate for stratospheric airship envelope. *Compos. Struct.*, 2006 **75**(1-4), 151-155.
- [7] R. Blum and H. Bögner-Balz, Evaluation method for the Elastic Moduli. [http://www.tensient.com/files/TenSiNet\\_Publications/TensiNews3\\_2002\\_09-1.pdf](http://www.tensient.com/files/TenSiNet_Publications/TensiNews3_2002_09-1.pdf). (2002)
- [9] MSAJ (Membrane Structures Association of Japan), M-02-1995 Testing method for elastic constants of membrane materials. *Membrane Structures Association of Japan*, Tokyo, 1995.
- [10] B. Foster and M. Mollaert, European design guide for tensile surface structures, *Tensinet*, Germany, 2004.

## MECHANICAL PROPERTIES OF TECHNICAL COATED FABRICS UNDER AXIAL AND OFF-AXIAL TENSILE TESTS

ALEXEY A. KUSTOV\*, NIKOLAY A. MOKIN<sup>†</sup> AND ALEXANDER M. IBRAGIMOV<sup>††</sup>

\* Department of Metal and Timber Structures  
Moscow State University of Civil Engineering (National Research University)  
Yaroslavskoye shosse, 26, 129337 Moscow, Russian Federation  
e-mail: alexeykustov@outlook.com, web page: <http://www.mgsu.ru>

<sup>†</sup> Department of Structural and Theoretical Mechanics  
Moscow State University of Civil Engineering (National Research University)  
Yaroslavskoye shosse, 26, 129337 Moscow, Russian Federation  
e-mail: mokiavelli@mail.ru, web page: <http://www.mgsu.ru>

<sup>††</sup> Department of Metal and Timber Structures  
Moscow State University of Civil Engineering (National Research University)  
Yaroslavskoye shosse, 26, 129337 Moscow, Russian Federation  
e-mail: igasu\_alex@mail.ru, web page: <http://www.mgsu.ru>

**Key words:** technical coated fabrics, membrane structures, laboratory tests, numerical simulation, digital image correlation

**Summary.** In the paper, laboratory tests carried out by the authors with axial ( $0^\circ$  - warp,  $90^\circ$  - weft) and off-axial ( $15^\circ$ ,  $30^\circ$ ,  $45^\circ$ ,  $60^\circ$ ,  $75^\circ$ ) tensile and also with biaxial tensile with shear with different load ratios are described. The purpose of the research was to determine the mechanical properties of material used at numerical simulations of membrane structures. Two different types of a technical coated fabrics used in the experiments - with and without Preconstraint<sup>®</sup> technology. To measure the displacement and strain fields on the surface of specimens, the method of digital image correlation has been used. Numerical simulation of technical coated fabrics, imitating carried-out laboratory tests, has been executed with using of software program Ansys Workbench. It is revealed owing to analysis of results of numerical simulations that shear stresses make a significant contribution to the stress-strain state of material in off-axial and biaxial tensile with shear. The possibility of applying several classical criteria for fracture strength of composite materials in order to predict and evaluate the behavior of technical coated fabrics under load is shown.

### Introduction

Technical coated fabrics (further in the text – TCF) are used in membrane structures. From pneumojacks to inflatable rubber dams (figure 1), from tanks to rescue equipment, from coating roofs of large-span structures to air-supported structures (figure 2), from pneumatic formwork to aqua parks, from aerostats and airships to inflatable structures of furniture and advertising, etc. – some areas where membrane structures made of TCF are used.



Figure 1. Inflatable rubber dam



Figure 2. Air-supported structures («The Verde Dickey Dome»)

Increasing number of buildings and structures made from TCF around the world, and also in Russia (for example, the form of coating roofs on a metal frame for two stadiums for the 2018 FIFA World Cup) requires detailed research of the behavior of the material taking into account its complex stress-strain state (further in the text - SSS).

The purpose of the research was to determine the mechanical properties of TCF used at numerical modelling of membrane structures. Also, it was important to establish necessary and sufficient number of laboratory tests in order to predict complex SSS of TCF at numerical modelling of material in tensile structures.

Laboratory tests under axial uniaxial and biaxial tensile until recently were considered the main tests for the research of the mechanical properties of the material used in the modelling of TCF and the estimation of the SSS of the material in the membrane structures. As noted in many modern researches, for example in<sup>1</sup>, usually in analysis of tensile structures made from TCF, the shear modulus of the material is neglected. According some normative documents, in particular in the American standard<sup>2</sup>, shear stresses in a material are usually small compared to normal tensile stresses, and for simplicity of calculation the influence of the shear modulus can be neglected. In many works, the modelling of TCF and principal verification of strength are carried out without taking into account the shear modulus, neglecting shear stresses, which in some cases leads to an overestimated strength of the material.

Recent reports have shown the importance of taking into account the shear modulus in the design of membrane structures made from TCF<sup>3-8</sup>. In work<sup>3</sup> it is said that the shear modulus of the material essentially affects the SSS tensile structures. For example, in inflatable beams or "Tensairity" type structures in which large shear deformations occur, taking into account the shear modulus contributes significantly to the accuracy of the structural behavior evaluation under load. Therefore, the research of the mechanical properties of the material, based only on the results of uniaxial and biaxial axial tensile tests, is not always sufficient for modelling a TCF in membrane structures. This is due both to the complex structure of the composite material and the features of the SSS of tensile structures.

Usually, the shear modulus is determined in the "pure shear" tests. This type of laboratory testing of TCF is researched well enough in the following works<sup>8-15</sup>. In work<sup>5</sup>, the possibility of determining the shear modulus from the test data under uniaxial off-axial tensile is shown. However, the material is assumed to be linearly elastic, which is only valid after applying

several load cycles and in the range up to 20% of the ultimate tensile strength (further in the text - UTS).

### Laboratory tests

In the paper, laboratory tests carried out by the authors with axial ( $0^\circ$  - warp,  $90^\circ$  - weft) and off-axial ( $15^\circ$ ,  $30^\circ$ ,  $45^\circ$ ,  $60^\circ$ ,  $75^\circ$ ) tensile and also with biaxial tensile with shear with different load ratios are described.

The test equipment was a biaxial tensile machine. To manage the experimental equipment and read the results, a specialized program STRAIN v1.0 was used.

In the laboratory tests, it was used TCF of the French company Serge Ferrari (402 Precontraint<sup>®</sup>) and the German company Mehler (Polymar 8212). Technical characteristics of the materials under study according to the manufacturer's data are presented in table 1. TCF 402 Precontraint<sup>®</sup> was manufactured with Precontraint<sup>®</sup> technology (the balanced and constant tension of the warp and weft threads before applying the polymer coating to the textile base), that is the main difference. It is known and investigated in many works that TCF manufactured with Precontraint<sup>®</sup> technology are less deformative in the direction of the weft threads than in the case of the material without the Precontraint<sup>®</sup> technology. Such comparison has been shown in work<sup>16</sup>.

Table 1. Specifications of tests materials

Type of TCF	Weight, g/m <sup>2</sup>	Thickness, mm	Type of weaves	UTS, N / 5 cm (warp / weft)
Polymar 8212 (Mehler )	650	0.5	Panama 2/2	2500 / 2500
402 Precontraint <sup>®</sup> (Serge Ferrari)	490	0.4	Panama 2/2	2500 / 2500

To measure the displacement and strain fields of the material, as well as to calculate the Poisson's ratio, the method of digital image correlation was chosen. This method has been successfully applied in many works in laboratory tests of TCF, for example, in articles<sup>4,8,17</sup>. GOM Correlate 2016 software was used for data processing.

*Uniaxial axial tests.* The preparation of specimens and the test procedure was carried out in accordance with GOST 30303-95 "Fabrics coated with rubber or plastic. Determination of breaking strength and elongation at break". Laboratory tests of TCF under uniaxial axial tensile were carried out before the specimens were fracture at a constant speed of 100 mm/min. On surface of the material, black paint was sprayed in order to use the optical method of digital image correlation.

By results of laboratory tests under uniaxial axial tensile (table 2), one can speak of satisfactory convergence between the UTS of the material obtained in experiments and the standard values given in the technical catalogs of the TCF. A difference approximately 20% in the direction of the weft threads in both types of TCF can be explained in the following ways:

- inevitable errors in the conduct of laboratory tests;
- possible overstating of the tensile strength of the TCF in the direction of the weft threads by the material producers.

Table 2. Comparison of the UTS TCF

	UTS, N / 5 cm	Polymar 8212	402 Preconstraint®
Warp	Normative value	2500	2500
	Experiment	2444.12	2283.74
<b>Difference</b>	<b>%</b>	<b>2.23</b>	<b>8.65</b>
Weft	Normative value	2500	2500
	Experiment	1975.82	2014.31
<b>Difference</b>	<b>%</b>	<b>20.97</b>	<b>19.43</b>

*Uniaxial off-axial tensile.* Off-axial is understood as test under uniaxial tensile test, in which the load application direction does not coincide with the direction of the main axes of the TCF (warp and weft yarns). For this purpose, the specimens in the form of rectangular strips or dumbbells are cut at a certain angle to the direction of the warp threads.

Normative documents by techniques of carrying out tests of TCF under uniaxial off-axial tensile are absent. The correct shape of the specimen was found by the results of preliminary experiments, which included a series of tests of various forms of material under uniaxial off-axial tensile. The main criterion for the quality of the found form of the specimen were the types of failure mechanism. Three main types of TCF fracture are distinguished in the case of off-axial tensile: even fracture (pure tensile failure), yarns pulled out (pure shear failure) and mixed fracture (mixed failure of tensile and shear)<sup>5,6</sup>.

All these types of fracture were obtained in a dumbbell specimen with dimensions of the central part of the specimen of 20x100 mm (figure 3). The shape of the material under uniaxial off-axial tensile tests is consistent with<sup>6</sup>, which uses a dumbbell specimens with similar dimensions and also shows three main types of TCF failure.

The material was tensile at a constant speed of 100 mm/min. The tests were carried out before the specimens were fracture. Under uniaxial off-axial tensile, method of digital image correlation could not be applied due to with the twisting of specimens, which already appeared at the very beginning of the experiment, which is explained by the peculiarity of the structure of the TCF.

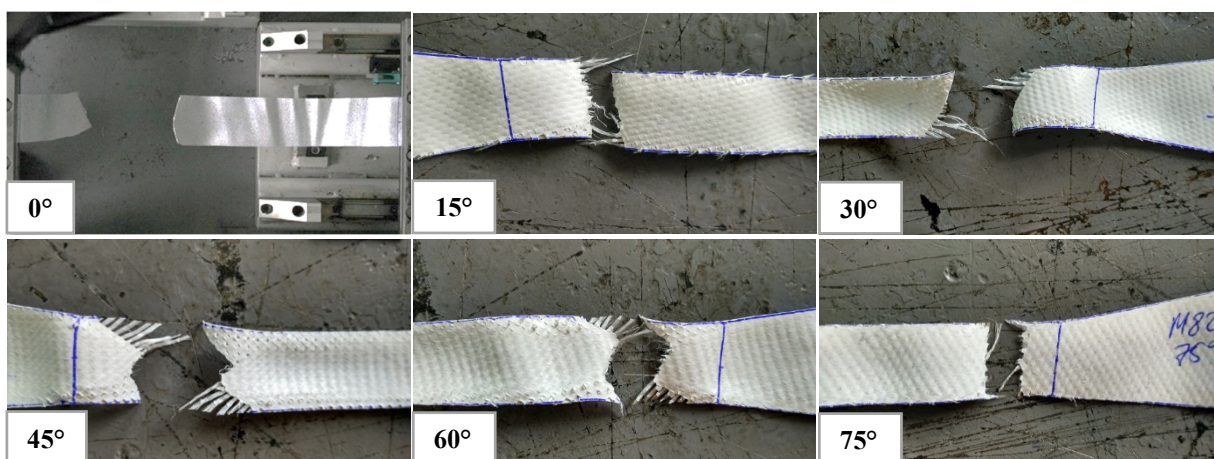


Figure 3. Three main types of TCF fracture: even fracture (0°, 15°, 75°), yarns pulled out (45°), mixed fracture (30°, 60°)

*Biaxial tensile with shear.* There are no domestic standards for laboratory tests under biaxial tensile of TCF yet. The foreign normative documents regulating and describing tests under biaxial tensile of TCF are the following: the Japanese standard<sup>18</sup>, the American standard<sup>2</sup>, the European design guide<sup>19</sup>.

The specificity of the laboratory tests carried out by the author consisted in the fact that the tests were carried out under biaxial tensile with shear. This is due to the fact that SSS of TCF in different membrane structures is complex. In particular, with wind influences on the structure, often the directions of the principal stresses in the TCF do not coincide with the principal axes of the material (directions along the warp and weft threads), which inevitably leads to the appearance of shear stresses. Usually, the influence of the shear modulus is neglected, which simplifies the SSS of the orthotropic material, however, it does not always reflect the real picture of stresses and strains distribution in the TCF.

In the work<sup>20</sup>, the material was studied not only under axial and off-axial uniaxial tensile, but also under off-axial biaxial tensile. The importance of such studies is shown, the results of experiments are presented and valuable conclusions in the end of the work are given.

Due to some characteristics of the tensile machine, the overall dimensions of the specimens were 400x400 mm. Next, a specimen was cut out in the form of a cross with an area of 80x80 mm in the center, the arm width has been 80 mm. The distance between the grips was 240 mm and 50 mm from each side are required for the grips of the testing machine. Two grips of the test equipment were stationary, the other two were moving at a constant speed of 100 mm/min. The tests were carried out before the specimens were fracture.

As well as in work<sup>21</sup>, two different types of material specimens have been chosen and tested: with cuts (type A) and without them (type B). The idea was to avoid the effect of transverse deformation on the material SSS. It was found that stress-strain curves of two different types (type A and B) of the TCF specimens are qualitatively and quantitatively almost identical, which agrees with the results of<sup>21</sup>. Figure 4 shows the measurement of displacement fields on the surface of two different types of specimens by the method of digital image correlation.

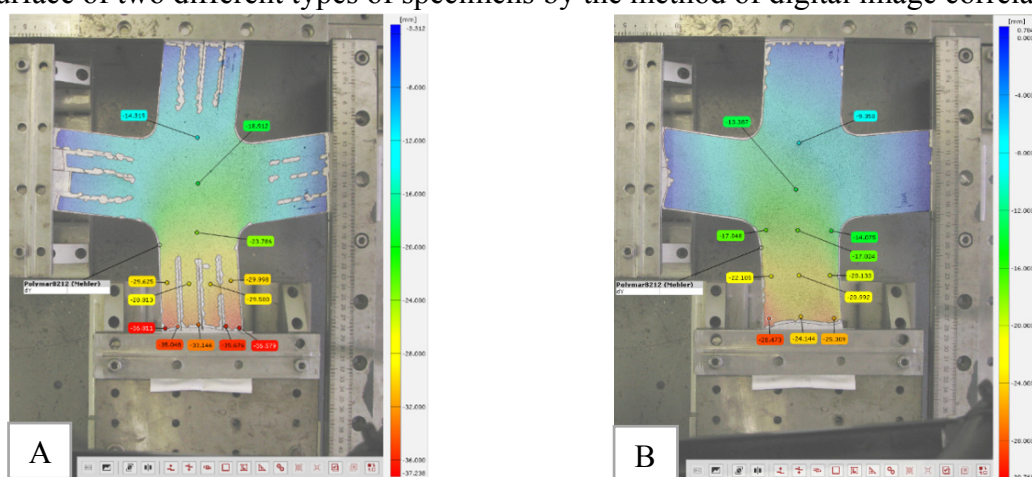


Figure 4. Measurement of the displacement fields on the surface of the specimen along the direction of the weft threads under biaxial tensile tests with shear of two types of specimens (type A and B)

The fracture of specimens occurred at the most intense point of material (figure 5), namely in places of concentration of the largest normal and shear stresses. It should be noted that shear stresses contributed approximately 15-25% of the total strength of the material.

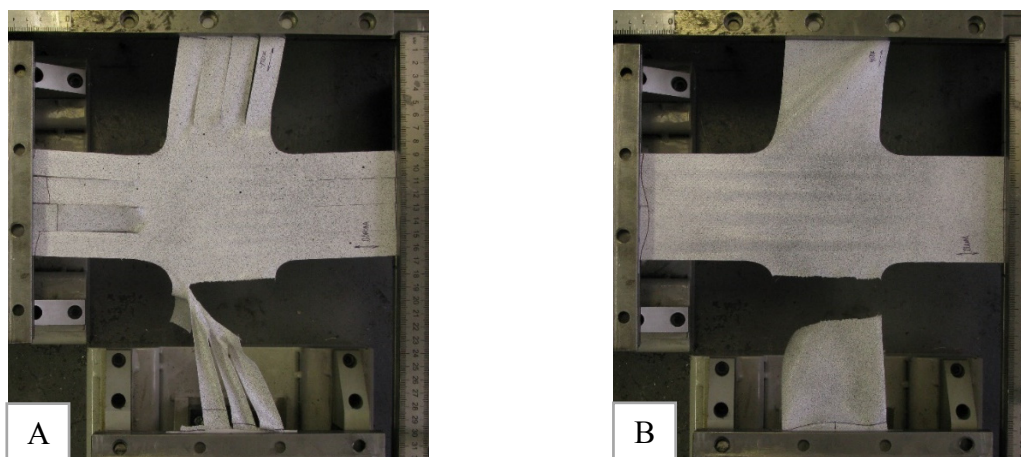


Figure 5. Fracture of specimens (type A and B) under biaxial tensile tests with shear

In laboratory tests, the ratio of modules of elasticity and Poisson's ratios for biaxial SSS was not observed. In the relation given in<sup>2</sup> for linear orthotropic material in biaxial SSS, it is necessary to introduce the coefficient  $K$ :

$$\frac{\nu_{fw}}{E_f} = K \frac{\nu_{wf}}{E_w} \quad (1)$$

where  $w$  – direction along warp threads,  $f$  – direction along weft threads.

In one article<sup>22</sup>, this coefficient is approximately equal to 0.6, in another paper<sup>23</sup> - 0.14. In our case, in laboratory tests under biaxial tensile with shear with load ratio 1:1, we obtained a coefficient  $K$  approximately equal to Polymar 8212 - 0.61, for 402 Preconstraint<sup>®</sup> - 0.82. It is noticeable that for a material with the Preconstraint<sup>®</sup> technology, the coefficient  $K$  is closer to 1.

By results of the carried-out laboratory tests stress-strain curves (figure 6 and 7) in which physically nonlinear and an orthotropic properties of the material is visually traced have been constructed. Engineering stresses are given in kN/m due to the fact that the mechanical properties of the TCF are not proportional to their thickness<sup>8</sup>.

Figure 8 shows the nonlinear dependence of the Poisson's ratio on the stress along the direction of the warp and weft yarns in two different types of TCF: with and without Preconstraint<sup>®</sup> technology.

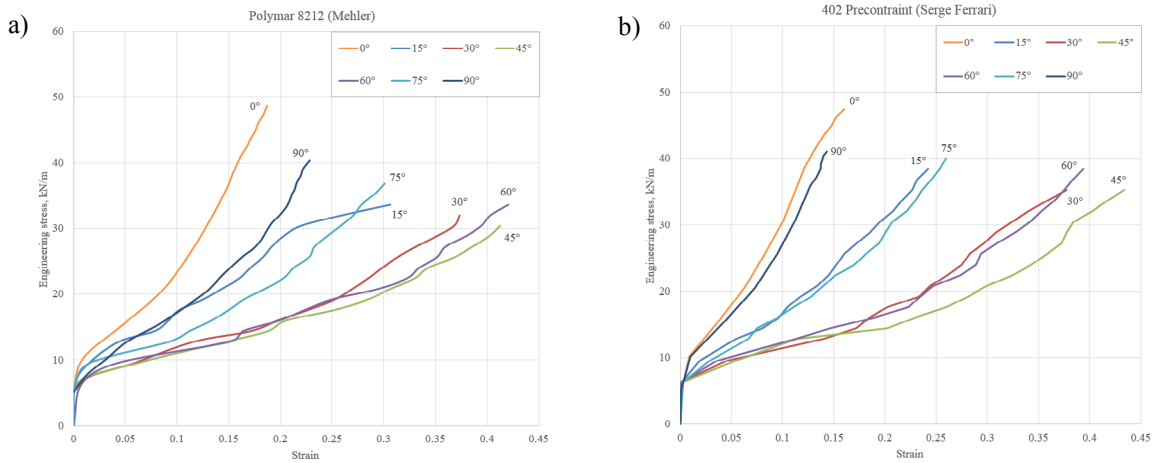


Figure 6. Stress-strain curves under uniaxial axial and off-axis tensile tests:  
a) Polymar 8212, b) 402 Preconstraint®

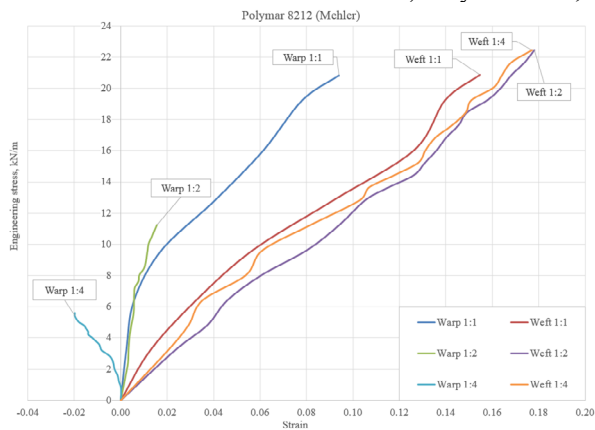


Figure 7. Stress-strain curves under biaxial tensile with shear with different load ratios for Polymar 8212

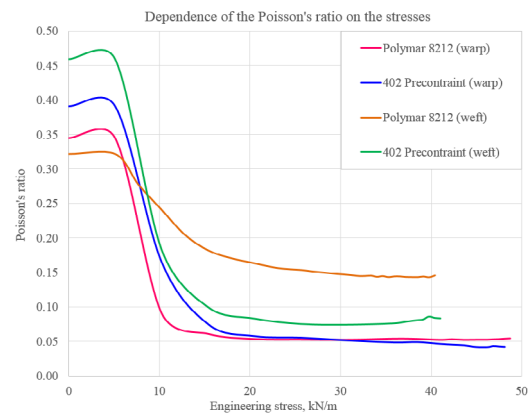


Figure 8. Dependence of the Poisson's ratio on stress under uniaxial axial tests

### Numerical simulations

The numerical simulations, imitating the carried-out laboratory tests, have been executed in Ansys Workbench. In numerical simulations under uniaxial axial tensile tests, the material was assumed isotropic and physically nonlinear that was considered by means of curve plasticity, which was set in the form of multilinear isotropic hardening. However, in numerical simulations of uniaxial off-axis and biaxial tensile with shear material must be specified as orthotropic and physically nonlinear. Modelling physically nonlinear orthotropic (a particular case of nonlinear anisotropic) materials is not a simple task.

To take into account the physically nonlinear orthotropic material, an anisotropic plasticity model was chosen that uses the Hill's yield criterion, taking into account the differences in yield stress in orthogonal directions. According to the Ansys manual<sup>24</sup>, the necessary six constants were calculated and necessary command APDL was registered in Ansys Workbench to take into account the anisotropic plasticity model. The analysis was performed taking into account the geometric nonlinear (large deflection).

TCF can only resist tensile load, almost without any flexural resistance. Therefore, in numerical simulations, the element type SHELL181 with a membrane option was used, which assumes that the element has only membrane stiffness. According to Ansys<sup>25</sup>, in numerical simulations with geometric nonlinear (large deflection) and with a membrane option in the elements of SHELL181 type, it is recommended to use the triangular shape of the element as more reliable. The load was set by the compelled displacement, simulating the carried-out laboratory tests.

The analysis of the work on the study of the shear modulus in a TCF showed that it can be taken with a sufficient accuracy linear. In articles<sup>4,5,7,8,17,26–28</sup> the value of the shear modulus of a TCF varies on average from 20 to 60 kN/m. In this work, the value of the shear modulus in the TCF was found in numerical simulations and amounted to 25 kN/m for the Polymar 8212, and 28 kN/m for the 402 Preconstraint<sup>®</sup>.

Convergence between laboratory tests and numerical simulations was determined:

- in numerical simulations – fracture of the specimens (maximum stress), coinciding with the place of fracture of TCF in laboratory tests (figure 9);
- on the qualitative and quantitative convergence of the "force-displacement" curves, obtained both in laboratory tests and in numerical simulations (figure 10 and 11);
- stresses in the TCF equal to the ultimate stresses, which were determined from the UTS of the material given in table 1 of this work.

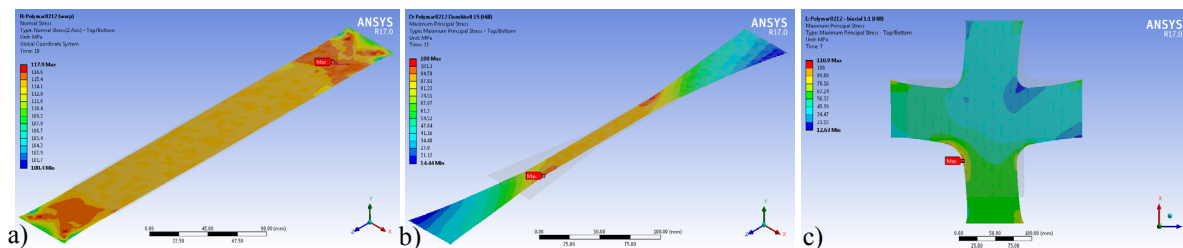


Figure 9. SSS of TCF Polymar 8212 in numerical simulations: a) under uniaxial axial tensile, b) under uniaxial off-axis tensile of the specimen 15°, c) under biaxial tensile with shear with load ratios 1:1

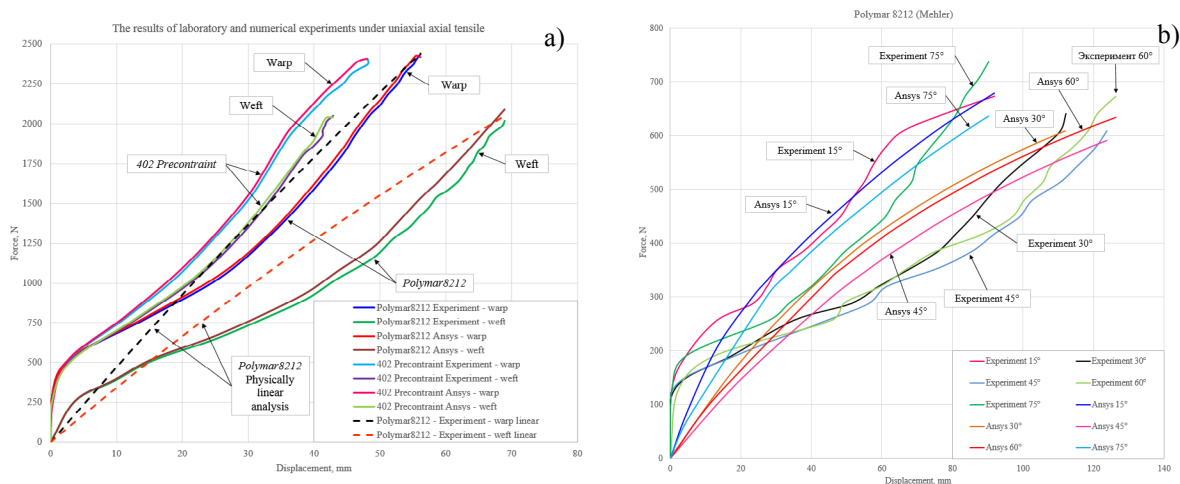


Figure 10. Comparison of the results laboratory tests and numerical simulations of TCF: a) under uniaxial axial tensile tests Polymar 8212 and 402 Preconstraint<sup>®</sup>, b) under uniaxial off-axis tensile tests Polymar 8212

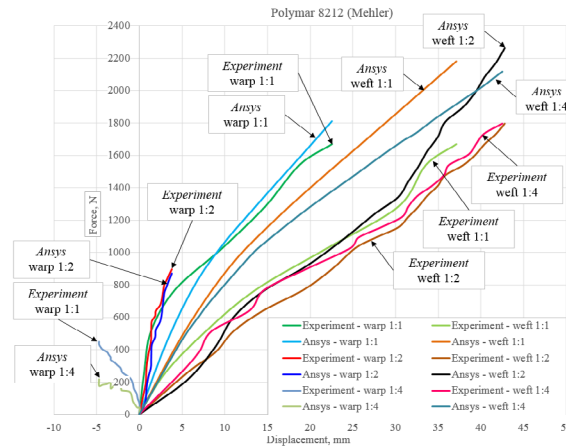


Figure 11. Comparison of the results laboratory tests and numerical simulations of TCF under biaxial tensile tests with shear with different load ratios Polymar 8212

### Strength criterion

At structures analysis, made from TCF, mechanical properties directed along the thickness of the material are always ignored, i.e. material work only in plane SSS is supposed. In this regard, some strength criteria of composite materials can be applied to TCF.

Here, several classical strength criteria are chosen to predict the UTS in numerical simulation under uniaxial off-axial tensile tests and estimates the factor of safety of a TCF under biaxial tensile with shear:

$$\text{Tsai-Hill: } \frac{\sigma_x^2}{X^2} + \frac{\sigma_y^2}{Y^2} - \frac{\sigma_x \sigma_y}{X^2} + \frac{\tau_{xy}^2}{S^2} = 1 \quad (2)$$

$$\text{Yeh-Stratton: } \frac{\sigma_x}{X} + \frac{\sigma_y}{Y} - \frac{\sigma_x \sigma_y}{X^2} + \frac{\tau_{xy}^2}{S^2} = 1 \quad (3)$$

$$\text{Hashin: } \left( \frac{\sigma_{11}}{X} \right)^2 + \left( \frac{\tau}{S} \right)^2 = 1 \quad (4)$$

$$\text{Norris: } \left( \frac{\sigma_x}{X} \right)^2 + \left( \frac{\sigma_y}{Y} \right)^2 - \frac{\sigma_x \sigma_y}{XY} + \frac{\tau_{xy}^2}{S^2} = 1 \quad (5)$$

where  $\sigma_x$  and  $\sigma_y$  are the normal stress in warp and weft,  $\tau$  – is the shear stress,  $X$  and  $Y$  – are the UTS in warp and weft, and  $S$  is the shear strength.

Figure 12 shows comparison of the UTS under uniaxial axial and off-axial tensile tests TCF between laboratory tests and numerical modelling with physically linear and physically nonlinear material model (anisotropic plasticity model), as well as predicting of the UTC by the Tsai-Hill strength criterion.

In table 3 shows a comparison between factors of safety calculated from the results of laboratory tests and determined using different strength criteria in numerical simulations. Factor of safety is the ratio of the technical characteristic UTS TCF to the breaking force obtained in the laboratory tests at the time of fracture material.

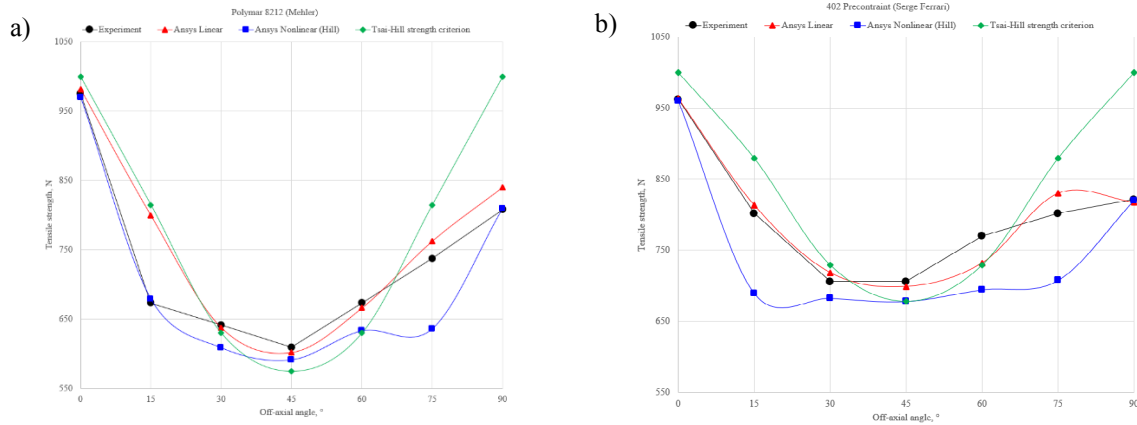


Figure 12. Comparison of the UTS TCF under uniaxial axial and off-axis tensile tests: a) Polymar 8212, b) 402 Precontraint®

Table 3. Comparison factor of safety by different strength criteria

Laboratory tests under biaxial tensile with shear for Polymar 8212					
Load ratios	Strength criteria / Factors of safety				
	Experiment	Tsai-Hill	Yeh-Stratton	Hashin	Norris
1:1	2.46	2.19	2.56	2.09	2.19
1:2	2.23	2.02	2.38	1.63	2.02
1:4	2.23	1.97	2.31	1.61	1.97

It can be seen that in a complex SSS (under biaxial tensile with shear), the TCF has a much smaller UTS than the UTS presented in the technical catalogs for the material. Also, in laboratory tests under uniaxial off-axis tensile, it is seen that the UTS decrease with increasing load angle to the warp yarns. The specimen of 45° have a 35-50% lower UTS that the UTS of TCF specimens under uniaxial axial tensile (specimens 0° and 90°).

Figure 13 shows factors of safety at Yeh-Stratton strength criterion in numerical simulations under biaxial tensile tests with shear with different load ratios.

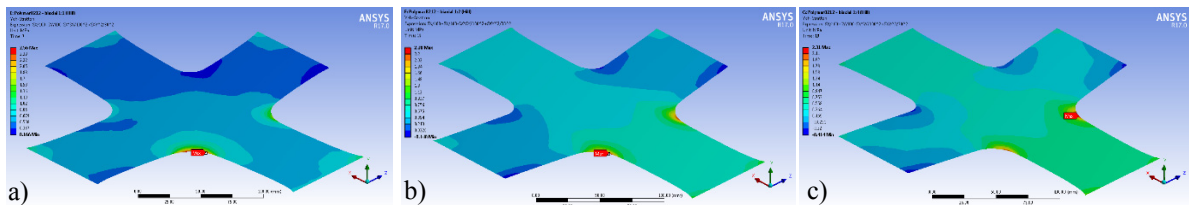


Figure 13. Factors of safety in numerical simulations of TCF Polymar 8212 under biaxial tensile tests with shear with different load ratios : a) 1:1, b) 1:2, c) 1:4

## Conclusions

*The most important findings of the research in laboratory tests:*

- the optical method of digital image correlation was the most suitable for measuring displacement and strain fields on the surface of the specimen in laboratory tests under uniaxial and biaxial tensile with shear;

- a TCF is an orthotropic and physically nonlinear material and the Poisson's ratio is not a constant that is consistent with the results of other researchers;
- shape of the specimen was revealed, which allows to determine correctly the mechanical properties of TCF under uniaxial off-axial tensile;
- found necessary and sufficient number of laboratory tests to determine the main mechanical properties used in modelling structures made from TCF.

*We got following results in numerical simulations:*

- satisfying quantitative and qualitative convergence between the results of laboratory tests and numerical simulations with a nonlinear material model was shown;
- shear stress make a significant contribution to the SSS of a TCF under uniaxial off-axial tensile;
- the Tsai-Hill strength criterion is suitable enough for prediction of the UTS TCF under uniaxial axial and off-axial tensile tests, except the specimens of 15° and 75°, which is explained by the peculiarities of the structure of TCF;
- the Yeh-Stratton strength criterion is quite suitable for estimating the factor of safety under biaxial tensile with shear with different load ratios.

*The following research tasks:*

- to find the most suitable nonlinear material model for describing of complex SSS;
- to perform laboratory test of tensile structures made from a TCF and numerical simulations with a nonlinear material model.

## REFERENCES

- [1] Beccarelli, P. Biaxial Testing for Fabrics and Foils: Optimizing Devices and Procedures. 9–34 (2015). doi:10.1007/978-3-319-02228-4
- [2] *ASCE/SEI55-10. Tensile membrane structures*. (ASCE standard. USA: American Society of Civil Engineers, 2010).
- [3] Galliot, C. & Luchsinger, R. H. The shear ramp: A new test method for the investigation of coated fabric shear behaviour - Part I: Theory. *Compos. Part A Appl. Sci. Manuf.* **41**, 1743–1749 (2010).
- [4] Galliot, C. & Luchsinger, R. H. The shear ramp: A new test method for the investigation of coated fabric shear behaviour - Part II: Experimental validation. *Compos. Part A Appl. Sci. Manuf.* **41**, 1750–1759 (2010).
- [5] Chen, S., Ding, X. & Yi, H. On the Anisotropic Tensile Behaviors of Flexible Polyvinyl Chloride-coated Fabrics. *Text. Res. J.* **77**, 369–374 (2007).
- [6] Zhang, L. Off-Axial Tensile Properties of Preconstraint PVDF Coated Polyester Fabrics under Different Tensile Rates. *Adv. Mater. Sci. Eng.* **2016**, 1–12 (2016).
- [7] Gosling, P. D. *et al.* Analysis and design of membrane structures: Results of a round robin exercise. *Eng. Struct.* **48**, 313–328 (2013).
- [8] Colman, A. G., Bridgens, B. N., Gosling, P. D., Jou, G. T. & Hsu, X. Y. Shear behaviour of architectural fabrics subjected to biaxial tensile loads. *Compos. Part A Appl. Sci. Manuf.* **66**, 163–174 (2014).
- [9] Willems, A., Lomov, S. V., Verpoest, I. & Vandepitte, D. Optical strain fields in shear and tensile testing of textile reinforcements. *Compos. Sci. Technol.* **68**, 807–819 (2008).

- [10] Lin, H., Clifford, M. J., Long, A. C. & Sherburn, M. Finite element modelling of fabric shear. *Model. Simul. Mater. Sci. Eng.* **17**, 15008 (2009).
- [11] Launay, J., Hivet, G., Duong, A. V. & Boisse, P. Experimental analysis of the influence of tensions on in plane shear behaviour of woven composite reinforcements. *Compos. Sci. Technol.* **68**, 506–515 (2008).
- [12] Kato, S., Yoshino, T. & Minami, H. Formulation of constitutive equations for fabric membranes based on the concept of fabric lattice model. *Eng. Struct.* **21**, 691–708 (1999).
- [13] Peng, X. Q. & Cao, J. A continuum mechanics-based non-orthogonal constitutive model for woven composite fabrics. *Compos. Part A Appl. Sci. Manuf.* **36**, 859–874 (2005).
- [14] Skelton, J. Fundamentals of fabric shear. *Text. Res. J.* **46**, 862–869 (1976).
- [15] Penava, Ž., Penava, D. Š. & Nakić, M. Woven Fabrics Behavior in Pure Shear. *J. Eng. Fiber. Fabr.* **10**, 114–125 (2015).
- [16] Zhang, Y., Zhang, Q. & Lv, H. Mechanical properties of polyvinylchloride-coated fabrics processed with Preconstraint (R) technology. *J. Reinf. Plast. Compos.* **31**, 1670–1684 (2012).
- [17] Dinh, T. D. *et al.* A new elasto-plastic material model for coated fabric. *Eng. Struct.* **71**, 222–233 (2014).
- [18] *MSAJ/M-02:1995 Testing method for elastic constants of membrane materials.* (Membrane Structures Association of Japan, 1995).
- [19] Forster, B. & Marijke, M. European Design Guide for Tensile Surface Structures. 332 (2001).
- [20] Yingying, Z., Xiaoguang, S., Qilin, Z. & Henglin, L. Fracture failure analysis and strength criterion for PTFE-coated woven fabrics. *J. Compos. Mater.* **49**, 1409–1421 (2015).
- [21] Ambroziak, A. & Klosowski, P. Mechanical properties for preliminary design of structures made from PVC coated fabric. *Constr. Build. Mater.* **50**, 74–81 (2014).
- [22] Chen, J. *et al.* Mechanical Behaviors and Elastic Parameters of Laminated Fabric URETEK3216LV Subjected to Uniaxial and Biaxial Loading. *Appl. Compos. Mater.* 1–30 (2017). doi:10.1007/s10443-016-9576-2
- [23] Gosling, P. D. & Bridgens, B. N. Computational Mechanics – A New Philosophy For. **23**, 215–232 (2008).
- [24] ANSYS Inc. ANSYS Mechanical APDL Material Reference. (2011).
- [25] ANSYS Inc. ANSYS Mechanical APDL Element Reference. (2012).
- [26] Bridgens, B. N., Gosling, P. D., Jou, G.-T. & Hsu, X.-Y. Inter-laboratory comparison of biaxial tests for architectural textiles. *J. Text. Inst.* **103**, 706–718 (2012).
- [27] Bridgens, B. N., Gosling, P. D. & Birchall, M. J. S. Tensile fabric structures: Concepts, practice & developments. *Struct. Eng.* **82**, 21–27 (2004).
- [28] Vysochina, K. Identification of Shear Stiffness of Soft Orthotropic Textile Composites: Part I - Development of a Mixed Method for Shear Elastic Constant Identification. *J. Ind. Text.* **35**, 137–155 (2005).

# Fracture failure analysis and bias tearing strength criterion for PVDF coated bi-axial warp knitted fabrics

Jianwen Chen<sup>\*†</sup>, Wujun Chen<sup>†</sup>, Mingyang Wang<sup>†</sup>, Bo Yao<sup>\*</sup>, Han Zhou<sup>\*</sup>, Bing Zhao<sup>†</sup>, Jianhui Hu<sup>†</sup>

<sup>\*</sup> School of Science, Nanjing University of Science and Technology, Nan Jing 210094, P.R. China [jianwench@yeah.net](mailto:jianwench@yeah.net) or [jianwench@njust.edu.cn](mailto:jianwench@njust.edu.cn)

<sup>†</sup> Space Structures Research Center (SSRC), Shanghai Jiao Tong University, Shanghai 200030, P.R. China [cw@sjtu.edu.cn](mailto:cw@sjtu.edu.cn)

<sup>+</sup> School of Mechanical Engineering, Nanjing University of Science and Technology, Nan Jing 210094, P.R. China

## ABSTRACT

This paper concerns the fracture failure and bias tearing strength criterion for a PVDF coated bi-axial warp knitted fabrics (BWKFs) widely used in air supported membrane structures (ASMSs). Central slit tearing tests were carefully conducted on bias specimens with seven off-axis angles, and the corresponding tearing properties, including failure behaviors and tearing strength criterion were discussed. Results show that coated bi-axial warp knitted fabrics are typical direction-dependent materials, and their tearing characteristics vary greatly with the bias angles. Typical tearing stress-displacement curves of bias samples could exhibit four characteristic regions: a co-deformation region, a shear deformation region, a plateau region, and a post peak region. No matter what the orientation of the initial slit or the yarn is, the propagation is always parallel to the secondary yarns. For specimens with different bias angles, some obvious differences in tearing behaviors are observed in terms of maximum displacement, damage mode, curve slope, and number of stress peaks, and these differences could be attributed to the material orthotropy and different failure mechanism of constituent materials. Unlike results of tensile strength for most of woven fabrics, for the studied BWKF composite, there is a W-shaped relationship between tearing strength and bias angle, with a local strength peak at 45° angle. The new tearing strength criterion proposed in the prior research is validated due to the strong agreements between the calculated and experimental results for the BWKF.

**Keywords:** Bi-axial warp knitted fabrics, Tearing strength, Bias angle, Propagation, Criterion, Air supported structures

## Introduction

Biaxial warp knitted fabric (BWKFs), a kind of non-crimp fabrics (NCF), is considered as one of the most important structural materials in pneumatic structures, which attract widespread attention [1, 2, 3]. A slit or a defect in coated fabrics may lead to the material fracture, and even cause the major collapse of the air supported membrane structures (ASMSs) under some severe conditions, e.g. high pressure of the internal air, strong wind, and heavy snow. Due to the significant effects of a slit or a defect on the material fracture development, the evaluation of the tearing strength of BWKFs with an existed slit is critical to the design and analysis of air supported structures.

The studying of tear propagation is an important subject due to its use in industrial applications. For instance, Krook and Fox [4] already discussed in 1945 the tongue tearing behaviors and described the del-shaped opening observed in the tearing damage. In the last several decades, this topic has received even more attention due to the increasing use of composite materials. Several kinds of tear methods are proposed and used to study the tearing behaviors of dry fabrics and coated (or laminated) fabrics. Some are in plane, such as trapezoidal tear method [5-9], central slit tear method [10-13], single edge notch tear method [14] and wing-shaped tear method [15-16], while other are out of plane, such as tongue tear method [17-20] and lounge-shaped tear method [15]. To date, the methods most widely used in tearing investigations of fabrics are the trapezoidal, central slit, and tongue tear methods, which have been adopted by some design code or guide [21,22]. The sample configurations of these tearing test methods can be found in Forster et al.[25], Ennouri et al. [23], and Huntington[24].

The trapezoidal tear method forming the basis of most design norms [22] has been studied extensively. Hager et al. [5], Turl [6], Chu et al. [7], Wang et al. [8], and Wang [9] conducted trapezoidal tearing tests, and some of them proposed analytical models to study the fracture failure and tearing strengths of the fabric materials. Tongue tearing behaviors of woven fabrics have also been investigated by many researchers through experimental and analytical approaches. For instance, Teixeira et al. [17], Scelzo et al. [18], Zhong et al. [19],

and Wang et al. [20] analyzed the contributions of structural parameters, including yarn type, weave pattern and weave structure, to the tongue tearing resistance of woven fabrics. For the central slit tear method, several investigations have been conducted on dry fabrics, coated or laminated fabrics. Godfrey et al. [11,12], Bigaud et al. [13], Maekawa et al. [10], and Chen et al. [25,26] investigated central slit tearing properties of woven fabrics by experimental or theoretical methods.

According to the aforementioned literatures, an experimental investigation is the main way to determine tearing behaviors of the woven fabrics and the data is often used as a standard for verifying the calculated results of the corresponding analytical or FEA models. Therefore, those tearing tests which can simulate the actual tear propagations in ASMSs are the most direct and effective means to determine tearing mechanism of coated fabrics. Among all the tear methods, the central slit tear method is considered to obtain closer tearing characteristics of the laminated fabrics to the engineering practice than the tongue, trapezoid, and wing tear methods in terms of the tension distribution and slit-opening shape. [21]

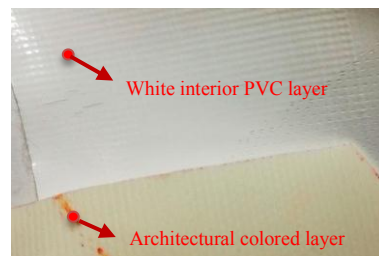
Proper design and analysis of membrane structures require a fundamental understanding of their mechanical behaviors [27], including the tear propagation, damage morphology and tearing mechanism. To the best of our knowledge, there are not enough studies focusing on the central slit tearing behaviors such as tearing stress-displacement relationships, tearing strength criterion, and damage morphology of coated fabrics for ASMSs.

Moreover, as the NCFs are typical direction-dependended materials, their characteristics vary greatly with the bias angles[28]. More researches are required to figure out how and to what extent the anisotropy and off-axis angle affect the tearing behaviors and tearing strength. Therefore, a series of central slit tearing tests were carefully conducted on bias specimens, and the corresponding tearing properties, including failure mechanisms and material strengths of a typical PVDF coated bi-axial warp knitted fabric were discussed. The findings would be of significant interest to the understanding on the tearing mechanism of laminated fabrics and to the structural safety assessment of membrane structures.

## Material and methods

### Materials

The envelope of ASMSs is made of coated bi-axial warp knitted fabrics. In this paper, the fabric material Shelter-Rite#8028 shown in Fig.1 consists of five functional layers, including the architectural colored layer (or wearable layer), white exterior PVDF layer, the structural layer, the blackout opaque layer, and the white interior PVC layer.



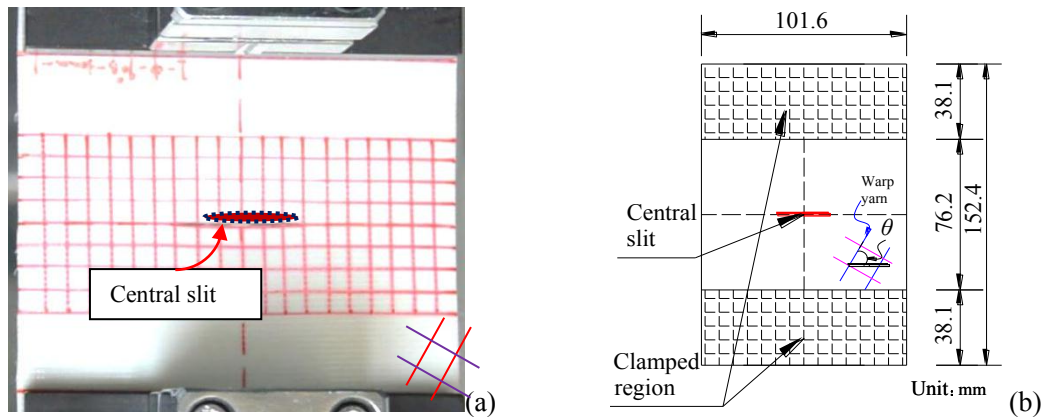
Nine and eight bundle counts per centimeter are laid in the warp and weft directions, respectively. This envelope fabric shows 950 g/m<sup>2</sup> areal density with a thickness of 0.70 mm, and is widely used in large and medium sized ASMSs. Specifications of the fabric material are listed in Table 1.

### Specimens

The uniaxial tearing tests were performed on rectangular specimens with a central slit. The photograph and geometrical dimension of tested samples which is based on the “airship design criteria” FAA-P-8110-2 [21] are illustrated by Fig.2. The shadow zones in the Fig.2(b) represent clamping areas in the upper and lower jaws, and the effective area of the specimen is 76.2×101.6 mm<sup>2</sup>. As shown in Fig.2(b), the slit was made by striking the fabric with a utility knife at an angle of 90° to the loading direction, and the off-axis samples were prepared by cutting the fabrics at the off-axis angles of 0°, 15°, 30°, 45°, 60°, 75°, and 90° from the warp direction. In other words, the tests of off-axis angles of 0° and 90° indicate the on-axial tearing tests in weft and warp directions respectively.

**Table 1.** Specifications of the envelope fabric

Variable	Mean value	Sample standard deviation	Coefficient of variability
Ultimate tensile strength (kN/m) (Warp)	71.8	2.87	0.040
Ultimate tensile strength (kN/m) (Weft)	64.5	4.78	0.074
Young modulus (kN/m) (Warp)	967.2	9.79	0.010
Young modulus (kN/m) (Weft)	558.5	8.53	0.015
Weave density (ends/1 cm) (warp × weft)	9 × 8	--	--
Areal density (g/m <sup>2</sup> )	950.0	--	--
Thickness (mm)	0.70	0.011	0.016
Hydrostatic resistance (MPa)	3.45	--	--

**Fig. 2.** The specimen of the central slit tearing tests:(a) photograph of the specimen;(b)geometrical dimension (mm).

All specimens were carefully fabricated along the yarn orientations, avoiding the loss of yarns. Coated fabrics are known to have a significant level of variability across the width of a single roll due to bowing or skewing of the fabric during manufacture [29]. For this work these effects were minimized by cutting the specimens from the center of the roll. At least three test samples for each test are conducted to guarantee the reliability of the results. The layout of the experimental protocol is shown in Table 2.

### Testing process

The uniaxial tearing tests were carried out on UTM-4000 tester. In order to reduce dynamic effects, the tensile speed was set up at 10 mm/min, which is a very low speed compared with those in conventional tensile tests. The initial tearing and the tear propagation of the specimens with different slit lengths were observed using a camera device.

**Table 2.** Layout of the experimental protocol.

Loading speed (mm/min)	Slit length $2l_c$ (mm)	Off-axis angle $\theta$ (°)	Number of specimens for each test	Total number of specimens
10	20 30	0 15	3	42
		30 45		
		60 75 90		

## Environmental conditions

All tests were done at a relative humidity of  $65 \pm 4.0\%$  and a temperature of  $20 \pm 2.0\text{ }^\circ\text{C}$  according to the ISO 139-2005 standard [30].

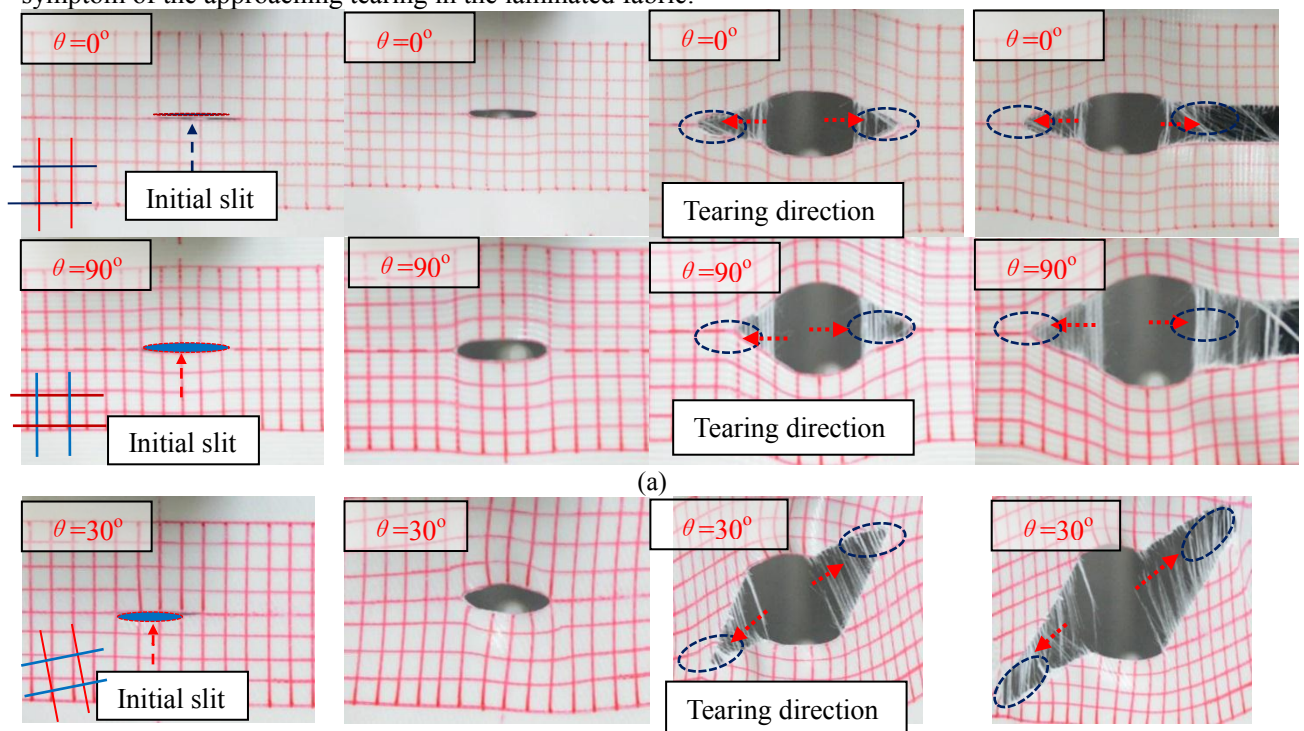
## Results and discussions

### Tearing properties

#### Failure performance and tearing propagation

**Similarities.** Typical tearing damage morphologies are shown in Fig.3 and Fig.4. Comparing these images in Fig.3 and Fig.4 shows that there are many similarities in the failure performance and tearing propagation of the studied materials. First, as the load increases, the initial slit progressively takes an elliptic shape and the inelastic deformation and yarn slippage start to occur in the vicinity of slit tips. These increasing deformation and slippage could lead to the formation of large deformation regions.

Second, as shown in Fig.3 and Fig.4, with the increasing of the uniaxial tensile force, two local tearing delta zones, i.e. the stress concentration regions, in which load bearing yarns have been pulled out of the adhesives by the concentrated tensile stresses, will take shape in the large deformation regions. The progressive delta zone of the tear tip develops gradually and the load bearing yarns break one by one at the tear tip. As shown in Fig.3, the failure of load bearing yarns in the delta zones is mainly due to direct tensile fracture. Here, the yarns in the delta zones can be generally divided into two categories: the principal and secondary yarns. Specifically, the load bearing yarns are the principal yarns and the non-load bearing yarns or less important yarns belong to the secondary ones. As the load increases, slippage on the principal yarns becomes more and more difficult, and thus the load is progressively delivered to the secondary yarns. The load transferred by the secondary yarns or other laminated layers ( including adhesives ) is delivered to other principal yarns again which are beyond the first intact yarn in the delta zone. And therefore, the pulled-out length of adjacent principal yarns increases and then the size of the delta zone is enlarged. As the load builds up further, some of the principal yarns fail once more and again yarns slip by each other to produce a new delta zone, and so on, in a cycle, until the failure extends over the length tested. For the uniaxial tests, in fact, the local delta zone is the symptom of the approaching tearing in the laminated fabric.



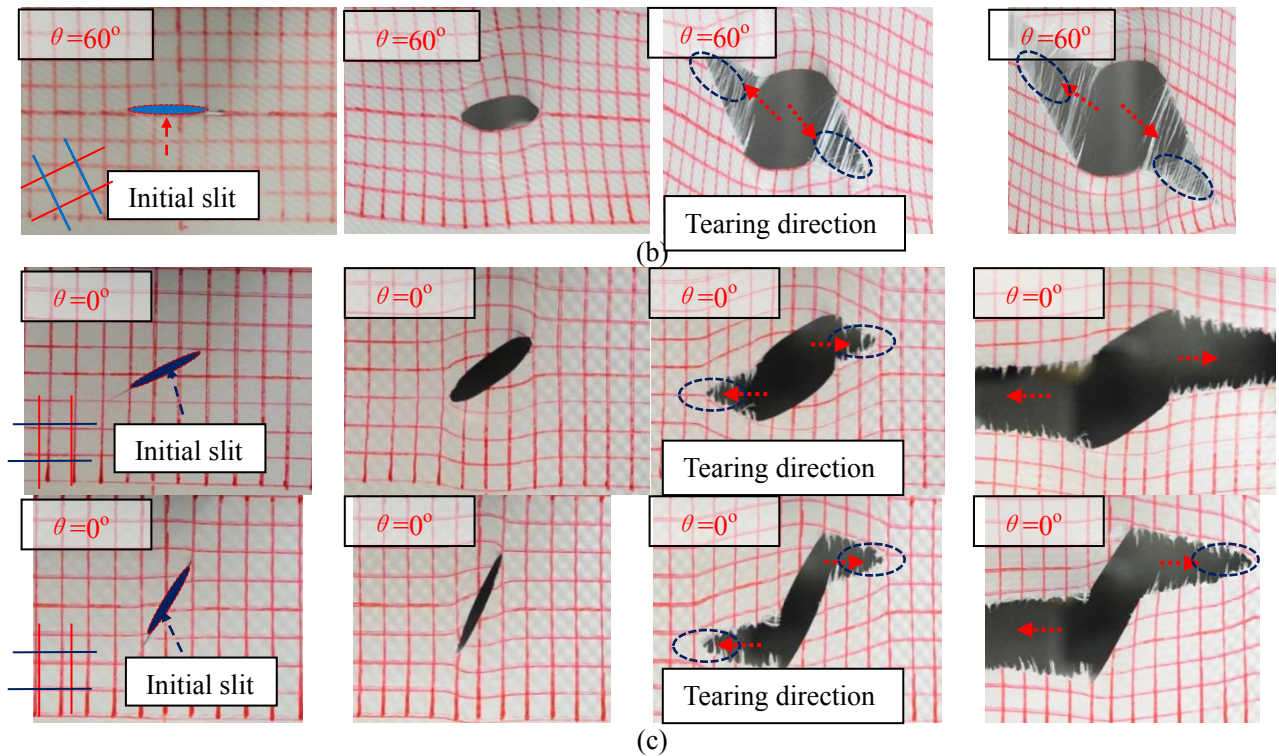


**Fig. 3.** Typical tear propagation processes of on-axial (a), off-axial samples (b) and inclined slits (c).

**Differences.** Nevertheless, some differences still exist between the tearing specimens with different slit parameters or yarn orientations.

The most significant is the slit-opening shapes due to the rotation of slit or yarns. As shown in Fig.4, the tearing of the envelope fabric could produce three kinds of appearance in terms of the orientation of the tear: line-shaped, Z-shaped, and parallelograms-shaped opening. Specifically, for on-axial specimens, a slit could result in a line-shaped opening or a Z-shaped opening depending on their slit orientation[28], whereas, for off-axial specimens, their slits could form parallelograms-shaped openings.

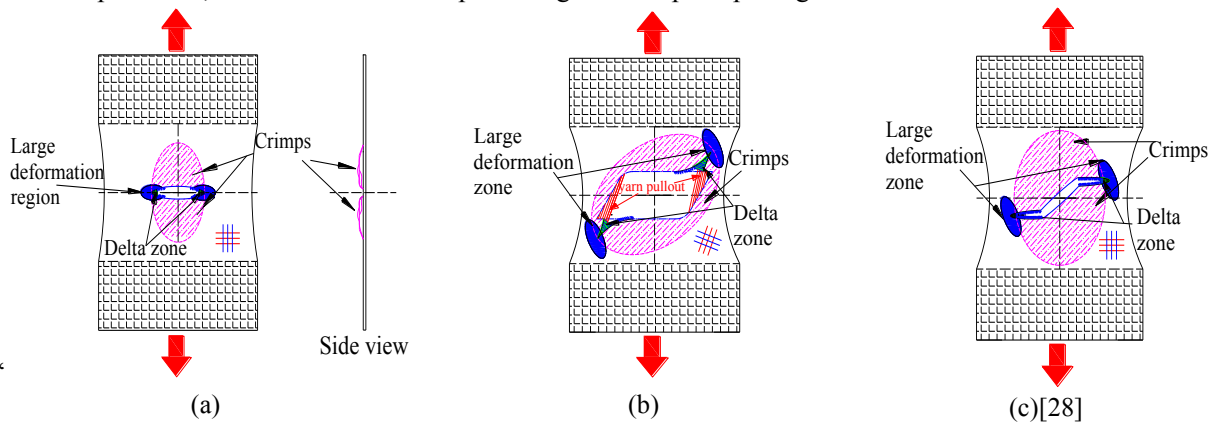


**Fig. 4.** Schematic drawings of typical damage modes of the tearing specimens: (a) line-shaped opening; (b) parallelograms-shaped opening; and (c) Z-shaped opening.

According to Bigaud et al. [13] and Chen et al. [26], the failure mode and the slit propagation direction can be mainly decided by these factors as follows:

- ✧ Slit equivalent length (related to the effective length and orientation),
- ✧ Loading ratios,
- ✧ Mechanical properties of the yarns in both directions,
- ✧ The orthotropy of the material.

Besides the factors mentioned above, the tearing failure of the envelope fabrics possibly involves a

variety of factors: yarn orientation (see Fig.5 ), specimen size and geometry, displacement versus load control, compliance of test fixture and test machine, etc. For example, the tear always propagates along the direction of yarns, as shown in Fig.5. As off-axis specimens could show great shear deformation and large area of yarn pullout, when the slit starts to propagate, these shear deformation and yarn pullout could absorb more energy and reduce the stress concentration in the yarns at the slit tip and, therefore, during the tests, most of the specimens failed in a progressive mode, and they exhibited progressive damages of the yarns and other functional layers before the failure of these specimens.

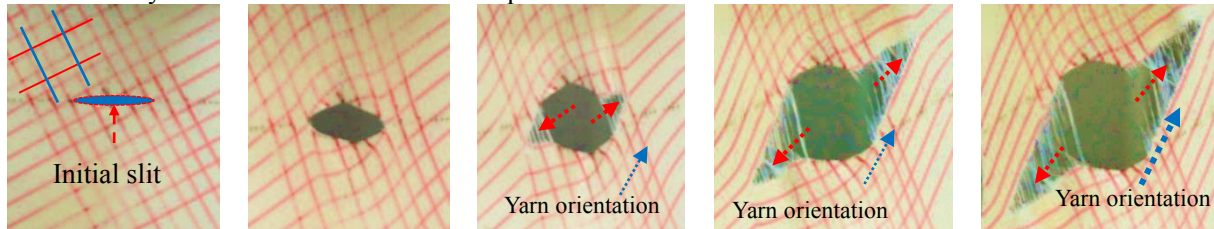


**Fig. 5.** The tearing propagation direction and the yarn orientation.

Fig.6 shows the typical damage modes of tearing specimens with different slit orientations and yarn orientations. Here, the results shown in Fig.6(a) is a summary of on-axial tearing tests with different slit orientations. It is obvious that for uniaxial tearing tests, whatever the orientation of the initial slit is, the propagation is always perpendicular to the tensile loading direction. Consequently, only lengthways yarns are broken, and the path is thus as energetically economical as possible.

Unlike the slit orientation, yarn orientations could affect the slit propagation direction of the envelope fabric significantly. As shown in Fig. 6(b), with the increase of off-axis angle changing from  $0^\circ$  to  $90^\circ$ , the slit propagation angle, which is the angle between the loading direction and slit propagation direction, first decreases and then increases. The location of the local delta zone changes obviously as the yarn rotates. The variation of the slit propagation angle could be attributed to the rotation of principle yarns in the local delta zone. Due to the yarn rotation, the contributions to bearing capacity of warp and weft yarns vary with the bias angle. The effects of the yarn rotation on tearing strengths will be discussed later. In addition, as illustrated in Fig.3 and Fig.5, it is obvious that whatever the orientation of the initial slit or the yarn is, the propagation is always parallel to the secondary yarns.

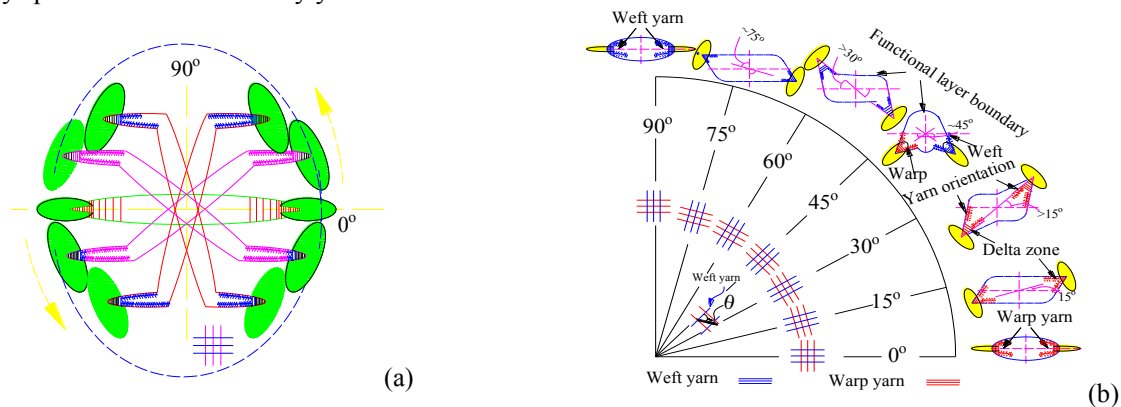


**Fig. 6.** Schematic drawings of typical damage modes of the tearing specimens with different slit orientations (a) and off-axis angles (b).

### Tearing behaviors affected by off-axis angles

The tearing stress- displacement curves of different bias specimens are shown in Fig.7. According to Fig.7, the studied material is typically orthotropic and the tearing behaviors depend strongly on the yarn orientations. The peak stresses (or tearing strengths) and slopes of tearing stress-displacement curves before the corresponding peak stresses vary markedly with increasing bias angles.

The average tearing strengths and corresponding displacements are shown by Fig.8. Here  $0^\circ$  (or  $180^\circ$ ) and  $90^\circ$  (or  $270^\circ$ ) angles represent the warp and weft directions, respectively. The results of the tearing tests show a W-shaped relationship between tearing strength and off-axis angle, with a local strength peak at  $45^\circ$  angle, and an inverted V-shaped relationship between displacement and off-axis angle. There is a local peak strength at bias angle of  $45^\circ$ . Specifically, for the slit length of 20 mm, the strength of  $45^\circ$  reaches 36.3 kN/m, which is

nearly equal to those of on-axial specimens. In addition, the corresponding displacement of 45° at its peak stress reaches the highest value (60.5mm), which is about four times of those of on-axial values (see Fig.8b).

Ambroziak. [31] and Zhang et al. [27] found that the relationship between tensile strength and strain of the bias specimen is U-shaped, declining from a moderate level at 0° and then increasing steadily up to the highest level at 90°. The results of tearing strength are inconsistent with the existing results for tensile strength[31,27].

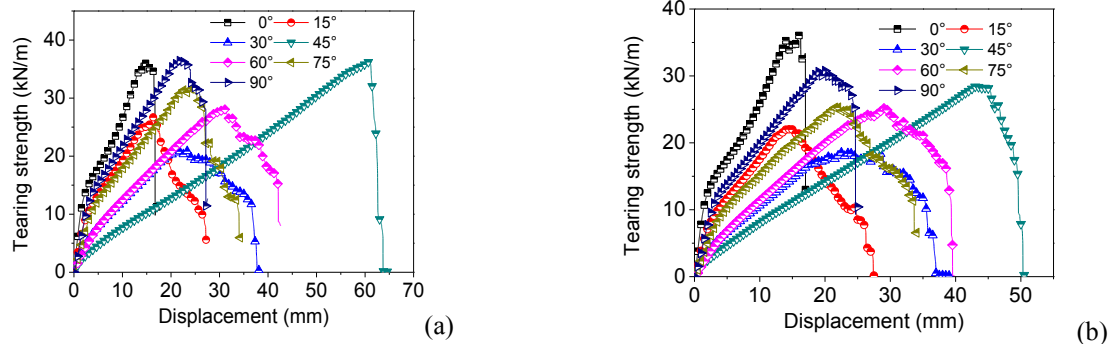


**Fig. 7.** The tearing stress-displacement curves for bias specimens with slit of (a) 20 mm and (b) 30mm.

In addition, Fig.7 reports two types of failure modes: progressive failure and brittle failure, which is analogous to Bigaud et al.[13]

**Progressive failure:** In some fabrics, a few yarns at the tip of the slit rupture while the load is still generally increasing on the specimen. The initial slit propagates alternately on each side, the tearing stress decreases gradually to the residual strength. The residual strength is a low level of stress after the peak of the stress. This failure mode occurs mainly for a bias angle (with respect to 45°) larger than a certain threshold  $|\theta_0 - 45^\circ|$ .

**Brittle failure:** The failure process in the fabrics was very sudden, with a rapid tear propagating across the center section of the specimen and an associated sudden drop in the applied load. For tests involving sudden catastrophic tearing, the load associated with first yarn rupture nearly coincides with the maximum load. During the experiment, many yarns broke almost simultaneously. Hence, the tearing stress of the specimen plunges to the residual strength immediately after the peak.

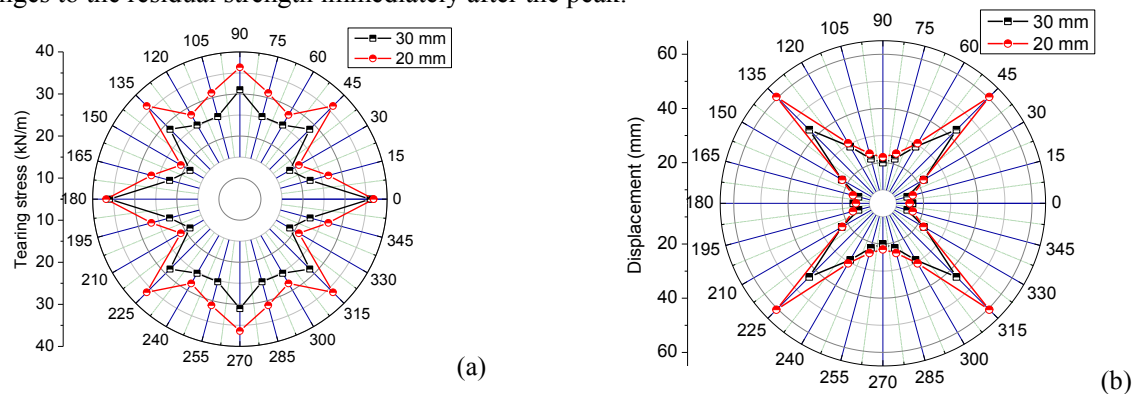


**Fig. 8.** Test results of tearing strengths (a) and corresponding displacements (b).

For the composite membrane used for air inflatable or supported membrane structures, it is important to extract a limiting value to the stress for which the slit starts propagating, leading more or less quickly to the sample global failure. This force can be described as the “propagation threshold strength”. The threshold strength, maximum strength (tearing strength) and their corresponding displacements for bias specimens could be predicted by Fig.9 and Fig.10, respectively. The distances between two curves of angles near 45° are larger than those of angles near 0° or 90°, and the threshold angle  $|\theta_0 - 45^\circ|$  is about 30°. That is to say, for angles larger than 15° or smaller than 75°, their failure modes are progressive failure.

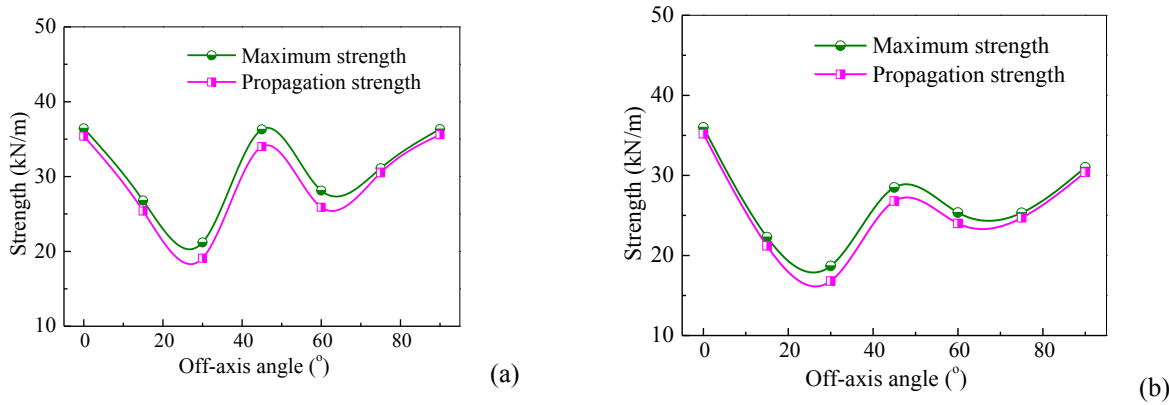


**Fig. 9.** Propagation threshold stresses and maximum stresses for slits of (a) 20 mm and (b) 30mm.

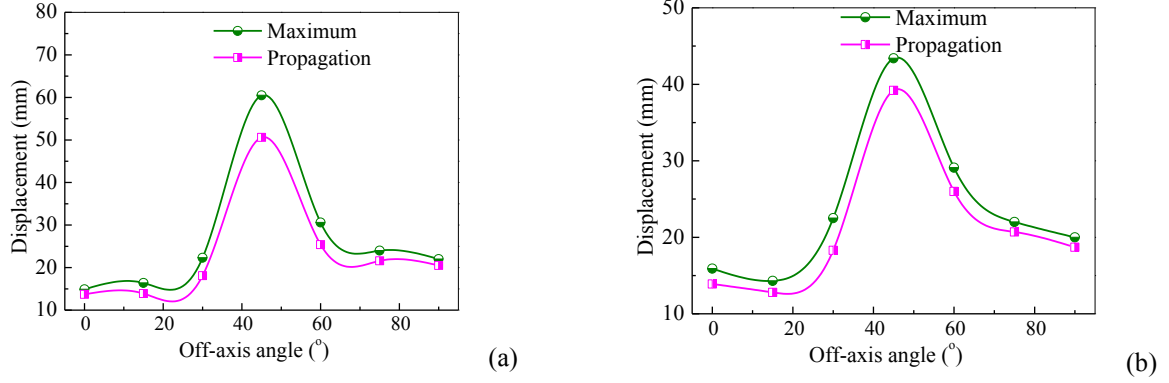


**Fig. 10.** Displacements for Propagation threshold stresses and maximum stresses for slits of (a) 20 mm and (b) 30mm.

According to Fig.9 and Fig.10, the tearing behaviors of the laminated fabric exhibit significant orthotropy. Take results of 30mm as an example, the average tearing strength at 90° reaches 31.0 kN/m with a displacement of 20 mm, while the average tearing strength at 0° reaches 36.0 kN/m with a displacement of 15.9 mm. Although the equivalent slit lengths in warp are as great as those in weft, it can also be observed that the tearing strengths in 75° and 60° could be up to 13.6% (75°) and 35.5 % (60°) higher than those in 15° and 30°, respectively. However, the displacements also show the similar tendency to the tearing strengths.. As we all know, the unbalanced properties (i.e. orthotropy) of the fabric material mainly originate in the different weaving parameters, such as yarn densities, levels of the crimp, and yarn looseness, resulting from manufacturing process of the laminated fabrics. Concerning the design practice and structural safety assessment, it might be recommendable in light of the great variation of the tearing strengths to conduct fabric structures analysis with a lower limit of tearing strength. For the studied material, the lower limit could be obtained from the tests of 30° or 60° off-axis angle. Of course, the upper limit could be obtained from the tests of 0° or 90° off-axis angle.

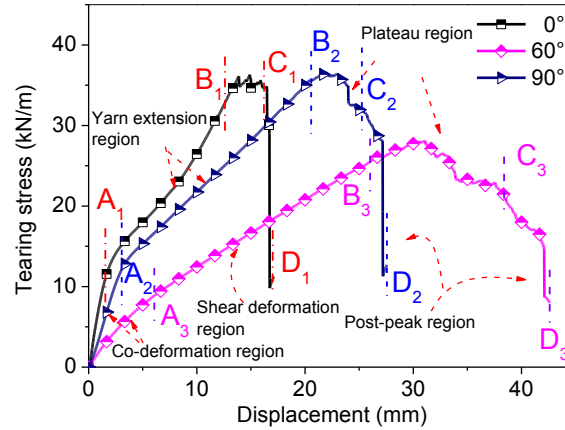
*Model for the tearing stress- displacement curve*

Fig.11 presents three typical models for the tearing stress-displacement curves, including two on-axial curves and an off-axial curve. The typical tearing curves of the envelope fabric can be modeled with several characteristic regions. Here, for the on-axial specimens, their curves consist of four characteristic regions, including a co-deformation region, a yarn extension region, a plateau region, and a post peak region. For the bias specimens, the yarn extension region is replaced by a shear deformation region. These four characteristic regions are displayed:

**i).(OA) the co-deformation region:** In this region, the tensile and shearing behaviors of the envelope fabric are not mainly dominated by the structure layer, but the other functional layers, such as the PVF film; and thus the typical curves of on-axial and off-axial samples are similar to each other in terms of the tendency and slopes of curves. Here, the on-axial slopes are relatively greater than those of off-axial ones. There are no initial crimps in the woven fabrics, and the load in this region essentially straightens the yarns by removing the

looseness, which is not consistent with those woven fabrics[28].

**ii. (AB) the yarn extension region or the shear deformation region:** Due to the obvious shear deformations in off-axial specimens, the bias curve slope is smaller than those of on-axial ones. For the on-axial samples, the structural layers control the mechanical behaviors, and in contrast, for the off-axial samples, the adhesives and PVF films control their deformation characteristics. In this region, yarn-adhesive interface debonding occurs and rupture of some yarns takes place in the vicinity of the tear tips.



**Fig. 11.** Typical model of tearing stress-displacement curves.

**iii. (BC) the plateau region:** As the delta zones move with a nearly approximate area (see Fig.12), the curves show oscillation behaviors in this region. After reaching the propagation stress  $\sigma_{cr}$ , the length of the non-tear region whose yarns elongate with the same strain synchronously in the principal direction, decreases due to rupture of yarns in the delta zones[25]. However, the stresses of yarns in non-tear stable region increase, as the displacement increases. Therefore, the tearing stress of the specimen can reach a plateau at a high level. The peak stress in this region is known as the ultimate tearing strength  $\sigma_{ult-T}$ .

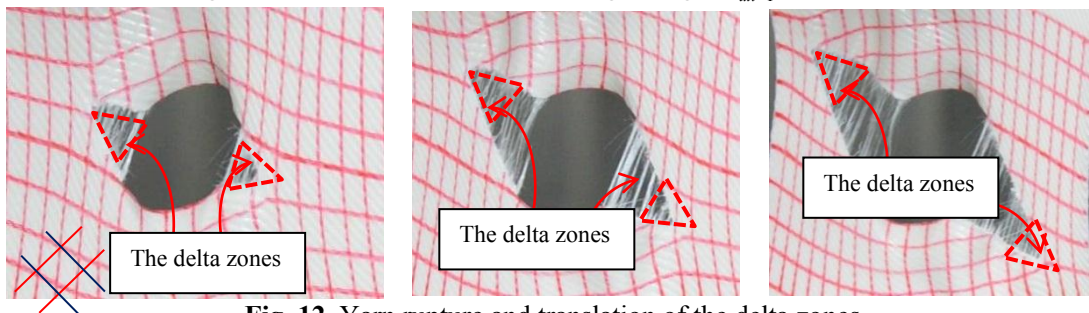


**Fig. 12.** Yarn rupture and translation of the delta zones

Some differences still exist between the on-axial and off-axial curves. For example, more peaks are observed off-axial curves, which is mainly attributed to the different phenomenon of yarn failure and durations of the plateau region[28]. In the off-axial specimens, more yarn pullout and yarn slip could be observed, as shown in Fig.3. The yarn pullout process needs to absorb more energy than the rupture process [25,32,33] and yarn slip at crossover points may significantly toughen tear damaged woven fabrics against tear propagation; therefore, the plateau region of off-axial specimens could last much longer and present more peaks than those of on-axial specimens.

**iv. (CD) the post-peak region:** After the plateau region, as the tear propagates, more and more principal yarns ruptured. During the tests, two or three yarns (or, even more) often ruptured simultaneously (see Fig.13). Therefore, the tearing stress of the specimen plunges to a lower level, namely the residual strength of the specimen. Some samples may show another fluctuation stage after the peak. Actually, at the last stage of a tearing test, the yarns in the last delta zone are damaged not so much in a tearing manner as in a pullout manner (see Fig.13).

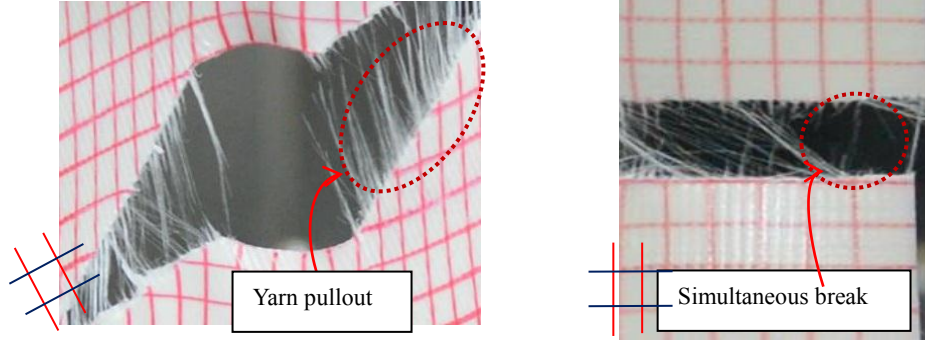


**Fig. 13.** Yarn pullout and simultaneous break

### *Tearing strength criterion*

The tear propagation in woven-fabric materials has been the subject of a number of investigations during the past several decades. Many fracture models have been proposed and used to predict the tearing strength for woven-fabrics under uniaxial loads. Among these fracture models, Hedgepeth's stress concentration factor [34], Thiele's formula [10] and method of stress field consideration [10] are three typical theories predicting the tearing strength. However, it should be noted that all these fracture models apply only to on-axial tearing specimens. It is necessary to explore a new fracture model or a new tearing strength criterion for the accurate predictions of bias tearing strengths.

Several tensile strength criteria used in composite materials may be applicable, such as the maximum stress criterion, the maximum strain criterion, Tsai-hill criterion and quadratic interaction criterion[35]. Among them, Tsai-hill criterion and the quadratic interaction criterion have both taken the interaction item of the two principal stresses into consideration, and they are more convenient to use than the others. To date, Tsai-hill criterion has been widely used to predict the tensile strength of coated fabrics in many studies[35]. As there are many similarities between the tensile and the central tearing tests, in terms of loading conditions, characteristics of load-deformation curves, the tearing strength of bias specimens also could be predicted by the Tsai-hill criterion.

The authors have proposed a new tearing strength criterion for plain woven fabrics based on the Tsai-hill criterion[28]. The new criterion contains two parts: one is a U-shaped relationship from the Tsai-hill criterion  $[\sigma_{1\theta}]$ , and another is an inverted V-shaped relationship from the off-axial constitutive relationship for shear modulus of orthotropic materials  $[\sigma_{2\theta}]$ , i.e.,

$$\sigma_{\theta} = [\sigma_{1\theta}] + [\sigma_{2\theta}] \quad (1)$$

For the U-shaped part, the modified Tsai-hill criterion for tearing strength can be expressed as follows:

$$\frac{1}{[\sigma_{1\theta}]^2} = \frac{1}{X^2} \cos^4 \theta + \left( \frac{1}{(\frac{1}{2}S)^2} - \frac{1}{X^2} \right) \cos^2 \theta \cdot \sin^2 \theta + \frac{1}{Y^2} \sin^4 \theta \quad (2)$$

where  $X$ ,  $Y$  and  $X_{45}$  indicate the tearing strengths in the weft, warp and  $45^\circ$  angle directions, respectively.

For the inverted V-shaped part, the modified equation could be expressed as follows:

$$\frac{1}{[\sigma_{2\theta}]^2} = \frac{1}{(\alpha S)^2} + 4 \left( \frac{1}{(\alpha X)^2} + \frac{1}{(\alpha Y)^2} - \frac{1}{(\alpha S)^2} + \frac{2\nu}{(\alpha X)^2} \right) \cdot \cos^2 \theta \cdot \sin^2 \theta \quad (2)$$

where  $\alpha$  is the parameter for the strengths  $X$ ,  $Y$ , and  $S$ . For the material studied in this paper, the parameter  $\alpha$  is equal to 0.45.

Two parts of the tearing strength mentioned above could give proper predictions for the part of U-shaped relationship and inverted V-shaped relationship, respectively. The results of tearing strengths obtained from central slit tearing tests are compared with the predictions in Fig.14. It is evident that the predictions are fairly similar to their test counterparts, and the proposed tearing strength criterion could accurately represent test data. The high similarity confirms the feasibility of the proposed criterion, and the current findings expand prior work. This W-shaped relationship revealed by the formulas is useful in structural safety assessment, and the proposed formulas extend some existing criteria for tensile strengths to predict the tearing strengths of NCFs.

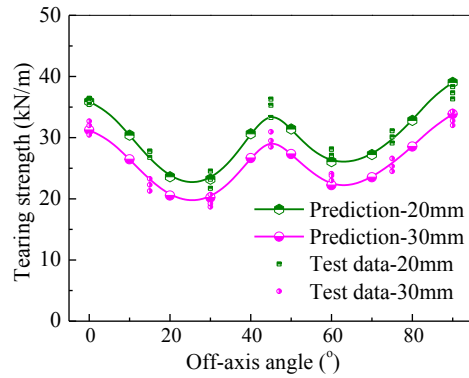


**Fig. 14.** Comparison of the tearing strength between test data and predictions by the proposed criterion.

Overall, both the test data and predictions show typical W-shaped curves in Fig.14 for different slit lengths, which is not consistent with the results for bias tensile strengths obtained in previous researches [27,31,36]. There is a local peak at off-axis angle  $45^\circ$  in every curve, which is probably attributed to the yarn pullout and joint action of yarns of two directions in the vicinity of the slit tips[28].

## Conclusions

This paper presents the research on fracture failure analysis and tearing strength criterion for ASMSs' fabrics. The following conclusions can be drawn from the present study.

This NCF is typical direction-depended materials, and their failure characteristics vary greatly with the bias angles. As off-axial specimens could show great shear deformation and large area of yarn pullout, when the slit starts to propagate, these shear deformation and yarn pullout could absorb more energy and reduce the stress concentration in the yarns at the slit tip and, therefore, during the tests, most of the specimens failed in a progressive mode, and they exhibited progressive damages of the yarns and other functional layers before the failure of these specimens. The slit propagation direction can be mainly decided by yarn orientation, slit orientation, and the orthotropy of the material. Overall, whatever the orientation of the initial slit or the yarn is, the propagation is always parallel to the secondary yarns.

Typical tearing stress-displacement curves of the NCF could be defined as four characteristic regions: a co-deformation region, a shear deformation region, a plateau region, and a post peak region. Among bias specimens, there are many obvious differences in tearing behaviors in terms of maximum displacement, damage mode, curve slope, and number of stress peaks, which could be attributed to the material orthotropy and different failure mechanism of constituent materials.

For the tearing strength criterion for NCFs, there is a W-shaped relationship between tearing strength and off-axis angle, with a local strength peak at  $45^\circ$  angle. The W-shaped relationship could be regarded as a superposition of two parts: one is a U-shaped relationship from the Tsai-hill criterion, and another is an inverted V-shaped relationship from the off-axial constitutive relationship for shear modulus of orthotropic materials. Accordingly, the proposed tearing strength criterion is validated due to the high precision between the calculated and experimental results for the BWKF.

## Acknowledgements

This work was supported by the National Natural Science Foundation of China (Grant No.51608270), the Fundamental Research Program of Jiangsu Province (Grant No.BK20150775), the Fundamental Research Funds for the Central Universities (Grant No.30916011342), and the China Postdoctoral Science Foundation (Grant No.2016M601816 and No.2017T100371). The tested fabric materials were supplied by Richard Jiang of Seaman Corporation Shanghai Representative Office. Some of the tests were conducted in School of Naval Architecture, Ocean & Civil Engineering, Shanghai Jiao Tong University. The authors acknowledge with thanks all these help and other unmentioned ones.

## REFERENCES

- [1] H. Kong, A.P. Mouritz, R. Paton, "Tensile extension properties and deformation mechanisms of multi-axial non-crimp fabrics", *Compos Struct*, Vol. **66**, No.1, pp. 249-259, (2004).
- [2] Y. Luo and H. Hu, "Mechanical properties of PVC coated bi-axial warp knitted fabric with and without initial cracks under multi-axial tensile loads", *Compos Struct*, Vol. **89**, No. 4, pp. 536-542, (2009).
- [3] L. Jin, H. Hu, B. Sun, et al, "A simplified microstructure model of bi-axial warp-knitted composite for ballistic impact simulation", *Compos Part B-Eng*, Vol. **41**, No. 5, pp. 337-353, (2010).
- [4] C.M. Krook and K.R. Fox, "Study of the tongue-tear test", *Text Res J*, Vol. **15**, No. 11, pp. 389-396, (1945).
- [5] O.B. Hager, D.D. Gagliardi, H.B. Walker, "Analysis of tear strength", *Text Res J*, Vol. **17**, No. 7, pp. 376-381, (1947).
- [6] L.H. Turl, "The measurement of tearing strength of textile fabrics", *Text Res J*, Vol. **26**, No. 3, pp. 169-176, (1956).
- [7] C. Chu, R. Dhingra, R. Postle, "Study of tearing properties of membrane coated fabrics", *J Donghua Univ*, Vol. **4**, No. 8, pp. 1-9, (1991).
- [8] P. Wang, B. Sun, B. Gu, "Comparisons of trapezoid tearing behaviors of uncoated and coated woven fabrics from experimental and finite element analysis", *Int J Damage Mech*, Vol. **22**, No. 4, pp. 464-489, (2013).
- [9] S. Wang, "Analytical modeling on mechanical responses and damage morphology of flexible woven composites under trapezoid tearing", *Text Res J*, Vol. **83**, No. 12, pp. 1297-1309, (2013).
- [10] S. Maekawa, K. Shibasaki, T. Kurose, et al, "Tear propagation of a high-performance airship envelope material", *J Aircraft*, Vol. **45**, No. 5, pp. 1546-1553, (2008).
- [11] T.A. Godfrey and J.N. Rossettos, "The onset of tear propagation at slits in stressed uncoated plain weave fabrics", *J Appl Mech-Tasme*, Vol. **66**, No. 4, pp. 926-933, (1999).
- [12] T.A. Godfrey, J.N. Rossettos, S.E. Bosselman, "The onset of tearing at slits in stressed coated plain weave fabrics", *J Appl Mech*, Vol. **71**, No. 6, pp. 879-886, (2004).
- [13] D. Bigaud, C. Szostkiewicz, P. Hamelin, "Tearing analysis for textile reinforced soft composites under mono-axial and bi-axial tensile stresses", *Compos Struct*, vol. **62**, No. 2, pp. 129-137, (2003).
- [14] L. Liu, M. Lv, H. Xiao, "Tear strength characteristics of laminated envelope composites based on single edge notched film experiment", *Eng Fract Mech*, Vol. **127**, pp. 21-30, (2014).
- [15] B. Witkowska, I. Frydrych, "A comparative analysis of tear strength methods", *Fibres Text East Eur*, Vol. **12**, No. 2, pp. 42-47, (2004).
- [16] B. Witkowska and I. Frydrych, "Static tearing, Part II: Analysis of stages of static tearing in cotton fabrics for wing-shaped test specimens", *Text Res J*, Vol. **78**, No. 11, pp. 977-987, (2008).
- [17] N.A Teixeira, M.M. Platt, W.J. Hamburger, "Mechanics of elastic performance of textile materials: part XII: relation of certain geometric factors to the tear strength of woven fabrics", *Text Res J*, Vol. **25**, pp. 838-861, (1955).
- [18] W.A. Scelzo, S. Backer, M.C. Boyce, "Mechanistic role of yarn and fabric structure in determining tear resistance of woven cloth: Part II: Modeling tongue tear", *Text Res J*, Vol. **64**, No. 6, pp. 321-329, (1994).
- [19] W. Zhong, N. Pan, D. Lukas, "Stochastic modelling of tear behavior of coated fabrics", *Model Simul Mater Sc*, Vol. **12**, No. 12, pp. 293-309, (2004).
- [20] P. Wang, Q. Ma, B.Z. Sun, et al, "Finite element modeling of woven fabric tearing damage", *Text Res J*, Vol. **81**, No. 12, pp. 1273-1286, (2011).
- [21] FAA-P-8110-2-1995, Airship Design Criteria, Federal Aviation Administration of USA, 1995.
- [22] B. Forster and M. Mollaert, *European design guide for tensile surface structures*, Germany, Tensinet, 2004.
- [23] T. Ennouri, D. Patricia, V.K. Toan, "Tear resistance of woven textiles-criterion and mechanisms", *Compos Part B-Eng*, Vol. **42**, No. 7, pp. 1851-1859, (2011).
- [24] C. G. Huntington, *Tensile Fabric Structures*. Virginia, American society of civil engineers-ASCE, 2010.
- [25] J.W. Chen, W.J. Chen, B. Zhao, et al, "Mechanical responses and damage morphology of laminated

- fabrics with a central slit under uniaxial tension: a comparison between analytical and experimental results”, *Constr Build Mater*, Vol. **101**, pp. 488-502, (2015).
- [26] J.W. Chen and W.J. Chen, “Central crack tearing testing of laminated fabrics Urettek3216LV under uni- and bi- axial static tensile loads”, *J Mater Civil Eng*, Vol. **28**, No. 7, Doi:10.1061/ (ASCE) MT.1943-5533.0001537, (2016).
- [27] Y.Y. Zhang, Q.L. Zhang, C. Zhou, et al, “Mechanical properties of PTFE coated fabrics”, *J Reinf Plast Comp*, Vol. **29**, No. 29, pp. 3624-3630, (2010).
- [28] J.W. Chen, W.J. Chen, H. Zhou, et al, “Central tearing characteristics of laminated fabrics: Effect of slit parameter, off-axis angle, and loading speed”, *J Reinf Plast Comp*, 0731684417695460, (2017).
- [29] G.K. Wang, S. Youngwook, W. Kyeongsik, et al, “Mechanical property characterization of film-fabric laminate for stratospheric airship envelope”, *Compos Struct*, Vol. **75**, pp. 151-155, (2006).
- [30] B. Bridgens, P. Gosling, G.T. Jou, et al, “Inter-laboratory comparison of biaxial tests for architectural textiles”, *J Text I*, Vol. **103**, No. 7, pp. 706-718, (2012).
- [31] BS EN ISO 139-2005, Textiles- Standard atmospheres for conditioning and testing, British Standard Institution (BSI), 2005.
- [32] A. Ambroziak, “Mechanical properties of PVDF-coated fabric under tensile tests”, *J Polym Eng*, Vol. **35**, No. 4, pp. 377-390, (2015).
- [33] K.M. Kirkwood, J.E. Kirkwood, Y.S. Lee, et al, “Yarn pull-out as a mechanism for dissipating ballistic impact energy in kevlar® km-2 fabric part i: quasi-static characterization of yarn pull-out”, *Text Res J*, Vol. **74**, No. 10, pp. 920-928, (2004).
- [34] M. Valizadeh, S.A.H. Ravandi, M. Salimi, et al, “Determination of internal mechanical characteristics of woven fabrics using the force-balance analysis of yarn pullout test”, *J Text I*, Vol. **99**, No. 1, pp. 47-55, (2008).
- [35] A.D. Topping, “The critical slit length of pressurized coated fabric cylinders”, *J Ind Text*, Vol. **3**, pp. 96-110, (1973).
- [36] S. Chen, X. Ding, H. Yi, “On the anisotropic tensile behaviors of flexible polyvinyl Chloride-coated fabrics”, *Text Res J*, Vol. **77**, No. 6, pp. 369-374, (2009).
- [37] Y.Y. Zhang, X.G. Song, Q.L. Zhang, et al, “Fracture failure analysis and strength criterion for PTFE-coated woven fabrics”, *J Compos Mater*, Vol. **49**, No. 12, pp. 1409-1421, (2015).

TEST AND MESOSCOPIC FINITE ELEMENT ANALYSIS ON  
MECHANICAL PROPERTIES DEGRADATION OF AGED COATED FABRICS  
**STRUCTURAL MEMBRANES 2017**

**QILIN ZHANG<sup>\*</sup>, YUNTING LI<sup>†</sup>**

<sup>\*</sup> College of Civil Engineering  
Tongji University  
200092 Shanghai, China.  
E-mail: zhangqilin@tongji.edu.cn

<sup>†</sup> College of Civil Engineering  
Tongji University  
200092 Shanghai, China.  
E-mail: liyunting0715@sina.com

**Key words:** PVDF-coated Fabrics, Ageing Behavior, Mechanical Property, Mesoscopic Finite Element Analysis.

**Summary.** In this paper the mechanical properties degradation of aged coated fabrics is investigated. Tests on the tension strength and the tearing strength of the aged fabrics are carried out, which is from the membrane roof of Qingdao Stadium used for more than 13 years. The strength degradation degrees of the aged fabrics are obtained. Due to the configuration of fabrics the numerical simulation on its stress state as well as its fracture process and mechanism is very difficult. In this paper, a mesoscopic finite element model for plain woven fabrics stress analysis is established based on woven configuration fabric cells. The numerical analysis shows that a firm yarn-yarn connection at interlacing point would make fabrics has high shear stiffness and concentrates tensile stress on the edge of the fabrics in which applied load. It coincides with the bi-axial tensile test, in which cruciform specimen fracture always at the arms instead of core area. Finally the fracture criterion is built up for new and aged fabrics on the basis of the test and analysis results of this paper.

## 1 INTRODUCTION

Membrane structure, with many advantages including a light weight, good light transmission, flexible stretch, strong sense of shape and great architectural performance, is well received and has been widely used in public shelter structures. Built on a bend in the River Thames in Greenwich, London, the Millennium Dome is one of the most famous Britain's landmarks. The world's most luxurious United Arab Emirates BurjAl-Arab hotel in Dubai is a double-layer membrane structure of the building. It is built on a man-made island with a light graceful sailboat styling shape and integrated into the surrounding landscape. Besides, the membrane structures are preferred in the many public buildings, such as Stadium and Airport. However, the membrane structure also has essential shortcoming, that is, compared with the steel, concrete, glass and other building material, membrane material is more easily aging and could cause the destruction of the structure. To ensure safety, aging of

membrane materials is an important subject.

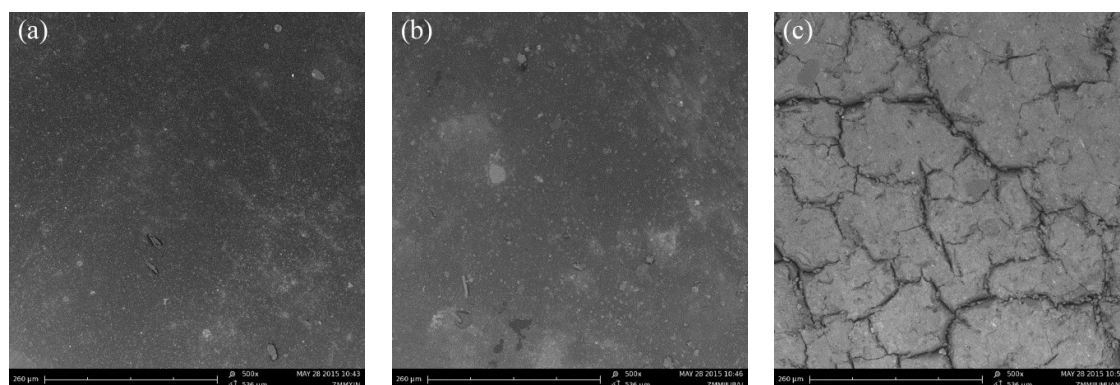
Many research on the effects of different factors on the aging of membrane materials have been carried out with artificial accelerated ageing method [1-8] or outdoor ageing method [9-12]. These studies are the basis for the study of aging properties of membrane materials. For further understanding of material aging, the aging coated fabrics removed from a stadium been selected as research objects, a list of mechanical tests are carried out. To figure out its aging mechanism, numerical simulations are also performed. This paper consists of two main parts, experiment study and numerical analysis.

## 2 AGING PROPERTIES OF PVDF

To evaluate the durability of coated fabrics after aging in a structure outdoor, a series of contrast experiments was carries out between the natural ageing coated fabrics removed from a stadium built in 2007 and the new specimens of the same type of coated fabrics. Mechanical properties of coated fabrics, including tensile, tearing and bonding strength, are tested according to DG/T J082019-2007 (2007) [13]. The main test results and analysis are as follows [14].

### 2.1 Coating

The reduction of brightness at the sunny side is 56.42%, while that at the shaded side is 30%. According to the microscopic morphology of the fabric coatings (Fig. 1), the ageing coating at the shaded side has some bulges, but there is not crack and pulverization. However, the ageing coating at the sunny side is full of cracks, with bulges and pulverization. The color change and cracks caused by ageing at the sunny side is more severe than that at the shaded side. According to the aging principle of polymers, it is mainly due to the ageing mechanism of high polymer material, namely rupture of molecular chain (degradation) and crosslinking of macromolecular chain [15].



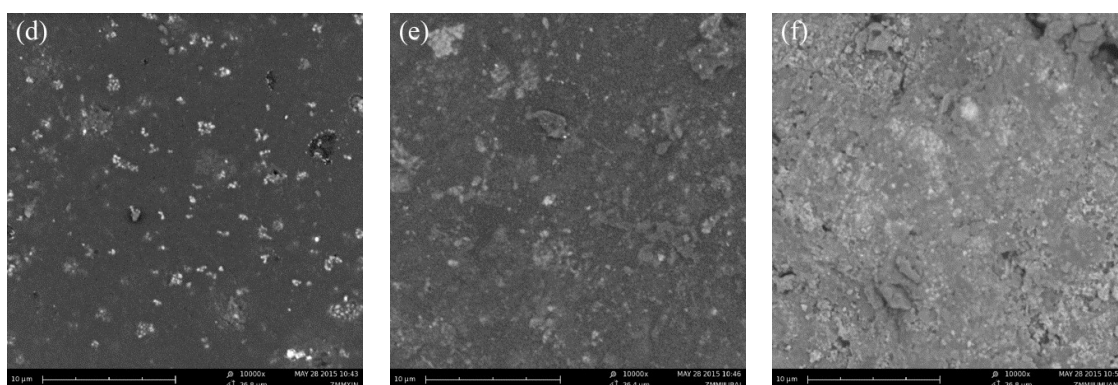


Figure 1: Photographs of the coating by SEM: (a) new coating×500 (b) ageing coating at the shaded side×500 (c) ageing coating at the sunny side×500 (d) new coating×10000 (e) ageing coating at the shaded side×10000 (f) ageing coating at the sunny side×10000

## 2.2 Force at failure & tearing strength

The results of force at failure and tearing strength tests are presented in Table 1. In warp direction, force at failure of the new fabrics is 8132 N/5 cm, while that of the ageing is 7329 N/5 cm. In weft direction, force at failure of the new fabrics is 7051 N/5 cm and that of the ageing one is 6792 N/5 cm. Test results show the force at failure of fabrics decreases by 9.9% in warp direction and decreases by 3.7% in weft direction. In warp direction, tearing strength of the new coated fabrics is 1217 N, while that of the ageing is 937 N. In weft direction, tearing strength of the new coated fabrics is 1163 N and that of the ageing is 818 N. Experimental results show that tearing strength of aging coated fabrics decreases by 23% in warp direction and 29.6% in weft direction. Possibility P of significant difference are 1.5E-18 and 2.8E-29 in warp and weft respectively, which are lower than 0.05. T-test proves that tearing strength of the new and aging material has notable difference in warp and weft directions. In addition, it can be found that the degradation of tearing strength is more obvious than that of force at failure, which is consistent with other researches [4, 8, 24].

Table 1: Force at failure testing results

Material	Tensile force (N/5cm)		Tearing strength (N)	
	Warp	Weft	Warp	Weft
New	8132	7051	1217	1163
Ageing	7329	6792	937	818
Reduction	9.9%	3.7%	23.0%	29.6%

## 3 NUMERICAL ANALYSIS

In order to analyse stress of aging membrane material. The numerical model of coated fabrics is built. There are three parts in this section. Stress characteristics of the coated yarn were analysed and tangential action at the interlaced point of fabrics was discussed. Besides, the effect of coating hardening on fabric was studied.

### 3.1 Method

Coated fabrics membrane can be analyzed on three scales: macroscopic, mesoscopic and microscopic. In this paper, modelling and analysis are on the mesoscopic. A yarn is the basic constituent material.

Modelling tool is Texgen which [16, 17] is developed by the Polymer Composites Group at the University of Nottingham as a modelling pre-processor for a variety of applications including solid mechanics. It provide a graphical user interface to define path, section shapes and dimensions of a yarn and discretize yarns by a built-in mesh generator.

In this paper, two weft yarns and two warp yarns are interlaced vertically to form a unit cell as fig. 2 shown. In Texgen, yarn path is represented by a spline  $S(u)$ . As fig. 3 shown, 9 control points are defined and Natural cubic spline is selected. Section shape of yarns are lenticular according to SEM above. Width and height is 1.8 and 0.4 respectively. Other parameters are shown in the Table 2. Geometric information is according to SEM of the yarn.

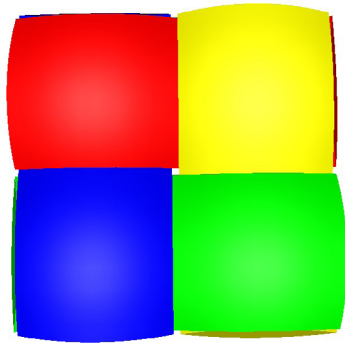


Figure 2: Unit cell

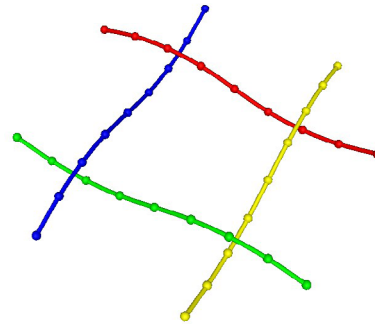


Figure 3: Yarn path and control points

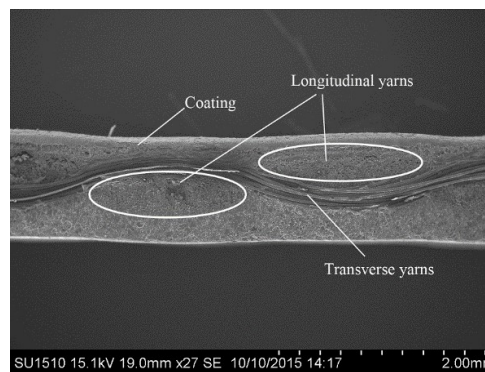


Figure 4: The cross section of ageing coated fabric

Table 2: Parameters of yarns

Parameters	Warp	Weft
Yarn linear density	0.0002002 kg/m	0.00011 kg/m
Fiber density	1.37g/cm <sup>3</sup>	1.37g/cm <sup>3</sup>
Total fiber area	0.146554mm <sup>2</sup>	0.08052 mm <sup>2</sup>
Fiber diameter	25μm	25μm
Fiber per yarn	300	165

Mechanical model of yarns are defined in Abaqus [18]. Tensile properties are defined using experimental data as isotropic hyperelastic materials. The stress-strain curves are shown in Figure 5. The Poisson's ratio is 0.4. The coating is defined as elastic material.

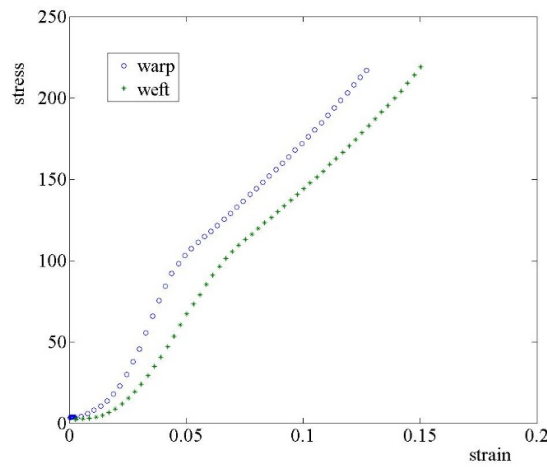


Figure 5: Stress-strain curves of yarns

### 3.2 Results and analysis

In the coating process of the fabric, there may be two modes of action in the intersection of warp and weft yarns. The first situation is that warp and weft yarns is bonded at the interlace points. The second is the coating material is not penetrated inside and there is only tangential friction at the interlace points. In this paper, the stress state of the yarn under tension in above two cases is compared and analysed.

From fig. 6-a, in the bonding mode, stress of the whole yarns are more concentrated at some location, while it is uniform in the friction-mode. In the bonding mode, the maximum and minimum values differ by 1/3, however, stress are kept at the same level in the friction mode. According above, when the yarns are independent at the interlace point, the fabrics would show a greater strength due to a reasonable stress distribution. After applied coating, if yarns of the fabrics bonding together, the stress of yarns concentrated in the free area between the interlace points and it reaches to the maximum at both ends of the lenticular section.

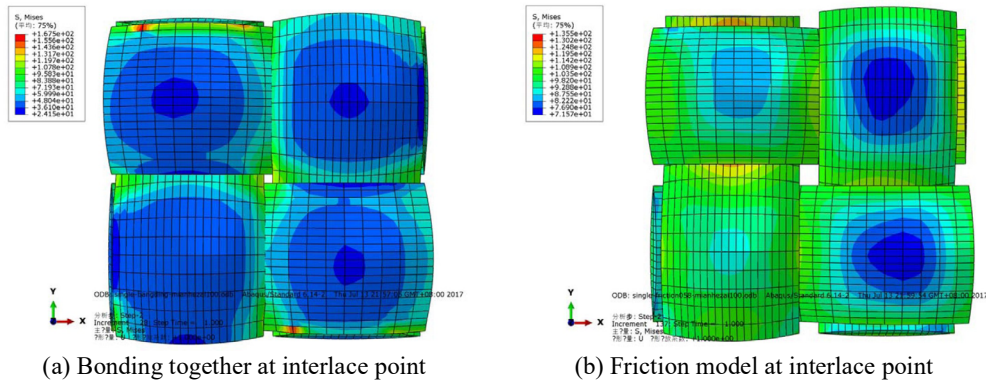


Figure 6: Stress nephogram of two models

Considering the modulus of elasticity changes when the coating is aged, the following sections compare the effect of the coating hardening on the internal stress of the fabric.

With two different elastic modulus of coating, stress of yarns in a unit cell are shown in Figure 7. In Figure 7-a, when elastic modulus of coating  $E$  is 15 MPa, the stress concentrate on the edge of a yarn. From Figure 7-b, when elastic modulus of coating  $E$  is 150 MPa, there is average distribution stress in a yarn. In addition, stress are contrasted at three typical positions of a yarn, as Figure 8 shown. Under the same load, stress-strain curves of three points on a yarn was show in Figure 9. From Figure 9-a, it is easy to find that there is a great difference at three points. However, in Figure 9-a, stress in the three positions is much closer. Hardening of the coating tend to a more equal distributions of stress. The improvement of stress concentration can make the yarn force more uniform and the fabric strength higher

It should be emphasized that the elastic modulus of the coating discussed above is much smaller than that of the yarn. If the modulus of coating and yarn on the same level, it will cause stress concentration in the coating and the bonding position, and the force condition needs a further studies.

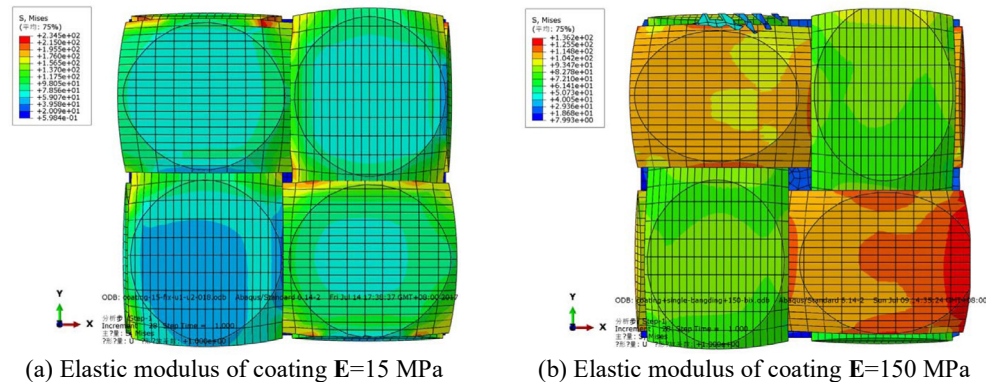


Figure 7: Stress of two models

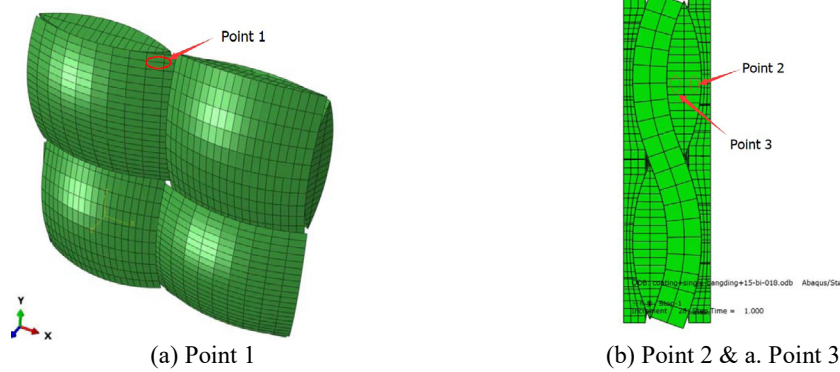


Figure 8: Typical position

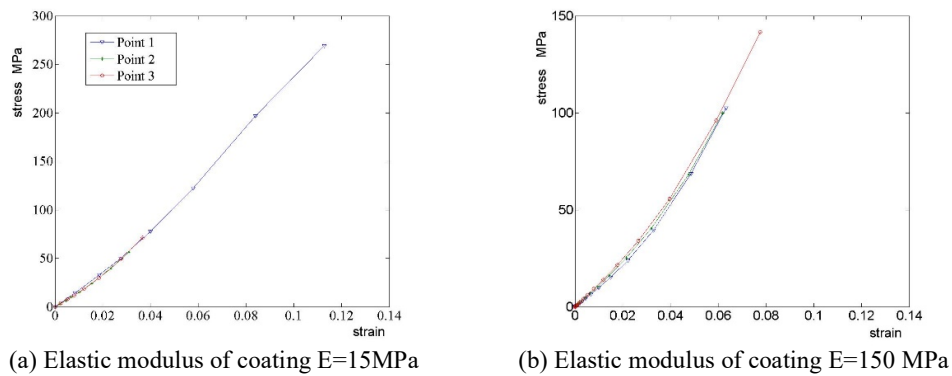


Figure 9: Stress-strain curve

#### 4 CONCLUSIONS

Based on the above research, the following conclusions are obtained:

- Aging coating has cracks, powder and other aging characteristics.
- Tensile strength of coated fabrics decrease by less than 10% and tearing strength decreased to 20%~30%
- Numerical analysis shows that tangential action at the interlaced point of fabrics greatly affect the distribution of stress. When the warp and weft are bonded at the interlace points, stress is concentrated on the edge of a yarn. If there is only friction in tangential at the interlace points, stress distribution of a yarn is more even.
- After aging, the hardening of the coating will lead to a more uniform stress distribution of the yarn. This may be one of the reasons why the tensile strength of the fabric does not decrease significantly after aging

#### REFERENCES

- [1] Zhang YY. Effect of Temperature and Water Immersion on the Mechanical Properties of

- Coated Fabrics. *Advanced Materials Research*. Vols.129-131(2010): 230-234.
- [2] Real L P, Gardette J. Ageing and characterisation of PVC-based compounds utilised for exterior applications in the building construction field 1: Thermal ageing. *Polymer Testing*. 2001, 20(7): 779-787.
- [3] Berdahl P, Akbari H, Levinson R, et al. Weathering of roofing materials - An overview. *Construction and Building Materials*. 2008, 22(4): 423-433.
- [4] Razak H A, Chua C S, Toyoda H. Weatherability of coated fabrics as roofing material in tropical environment. *Building and Environment*. 2004, 39(1): 87-92.
- [5] Chen ZR, Zhang QL, Xue WL. Experimental Research on Mechanical Properties of PVC Membrane after Ageing. *Proceedings of international Association for Shell and Spatial Structures*, Wroclaw, Poland, 2013.
- [6] Kuai BL. Aging Tests of PVC Membrane Material. *Tensinet instambul Symposium*, 2013
- [7] Triki E, Arrieta C, Boukehili H, et al. Tear behavior of polyester-based coated textiles after thermo-oxidative aging. *Polymer Composites*. 2012, 33(6): 1007-1017.
- [8] Andelko O, Haramina T. Effect of aging on mechanical properties of polymeric ripstop fabrics. *J. Polym*. 2012.
- [9] Joneydi S, Khoddami A, Zadhoush A. Novel superhydrophobic top coating on surface modified PVC-coated fabric. *Progress in Organic Coatings*. 2013, 76(5): 821-826.
- [10] Zhou S, Ding X, Wu L. Fabrication of ambient-curable superhydrophobic fluoropolysiloxane/TiO<sub>2</sub> nanocomposite coatings with good mechanical properties and durability. *Progress in Organic Coatings*. 2013, 76(4): 563-570.
- [11] Ahmed H. Improving UV Resistance of High Performance Fibers. *ProQuest Dissertation and Theses*, North Carolina State University, Raleigh, NC, 2011.
- [12] Ambroziak A. Mechanical properties of PVDF-coated fabric under tensile tests. *J.Polym. Eng*. 2015; 35(4): 377-390.
- [13] DGTJ08—2019—2007. Technical Specification for Inspection of Membrane Structures. Shanghai Construction and Traffic Committee: Shanghai, 2007.
- [14] Li YT, Liu T, Yang B, et al. Effects of Natural Ageing on Mechanical Properties of PVDF-Coated Fabrics. *Structural Engineering International*. 2016, 26(4): 348-356.
- [15] Wen JB. *Mechanical engineering materials*. Machinery Industry Press, 2009: 302.
- [16] Long. H L L B. Modelling and simulating textile structures using TexGen. 2011.
- [17] Lin H, Clifford M J, Long A C, et al. A finite element approach to the modelling of fabric mechanics and its application to virtual fabric design and testing. 2012.
- [18] Al. H L X Z. Automated geometric modeling of textile structures. *Textile Research Journal*. 2012.

## IMPROVED DAYLIGHT COMFORT BY A NEW 3D-FOIL THAT ALLOWS TO TRADE OFF SOLAR GAINS AND LIGHT INDIVIDUALLY

JAN CREMERS<sup>\*</sup>, HANNES MARX<sup>†</sup>

<sup>\*†</sup> University of Applied Sciences Stuttgart (HFT Stuttgart)  
Schellingstr. 24, 70174 Stuttgart, Germany

Email: jan.cremers@hft-stuttgart.de - Web page: <http://www.hft-stuttgart.de>

Email: hannes.marx@hft-stuttgart.de

**Key words:** ETFE, membrane structure, daylight quality, solar energy, solar shading, visual comfort.

**Summary.** *This paper presents a new shading approach for ETFE-membrane cushions. Due to the high visible transmission of an ETFE-foil (one layer transparent ETFE foil  $\approx 92\%$  @  $200\mu\text{m}$ ) the risk of overheating and glare effect in the summer is very high. Therefore, a new angle-selective shading system blocks off direct sunlight but diffuse sunlight can enter the building. Especially, this measure means a reduction of the cooling energy loads and should improve the thermal- and visual comfort. In this paper we focus on the visual comfort of the daylight factor, brightness and glare effect through the new 3D-foil.*

### 1 INTRODUCTION

From an energy perspective, transparent membrane constructions with a U-value of about  $2.1 \text{ W/m}^2\text{K}$  (@ three-layer construction) [1, pp. 216] will always act as a heat sink compared to opaque exterior walls or roofs with a U-value of about  $\approx 0.28 / 0.20 \text{ W/m}^2\text{K}$  [2] due to the worse thermal transmission coefficients (U-value). Therefore, the heating energy demand will be increased by reducing the solar gains. But on the other hand, the high visible transmission of membrane construction leads to a high utilization of the incoming daylight and reduces artificial lighting inside the building. Otherwise the risk of overheating without an appropriate sun protection by increased solar gains in summer is very high. Typical materials for transparent membrane constructions are ethylene-tetra-fluoro-ethylene (ETFE). ETFE does not become brittle or yellowed because it absorbs a minimum amount of the UV-radiation and has a self-cleaning effect [1, pp.97]. These properties allow for long lasting applications.

ETFE-foils can be printed (fritting) with different printing patterns (e.g. points) and colors (optimal colors have a high reflection capacity). Furthermore tinted ETFE material can be used in several colors. Thereby the optical properties (transmittance  $[\tau]$ , reflectance  $[\rho]$  and the absorption  $[\alpha]$  coefficients) can be controlled by the pigmentation grades and printing patterns. The current sun protection solutions are summarized in [5].

The main disadvantage of current state-of-the-art shading solutions for foils is the constant transmittance and reflection coefficient regardless of the incidence angle of the sun.

However, if a sun protection is used the natural daylight in the room will be decreased. Nevertheless sufficient illumination through daylight without glare phenomena needs to be

ensured in order to reduce the energy consumption for artificial lighting. Visible light consists of electromagnetic radiation which can be perceived by the human eye. The visual range ( $T_{vis}$ ) is in the wavelength range of between approx. 380 and 780 nanometers (nm) [1, pp.113]. When using transparent ETFE-foils the high visual transmission can often cause glare phenomena, according to [4]. Glare can be caused by the contrast of light and dark surfaces or by direct and/or indirect reflections. Thereby, the luminance distribution describes the brightness impression of a surface thus high luminance should be avoided, because glare can occur. Uniform contrast relation should prevail, because too high contrast can lead to fatigue and too low luminance contrasts may make the work or lounge area unattractive. [3]

To avoid some of the above mentioned daylight problems, the design of the shopping mall "Dolce Vita Tejo" in Lisbon (Amadora) has been inspired by the widely use of the architectural idea of a shed roof (saw-tooth roof), see Figure 1. The aim was an optimal use of daylight with good thermal comfort inside the building. This was achieved by printing the foil-layers, with partly double printed ETFE-foils.

Through the roof shape and the foil-printing it is possible to let diffuse sunlight enter the building from the northern part of the cushion surface equipped with a transparent ETFE-foil and block off direct sunlight from the southern part of the cushion surface thought out the printing. The membrane cushions are installed as an overhead roof system with dimensions of each membrane cushion of approx. 10 m x 10 m [1, pp.256].



Figure 1: Shopping mall: Dolce Vita Tejo in Lisbon. Source: Hannes Marx

The shading approach discussed here is similar to the project "Dolce Vita Tejo" and is also inspired by a shed roof structure. However, the saw-tooth structure is downsized to a millimeter scale (3D-Foil). Compared to the membrane cushions in "Dolce Vita Tejo" the working model of the new shading approach is much smaller, the scale factor is about 500, see Figure 2. This requires a special modification of the applied ETFE-foil. The foil will not only be printed but also additionally spatially transformed, so that the printing pattern can be adjusted in the design phase considering the sun position and the direct sunlight radiation.

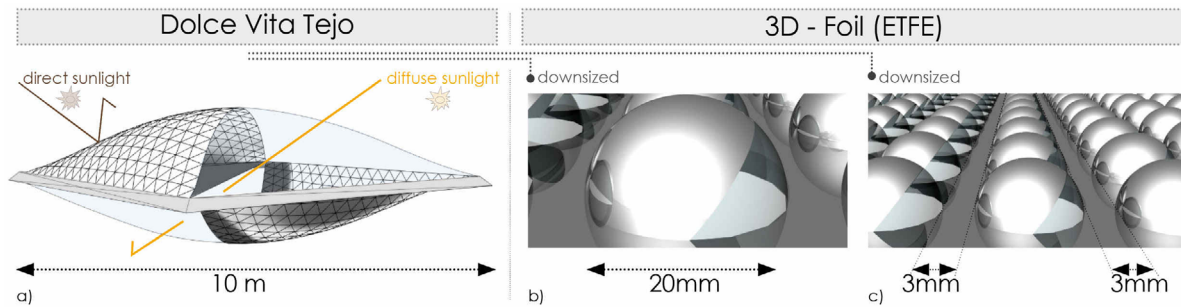


Figure 2: a) "Dolce Vita Tejo" in Lisbon, b) c) hemisphere geometry of the new shading approach: downsized to a millimeter scale ( $r = 10\text{mm}$ )

In this paper we focus on the visual comfort (daylight factor and glare phenomena) by using a fixed geometry (hemisphere: radius = 10 mm) with optimized printing pattern for Stuttgart, Germany. In [5] and [7] we describe the thermal simulation method with TRNSYS 17 because it's a special requirement to represent the small structure for the energy loads (cooling and heating).

### 1.1 3D – Foil (form optimization and material samples)

The hemisphere geometry is the best option for the new spatially transformed shading approach, because the significant benefits compared with location- and orientation specific geometries are too expensive in the manufacturing for the tooling. Therefore, only the printing part on the hemisphere can exactly be adjusted to the sun position by each project. Consequently, a hemisphere can be applied for both, façades- and roofs.

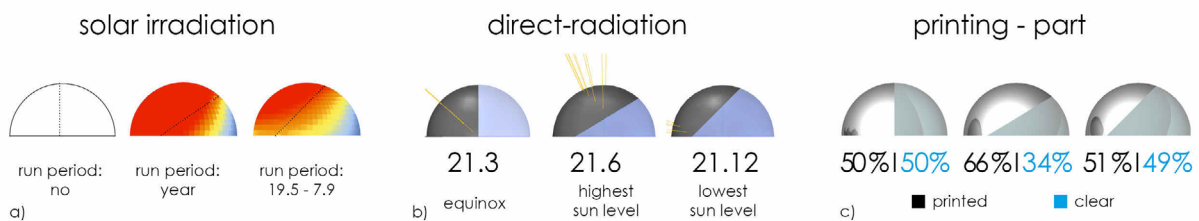


Figure 3: Printing optimization: hemisphere  
 a) solar irradiation (run period) b) direct-radiation (sun position) c) printing part

In order to achieve the ideal printing pattern, different influencing factors have to be analyzed:

intensity of the solar irradiation [ $\text{kWh}/\text{m}^2$ ], sun position (direct radiation), sun hours as well as time limits to guarantee solar gains in the winter case (Stuttgart: 8<sup>th</sup> Sept. to 20<sup>th</sup> May).

In [7] the thermal simulations of the total energy load (cooling/heating) are presented for different geometries (saw-tooth structure, pyramid, hemispheres) and different printing patterns. The results show a considerable reduction of the solar gains in the winter months (comparing the variants) and thus indicate a higher total energy loads for some geometries. These results are essential for the sun protection solution, which have an optimal printing pattern for Stuttgart with 51%, see Figure 3c. An optimal printing pattern improves the

thermal comfort, saves cooling energy because the direct radiation is blocked off and solar gains in the winter month can enter the room. Furthermore, it is intended to generate a glare- and shadow free situation with sufficient daylight by diffuse radiation.

The new spatially transformed foils are installed in the middle-layer of a membrane cushion. The building integration of the new spatially transformed foil is described in [5] in more detail.

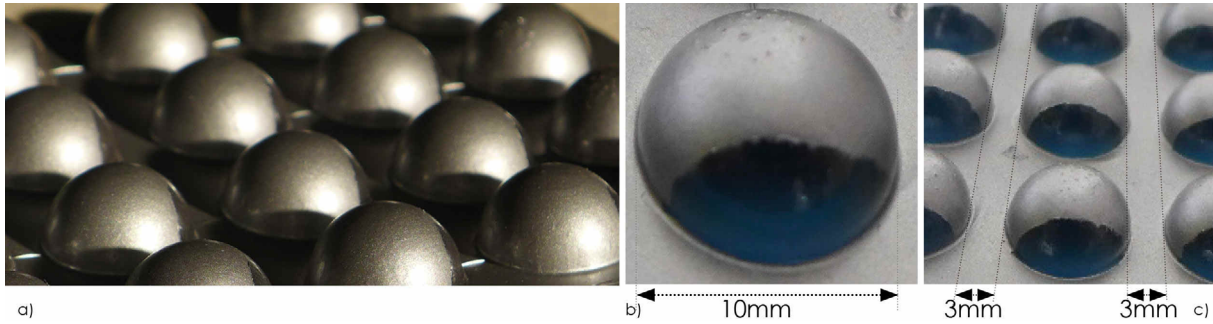


Figure 4: Material samples spatially transformed: 3D – Foil, optical impression

First material samples are made of PVC (polyvinyl chloride) in lab-scale 1:1 in the university’s workshops with a thickness of 200  $\mu\text{m}$  regarding the producible and optical impression, see in Figure 4. Based on the previous findings and results prototypes with the dimension of 700 x 700 mm are currently produced. These prototypes will then be measured to gather angle-dependent measurement data for the transmission  $[\tau]$ , reflection  $[\rho]$  and total energy transmittance (g-value) and finally they will be used for demonstration as well.

## 2 SIMULATION METHOD

First of all, the light foundations are based on the spectral data of transparent and nearly 100% printed ETFE-foil with a thickness of 200  $\mu\text{m}$ . This is required to calculate new materials for the material list [rad-file] to use it in DIVA 3.0 (Radiance), see Table 1.

Table 1: Material input for DIVA: ETFE-foil

<b>Window</b> <i>Description</i>	<b>color</b> <i>red/green/blue</i>	<b>specularity</b> <i>[-]</i>	<b>roughness</b> <i>[-]</i>	<b>transmission</b> <i>[-]</i>	<b>transmitted</b> <i>specularity</i>
ETFE - clear	0.98	0.08	0.00	0.99	0.98
ETFE – printed	0.44	0.29	0.00	0.16	0.40

Then a fictitious 3D-building model (Figure 5) was built in Rhino to simulate the illuminance  $[\text{cd}/\text{m}^2]$ , brightness impression and daylight factor (DF) with the aid of dynamic simulation in DIVA 3.0. Two different variants were created for this study, one for the visual comfort (intensity of daylight) and another for the daylight factor (sufficient natural daylight). The basic simulation model is a three-layer membrane cushion with 2 air chambers in which the sun protection (i.e. the spatially transformed 3D-foil with hemisphere geometry) is installed (cf. Figure 5a).

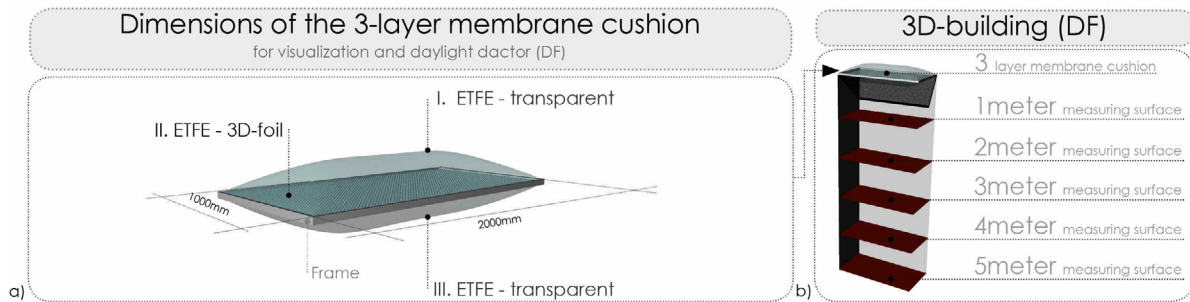


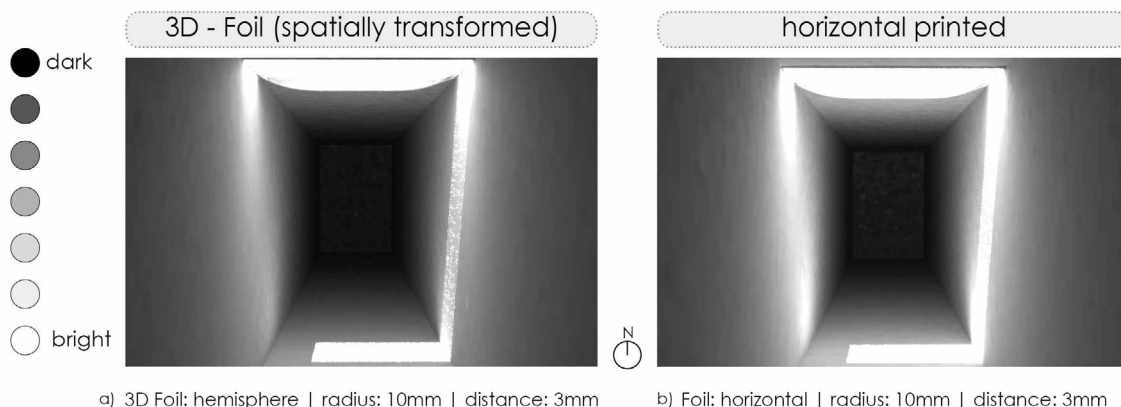
Figure 5: 3D simulation model:  
 a) three-layer membrane cushion (1000 x 2000 mm, high: 500 mm) c) sufficient daylight factor (DF) dependent of height.

### 3 RESULTS AND DISCUSSION

In the following simulations the spatially transformed sun protection (hemisphere geometry) with a radius of 10 mm and distance to each geometry of 3 mm cf. Figure 2c, will be compared within the membrane system with a conventional horizontal printed ETFE-foil (without spatially transformation). Furthermore, the identical printing part is analyzed in more detail with respect to the incoming of the daylight factor (DF) and glare phenomenon by using false colors ( $\text{cd}/\text{m}^2$ ) as well as the contrast differences and impact of shadow incidence. Only a small part of the 3D – foil (1000 x 2000 mm) is considered because through the small structure, the simulation time for a large area takes too long. In a next step, the prototypes can be measured in the artificial sun at the university’s workshops to analyse the daylight factor (DF).

#### 3.1 Visual comfort

Figure 6 depicts the results for the 21<sup>st</sup> of June at 1pm with direct radiation. The 21<sup>st</sup> of June is the day with the highest sun position at 13:25 am (azimuth:  $179.49^\circ$ , zenith:  $64.66^\circ$ ) in Stuttgart cf. Figure 3b. Comparing the visualization of the spatially transformed 3D-foil and the conventional horizontal printed foil, both variants are distinguishable regarding the brightness.



a) 3D Foil: hemisphere | radius: 10mm | distance: 3mm      b) Foil: horizontal | radius: 10mm | distance: 3mm

Figure 6: Visualization in DIVA: brightness impression, view from the south side.  
 a) 3D-Foil b) conventional horizontal printed

The visualizations in Figure 6 show the benefits of the new spatially transformed ETFE-foil regarding the impact shadow and brightness impression. The direct sunlight is blocked off and leads to less reflection glare inside the room. The further reflection properties of the components are listed in Table 2.

Table 2: Material (reflecion properties)

Input materials	Material name (DIVA)	Description
wall, floor, ceiling	GenericInteriorWall	50% reflectance
Frame	metal diffuse	50% reflectance

A clear sky with sun has a calculated illuminance of about 25.000 cd/m<sup>2</sup> (based on the climate data by the German Meteorological Service, Stuttgart). Figure 7 shows a false-color illustration and analyzes illuminance of the direct incidence of sunlight on the floor and a small part of the wall.

The achieved illumination requirements for a good comfort such as for a workplace (technical drawing) are an illuminance of 750 cd/m<sup>2</sup>; a color inspection of 1000 cd/m<sup>2</sup> and painting of 1000 cd/m<sup>2</sup> [3].

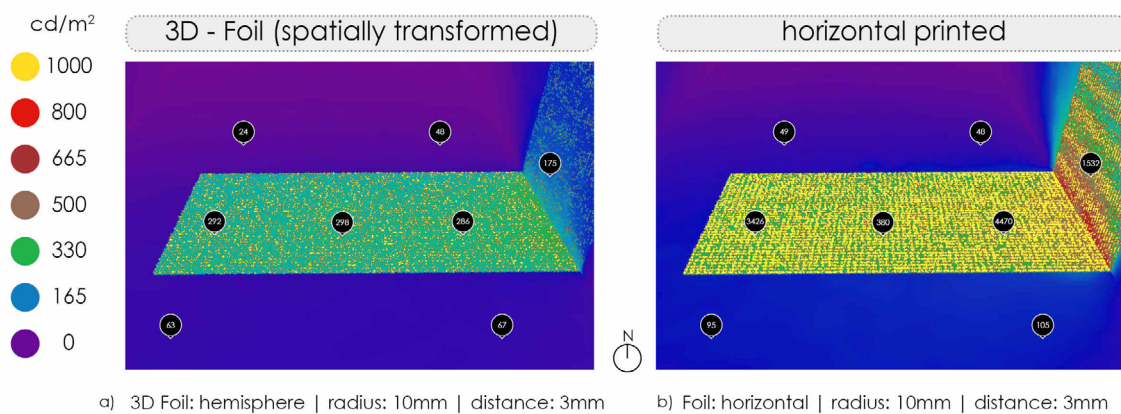


Figure 7: False-color  
a) 3D – ETFE- Foil b) horizontal ETFE-foil

Figure 7a (3D-foil) shows the highest illuminance with 1774 cd/m<sup>2</sup> compared to the horizontal printed ETFE-foil where the highest illuminance is at 7302 cd/m<sup>2</sup>. The average of the illuminance on the floor is for the 3D-Foil 528 cd/m<sup>2</sup> and for the horizontal printed foil at 1981 cd/m<sup>2</sup> in this viewing angle. This is a reduction of the illuminance (direct sunlight) of about 73%.

### 3.2 Daylight quality (DF)

The aim of the daylight factor analysis is to show the benefits and risks of the new 3D foil regarding to the natural daylight supply beginning from the floor of the room up to the spatial transformation (3D-Foil). Because of different levels of direct sunlight blocking partly 100%

due to the adjusted printing pattern, different variants were used. The daylight factor is calculated by diffuse sky conditions, i.e. without direct radiation as follows:

$$DF = (E_p / E_a) * 100 \tag{1}$$

Thereby, the diffuse sky is calculated with 17.900 cd/m<sup>2</sup>. Aimed daylight factors (DF) with rooflights should not be less than  $D_{min} < 2\%$ . Regarding the overheating in the summer the "DF" should not be higher than  $D_{max} > 10\%$  for rooms with a limited room height [8].

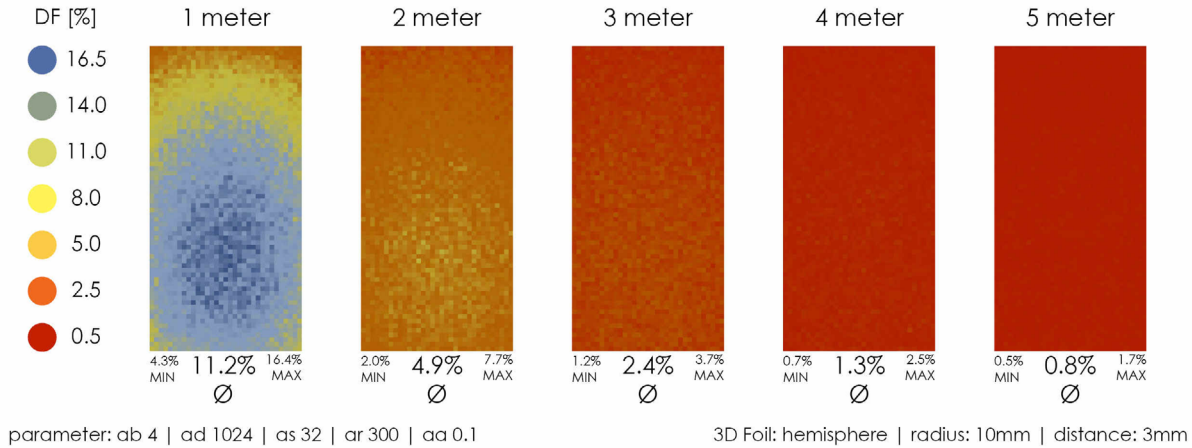


Figure 8: Daylight Factor (DF)

The daylight factor (DF) at a distance of 1 meter from the roof amounts 11.2%, at a distance of 3 meter 2.4% and at a distance of 5 meter it is only 0.8%. Therefore, the "DF" is sufficient up to a distance between of 3 and 4 meter.

Another criterion for the daylight conditions is the uniformity [G] of the daylight factor:

$$G = (D_{min} / D_{max} ) \tag{2}$$

A ratio from 1:4 is very good, but in case of  $G < 1:10$  the uniformity is described as insufficient [8]. At a distance of 4 meters the minimum "DF" ( $D_{min}$ ) is 0.7% and the maximum is ( $D_{max}$ ) is 2.5% this is a uniformity [G] of 1:3,6.

Compared with a horizontal printed ETFE-foil at the distance of 4 meter the "DF" is also by 1.3%,  $D_{min} = 0.7\%$  and  $D_{max} = 2.3\%$ .

#### 4 CONCLUSION & OUTLOOK

This paper is a short evaluation of the new shading approach for membrane structures. The general problem is the fixed transmission- and reflexion coefficient for conventional ETFE sun protection. This is addressed by the new spatially transformed ETFE-foil (3D-foil). Thereby, the idea of the shed roof (saw-tooth structure) is downsized to a millimetre scale. However, the new shading approach is installed in the middle of a multi-layer membrane cushion. An optimal geometry is a hemisphere, because the printing pattern can be adjusted exactly to the sun position independently from the spatial transforming process. In this paper the new sun protection is analyzed for Stuttgart (Germany) with an optimal printing pattern of

about 51%. This allows for a reduction of the cooling energy loads of about 69% according to a thermal simulation with TRNSYS 17 compared to a horizontal printed ETFE-foil [7]. A sufficient daylight factor (DF) allows from about 2.5 to 1.3% at a distance up to 4 meters. Because of the diffuse sky condition there is no significant difference between the new 3D-foil and a conventional horizontal printed ETFE-foil.

Furthermore, the glare risk can be reduced especially for the direct and reflection glare by the new shading approach. Based on the reduction of the illuminance (direct sunlight) of about 73%, this ensures even an uniform illumination inside the room. Therefore, the essential effect at the new angle-selective shading system for membrane structure is to block off a high amount of the direct sunlight and enter sufficient natural daylight for the thermal and visual comfort. The simulation results (DF) will be validated by measurements of the prototypes in the coming month.

## ACKNOWLEDGEMENTS

The project "FMESG" is funded by the German Federal Ministry for Economic Affairs and Energy (BMWi, project code 03ET1309F).

Supported by:



on the basis of a decision  
by the German Bundestag

## REFERENCES

- [1] Knippers J., Cremers J., Gabler M., Lienhard J., Construction Manual for Polymers and Membranes. Munich: BIRKHÄUSER/ DETAIL, 2011. p. 216.
- [2] Verordnung über energiesparenden Wärmeschutz und energiesparende Anlagentechnik bei Gebäuden (Energiesparverordnung – EnEV), 24.10.2015. p.30
- [3] DIN EN 12464-1: Light and lighting – Lighting of work places – Part 1: Indoor work places; German Version EN 12464-1:2011
- [4] Lau B., Masih D., Ademakinwa A., Low S., Chilton J.: Understanding Light in Lightweight Fabric (ETFE Foil) Structures through Field Studies, TensiNet 2016, Newcastle/UK, Procedia Engineering 155; 2016. p. 479 – 485
- [5] Cremers J., Marx H.: A new printed and spatial transformed ETFE foil provides shading and improves natural light and thermal comfort for membrane structures, PLEA 2017, Edinburgh/UK.
- [6] Cremers J., Marx H.: Comparative Study of a New IR-Absorbing Film to Improve Solar Shading and Thermal Comfort for ETFE Structures, Procedia Engineering 155 (2016) 113-120.
- [7] Cremers J., Marx H.: 3D-ETFE: Development and evaluation of a new printed and spatially transformed foil improving shading, light quality, thermal comfort and energy demand for membrane structures, CISBAT 2017, Lausanne/CH (currently still unpublished).
- [8] DIN EN 5034-6: Daylight in interiors – Part 6: Simplified determination of suitable dimensions for rooflights; German Version: 2007

## PERFORMANCE OF CURVED ORGANIC PHOTOVOLTAICS MODULES FOR MEMBRANES INTEGRATION: SOLAR SIMULATION TESTS

IBRAHIM ALI H.<sup>\*</sup> AND BECCARELLI P.,<sup>†</sup>

<sup>\*</sup> Department of Architecture and Built Environment  
The University of Nottingham  
University Park, NG72RD Nottingham, UK

<sup>\*</sup> Hend.ibrahimali@nottingham.ac.uk

<sup>†</sup> Paolo.beccarelli@nottingham.ac.uk

**Key words:** MIPV, Membrane Integrated Photovoltaic, Organic Photovoltaic Performance, ETFE, Solar Simulation Tests, OPV.

### Summary:

Photovoltaic (PV) solar technology is considered among the best product renewable energy sources for building applications. Flexible thin-film technology has potentials not only for traditional architectures, but also the most innovative applications that favor envelopes characterized by free morphologies such as membrane structures. Integrating flexible solar modules in pre-tensioned membrane structures allows for wide design varieties of shapes and geometries. However, the fact that curved and inclined PV modules whose orientation is guided by the membrane roof surface receive inhomogeneous radiation intensities across the module makes it necessary to measure the I-V characteristics in a testing environment to calculate the overall modules performance. This paper will be dedicated to investigating the yield of Organic Photovoltaics Modules and how the integration of organic flexible PV module onto a curved membrane surface has an impact on the PV module's output in a solar simulation test environment.

### 1 INTRODUCTION

The wide application of ETFE into architecture and the material characteristics starting from its lightweight, transparency, flexibility and ending with the sustainability and the durability make it a recommended substrate for the cheapest pv technology, Organic Photovoltaics. Although the OPV's efficiency is still low compared to the first and the second PV generations but this integration between the ETFE and OPV should represent a more cost-effective solution for the creation of a new kind of facade employable both in existing and new construction. Moreover, as Organic PV cells is mainly manufactured from polymers which is responsible for the module translucency unlike common Silicon PV technologies,

this makes OPV's are the best candidate when integrated with transparent ETFE cushions for maximizing the daylighting performance of building envelopes.

The integration of Flexible Photovoltaic Technology into membrane structures offers a promising significant step in the market development. However, some challenges and questions are arising relating to the applicability of such systems and how they are significantly dependant on a list of complex aspects that should be considered during the design phase. Among those aspects: I. Estimating the yield of PV system attached to membrane geometries whom surfaces are characterised by single or double curvature is a complex process. II. The distribution of stresses and deflection over the membrane surface and their impact on PV modules arrangement. III. The optimum orientation of PV modules to solar radiation in the determined geographic zone. IIII. The complex forms for membranes make it difficult to follow the areas under shadowing effect that should be avoided for locating modules.

## 2 ORGANIC PV SOLAR SIMULATION TESTS

The tests are conducted at the laboratory of General Electric Global Research Centre in Munchen, Germany using photovoltaics modules of Konarka power plastic lightweight thin-film organic solar module, Model 540 and 120 as shown in Fig.1, 2& 3. The target of these tests is to investigate how the integration of organic flexible PV module onto a curved membrane surface has an impact on the PV module's output. The fact that curved and inclined PV modules whose orientation is guided by the membrane roof surface receive inhomogeneous radiation intensities across the module makes it necessary to measure the I-V characteristics in a testing environment to calculate the overall modules performance. This part of the research will be dedicated to investigating the yield of Organic Photovoltaics Modules in relation to curvature in a solar simulation test environment.

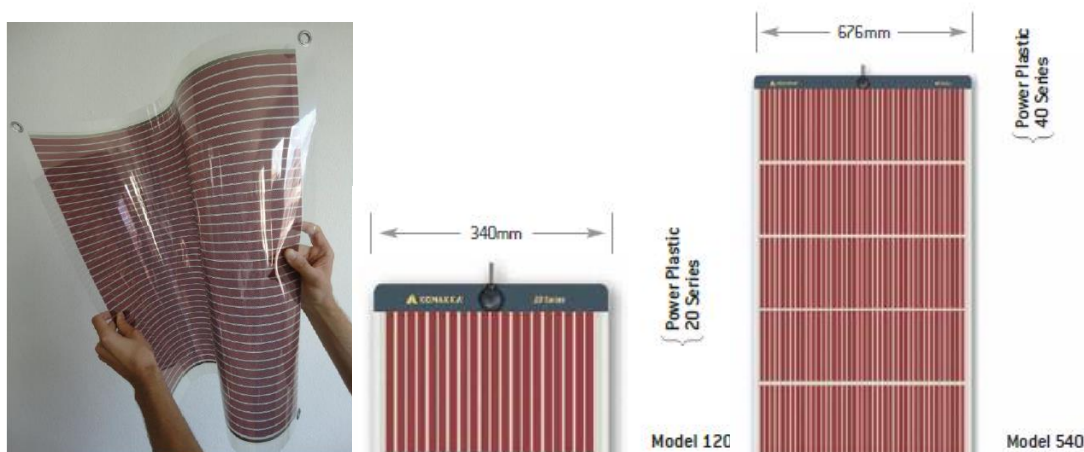


Fig.1, Fig.2. & Fig.3: Konarka OPV modules (Konarka power plastic)

## 2.1. Test Setup

The test facility at the laboratory of GE composes of a solar simulator of 6 metal-halide lamps arranged in two rows. Each lamp can be adapted to a range of radiation values starting from 400 to 1200 W/M<sup>2</sup>. A PVPM Meter (PVPM1000C40) device is connected to the module to measure the I-V characteristics of the modules using PVPM Display software. A Radiation sensor is located at the level of PV surface and transfer the measured values to the PVPM meter. A temperature sensor is connected to the backside of the module surface to monitor the temperature. Fig.4. indicates a model of the test facility.

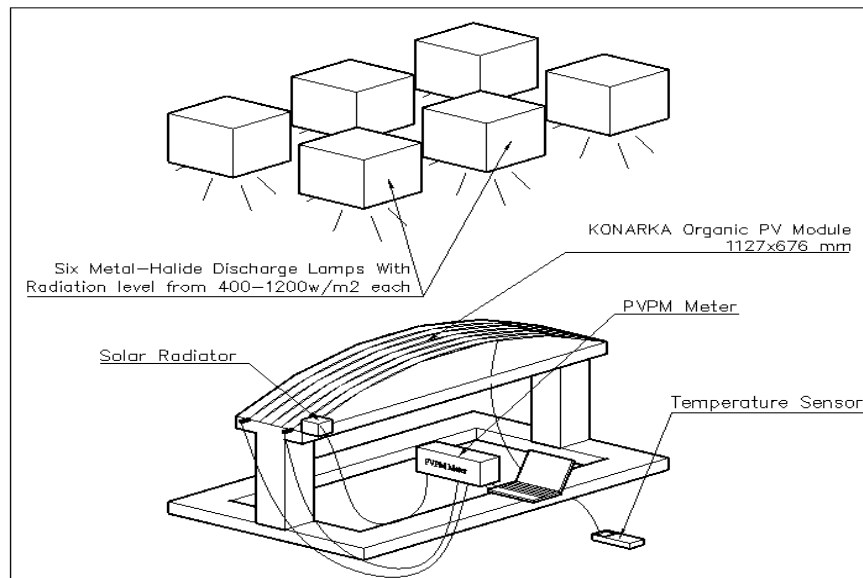


Fig.4. : The test stand and Equipments

## 2.2. Testing the Exact Performance Values

The first tests were done to measure the modules actual performance using the FLASHER equipment as shown in Fig.5. The target was to assess the modules technical values provided by the manufacturer's datasheet. The modules output was measured for the two 120 and 540 modules types. The obtained measurements are as follow:

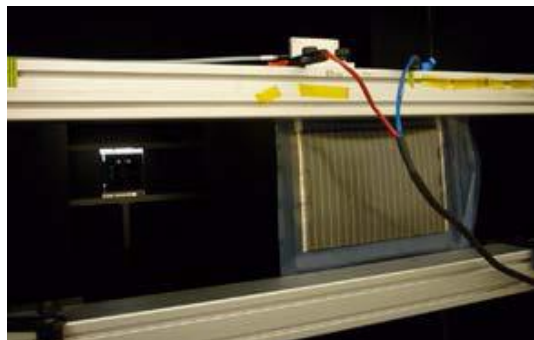


Fig.5: Measuring the modules output by a Flasher device

Module Type	Irradiance w/m <sup>2</sup>	Isc (A)	Voc (V)	MPP (W)	Efficiency (%)
Power Plastic 540	1000	0.96	23.2	12	1.6
Power Plastic 120	1000	0.2	11.63	1.18	1.3

Table 1: The exact performance values of Konarka OPV modules

### 2.3. Testing the Dependency of Curvature from Efficiency

Test Description: These tests are dedicated to monitoring the modules performance in relation to their curvature. A module’s performance of Power Plastic 540 is tested in six different curved positions starting from the flat zero curvature position till 9% curvature, as shown in Fig. 6. The GE laboratory test facility allows setting the module at different curvatures by fixing them on metal bars that could be clamped at their ends from both sides by controlling the distance “R” thus the curvature desired. See Fig.6, 7&8.

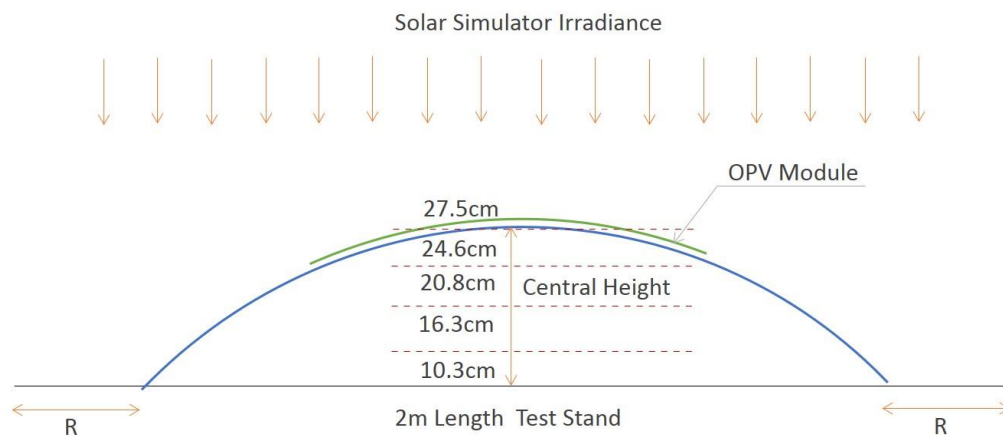


Fig.6: Testing stand

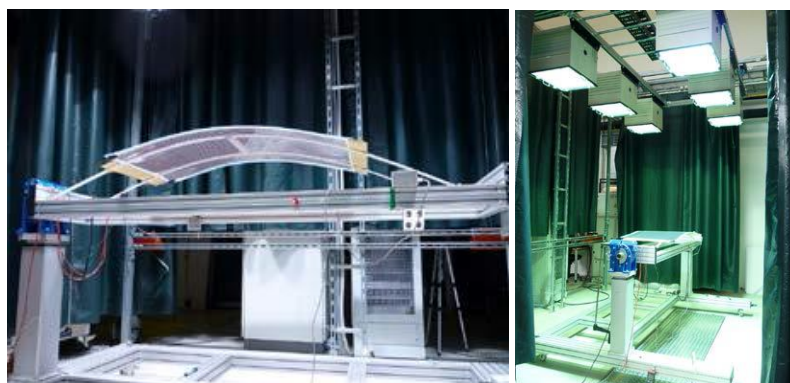


Fig.7 & Fig.8.: Testing the modules performance under curved positions

The module’s output in the flat position resulted in 9.2W while the performance has decreased to 9.1, 9.0, 8.9, 8.7 and 8.6 W corresponding to 3%, 5%, 7%, 8% and 9% respectively as indicated in Table:2.

Module Type	Voc (V)	Isc (A)	MPP (W)	T Mod	Irradiance w/m <sup>2</sup>	Central Height (cm)
Flat Position	21.97	0.7	9.2	51.8	699	0
3% Curvature	21.88	0.6	9.1	42.4	352	10.3
5% Curvature	21.91	0.6	9.0	41.8	340	16.3
7% Curvature	21.91	0.6	8.9	42.3	330	20.8
8% Curvature	21.90	0.6	8.7	43.3	342	24.6
9% Curvature	21.90	0.6	8.6	55.2	326	27.7

Table 2: The modules output at curved positions

**2.4. Analysis of Measurements:**

The first results showed that the performance of modules increase with increasing the curvature which seemed irrational as the flatter surfaces should receive the maximum radiation quantity and thus produce the higher output. The reason behind that the more curvature the module has the less distance between the module and the radiation source becomes. This is unlike the real conditions where the sun is far from earth by millions of kilometers. Therefore, an adjustment to the test setting was made by keeping the distance between the module peak point and the laps fixed by lowering the whole test structure by the same distance of the module rise resulted from increased curvature. Fig.9 indicates the results after the performed correction and show that the flatter the solar module is the higher performance the module achieves.

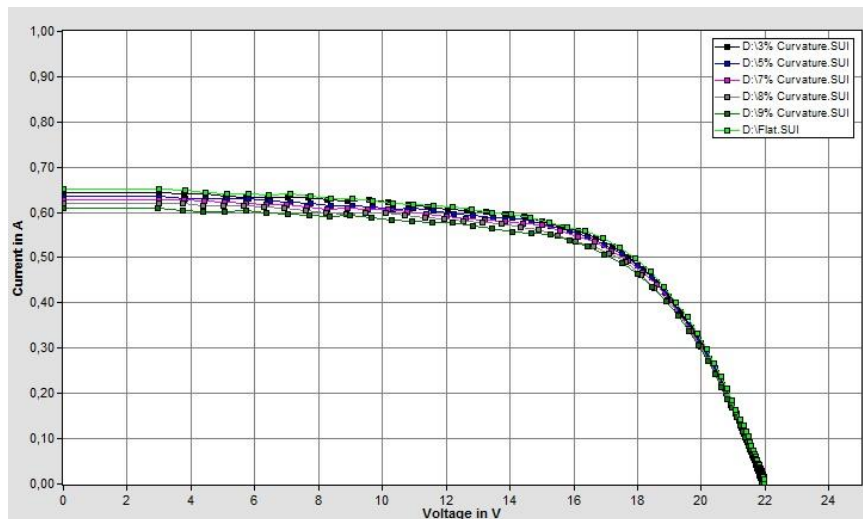


Fig.9: Indicates the I-V output for different curvatures of Konarka 540 module

### 3 CONCLUSION

The tests showed that Organic PV resulted in good performance rates when applied to curved surfaces. The yield of the modules decrease with increasing curvature and inclination as they receive less amount of perpendicular radiation to their plane. For an optimum performance, modules should be flat. Moreover, a comparison between Organic modules and Amorphous silicon is performed to calculate the rate of performance loss for both technologies. The Amorphous Silicon Tests Results is a part of Masters dissertation by Lakatos, 2011 in which he conducted his research using the same testing settings and thus the results can be comparable. The first and last reading for flat and 9% curvature were excluded from the comparison because of the inhomogeneous radiation value. The study showed that for the organic modules, a performance value of 0.028 Watt is reduced every 1cm increasing of central height. Whereas for Amorphous silicon modules, the reduced value is 0.03 Watt/1cm [3]. This comparison shows that both technologies have similar behavior in this aspect and that OPV has good potentials to compete with other PV technologies.

### REFERENCES

- [1] Cremers J., *Energy Saving Design of Membrane Building Envelopes*, International Conference on Textile Composites and Inflatable Structures, Structural membranes, Barcelona, 2011
- [2] Ibrahim H., *Membrane Integrated Flexible Photovoltaics: Integrating Organic and Thin-Film Photovoltaics Modules into ETFE and PTFE/Glass Membrane Structures*, PhD Dissertation, Politecnico di Milano, Italy, 2013.
- [3] Lakatos Z, “*Untersuchung einer membrandach-konstruktion mit integrierten flexible photovoltaikzellen*”, Hochschule für Angewandte Wissenschaften Hamburg, 2011

## **COMMON PROBLEMS IN THE DESIGN AND CONSTRUCTION OF MEMBRANE STRUCTURES**

### **STRUCTURAL MEMBRANES 2017**

**Dipl.-Ing. Florian Weller**

Florian Weller GmbH  
Donatusstrasse 6, 41352 Korschenbroich, Germany  
E-mail : [office@florian-weller.de](mailto:office@florian-weller.de), web page : <http://www.florian-weller.de>

**Key words: Membrane structures, design, construction**

**Summary.** This paper presents and discusses common problems frequently encountered in the design and construction of membrane structures.

Most of these problems can be avoided by careful design and preparation, which would take into account intermediate assembly and erection conditions. The following points should be considered, by assuring that:

- Realistic load assumptions are made, if necessary, with supporting load tests
- Individual fields are not too large
- Pre-assembly damage and kinks are avoided
- Slippage from snow, if possible, is avoided

When parallel to design, manufacture and assembly, a construction supervisor is tasked with reviewing and supervising all the stages, major damage can be avoided.

## **1 Introduction**

Membrane construction is an interesting field of activity, which is often unknown to the civil engineer.

Membrane structures fascinate by their interesting shape and their often prominent locations.

Following several, sometimes spectacular membrane failures, a certain degree of uncertainty has been experienced by structural designers and clients.

The following article is intended to describe the common causes of damage observed by the author who has been engaged to monitor and assure the quality of membranes and membrane systems.

The author has not undertaken any design work or conceptual planning works in membrane-related projects. Instead, involvement has always been restricted to managing and / or supervising such projects on site on behalf of the client. In addition, the author has gained further extensive knowledge and experience of this technology from dealing with inspection and maintenance issues related to completed construction projects.

Experience shows that the greatest problems lie with the implementation of the design (during manufacturing and assembly) which is often the cause of the ensuing damage (both before or after construction is complete). In order to be able to explain more clearly the problems associated with all the stages of construction, it is first necessary to explain the individual steps involved in the design, manufacture and final installation of a typical membrane project.

## **2 DEFINITION OF A MEMBRANE STRUCTURE**

In the context of this article, a membrane structure is defined as a surface of a flexurally soft building material, doubly curved and pre-tensioned and only capable of functioning in tension.

### **2.1 How does a membrane project work?**

Compared to traditional methods of construction such as reinforced concrete or steel construction, membrane design and final assembly can be highly complex, dealing with changing dynamic loads, sensitivity in the quality and performance of the manufactured fabric and final on-site installation.

To understand the differences compared with classical construction, it is helpful to describe the individual steps of a membrane project.

#### **2.1.1 Concept design and development of membrane shape**

The design of a membrane structure is relatively complex because the shape is the result of a form-finding process due to the inherent flexibility of the material. This form-finding is iterative, since the selection of the material, the boundary conditions and the chosen pre-tension always influences the form, repeatedly.

Due to the exclusive tensile characteristics of the material, care must be taken during the design of the membrane surface that the applied pre-stress must never be reversed into compression under the influence of external loads. Compressive stresses can lead to wrinkling and loss of the intended shape.

It is a particular characteristic of all membrane surfaces that their shape and loading condition are interdependent.

Therefore, the geometry depends upon the interacting forces - and vice versa.

The process of creating and defining a final membrane surface is now made by form-finding software, which has largely displaced the previously customary iterative, experimental methods.

### **2.1.2 Structural analysis**

The basic definition of the shape is followed by defining critical loads and deformation conditions. Particular structural analysis includes a focus upon the localised failure of any one membrane field, as well as the influence on loading due to snow and the potential for ponding of water.

Once these loads have been determined, the actual sizing of the membrane material and the surface and edge details are then designed.

Within the scope of this article, a particular topic which will be mentioned relates to the safety concept of membrane design, based upon partial safety factors.

An attempt is made to detect and cover some of the (negative) properties of the membranes by means of certain partial safety factors. Typical partial safety coefficients measure the influence of the biaxial stresses, long-term effects, environmental and temperature influences, the membrane material itself and influences from the erection. In addition, there is then a global safety factor for global influences.

This usually results in total safety factor coefficients of 5 to 7. Whether and to what extent these apparent high safety factors are able to achieve an adequate safety of a membrane construction must be examined separately in each individual case.

### **2.1.3 Cutting patterns**

The pre-tensioned, spatially curved membrane surface has to be cut out by the manufacturer from planar surface elements and then joined together in such a way that the desired three-dimensional shape is created subsequently through pre-stressing.

Influence on the cutting patterns and fabrication geometry is based not only on the width of the available material but also a minimization of the blending and questions relating to the assembly technology.

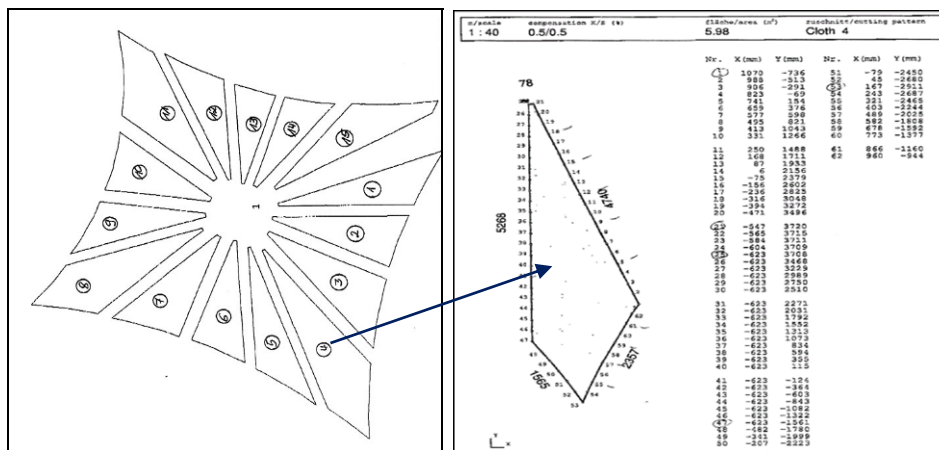


Figure 1 Cutting patterns from overview to single pattern

A particular difficulty for parties involved in supervision is that the design of the cutting patterns cannot be checked, unless undertaken by another independent designer. It is often not possible to determine whether the membrane has the desired shape under pre-tension (the more important would be an adjustable fastening of the membrane edges, see chapter 4.9).

### 2.1.4 Material selection

The choice of the most appropriate membrane material depends on many factors, such as:

- Strength,
- Durability,
- Cost effectiveness,
- Installation possibilities

A distinction is made between coated fabrics and single films.

Fabrics usually tend to be either Polyester-PVC or Glass-PTFE. For the most part, the types of films used are from transparent ETFE.

### 2.1.5 Determination of material characteristics, determination of compensation

Material characteristics, such as strength in the warp and weft direction, are initially specified by the manufacturer.

Within the scope of monitoring (see Section 2.1.6, approval in individual cases), this information is checked for each production batch.

Bi-axial stress-strain tests, partly influenced by temperature, are carried out on the cutting patterns and the relevant compensation required. These bi-axial tests provide important

knowledge and guidance into the strain behaviour of the membrane under load as well as the time-dependent relaxation of the membrane.

If the compensating values, on which the cutting patterns are based, are not determined correctly, then the membrane will be either too small or too large, and subsequently cannot either be installed or has too little pre-stress and / or folds.

### **2.1.6 Approval in individual cases**

In Germany construction projects using membranes are largely unregulated. The German Standard DIN EN 13782 is used for designing tensioned, membrane-type structures, including marquees and tents. In principle, in individual cases, it should be assumed in Germany that a building permit is required when choosing to build a membrane structure.

In order to monitor production, the accompanying material- and welded seam tests are usually prescribed. For this purpose, before the start of production and also during production, material samples and sampling of the most important details, are inspected and tested to destruction.

The author has experienced however, that in many cases, the quality of inspection and monitoring of the manufacture and final assembly of membranes is grossly inadequate. In the majority of cases, only one inspection of the manufacturing process and final installation is undertaken.

### **2.1.7 Assembling process in manufacture**

During the assembling process, the membrane is cut from raw material and put together.

At the beginning of the material inspection (mostly sampled from a roll), a check is carried out on a light table in order to detect faults in the fabric or the coating and to consider these in the context of the cutting process.

This is followed by cutting of the membrane shapes, mostly on CAD-CAM controlled machines. Another possibility to draw stencils on plotters, cut them out, and then mark the sub-fields on the membrane material.

The joining of the individually-tailored shapes into a membrane field is usually carried out by means of welding. In the case of Polyester PVC this is by means of high frequency welding, or in the case of glass PTFE fabric by means of a welding beam. For Polyester PVC fabrics, details are welded with the application of a hot-air gun.

Depending on the material type, joints can also be sewn.



**Figure 2** Welding of Polyester-PVC fabric with high frequency welding machine (Photo: CenoTec)

In addition, membrane details such as corners or reinforcements are manufactured; cable pockets are attached; and belts are sewn on.

After final visual- and dimensional inspections, the finished membrane bay is packed (see next chapter).

During the joining process, care must be taken that the material is treated with care. Especially for Glass PTFE fabrics wrinkles and kinks can occur and must be avoided at all cost.

### **2.1.8 Packaging / shipping**

Especially with kink-sensitive Glass-PTFE membranes, sufficient attention must be paid to careful packaging. Irreversible damage to membrane fabrics and coating can occur as a result of improper packaging.

For the packaging of large membrane panels a considerable number of personnel is required. Close bending radii must be avoided or compensated for by using cardboard or foam rolls.



**Figure 3** Folding of a large membrane panel

The more carefully a membrane can be packed, the less chance there is of damage occurring.



**Bild 4** Folding of excess area at a large membrane panel, mind the foam rolls at photo on left, these are too small and do not prevent kinks when fabric is folded

The designers should, in any case, create a folding and packaging plan for the jointed sections and specify the minimum size of the folded packages.

### 2.1.9 Assembly

As a part of the installation preparation, auxiliary structures- and scaffolding are erected. The delivered membrane is unpacked and then spread either on the ground and lifted up as a whole or spread out at the appropriate installation height.

The membrane must then be connected to the substructure relatively quickly in order to be able to control the membrane in the event of wind.

This is followed by the application of pre-tensioning.

The tensioning of a membrane between fixed edges, in part, entails a great deal of effort for tensile stresses up to 5 kN/m.

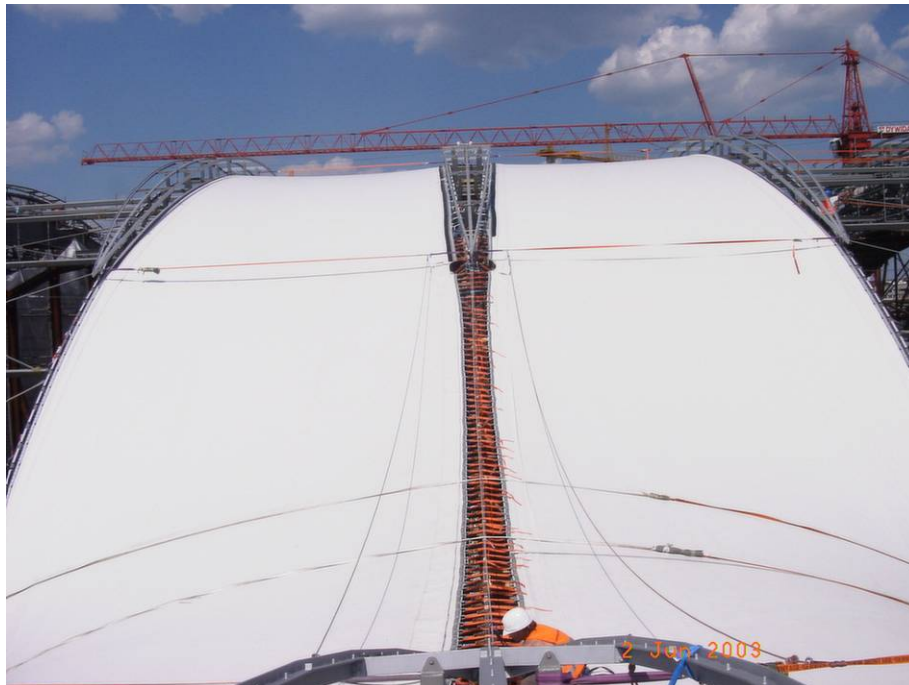


**Figure 5** Battery of ratchet belts for tensioning of two adjacent membrane bays

In the case of adjustable high or low points, the stresses can be entered relatively easily, with appropriate design of the anchor points.



**Figure 6** High point of a membrane panel during tensioning with hydraulics (© form-TL)

## 2.2 Typical detail solutions

There are many different solutions to join patterns to the surface or to attach to the edges of the membrane.

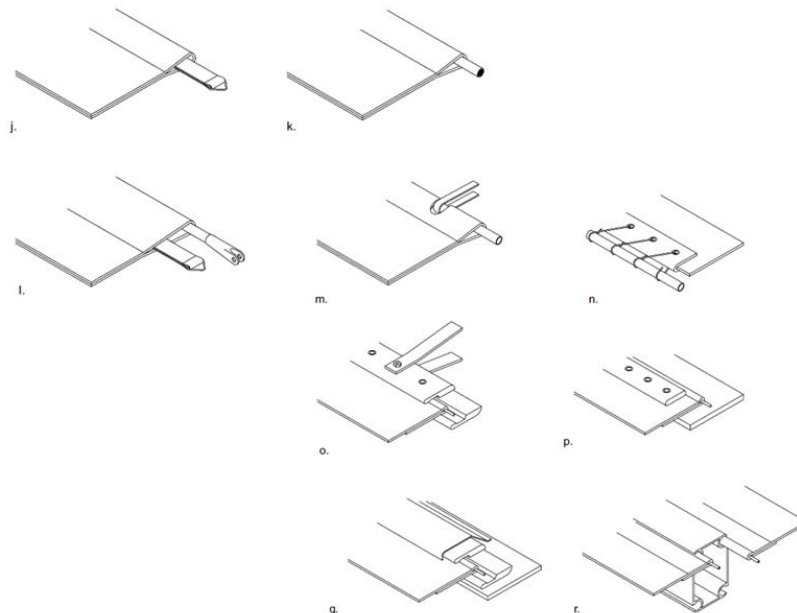


**Figure 7** Schematic overview of edge details [2]

A comprehensive explanation of the many different detail solutions for edges, corner and area details would be beyond the scope of this article.



**Figure 8**      **Examples of good edge and corner details**

At this point, it should be pointed out that it is generally advantageous if the fastening of the membrane is carried out adjustable on rigid edges so that, if necessary, it can be adjusted.

This allows the pre-tensioning in the membrane to be adjusted so that stress reductions from relaxation can be compensated for. Therefore, in the case of adjustable edge fixtures, the original pre-tension in the membrane can be lower, as long-term effects can be compensated for.

In the following, four typical and frequently occurring detailed solutions are described.

### **2.2.1 Clamping edge**

At the clamping edge of the membrane a keder stripe, welded to the edge of the fabric, is bolted between clamping plates. One of the two clamping plates is thereby wider than the others and can then be secured to the substructure.



**Figure 9** Clamping edge, bolted to concrete structure (© Birdair)

This solution has the advantage that the tensioning tools are fixed to the wider clamp plate for pre-tensioning and not directly to the membrane via auxiliary clamps. A worse version of the clamping edge is described in chapter 4.7.1.

### 2.2.2 Keder profile

By using a keder profile, the membrane is threaded into a keder profile, which in cross-section is a three-quarters-rounded track, usually manufactured from aluminium, using the same principal adopted for feeding sails onto the mast of a sailing boat.

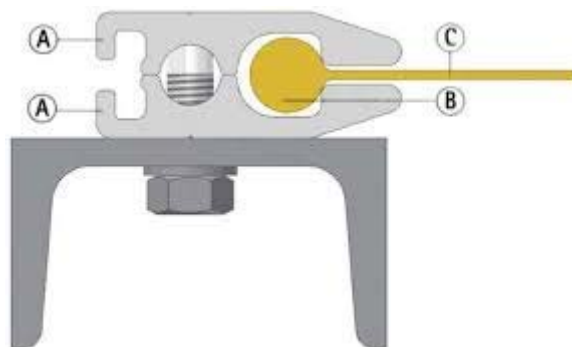


**Figure 10** Cross section keder profile

The advantage of using keder profiles is that first the membrane can be spread out and the profile can be subsequently pushed on (see next photo).



**Figure 11** Keder profile is pushed onto the edge of an ETFE foil

### 2.2.3 Rope edge

When connecting the membrane to an edge cable, there are basically two possibilities.

In the case of the cable pocket, the membrane is laid over and an edge pocket is created. In the edge pocket there is a rope or cable which is connected to the substructure.

There is also the possibility to allow the cable to run next to the membrane edge and to connect the membrane to the cable with clamping bars and straps.

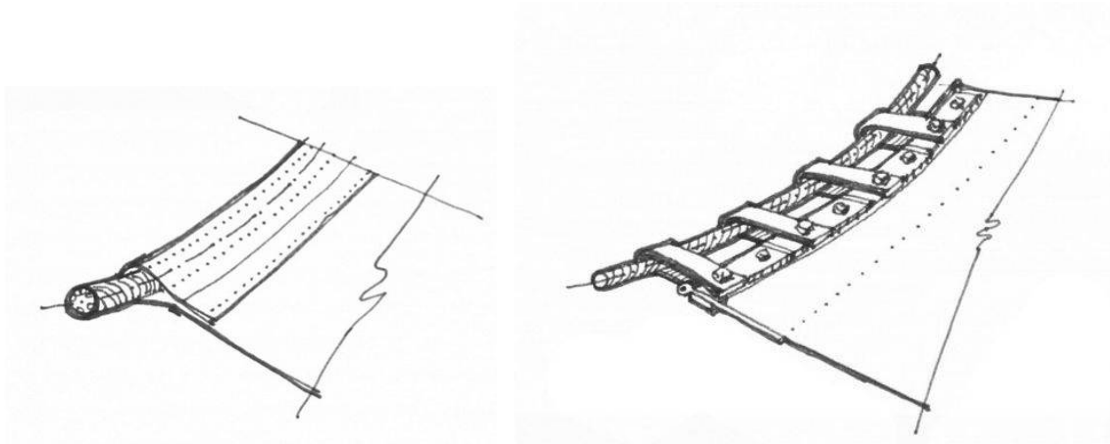


**Figure 12** Cable pocket (LHS) und cable edge with clamping bars and straps (RHS)

## 2.2.4 Support arches

Membrane support arches are a relatively simple concept in order to create saddle surfaces, especially when installed on cable nets.

The membrane arches are frequently equipped with keder profiles on the upper side. A keder stripe at the underside of the membrane is then threaded into these profiles. This keder stripe has two tasks. It prevents the membrane from being lifted off the arch and, at the same time prevents the movement of the pivoted.



**Figure 13** Membrane arches prepared for lift of membrane

For some projects, e.g. In the case of the fixed roof of the BC Place stadium (see figure 16), the membrane is exposed freely on the arches. The arches are coupled to one another by a cable extending in the longitudinal direction under the apex angles of the arches and are secured to prevent deflection.

## 3 INSTALLATION

The individual working steps of a membrane project have already been described in Chapter 2.

The actual installation procedure of the membrane is often neglected during design, however, particularly in the case of complex and large membranes, this places great demands on the personnel undertaking the work. Therefore, for this, the most important working steps are described in detail below.

When assembling a membrane, it is important to ensure that this is done, especially with glass PTFE fabrics, only at permissible temperatures and without damage and kinks.

### 3.1 Spreading out the Membrane

The process of spreading out the delivered membrane is not easy on the construction site in wind and rain. Usually, the package is placed on a scaffold table or belt net and spread there, usually with the help of a crane.

In the case of large panels, the membrane is often pulled over auxiliary belts and guided laterally. Care must be taken to ensure that under no circumstances shall any kinks be allowed to develop.

It is preferable if the membrane is delivered in a rolled form, and can be unrolled subsequently using a crane. However, this is only possible with modestly curved surfaces.



**Figure 14 Unrolling of membrane with use of crane traverse (Photo: Montageservice LB)**

During the spreading of the membrane, a temporary position must be securable at any time.

### 3.2 Connection to the sub-construction

After spreading and temporarily securing the membrane, it is connected to the substructure.

Keder profiles are slipped, clamping plates are screwed on, or edge cables are pulled into their pockets.

Often auxiliary structures are necessary for the introduction of the tensile forces. In some cases, auxiliary keder stripes (stripes welded on in the factory, which are later cut off) are of considerable assistance in installation.

### 3.3 Applying the pre-tension

In the case of a membrane with high or low points, the introduction of the pre-tensioning is usually simple: first the membrane edges are connected and then the high or low point is pushed or pulled.

At any rigid edge location, the membrane must be pulled continuously along its entire length. This means that in most cases numerous ratchet belts or threaded rods are used. During the installation design process, specifications for the forces are established, including rest periods required during tensioning.

The application of the pre-tension should be monitored with appropriate measurement device (e.g., load cells) so as not to exceed the scheduled pre-tensioning at any time.

#### **4 COMMON CAUSES OF DAMAGE**

There are a variety of different causes for possible damage to a membrane structure. Usually, a single circumstance is not the cause of damage, but a combination of different factors.

According to the author's experience, the defects listed below are relatively frequent causes of damage.

##### **4.1 Unrealistic load assumptions**

In complex shapes or roof surfaces, it is often difficult to make realistic load assumptions.

It is important to ensure that loads from wind, snow and ice are correctly understood and that the design prevents the formation of water ponding. See also the Dresden Central Station, chapter 5.2.

The dynamic effects of slipping snow are extremely difficult to take into account. In addition, there is the fact that the snow is often lumpy and compact and an ice layer can form under the snow. This prevents realistic assumption of the actual loads, therefore is almost impossible. If possible, the elimination of the risk of snow slippage should be considered and designed out of the final solution.

##### **4.2 Unconsidered constraints or load peaks**

Possible constraints or load peaks are a sub-topic of the load assumptions. However, since a membrane is very sensitive to the introduction of local loads, this point should be considered separately.

Any hindrance to the free deformation of the membrane must be avoided or taken into account as a specific load case. If a peak load can occur, corresponding reinforcement must be provided.

Disregarding deformations and the resulting contact with other components can lead to partially large load peaks. At the Metronom Theatre in Oberhausen, on the rigging level in the interior of the theatre, a steel construction was installed retrospectively, which was physically quite close to the inner membrane. During heavy winds, the inner membrane was subsequently pressed against the sharp edges of the steel construction and tore along a length of about 20 metres.

### **4.3 Very large membrane fields**

Very large membrane fields (individual sizes of more than 500 m<sup>2</sup>) lead to problems in several respects.

The handling of the membrane in the joining process is only possible by using a considerable number of personnel and by using cranes. The larger the membrane, the more likely folds are kinked or stepped upon - with the inevitable consequence of damage.

The given packing dimension (i.e. container dimensions, air transport) may not permit the necessary bending radiuses to be sustained or maintained

The membrane, which has a light surface, develops a considerable weight in several layers, which then causes the folds to become damaging creases or kinks.

During installation, large individual surfaces are difficult to handle and, above all, they cannot be secured temporarily.

In the case of more extensive damage, correspondingly larger sub-panels must be replaced.

Therefore, oversized membrane fields should be avoided. Large areas can be subdivided into individual membrane fields and these can then be connected with clamps or two-sided keder profiles.

### **4.4 Inadequate packaging**

The temptation to convert a membrane panel, which is sometimes hundreds of square metres in size, into a transport package that is as small as possible, while at the same time minimizing the minimum bending radii of the material, is relatively high.

The pressure to meet agreed deadlines, and the intention to ship the membrane by air transport, often leads to inadequate packing being used.

The following photo shows a two-layer Glass-PTFE membrane of approx. 800 m<sup>2</sup> total area after opening of the transport crate. It is evident from the snow rests at the edge of the photograph that temperatures around the freezing point appear to prevail. This membrane thus transported and installed at sub-zero temperatures failed completely nine months after installation from snow load.



**Figure 15** Glas-PTFE Membrane (approx. 800 m<sup>2</sup>) packed particularly small

#### **4.5 Folds and kinks**

Folds and kinks, especially with Glas-PTFE membranes, lead to a reduction in the load-bearing capacity of the fabric.

Folds and kinks can be developed at several points during the production process, the packaging process and, of course, during installation.

In the case of Glas-PTFE membranes, kinks must always be avoided. According to the author's experience, instructions on this alone are not sufficient, therefore instead the individual work steps should be monitored.

#### **4.6 Unfavourable installation conditions**

Unfavourable assembly conditions can have many causes and characteristics. One example being the existence of quite a high height combined with limited accessibility for installation.

In addition, unfavourable conditions during membrane assembly can arise from time pressure, wind and low temperatures.

Substantially greater time pressure can lead to unsatisfactory handling or care of the membrane, including lack of regard for the necessary relaxation of the membrane during the tensioning process.

Time pressure also means that often the requirement for a favourable weather window is ignored. If strong winds occur during an (unsecured) assembly condition, damage is almost

certainly pre-programmed. An example of this is the façade of the Cape Town Stadium (see chapter 5.3).

Glass-PTFE membranes cannot be installed at low temperatures. The temperature limit is discussed repeatedly, but it is essential that a minimum temperature of  $+5^{\circ}\text{C}$  is observed at all cost.

A further repeated discussion is to ensure that the membrane is heated, preferably whilst contained inside the transport box, in order to avoid damage to the fabric by transport movement at low temperatures. The approach is not incorrect, however, it must be noted that the membrane will subsequently assume the ambient temperature once again immediately after it has been spread out.

#### 4.7 Difficult to install details

The conditions and requirements of the subsequent installation must be taken into consideration as early as the design stage. Potentially cost-effective or easy-to-maintain details may be difficult to mount on the construction site, possibly at high cost or leading to damage of the membrane.

Two examples will illustrate this.

##### 4.7.1 Clamping edge

The very simple clamping edge of the membrane, at which the membrane is fixed with a keder stripe by means of threaded bolts and a clamping bar, can hardly be installed if there are no adjustment possibilities on the edges. This detail can only be mounted free of stress, for example, when a high-point membrane is used.



**Figure 16** Clamping edge, planned details on RHS, LHS shows situation during installation with auxiliary clamps

A substantially better clamping edge is that which uses two clamping profiles from which the wider one can be secured to the sub-construction (see Chapter 2.2.1)

#### 4.7.2 Keder profile on membrane arches

The membrane arches described in Chapter 2.2.4 with the keder profile, into which a keder stripe on the underside of the membrane must be threaded, considerably complicate the installation of the membrane. Not only must the arches be corrected in their lateral inclination, as the membrane is pulled over, it is also necessary for the installation team on the underside of the membrane to monitor and ensure correct threading of the keder stripe onto the membrane arch.

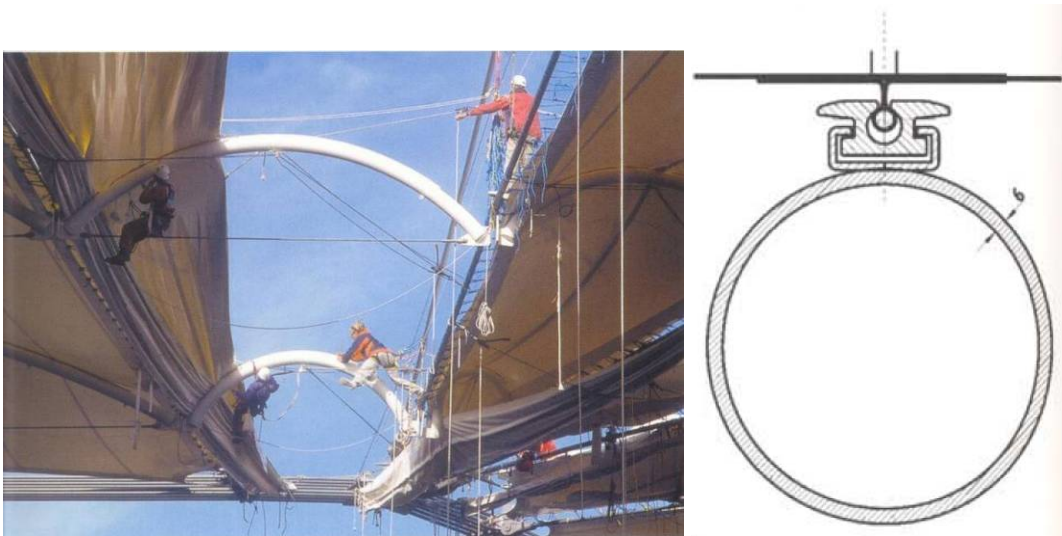


**Figure 17** Membrane arches with membrane pulled over, mind the workers hanging under the arches (LHS), Detail of arch with keder profile (RHS)

It would be better if a keder profile could be pushed onto the keder stripe on the underside of the membrane after assembly and then connected to the membrane arch.

It would also be conceivable to screw a clamping bar from above through the membrane into a corresponding profile on the arch.

#### 4.8 Missing installation aids

The author can confirm that on several construction sites only the final installed condition of the membrane edge details were considered, instead of planning the actual sequence of installation steps which resulted in this final condition.

The following photo shows a battery of small tirsers, which have been hooked to the underside of a metal flashing. There was simply no other method to initiate the necessary pre-tensioning forces at the edge of the membrane since no assisting installation device or methodology was planned at design stage.



**Figure 18** Battery of turfers to tension a membrane bay

The following photo shows another example, the tensioning process of a single-ply ETFE film. Although the pre-tensioning forces are rather small here, the assembly team had to build an expensive (and not altogether trustworthy) tensioning device in order to ensure that the tensioning in the foil was achieved.



**Figure 19** Tensioning of a single layer ETFE-foil

This lack of installation assistance leads to the installation being made more difficult and attention is no longer paid to ensure any necessary and careful treatment of the membrane.

Unfavourable installation conditions also lead to the pre-stressing forces being applied too quickly in the membrane in order to be able to complete the installation as quickly as possible.

#### 4.9 Non-adjustable edges

Attaching the membrane to the substructure with clamping edges without properly designed adjusters causes two major problems.

If the attachment of the membrane to the rigid edges is adjustable, long-term effects, such as creep and relaxation, which lead to reduced tension in the membrane, can be compensated for. In this instance, the applied pre-stress to the membrane can be lower because re-tensioning would then be possible. Without an adjustable clamping edge, considerable pre-stresses must be introduced, with the associated extra effort required during assembly. In addition, the membrane must then be tensioned over a longer period of time until the material has reached the desired geometry without the need for excessive forces. These extended periods of time have a corresponding influence on the cost of resources required (i.e. personnel, equipment and materials).

A second, negative aspect of the fixed, non-adjustable clamping edge relate to the ensuing tolerances in the substructure to which is connected. Deviations from the intended geometry then influence the membrane directly, which can lead to considerable damage. The following photo shows a membrane which has been connected to a steel substructure with clamping plates. Dimensional deviations in steel construction lead to an offset between adjacent clamping plates, to shear forces in the membrane edge and ultimately to a tearing of the membrane through the clamping edge.



**Figure 20** Offset of clamping plates fixed to steel structure

## 5 DAMAGED MEMBRANES - EXAMPLES

The following is a description of the damage known to the author. The selection of these examples of damage is not entirely arbitrary, instead they demonstrate common causes of damage.

### 5.1 Veltins-Arena Gelsenkirchen

At the Veltins Arena in Gelsenkirchen in the winter months of 2010/11, damage to 7 of the 40 roof fields occurred within three days. The roofs were largely irreparably damaged. Fortunately no one was injured.



**Figure 21** Aerial view of Veltins-Arena, end of December 2010

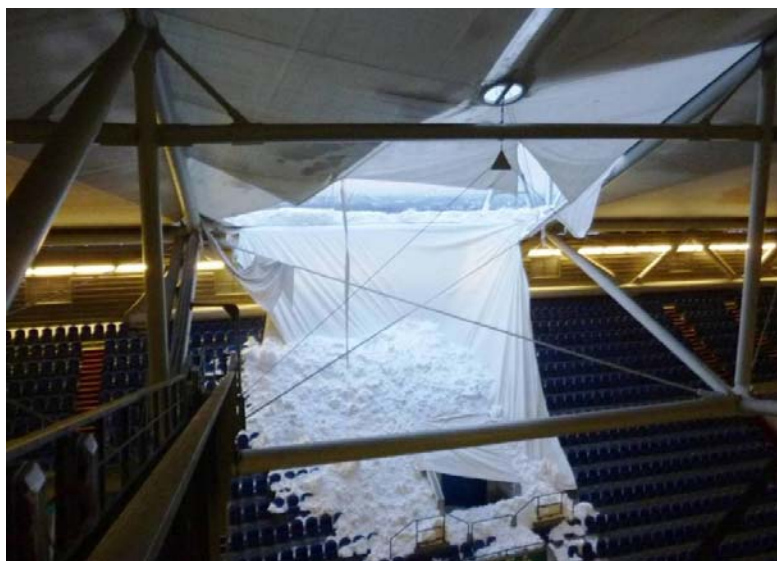


**Figure 22** Veltins-Arena, snow loads on the stand after failure of a roof panel



In addition, pre-damage to the membrane could be confirmed by the observation of kinks which had arisen during assembly and / or during installation.

Both factors led to a reduction in the load-bearing capacity of the membrane.

### **5.1.3 Dynamic effects caused by slipping snow**

Regarding the various identified damage, which occurred in part only a few hours after each other, the effect of snow on the roof areas was varied. On some fields, the snow lay more or less evenly distributed over the entire roof surface compared to the field which failed. Here, the above-described load peaks at the unintended suspension points may have been decisive in defining the cause of the damage.

In other fields the snow had slipped down to the gutter. Dynamic effects, culminating in the fact that the compacted snow mass, which slipped with increasing speed, strongly deformed the membrane at the lower connection to the steel structure and probably also pressed against the steel structure. As a result, local load peaks occurred, which led to initial tears.

### **5.1.4 Build-up of ice under snow on the roof**

The effects described above, during which time the snow had slipped off the membrane, were aggravated by the fact that under the snow layer a several centimetres thick ice layer had formed on the membrane. As a result, this ice had acted as a knife during the slipping process, thus slicing through the membrane material.

The ice forms under the snow layer, when the snow heats up from underneath, i.e. from the interior of the stadium, and freezes again once temperatures drop. In addition, rainwater is able to seep through the snow layer, and can subsequently freeze at the boundary layer to the membrane.

Conclusion: Peak loads were not identified and the membrane material had been pre-damaged by kinks. The membrane was locally damaged by the dynamic effects of unhindered slipping snow, together with the formation of ice below.

## 5.2 Main railway station, Dresden

At the membrane roof of Dresden's main railway station, which was built between 2001 and 2006, 5 to 14 m wide fields of Glas-PTFE fabric are stretched between a secondary structure on the historical framework arches. For every second axis, the membrane forms a funnel for dewatering the roof surface.



**Figure 24** Main station Dresden, partial view of roof with funnels

In the winter of 2009/2010 a large tear occurred at one of the funnels. The membrane was cut at a height of about 3 m, permitting a lens-shaped opening to be observed. Inside the funnel lay a compact lump of ice and snow to a height estimated to be 2.0m.



**Figure 25** Main station Dresden, ruptured funnel with snow filling

At first, it was assumed that this was a singular event due to damage to the funnel membrane. In the winter of 2010/11, however, a further eight funnels with a similar damage pattern tore.



**Figure 26** Main station Dresden, ruptured funnel with snow filling

In the structural calculation of the membrane roof, snow loads on the basis of a wind and snow load report were taken into account. Local snow accumulations and filling of funnels with snow were also considered.

The actual snow in the funnels, however, was heavily compressed and had developed a density almost the same as ice. Moreover, the surface of the clumped snow was not smooth, but partly exhibited fist-sized depth between peaks and troughs.



**Figure 27 Main station Dresden, clumped snow in funnel with local peaks**

The cause of the damage lay in an overloading of the membrane by the formation of snow and an ice wedge in the funnel. Due to this wedge, very high stresses occurred locally in the membrane, which finally led to the failure of the material.

It could be proven that in the wind and snow report as well as in the structural analysis of the membrane, a sufficiently high snow weight was calculated.

However, it was clear that in the case of the local observations, that is to say in the funnels themselves, inadequate high snow loads or ice loads were assumed in the structural analysis of the membrane, therefore were inadequate to cover the prevailing conditions at the time, including the slippage of snow.

The resulting combination of snowfall, low temperatures over an extended period of time and a subsequent rainy season caused unfavourable conditions for the load on the hoppers. It is extremely difficult to calculate or assess the dynamic effects of slipping snow, especially when assessing large quantities (of it).

Conclusion: The load assumptions adopted in the area of the funnel were totally inadequate for the eventual prevailing load conditions. Additionally, the dynamic effects from slipping snow were not considered.

### **5.3 Green Point Stadium, Cape Town, South Africa**

The assembly of the façade at the Greenpoint Stadium in Cape Town had to be carried out at the end of a tight program, therefore there was extreme time pressure to complete this.

Although several fields were already assembled and a degree of expertise should have been gained as a result, wind forecasts were ignored under the prevailing time pressure.

Strong wind during the installation of a façade field led to the destruction of the Glass-PTFE mesh fabric, since the high forces developed during assembly could at times only be transferred at certain individual points.



**Figure 28** Green Point Stadium, facade during installation



**Figure 29** Green Point Stadium, wind damage to facade panel

Conclusion: It was installed under unfavourable weather conditions so that strong wind could damage the membrane during intermediate assembly conditions. The loss of time due to the loss of the façade field was, of course, significantly higher than the waiting time which should have been taken in order to ensure optimum installation conditions.

## 5.4 Velodrome, Abuja, Nigeria

The Velodrome in Abuja, the capital of Nigeria, was built in 2003 and used for the All-African Games, together with the adjacent National Stadium.



**Figure 30** Velodrome Abuja, Nigeria

On the last day of the All-African Games the membrane roof was almost completely destroyed during a thunderstorm.



**Figure 31** Velodrome Abuja, Membrane damaged after thunder storm  
© Getty Images

As is often the case, the cause of damage has several sources.

The original design anticipated that the membrane of the entire dome should be assembled on the ground and then suspended from a rope net.

This led to extremely large membrane fields being created, which had to be spread and assembled on the ground. Due to the significant 3-dimensional curvature of the roof, the membrane laid on the floor had a great many folds. Due to a lack of supervision, the assembly team was permitted to walk over these folds, leading to initially unobservable kinks being created in the material.

With the aid of structural calculation, the deformations of the roof under wind influence were investigated. Above all, the catwalk suspended under the membrane on the rope net had to be able to absorb the deformations. However, a critical point was not taken into account when considering membrane deformations, namely access to the catwalk. At a particular point, a ladder is connected to the catwalk from the ground. This location formed a fixed position within the catwalk, at which point deformations were restricted.

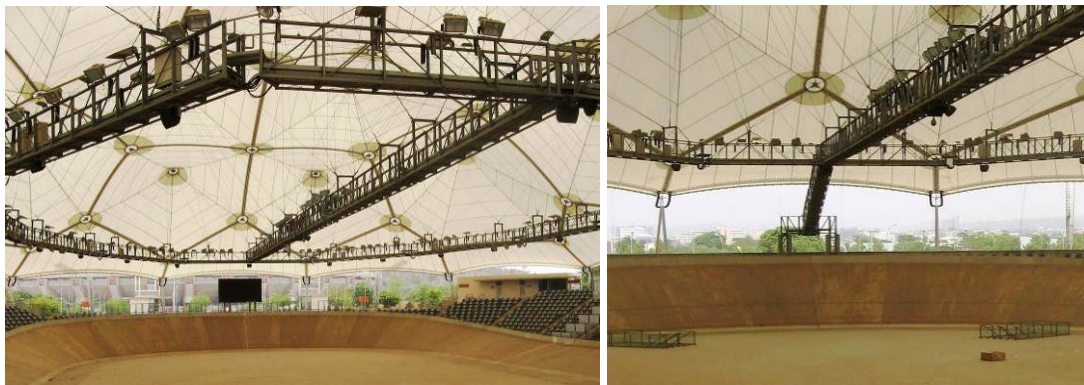


**Figure 32** Velodrome Abuja, catwalk under the roof, photo RHS shows access from ground level to catwalk

During a strong thunderstorm with high wind loads and corresponding deformations of the roof, the membrane was pressed against the railing of the catwalk at the fixed point and tore. As a result of the above-described damage (kinks) during assembly, the initial tear propagated further and ultimately led to the complete destruction of the membrane.

Conclusion: Constraints had not been considered, the membrane fields were too large for appropriate assembly, and assembly had not been monitored, resulting in membrane material being kinked and damaged.

## 6 SUMMARY

This paper has discussed and clarified the frequent problems relating to the design, manufacture and installation of membrane structures, including offering solutions to avoid expensive damage.

The main and most frequent causes of problems with the construction of membrane structures and subsequent damage are:

- Unrealistic assumption of loads, especially with regard to snow loads and dynamic effects from slipping snow
- Lack of foresight of possible peak loadings
- Oversized membrane fields and thus also inadequate packing requirements
- Folds and wrinkles
- Unfavourable installation conditions
- Installation-unfriendly details and missing installation aids
- Absence of adjustment possibilities

Most of these problems can be avoided by careful design, which should also take account of the intermediate and final installation conditions. The following points should be observed:

- Adopt realistic load assumptions, if necessary, with tests and/or mock ups
- Do not select individual fields to be too large, observe packing requirements, and take into account installation options
- Monitor the manufacture and installation sufficiently in order to ensure quality and to avoid damage or kinks

Slipping of snow should be prevented wherever possible. If a membrane surface is designed for snow loads, this should be in a manner to permit the snow to remain on the roof surface and to thaw gradually. If slipping of snow cannot be prevented, the membrane edges should be designed so as to offer as little resistance as possible to the sliding snow.

In Germany, the membrane material itself as well as the surface and edge details are tested thoroughly in all membrane projects. However, due to a lack of published guidance for use at the design stage, attention to monitoring the various processes of membrane construction, right through from initial concept design to production and installation, is inadequate.

The obvious conclusion is that if a dedicated person were to be appointed to supervise all aspects of the design, factory manufacture and installation on site, this appointment would go a long way to ensuring that significant damage to membrane structures is avoided.

## 7 REFERENCES

- [1] Bauen mit Membranen DETAIL Zeitschrift für Architektur, Heft 6, 2000.
- [2] Koch, Klaus-Michael; Habermann, Karl J.: Membrane Structures: The Fifth Building Material, Prestel Verlag, 2004.
- [3] Seidel, M.: Textile Hüllen, Bauen mit biegeweichen Tragelementen, Ernst & Sohn, Berlin, 2008.

## DESIGN AND CONSTRUCTION OF THE ASYMPTOTIC PAVILION

Eike Schling<sup>\*</sup>, Denis Hitrec<sup>†</sup>, Jonas Schikore<sup>\*</sup> and Rainer Barthel<sup>\*</sup>

<sup>\*</sup> Chair of Structural Design, Faculty of Architecture, Technical University of Munich  
Arcisstr. 21, 80333 Munich, Germany  
e-mail: eike.schling@tum.de, web page: <http://www.lt.ar.tum.de>

<sup>†</sup> Faculty of Architecture, University of Ljubljana  
Zoisova cesta 12, SI – 1000 Ljubljana, Slovenia  
e-mail: hitrec.denis@gmail.com - web page: <http://www.fa.uni-lj.si>

**Key words:** Asymptotic curves, Minimal Surfaces, Strained Gridshell.

**Summary.** *Digital tools have made it easy to design freeform surfaces and structures. The challenges arise later in respect to planning and construction. Their realization often results in the fabrication of many unique and geometrically-complex building parts. Current research at the Chair of Structural Design investigates curve networks with repetitive geometric parameters in order to find new, fabrication-aware design methods. In this paper, we present a method to design doubly-curved grid structures with exclusively orthogonal joints from flat and straight strips. The strips are oriented upright on the underlying surface, hence normal loads can be transferred via bending around their strong axis. This is made possible by using asymptotic curve networks on minimal surfaces<sup>1, 2</sup>. This new construction method was tested in several prototypes from timber and steel. Our goal is to build a large-scale (9x12m) research pavilion as an exhibition and gathering space for the Structural Membranes Conference in Munich. In this paper, we present the geometric fundamentals, the design and modelling process, fabrication and assembly, as well as the structural analysis based on the Finite Element Method of this research pavilion.*

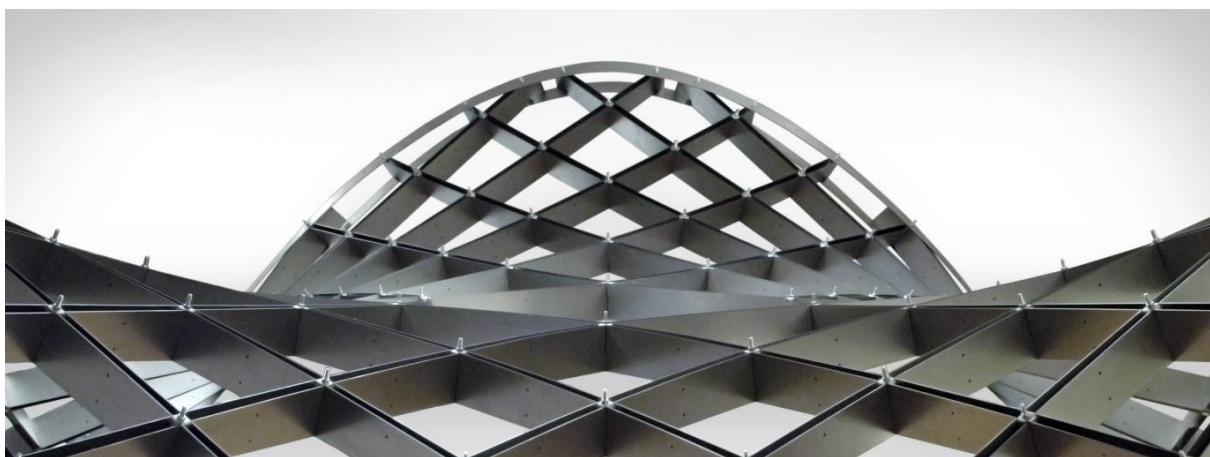


Figure 1 Prototype of an asymptotic gridshell. The structure is built from straight strips of steel. The lamellas are oriented normal to the design surface. All slot joints are identical and orthogonal. *Image:* (Eike Schling)



Figure 2: Grid structure based on asymptotic curves: The model is built from straight strips of beech veneer. All joints are orthogonal. *Image: (Denis Hitrec)*

## 1 INTRODUCTION

There are a number of design strategies aiming to simplify the fabrication and construction process of doubly-curved grid structures. Therein, we can distinguish between discrete and smooth segmentations<sup>3</sup>. One strategy, to build smoothly curved structures relies on the elastic deformation of its building components in order to achieve a desired curvilinear geometry from straight or flat elements<sup>4</sup>. Consequently, there is a strong interest in the modelling and segmentation of geometry that can be unrolled into a flat state, such as developable surfaces<sup>5</sup>. Recent publications have given a valuable overview on three specific curve types – geodesic curves, principal curvature lines, and asymptotic curves (Fig. 3) – that show great potential to be modelled as developable strips<sup>6</sup>. Both geodesic curves and principle curvature lines have been successfully used for this purpose in architectural projects<sup>7</sup>. However, there have been no applications of asymptotic curves for load-bearing structures. This is astounding, as asymptotic curves are the only type which are able to combine the benefits of straight unrolling and orthogonal nodes (Fig.2).<sup>1,2</sup>

In this paper we present a method to design strained grid structures along asymptotic curves on minimal surfaces to benefit from a high degree of simplification in fabrication and construction. They can be constructed from straight strips orientated normal to the underlying surface. This allows for an elastic assembly via their weak axis, and a local transfer of normal loads via their strong axis. Furthermore, the strips form a doubly-curved network, enabling a global load transfer as a shell structure.<sup>2</sup>

In Section 2, we describe the geometric theory of curvature and curve networks. In Section 3 we introduce our computational design method of modelling minimal surfaces, asymptotic curves and networks. In Section 4, we implement this method in the design of a research pavilion for the Structural Membranes Conference. In Section 5, we discuss the fabrication, construction details and assembly by means of two prototypes, in timber and steel. Section 6, gives insights into the local and global load-bearing behavior, and describes the structural analysis based on Finite Element Method. We summarize our results in Section 7 and conclude in Section 8, by highlighting challenges of this method, and suggesting future investigations on structural simulation and façade development.

## 2 FUNDAMENTALS

### 2.1 Curvature of curves on surfaces

To measure the curvature of a curve on a surface, we can combine the information of direction (native to the curve) and orientation (native to the surface) to generate a coordinate system called the Darboux frame (Fig.3 *right*). This frame consists of the normal vector  $\mathbf{z}$ , the tangent vector  $\mathbf{x}$  and their cross-product, the tangent-normal vector  $\mathbf{y}$ . When moving the Darboux frame along the surface-curve, the velocity of rotation around all three axes can be measured. These three curvature types are called the geodesic curvature  $k_g$  (around  $\mathbf{z}$ ), the geodesic torsion  $t_g$  (around  $\mathbf{x}$ ), and the normal curvature  $k_n$  (around  $\mathbf{y}$ )<sup>6</sup>.

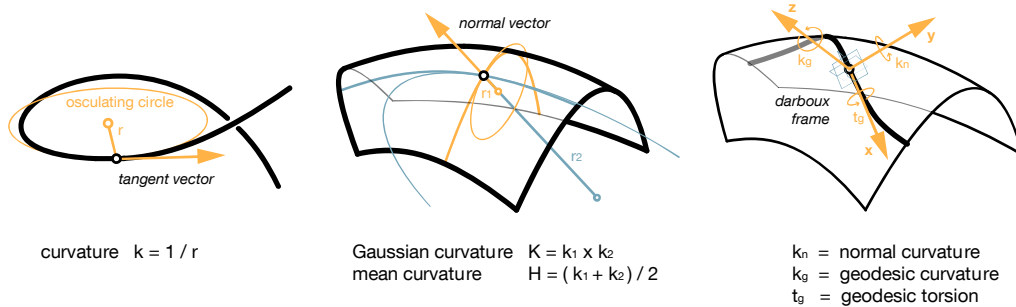


Figure 3: Definitions of curvature. *Left*: Curvature of a curve is measured through the osculating circle. *Middle*: The Gaussian or mean curvature of a surface is calculated with the principle curvatures  $k_1$  and  $k_2$ . *Right*: A curve on a surface displays normal curvature  $k_n$ , geodesic curvature  $k_g$  and geodesic torsion  $t_g$ .

### 2.2 Curvature related networks

Certain paths on a surface may avoid one of these three curvatures (Fig. 4). These specific curves hold great potential to simplify the fabrication and construction of curved grid structures. **Geodesic curves** have a vanishing geodesic curvature. They follow the shortest path between two points on a surface. They can be constructed from straight, planar strips tangential to the surface. **Principle curvature lines** have a vanishing geodesic torsion — there is no twisting of the respective structural element. They can be fabricated from curved, planar strips, and bent only around their weak axis. Their two families intersect at 90 degrees. **Asymptotic curves** have a vanishing normal curvature, and thus only exist on anticlastic surface-regions. Asymptotic curves combine several geometric benefits: They can be formed from straight, planar strips perpendicular to the surface. On minimal surfaces, their two families intersect at 90 degrees and bisect principle curvature lines.<sup>1</sup>

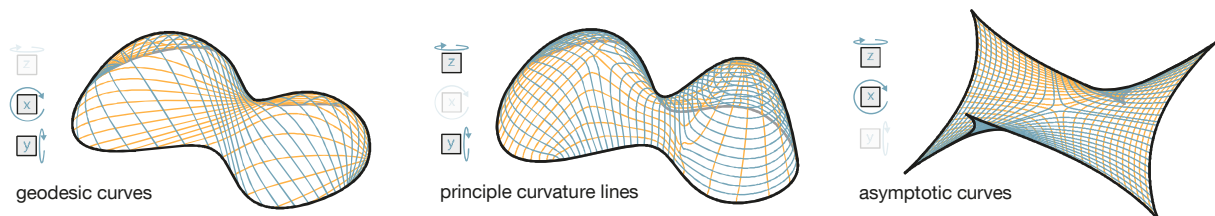


Figure 4: Surface-curves have three curvatures: Geodesic curvature ( $z$ ), geodesic torsion ( $x$ ), and normal curvature ( $y$ ). For each of them, if avoided, a related curve type exists: geodesic curves, principle curvature lines and asymptotic curves.

### 3 METHOD

#### 3.1 Minimal surface

A minimal surface is the surface of minimal area between any given boundaries. Minimal surfaces have a constant mean curvature of zero. In nature such shapes result from an equilibrium of homogeneous tension, e.g. in a soap film.

Various tools are capable of approximating minimal surfaces based on meshes, with varying degrees of precision and speed (Surface Evolver, Kangaroo-SoapFilm, Millipede, etc.). They are commonly based on a method by Pinkall and Polthier (1993)<sup>8</sup>.

The Rhino-plugin TeDa (Chair of Structural Analysis, TUM) provides a tool to model minimal surfaces as NURBS, based on isotropic pre-stress fields<sup>9</sup>.

Certain minimal surfaces can be modelled via their mathematical definition. This is especially helpful as a reference when testing the accuracy of other algorithms.

#### 3.2 Asymptotic curves

Geometrically, the local direction of an asymptotic curve can be found by intersecting the surface with its own tangent plane. We developed a custom VBScript for Grasshopper/Rhino to trace asymptotic curves on NURBS-surface using differential geometry.

A detailed description of this method and the generation of accurate strip models is being published parallel at the Design Modelling Symposium 2017<sup>1</sup>.

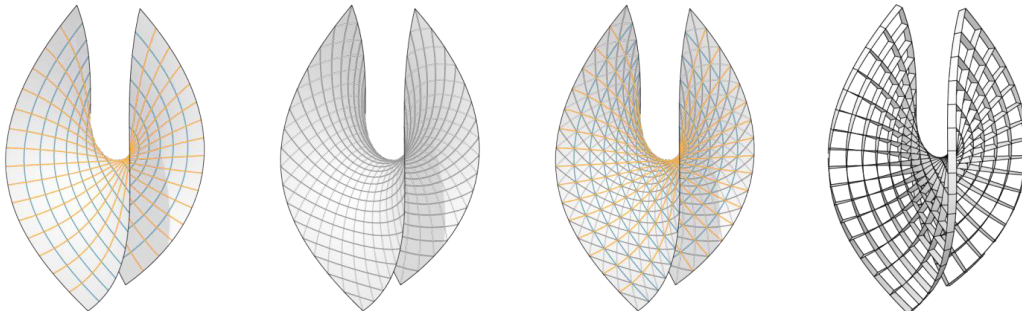


Figure 5: Enneper surface with a) asymptotic curves b) principle curvature lines c) web of both networks d) strip model of the asymptotic network

#### 3.3 Network design

Asymptotic curve networks consist of two families of curves that follow a direction field. The designer can only pick a starting point, but cannot alter their path. If the surface is locally planar, the quadrilateral network forms a singularity with a higher valence.

To achieve a homogeneous network, we take advantage of the bisecting property between asymptotic curves and principle curvature lines (Fig. 5)<sup>10</sup>. By alternately drawing each curve and using their intersections as new starting point, we create an “isothermal” web with nearly quadratic cells<sup>11</sup>.

The node to node distance, measured along the asymptotic curves, is the only variable information needed to mark the intersections on the flat and straight strips before bending and twisting them into an asymptotic support structure.

## 4 DESIGN

### 4.1 General insights

A minimal surface can be defined by one (a, b), two (c), or multiple (d, e) closed boundary-curves (Fig. 6). Symmetry properties can be used to create repetitive (a, b, c) or periodic (e) minimal surfaces. Boundary-curves may consist of straight lines (a), planar curves (d), or spatial curves (b, c, e). Straight or planar curves are likely to attract singularities (a, c, d). A well-integrated edge can also be achieved by modelling a larger surface and “cookie-cutting” the desired boundary. The Gaussian curvature of the design surface directly influences the density of the network, the position of singularities and the geodesic torsion of asymptotic curves.

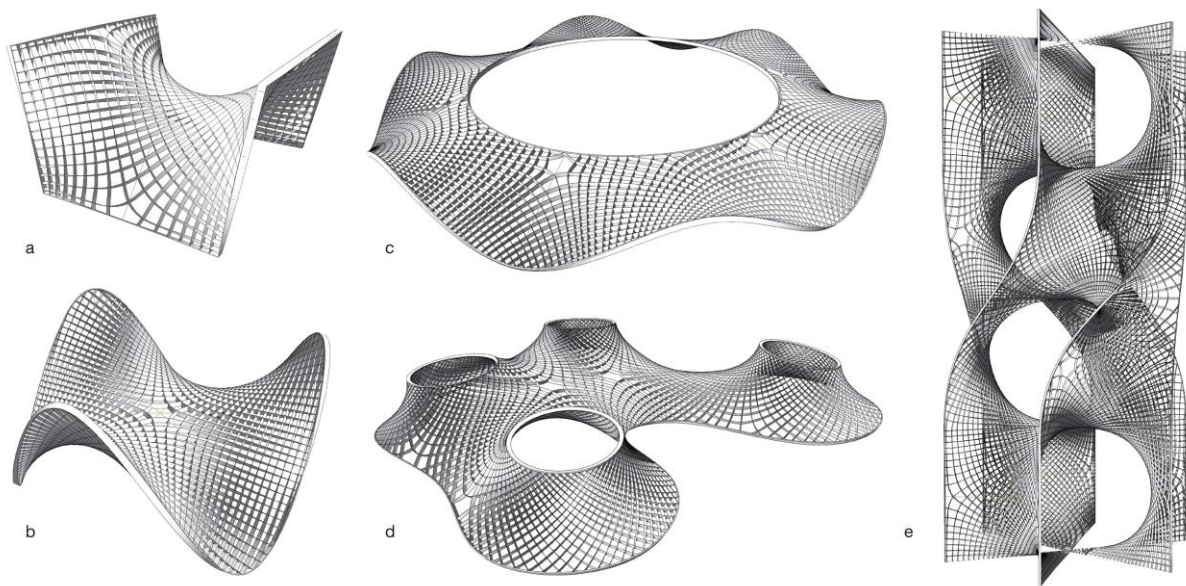


Figure 6: Examples of asymptotic strip networks on minimal surfaces. a) One polygonal boundary, creating a saddle shape with singularities appearing along the edges. b) One spatially curved boundary, creating a network with central singularity. c) Two boundary curves creating a rotational repetitive network with regular singularities. d) Multiple boundaries creating a freely designed network. e) Variation of a singly-periodic Sherk’s 2nd minimal surface, with six interlinking boundaries.

### 4.2 Implementation

We applied this method in the design of a large scale research pavilion for the Structural Membranes Conference in Munich. The design is based on a catenoid – the minimal surface between two circles (Fig. 7). By adjusting the position and shape of these two boundary curves we created an architectural space that reacts to the specific site requirements.

The design of this self-supporting grid structure needs to fulfill **geometric requirements**, creating a homogenously curved minimal surface with well positioned singularities and an aesthetic curve network; **constructional requirements**, considering the allowable bending and torsion of all strip profiles; and **structural requirements** creating a doubly curved structure with well positioned vertical and horizontal supports and efficient arched edges.

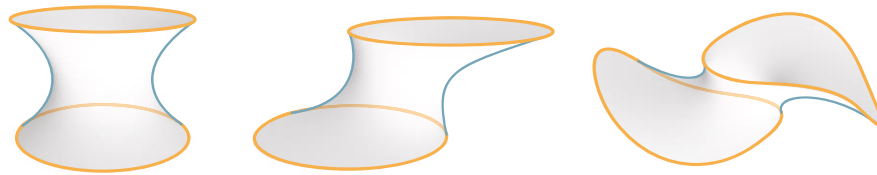


Figure 7 : Design Process : A catenoid is manipulated by shifting and shaping its boundary circles, to create an architectural space with a circular courtyard and two archways.

The pavilion has a span of approx. 9 x 12m at 5m height. The catenoid creates a circular courtyard, embracing one of the green islands on site. Two archways allow circulation to connect the campus to the conference rooms (Fig. 8). At the time of submission of this paper, we are working with sponsors to develop a finance and construction strategy.



Figure 8 : The Asymptotic Pavilion is located at the central campus of the TUM. It is fitted to the specific site requirements of this green courtyard.

## 5 CONSTRUCTION

### 5.1 Strained grid

Our construction process follows the reference of Frei Otto's strained gridshells. This paradigm utilizes elastic deformation to create a doubly-curved lattice structure from straight wooden laths<sup>12</sup>.

In our method, we fabricate flat strips of timber or steel and subsequently bend them into their spatial geometry. As asymptotic curves admit no normal curvature, no bending around the y-axis of the profiles is necessary during assembly. Subsequently, the grid can be constructed from straight lamellas orientated perpendicular to the surface. The geodesic curvature results in bending around the z-axis. The geodesic torsion results in twisting of the lamellas (around their x-axis). When choosing the profiles, the section modulus and thickness

need to be adjusted to the maximum twist and minimal bending radii in order to keep deformation elastic. At the same time, the profiles need to provide enough stiffness to resist buckling under compression loads. These opposing factors can be solved by introducing two layers of lamellas. Each layer is sufficiently slender to easily be bent and twisted into its target geometry. Once the final geometry is installed, the two layers are coupled with a shear block in regular intervals to increase the overall stiffness similar to a Vierendeel truss. This technique was applied in the construction of two prototypes, first in timber and then in steel, each with an approx. 4 x 4m span (Fig. 9, 10).

## 5.2 Timber prototype – spatial construction

For the timber prototype, the two asymptotic directions were constructed on separate levels out of 4mm poplar plywood. This allowed for the use of continuous, uninterrupted profiles (Fig. 9, *bottom*). The upper and lower level were connected with a square stud, enforcing the orthogonal intersection angle. This rigid connection could only be fitted if all elements are curved in their final spatial geometry. Consequently, this prototype had to be erected spatially using framework and edge beams as temporary supports. The height of the planar edge profiles was determined by their intersection angle with the lamellas, creating a dominant frame (Fig. 9, *top*).



Figure 9: Timber prototype. The lamellas are doubled and coupled to allow for low bending radii and high stiffness. *Image:* (Eike Schling)

### 5.3 Steel prototype – elastic erection

The steel prototype was built from straight, 1.5mm steel strips. Both asymptotic directions interlock flush on one level. Therefore, the lamellas have a double slot at every intersection (Fig. 10, *top*). Due to a slot tolerance, the joints were able to rotate by up to 60 degrees. This made it possible to assemble the grid flat on a hexagonal scaffolding. The structure was then “eased down” and “pushed up” simultaneously and thus transformed into its spatial geometry (Fig. 10, *middle*)<sup>13</sup>. During the deformation process, a pair of orthogonal, star-shaped washers were tightened with a bolt at every node, enforcing the 90-degree intersection angle.

Once the final geometry was reached, the edges were fitted by attaching steel strips on top and bottom. The edge-beam locks the shape in its final geometry, generates stiffness and provides attachments for the future diagonal bracing and façade. (Fig. 10, *bottom*).

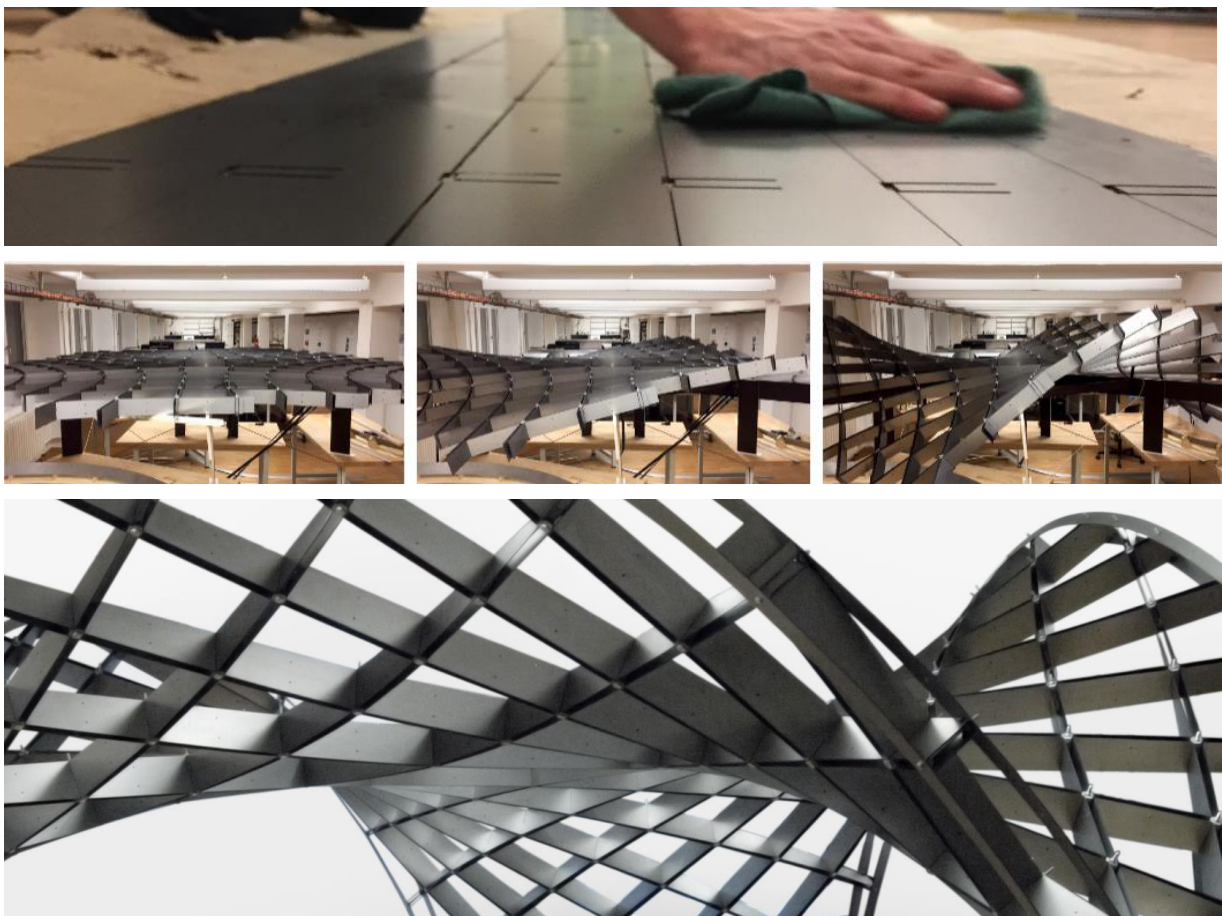


Figure 10: Steel prototype. *Top*: The grid is built from straight and flat steel strips. A double slot allows to interlock both directions in one level. *Middle*: Assembly process showing the elastic transformation from flat to curved geometry. *Bottom*: The final geometry is fixed via tangential edge strips.

## 6 STRUCTURAL ANALYSIS

### 6.1 Load-Bearing Behavior

We observed a hybrid load-bearing behavior of two competing mechanisms; a grillage and a gridshell.

The profiles are oriented normal to the surface. Due to the bending stiffness in their strong axis, the grid is able to act as a beam grillage. This is needed to account for the local planarity of asymptotic networks (due to their vanishing normal curvature) and to stabilize open edges. At the same time, the strips form a doubly-curved network. Bracing the quadrilateral network with diagonal cables and supporting it horizontally activates the form-active behavior of a gridshell.

Which of the two mechanism dominates, depends on the overall shape, the grid layout (direction, orthotropy, density and curvature), stiffness ratios (bending and axial stiffness), loads and constraints. These factors were taken into account, when designing both the pavilion and prototypes, in order to promote a shell like behavior.

The elastic erection process, results in restraint (residual) stresses inside the curved and twisted grid elements. When using suitable section dimensions, the initial bending moments stay low and have minor effects on the global behavior.

However, compression of these curved elements increases the bending moment in their weak axis. The strategy of doubling and coupling lamellas (Section 5.1) is therefore essential to control local buckling. The buckling behavior is dependent on the grid size as well as the offset and coupling interval of parallel lamellas.

### 6.2 FEM - Analysis

The design for the Asymptotic Pavilion (Section 4.2) was analyzed based on the Finite Element Method. The parametric line geometry was modelled in Rhino/Grasshopper and exported to RFEM. Material and joints are based on the steel prototype as described in section 5.3, including diagonal bracing and nondisplaceable supports. The grid nodes are considered rigid. To represent the weakening of the lamellas at the cross-nodes, the joints are modelled as plastic hinges.

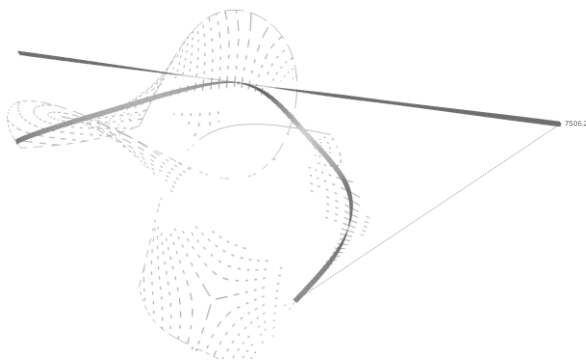


Figure 11: Due to the induced strain loads, a sample lamella will straighten, when extracted from the grid.

The final development of an FEM-Model requires some unusual strategies and is not yet fully completed. The model needs to consider high elastic deformations and their resulting residual stresses, as well as a system change due to the later coupling of parallel lamellas.

The values of geodesic curvature and torsion are measured along each curve and transferred into strain loads, which are then applied as initial load case to the curved geometry. This strategy enables us to induce the residual stresses, without modelling the assembly process.

To verify this method, a sample lamella is extracted from the grid. The applied loads straighten the lamella into its unstrained shape demonstrating correctness of the strain load values (Fig. 11).

Figure 12, shows the surface stress of the final pavilion, including restraint and self-weight. The maximum stresses are mainly caused by the initial bending process and can be adjusted by changing the stiffness in the weak axis or changing the surface curvature.

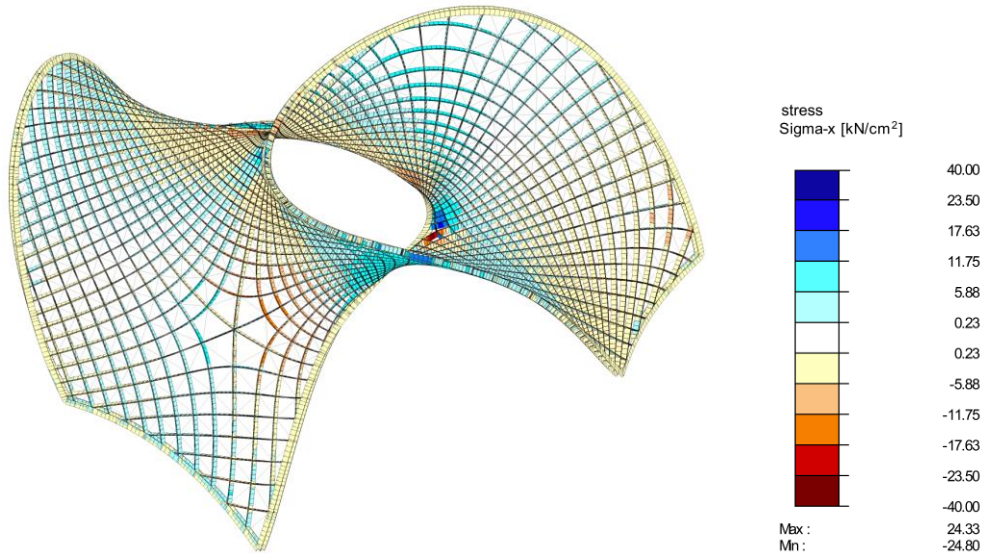


Figure 12: Surface stresses of the grid structure resulting from both the elastic erection process and self-weight.

Due to intense twisting of the lamellas, we expect further stresses according to the theory of helix torsion<sup>14</sup>. These effects are not yet considered in the FEM analysis and need to be quantified in further calculations.

### 6.3 Strain energy analysis

To evaluate and quantify the structures behaviour, the balance of strain energy is observed under self-weight, excluding the initial restraint stresses. For this, the energy due to internal forces  $M_x$ ,  $M_y$ ,  $M_z$  and  $N$  are compared.  $M_y$  and  $M_t$  are attributed to a grillage-like behavior,  $N$  and  $M_z$  are categorized as a shell-like behaviour. The calculated energy ratio, indicates a dominating shell-like load-bearing behaviour.

$$W = \frac{1}{2} \int_0^l \left[ \underbrace{\frac{M_x^2(x)}{GI_P} + \frac{M_y^2(x)}{EI_y}}_{\text{Grillage behaviour 20\%}} + \underbrace{\frac{M_z^2(x)}{EI_z} + \frac{N^2(x)}{EA}}_{\text{Shell behaviour 80\%}} \right] dx$$

Figure 13: Formula for strain energy  $W$ <sup>14</sup>. Indicated below is the balance between  $M_x$ ,  $M_y$ , and  $M_z$ ,  $N$ .

## 7 RESULTS

We compared the geometric properties of three specific curve networks: geodesic curves, principle curvature lines and asymptotic curves, and identified that only asymptotic curves are able to combine the benefits of straight unrolling and orthogonal nodes. They can be formed from straight strips perpendicular to the underlying anticlastic surface. This way, they resist loads normal to the surface by bending in their strong axis. On minimal surfaces, asymptotic curves intersect at 90 degrees, which allows the use of identical nodes throughout the structure. The bisecting property with principle curvature networks offers further geometric advantages for substructure and façade.

We developed a custom VBScript that can trace asymptotic curves on anticlastic surfaces with sufficient accuracy for design and construction, and implemented this method in a pavilion design for the Structural Membranes Conference 2017.

Due to an initial deformation, both twisting (geodesic torsion) and bending (geodesic curvature) have to be considered when choosing profiles for this construction. We have presented a strategy of doubling and coupling the bent structural elements to achieve sufficient stiffness of the final grid. The findings were demonstrated in the realization of two prototypes: One in timber and one in steel, each with a span of 4 x 4m.

We discussed the structural behavior based on two competing mechanism, a grillage and a gridshell and finally developed a workflow to compute the residual stress of the elastic erection process on the basis of the local geometric curvature and torsion, without simulating the assembly process.

## 8 CONCLUSION

An analytical approach to both geometry and material properties is required to achieve a symbiosis of form, structure and fabrication. Even though the design freedom is limited to the choice of boundary curves, there is a wide range of design solutions applicable to all scales and functions. The construction of asymptotic grids as strained grids offers advantages for both fabrication and assembly. Structurally, asymptotic gridshells show great potential, as they combine the benefits of upright sections with a doubly-curved grid. Hence, loads can be transferred locally via bending, and globally as a shell structure.

We are continuing to investigate the structural behavior of strained asymptotic structures, comparing grid orientations, shapes and supports. Another ongoing development is the implementation of constructive details: This includes cable bracing and façade systems using planar quads, developable façade strips and membranes.

## ACKNOWLEDGEMENTS

This paper is part of the research project, Repetitive Grid Structures, funded by the Leonhard-Lorenz-Stiftung and the Research Lab of the Department of Architecture, TUM. Both the geometric background as well as the digital workflow were developed in close collaboration with the Department of Applied Geometry and the Center for Geometry and Computational Design, Prof. Helmut Pottmann, TU Wien. The plugin TeDa was provided and supported by Anna Bauer and Bendikt Phillipp from the Chair of Structural Analysis, TUM. Further support in MESH modelling was granted by Alexander Schiftner and the Evolute GmbH in

Perchtoldsdorf, Austria. We would like to thank Matthias Müller, locksmith at the Technisches Zentrum, TUM, as well as Thomas Brandl and Harry Siebendritt of the Brandl Metallbau GmbH&Co. KG in Eitensheim for their extensive support in steel fabrication.

## REFERENCES

- [1] E. Schling, R. Barthel, 2017: *Experimental studies on the construction of doubly curved structures*. In: DETAILstructure 01/17, Munich, Institut für Internationale Architektur-Dokumentation, pp. 52-56
- [2] E. Schling, D. Hitrec and R. Barthel, 2017: *Designing grid structures using asymptotic curve networks*. In: Design Modelling Symposium, Paris, In press: SpringerVerlag
- [3] H. Pottmann, M. Eigensatz, A. Vaxman and J. Wallner, 2015: *Architectural Geometry*. In: Computers and Graphics. Available Online: <http://www.geometrie.tuwien.ac.at/geom/fg4/sn/2015/ag/ag.pdf>, Accessed 9. May 2017
- [4] J. Lienhard, 2014: *Bending-Active Structures. Form-finding strategies using elastic deformation in static and kinetic systems and the structural potentials therein*. Stuttgart: ITKE
- [5] C. Tang, P. Bo, J. Wallner and H. Pottmann, 2016: *Interactive Design of Developable Surfaces*. In: ACM Transactions on Graphics, Vol. 35, No. 2, Article 12, New York  
Available Online: <http://www.geometrie.tugraz.at/wallner/abw.pdf>, Accessed 9. May 2017
- [6] C. Tang, M. Kilian, H. Pottmann, P. Bo and J. Wallner, 2016b: *Analysis and Design of Curved Support Structures*. In: Adriaenssens, S. et al. (eds.): *Advances in Architectural Geometry*, Zürich, VDF, pp. 8-22
- [7] A. Schiftner, N. Leduc, P. Bompas, N. Baldassini, M. Eigensatz, 2012: *Architectural Geometry from Research to Practice: The Eiffel Tower Pavilions*. In: Hesselgren, L. et al. (eds.): *Advances in Architectural Geometry*, Paris, SpringerWienNewYork, pp. 213-228
- [8] U. Pinkall and K. Polthier, 2013: *Computing Discrete Minimal Surfaces and Their Conjugates*. In: *Experimental Mathematics* 2 (1), pp. 15-36
- [9] B. Philipp, M. Breitenberger, L. D'Áuria, R. Wüchner and K.-U. Bletzinger, 2016: *Integrated design and analysis of structural membranes using Isogeometric B-Rep Analysis*. In: *Computer Methods in Applied Mechanics and Engineering*, Vol. 303, pp. 312-340
- [10] H. Pottmann, A. Asperl, M. Hofer and A. Kilian, 2007: *Architectural Geometry*, Exton, Bentley Institute Press, p.648
- [11] S. Sechelmann, T. Rörig, A. Bobenko, 2012: *Quasiisothermic Mesh Layout*. In: Hesselgren, L. et al. (eds.): *Advances in Architectural Geometry*, Paris, SpringerWienNewYork, pp. 243-258
- [12] S. Adriaenssens and B. Glisic, 2013: *Multihalle Mannheim*, Princeton University, Department of Civil and Environmental Engineering, Available Online: <http://shells.princeton.edu/Mann1.html>, Accessed: 9.5.2017
- [13] G. Quinn and C. Gengnagel, 2014: *A review of elastic grid shells, their erection methods and the potential use of pneumatic formwork*. In: N. De Temmerman and C. A. Brebbia (eds.): *MARAS 2014*. Ostend, WIT PressSouthampton, pp. 129-143
- [14] Günter Lunpe, Volker Gensichen, 2014: *Evaluierung der linearen und nichtlinearen Stabstatik in Theorie und Software*, Chapter 4.2 pp. 118-128

## IMPORTANCE OF THE CONTEXT FOR THE DESIGN OF THE MEMBRANE STRUCTURES

SIMONE TOSO\*, MAURÍCIO R. P. CHIVANTE \*, KARSTEN MORITZ\*

\*Taiyo Europe GmbH  
Muehlweg 2  
82054 Sauerlach, Germany  
Email: info@taiyo-europe.com - Web page: <http://www.taiyo-europe.com>

**Key words:** ETFE cushion, PTFE membrane, PVC membrane.

**Summary.** This work underlines the importance of the context for the design of membrane structures. There are many aspects that can influence the design and it is difficult to summarize all of them in few points, especially because structural membranes are mainly chosen by clients and architects because of their capability to reach shapes and limits that other structural types are not able to.

However, three main aspects should always be considered while designing a membrane structure: shape, environment and installation. The architects, designers and engineers mainly focalize their attention in one of them together with others like: light, space, structure, ecc., but I believe that these aspects need to be always simultaneously evaluated. The shape is important following the architectural signature and the aesthetical result. The second aspect, environment, can be considered as: natural environment (respect of the Nature), architectural environment (harmony with the existing surrounding), and comfort environment (respect of the comfort for the users). The third aspect that is frequently neglected or underestimated on earlier design stages is the method of installation and how this can influence the result of the final structure.

In order to exemplify each of the three mentioned aspects, this work presents three different membrane projects executed by Taiyo Europe. In these three projects, each one of the mentioned aspects was particularly emphasized. The first project, where the shape aspect was particularly important, is the ETFE skylight of the Podium Zaha Hadid realized in Milano (Italy). The second one, where the environment was prevalent, is the PTFE roof covering the prehistorical temple of Tarxien (Malta). The third one is the Cardo and Decumano PVC structure realized for Milano Expo 2015, in this project the installation method was essential once several different structures were being simultaneously executed in a very narrow space.

By these examples this work emphasizes the importance of carefully assessing that the shape, environment and installation conditions during the entire develop of a membrane structure.

## 1 INTRODUCTION

Membrane structures are well known for its ability to span large distances in a structurally efficient and lightweight manner, simultaneously offering a large array of shapes, visual and architectural effects which no other material could efficiently provide (Figure 1 and Figure 2).



Figure 1: Millennium Dome Greenwich, London (UK), PTFE coated fiberglass fabric, completed in 1998.



Figure 2: Municipal Waste Management Department parking cover, Munich (Germany), triple layer ETFE cushions incorporated with photovoltaic cells, completed in 2011.

The design of such systems is however a complex procedure, consisting on an iterative assessment of different aspects related to the structure; e.g. the intended shape and the loading criteria must be concomitantly analyzed, as the flexibility of the structure also means that applied loads impact the shape; the location where the structure will be installed influence the installation methodology, which in turns may (both) affect the shape.

The design process of a membrane structure may include the following tasks: conceptual design; physical modelling; computer modelling; form finding; analysis; fabrication design and cutting pattern generation; installation design; and maintenance concept.

As a successful journey starts with making a first step on the right direction, following it will be further explored the importance of a holistic approach during the concept design.

## **2 CONCEPTUAL DESIGN OF MEMBRANE STRUCTURES**

The conceptual design usually commences with an intent and a sketch developed by the creator (usually represented by the architect). This intent provides the basis for the following conceptual design, which includes tasks such as material selection identification, form finding, environmental impact, comfort assessment, preliminary installation concept and a cost-benefit analysis.

Several contextual dimensions in which the membrane structure is inserted impact the conceptual design. This work focus will further assess three of them: the shape desired; the environment in which the structure will be implemented; and the future installation context.

## **3 SHAPE**

Architects and designers are often looking for a type of material that can be as much versatile as possible in order to follow the desired shapes that, most of the time, are their brand of identification.

This was the case of the podium in CityLife Milano, where the archistar Zaha Hadid has the necessity to create a skylight on the podium of her tower in order to spread the sun light inside the shopping center. She was also looking for a material able to be transparent and light because the almost 200 m tower above the podium had to be visible from inside and the steel structure should not be dominating. Moreover, the solution had to be thermal insulated in order to guarantee the inner comfort and, especially, had to follow the rotundity of the building. The membrane structure, in this such case the ETFE, is the perfect material that can reply to all these requirements, especially when it is used as multilayer cushions able to have thermal and optical properties similar to the glass, but with a self-weight that is practically neglectable.

The main shape of the roof was identified by 16 different beams each one realized by two straight segments connected by an arch, this geometry, that can appear simple, is however quite complicate to obtain because the convexity of the arch is going against the natural shape of inner layer, so only with an accurate form finding and the proper cutting pattern it is possible to reach this required result.



Figure 3: Top view of the CityLife Zaha Hadid's podium.



Figure 4: Top view of the ETFE skylight.



Figure 5: Inner view of the ETFE skylight.

## 4 ENVIRONMENT

The environment is the second point here analyzed; in the last period, this is becoming one of the key point regarding the choice of the materials and the architectural and static solutions. The environmental aspects can be studied from multiple points especially because many disciplines are including them in their studies. Here below it is possible to find three of these aspects especially related to our project realized in Malta for the archeologic site of Tarxien.

### 4.1 Natural environment

The Megalithic Temples of Tarxien was accepted as a UNESCO World Heritage site in 1992 and soon was clear to the Heritage Malta that the limestone used to realize the temples were slowly but inexorably deteriorate by the UV radius and the rain. It was therefore necessary to

cover the 3000 m<sup>2</sup> site with a structure able to have the biggest span and the lowest number of supports in order to be as less invasive as possible and to preserve the rest of the finds not yet discovered and safeguarded them for the next generations.

Also in this case a membrane structure is used, particularly a fiberglass PTFE that, because of its neglectable self-weight and high resistance, can be supported only by two steel arches with a span of 70 m.



Figure 6: View of the PTFE roof from outside (Tarxien temple site)

#### 4.2 Architectural Environment

To protect the archeologic site was mandatory, but on the same time it was necessary to find a solution harmoniously inserted in the architectural environment of the city of Tarxien. It is why the total height of the structure was imposed by the municipality, and the modern shape of the new structure had to be in harmony with the shape of the existing surrounding buildings.



Figure 7: Top view (of the Tarxien temples site).

### 4.3 Comfort environment

The site is receiving almost 65.000 people per year and normally the peak of the visits is during summer time, it is why the choice of the PTFE membrane was dictated also by the necessity to have a product able to stop the sun radiation but not the translucency in fact, this kind of material is able to block almost the entire part of the UV light spectrum but about the 12% of the visible light is still passing through it. This means that the prehistorical finds and visitors even if with a comfortable light, they are not exposed to the direct energy of the sun.



Figure 8: View of the PTFE roof from inside.

## 5 INSTALLATION

When everything is design by the Architects and Engineers, there can be a last aspect that can call into question the entire project if it was not properly considered, this is the installation methodology. Most of the time, the membrane structures are used to cover huge surfaces, cantilevers or spans, and these can be translated with the necessity to adopt heavy equipment or a numerous team that need space and a proper time and sequence to complete the work.

The job site of the Milano Expo 2015 was particularly indicative from this point of view, in fact in the last months, almost 6.500 laborers were working in the entire area and almost all of them need to pass along the Cardo and Decumano streets to reach their pavilions. On the same time, our team was occupied to install 2.900 ton of steel and 65.000 m<sup>2</sup> of PVC canopy to cover the Cardo and Decumano.



Figure 9: Top view of the Decumano.

The method of installation had to consider that the 14 m height columns had to be installed without using the surface dedicated for the pavilions jobsites, this means that only the surface of the Cardo and the Decumano with their 35m width can be used, but on the same time it was possible to close these streets only for few hours in order to permit the flow of the other workers.

Considering these restrains, the entire structure was designed in order to be lifted in the quickest way: the columns were fixed on the base with a hinge connection and between them with an upper support and lower tension cables connected by hangers.



Figure 10: View of the crossing between Cardo and Decumano

All the expedients studied during the design phase permitted to install one complete modulus composed by about 90 ton of steel and 2.000 m<sup>2</sup> of membrane in less than one week, and the 5 axes of columns were lifted in less than 5 hours.

This kind of result is possible to reach only with the proper knowledge of an experience company, otherwise this last step of the project, if not properly studied and developed, can be extremely demanding especially from the financial point of view.



Figure 11: View of the Decumano during installation

## 6 CONCLUSIONS

By the three-example illustrated here above, it is clear and evident how the described aspects: shape, environment and installation are mutually and simultaneously important during the design of a membrane structure. It is also important to note that none of these aspects can be neglected, for instance, the Tarxien project was used in this article to focalize the environment,

but the shape of this structure was likewise important during the design in order to respect the landscape restraints, and the installation aspect were likewise important because the existing archeological finds cannot be touched.

The same mutual connection between shape, environment and installation can be found in the Zaha Hadid and Milano Expo projects and, in general, in all the projects related to the membrane structures.

Although not complete and exhaustive, this work brings an awareness to the importance of a holistic understanding and assessment on the different dimensions involved on the design of a tensile structure.

Moreover, it also emphasizes the importance of bringing to the team an specialist in implementing such membrane structures in an early stage, ensuring to the best the right first steps towards the successful execution of the structure

## REFERENCES

- [1] Zaha Hadid project: <http://www.zaha-hadid.com/architecture/citylife-milano/> <http://www.city-life-shoppingdistrict.it/> <http://www.redesco.it/projects/14/zaha-hadid-commercial-podium-in-citylife-development-milan>
- [2] Tarxien project: [https://en.wikipedia.org/wiki/Tarxien\\_Temples](https://en.wikipedia.org/wiki/Tarxien_Temples) <http://www.taiyo-europe.com/textile-architektur-etfe/projectportfolio/tarxien-temples/detail/>
- [3] Expo 2015 project: <http://www.taiyo-europe.com/textile-architektur-etfe/projectportfolio/cardo-e-decumano-expo-milano-2015/detail/>

## A MULTISCALE NON-ORTHOGONAL MODEL FOR TENSILE PROPERTIES OF UNCOATED AND COATED F-12 ARAMID FABRIC

HUIFENG TAN<sup>\*</sup>, XILIN LUO, GUOCHANG LIN

<sup>\*</sup> Center for Composite Materials and Structures  
Harbin Institute of Technology  
No.2 Yikuang Street, Harbin, 150080, China  
e-mail: [tanhf@hit.edu.cn](mailto:tanhf@hit.edu.cn) - web page: <http://www.hit.edu.cn>

**Key words:** F-12 aramid fabric, multiscale, non-orthogonal, off-axial tensile

**Summary.** Coated F-12 aramid fabric can be used as the balloon envelopes material because of the high strength and light weight performance. In this paper, a multiscale non-orthogonal material model was established to capture the tensile properties of F-12 fabric with and without polyethylene terephthalate-aluminum (PET-Al) coating. Off-axial monotonic tensile tests were carried out to validate the material model. The nonlinearity and anisotropic properties of the coated and uncoated fabrics were investigated. In this model, the stress was obtained based on the equilibrium equations and yarn constitutive model in mesoscale. The mesoscale configuration was observed through optical microscope and SEM. The material orientation was aligned with the yarn directions and the stress was updated in real time. The material model was implemented by user material subroutine in ABAQUS and simulate fabric off-axial tensile test. In addition, a theory model to calculate the elastic property of the fabric was also set up using the mesoscale deformation mechanism. The simulation results were compared with the test and theory results. Results suggest that simulation results were agree well with test results. The fabrics were nearly linearity in weft direction, while the stress-strain curve exhibited obvious nonlinearity in warp direction. The tensile modulus of the fabric showed orthotropic behaviour rather than the strength. The coating can affect the strength and failure model of F-12 fabric. Yarn slip was the mostly failure model in uncoated fabric while break in coated fabric. Research in this study provides certain reference in analysis and design for balloon envelopes.

### 1 INTRODUCTION

F-12 aramid fibers is spun from aromatic polyamides and copolyamides with heterocycles in the chain, whose strength (4.35-4.67GPa) is 1.69 times higher than that of Kevlar-49. It is developed by the 46<sup>th</sup> Institute, Sixth Academy of China Aerospace Science & Industry Corp. PET-Al coated F-12 aramid fabric is a suitable envelope material in stratospheric airship and super-pressure balloon. The PET-Al coating contains helium barrier layer and can be utilized to resistant the UV radiation and heat, while the fabric is used as the load carrier layer. The mechanic performance of the envelope membrane is related to the carrying capacity and service life of the aerostatics structures. Hence, the demands for the envelope material are more complex than that of architectural textiles [1].

The coated F-12 aramid fabric is a flexible laminated material, whose mechanic properties are determined by fabric layer. On the early research of fabric mechanics, a basis theoretical

model developed by Pierce [2] was only used to geometrical analysis based on the weave architecture and yarn properties. Kawabata [3], Hearle, et al. [4] detailed and expanded the model to mechanical analysis. The simplifying assumptions made the theoretical model different from the actual fabric. Hence, there are certain limitations in the theoretical analysis results.

In the former research, experiment is another main tool to investigate the mechanical behavior of the fabric [5-6]. Since coated fabric is usually used in tensioned membrane structure and inflatable structure. Hence, tensile test is the most common method, which consist mono-uniaxial test, biaxial test, cyclic test. However, the macroscopic test is unable to capture the deformation mechanism in yarn scale. The mesoscale or multiscale numerical analysis approach combined with experimental method was commonly carried out to study the systematic information of the tensile behavior of fabric.

Due to the hierarchical of the fabric, numerical method [7] can be divided into three categories, including microscopic (fiber level), mesoscopic (the yarn level) and macroscopic (the fabric level). The homogenization method, which takes the yarns and fabric as a continuum, is required in mesoscopic and macroscopic approach. Usually, the solid element and shell element are used to simulate the yarn and fabric. Many deformation and the inter-fiber or intra-fiber interaction mechanisms are ignored. The result is that as the scale increase, the computational efficiency improved, while the accuracy reduced. Some researchers developed the multiscale material model, which is a macroscale models based on mesoscale properties. However, most of their study focused on dry fabric. In this paper, a multiscale material model based on mesoscale behavior was developed to simulate the coated and uncoated fabric. The coating properties and yarn bending and shear responses were considered. The off-axial tensile tests were carried out to verify the material model. The extension responses, such as the anisotropic properties, tensile strength, deformation field, elongation at break and failure modes were analyzed. The effect of the PET-Al coating to the aramid fabric was investigated.

## 2 EXPERIMENTAL PROGRAMS

### 2.1 Test material and specimens

In this study, a plain weave fabric made of F-12 aramid fibers with and without PET-Al coating were investigated, as shown in Fig. 1. The line density of the yarn is 23 tex and the weave density is 16 yarns/cm. The uncoated fabric shows  $60.2\text{g/m}^2$  area density with a thickness of 0.130mm. The coated fabric shows  $127\text{g/m}^2$  area density with a thickness of 0.177mm. The surface morphology and cross section shape of the fabric are investigated by SEM and optical microscope respectively, as shown in Fig. 2. The figures were imported into AutoCAD software and then the structural parameters were calibrated, as shown in Tab. 1.

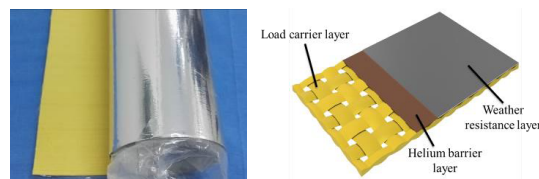


Fig. 1 F-12 aramid fabric with PET-Al coating

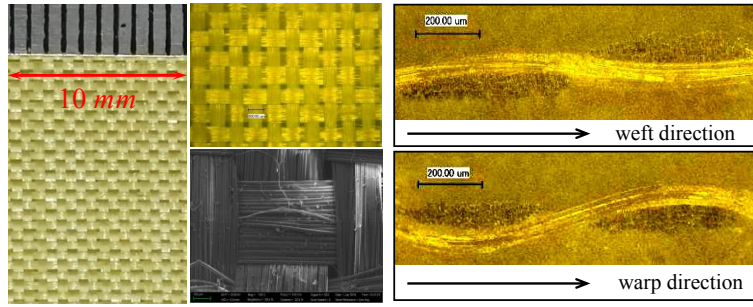


Fig. 1 Macro and mesostructure of F-12 fabric: surface morphology (left) ;cross section (right)

Tab. 1 Material properties and unit cell geometry for F-12 fabric

Properties	Values
Yarn count (yarn/cm) warp/weft	16
Yarn linear density (tex) warp/weft	23
Fiber density (g/cm <sup>3</sup> )	1.44
Yarn spacing (mm) warp/weft	0.584 / 0.672
Yarn width (mm) warp/weft	0.523 / 0.470
Yarn height (mm) warp/weft	0.068 / 0.074
Crimp amplitude (mm) warp/weft	0.072 / 0.015
Crimp length (mm) warp/weft	0.703 / 0.586
Yarn inclined angle (°) warp/weft	16 / 3
Crimp (%) warp/weft	4.61 / 0.34
Fabric thickness (mm)	0.13

Mono-uniaxial extension tests with seven different off-axis angles ( $\theta=0^\circ, 15^\circ, 30^\circ, 45^\circ, 60^\circ, 75^\circ, 90^\circ$ ) were conducted, according to the standard of ISO 1421-1998. The samples for the coated and uncoated fabrics were tailored into long strips by  $300 \times 50$  mm, with four aluminum reinforced plates pasted on the end of the samples. The angle between the warp direction and the loading direction was defined as off-axis angle, as shown in Fig. 3. In coordinate system  $OXY$ ,  $X$ -axis and  $Y$ -axis indicate the warp and weft direction, respectively, while in  $Oxy$ , axis  $x$  represents loading direction. The tests were conducted using INSTRON 5965 at the loading rate of 50mm/min. Both video extensometer and digital image correlation (DIC) were used to measure the strains, as shown in Fig. 4.

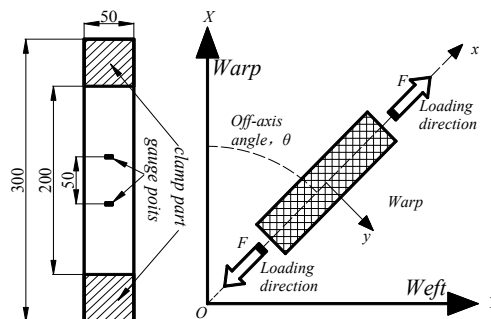


Fig. 2 Geometry and the tailor direction of the off-axes extension sample



Fig. 3 Deformation measurement in tensile test (a)video extensometer (b)DIC

The yarn tensile properties are required in the multiscale model. Hence, yarn extension test was carried out refer to ASTM D2256. The sample was extract from fabric exactly. The yarn sample was cut into 350mm. Aluminum plates with the size 30mm  $\times$  50mm were pasted at the end of the sample. The effective cross section area can be calculated by the linear density and the volume density.

All the tests are conducted in the tensile test machine INSTRON5965. Two different load cells with loading range in 0-0.5KN and 0-5KN are used in yarn test and fabric test, respectively.

### 3 NUMERICAL SIMULATED

#### 3.1 Material model based on meso-structure

The mechanical behavior is related to the fiber properties and yarn woven architecture. As seen in Fig. 2, F-12 fabric shows a repetitive orthogonal configuration that warp yarns interlace weft yarns one by one. It means that a representative element can be built to analyze the entire structure. In this study, a shell element which contains the cross-over point and yarns with half lengths of unit cell based on meso-structure was established, to relate macroscale material model to yarn scale, as shown in Fig. 5. The shell element is orthotropic at the initial state. In the case of shear deformation, the warp yarns and the weft yarns would rotate around the cross-over points. The angle between warp and weft yarns changed with the deformation. Hence, the shell element will be non-orthotropic. An actual material model requires the material orientation in the shell element tracking with the yarns direction in real time [8-9]. The coating will shear the load. Especially in the shear case, coating would increase the shear resistance obviously. In the case of coated fabric, coating stretching and shear items were added to the uncoated fabric model.

#### 3.2 Tracking yarn direction

Off-axes extension test would cause shear deformation. As mentioned before, the fiber orientation has been constantly changing in the test. Based on the theory of continuum mechanics, the fiber orientation can be tracked as the following method.

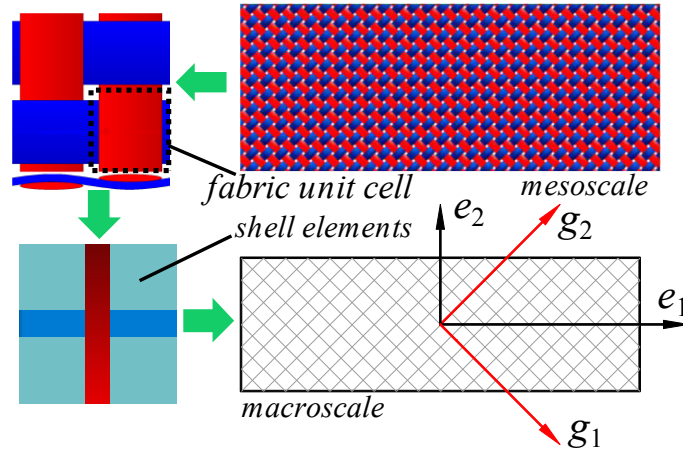


Fig. 5 The principle of non-orthogonality macro-model based on mesoscale

The coordinate systems on the fabric before and after deformation are shown in Fig. 6.  $e_i$  was the orthogonal local frame attached to the element which is called co-rotational frame.  $g_i$  was a non-orthogonal frame attached to the yarn directions. The new yarn orientation can be calculated from the initial vectors and the deformation gradient, while the new co-rotational frame can be related to the initial vectors and the rotational gradient, as shown in formula (1) and (2):

$$\mathbf{g}_i = \mathbf{F} \cdot \mathbf{g}_i^0 \quad (1)$$

$$\mathbf{e}_i = \mathbf{R} \cdot \mathbf{e}_i^0 \quad (2)$$

$$\mathbf{R} = \mathbf{F}\mathbf{U}^{-1} \quad (3)$$

where  $\mathbf{F}$  represents the deformation gradient,  $\mathbf{U}$  is the right-stretch tensor,  $\mathbf{R}$  is the rotational tensor.  $\mathbf{g}_i^0$  and  $\mathbf{e}_i^0$  are the initial unit vectors of material frame and co-rotational frame, respectively.

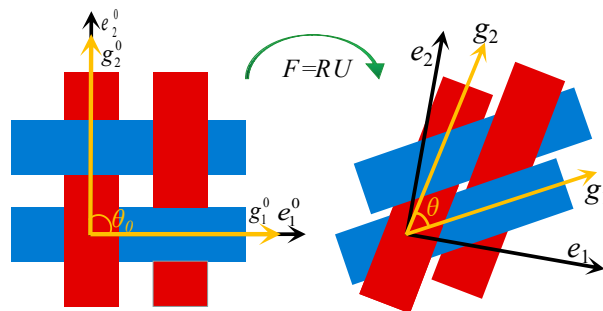


Fig. 6 The coordinate systems on the fabric (a) before deformation (b) after deformation

The current yarn stretch can be determined from:

$$\lambda_i = \sqrt{\mathbf{g}_i^T \cdot \mathbf{g}_i} = \sqrt{(\mathbf{F} \cdot \mathbf{g}_i^0)^T \cdot (\mathbf{F} \cdot \mathbf{g}_i^0)} = \sqrt{\mathbf{g}_i^{0T} \cdot \mathbf{C} \cdot \mathbf{g}_i^0}, \quad \mathbf{C} = \mathbf{F}^T \mathbf{F} \quad (4)$$

where  $\mathbf{C}$  is the Green deformation tensor. The angle between the warp yarns and weft yarns can be calculated by the following formulas:

$$\cos \theta = \frac{\mathbf{g}_1^{0T} \mathbf{C} \mathbf{g}_2^0}{\lambda_1 \lambda_2} \quad (5)$$

Hence, the shear angle is defined as following:

$$\gamma = \frac{\pi}{2} - \theta \quad (6)$$

### 3.3 Determination of stress

After shear deformation, the balanced force generated on the boundary of the shell element is shown in Fig. 7. The relationship between each force components can be established through the equilibrium equation [9].

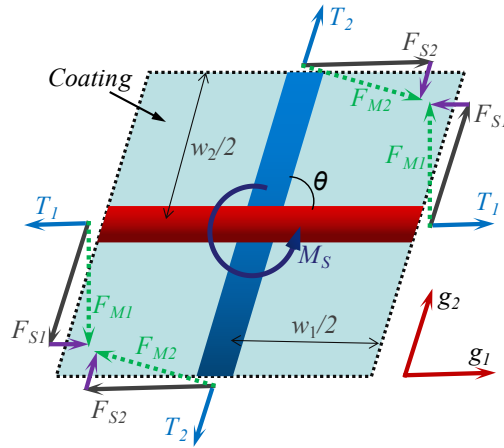


Fig. 7 Forces balance at the boundaries of unit cell

The shear force on the boundary can be determined by following formulas:

$$F_{Mi} = \frac{M_S}{w_i}; i = 1, 2 \quad (7)$$

$$F_{Si} = F_{Mi} / \sin \theta; i = 1, 2 \quad (8)$$

The traction force vector is defined as:

$$\mathbf{t} = \boldsymbol{\sigma} \mathbf{n} dS \quad (9)$$

Where  $\mathbf{t}$ ,  $\boldsymbol{\sigma}$ ,  $\mathbf{n}$ ,  $dS$  are the traction force vector, Cauchy stress tensor, the unit normal of the surface, and small surface area. In conclusion, the Cauchy stress can be decided by yarn tension  $f_{yarn,1}$ , coating tension  $f_{ct,1}$ , yarn bending moments  $M_{bi}$ , the shear force  $F_{Si}$ :

$$\sigma_{11} = \frac{f_{yarn,1} \cdot \cos \theta_1 + f_{ct,1} - M_{b1} / (l_1 \cdot \sin \theta_1) - F_{S1} \cdot \cos \theta}{A_2 \sin \theta}; \quad (10)$$

$$\sigma_{22} = \frac{f_{yarn,2} \cdot \cos \theta_2 + f_{ct,2} - M_{b2} / (l_2 \cdot \sin \theta_2) - F_{S2} \cdot \cos \theta}{A_2 \sin \theta}; \quad (11)$$

$$\sigma_{12} = \sigma_{21} = \frac{F_{S1}}{A_2} = \frac{F_{S2}}{A_1} = \frac{F_S}{w_1 w_2 t_f^0 \sin^2 \theta} \quad (12)$$

### 3.4 Constitutive relations

As indicated above, the material model established was based on the yarn mechanical properties and geometry. From formula (10), the yarn tensile and bending constitutive relation, the coating tensile behavior, the fabric shear behavior are required.

The tensile force in the yarns is determined by:

$$f_{yarn,i} = E_i(\varepsilon_i) A_i \varepsilon_i \quad (13)$$

The tensile force in the coating is determined by:

$$f_{ct} = E_{ct} A_{ct} \varepsilon_i \quad (14)$$

The bending behavior of the yarns are calculated from:

$$M_{bi} = k_{bi} (\theta_i - \theta_i^0) \quad (15)$$

The fabric shear behavior is determined by bias tensile test. Polynomial function is used to fit the relation between normalized shear force and shear angle. Then, the parameters are obtained.

$$F_{sh}(\gamma) = \frac{1}{(2D-W)\cos(\gamma)} \left( \frac{FD}{W} (\cos(\frac{\gamma}{2}) - \sin(\frac{\gamma}{2})) - W \cos(\frac{\gamma}{2}) F_{sh}(\frac{\gamma}{2}) \right) \quad (16)$$

$$F_{sh}(\gamma) = a\gamma^5 + b\gamma^4 + c\gamma^3 + d\gamma^2 + e\gamma + f \quad (17)$$

## 4 THEORETICAL MODEL

According to mesoscopic model, the elastic constant of the fabric can be calculated based on energy method and Castigliano's theorem [10]. three dimensional sawtooth model was established to model the unit cell of fabric, as shown in Fig. 7. At initial state or on-axial tensile deformation, the warp yarns and weft yarns are orthogonal. The tensile mechanism are crimp change and yarn extension. The main load on the yarns are tensile force and bending moment. In Fig. 8,  $f_i$  is the in-plane axial tensile loading, which is decomposed into the yarn part ( $f_{yarn}$ ) and the coating part ( $f_{ct}$ ).  $v_i$  is the compress loading between warp yarns and weft yarns.

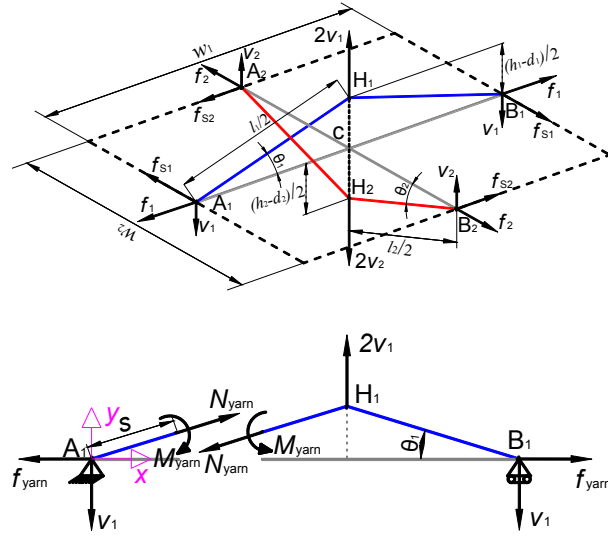


Fig. 8 The force analysis of the saw-tooth model

The extension strain energy of the yarn is given as:

$$U_{yarn,E} = \frac{l_1 \left( f_{yarn,1} \cos \theta_1 + v_1 \sin \theta_1 \right)^2}{2E_1 A_1} + \frac{l_2 \left( f_{yarn,2} \cos \theta_2 + v_2 \sin \theta_2 \right)^2}{2E_2 A_2} \quad (18)$$

The bending strain energy of the yarn is given as:

$$U_{yarn,B} = \frac{l_1^3 \left( -f_{yarn,1} \sin \theta_1 + v_1 \cos \theta_1 \right)^2}{24E_1 I_1} + \frac{l_2^3 \left( -f_{yarn,2} \sin \theta_2 + v_2 \cos \theta_2 \right)^2}{24E_2 I_2} \quad (19)$$

The total strain energy of the yarn is given as:

$$U_T = U_{yarn,E} + U_{yarn,B} \quad (20)$$

The elastic modulus in uniaxial loading can be determined as:

$$E_1 = \frac{12B_1 w_2}{w_1 l_1^3 \sin^2 \theta_1} \left( 1 + \frac{B_2 l_1^3 \cos^2 \theta_1}{B_1 l_2^3 \cos^2 \theta_2} \right) \quad (21)$$

where  $l_i$  is the yarn length,  $w_i$  is the yarn spacing,  $h_i$  is the crimp amplitude,  $\theta_i$  is the yarn incline angle,  $B_i$  is the yarn bending stiffness, which can be calculated from  $B=EI$ . Then, the bending stiffnesses are obtained,  $B_{warp}=0.56 \text{ N}\cdot\text{mm}^2$ ,  $B_{weft}=0.63 \text{ N}\cdot\text{mm}^2$ . Plug the values in Tab. 1 and the bending stiffness into formula (23), the theoretical value of initial modulus can be calculated.

## 5 RESULTS AND DISCUSSION

### 5.1 Test results

The yarn tensile behavior is shown in Fig. 9. Solid lines and dashed lines represent warp direction and weft direction, respectively. Five effective samples were test in each type of yarns. The stress-strain curves of each type of yarns show excellent repetition, which indicate the performance and the fiber damage in weaving process are stable. The piecewise linear functions are used to fit the curves. Then, the tensile modulus are obtained:

$$E_{weft} = \begin{cases} 119.04 \text{ GPa}; & \varepsilon \leq 0.01 \\ 83.24 \text{ GPa}; & \varepsilon > 0.01 \end{cases}, \text{ in weft direction}$$

$$E_{warp} = \begin{cases} 64.65 \text{ GPa}; & \varepsilon \leq 0.25\% \\ 112.41 \text{ GPa}; & 0.25\% < \varepsilon \leq 1\% \\ 79.75 \text{ GPa}; & 1\% \leq \varepsilon \end{cases}, \text{ in warp direction}$$

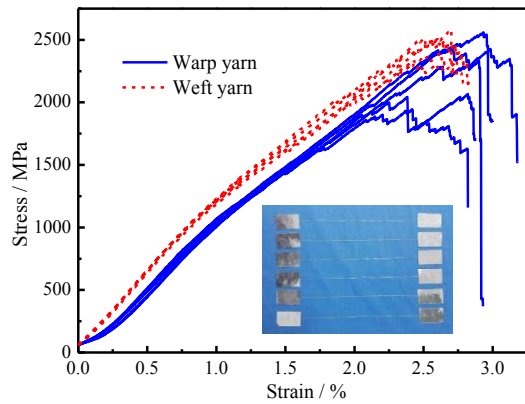


Fig. 9 The stress-strain relation of F-12 single yarn

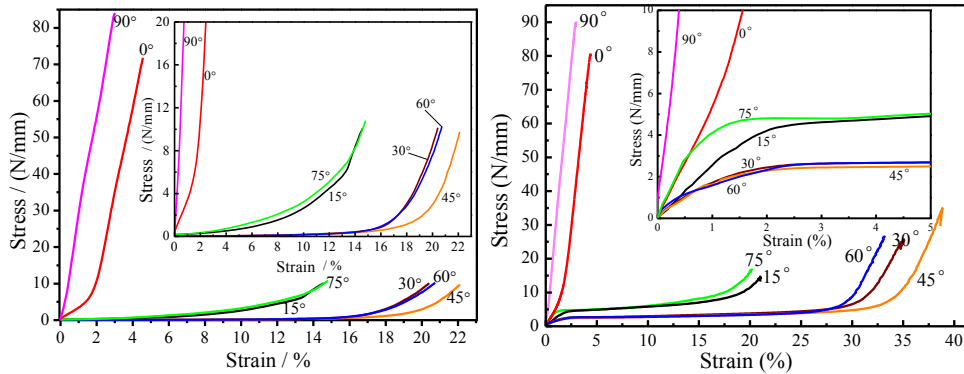


Fig. 10 The stress-strain curves of membrane material (a)uncoated fabric (b)coated fabric

The on-axial and off-axial extension performance is seen in Fig. 10. The modulus of on-axial samples is greater than that of off-axial samples both for uncoated and coated fabric. The relation on the weft direction is linear, while nonlinear in warp direction. It can be explained from Fig.2, the crimp in warp yarns is significantly larger than that in weft yarns. For the complementary angles 15 ° and 75 ° or 30 ° and 60 °, the curves are approximated, which means the fabric is orthogonal. The elongation is increase with the bias angles and

come to maximum value at 45°. Then the elongation decrease with the bias angles increase. The difference between the uncoated and coated fabric is that the resistance in the cross-over points of coated fabric is greater than that of uncoated fabric. It caused that in the initial bias tensile curves, the loading between the interwoven yarns need to come to the limit static friction to rotate. Hence, the tangent modulus of coated fabric is larger than that of uncoated fabric.

The tensile strength and the failure modes of uncoated and coated fabric are shown in Fig.11 and Fig. 12, respectively. Both for uncoated and coated fabric, the values of breaking forces of on-axial samples are larger than that in other directions. For the uncoated fabric, the values of breaking forces of the samples are decrease with the bias angles and come to minimum values at 45°. Then the breaking force increase with the bias angles increase. The trend is similar to classical laminate theory. However, the breaking force for the complementary angles of 30° and 60° are larger than for angles of 15° and 75°. The breaking force for an angle of 45° increases as compared to other different bias angles. This probably due to the resistance pf PET-Al coating to the yarn rotation makes the force increases when the direction of the force are coinciding the direction of yarns. Another effect of the coating to the fabric is the failure modes. The failure mode of on-axial uncoated samples is fiber fracture, while interface damage appears in coated samples. For off-axial uncoated samples, the necking effect due to yarn slips occurs, while for coated samples, the samples breaking because of shear failure in intra-yarns.

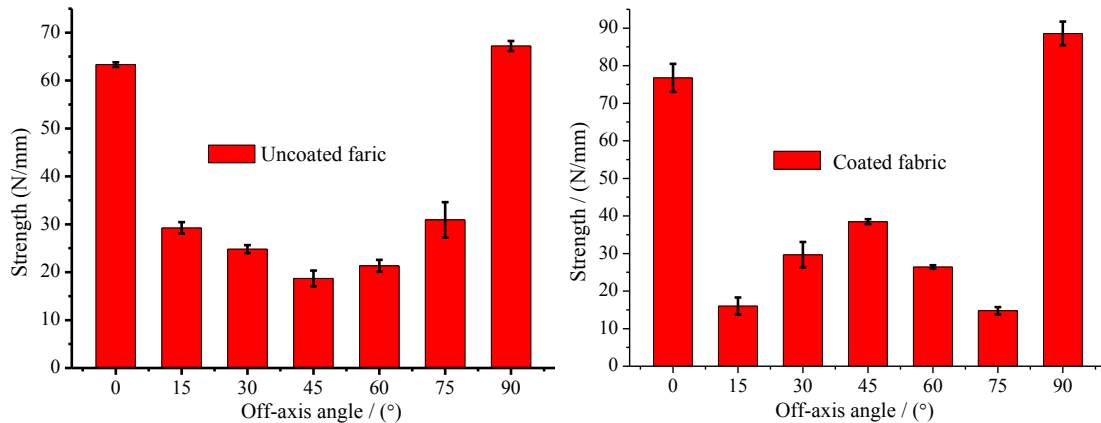


Fig. 11 The tensile strength of membrane material

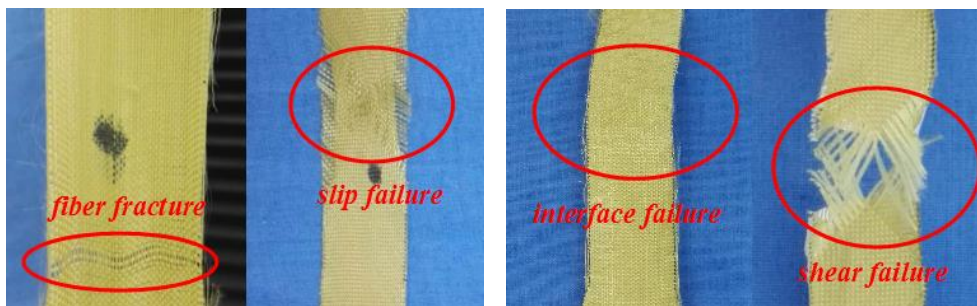


Fig. 12 Damage modes of membrane material: uncoated fabric (left), coated fabric (right)

### 5.2 Numerical simulation results

Fig. 13 shows the load-extension relation for 45° off-axial tensile of uncoated and coated fabric. The discrete points represent test results, while the lines are FEM results. Blue represent the results of uncoated fabric and red represent that of coated fabric. FEM results agree well with the experiment results. The PET-Al coating affects the shear properties of the fabric obviously. The value elongation of coated fabric is larger than that of uncoated fabric. Besides, at the initial state, the shear stiffness of coated fabric is greater than that of uncoated fabric. This is due to the resistance of the coating to the yarns rotation.

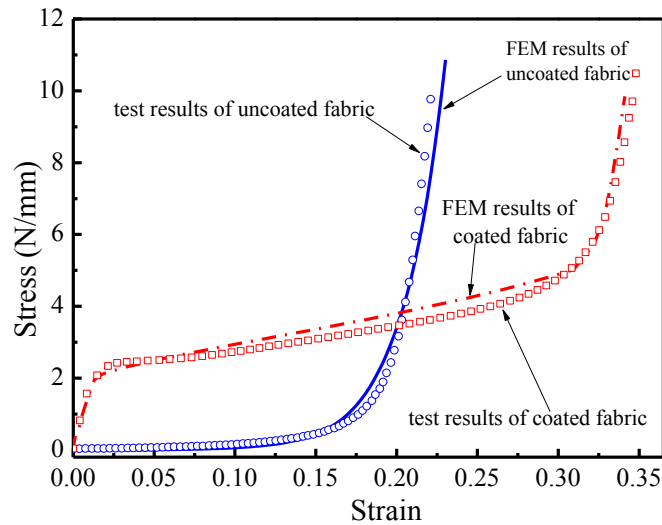


Fig. 13 Load-extension relation for 45° off-axial tensile of uncoated and coated fabric

Fig. 14 and Fig. 15 are the compared deformation results of FEM and experiment for the uncoated and coated fabric on off-axial tensile, respectively. Left side of Fig. 14 is the shear angle contour obtained by FEM. The other side is the actual deformation in tensile test. The deformation is basically symmetrical. However, out-plane displacement appears in the experiment, which is not consider in this material model. Fig. 15 shows the displacement contours obtained by FEM (left) and DIC (right). Both the distribution and the values are agreement. Therefore, the accuracy of the model is further validated.

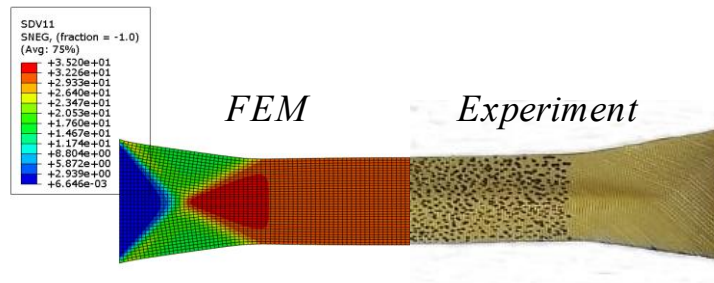


Fig. 14 The FEM results compared with test results on 45° off-axial tensile of uncoated fabric

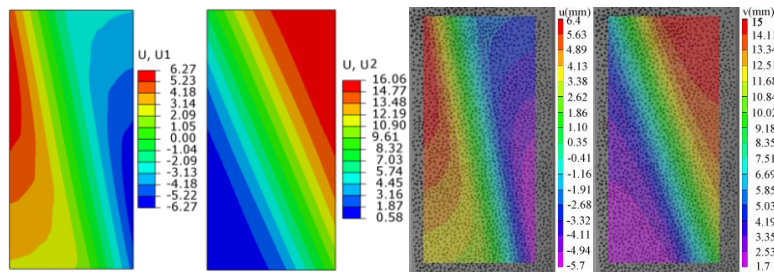


Fig. 15 The FEM results compared with test results on 15° off-axis tensile of coated fabric

## 6 CONCLUSIONS

In this paper, a multiscale non-orthogonal material model based on mesoscopic properties was established to capture the tensile properties of F-12 fabric with and without PET-Al coating. Off-axis tensile tests were conducted to validate the model and investigate the tensile properties. 15° and 45° test results were taken to compare with the simulation results. The simulation results by the material model agreed well with the experiment of the fabric. The test results show that both uncoated fabric and coated fabric are orthogonal. The PET-Al coating will affect the tensile properties and failure modes of the fabric.

## REFERENCES

- [1] F. Wang, Y. Chen, W. Xu, et al. "Experimental study on uniaxial tensile and welding performance of a new coated fabric for airship envelopes", *J. Text. Inst.*, 46(7): pp. 1474-1497, (2017).
- [2] F. T. Peirce, "The geometry of cloth structure." *J. Text. Inst.* , 28.3: T45-T96, (1937).
- [3] S. Kawabata, M. Niwa and H. Kawai, "The finite deformation theory of plain-weave fabrics. part III-the shear-deformation theory", *J. Text. Inst.*, vol. 64(2), pp. 62–85, (1973).
- [4] Hearle, J. W. S., and W. J. Shanahan. "11—An energy method for calculations in fabric mechanics part i: principles of the method." *J. Text. Inst.*, 69.4, pp. 81-91, (1978).
- [5] Y.Y. Zhang, J.H. Xu, and Q.L. Zhang. "Advances in mechanical properties of coated fabrics in civil engineering", *J. Ind. Text.*, 1528083716679159, (2016).
- [6] J.H. Hu, C.J. Gao, S.Z. He, et al. "Effects of on-axis and off-axis tension on uniaxial mechanical properties of plain woven fabrics for inflated structures", *Compo. Struc.*, Vol. 171, pp. 92-99, (2017).
- [7] M. V. d'Agostino, , Giorgio, I., et al. "Continuum and discrete models for structures including (quasi-) inextensible elasticae with a view to the design and modeling of composite reinforcements", *Int. J. Solids. Struct.*, 59, 1-17. (2015)
- [8] O. Erol, B. Powers and M. Keefe, "Development of a non-orthogonal macroscale material model for advanced woven fabrics based on mesoscale structure", *Compos. Part B-Eng.*, Vol. 110, pp. 497-510, (2017).
- [9] M. J. King, P. Jearanaisilawong and S. Socrate. "A continuum constitutive model for the mechanical behavior of woven fabrics", *Int. J. Solids Struct.*, Vol. 42.13, pp. 3867-3896, (2005).
- [10] Leaf, G. A. V., and K. H. Kandil. "1—The initial load–extension behaviour of plain-woven fabrics." *J. Text. Inst.*, 71.1, pp. 1-7, (1980).

## INVESTIGATION OF THE STRUCTURE AND PROPERTIES OF FLEXIBLE POLYMERIC MATERIALS FOR INTEGRATION WITH THIN HEAT CONDUCTORS

STRUCTURAL MEMBRANES 2017

IRINA V. CHERUNOVA<sup>1</sup>, MARIA P. STENKINA<sup>2</sup>, PAVEL V. CHERUNOV<sup>3</sup>

<sup>1</sup>Doctor of Technical Sciences, Professor

Don State Technical University

55, 37 Voroshilova Street, Shakhty, Rostov Region, 346527, Russian Federation

e-mail: [i\\_sch@mail.ru](mailto:i_sch@mail.ru), phone number: +7(928)9056619, skype: cherunova\_irina

<sup>2</sup>student

Don State Technical University

322, 90A, Lenina Street, Shakhty, Rostov Region, 346500, Russian Federation

e-mail: [s-akura@yandex.ru](mailto:s-akura@yandex.ru), phone number: +7(908)5119112, skype: Maria Stenkina

<sup>3</sup>student

Don State Technical University

55, 37 Voroshilova Street, Shakhty, Rostov Region, 346527, Russian Federation

e-mail: [ch.opel@yandex.ru](mailto:ch.opel@yandex.ru), phone number: +7(928)9045390, skype: a605oa161

**Key words:** Heat conductor, Hating, Flexible polymeric material, Laser engraving, Cold conditions.

**Summary:** This article presents the results of analysis of the methods of connecting heaters with materials. Limitations and disadvantages of the ways of integration of materials with heat conductors are revealed. The method of glueless thermoplastic fixing has been proposed. The thermophysical characteristics of the selected polymeric materials were experimentally determined. Experimental studies of the maximum strength for selected materials were carried out. Recommendations for creating heat-protective garments with polymeric materials have been obtained.

Climatic conditions are severe for most parts of Russia, Canada, Finland, Sweden, Norway, as well as Iceland, Greenland, Alaska [1]. People work and live in cold conditions. Cold adversely affect on the human body. It reduces the motor activity of a person and causes impaired coordination [2]. There is a risk of frostbite during a short stay in conditions of low temperatures, strong wind and high humidity [2,3].

Nowadays the development of the cold regions is an actual direction. A particularly important direction is the development of materials adapted to the conditions of cold regions. The development of technical means that they can work in the cold is also relevant [4].

There is a large number of garments that protect people from the cold. They have disadvantages. First, most of these products are made of textiles with heat conductors. Such products give heat to the cold environment [5,6]. Secondly, most of these products heat the entire surface. Here the features of human physiology are not taken into account [7-9]. The solution is the integration of flexible polymeric materials with heat conductors according to a given contour.

Polymers exhibit low thermal conductivity due to their relatively fair atomic density [10].

The tasks of supplying heat to specified areas of products are relevant for many industries. This is not only the creation of clothing, but also footwear, gloves, covers for storage and transportation of equipment, and others [11,12].

The goal of this work is studying the properties of polymeric materials for integrating technologies with heat conductors.

The tasks are:

- research and classification of heat conductors;
- analysis of the methods of connecting heaters with materials;
- selection of materials for research;
- research of thermophysical properties of the selected materials.

According to the data of [13], the classification of flexible heaters into three groups is given: type of heating element, purpose, type of shell around the heating element. However, there is no information on how to join the heat conductors to the material.

The literary analysis [14-18] revealed the main materials to join with heat conductors: silicone, polyamide, polyester. This increases the cost of heating the garments. The analysis of the methods of fixing the heating elements is presented (Table 1).

Table 1: Analysis of the methods of fixing the heating elements

Heat conductor type	Basis material	The method to join the heater to the base material	Method of attachment to the details of garments	Disadvantages
Metal/carbon thread	silicone	vulcanization	glue	costs for glue; the heater is covered with a layer of material, which reduces the heat transfer
Metal/carbon thread	polyamide	lamination	glue	costs for glue; two layers of laminating material
Metal/carbon thread	polyester	lamination	glue	costs for glue; two layers of laminating material
Metal/carbon thread	foil heaters	lamination	glue	costs for glue; two layers of laminating material
Metal/carbon thread/ thermally conductive polymer	textile, non-textile	topstitch, woven with a conductive thread, gluing	production of heating part of garment from a heating element	quickly give heat to the cold environment

The limitations of creating a heat-conducting contour of the required depth in the material structure are revealed. It is necessary for more efficient heat transfer.

Today, the use of 3d printing technologies is increasing to apply thermal conductive polymer to materials. It is possible due to the development of the thermal conductivity of filaments. Technology of 3d printing is used for manufacturing low cost thermally conducting devices[19]. Also, it is known the laser engraving technology [20]. It allows to get depressions in the structure of the material - canals of the necessary configuration and depth. We propose to string together the technologies of 3d printing and laser engraving in order to obtain a method of glueless thermoplastic fixing of heat conductors in the structure of the polymeric materials. This method eliminates the cost of glue, provides a higher contact of the heater with the material (however, it is possible to change the technical characteristics of the modified material).

The method of glueless thermoplastic fixing: the canal of required depth and configuration is cut out in the structure of the material using laser engraving technology. At the same time, the polymer thermo-conductive thread is laid in this canal. The internal surface of the canal is a fixing surface based on the established physical and chemical conditions (Figure 1).

The technical characteristics were experimentally established in order to obtain the canal of required depth. Thermally conductive polymer thread (ITP Textile Materialien, Germany) was selected to conduct experiments [21].

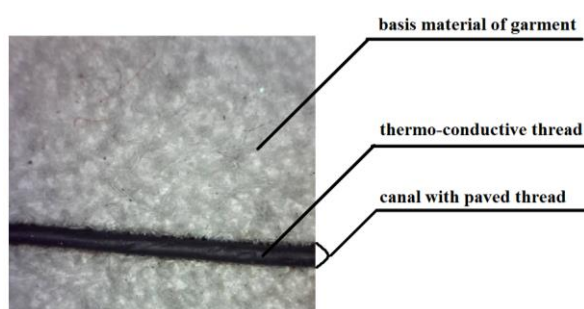


Figure 1: Thermo-conductive thread in a canal

There were selected some polymeric materials such as: neoprene, genuine leather, faux leather, silicone plate for the research. The selection criteria are: thermal conductivity, the possibility of using glueless fixing of the heater, the possibility of using laser engraving technologies, availability in the market.

The thermophysical characteristics of the selected materials were experimentally determined (Table 2).

Table 2: Thermophysical characteristics of selected garment materials

Name of material	Thickness, m	Bulk density, kg/m <sup>3</sup>	Thermal conductivity coefficient, W/(m*K)
Neoprene	0,001	314,46	0,1064
	0,002	471,7	0,1018
	0,003	523,83	0,0677
	0,004	550,1	0,0797
	0,005	565,8	0,0801
Genuine leather	0,001	157,23	0,1111

	0,002	235,85	0,0932
	0,003	209,53	0,0789
Faux leather	0,001	314,30	0,1831
	0,002	314,34	0,1512
	0,003	550,31	0,1174
	0,004	628,93	0,1276
	0,005	1572,33	0,1339
Silicone plate	0,001	1152,43	0,0404
	0,002	1194,6	0,0335
	0,003	1257,37	0,0327
	0,004	1336,48	0,0329
	0,005	1428,58	0,0341

The canal in structure of material might change the overall tensile strength. Experimental studies of the maximum strength for selected materials were carried out. Studies were conducted in two forms: with a cutted out canal and without.

Using the laser engraving technology, according to GOST [22-25], the samples of the following kind were made:

- "duble-shoulder blade" with and without a canal ((silicone plate, neoprene, genuine leather) Figure 2);
- rectangular appearance (faux leather);
- round appearance (all materials for abrasion tests) [6-9].



a) with a canal



b) without a canal

Figure 2: Scheme of the material sample "duble-shoulder blade" with (a) and without (b) a canal

It was established that the tensile strength for samples with a canal has not decreased for neoprene and a silicone plate (Figure 3).

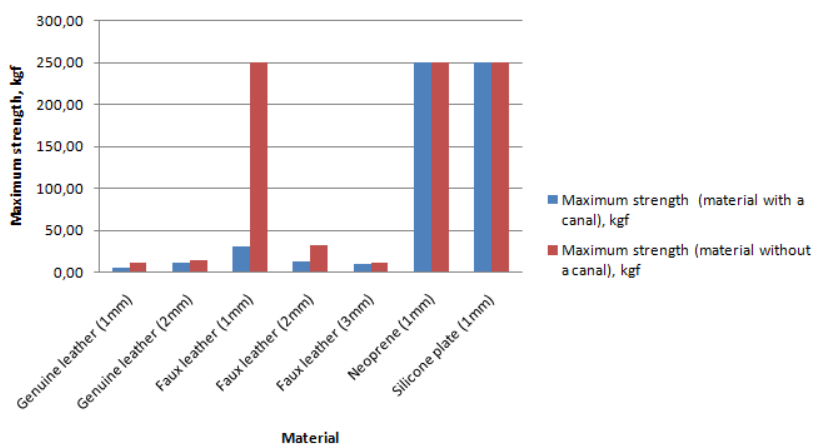


Figure 3: Characteristics of maximum strength of materials

Neoprene was less resistant to abrasion, in contrast to the genuine leather and silicone plate. Silicone plate thickness of 3 mm and genuine leather thickness of 3 mm have shown the highest values of thermal protection and wear resistance.

It was revealed the deviation of sizes of finished samples of materials (thickness 1 mm) from projected dimensions (Table 3).

Table 3: Deviation of sizes of finished samples of materials from projected dimensions

Name of material	Deviation by length, %	Deviation by width, %
Genuine leather	0,5	0
Faux leather	0,5	0
Neoprene	0,9	4,0
Silicone plate	0,5	0

It has amounted to 4% for neoprene; 0.5% for genuine leather; 0.5% for the silicone plate. Neoprene has shown high melting and charring.

Samples of materials thicker than 1 mm have shown a deviation more than 3%. This error has exceeded the permissible norm in accordance with the relevant standards [22-25].

According to [20, 26] the laser radiation power is recommended to be from 500 W to ensure a minimum deviation in the dimensions of samples of materials with a thickness of more than 1 mm.

During the evaluation of the quality of the contour laser treatment, it has been revealed that the canal surface in the structure of the silicone plate has been slightly damaged. It has remained smooth without charring.

The processing of neoprene and genuine leather have resulted in a strong charring. The surface structure of the canal has been severely damaged.

The surface of the canal in the structure of the faux leather had inclusions of textile material. It does not match to the proposed technology of glueless thermoplastic fixing [12-14].

As a result, limitations and disadvantages of the ways of integration of materials with heat conductors are revealed. The method of glueless thermoplastic fixing has been proposed, which was based on laser engraving technology and filament feeding using 3d printing technology. The thermal and physical characteristics of the selected polymer materials were experimentally established.

It was recommended:

- use a silicone plate or genuine leather as the main material to join with the heat conductor;
- take into account the power of the laser-engraving equipment;
- take into account the established deviations in the dimensions of the finished sample of the material from the projected one.

Integration of polymer materials with heaters allows to reduce the weight, volume and cost of heat-protective garments (clothes, shoes, gloves, covers). It also expands the use of such products. They become more mobile and ergonomic, with an extended time resource for

continuous use. Despite this, many tasks of supplying heat to specified areas of polymer materials remain unresolved. It requires additional research.

## REFERENCES

- [1] Lukin Yury F. Performance of an ethno cultural landscape of Arctic regions in global and regional measurements / Arctic and North. (2011) 1: 29 pp.
- [2] Modes of work and rest, work in the cold in an open area or in unheated rooms. Guidelines. MR 2.2.7.2129-06. (2006) 15 pp.
- [3] M.P. Stenkina and I.V. Cherunova, Evaluation of development resources for heated garments for operation in critical cold, The Future of Science-2016, Collection of Scientific Articles of the 4th International Youth Scientific Conference, Southwestern State University Kursk, 2016, 4: 262-266.
- [4] Decree of the Government of the Russian Federation of April 21, 2014 No. 366 The State Program of the Russian Federation "Social and Economic Development of the Arctic Zone of the Russian Federation for the Period to 2020", 39 pp.
- [5] P. Cherunov, I. Cherunova, S. Knyazeva, M. Stenkina, E. Stefanova, N. Kornev, The development of the research techniques of structure and properties of composite textile materials when interacting with viscous fractions of hydrocarbon compounds, Structural Membranes, 2015, pp. 555-564.
- [6] Syed Talha Ali Hamdani, Prasad Potluri and Anura Fernando, Thermo-Mechanical Behavior of Textile Heating Fabric Based on Silver Coated Polymeric Yarn, Materials, 2013, pp. 1072-1089.
- [7] Riikka Holopainen, A human thermal model for improved thermal comfort, Thesis for the degree of Doctor of Science in Technology, Dissertation, Espoo, 2012, VTT Science, 23: 141 p.
- [8] I. Cherunova, N. Kornev, G. Jacobi, I. Treshchun, A. Gross, J. Turnow, S. Schreier, M. Paschen, Application of calculations of heat transfer and computational fluid mechanics to the design of protection cloths, Engineering and Physics Journal, 2014, 87/4: 829-837.
- [9] I. Cherunova, N. Kornev, I. Brink, Mathematical model of the ice protection of a human body at high temperatures of surrounding medium, Forschung im Ingenieurwesen, 2012, 76/3-4: 97-103.
- [10] I.A. Tsekmes, R. Kochetov, P.H.F. Morshuis, J.J Smit, Thermal Conductivity of Polymeric Composites: A Review, IEEE International Conference on Solid Dielectrics, Bologna, Italy, June 30 – July 4, 2013, pp. 678-681.
- [11] I. Cherunova, N. Kornev, G. Jacobi, I. Treshchun, A. Gross, J. Turnow, S. Schreier, M. Paschen, Application of computational fluid mechanics for protection cloth design, 11th World Congress on Computational Mechanics, WCCM 2014, 5th European Conference on Computational Mechanics, ECCM 2014 and 6th European Conference on Computational Fluid Dynamics, ECFD 2014, pp. 7262-7273.
- [12] M. P. Stenkina and I.V. Cherunova, Development of technology for the design of protective devices for communication facilities with built-in heat transfer systems, XVIII Youth International Scientific and Technical Conference of students, students, graduate students and young scientists "High technology and Intelligent Systems - 2016"

- (TECHNOLOGY & SYSTEMS-2016), is dedicated to the 55th anniversary of the First Man in Space, Bauman Moscow State Technical University, 2016, pp.115-122.
- [13] A. K. Sysoev, Efficiency of the use of flexible surface heating elements, *Electronic scientific journal, "Engineering Bulletin of the Don*, 2017, 1: 13 p.
  - [14] Yu. Xiaowei, K. Bikram, Mahajan, Wan Shou, Heng Pan, *Materials, Mechanics, and Patterning Techniques for Elastomer-Based Stretchable Conductors, Micromachines*, 2016, 8(1):7, 30 pp.
  - [15] *Flexible heaters design guide*, Minco, 2007, 45 pp.
  - [16] *Flexible Heaters*, Watlow, 2010, 20 pp.
  - [17] Christopher Oshman, Qian Li, Li-Anne Liew, Ronggui Yang, Victor M. Bright, Y C Lee, *Flat flexible polymer heat pipes, Journal of micromechanics and microengineering*, 2013, 23: 6 pp.
  - [18] Ashok Kumar, *Study on Different Techniques of Fabricating Conductive Fabrics for Developing Wearable Electronics Garments, Textile Science & Engineering*, 2015, 5(5): 6 pp.
  - [19] U. Kalsoom, A. Peristyy, P.N. Nesterenko, B. Paull, *A 3D printable diamond polymer composite: A novel material for fabrication of low cost thermally conducting devices, RSC Advances*, 2016, 6(44): 38140-38147.
  - [20] P. Shukla, J. Lawrence, Y. Zhang, *Understanding laser beam brightness: A review and new prospective in material processing, Optics & Laser Technology*, 2015, 75: 40–51.
  - [21] ITP Textile Materialien, URL: <http://itp-gmbh.de/de/technologiekompetenzen/textile-heizsysteme/niedertemperatur>.
  - [22] GOST R ISO 3376-2013. *Leather. Determination of tensile strength at break and elongation*. Moscow, Standartinform, 2014, 7 p.
  - [23] GOST R 56284-2014. *Imitation leather. Method for determining the breaking load and elongation at break*. Moscow, Standartinform, 2015, 8 p.
  - [24] GOST 11721-78. *Rubber is porous. Method for the determination of tensile strength properties*. M., Interstate Standard, 1980, 6 p.
  - [25] GOST 270-75. *Rubber. Method for the determination of tensile strength properties*. M., IPK Publishing house of standards, 1978, 11 p.
  - [26] A. Stepanov, M. Manninen, I. Pärnänen, M. Hirvimäki, A. Salminen, *Tool for Industry or Designers? 15th Nordic Laser Materials Processing Conference, Nolamp 15, Physics Procedia*, 2015, 78:157-162.

## INVESTIGATIONS INTO THE LONG-TERM BEHAVIOUR OF FABRICS

HASTIA ASADI\*, JÖRG UHLEMANN\*, THOMAS STEGMAIER†, VOLKMAR  
VON ARNIM†, NATALIE STRANGHÖNER\*

\* Institute for Metal and Lightweight Structures  
University of Duisburg-Essen  
45117 Essen, Germany  
Email: [iml@uni-due.de](mailto:iml@uni-due.de), web page: <http://www.uni-due.de/iml>

† Deutsche Institute für Textil- und Faserforschung (DITF)  
73770 Denkendorf, Germany  
Email: [thomas.stegmaier@ditf.de](mailto:thomas.stegmaier@ditf.de) - Web page: <http://www.ditf.de/>

**Key words:** Coated woven fabric, tensile strength, weathering, long-term loading, top coat

**Summary.** The design process of membrane buildings and structural fabrics has to consider changes of the material properties due to long-term exposure to the environment. For the structural engineer the loss of tensile strength in the fabric, in the seams and in the mechanical fastenings is of major concern, further variations in tear strength and stiffness should be known. The degradation of the protective coating normally becomes apparent in the decrease of the optical properties, first.

For basic synthetic materials the strength deterioration resulting from certain environmental impacts are known. But the prediction of properties for material compositions typically found in structural membranes are vague and a change of these properties during lifetime due to a time dependent environmental load spectrum containing UV radiation, condensate, rain, temperature and pollutants is not possible without experimental testing.

Regarding long-term loading behaviour of structural membranes, creep-rupture or time-to-failure-tests are state of the art. A reevaluation of existing literature and new experimental results show that these tests do not cover loads with limited duration like snow.

The objective of the present paper is to broaden the data basis for long-term behaviour of typical structural membranes for both environmental impacts and mechanical loading. Both aspects are investigated in contribution to the development of a new European design standard for structural membranes.

PVC-coated polyester (PES) fabrics and PTFE-coated glass fiber fabrics are in the main focus of the standardization work as they cover the gross market for structural fabrics. In this paper, environmental impacts to the top coat, particular due to humidity are discussed for PES/PVC and glass/PTFE fabrics. Furthermore, effects of “long-term loading” but with limited duration are presented for glass/PTFE fabrics. Moreover, consequences on the linked strength reduction factors derived from the test results are analyzed and the implications on the design concept and test methods are discussed.

### 1 INTRODUCTION

Today, the application of coated fabrics as architectural membrane material for light weight structures is growing dramatically. New generations of membrane materials have been developed over the last decades based on high strength fiber fabrics, coated by high performance materials. For some composites, such as PVC-coated polyester fabric, the

coating actually consists of several layers. The main coat made from plasticized PVC protects the fabric and thin top coats on the exterior surface containing e. g. polyvinylidene fluoride (PVDF) protect the main PVC coat. Ideally, the top coat provides a barrier to and from the environment blocking incoming UV radiation, moisture, dirt, corrosive gases and mitigates the plasticizer migration to the surface.

Under weathering, every layer degrades according to its own sensitivity and the permeability of the covering layers with the result of variable functional losses especially concerning the optical and mechanical properties. Until now, rough assumptions are made for testing architectural membranes and calculating strength reduction factors [1, 2].

In this work, PVC coated polyester fiber membranes taken from two dismantled architectural projects located in Germany are investigated by evaluating existing test results available in the Essen Laboratory for Lightweight Structures (ELLF) at the University of Duisburg-Essen. Furthermore, the effect of wetting on the short term tensile strength of PES/PVC and glass/PTFE are assessed.

In addition, changes in top coat structure and chemical composition of PES/PVC membranes due to rapid artificial weathering at the German Institutes of Textile and fiber research (DITF Denkendorf) are shown up, deploying ATR-IR spectroscopy and a dyeing procedure.

In the design practice long-term loading impacts are considered in a simplified manner, using a safe sided strength reduction factor of approximately 2 for glass/PTFE fabrics. The prediction presently based on long-term loading simulations of “unlimited” duration can be improved considering effects of long-term loads with limited duration as for example snow, discussed below for a glass/PTFE fabric.

## 2 CONSIDERATION OF ENVIRONMENTAL IMPACTS AND STRENGTH REDUCTION FACTORS

### 2.1 General

In general, environmental impacts can be investigated using three procedures: natural ageing (weathering) of test specimens in natural weathering test rigs, artificially accelerated ageing in weathering chambers and ageing by practical application [3]. The last method means the investigation of dismantled material from a realized project.

In the framework of the German “A-factor”-concept, the reduction factor considering environmental impact is calculated according to equation (1) [4]:

$$A_2 = \frac{n_{23}}{n_{w,23}} \quad (1)$$

where  $n_{23}$  is the short term tensile strength at room temperature of 23°C and  $n_{w,23}$  is the tensile strength at room temperature of 23°C for a weathered test specimen. One aim of the present research is to quantify this ratio for the typically used materials in textile architecture, considering typical lifetimes of architectural structures made from the common composites PES/PVC and glass/PTFE.

### 2.2 Assessing strength reduction factors of two dismantled architectural fabrics

Architectural PES/PVC membranes applied in two membrane buildings are evaluated in this chapter, see also [5]. Table 1 gives details about these materials and their background. After each interval of inspection a sample was taken and the mechanical performance was assessed using a CRE (constant rate extension) tensile testing machine according to EN ISO

1421 [6]. The results are presented in Figure 1.

**Table 1:** General features of projects A and B

Name of the project	Year of installation	Location	Application	Material type
A	1979	Germany	Stand canopy	PES/PVC type V Color green Top coat: Acrylic
B	1994	Germany	Multifunctional stadium roof	PES/PVC type III Color white TiO <sub>2</sub> Top Coat pure PVDF

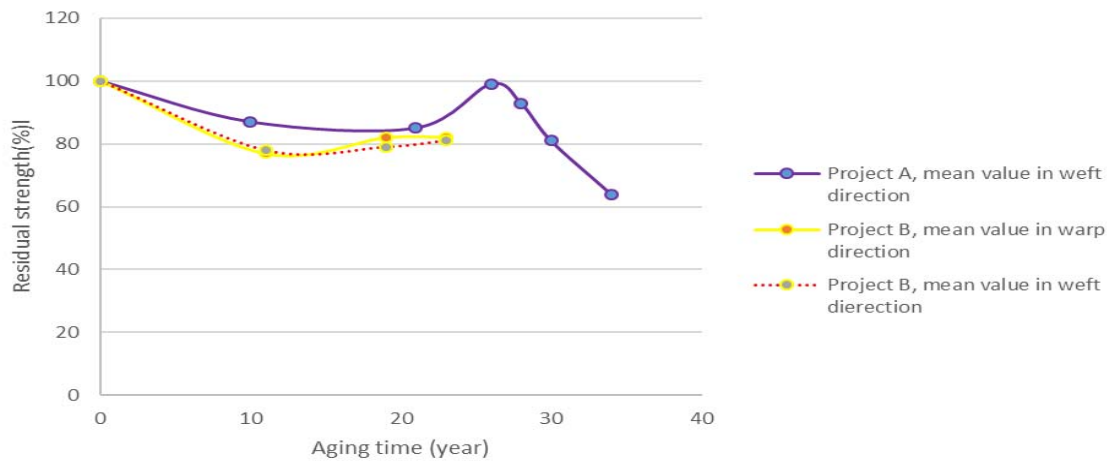


**Figure 1:** Residual strength-ageing time curves of projects A and B

With curves in Figure 1, the  $A_2$  factors (strength reduction factors) of two projects could be calculated for different ageing duration. But for the designer, the  $A_2$  factor for a specific material considering its typical lifetime is decisive. Presuming a typical service life of 15 years for PES/PVC it results  $A_2 = 1.18$  for material (A) in weft direction and  $A_2 = 1.32$  for Material (B), both in weft and warp direction.

### 3 CHARACTERIZATION OF WETTING AND WICKING

#### 3.1 General

Many physical properties of fibers are affected by the amount of water absorption such as dimensions, tensile strength and elastic recovery. Pollutants can accompany the water which eases the penetration into the material. The water transport is driven by capillary forces and requires a porous media [7].

In Figure 2 the cross section of a PVC coated membrane is depicted showing the foamy, porous structure of the soft PVC coating. The PVC hardly infiltrates the PES-yarn. The PVDF-topcoat is 15-20  $\mu\text{m}$  thick. In general, the wicking process can be distinguished according to the transport direction in transverse or in-plane wicking[8].

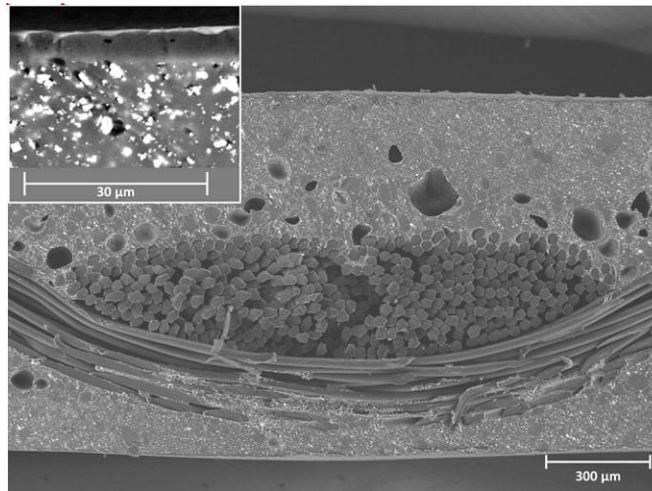


**Figure 2:** SEM cross section of a PVC coated PES membrane. Enlarged detail shows PVC coating and PVDF topcoat. Bright particles are inorganic fillers in PVC.

### 3.2 Wetting mechanism in architectural fabrics

In architectural fabrics, the exterior surface is sealed and therefore water (rain or melting snow) should not seep into fabric yarns by passing the coating surface as long as the top coat keeps intact. With the passage of time ageing cracks develop, delamination occurs and the protection is reduced. Via the seams and uncovered edges, in-plane wicking along the yarns which are coated but not filled by PVC or any other materials, might take place. Additionally, these cracks cause transverse wicking and water penetrates through the thickness of the fabric. In many technical polyester fabrics the wicking process is reduced by supplying a “low-wick” system, but as not all materials are equipped and the effectiveness of the low-wick system itself decreases under environmental influence, the impact of humidity or water on the material properties is of interest.

### 3.3 Effect of water on tensile properties of PES/PVC and glass/PTFE fabrics

The changes of tensile strength due to the influence of water penetration has been examined through wet tests based on EN ISO 1421 [6], carried out on virgin and aged, dismantled PES/PVC fabrics and on virgin glass/PTFE fabric. The dismantled PES/PVC fabric investigated was given from a three-year old inner layer of a biogas plant. The inner layer of biogas plants is affected by some aggressive chemical gases such as hydrogen sulfide. In these tests, test specimens were placed in a bath of water and surfactant for 24 hours, see Figure 3. The surfactant was used in order to lower the surface tension. Comparison samples were kept dry. Dry and wetted test specimens were subsequently tested with the CRE tensile testing machine at the ELLF. Table 2 shows the change of weight after the water bath. With the exception of the dismantled fabric, which has some micro cracks, the average changes in weight of the samples investigated after wetting are almost the same for both PES/PVC and glass/PTFE fabrics.

Table 3 presents the change in tensile strength of the wetted materials related to the dry ones. The amount of mean tensile strength of PES/PVC fabrics after wetting does not decrease dramatically. On the contrary, it increases slightly in some cases. Overall, the changes are rather insignificant. In contrast, for the glass/PTFE fabric, a considerable decrease in tensile strength of 6.81% and 6.64% is observed for warp and weft direction, respectively. This illustrates, that glass/PTFE fabric is more sensitive to water influences, particularly as it

absorbed the smallest amount of water of all tested materials, see Table 2. This effect is known as hydrolysis, which leads to stress corrosion cracking of the glass fibers, see e.g. [9]. It can be concluded, that for the weathering test of glass/PTFE fabrics – natural or artificial – it is important to cover edges of the test specimens.



**Figure 3 :** Wet test procedure, bath of water and surfactant (left) and drying with paper towel (right)

**Table 2:** Average weight changes (%) of different fabrics after wetting

Name of fabric	Average weight changes after wetting (%)	
	Warp strip specimens	Weft strip specimens
PES/PVC, Type I, Dismantled (3 years old) , Biogas Plant	9.09%	9.06%
PES/PVC, Type I, virgin	4.11%	4.24%
PES/PVC, Type II, virgin	4.96%	4.82%
PES/PVC, Type III, virgin	3.49%	2.79%
Glass/PTFE, Type III, virgin	3.18%	3.23%

**Table 3:** Average tensile strength changes (%) of different fabrics after wetting

Name of fabric	Change in mean tensile strength after wetting (%) related to the dry state			
	Warp stressing		Weft stressing	
	Increase	Decrease	Increase	Decrease
PES/PVC, Type I, Dismantled, Biogas Plant	3.91%			0.46%
PES/PVC, Type I, virgin		0.89%		1.49%
PES/PVC, Type II, virgin		2.06%		2.72%
PES/PVC, Type III, virgin	4.62%		1.28%	
PES/PVC, Type IV, virgin	1.39%		1.95%	
Glass/PTFE, Type III, virgin		6.81%		6.64%

Table 4 shows the changes in amount of mean tensile strain at breaking point after wetting. It becomes obvious that the differences between virgin samples of PES/PVC and glass/PTFE are not considerable. In contrast, for dismantled biogas PES/PVC samples, these changes are about 6.87% and 4.76% in warp and weft direction, respectively. With reference to Table 2, the highest amount of water seepage belongs to these dismantled samples: 9.09% in warp and

9.06% in weft. It could be concluded that the more water seeps into PES/PVC samples, the more growth in mean tensile strain at break can be observed. But the data are not stringent. For instance, the type II virgin material has a relative high water absorption, but low increase in tensile strain at break.

**Table 4:** Average breaking tensile strain changes (%) of different fabrics after wetting

Name of fabric	Change in mean tensile strain at break after wetting (%) related to the dry state			
	Warp stressing		Weft stressing	
	increase	decrease	Increase	decrease
PES/PVC, Type I, Dismantled, Biogas Plant	6.87%		4.76%	
PES/PVC, Type I, virgin	1.57%			0.73%
PES/PVC, Type II, virgin	1.55%			1.18%
PES/PVC, Type III, virgin	4.68%		3.02%	
PES/PVC, Type IV, virgin	0%		1.99%	
Glass/PTFE, Type III, virgin		3.75%		2.49%

## 4 ARTIFICIAL WEATHERING OF TOP COATING

### 4.1 General functionality

The purpose of a top coat is to increase the appearance, reduce the maintenance and to extend service life. In particular, this is accomplished by blocking environmental penetration of chemicals, moisture and UV radiation; mitigating the loss of plasticizer; increasing the surface quality regarding cracking, crazing and abrasion; reducing the adherence of moisture, dirt, biological films and preserving gloss, color and reducing solar heating.

The durability and effectivity depend on the chemical composition, the thickness and the surface quality of the coating. In general, only limited information concerning the layered build up is published by the manufacturers allowing not more than a rough assignment to the material classes e.g.: PVF-film, PVDF-film, acrylic-resin, resin of acrylic blended with PVDF or other materials, PVDF-resin, TiO<sub>2</sub>. Further, the thickness of the resins range in the order of 1 to 10 µm while the films thickness is > 20 µm. The unprecise knowledge of the material composition influences the model concept of the ageing process and influences the examination method for assessing aged materials.

In the following, two methods are presented for examining changes in top coats after artificial weathering in a wet-dry industrial environment characterized by temperature changes between -30 to +70°C with condensing water and sulfur dioxide SO<sub>2</sub> turning into sulfurous acid H<sub>2</sub>SO<sub>3</sub>. The cycle Global-UV-test is subdivided into four periods with different conditions of temperature, humidity and UV-radiation. During the 10 hour lasting periods I and III the chamber temperature is kept at 50°C, the relative humidity at 90 % and the global UV radiation has an intensity of 50 W/m<sup>2</sup> on the top surface. Between these periods lays an interval with rain at 30°C without UV-radiation. This cycle is characterized by high UV-irradiation at high humidity under moderate temperature. It simulates an application in a humid tropical or subtropical climate without industrial pollution.

The cycle noxious gas/climate change consists also of four periods with changing conditions of humidity, temperature and concentration of noxious gases. During the 6 hour lasting periods I and III the chamber temperature lays at 70°C, the relative humidity at 90 %

and the concentration of each SO<sub>2</sub> and NO<sub>x</sub> at 15 ppm. A 6 hour frost period with -30°C under continuing affection by SO<sub>2</sub>/NO<sub>x</sub> is simulated in the interval between the periods I and III. The final 6 hour period IV simulates moderate climate conditions with 20°C at 35 % relative humidity. This cycle is characterized by strong temperature and humidity changings at high concentrations of corrosive gases. It simulates an application in moderate climates with seasonal temperature changings and high industrial pollution.

**Table 5:** Environmental simulation, cycle Global-UV-test, cycle time 24 h

period		I	II	III	IV
time	[h]	10	2	10	2
temperature	[°C]	50	30	50	30
relative humidity	[%]	90		90	
UV-intensity *	[W/m <sup>2</sup> ]	50	0	50	0
rain		none	+	none	+

\* UV-irradiation only on the upper side

**Table 6:** Environmental simulation, cycle noxious gas/climate change, cycle time 24 h

period		I	II	III	IV
time	[h]	6	6	6	6
temperature	[°C]	70	-30	70	20
relative humidity	[%]	90		90	35
noxious gas SO <sub>2</sub> / NO <sub>x</sub>	[ppm]	15 / 15	15 / 15	15 / 15	0

**Table 7:** Cycle arrangement of series 1 and 2

days		1	2	3	4	5	6	7	8	9	10	11	12	13	14	15	16	17	18	19	20
series 1(b)	Global-UV-test	X		X		X		X		X		X		X		X		X		X	
	noxious gas/climate change		X		X		X		X		X		X		X		X		X		X
series 2(c)	noxious gas/climate change	X	X	X	X	X	X	X	X	X	X	X	X	X	X	X	X	X	X	X	X

Changes in chemical composition of the top layer can be analyzed deploying an ATR-IR spectroscope. The search for cracks and capillary systems can be analyzed by applying a dyeing procedure.

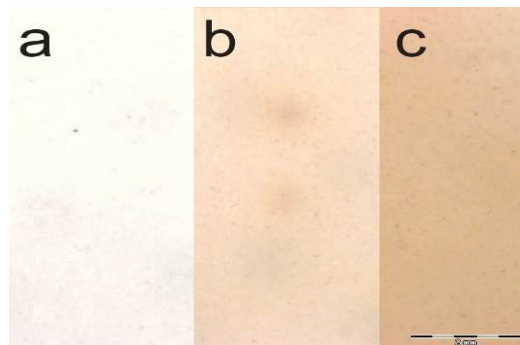


**Figure 4:** Microscopic picture of material (a) and in condition after 20 days of aging (series 1, b / series 2, c)

A weak yellowing appears on the membrane surfaces from series 1. The edges of the samples show a stronger yellowing effect, which indicates that humidity and noxious gases which penetrate into the laminate along open laying fabrics and layers are more responsible for the yellowing than the UV-radiation.

According to the visual appearance the chosen environmental treatment conditions cause external alterations of the membrane but keep the material functionally intact. This is in harmony with the typical observation that changings in color appear on membranes much earlier before serious material destruction takes place.

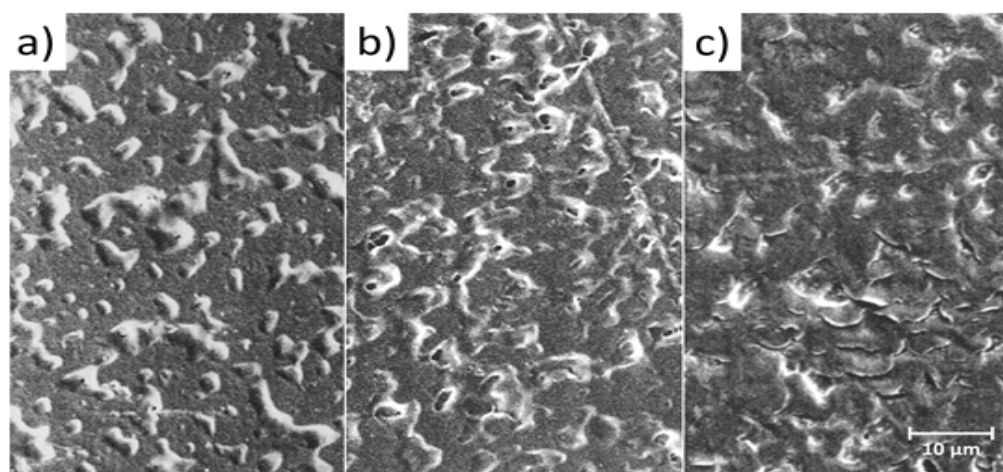


**Figure 5:** SEM picture of material as-received (a) and in condition after 20 days of aging (series 1, b / series 2,c)

Blisters in the top coat or in layers beneath tend to open up during ageing. This causes pores in the top coat which reduce the function of the top coat as protecting coating and diffusion barrier.

#### 4.2 ATR-IR spectroscopy

The IR spectroscopic examination of the top coat surface containing PVDF has been conducted with a Biorad FT60 spectrometer, a Specac Golden Gate single reflection ATR accessory and a germanium crystal. The high refraction index of the Ge-crystal limits the penetration depth of the IR ray into the material to approximately 1  $\mu\text{m}$ . Thus the chemical information is from the very top layer of the PVDF-top coat. The PVDF coating contains also acrylic binder which results in relatively strong C=O vibration at 1728  $\text{cm}^{-1}$  in the IR-spectrum. After the artificial ageing, especially the samples in series 2 display strong OH-vibrations at 3300  $\text{cm}^{-1}$  and signals at 1640 – 1660  $\text{cm}^{-1}$  in the IR-spectrum of the PVDF-coating. This can be explained with hydrolytic degradation of ester groups. Furthermore, one can recognize that the intensity of the carbonyl vibration at 1728  $\text{cm}^{-1}$  decreases during ageing. Apparently this goes together with an increasing signal at 1660  $\text{cm}^{-1}$ . A decreasing signal intensity means that chemical alterations take place with a non (or slow) diffusing component. This might assume that the PVDF coating acts as an efficient diffusion barrier for PVC plasticizers.

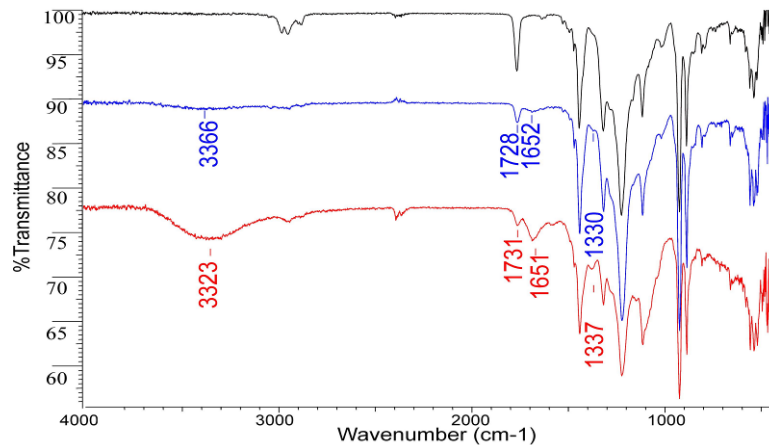


**Figure 6:** IR spectrum of Membrane PVDF-topcoat surface: as-received (top, black) and in condition after aging (series 1, middle, blue / series 2, bottom, red)

### 4.3 Dyeing according to the Neocarmin TA-Standard procedure

The varyingly aged membranes were afterwards treated with a dye in the Neocarmin TA process. After the dyeing procedure the surface was investigated with a stereo-microscope, see Figure 7. The penetration of the colored fluid uncovers capillary capabilities of the material and differences in color intensity and color shade depict differences in material and thickness as well as changes in chemical composition during ageing.

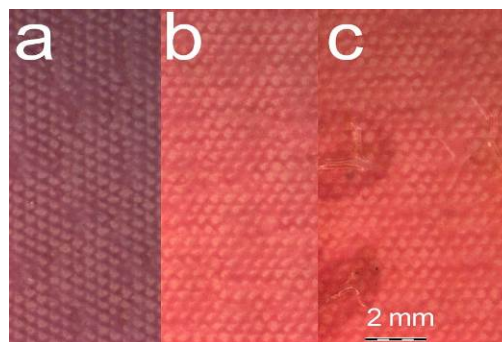


**Figure 7:** Microscopic picture of dyed material as-received (a) and in condition after 20 days of aging (series 1, b / series 2, c)

## 5 LONG-TERM LOADING IMPACTS ON GLASS-PTFE FABRICS

In German design practice, long-term loading is typically considered as decreasing the tensile strength and is taken into account by the strength reduction factor  $A_1$  [2]:

$$A_1 = 1.1 \cdot \frac{n_{23}}{n_{t,23}} \quad (2)$$

where  $n_{23}$  is the short term tensile strength and  $n_{t,23}$  is the tensile strength after long-term loading over time  $t$  in “time-to-failure”-tests, both at room temperature ( $T = 23^\circ\text{C}$ ). The “extrapolation factor” of 1.1 was introduced by Minte. It aimed to cover uncertainties of the extrapolation for the time between  $t = 10^3$  h and  $t = 10^5$  h because only a few tests existed for this period of time.

On the other hand, [5, 10] show for PES/PVC fabrics that “long-term” load of limited duration like snow does not reduce the strength. In order to investigate the effect “long-term”

loading of limited duration on PTFE-coated glass fiber fabrics, experimental “long-term” loading tests have been performed in the ELLF on a glass-PTFE fabric type II according to the classification proposed in [4]. In the framework of these tests, the duration of “long-term” is defined as three months, which is able to cover a snow load duration in most regions of Europe. For safety purposes, the magnitude of the membrane stress resulting from the snow load is considered as the maximum design stress, assumed here to be 25 % of the short term tensile strength given in the data sheet. This assumption is deduced from the typical safety factor of 4. Presuming a damaging effect, a subsequent period of 2.5 months at prestress level is scheduled for half of the tests specimens in order to identify a possible recovery after unloading. The prestress level is set to 2 % of the short term tensile strength. The tests were carried out in two phases:

- Phase 1: Loading of all test specimens with the full design stress and holding it constant for three months; for half of the test specimens a subsequent recovery time of 2.5 months on prestress level was scheduled;
- Phase 2: Unloading of the test specimens, removal from the long-term loading test rig and immediate mounting in the 50-kN tensile testing machine for the experimental determination of the residual tensile strength.

In total, 12 test specimens were tested, six warp and six weft specimens. They were mounted on the ELLF creep test stand as shown in Figure 8 on the left.



**Figure 8:** Installation situation of the long-term loaded test specimens in the creep test stand (left), examples of the kind and position of fractures during the tensile tests after long-term loading (right)

In phase 2, every single test specimen was demounted from the long-term test stand individually and mounted immediately in the tensile testing machine within a time period of less than five minutes. Figure 8 on the right gives an example of material fractures obtained in these tensile tests. No clamping fractures occurred. For comparison reasons, also virgin material was tested in the tensile testing machine. Table 8 shows the results of the measured residual strengths after three months of full design stress and in comparison the virgin state strengths. The strength did not decrease after three months loading, but instead increased by 4-5 % regarding mean values. Only the 5%-fractile in weft direction shows a constant level. This is due to a slightly higher coefficient of variation after the long term loading in weft direction. But it should be mentioned that the coefficient of variation was generally low with max.  $V_x = 3.2\%$ .

**Table 8:** Comparison of virgin tensile strengths to residual tensile strengths after three months loading on full design stress level

	Warp		Weft	
	Mean	5%-Fractile	Mean	5%-Fractile
Short term tensile strength of the virgin material [kN/m]	117,2	113,2	122,8	116,2
Residual strength after three months of full design stress [kN/m]	122,4	121,3	129,4	116,5
Residual strength/virgin strength [%]	104,55	107,16	105,37	100,26

As almost no strength decrease due to long-term loading could be identified, the additional recovery time was valued to be obsolete. However, Table 9 gives the results of the residual strengths after the additional recovery time of 2.5 months on prestress level. For warp as well as for weft direction, the mean tensile strength even rises! But as the deviations are little higher now with  $V_x = 3-4\%$ , the 5%-fractiles are more or less on virgin state level again. In warp direction the “usable” strength value in the design even decreased slightly by 2 %.

In summary, long-term loading of limited duration did not damage glass/PTFE fabric. On the contrary, the full design load initially even strengthened the material. But this increase was lost again during the subsequent period at prestress level.

From this it follows, that in the current design practice the impact of long-term loading, considered with a strength reduction factor of approximately  $A_2 = 2$  or more for glass/PTFE fabrics, seems to be much too high and leads to very conservative values. Possibly, the strength reduction factor for long-term loading in the future design standard could be applied on load combinations including prestress, but excluding snow. For the definition of safe strength reduction factors in the framework of the establishment of a Eurocode, further research is recommended.

**Table 9:** Comparison of virgin tensile strengths to residual tensile strengths after three months loading on full design stress level plus 2.5 months recovery on prestress level

	Warp		Weft	
	Mean	5%-Fractile	Mean	5%-Fractile
Short term tensile strength of the virgin material [kN/m]	117,2	113,2	122,8	116,2
Residual strength after three months of full design stress plus 2.5 months recovery [kN/m]	123,5	111,2	134,5	117,7
Residual strength/virgin strength [%]	105,38	98,23	109,53	101,29

## 6 CONCLUSIONS

Environmental impact causes some changes in both optical and mechanical properties of building polymers. PVC-coated polyester and PTFE-coated glass fiber fabrics are affected where they are exposed directly to the atmospheric environment during their long-term services in textile architecture structures.

Experimental tests presented in this contribution simulated water seepage from uncovered

edges of PES/PVC and glass/PTFE fabrics and investigated the development of tensile strength for the wetted test specimens. All polyester fabrics investigated revealed no significant loss of tensile strength due to water penetration, whereas the glass/PTFE fabric showed a considerable loss of strength of approximately 7 % – although the lowest amount of water was absorbed compared to all other tested material. Due to this sensitivity, it is strongly recommended to cover edges of test samples made from glass fiber fabric in both natural and artificial weathering tests.

Experimental long-term loading tests on glass/PTFE fabric simulating high stress with a load duration of three months revealed that the glass fiber fabric did not respond with a decrease in tensile strength but actually an increase. In fact, this favorable effect got lost when the high stress was withdrawn again. In contrast to the current design practice, it is imaginable that future design rules omit a strength reduction for “long-term” loads with limited duration like snow and only apply it to long-term loads of unlimited duration like prestress.

## REFERENCES

- [1] B. Meffert, *Mechanische Eigenschaften PVC-beschichteter Polyestergewebe*, PhD-Thesis, RWTH Aachen University, 1987.
- [2] J. Minte, *Das mechanische Verhalten von Verbindungen beschichteter Chemiefasergewebe*, Dissertation, RWTH Aachen University, 1981.
- [3] Z. h. Chen, Z. h. Qilin, and W. Xue, *Experimental research on Mechanical Properties of PVC Membrane After Aging*, Proceedings of the International Association for Shell and Spatial Structures Symposium, Wroclaw, Poland, 2013.
- [4] N. Stranghöner et al., *Prospect for European Guidance for the Structural Design of Tensile Membrane Structures, Support to the implementation, harmonization and further development of the Eurocodes*, JRC Science and Policy Report, European Commission, Joint Research Centre, Editors: M. Mollaert, S. Dimova, A. Pinto, St. Denton, EUR 25400 EN, European Union, 2016.
- [5] J. Uhlemann, H. Asadi, and N. Stranghöner, *A survey on strength deterioration of Polyester-PVC fabrics*, Proceedings of the IASS Symposium, Hamburg, 2017.
- [6] EN ISO 1421:2017-03, *Rubber- or plastics-coated fabrics – Determination of tensile strength and elongation at break (ISO 1421:2016)*
- [7] A. Chatterjee and P. Singh, *Studies on wicking behavior of polyester fabric*, Hindawi Journal of textiles (2014), 1-11.
- [8] A. Patnaik, R. S. Rengasamy, V. K. Kothari and A. Ghosh, *Wetting and Wicking of textiles*, Taylor & Francis, 2006.
- [9] W. Terchüren and L. Kido, *Neuartige Glasfasern mit innovativen Beschichtungen für Riemenanwendungen*, in: „14. Tagung Zahnriemengetriebe“ am Institut für Feinwerktechnik und Elektronik-Design der TU Dresden (2010), 64–79.
- [10] U. Schulz, *Einfluß der Freibewitterung bei Membranwerkstoffen und ihren Verbindungen*, Berichte der Versuchsanstalt für Stahl, Holz und Steine der Universität Fridericiana, Karlsruhe, 1987.

## Saturation behaviour and load-induced thickness change of woven glass fibre fabrics

JÖRG UHLEMANN\*, DANIEL BALZANI<sup>†1,2</sup>, NATALIE STRANGHÖNER\*,  
MEHRAN MOTEVALLI<sup>†1</sup>

\* Institute for Metal and Lightweight Structures  
University of Duisburg-Essen  
45117 Essen, Germany  
Email: [iml@uni-due.de](mailto:iml@uni-due.de), web page: <http://www.uni-due.de/iml>

<sup>†1</sup> Institute of Mechanics and Shell Structures  
Technical University of Dresden  
01219 Dresden, Germany  
Email: [imf@mailbox.tu-dresden.de](mailto:imf@mailbox.tu-dresden.de) - Web page: <http://www.imf.tu-dresden.de/>

<sup>†2</sup> Dresden Center for Computational Materials Science (DCMS)  
01062 Dresden, Germany  
Web page: <http://dcms.tu-dresden.de/de/>

**Keywords:** Glass fibre fabrics, stress-strain behaviour, saturation behaviour, secant modulus, Poisson's ratio, thickness change.

**Summary.** The stress-strain behaviour of woven and coated technical textiles for structural purposes is well known to be anisotropic, nonlinear and viscoelastic. Tensile tests with cyclic loads on woven structural fabrics show a saturating behaviour regarding the stress-strain characteristics. Permanent strains are well known to be considerable, particularly in the first load cycles. However, the increase of permanent strains reduces in the following load cycles until only negligible additional permanent strains are observed. In common experimental test practice for structural fabrics, three to five load cycles are applied in total. Results show, that the saturation process may be considered progressed at that point, but not yet finished. In general, elastic material behaviour could be adopted for material modelling in the framework of a numerical analysis when the saturation is finished by an acceptable tolerance. The present paper investigates, whether and when the saturation process is completely finished for a woven glass fibre fabric. For this purpose a specific experimental protocol was developed where longitudinal and transverse strains are considered in uniaxial tensile tests with multiple load cycles.

Furthermore, in order to reach beyond the state-of-the-art linear-elastic material model, a new nonlinear anisotropic hyperelastic material model formulated in a full three-dimensional continuum mechanics setup can be considered. That means, that a change in thickness due to axial loading may be taken into account. For this reason, a protocol was developed such that the thickness change is also measured in the saturation tests. The results from these investigations are presented and interpreted in the present paper.

## 1 INTRODUCTION

The stress-strain behaviour of woven fabrics is known to be anisotropic, nonlinear and inelastic in general, see Figure 1. But it is also well known that nonlinearity and permanent strain increments decrease from load cycle to load cycle, particularly in the first load cycles. In common experimental test practice linked to textile architecture, three to five repeated load cycles are used to stabilise the stiffness behaviour in uniaxial or – more typical – biaxial tensile tests aiming to derive stiffness parameters [1–4]. Only two investigations are known in which ten or twenty load cycles were examined [5, 6]. Therein, the longitudinal strain development of PVC-coated polyester fabric was analysed, but transverse strains were disregarded. Up to now, no studies with multiple load cycles are known for PTFE-coated glass fibre fabrics, besides PES-PVC the other mostly used material for textile architecture.

Moreover, the material's residual or permanent strain has to be considered in the compensation planning in order to ensure a certain safe level of prestress in the structural membrane. Altogether, it always seemed justified to presume elastic material behaviour for the structural analysis in the framework of a membrane structure's design verification. But, up to now, this presumption has never been thoroughly investigated and proven. Is the material behaviour really properly saturated after three or five load cycles?

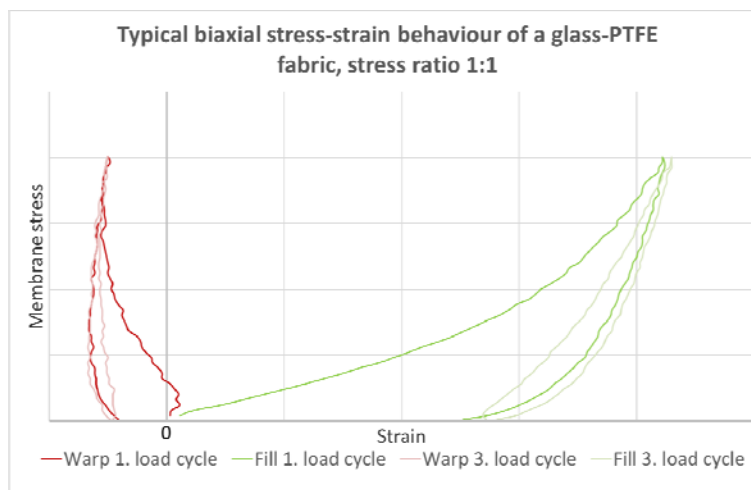


**Figure 1:** Typical stress-strain diagram for a glass-PTFE fabric under biaxial stress ratio warp:fill 1:1 showing nonlinearity, inelasticity and anisotropy

The first aim of this contribution is to investigate whether and when a woven glass-PTFE fabric saturates, i. e. gets into a stable state where the stiffness parameters do not vary significantly anymore from load cycle to load cycle. This state is also referred to as the “stable state of a woven fabric” in [3], there assumed to be reached within five load cycles with acceptable tolerance for practical applications.

The second aim is to investigate the load-induced change in thickness for the investigated glass fibre fabric. For the currently used plane-stress linear-elastic constitutive model, a change in thickness is not considered. However, for the development of a new anisotropic polyconvex hyperelastic material model formulated in a full three-dimensional continuum

mechanics setup in the sense of [7, 8], knowledge about this physical property is required. Different methods for measuring the thickness of a coated fabric as well as results for thickness and load-induced thickness changes are presented and discussed.

## 2 MATERIALS AND METHODS

The investigated material is a PTFE-coated glass fibre fabric. Table 1 illustrates basic characteristics of the material as measured in the Essen Laboratory for Lightweight Structures (ELLF) at the University of Duisburg-Essen. Due to the measured tensile strength  $f_t$  it can be classified as type II according to the harmonised classification in [9], although it is quite near to a type III.

Uniaxial cyclic strip tensile tests were performed on the 20-kN biaxial test rig of the ELLF. The test setup is illustrated in Figure 2. The reason for using a biaxial test rig for uniaxial tests was the ability to measure in-plane transverse strain and to have enough space to realise thickness changes and surface roughness measurements during the tensile tests. Longitudinal and transverse strains in the membrane plane were detected optically by a camera system continuously tracking four markers in the measurement field.

**Table 1:** Characteristics of the investigated glass-PTFE-material

Property		Standard	Measured value	Unit
Tensile strength $f_t$ Warp / Fill	Mean	DIN EN ISO 1421 – strip method	135.5 / 117.5	kN/m
	5%-fractile*		132.1 / 112.0	
Type**		according to [9]	II	-
Total weight		DIN EN ISO 2286-2	877	g/m <sup>2</sup>
Thickness		DIN EN ISO 2286-3	0.57	mm
Weave		-	Plain weave 1/1	-
Yarn density Warp / Fill		DIN EN 1049	12.3 / 14.4	yarns/cm
Yarn size Warp / Fill		DIN EN ISO 2060	1360 / 1360***	dtex

\* according to EN 1990 with a fractile factor  $k_n = 2.33$

\*\* according to proposed classification in [9] based on the measured tensile strength  $f_t$

\*\*\* manufacturer information

Three tests with yarn-parallel warp strips and three tests with yarn-parallel fill strips were conducted for statistical reasons. The load rate was set to 1.0 kN/m/s. Additionally, one test in each fabric direction was scheduled with a load rate ten times lower, i. e. 0.1 kN/m/s, in order to check whether the load rate had an impact on the recorded data.

Fifty regular load cycles (LCs) have been performed in each test. The maximum test stress in each cycle was 25 % of the lower tensile strength  $f_{t,min}$  given in the material data sheet:  $\max \sigma = 116/4 = 29$  kN/m. Note that the notion of stress refers here to the stress resultant defined as the integral over the thickness. The chosen maximum test stress matches the typical

value obtained by applying a safety and strength reduction factor of four in the field of structural membrane constructions. The minimum test stress in each cycle was zero. In order to ensure that creep processes were completely finished before load cycle N° 50, a hold time of 30 minutes on the maximum test stress was scheduled in the 49<sup>th</sup> load cycle. After load cycle N° 50, another hold time of 60 min. on max  $\sigma$  was scheduled. This procedure was only chosen for providing time to perform thickness and roughness measurements with different methods. The complete load protocol is given in Figure 3.

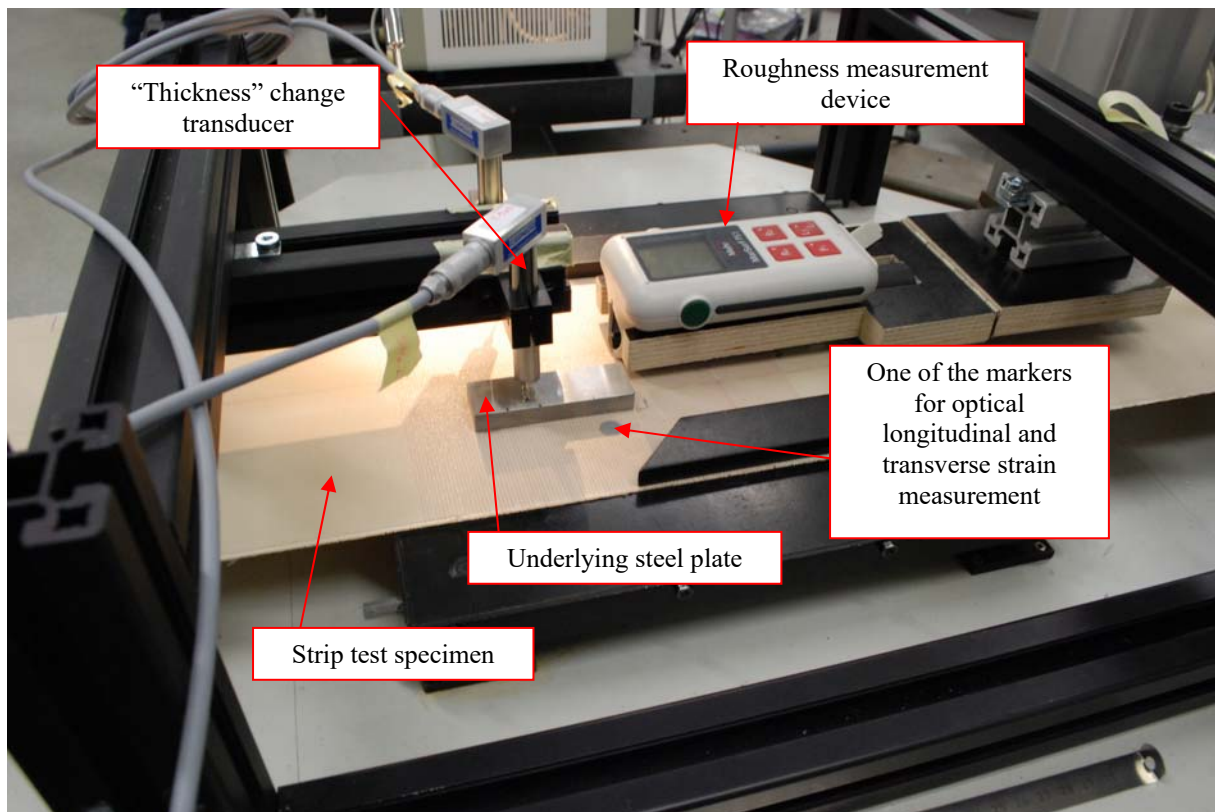


**Figure 2:** Test setup for the uniaxial cyclic tensile tests

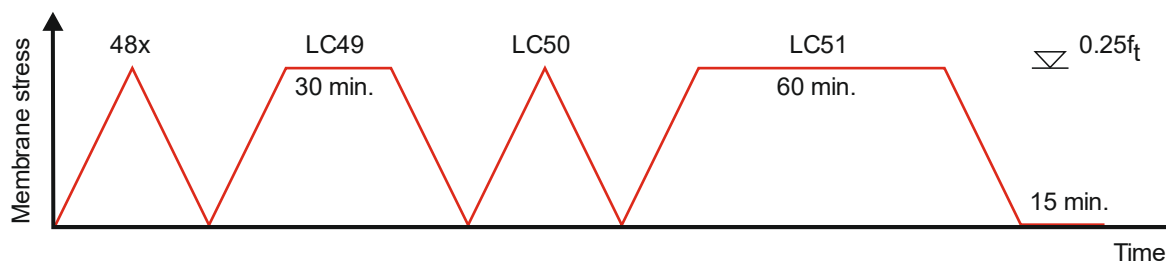


**Figure 3:** Load protocol of the uniaxial cyclic tensile tests

Preliminary studies on the thickness measurements with different measurement devices such as a thickness tester according to EN ISO 2286-3 [10], a digital calliper, a digital micrometer screw and a microscope as an optical method revealed that the result depends – partially heavily – on the chosen measurement device, see Table 2. This is assumed to be mainly due to different pressures normal to the membrane surface applied by the different devices. Apparently, the investigated material is quite sensitive to this impact. But also the different surface areas covered by the devices could possibly affect the results because single ridges on the surface are considerable higher than others.

**Table 2:** Different thickness measurement results obtained by different measurement methods for one and the same test sample piece

Measurement device / method	Mean thickness* [mm]
Thickness tester acc. to DIN EN ISO 2286-3	0.53
Digital calliper	0.52
Digital micrometer screw	0.50
Evaluation of microscopic cross section	0.52
Displacement transducer with underlying steel plate	0.54

\* Mean of four single measurements per method, rounded to two decimal places.

For future considerations of the thickness and thickness change in a 3D material model an extensive, reproducible and non-invasive measurement method is required. Finally, it was decided to measure the thickness of the virgin material with the same method as developed for detecting the thickness change: a displacement transducer normal to the membrane surface with a steel plate lying between the transducer and the membrane surface, see Figure 4. The steel plate’s surfaces are smoothed. To avoid any significant bending of the steel plate under the spring force of the transducer, the thickness of the steel plate is chosen to  $t = 10$  mm while the length and width of the steel plate were  $l = 75$  mm and  $b = 25$  mm. Of all compared mechanical thickness measurement methods, the transducer with steel plate underlayment led to the highest values, see Table 2. This indicates that this method is least affecting the measurement. If – for simplification reasons – a constant distribution is assumed, the stress between the steel plate and the membrane caused by the dead load of the steel plate and the transducer spring force becomes only  $0.0009$  N/mm<sup>2</sup>, calculated with a given spring constant of  $D = 0.056$  N/mm according to the producer’s data and an initial displacement of the spring of 4.5 mm. As a comparison: the stress due to the standardised thickness measurement according to EN ISO 2286-3 is ten times higher! Moreover, the transducer-steel plate combination covers the greatest area and spans from peak to peak in this area, see also Figure 4. Both features combined, increases the probability to cover peaks and leads to larger values. On the contrary, the more locally working measuring devices as thickness tester, calliper and micrometer screw (listed in order of increasing “locality”) – and also the evaluation of microscopic cross sections – have a lower probability to cover the highest peaks.

In order to ensure a high quality of the thickness change measurement with the transducer-steel plate combination, the planar position of the steel plate within the test setup was checked before each test in the individual setup.

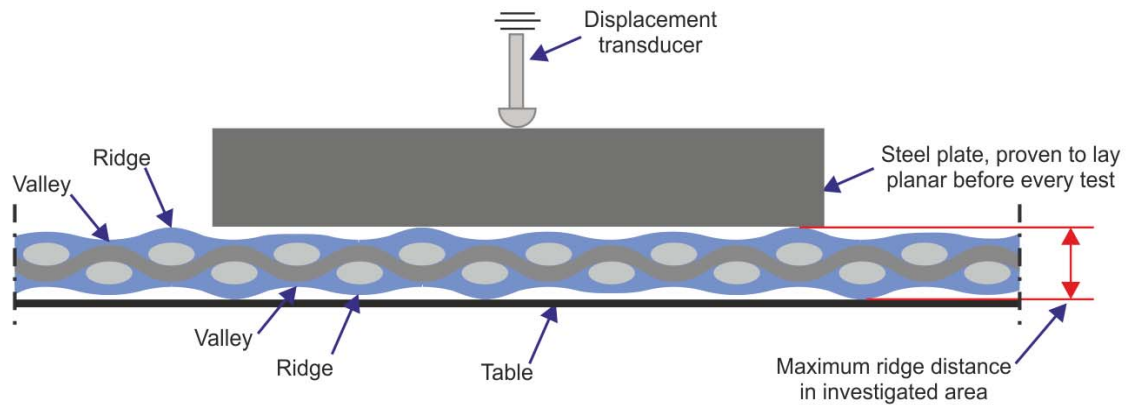


**Figure 4:** Measurement of thickness and thickness change: displacement transducer with a steel plate lying between transducer and membrane surface (not drawn to scale)

In fact, the ridge heights deviate. This is indicated in Figure 4. The chosen measurement method actually detects the membrane's "maximum ridge distance" in the area which is covered by the steel plate. This is in principle very similar to all other mechanical methods described above: they all measure the maximum thickness in the area covered by the measurement device – disregarding that they might reduce the maximum by compressing particularly the highest ridges.

During the cyclic tensile tests, the change of the ridge distance was continuously recorded with the transducer-steel plate combination. Additionally, the surface topography of the membrane was measured before and in the final phase of the tests under full load with a roughness measurement device within a range of 17.5 mm, see Figure 2. The surface roughness results are not presented in this paper.

### 3 EXPERIMENTAL RESULTS AND DISCUSSION

#### 3.1 General

Longitudinal and in-plane transverse strains were directly recorded by the optical measurement system of the biaxial test rig. The thickness change was externally recorded as the ridge distance change by the displacement transducer with underlying steel plate. The results of the strip tests with stress in warp and fill direction are presented and discussed in this section. The interpretation focusses on whether and when the stress-strain behaviour saturates, i. e. becomes elastic. As main indicators, the elastic moduli in form of the secant moduli and in-plane Poisson's ratios are calculated for each load cycle separately.

### 3.2 Longitudinal and transverse strain in the membrane plane

Figure 5 shows the results of all three “fast” tests and the one “slow” test in warp direction as strain versus time diagrams until the end of the 50<sup>th</sup> load cycle. In general, the deviations over all tests are low. Even the test with low stress rate does not result in significantly different strain values. Looking only on the transverse strains, the first fast test appears to be an outlier with much lower absolute strain values than the other test specimens. The turning points of longitudinal strains (minimal and maximal value in each cycle) saturate apparently after ca. ten load cycles at a strain level of approximately  $\varepsilon = 1.9\%$ . Then, the permanent strains have also saturated. During the hold time in the 49<sup>th</sup> load cycle, creep strain is negligible.

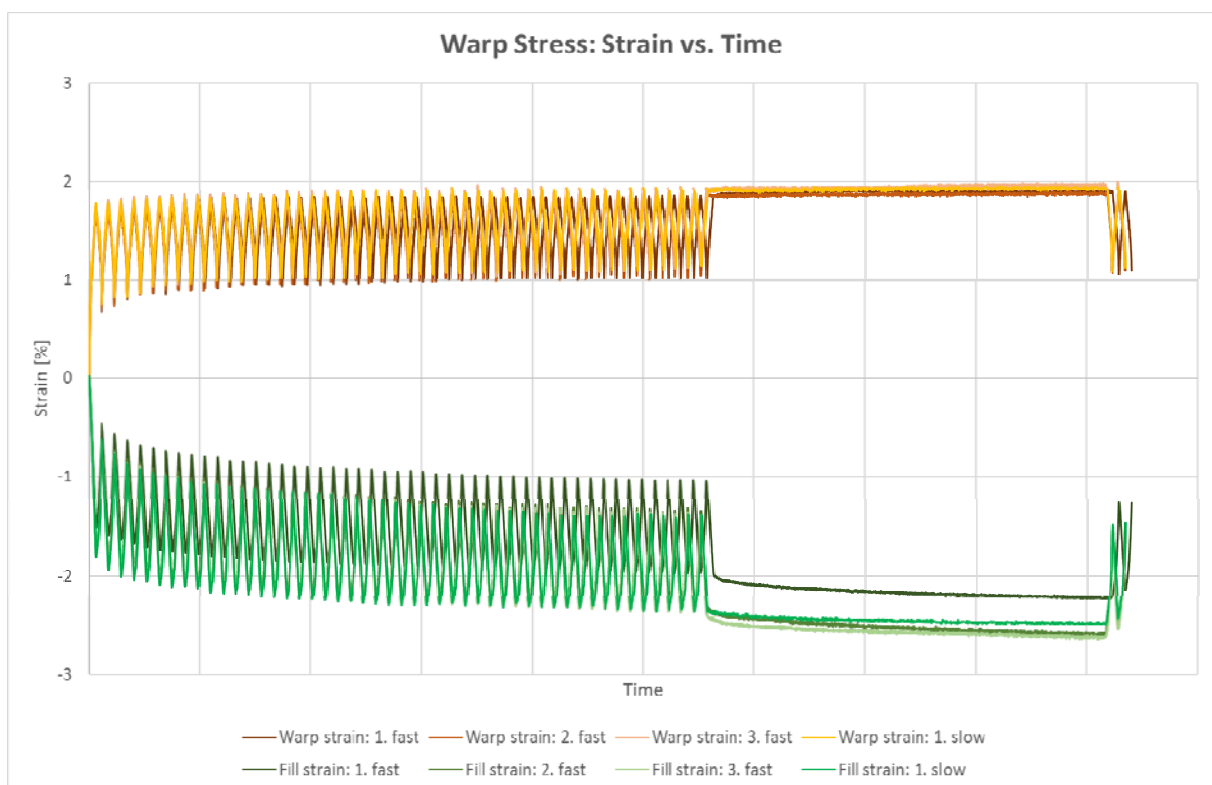


**Figure 5:** Longitudinal strain and transverse strain in membrane plane vs. time for all cyclic tensile tests in warp direction (timeline of the slow test compressed for comparability reasons)

However, transverse strain does not seem to saturate at all. Even after 48 load cycles with full design stress a clearly visible growth of strain is observed. Additionally, creep strain during the hold time is increasing constantly. After 30 minutes, a growth of ca. 10 % strain relating to the beginning of the hold time is observed and still the strain-time curves show no evidence to converge. Surprisingly, this happens while at the same time no creep is detected in longitudinal direction.

The recorded data appear to be independent of the stress rate. Remarkable is that the transverse strains are greater than the longitudinal strains, although this is known to be typical

for glass fibre fabrics!

Figure 6 shows the results of all three “fast” tests and the one “slow” test in fill direction as strain versus time diagrams, again until the end of the 50<sup>th</sup> load cycle. Due to the complex test setup, the camera temporarily lost two markers in the 3<sup>rd</sup> fast and in the slow test. This is marked in Figure 6. These failures could be fixed within a short time so that the rest of the test delivered reliable data.



**Figure 6:** Longitudinal strain and transverse strain in membrane plane vs. time for all cyclic tensile tests in fill direction (timeline of the slow test compressed for comparability reasons)

The first fast test shows a very different behaviour than all the others: the absolute strain magnitudes are considerably smaller in general and even decrease over time. All other test specimens responded very similar to each other so that single curves appear to be invisible in the diagram. Saturation is observed after approximately ten load cycles. The maximum and minimum strain values are constant afterwards for all load cycles and even during the hold time in the 49<sup>th</sup> load cycle. That means, all creep is removed in the load cycles before. As for the warp tests, there is no significant difference observed between the high and low stress rates. During fill stressing, the transverse strains are smaller than the longitudinal strains – except for the first fast test.

In order to investigate whether elastic parameters saturate in the same manner as the strain values, two linear-elastic parameters are derived for each load cycle  $i$ :

- the elastic modulus as secant modulus, calculated as the longitudinal strain increment  $\Delta\epsilon_{L,i}$  over the stress increment  $\Delta\sigma_i$  and

- Poisson's ratio as the negative transverse strain increment  $\Delta\varepsilon_{T,i}$  over the longitudinal strain increment  $\Delta\varepsilon_{L,i}$ .

For example, the determination of the elastic moduli is indicated for fill direction in Figure 7. It can be recognised that nonlinearity decreases over the load cycles. The results for the elastic moduli and the Poisson's ratios are illustrated in Figure 8.

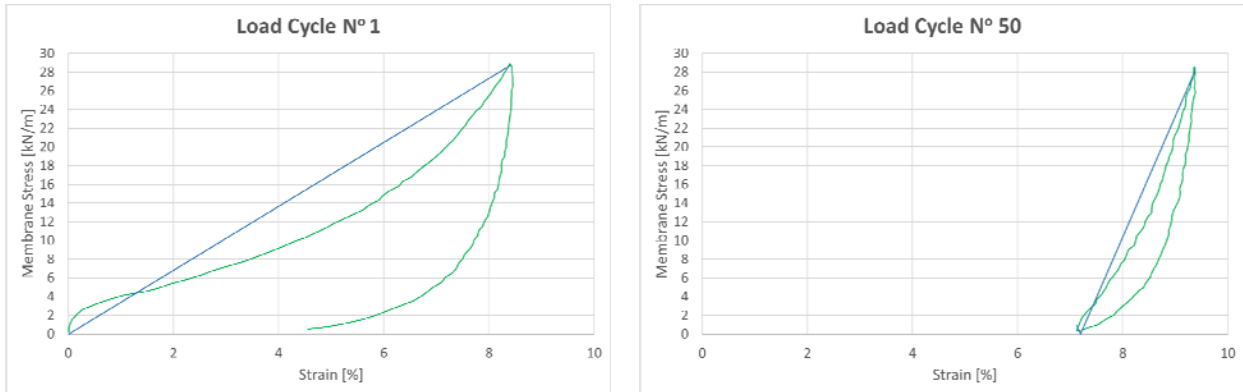


Figure 7: Determination of elastic moduli, exemplarily illustrated for fill direction in load cycle N° 1 (left) and load cycle N° 50 (right)

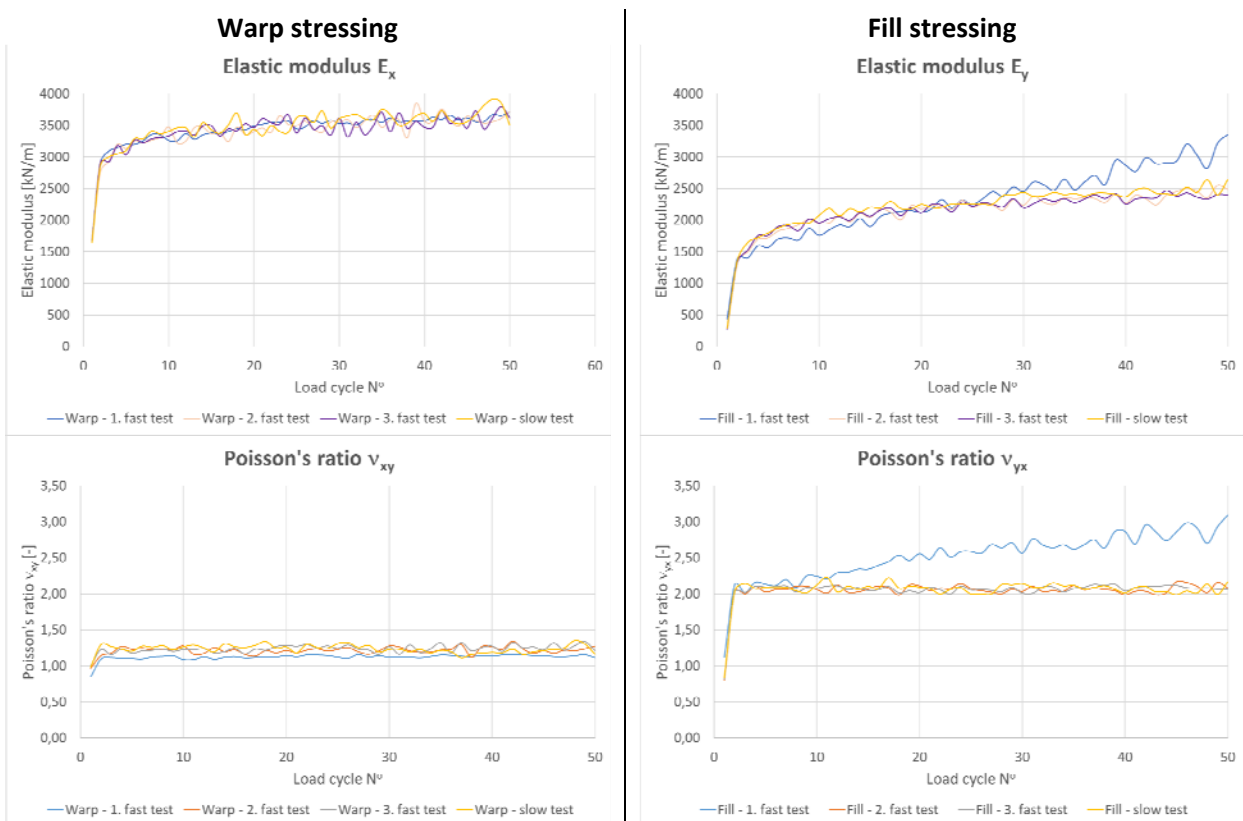


Figure 8: Saturation behaviour of elastic parameters

In fact, for warp stressing, the elastic moduli stabilise after ca. ten load cycles. Afterwards the increase yields to about 7 %, which has for sure a minor impact on analysis results. But for fill stressing, a further increase of about 30 % after load cycle N° 10 is observed – and the elastic moduli are still not saturated. This is surprising at first glance, because the strain peaks appeared to be saturated quite early in Figure 6. The reason for this behaviour can be found in the increasing permanent strains (minimal values of strains per cycle). This leads to decreasing strain increments for almost constant maximum strains.

Regarding the impact of the Poisson’s ratio on membrane structural analyses, it can be stated that the observed variation over the load cycles of ca.  $\Delta v = 0.1$  to  $\Delta v = 0.2$  beyond load cycle N° 2 is insignificant for both warp and fill stressing.

### 3.3 Thickness or ridge distance change

The recorded thickness change in form of the ridge distance change during load cycling is illustrated in Figure 9. Usually an increase in the ridge distance is registered. Only the first fast test under warp stressing behaves completely different. It also starts with increasing thickness during increasing load, but later the measured data become unstructured. Due to that, this measurement is assessed erroneous. Another inaccuracy appears in the slow test under fill stressing. Several significant jumps can be recognised in the test data curve. In this test, several times helping weights had to be adjusted, which could have been enough interfering factors to disturb the measurement. This shows how sensitive the test equipment is. The absolute values should be handled with caution because oftentimes the change of the ridge distance becomes only a few micrometers during later load cycles, a magnitude which lies within the measuring inaccuracy of the transducer. Apart from that, values and trends were repeatable and thus appear to be reliable.

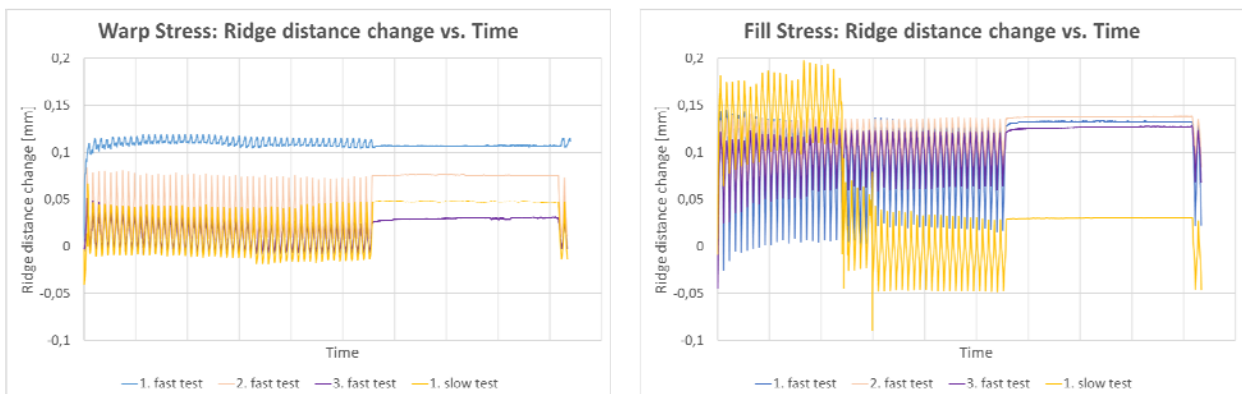


**Figure 9:** Recorded ridge distance change of all tests, under warp stressing (left) and under fill stressing (right)

In general, an increase of thickness is observed when stress raises. This effect is larger during fill stressing than during warp stressing. It is assumed that this effect is caused by the larger yarn crimp of the fill yarns: when they straighten under normal stress, they strongly force the warp yarns in new “height spots”.

With the initial thickness and the ridge distance change, the through-thickness strain and

the Poisson's ratio in through-thickness direction can be calculated, the latter one as the ratio of the through-thickness strain over the longitudinal strain increment in each load cycle. The resulting values are displayed in Figure 10. Poisson's ratios are negative because the material does not contract but expands in through-thickness direction.

The magnitude of thickness increase is relatively high. The thickness change was observed up to  $\Delta t = 0.08$  mm under warp stressing and up to  $\Delta t = 0.14$  mm under fill stressing in the single load cycles of the reliable tests. Related to an initial thickness in the beginning of the individual load cycles of approximately  $t = 0.58$  mm to  $0.66$  mm, the strain in through-thickness direction becomes approximately 14 % during warp stressing and 30 % during fill stressing. This yields extreme Poisson's ratios in through-thickness direction of minimal approximately  $\nu_{zx} = -15$  and  $\nu_{zy} = -7$ , respectively. The Poisson's ratio under fill stressing is considerably smaller due to higher longitudinal strains. Except for the slow test in warp direction, the through-thickness Poisson's ratios saturate for the reliable tests early, latest after approximately five load cycles.

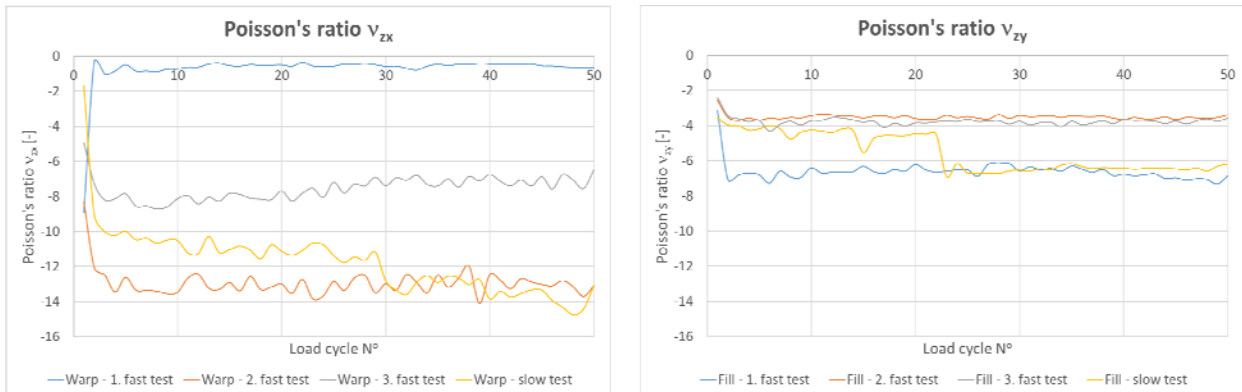


**Figure 10:** Poisson's ratios in through-thickness direction under warp stressing (left) and under fill stressing (right)

#### 4 CONCLUSIONS

The application of an elastic material model requires an elastic material behaviour in acceptable tolerances. The aim of this contribution was to investigate for a structural glass-PTFE fabric whether and when stiffness properties saturate under cyclic loading. Uniaxial cyclic tensile tests have been performed independently in warp and fill direction with 50 load cycles. Longitudinal and in-plane transverse strain were measured.

From a practical application's point of view, the elastic modulus in warp direction is saturated after approximately ten load cycles and both Poisson's ratios in membrane plane are saturated already in the second load cycle for the material investigated. On the contrary, the elastic modulus in fill direction continuously grows until the 50<sup>th</sup> load cycle.

In order to support the development of a new hyperelastic material model based on 3D continuums mechanics, additionally the thickness and load-induced thickness change of the fabric was measured in form of the ridge distance and change of the ridge distance during uniaxial cyclic tests. Different thickness measurement methods have been investigated and discussed. The thickness change was observed to values up to 0.08 mm under warp stressing

and up to 0.14 mm under fill stressing. This leads to extreme Poisson's ratios in through-thickness direction of approximately -15 and -7, respectively. The Poisson's ratios in through-thickness saturate early, latest after five load cycles. These results should be however interpreted with view to the precision of the transducer, which is in the order of magnitude of the measured ridge distance change.

## ACKNOWLEDGMENTS

The authors gratefully acknowledge the funding of this research by the Deutsche Forschungsgemeinschaft (DFG) in the framework of the research project „Characterisation and modeling of the nonlinear material behaviour of coated fabrics for textile architecture“ (GZ: STR 482/5-1, BA 2823/10-1).

## REFERENCES

- [1] pr EN 17117-1:2017, Rubber or plastics-coated fabrics – Mechanical test methods under biaxial stress states – Part 1: Tensile stiffness properties.
- [2] Membrane Structures Association of Japan, MSAJ/M-02-1995, Testing Method for Elastic Constants of Membrane Materials, 1995.
- [3] J. Uhlemann, *Elastic constants of architectural fabrics for design purposes*, Dissertation, Institute for Metal and Lightweight Structures, University of Duisburg-Essen, Shaker Verlag, Aachen, 2016.
- [4] R. Blum, H. Bögner and G. Némóz, *Testing Methods and standards*, European Design Guide for Tensile Surface Structures, B. Forster and M. Mollaert (Eds.), TensiNet Ass., Brussel, 2004, pp. 219–241.
- [5] H.-W. Reinhardt, *Ein- und zweiachsige Verformungs- und Festigkeitsuntersuchungen an einem beschichteten Gittergewebe*. Mitteilungen des SFB 64 No. 31/75. Stuttgart, 1975.
- [6] G. Rehm and R. Münsch, *Zum Spannungs-Dehnungs-Verhalten im Gebrauchslastbereich und zum Bruchverhalten von PVC-beschichteten Polyestergeweben*, 2. Internationales Symposium Weitgespannte Flächentragwerke: 1. Vorberichte zum Kolloquium, Stuttgart, 1979.
- [7] D. Balzani, P. Neff, J. Schröder, G.A. Holzapfel, *A polyconvex framework for soft biological tissues. Adjustment to experimental data*. International Journal of Solids and Structures, Vol. 43, 2006.
- [8] J. Schröder, D. Balzani, N. Stranghöner, J. Uhlemann, F. Gruttmann, K. Saxe, *Membranstrukturen mit nicht-linearem anisotropen Materialverhalten – Aspekte der Materialprüfung und der numerischen Simulation*, Der Bauingenieur, Vol. 86, 2011.
- [9] N. Stranghöner et al., *Prospect for European guidance for the Structural Design of Tensile Membrane Structures: Support to the implementation, harmonization and further development of the Eurocodes*, JRC Science and Policy Report, European Commission, Joint Research Centre, Editors: M. Mollaert, S. Dimova, A. Pinto, St. Denton, EUR 25400 EN, European Union, 2016.
- [10] EN ISO 2286-3:2016, Rubber- or plastics-coated fabrics – Determination of roll characteristics – Part 3: Method for determination of thickness.

## **STRETCH CONTROLLED SHADING CAPABILITIES OF SPECIAL ELASTOMERIC SILICONE FILMS**

**THOMAS STEGMAIER<sup>\*</sup>, VOLKMAR V. ARNIM<sup>\*</sup>, ANDREAS KUNZE<sup>\*</sup>,  
BENJAMIN EWERT<sup>\*</sup>, GÖTZ T. GRESSER<sup>\*</sup>, ANDRÉ TEIXEIRA<sup>†</sup>, FLORIAN  
WEININGER<sup>†</sup>**

<sup>\*</sup> Deutsche Institute für Textil- und Faserforschung Denkendorf (DITF)  
Körschtalstraße 26, 73770 Denkendorf, Germany  
e-mail: thomas.stegmaier@ditf.de, web page: www.ditf.de

<sup>†</sup> LEICHT Structural engineering and specialist consulting GmbH  
Landwehrstraße 60/62, 80336 München, Germany  
e-mail: F.Weininger@LEICHTonline.com, web page: www.LEICHTonline.com

**Key words:** silicone, film, shading, stretch, facade, window

**Summary.** A hitherto unexploited effect: the reversible stretch-induced change of translucency and transparency of certain silicone materials is experimentally investigated with regard to an application in a new type of shading system for biaxial bent, free-form building envelopes.

In a first step the silicone raw materials showing the effect are processed into membrane shape and the stretch-dependent optical characteristics of the silicone film samples are examined.

Shading effects are measured during cyclic and long term uniaxial tension tests. For multiaxial loading conditions, as appearing in planar biaxial tension tests with cross shaped specimens and bulge tests with inflated circular specimens, optical inhomogeneity effects due to locally varying elongations are documented.

Further results concerning a variable transparency depending on the distance of the observer and an object behind the membrane are discussed.

A conceptual application of the materials into translucent facades for shading purposes is presented. The closed cavity concept of planar stretched films located between window screens and the implementation of silicone films as inflatable shading structures are discussed. Furthermore, the advantages of silicone films in these kinds of cladding types are pointed out, as typical problems i.e. fogging and high-temperature stability pose no major issue.

### **1 INTRODUCTION**

In facades of residential and office buildings sun shading systems are installed to prevent excessive insolation associated with heating and dazzling effects. By regulating the transmittance of sunlight the ambient lighting can be controlled. The technical boundary conditions of present shading systems limit the design of free-form building envelopes, because the drapability of slatted blinds and roller blinds is thus far unidimensional.

Starting point for extending the design space of shading systems into biaxial bent surfaces was the discovery of a reversible effect: certain transparent silicones change their colour into pure white when stretched. Thereof the idea was developed to install thin silicone shading membranes in closed window cavities and to change their optical properties in a controlled manner due to mechanically or pneumatically caused stretching. In the following material, its performance and possible application scenarios are exemplarily presented.

## 2 MATERIALS

The effect of strain induced transparency change was first discovered on a commercial silicone product of unknown source. Through producer and material screening two silicone producers were found who knew about the effect and three materials could be identified for further examination. A proven theory explaining the effect is hitherto unknown to the authors. The silicone materials have in common, that they are filled and peroxide crosslinked. Since the phenomenon only could be observed on filled materials the assumption exists that the filling is responsible for the effect. At first the producers delivered the materials in highly viscous blocks of silicone, blended with a crosslinking agent. Later crosslinking agents were exchanged and adapted to an individual industrial production method based on solving the silicone block with petroleum. The following findings refer to the material Wacker, CENUSIL R360.

## 3 DEVELOPMENT OF FILMS

The production of test specimen was carried out in a vacuum press. A lump of silicone was placed between two massive steel plates and flattened to a circular cake with a diameter of 70 cm. 250  $\mu\text{m}$  thick Teflon membranes were used as abherent. The silicone film thickness was 1 mm in the centre of the cake and decreased continually to 0,2 mm at the edges. The parameters of the production process were:

Compressive force:	4500 kN
Steel plate area:	max. 1 m <sup>2</sup>
Abs. pressure evacuated:	200 mbar
Heating-up time:	30 min
Temperature holding:	160 °C, 15 min
Cooling time:	15 min.

The produced silicone film was transparent. Under tensile stress, which led to high strain, the transparency decreased as expected and the silicone turned white while remaining translucent. After unloading and elastic recovery the film again turned transparent.

By admixing petrol to the silicone, the viscosity was reduced to the extent, that sheets with a thickness of 50 to 200  $\mu\text{m}$  could be produced, through transfer coating the dissolved silicone onto a Teflon membrane with a doctor blade. Due to deficient film quality, leading to early film rupture at high strain, a survey of the properties thus far has only been conducted for samples produced in the press.

## 4 MECHANICAL PROPERTIES

The mechanical properties were determined by uniaxial tensile testing on a universal testing machine Zwick Z 020. New samples reached tensile strains at break  $> 600\%$ , which dropped to a value of  $300\%$  after 1000 load cycles ranging between 0 and  $200\%$  strain. The visual impression of maximum whiteness occurred at a strain of approximately  $130\%$ . On a new material the necessary tensile stress to reach a strain of  $100\%$  is  $1,4 \text{ N/mm}^2$ . Cyclic loading of the specimens led to a load drop of  $30\%$  in the first cycle and progressively another  $20\%$  during the following 999 load cycles. In clamped condition, strained to  $100\%$  for one hour, the stress relaxed to  $78\%$ .

As the exploitation of the optical effect requires considerable strains, lateral contraction gains importance for determining the strain dependent area of the silicone shading membrane. The lateral contraction of a slender,  $200 \text{ mm}$  long and  $50 \text{ mm}$  wide specimen decreased linearly from  $0,42$  at a strain of  $20\%$  towards  $0,31$  at a strain of  $100\%$ . On membrane panels with lower slenderness ratios, the obstruction of the lateral contraction exerted by the rigid clamping increases, leading the free edges to be bent.

The strip tensile test revealed residual strain in the specimen. Cyclic loading with growing strain showed proportionality between residual and applied strain. A yield point could not be identified. The residual strain was  $4\%$  for samples strained to  $100\%$ .

## 5 OPTICAL PROPERTIES

### 5.1 Visual effects

The visibility of a high-contrast image, placed  $23 \text{ mm}$  behind the silicone film constantly decreased with the films strain. An abrupt change of transparency due to stretching was not observed.

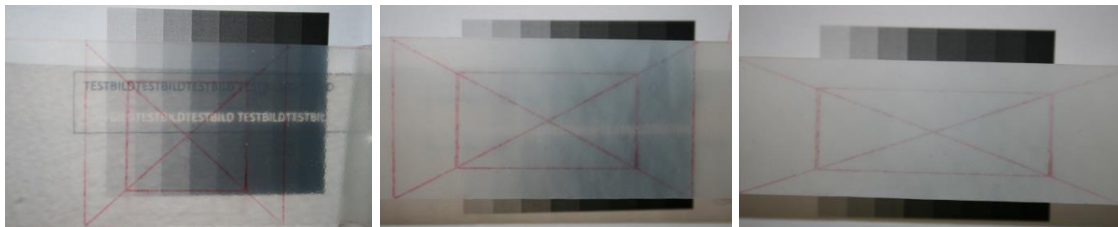


Figure 1: Image located  $23 \text{ mm}$  behind the silicone film strained to  $6,67\%$ ,  $53,33\%$  and  $100,00\%$ .

The transparency as depicted in figure 1 is only achieved for objects located close behind the film, since the visual effect depends on the distances as well between the object and the film, as between the observer and the film. In an unstrained condition the silicone film appears transparent for an image-film distance of  $0$  to  $100 \text{ mm}$ . At a distance of  $400 \text{ mm}$  the background image appears completely blurred and opaque for recognizing details.

In reverse a  $106\%$  strained film appears opaque and pure white to the observer except for one occasion. When the image touches the film and the distance becomes  $0 \text{ mm}$ , despite stretching, full transparency is given.

It can therefore be concluded, that light scattering plays a decisive role in the visible whitening effect. Consequently the measurement of the stretch induced translucency was of interest for inquiring, whether the light scattering goes along with a shading effect.

## 5.2 Shading performance

To prove the shading effect, a silicone film with a thickness of 700  $\mu\text{m}$  and the dimensions 180 mm x 280 mm was strained in a uniaxial stretching frame and the transmitted sunlight was measured with a global radiation measuring head including three integrating sensors. The spectral sensitivities were: UV-A (310 – 400 nm), VIS (360 – 760 nm) and NIR (700 – 1100 nm).

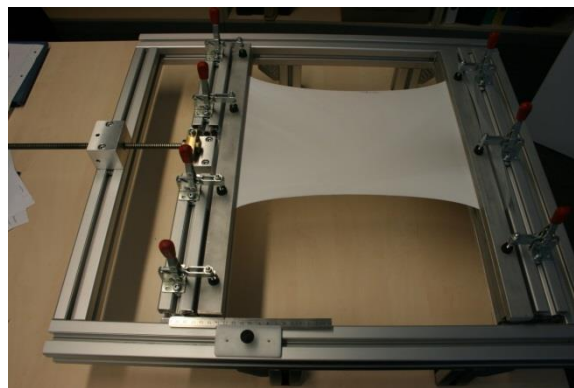


Figure 2: Stretching frame measuring 500 mm x 450 mm

Compared to the unshaded measuring head a clear, negative correlation appeared between strain and transmission in all radiation ranges: UV-A, visible light (VIS) and near infrared light (NIR). An abrupt change of translucency has not been observed. For the strain of 0% and 100% the reflexion and transmission were measured with an IR-spectrometer (Bruker, Vertex 80).

The optical properties of the unstretched film are as shown in figure 4. The VIS region is highly translucent (80%). In the NIR region the translucency drops from 85 to 5%, whereas the absorption increases from 10 to 95%.

The optical properties of the 100% stretched film are as shown in figure 5. The reflection increases to 60% due to the stretch-dependent white colouring, whilst the transmission decreases.

The ratio of the stretched to the unstretched optical properties in dependence of the wavelength is depicted in figure 6. The transmission is reduced to 50% by stretching, whilst the NIR absorption doubles and the reflection increases by a factor of 3 to 6.

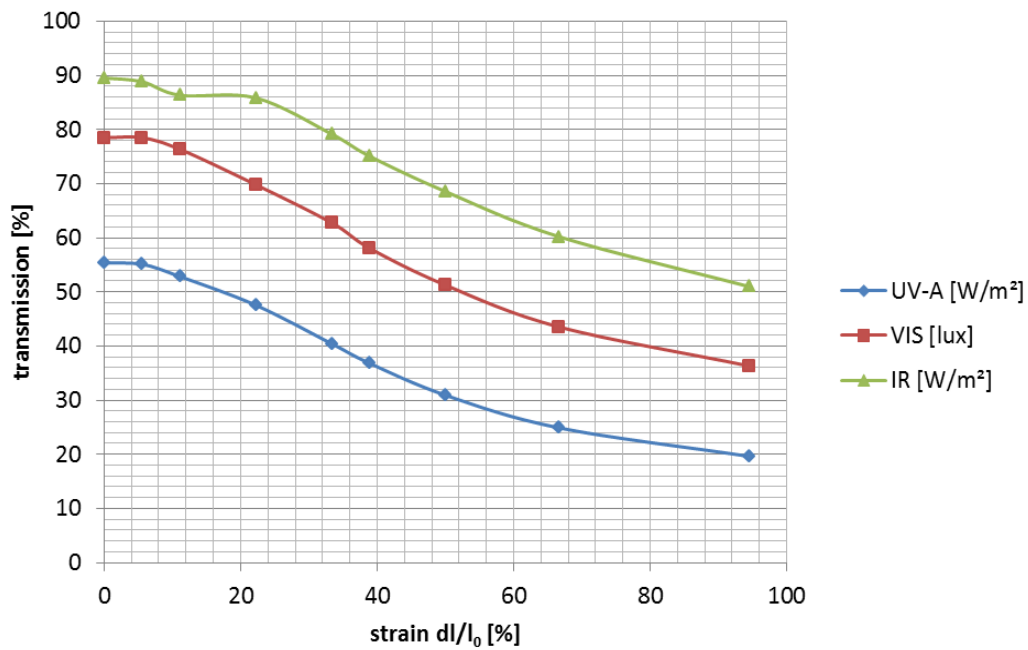


Figure 3: Transmission of sunlight through 700 µm thick silicone film versus strain

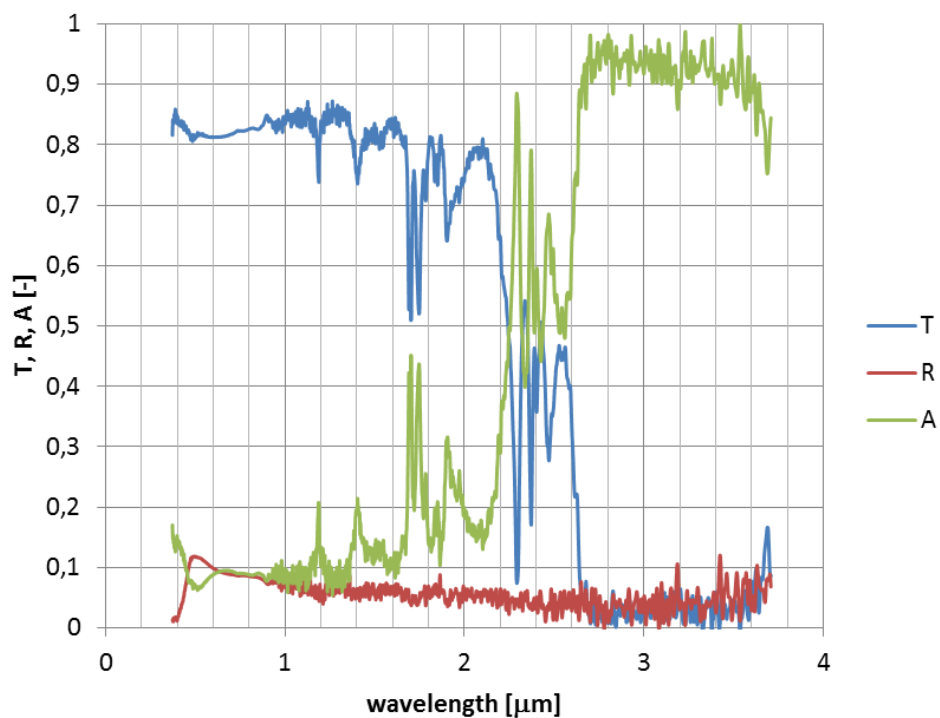


Figure 4: Optical properties of the unstretched film: transmission T, reflection R and absorption A in dependence of the wavelength

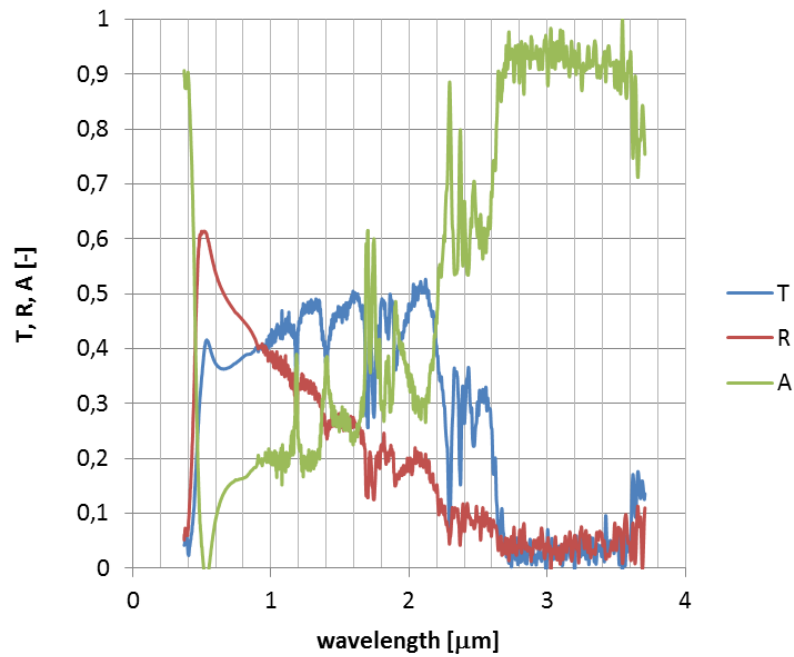


Figure 5: Optical properties of the 100% stretched film: transmission T, reflection R and absorption A in dependence of the wavelength

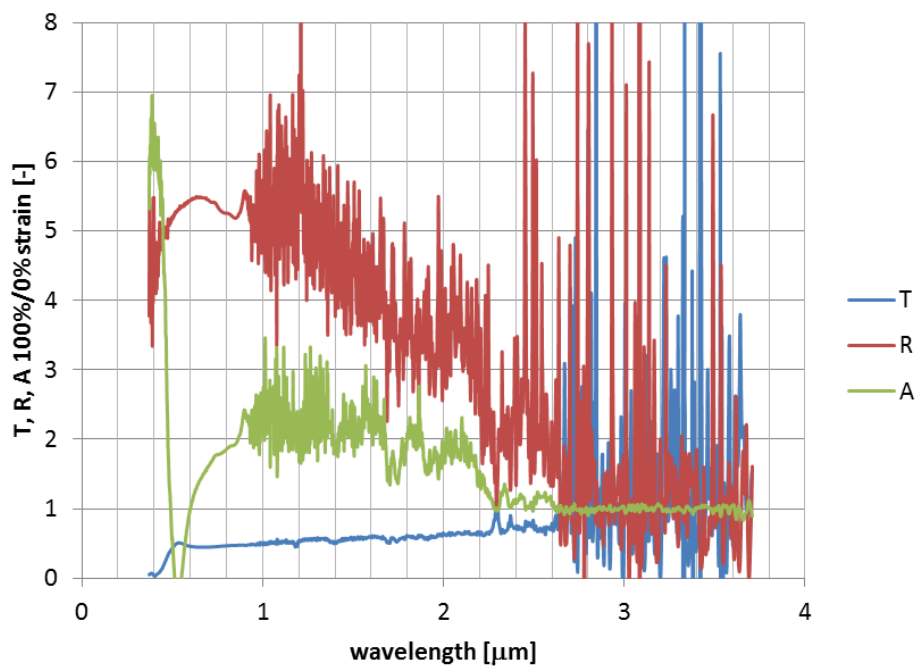


Figure 6: Ratio of the optical properties 100% stretched to unstretched film: transmission T, reflection R and absorption A in dependence of the wavelength

The stretching of the film does not affect the optical properties in the middle infrared region (MIR) as shown in figure 9. The radiation is largely absorbed as depicted in figures 7 and 8. The IR emission coefficient  $\epsilon_{IR} = 0,88$ .

Figure 2 was taken after 5 weeks, clamped at 100% strain. A decrease in whiteness was not detected. The transmission measurement of figure 3 was conducted after the 5 weeks in strained condition. After elastic recovery the film was transparent. Visual time-dependent effects have not been observed. The white effect is long-lasting and reversible.

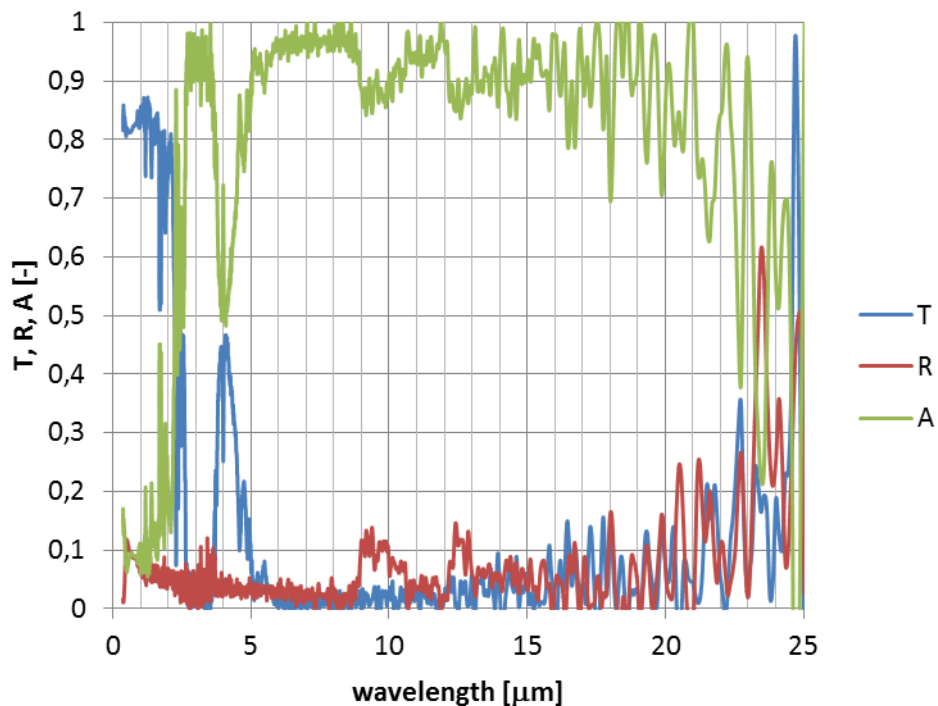


Figure 7: Optical properties of the unstretched film: transmission T, reflection R and absorption A in dependence of the wavelength

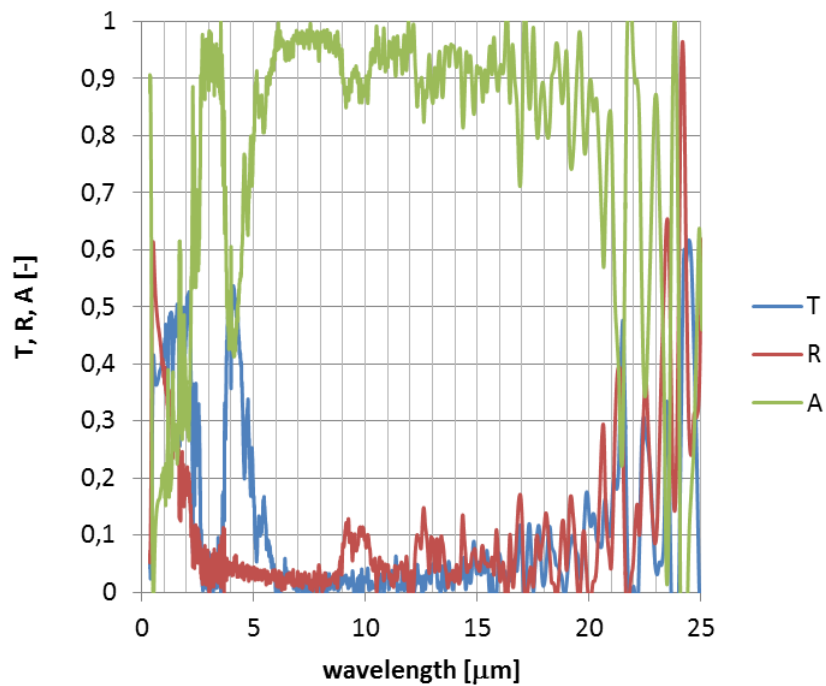


Figure 8: Optical properties of the 100% stretched film: transmission T, reflection R and absorption A in dependence of the wavelength

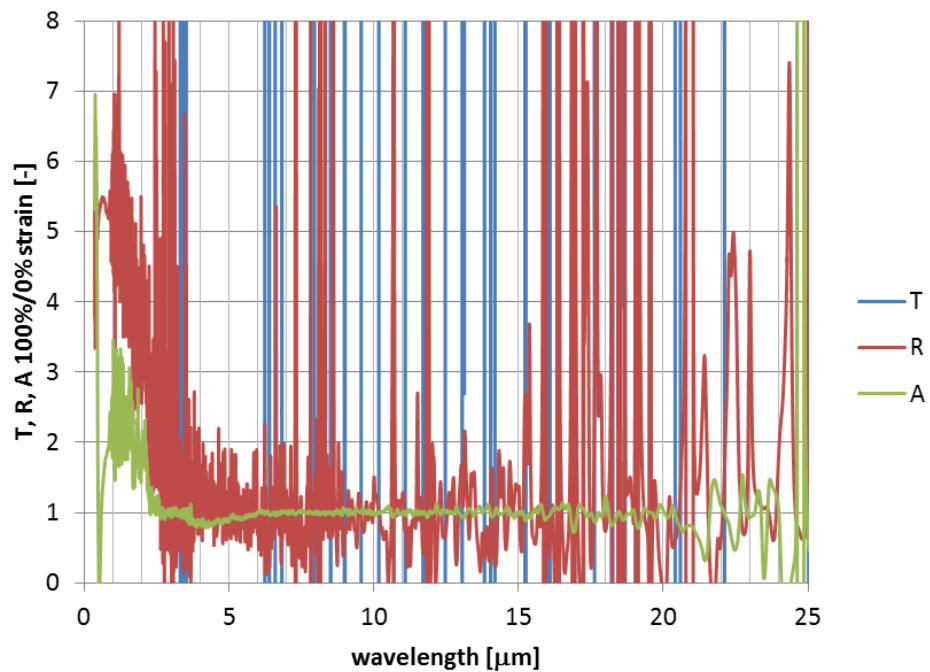


Figure 9: Ratio of the optical properties 100% stretched to unstretched film: transmission T, reflection R and absorption A in dependence of the wavelength

## 6 BIAXIAL STRETCHING

Two basic well-known procedures for stretching the film biaxially were tested for changing the optical properties: pneumatic pre-tensioning within a rigid boundary and mechanical pre-tensioning with moving edge supports.

The pneumatic pre-tensioning was effected in a bulge test with a clamp-opening diameter of 150 mm. The rigid edge prevents transverse contraction. The first whitening appears hence at the apex as shown in figure 10. By further inflation, the whitening extends over a larger dome area, but variable shades of white remain, as shown in figure 11. An application of the film in a pneumatic pillow will thus lead to uneven shading. If the whitening of the apex is valued as uncomplete, then inflation requires higher strains than uniaxial tensioning for the same shading effect.



Figure 10: Sample of Wacker R360 inflated to an apex stretching of 86%



Figure 11: Sample of Wacker R360 inflated to an apex stretching of 135%

The mechanical biaxial pretensioning was exerted on a cross shaped specimen with film arm widths of 50 mm. Because of the limited moving range of the test facility, the film was clamped in pre-tensioned condition. The first marked whitening effect occurred at the curved junction of the arms of the cross, then was extended to a circle surrounding the center, which became white at last. As can be seen by the distortion of the markings, the strain is unevenly distributed. The whitening strain of the diagonals of the square marking was 43%. The strain in vertical direction was 52 to 68% . The strain

in horizontal direction was 32 to 52%. An even whitening effect could not be achieved at mean strains in the cross-shaped specimens, but the necessary strain for coloring the specimen pure white could be halved.

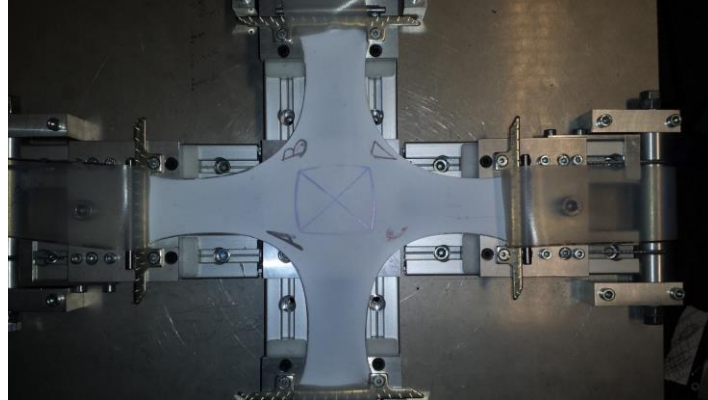


Figure 12: Cross shaped specimen of Wacker R360, biaxially tensioned

## 8 CLOSED CAVITY CONCEPT

LEICHT's research focused on integrating enclosed membrane elements into tessellated facade designs. The installation of the silicone shading mechanism inside of a closed cavity leads to a better control of the films surface environment. Translucent materials, which are more robust to environmental impacts act as exterior protection layers and provide the covering of the enclosure. Window glass for example possesses a smaller reactivity to mechanical weather influences, has better puncture resistance and shows less dirt adherence.

The results of the design studies are, that pneumatic inflation is the simplest and most reliable way of imposing and maintaining the necessary deformation of the silicone film, since only hose lines and air pumps are necessary for its actuation and; that an alternative possibility, the mechanical stretching through moving edge supports, requires relatively complex and delicate mechanisms in order to fully exploit the effect.

A simplified pneumatic design can be seen in the exploded view of figure 13. The two silicon membranes that form the basis of the shading system are installed between two stiff frames, that permanently seal off the pressurized inflatable. The films immediate environment is again separated from the outer environment by two transparent panels. The lateral enclosing system, which is necessary to fix all of the planar elements, is not depicted.

Particularly closed cavities with small spans allow an integration of the inflatable silicone films into transparent architectural design elements and can provide an aesthetic gain for a structural solution. The inflatable surfaces do not have to be planar. An adaption of the concept to curved enclosures with a multitude of membrane setups is conceivable. The vast array of possible designs based on the proposed concept still needs full exploitation.

For a practical, more in-depth approach, larger film samples are needed. The lack of large-scale production methods able to produce larger silicone film samples with reproducible optical and qualitatively valuable mechanical properties at date still poses a significant obstacle to the advancement of the concept.

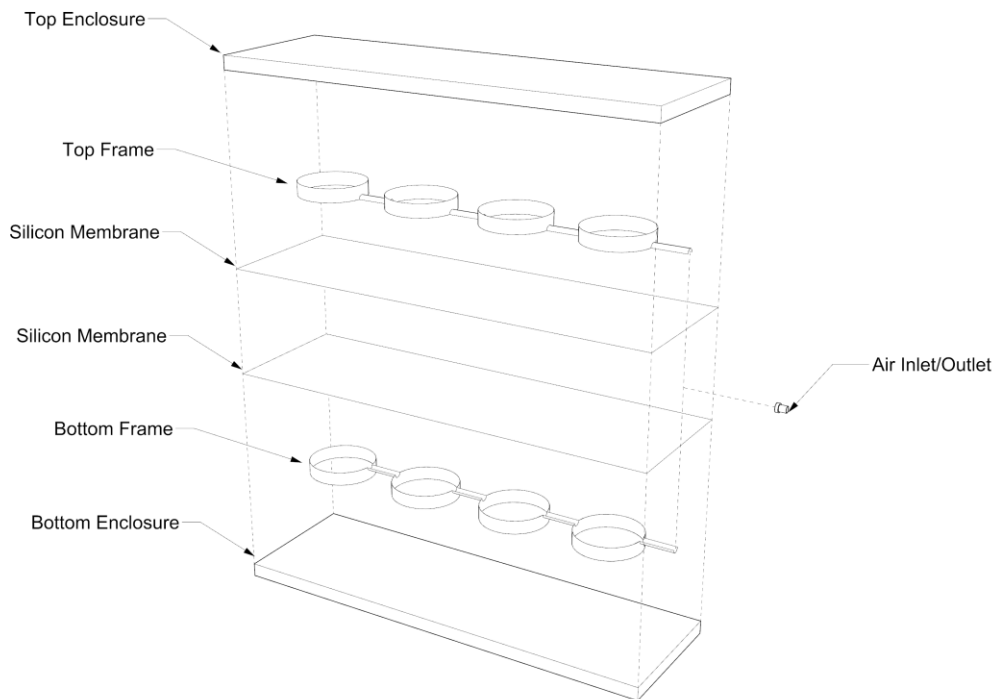


Figure 13: Exploded view of base closed cavity configuration.

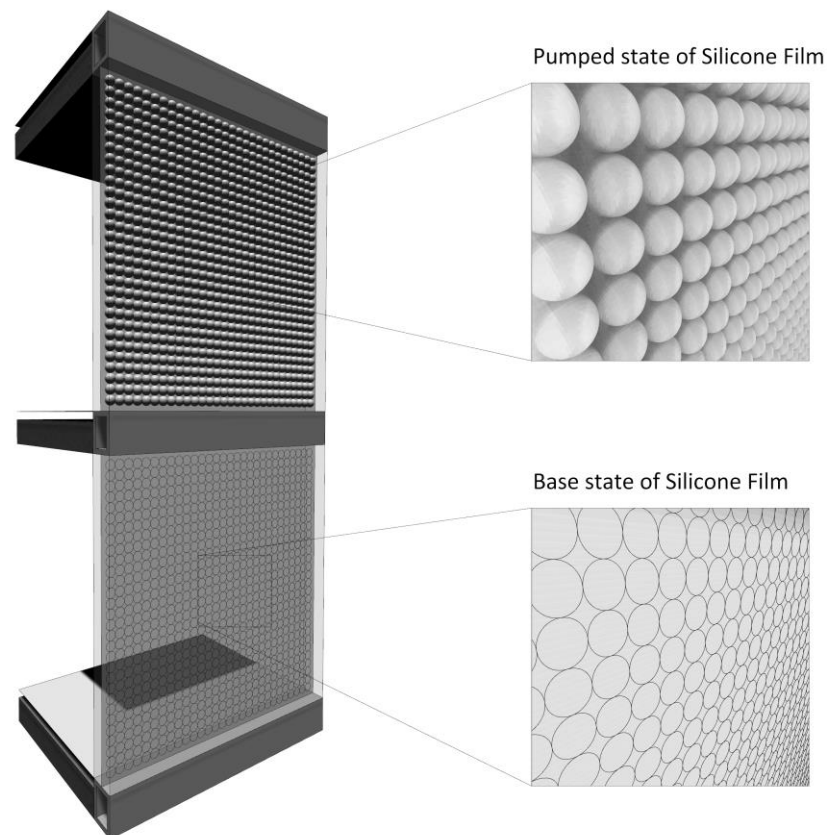


Figure 14: Rendered view of the possible façade application with closed cavities.

## 9 CONCLUSION

Up to now, unexploited shading effects were presented, by using a specific raw silicone product (Wacker R360), producing small film samples and quantifying their mechanical and optical properties in several test setups. Further, a possible application was explained.

On the basis of the published performance values, alternative application concepts can be developed. The presented prototypical production of silicone films only allows for building small-scale demonstrators. For an implementation into building facades, the industrial production of silicone films has to be advanced. In order to modify the films properties purposely and develop a broad range of similar materials, future research directed towards the understanding of the physical mechanism is needed.

### Acknowledgement

The authors like to thank the “Bundesministerium für Wirtschaft und Technologie” for funding the research project “Verschattungssysteme” within the framework of the “Zentrales Innovationsprogramm Mittelstand (ZIM)” by mandate of a “Deutsche Bundestag” resolution.

## Viscous characteristics of ETFE film sheet under temperature change

TATSUYA YOSHINO\* AND SHIRO KATO†

\* Taiyokogyo Corporation  
3-20, Syodai-Tajika, Hirakata-shi, Osaka, 573-1132, Japan  
e-mail: yt003051@mb.taiyokogyo.co.jp, web page: <http://www.taiyokogyo.co.jp/>

†Toyohashi University of Technology  
1-1 Hibarigaoka, Tempaku-cho, Toyohashi-shi, Aichi, 441-8580, Japan  
Email: kato-shiro@tg.commufa.jp

**Key words:** ETFE film, Viscous characteristics, Constitutive equation.

### 1 INTRODUCTION

Because ETFE film is a high polymer material its visco-elastic characteristics are observed by the researchers. Besides, the linear expansion coefficient of the ETFE is 10 times greater compared to steel products or the like. For that reason, due to change in temperature, there are cases where expansion and contraction are regarded as an issue. Therefore, in order to design and construct ETFE film membrane structures, research focused on its visco-elastic characteristics has been done.

For research focused on viscosity of ETFE film, in addition to that carried out by the authors, there is research by Moriyama and Kawabata<sup>1,2</sup>, by Jeong and Kawabata<sup>3</sup>, by Wu<sup>4</sup>, by Galliot and Luchsinger<sup>5</sup> and by Li and Wu<sup>6</sup> and so on. These studies take into account either the viscosity, the change in temperature or introducing the constitutive equation of FEM. There is no research that takes into account all of them.

The authors<sup>7</sup>, under the condition of fixed temperature, (1) based on MSJ Standards<sup>8,9</sup>, carried out biaxial tension tests and shearing tests of ETFE Film. (2) With respect to 5 types of stress ratio, biaxial tensile test was conducted, and the relationship between equivalent stress and equivalent plastic strain was identified. From the results, regardless of stress ratio, the curves of equivalent stress and equivalent plastic strain were consistent. (3) It was confirmed that the yield stress as well as stress after break down and the strain relationship can be expressed by the proposed elastic-plastic constitutive equation. (4) Performing pressurization test on membrane of a square plan showed that it can be sufficiently expressed by the proposed elastic-plastic constitutive equation.

Moreover, in reference<sup>10</sup>, the proposed incremental nonlinear viscoelasticity constitutive equation regarding the uniaxial tension field is extended to biaxial tension field in reference<sup>11,12</sup> and the validation is performed. This constitutive equation is formulated in the incremental form on the assumption of integration with FEM. Also, elapsed time, stress change and temperature difference can be taken into account. However, regarding the temperature, 1) the effect of temperature difference on the viscosity component can be taken into account using Time-temperature superposition principle but, 2) expansion and contraction due to temperature change cannot be taken into account.

Upon this, in this paper, the incremental form of the nonlinear viscoelasticity constitutive

equation of the biaxial tension field - mentioned in the previous paper - is extended into a constitutive equation that takes into account the expansion and contraction due to temperature change. Confirming that this constitutive equation is capable of taking into account elapsed time, stress change and temperature change.

Specifically:

1) Extend the incremental constitutive equation for the biaxial tension field proposed in the previous paper into an equation where expansion and contraction due to temperature change are added.

2) Perform uniaxial creep test accompanied with temperature change and show the results. From these results, focusing on expansion and contraction due to temperature change, compute various constants necessary for the constitutive equation.

3) Use the proposed constitutive law and computed constants to perform simulation of uniaxial creep test accompanied with temperature change.

## 2. FORMULATION OF INCREMENTAL CONSTITUTIVE EQUATIONS FOR ETFE FILM

### 2.1. Incremental constitutive equations are extended to be used in biaxial stress

The generalized Voigt model in figure 2.1.1 is used for incremental constitutive equations. In order to understand biaxial stress condition, variables related to Maxwell elements and Voigt elements are divided into deviatoric components and volumetric components. Divided variables are shown in Table 2.1.1.

#### 2.1.1. Incremental stresses

Consider the stress and temperature at a time of the  $j$ -th step, where  $\sigma(t_j)$  denotes the stress and  $T_j$  denotes the temperature at the time  $t_j$ . After a time increment  $\Delta t$ , the stress and temperature will change by incremental step  $\Delta\sigma$  and  $\Delta T$  respectively as follows.

$$t_{j+1} = t_j + \Delta t \quad (2.1.1)$$

$$\sigma(t_{j+1}) = \sigma(t_j) + \Delta\sigma \quad (2.1.2)$$

As shown in Figure 2.1.2, assuming that during the time interval  $\Delta t$ , stress changes linearly from  $\sigma(t_j)$  to  $\sigma(t_{j+1})$  which makes it possible to be expressed by the following formula.

$$\frac{\Delta\sigma}{\Delta t} = \frac{\sigma(t_{j+1}) - \sigma(t_j)}{t_{j+1} - t_j} = \text{const.} \quad (2.1.3)$$

$$\sigma(\tau) = \sigma(t_j) + \frac{\Delta\sigma}{\Delta t}(\tau - t_j) \quad (2.1.4)$$

Similarly for temperature change  $\Delta T$ ,

$$T(\tau) = T(t_j) + \frac{\Delta T}{\Delta t}(\tau - t_j) \quad (2.1.5)$$

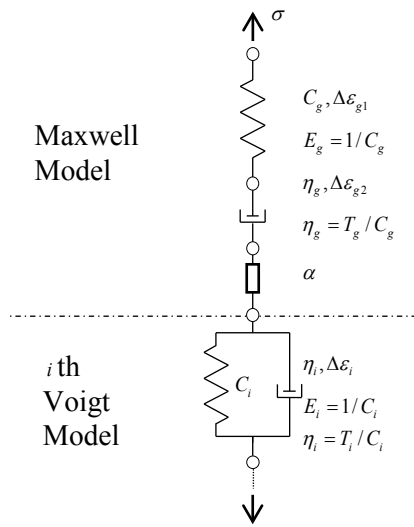


Figure 2.1.1 : generalized Voigt model

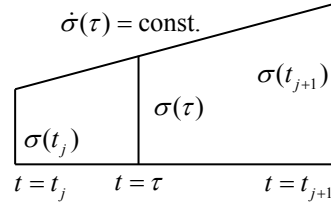


Figure 2.1.2 : Linear variation of stress during a time increment  $\Delta t$  step

Table 2.1.1 : Variables of the constitutive equations of biaxial tension

Item	Variable
For Maxwell model	Suffix g
For Voigt model	Suffix i
Time increment	$\Delta t$
Temperature increment	$\Delta T$
stress increment	$\Delta\sigma', \Delta\sigma_m$
Viscoelastic strain increment	$\Delta\epsilon^{el}$
Incremental strain for Maxwell element	$\Delta\epsilon_{g1}', \Delta\epsilon_{g1m}, \Delta\epsilon_{g2}', \Delta\epsilon_{g2m}$
Incremental strain for voigt element i	$\Delta\epsilon_i', \Delta\epsilon_{im}$
Compliance of elastic spring element	$C_{Gg}, C_{Kg}, C_{Gi}, C_{Ki}$
Viscosity	$\eta_{Gg}, \eta_{Kg}, \eta_{Gi}, \eta_{Ki}$
Relaxation and retardation time	$T_g = T_{Gg} = T_{Kg}, T_i = T_{Gi} = T_{Ki}$
Coefficient of linear expansion	$\alpha(T)$

### 2.1.2. Incremental visco-elastic strains for each element

Consider the evaluation of deviatoric (') and volumetric (m) components of the viscoelastic strain increment  $\Delta\epsilon^{el}$  for the Voigt model shown in Figure 2.1.1. The expansion and contraction component accompanying the temperature change is only considered for Maxwell elements.

### A) Maxwell elements

The incremental strain of Maxwell elements is divided into deviatoric (') and volumetric (m) components. The incremental strain during time interval  $t_j, t_{j+1}$  will be calculated by integration. The resultant equations are shown below;

$$\Delta \varepsilon_{g1}^{el'} = C_{Gg} \cdot \Delta \sigma', \quad \Delta \varepsilon_{g1m}^{el} = C_{Kg} \cdot \Delta \sigma_m \quad (2.1.6)$$

$$\Delta \varepsilon_{g2}^{el'} = \frac{1}{\eta_{Gg}} \Delta t \left( \sigma'(t_j) + \frac{1}{2} \Delta \sigma' \right), \quad \Delta \varepsilon_{g2m}^{el} = \frac{1}{\eta_{Kg}} \Delta t \left( \sigma_m(t_j) + \frac{1}{2} \Delta \sigma_m \right) \quad (2.1.7)$$

In the next equation, the incremental heat strain  $\Delta \varepsilon^\theta$  accompany incremental temperature  $\Delta T$  is put in equation form by using coefficient of linear expansion  $\alpha(T)$ . Coefficient of linear expansion  $\alpha(T)$  is a function in temperature  $T$ .

$$\Delta \varepsilon^\theta = \alpha(T) \Delta T \quad (2.1.8)$$

### B) Voigt elements

Similarly, considering the deviatoric (') and volumetric (m) strain components for the Voigt model, the equations will be as follows;

$$\begin{aligned} \Delta \varepsilon_i^{el'} &= \left( C_{Gi} \sigma'(t_j) - \varepsilon_i^{el'}(t_j) \right) \left( 1 - e^{-\Delta t / T_i} \right) + C_{Gi} \cdot \Delta \sigma' \left( 1 - \frac{T_i}{\Delta t} \left( 1 - e^{-\Delta t / T_i} \right) \right) \\ \Delta \varepsilon_{im}^{el} &= \left( C_{Ki} \sigma_m(t_j) - \varepsilon_{im}^{el}(t_j) \right) \left( 1 - e^{-\Delta t / T_i} \right) + C_{Ki} \cdot \Delta \sigma_m \left( 1 - \frac{T_i}{\Delta t} \left( 1 - e^{-\Delta t / T_i} \right) \right) \end{aligned} \quad (2.1.9)$$

#### 2.1.3. Incremental constitutive equations for linear viscoelasticity

From Eqs. (2.4.6) - (2.4.9), the incremental stresses are obtained as follows;

$$\Delta \sigma = \Delta \sigma' + \Delta \sigma_m = \frac{2\Delta \varepsilon'}{C_G(t)} + \frac{3\Delta \varepsilon_m}{C_K(t)} - \frac{\Delta \varepsilon'_a}{C_G(t)} - \frac{\Delta \varepsilon_{am}}{C_K(t)} - \frac{\Delta \varepsilon^\theta}{C_K(t)} \quad (2.1.10)$$

where

$$\begin{aligned} \Delta \varepsilon' &= \frac{1}{2} \left( C_G + \frac{\Delta t}{2\eta_G} \right) \Delta \sigma' + \sum_i \frac{C_{Gi}}{2} \left\{ 1 - \left[ 1 - \exp \left( -\frac{\Delta t}{T_{Gi}} \right) \right] \frac{T_{Gi}}{\Delta t} \right\} \Delta \sigma' \\ &+ \frac{\Delta t}{2\eta_G} \sigma'(t) + \sum_i \frac{C_{Gi}}{2} \left[ 1 - \exp \left( -\frac{\Delta t}{T_{Gi}} \right) \right] \sigma'(t) - \sum_i \left[ 1 - \exp \left( -\frac{\Delta t}{T_{Gi}} \right) \right] \varepsilon_i'(t) \\ \Delta \varepsilon'_a &= \frac{\Delta t}{\eta_G} \sigma'(t) + \sum_i C_{Gi} \left[ 1 - \exp \left( -\frac{\Delta t}{T_{Gi}} \right) \right] \sigma'(t) - 2 \sum_i \left[ 1 - \exp \left( -\frac{\Delta t}{T_{Gi}} \right) \right] \varepsilon_i'(t) \end{aligned} \quad (2.1.11)$$

$$\begin{aligned} \Delta \varepsilon_m &= \frac{1}{2} \left( C_K + \frac{\Delta t}{3\eta_K} \right) \Delta \sigma_m + \sum_i \frac{C_{Ki}}{3} \left\{ 1 - \left[ 1 - \exp \left( -\frac{\Delta t}{T_{Ki}} \right) \right] \frac{T_{Ki}}{\Delta t} \right\} \Delta \sigma_m \\ &+ \frac{\Delta t}{3\eta_K} \sigma_m(t) + \sum_i \frac{C_{Ki}}{3} \left[ 1 - \exp \left( -\frac{\Delta t}{T_{Ki}} \right) \right] \sigma_m(t) - \sum_i \left[ 1 - \exp \left( -\frac{\Delta t}{T_{Ki}} \right) \right] \varepsilon_{mi}(t) \end{aligned} \quad (2.1.12)$$

$$\begin{aligned} \Delta \varepsilon_{am} &= \frac{\Delta t}{\eta_K} \sigma_m(t) + \sum_i C_{Ki} \left[ 1 - \exp \left( -\frac{\Delta t}{T_{Ki}} \right) \right] \sigma_m(t) - 3 \sum_i \left[ 1 - \exp \left( -\frac{\Delta t}{T_{Ki}} \right) \right] \varepsilon_{mi}(t) \\ \bar{C}_G(t) &= C_{Gg} + \frac{\Delta t}{2\eta_G} + \sum_i C_{Gi} \left\{ 1 - \left[ 1 - \exp \left( -\frac{\Delta t}{T_{Gi}} \right) \right] \frac{T_{Gi}}{\Delta t} \right\} \\ \bar{C}_K(t) &= C_{Kg} + \frac{\Delta t}{2\eta_K} + \sum_i C_{Ki} \left\{ 1 - \left[ 1 - \exp \left( -\frac{\Delta t}{T_{Ki}} \right) \right] \frac{T_{Ki}}{\Delta t} \right\} \end{aligned} \quad (2.1.13)$$

## 2.2. Incremental constitutive equations for nonlinear viscoelasticity under uniaxial tension

Depending on strain level of ETFE Film, the creep strain shows nonlinearity. Accordingly, the relation between linear strain vector,  $\{\varepsilon^{el}\}$  and nonlinear strain vector,  $\{\varepsilon^{nl}\}$  is expressed in the following equations with nonlinear viscoelastic coefficient,  $\beta(\bar{\sigma})$ . Provided that the expansion and contraction part accompanying temperature change is excluded.

$$\{\varepsilon^{nl}\} = \beta(\bar{\sigma}) \cdot \langle \{\varepsilon^{el}\} - \{\varepsilon^\theta\} \rangle + \{\varepsilon^\theta\} \quad (2.2.1)$$

where

$$\bar{\sigma} = (\sigma_x^2 - \sigma_x \sigma_y + \sigma_y^2 + 3\tau_{xy}^2)^{1/2} \quad (2.2.2)$$

Put equation of the nonlinear viscoelastic coefficient  $\beta(\bar{\sigma})$  in the following form where the coefficients  $B_2, B_1, B_0$  are calculated separately.

$$\beta(\bar{\sigma}_i) = B_2 \bar{\sigma}_i^2 + B_1 \bar{\sigma}_i + B_0 \quad (2.2.3)$$

Here, regarding each strain vector during time interval  $t_j, t_{j+1}$ , the equation will be as follows;

$$\{\varepsilon^{nl}_j\} = \beta(\bar{\sigma}_j) \cdot \langle \{\varepsilon^{el}_j\} - \{\varepsilon^\theta_j\} \rangle + \{\varepsilon^\theta_j\} \quad (2.2.4)$$

$$\{\varepsilon^{nl}_{j+1}\} = \beta(\bar{\sigma}_{j+1}) \cdot \langle \{\varepsilon^{el}_{j+1}\} - \{\varepsilon^\theta_{j+1}\} \rangle + \{\varepsilon^\theta_{j+1}\} \quad (2.2.5)$$

Subtract equation (2.2.5) from equation (2.2.4) to get the following equation of the nonlinear viscoelastic strain increment vector  $\{\Delta \varepsilon^{nl}_{j+1}\}$ ;

$$\begin{aligned} \{\Delta \varepsilon^{nl}_{j+1}\} &= \{\varepsilon^{nl}_{j+1}\} - \{\varepsilon^{nl}_j\} \\ &= [\beta(\bar{\sigma}_{j+1}) - \beta(\bar{\sigma}_j)] \langle \{\varepsilon^{el}_j\} - \{\varepsilon^\theta_j\} \rangle + \beta(\bar{\sigma}_{j+1}) [\{\Delta \varepsilon^{el}_{j+1}\} - \{\Delta \varepsilon^\theta_{j+1}\}] + \{\Delta \varepsilon^\theta_{j+1}\} \end{aligned} \quad (2.2.6)$$

From the above, we can obtain the nonlinear viscoelastic strain increment vector  $\{\Delta \varepsilon^{nl}_{j+1}\}$  by using the nonlinear viscoelastic coefficient  $\beta(\sigma)$ .

### 2.3. Time-temperature superposition principle

Consider the creep compliance  $C$  at two temperatures  $T$  and  $T_0$ . The principle of time-temperature superposition states that the change in temperature from  $T$  and  $T_0$  is equivalent to multiplying the time scale by a constant factor  $a_T$  which is only a function of the two temperatures  $T$  and  $T_0$ . In other words,

$$\log(a_{T_0}(T)) = \log(t/t') \quad (2.3.1)$$

where  $t$  and  $t'$  denote the original and shifted times, respectively. The shift factor,  $a_T$ , is also expressed as follows with the activation energy  $\Delta H$ ,

$$\log_{10} a_T(T) = \frac{1}{2.303} \frac{\Delta H}{R} \left( \frac{1}{T} - \frac{1}{T_0} \right) \quad (2.3.2)$$

where  $R = 8.314 \times 10^{-3} \text{ kJ}/(\text{mol} \cdot \text{K})$  is applied.

## 3. Evaluation of constants used in the incremental model constitutive equations

### 3.1. Creep compliance of ETFE

In our previous paper, in order for the mathematical expression to be compatible with the experimental results by Moriyama and Kawabata, a type of generalized Voigt model is proposed assuming several constants.

In this paper, in order to express in more details the high temperature characteristics, a minimum retardation time is assumed to be  $4.90\text{E-}07 \text{ sec}$ , then the constants are evaluated again. The results are shown in Table 3.1.1 and using  $C_g = 4.14\text{E-}04$ .

The deviatoric and volumetric components for compliance of elastic spring element are expressed as follows.

$$\begin{aligned} C_{Gg} &= 2(1+\nu_c)C_G, & C_{Gi} &= 2(1+\nu_c)C_i \\ C_{Kg} &= (1-2\nu_c)C_G, & C_{Ki} &= (1-2\nu_c)C_i \end{aligned} \quad (3.1.1)$$

where,  $\nu_c$  is creep Poisson's ratio.

Table 3.1.1 : Retardation time  $T_i$  and compliance  $C_i$

$i$	$T_i$	$C_i$	$i$	$T_i$	$C_i$	$i$	$T_i$	$C_i$
1	9.13E+13	9.12E-04	10	9.35E+06	1.72E-05	19	9.57E-01	1.25E-05
2	3.65E+12	2.37E-04	11	1.87E+06	2.69E-04	20	1.91E-01	6.04E-05
3	7.30E+11	6.65E-04	12	3.74E+05	4.70E-05	21	7.66E-03	1.66E-05
4	1.46E+11	2.65E-04	13	7.48E+04	1.98E-04	22	1.53E-03	8.20E-07
5	2.92E+10	1.07E-03	14	1.50E+04	2.22E-05	23	3.06E-04	1.48E-04
6	5.84E+09	1.54E-04	15	2.99E+03	1.35E-04	24	1.23E-05	1.92E-05
7	1.17E+09	7.95E-04	16	5.98E+02	3.49E-05	25	2.45E-06	5.54E-05
8	2.34E+08	1.21E-04	17	1.20E+02	1.28E-04	26	4.90E-07	7.44E-06
9	4.67E+07	4.61E-04	18	4.79E+00	6.30E-05			

### 3.2. Activation energy $\Delta H$

In this paper, similarly as in previous paper, the data of Moriyama and Kawabata<sup>1,2</sup> is used. Moriyama and Kawabata<sup>1,2</sup> evaluated and presented the activation energy,  $\Delta H$ , of ETFE. The results are shown in Table 3.2.1 and Figure 3.2.1. These values are to be utilized later in the present analysis.

Table 3.2.1 : Activation energy<sup>1,2</sup>

temperature $T$	activation energy $\Delta H$
$T < 40^\circ\text{C}$	113.707
$40^\circ\text{C} < T < 90^\circ\text{C}$	342.261
$90^\circ\text{C} < T$	447.237

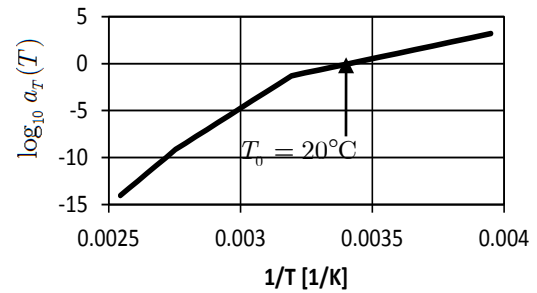


Figure 3.2.1 : Relationship between inverse of temperature  $T$  and shift factor represented in  $\log_{10} a_T(T)$  with reference temperature  $T_0$  of  $20^\circ\text{C}$

### 3.3 Coefficient of linear expansion $\alpha(T)$

Coefficient of linear expansion  $\alpha(T)$  is obtained through tests based on JIS K 7197-1991<sup>13</sup>. It's Testing method for linear thermal expansion coefficient of plastics by thermomechanical analysis. Rise Film temperature from room temperature to 423K then cool down to -223K. After that, Coefficient of linear expansion is obtained by rising it again to 423K. The results are shown in figure 3.3.1. The next approximate equation is obtained from these results.

$$\alpha(T) = -2.057 \times 10^{-8} T^4 + 3.289 \times 10^{-5} T^4 - 1.847 \times 10^{-2} T^2 + 4.443 T - 379.6 \quad (3.3.1)$$

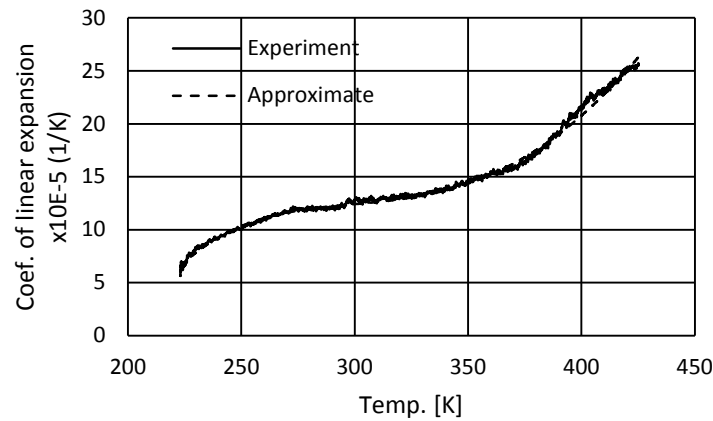


Figure 3.3.1 : Coefficient of linear expansion  $\alpha(T)$

#### 4. UNIAXIAL CREEP TEST OF ETFE FILM

##### 4.1. Uniaxial creep test of fixed temperature

Uniaxial tensile testing machine is used to carry out uniaxial creep test with fixed temperature. Shape of test specimen is shown in figure 4.1.1. Test conditions are shown in table 4.1.1. Results of the creep test are shown in table 4.1.2. When considering the temperature strain, it is necessary to pay attention to not only the temperature strain of the specimen but also to the temperature strain of the jig.

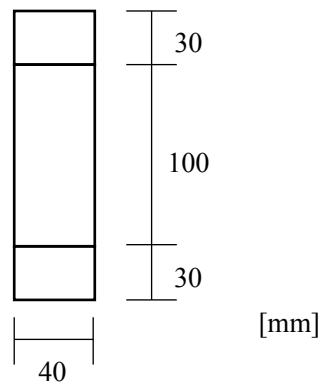


Figure 4.1.1 : Shape of test specimen for uniaxial creep test

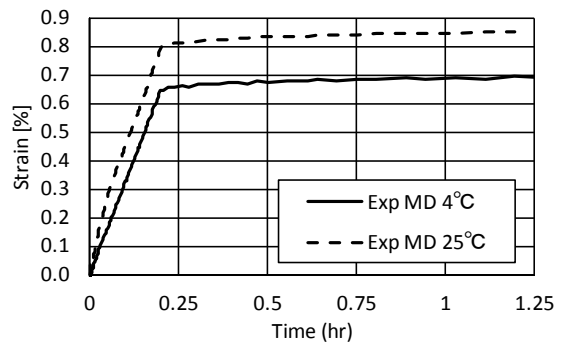


Figure 4.1.2 : Strain – Time relationship

Table 4.1.1 : Uniaxial tensile test conditions

Film thickness	250 $\mu$ m
Direction	MD
Width of test specimen	40mm
Distance between chucks	100mm
Max stress	6.1MPa
Loading rate	0.5MPa/min
Present temperature	Fixed temperature 4 and 25 °C

### 4.2. Uniaxial creep test of 30°C temperature change

Uniaxial tensile testing machine is used to carry out uniaxial creep test accompanied with change in temperature. Conditions of temperature change are shown in table 4.2.1. Shape of test specimen is shown in figure 4.1.1.

Preset temperature is shown in table 4.2.1 and temperature setting values during test is shown in figure 4.2.1. Test results are shown in figures 4.2.2 and 4.2.3.

Table 4.2.1 : Setting of temperature change

Initial temperature 30°C, loading time and 1 hour soaking 30°C - 0°C, 6 cycles Temperature rate is 30°C/hr for cycling time
--

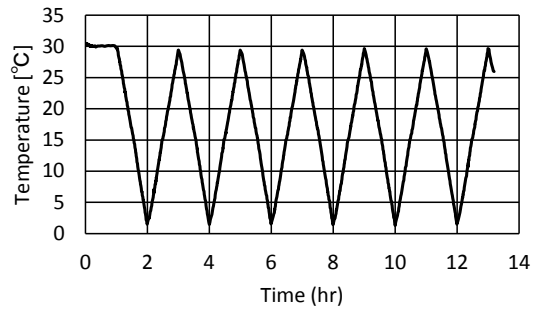


Figure 4.2.1 : Temperature of creep test

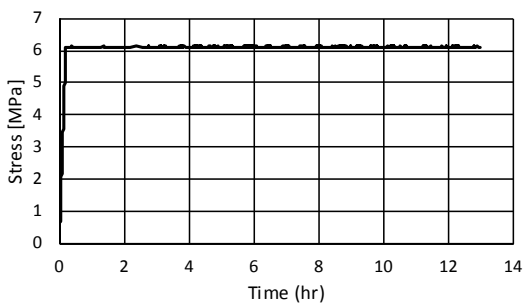


Figure 4.2.2 : Stress-Time relationship

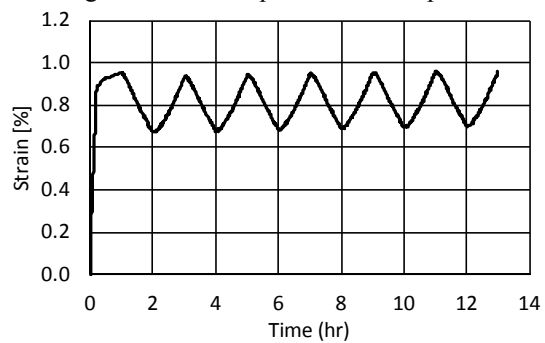


Figure 4.2.3 : Strain-Time relationship

### 4.3. Uniaxial creep test of 10°C temperature change

Uniaxial tensile testing machine is used to carry out uniaxial creep test accompanied with change in temperature. Conditions of temperature change are shown in table 4.3.1. Shape of test specimen is shown in figure 4.1.1.

Preset temperature is shown in table 4.3.1 and temperature setting values during test is shown in figure 4.3.1. Test results are shown in figures 4.3.2 and 4.3.3.

Table 4.2.1 : Setting of temperature change

Initial temperature 30°C , loading time and 3 hour soaking 30–0°C , 20–10°C , 10–0°C , 5 cycles each Temperature rate is 10°C/15min for cycling time
--

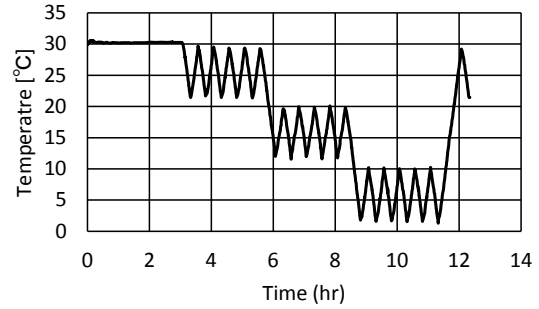


Figure 4.3.1 : Temperature of creep test

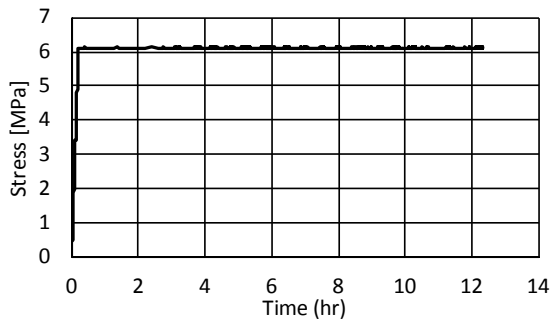


Figure 4.3.2 : Stress - Time relationship

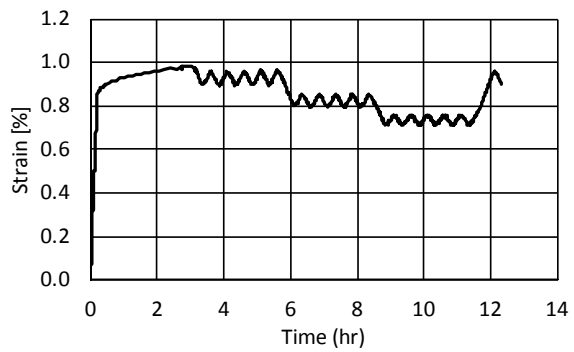


Figure 4.3.3 : Strain - Time relationship

## 5. SIMULATION OF EXPERIMENTAL TEST

Using the proposed constitutive equation, simulation of uniaxial creep test carried out in section 4 is performed. The values of the coefficients mentioned in section 3 are used. Simulation results are shown in figures 5.1~5.3. Creep strain in both of them can be confirmed to be sufficiently estimated.

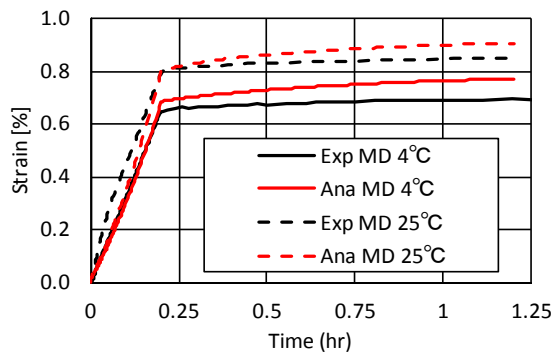


Figure 5.1 : Strain - Time relationship  
(fixed temperature)

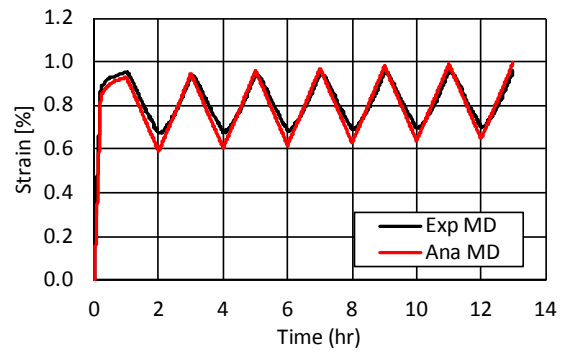


Figure 5.2 : Strain - Time relationship (30°C change)

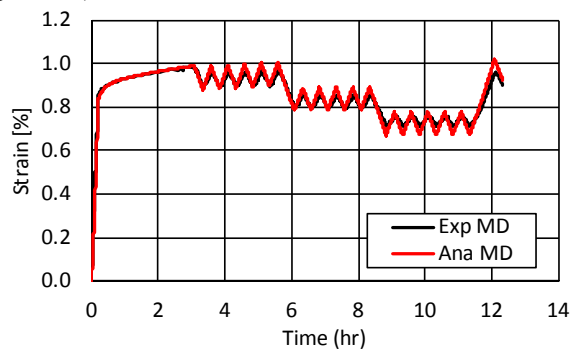


Figure 5.3 : Strain - Time relationship (10°C change)

## 6. CONCLUSION

In this paper, the incremental nonlinear viscoelasticity constitutive equation for biaxial tension field was extended to consider the expansion part due to temperature change. Through thermomechanical analysis, the characteristic of expansion due to temperature change is obtained as the coefficient of linear expansion.

As well, performing uniaxial creep test under fixed temperature and under temperature change, uniaxial creep characteristics depended on temperature was confirmed.

Again, using the proposed constitutive equation, simulation of uniaxial creep test that depended on temperature was carried out. Simulation results showed that creep characteristics can be expressed by the proposed equation.

From the above, it was confirmed that elapsed time, stress change and temperature change can be taken into account using the constitutive law. In order to make comparison with the test results of limited conditions, it is necessary to carry out additional comparative studies. For example, biaxial creep accompanied with temperature change in random stress ratio and so on.

## ACKNOWLEDGEMENT

We would like to express our gratitude to Dr. Hiroshi Aruga from Asahi Glass Co. for providing us with valuable data to conduct this research.

## REFERENCES

- [1] Kawabata K., Moriyama F., Study on viscoelastic characteristics and structural response of film membrane structures, Proceedings of the IASS-APCS 2006 International Symposium MB01.150-151, 2006.10
- [2] Moriyama F., Study on Viscoelastic Behavior of ETFE Film Pneumatic Structure, PhD Thesis, Yokohama National University, Japan, 2006.3 (In Japanese)
- [3] Eul-Seok JEONG, Masaya KAWABATA : Visco-Plastic Constitutive Equation of ETFE Film - Examination on the Stress Strain relationships of Uniaxial and Biaxial Tensile Deformation, IABSE-IASS 2011 Symposium Proceedings, Ref. No. 0799, 2011.9
- [4] Wu M., Li Y. : Revised finite element formulation for membrane creep analysis, Proc. of the IASS-SLTE 2014, Paper No. 209, 2014
- [5] Galliot C, Luchsinger RH. : Uniaxial and biaxial mechanical properties of ETFE foils, Polymer Testing; 30(4); 356-365, 2011
- [6] Li Y., Wu M., Wang H. : biaxial creep tests of ETFE foil, Proc. of the IASS-SLTE 2014, Paper No. 136, 2014
- [7] Yoshino T., Segawa S., Oda K., Material characteristics of ETFE film under bi-axial tension and stress-displacement analysis considering the elasto-plastic characteristics, Research Report on Membrane Structures 2004, 18, 31-39, 2005.2 (In Japanese)
- [8] Testing method for elastic constants of membrane materials, Standard of Membrane Structures Association of Japan, MSAJ/M-02-1995, 1995
- [9] Testing method for in-plane shear stiffness of membrane materials, Standard of Membrane Structures Association of Japan, MSAJ/M-01-1993, 1993
- [10] Tatsuya Yoshino, Shiro Kato : Formulation of non-linear incremental constitutive equation of ETFE film structure considering the dependence on temperature change, IASS 2013 Symposium, Paper ID 1331, 2013.9
- [11] Tatsuya YOSHINO, Shiro KATO : Viscous characteristics of ETFE film sheet under biaxial tensions, Proceedings of IASS Symposium 2015, No. IASS2015-419518, 2015.8
- [12] Tatsuya YOSHINO, Shiro KATO : Viscous characteristics of ETFE film sheet under equal biaxial tensions, TENSINET - COST TU1303 International Symposium 2016, Procedia Engineering, Volume 155, Pages 442-451, 2016.9
- [13] Testing method for linear thermal expansion coefficient of plastics by thermomechanical analysis, Japanese Industrial Standards, JIS K 7197-1991, 1991
- [14] The Society of Rheology, Japan : New course in Rheology, The Society of Polymer Science, Japan, 2001

## ACTIVE BENDING STARTING ON CURVED ARCHITECTURAL SHAPE

STRUCTURAL MEMBRANES 2017

JUERGEN BELLMANN<sup>†</sup>

\* SOFiSTiK AG 85764 Oberschleissheim, Germany  
e-mail: juergen.bellmann@sofistik.de, web page: <http://www.sofistik.com>

**Key words:** Active Bending, Membranes, Formfinding, Torsion

**Summary.** This paper describes the implementation of an analysis technique for active bending beams starting on a rough curved architectural system.

### 1 INTRODUCTION

In earlier applications active bending analysis started with a straight beam that was bent to a curved one. In this paper we show the technique starting with a curved architectural shape (see Fig. 1 left) and giving the beam the information that it originally was straight. So an internal bending prestress can be calculated and applied that corresponds to the input curvature of the beam chain.

In this paper we demonstrate the technique and check it by removing the membranes and fixings and let the beams relax. Then they must go back to an unstressed straight beam again.

Special focus is set on problems of torsion in active bending structures.

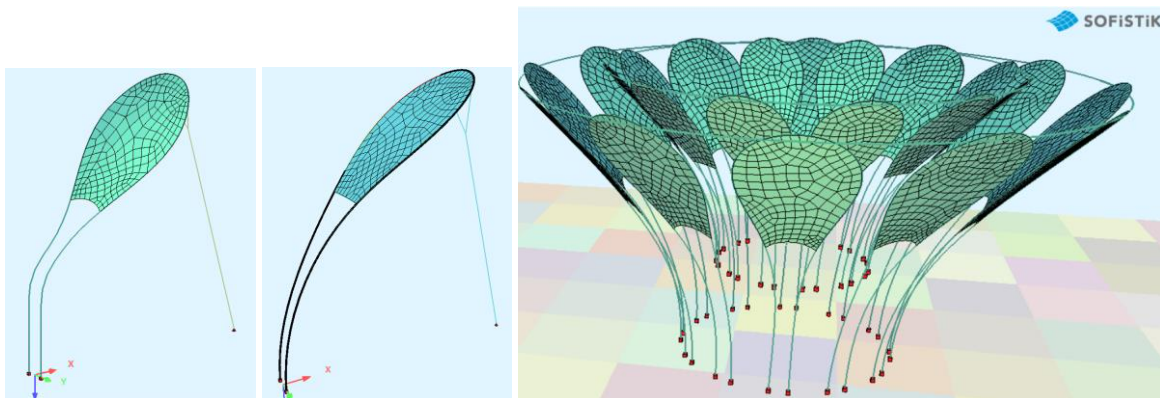


Figure 1: Leaf : rough input system – activated bending - multiple leaves added to an ensemble

## 2 SIMPLE BEAM

In earlier applications a straight beam was bent in a geometrical nonlinear analysis TH3 into a curved shape [1]. As a result, we got a stressed bended beam, see Fig. 2:

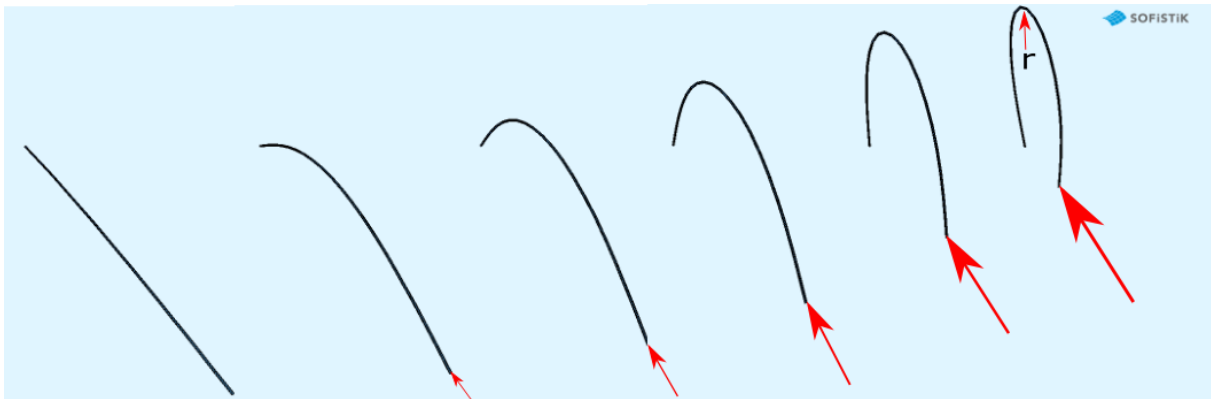


Figure 2: Bending up a straight beam

A new function ACTB uses another much easier way. The system is already input curved and you only give the beam chain the information that it originally was straight. In a first step the program calculates the curvature of the curved input beam chain and then applies an internal bending prestress that corresponds to this input curvature. This prestress would like to bend back the beam chain into a straight shape.

The input shape must not be totally correct. The beam will push itself automatically into an equilibrium active bending shape. In the following picture the beam behind is the just up-bended beam (group 1), the middle beam (group 2) has already got the final input shape in SOFiMSHA, the front beam (group 3) starts with a circular input geometry. In Fig. 3 left we see the result without ACTB input, then group 2+3 are stress-free. The result with input ACTB for groups 2+3 is shown on the right. Then all three beams end in the same stressed shape and bending moment as shown in Fig. 4.



Figure 3: Left system without ACTB, 3=circular input system, on the right result with ACTB

As a check we then remove the supports and let the beams *relax* freely (slow removal



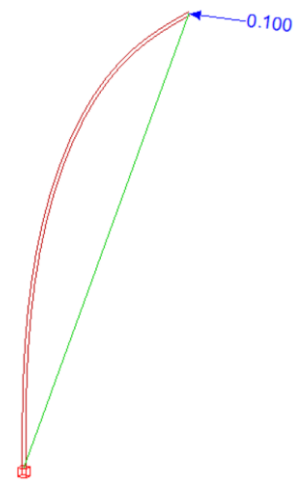


Figure 5: Torsion case study

In the following we demonstrate, that no torsional moment will appear in this case. Please notice that we can also start to bend the beam backward or under 30 degree, see Fig. 6.

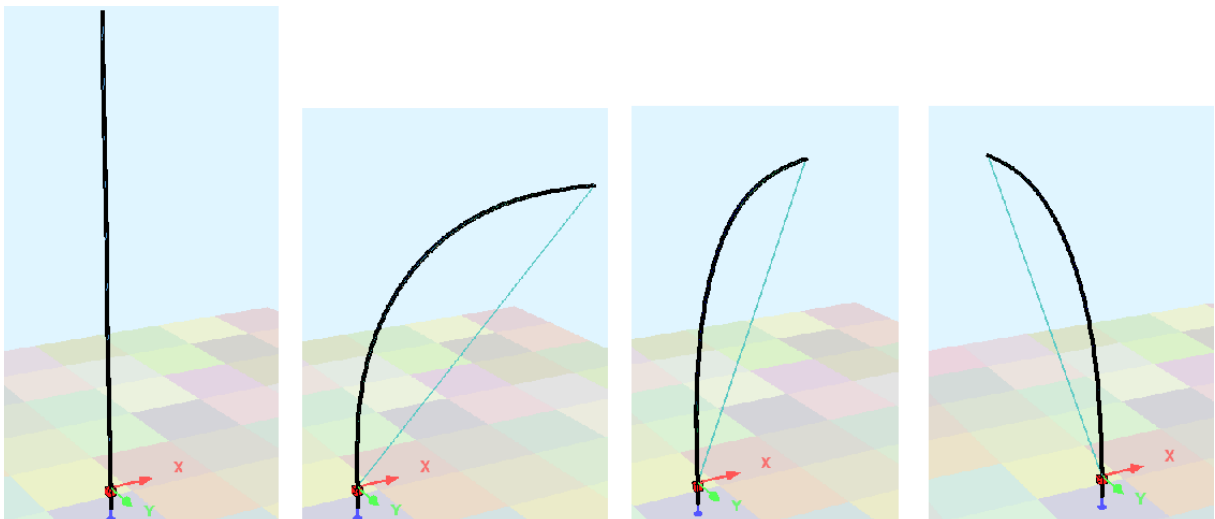


Figure 6: Torsion case study: left starting system, then bend to +x, under 30 degree or backward (-y)

The amount of energy is the same for all three cases. Therefore a horizontal deformation of the cantilever should not activate additional energy in the system. But this would mean that the system is unstable regarding rotation around the z axis. But the beam is fixed at the bottom - so this should not be the case.

But it is - with a horizontal deformation the beam just rolls away without a force into the new position, see Fig. 7 (at least theoretically). This happens for a perfect round beam, while the cable must be attached at the cross section center of the beam. In reality a beam is never perfect round - it will always bend into a favored direction.

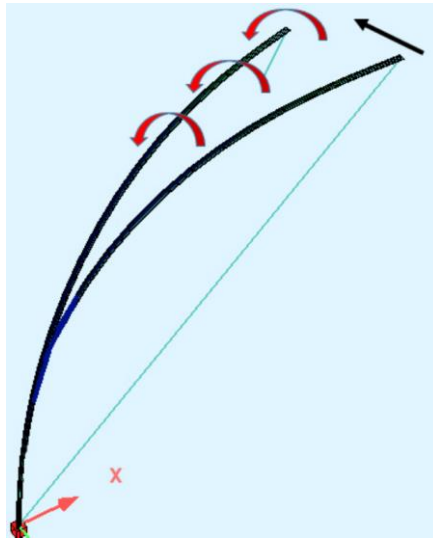


Figure 7: Horizontal deformation of the cantilever - the beam just rolls away without force

We (the SOFiSTiK team) have build a real model and proved that the beam really rolls away and no torsion appears, see YOUTUBE video with search term 'active bending torsion beam':



Figure 8: torsion test case - YOUTUBE video 'active bending torsion beam'

You can also compare the behavior with a tube-cleaning-spiral that you twist at one end. Also in case the spiral goes around in curves, you can twist it nearly without effort if the end of the spiral and the spiral in between is not fixed against rotation.

Conclusion: on many deformations and loadings an active bending beam just rolls away or rotates and withdraws itself from torsion.

### 3.2 Torsion on beam with fixed ends

So we use a beam with restrained ends in the next example according Fig. 8 - then we can introduce a torsion. To test it, we first bend the straight beam to a half circle (also requires bending moment at the end of the beam) and then apply torsion. Accordingly, we rotate the left support left and the right support also left. As a result we get a constant torsion in the beam.

Under torsion, little horizontal deformations occur vertical to the circle plane. If we now freeze the system and store it (SOFiSTiK-ASE: SYST STOR YES) and then start the active

bending procedure ACTB on the stress-free updated system, we get a torsion in the beam - as in the original system. In the active bending routine this is created with a rotational check that recognizes a torsion via the little horizontal deformations. You only have to tell the program that the active bending beam is restrained at both ends and that at both ends torsion can be applied (SOFiSTiK-ASE: ACTB MEND 'FIX' MT 'FIX'). Otherwise, ASE assumes that the beam does not have bending or torsional moments at both ends - as in the first example.

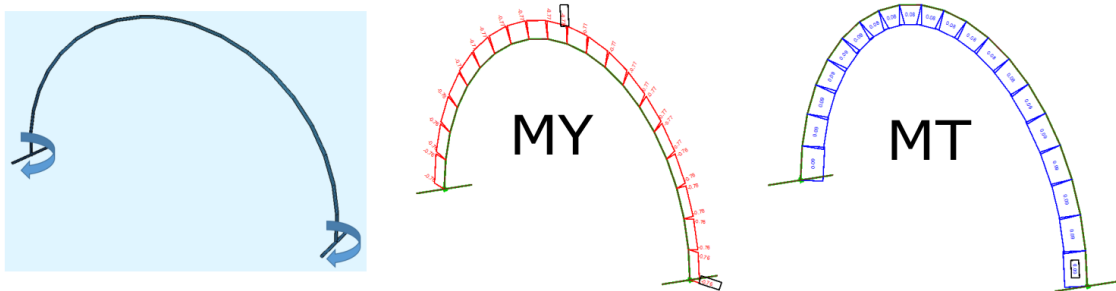


Figure 9: left: bend up a straight beam to a half circle and torsioned : center: MY right: MT

### 3.3 No torsion in case of constant beam rotation

If we rotate both ends in opposite direction, so the left to the left and the right to the right, we can rotate the beam without energy. The whole beam just rotates away, see Fig. 9. This happens because the active bending beam originally came from a straight beam and the stress-free length of the inner fiber has the same length as the outer fiber.

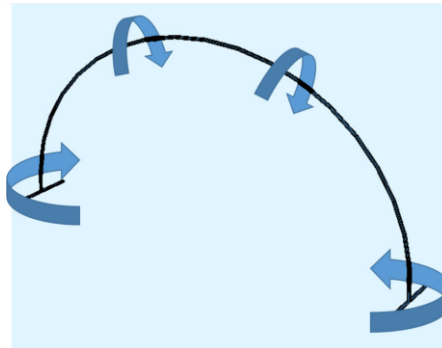


Figure 10: Bend up a straight beam to a half circle and torsioned contraverse: no torsion MT appears

This would not happen in case of a stress-free half circle - it has a shorter inner fiber and a longer outer fiber. A torsion would require energy. So again we see: it is not so easy to get torsion into an active bending beam.

### 3.4 Torsion caused by loading transverse to the main active bending plane

If we take the stressed system from the previous chapter and apply a horizontal force on top, see fig. 1, the load and the induced shear force acts transverse to the main active bending plane and we get a torsional moment MT. Depending on the torsional restraint at the bottom the system is more or less flexible for this transverse loading.

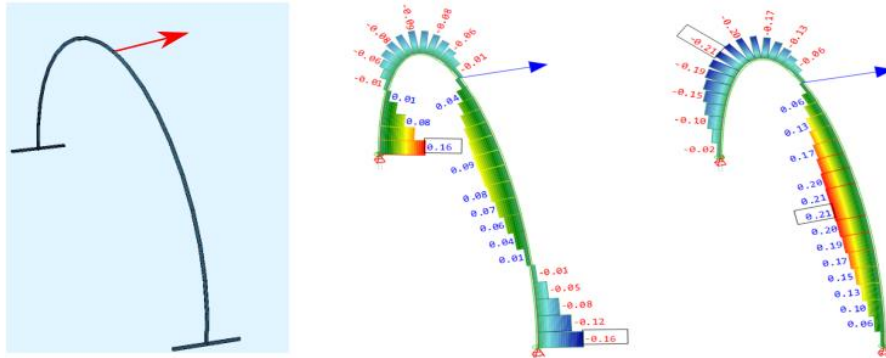


Figure 11: MT for loading transverse to main plane: middle full, right torsionfree bottom fixing

But the material stress is often small compared to the bending stress. In the example of fig. 12 max-tau-MT is less than 0.1\% in relation to the maximum bending stress.

#### 4 ACTIVE BENDING INCLUDING A MEMBRANE

In the next example similar to [3] we start only with a rough desired architectural form in a graphical input (AUTOCAD-SOFIPLUS) and immediately insert a formfinding membrane. The curvatures must not be exact in this input system. So the upper part with the membrane was input in a 45 degree plane to have an easy input, see Fig. 12:

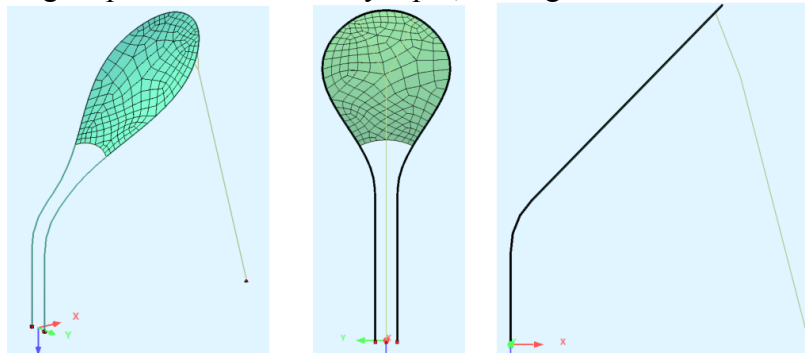


Figure 12: Input system: center: view in x, right: side view (straight membrane input plane)

With the special input ACTB, we specify now that the beam originated from a straight beam and so the system nearly playfully iterates to its stability shape. Due to the bottom restraint, the beams pull up and tension the anchorage cable. As the membrane is defined as a soap film with given prestress, it finds a stress-constant form as well, see Fig. 13. The bottom cable of the membrane can be input with a given length.

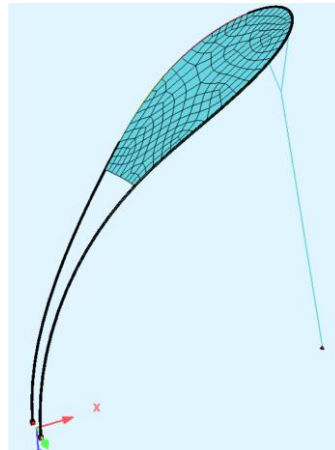


Figure 13: Result of formfinding with ACTB GRP 2 (beam elements)

Torsion: caused by the anchorage cable a slight torsion is induced compared to fig. 11. Max-tau-MT is less than 0.1\% in relation to the maximum bending stress. Depending on the torsional restraint at the bottom the system is more or less flexible against this horizontal loading of the anchorage cable.

To check if the active bending moment is correctly introduced in the curved input system, we now let the beam relax. For this we switch off the membrane and the cable and cut the beam into shorter pieces. With this we start a dynamic relaxation and as a result we really get straight pieces, see Fig. 14:

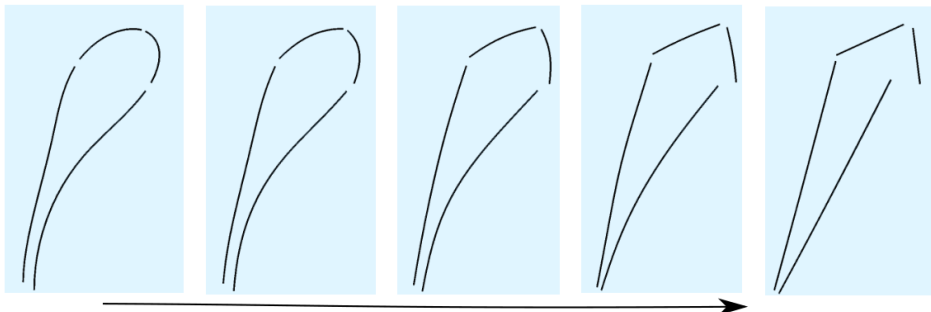


Figure 14: Dynamic relaxation to check if straight beams remain

The system is rather flexible and would swing or flutter on wind. Without wind it is stable, but the first buckling eigenfrequency is only a little bit greater than 1.0. Now it is easy to use the system several times as shown in Fig. 1. Similar shapes can be found in [3].

Also in the next example, we model the final form only roughly in the graphical input. To reduce the height of the tent, the upper arch was compressed a little bit. As a result, a kink was introduced in the beam. But this kink is not a problem and smoothed (straightened) by the active bending technique, see Fig. 15.

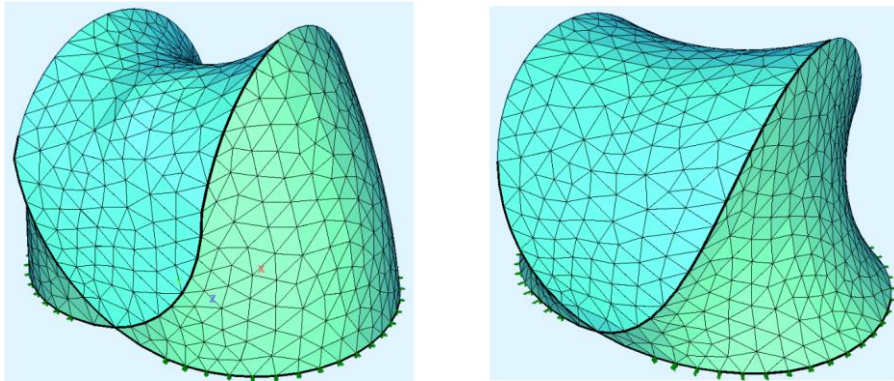


Figure 15: Throw tent: left input system, right: stressed system after ACTB active bending formfinding

With a four-node quad meshing, quads could be created at the kink with three nodes attached to an active bending beam, one node before the kink, one at the kink and one behind. If the active bending beam then gets nearly straight, at the kink an angle of nearly 180 degrees would be created and cause an error. Therefore, a triangle meshing is used here. As in membrane elements the nonconforming shape functions of a four-node quad are switched off, the use of triangle elements is sufficient.

Torsion: the rotation of the main active bending plane causes a slight torsion. But as the rod can nearly rotate free in the membrane pocket, the active bending beam withdraws himself as good as possible from torsion. Only in case the friction in the membrane pocket is high e.g. for a windsurf mast, a significant torsion may be induced on wind loading.

The last example of a sphere demonstrates how to reach various final shapes with different prestress input, see Fig. 16. Here no torsion appears in the building stage. The bending always acts in one plane. Vertical to this plane no shear force appears (disregarding of little gravity loading in the upper plane).

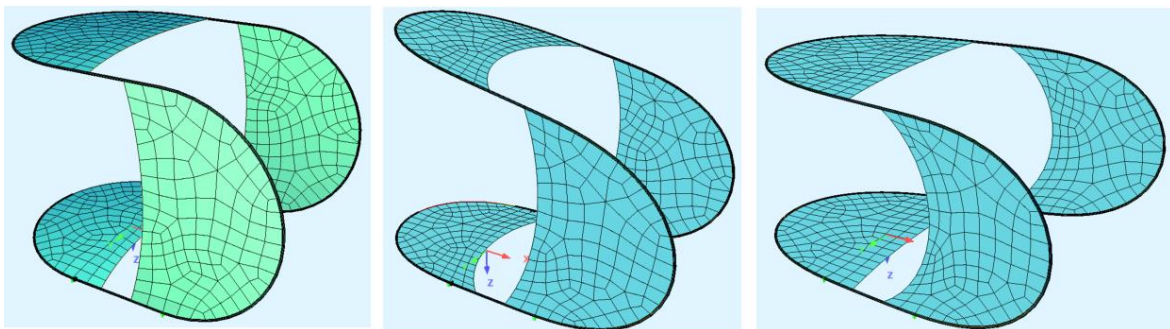


Figure 16: Spere : left input system, middle: upper areas prestressed higher, right : vertical areas stressed higher

## 5 CONCLUSIONS

On various examples a simple technique for creating finite element active bending beams has been represented. It is shown that in most cases it is difficult to introduce a significant torsional bending in an active bending structure.

## REFERENCES

- [1] Fabienne Garti, *Active-Bending Hybrid Structures*, Master Thesis, Berlin, June 12, 2015, KET Lehrstuhl für Konstruktives Entwerfen und Tragwerksplanung, presented at the INSA Strasbourg
- [2] Evy L. M. Slabbinck, *Modelling of torsion in bending-active tensile structures*, Young Engineers Colloquium, Stuttgart 2015, <https://www.researchgate.net/publication/275019159>
- [3] Lars De Laet, Evy Slabbinck, Tom Van Mele, Philippe Block, Marijke Mollaert, *Case study: A modular, self-tensioned, bending-active canopy*, Proceedings of the International Association for Shell and Spatial Structures (IASS) Symposium 2013 23-27 September, Wroclaw, Poland, <https://www.researchgate.net/publication/264119747>

## ADVANCED APPROACHES FOR ANALYSIS AND FORM FINDING OF MEMBRANE STRUCTURES WITH FINITE ELEMENTS

Jan Gade<sup>+</sup>, Manfred Bischoff<sup>+</sup> and Roman Kemmler<sup>\*</sup>

<sup>+</sup> Institute for Structural Mechanics  
University of Stuttgart  
Pfaffenwaldring 7, 70550 Stuttgart, Germany  
e-mails: Bischoff/Gade@ibb.uni-stuttgart.de - web page: <https://www.ibb.uni-stuttgart.de/>

<sup>\*</sup> Professorship for Engineering Mechanics and Structural Analysis  
Hochschule Konstanz University of Applied Sciences  
Alfred-Wachtel-Straße 8, 78462 Konstanz, Germany  
e-mail: Roman.Kemmler@htwg-konstanz.de - web page: <http://www.htwg-konstanz.de/>

**Key words:** Woven fabric membranes, microstructural modelling, anisotropic hyperelasticity, parameter identification, form finding, cutting patterning, optimisation

**Abstract.** *Part I* deals with material modelling of woven fabric membranes. Due to their structure of crossed yarns embedded in coating, woven fabric membranes are characterised by a highly nonlinear stress-strain behaviour. In order to determine an accurate structural response of membrane structures, a suitable description of the material behaviour is required. A linear elastic orthotropic model approach, which is current practice, only allows a relative coarse approximation of the material behaviour. The present work focuses on two different material approaches: A first approach becomes evident by focusing on the meso-scale. The inhomogeneous, however periodic structure of woven fabrics motivates for microstructural modelling. An established microstructural model is considered and enhanced with regard to the coating stiffness. Secondly, an anisotropic hyperelastic material model for woven fabric membranes is considered. By performing inverse processes of parameter identification, fits of the two different material models w.r.t. measured data from a common biaxial test are shown. The results of the inversely parametrised material models are compared and discussed.

*Part II* presents an extended approach for a simultaneous form finding and cutting patterning computation of membrane structures. The approach is formulated as an optimisation problem in which both the geometries of the equilibrium and cutting patterning configuration are initially unknown. The design objectives are minimum deviations from prescribed stresses in warp and fill direction along with minimum shear deformation. The equilibrium equations are introduced into the optimisation problem as constraints. Additional design criteria can be formulated (for the geometry of seam lines etc.). Similar to

the motivation for the Updated Reference Strategy [4] the described problem is singular in the tangent plane. In both the equilibrium and the cutting patterning configuration finite element nodes can move without changing stresses. Therefore, several approaches are presented to stabilise the algorithm. The overall result of the computation is a stressed equilibrium and an unstressed cutting patterning geometry. The interaction of both configurations is described in Total Lagrangian formulation.

The microstructural model, which is focused in Part I, is applied. Based on this approach, information about fibre orientation as well as the ending of fibres at cutting edges are available. As a result, more accurate results can be computed compared to simpler approaches commonly used in practice.

## **Part I: Comparison of a microstructural model with an anisotropic hyperelastic model gained by inverse problems of parameter identification**

### **1 INTRODUCTION**

The structure of a woven fabric embedded in coating, which is caused by the manufacturing process, leads to a significant physically nonlinear material behaviour. Moreover, membrane structures are characterised by a pronounced geometrically nonlinear behaviour as well. Hence, a realistic analysis demands for a suitable modelling of the material behaviour in context of finite deformations theory. For this purpose there are several approaches, which arise from different modelling scales.

At first, the test data from a biaxial tension test is presented with regard to its usage in parameter identification (Chapter 2). In Chapter 3 we give just the basic ideas about approaches for modelling material behaviour on different modelling scales. After that, we firstly present an established microstructural model with our enhancement (Chapter 4) and we secondly pose an anisotropic hyperelastic model (Chapter 5). In Chapter 6 the processes of identification of the model parameters are outlined. Finally, the results of the two material models are compared and discussed (Chapter 7). The contribution focuses on the elastic deformation behaviour. Neither viscoelastic, viscoplastic nor wrinkling effects are considered.

### **2 EXPERIMENTAL DATA FROM A BIAXIAL TENSION TEST**

In order to perform the identification of the parameters of the microstructural model (Chapter 6) as well as the anisotropic hyperelastic model (Chapter 5), data from a biaxial tension test are considered. The test data was kindly provided by Low and Bonar GmbH (former Mehler Technologies GmbH, Fulda/Germany). Figure 1 outlines the setup of the test. The specimen is a slotted woven fabric membrane, whose two families of fibres are orthogonal and orientated parallel to the load directions.

The test procedure as well as the evaluation method is performed in accordance to JIS

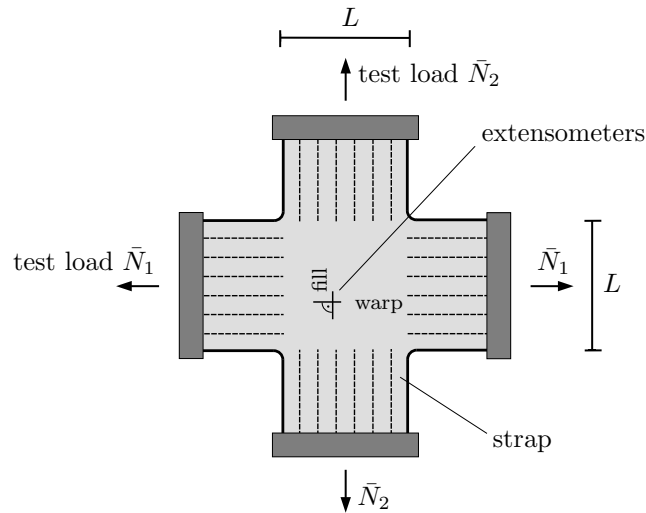


**Figure 1:** Biaxial tension test of a woven fabric membrane – outline of the setup (after [1])

MSAJ/M-02-1995 [14]. This means that load-strain curves corresponding to 5 load ratios are extracted for further regards. These 5 load ratios  $(\bar{N}_{1,i}/L) : (\bar{N}_{2,i}/L)$  are 2:1, 1:2, 2:0, 2:2 and 0:2, where the ratio value of 2 resp. 1 is equivalent to a load of 45.0 resp. 22.5 kN/m. It is a load-controlled test with a constant loading rate of  $\pm 0.2$  kN/(ms), which is assumed to be a quasi-static loading process. Since the loads are related to a reference dimension  $L$ , they act as first Piola-Kirchhoff stresses. Therefore,  $\bar{P}_{11,i} := \bar{N}_{1,i}/L$  resp.  $\bar{P}_{22,i} := \bar{N}_{2,i}/L$  (with regard to unit thickness) is assumed. Engineering strains are measured with extensometers in the inner area of the specimen. They are aligned parallel to the directions of the yarns. More details concerning the biaxial tension test, the specific test procedure and evaluation method are given in e.g. [7, pp. 51f.], [16, pp. 382f.].

There are a total of  $n_V = 380$  test data points indexed by the symbol  $i = 1, \dots, n_V$ . The measured and evaluated test data is shown in Figure 5.  $\bar{\lambda}_{11,i}$  resp.  $\bar{\lambda}_{22,i}$  is the  $i$ -th measured stretching in warp resp. fill direction (note: stretch  $\lambda =$  engineering strain + 1).

### 3 MODELLING APPROACHES FOR WOVEN FABRIC MATERIALS

Considering woven fabric materials in an engineering context, three distinct approaches can be utilised to model the stress-strain behavior accounting for the material structure:

- (a) **Micro-scale approach** The modelling of the particular components of the material (yarns, coating, contact) is applicable for determination of local phenomena like e.g. failure or damage behaviour.
- (b) **Macro-scale approach** The assumption of a phenomenological material model like a linear elastic, orthotropic model is a basic engineering approach and is used in practical applications. A hyperelastic material model falls in this category as well. The material parameters have to be determined by means of experimental methods

(e.g. [18], [7], [16]).

**(c) Meso-scale approach** Since a woven fabric membrane is characterised by a repetitive structure, the modelling of the material behaviour by means of a submodel at the meso-scale is reasonable. Such a submodel represents the smallest repetitive unit and is called a unit cell model or microstructural model (e.g. [5], [6], [1]).

In the present contribution, approach (c) is focused by assuming a microstructural model for plain-woven fabric materials. Inversely gained results are compared with results of an anisotropic hyperelastic material model (approach (b)). In order to perform numerical computations of full scale engineering structures, the microstructural model at the meso-scale (approach (c)) is coupled with the macro-scale in context of e.g. finite element computations (see Part II, Figure 6). Such an approach is denoted as multi-scale modelling or  $FE^2$  ([9]).

## 4 MICROSTRUCTURAL MODEL

In this section an established microstructural model is stated, enhanced and at last the governing model equations are mentioned.

### 4.1 Established model

The basis of Part I of the present contribution is the established microstructural model for plain-woven fabric membrane materials shown in Figure 2. An early publication of a

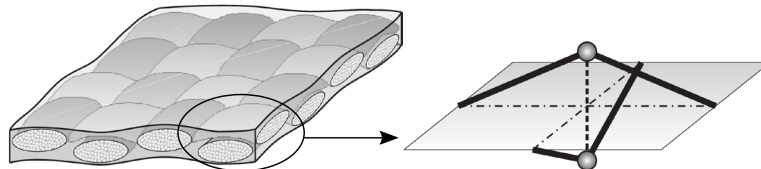


**Figure 2:** Left: Plain-woven fabric membrane; right: established microstructural model (from [1, p. 17])

mechanical description of the model is attributed to KAWABATA [12]. He modelled one single intersection point as inclined, piecewise linear bar elements coupled by another bar element, which represents the contact between the yarns. Amongst others, there were MEFFERT [13] as well as BLUM [5], who made further studies of the above-mentioned model. On this basis, BÖGNER reveals a considerable influence of the transversal compression of the yarns. Therefore she modelled a spring in between the two intersection points of the yarns [6]. Recently, KAISER/HAUG/PYTTEL/DUDDECK [11] used a beam model with bending stiffness as representatives for the yarns. They couple it with a finite element system and handle draping simulation problems by using material properties from earlier publications.

A methodological feature of the work mentioned above is, that the geometrical as well as the stiffness parameters of the models are directly obtained by means of experimental

methods. This means that for example geometrical dimensions of the particular woven fabric like yarn diameters and yarn spacings were obtained by means of experimental measurement. In contrast to this, in the present paper model parameters are gained as solutions of inverse problems on the basis of test data of a standardised biaxial tension test (see Chapter 6). An advantage is the flexible adaption to other test data. Moreover, there is no need for special measurement equipment. On the other hand, a direct physical meaning of the determined parameters is not ensured at all times.

#### 4.2 Enhancement of the established model

A well-described deformation mechanism is the crimp interchange (e.g. [7], [1]), which is essentially responsible for the nonlinear material behaviour. Figure 3 outlines the mechanism in context of the established unit cell modell. In cases, where the load in one direction dominates (e.g.  $F_1 \ll F_2$ ), the coating is lengthened resp. shortened and tension resp. compression stresses are activated, whose magnitudes are functions of the coating stiffness and contact stiffness of the yarns. Hence, the model is enhanced by

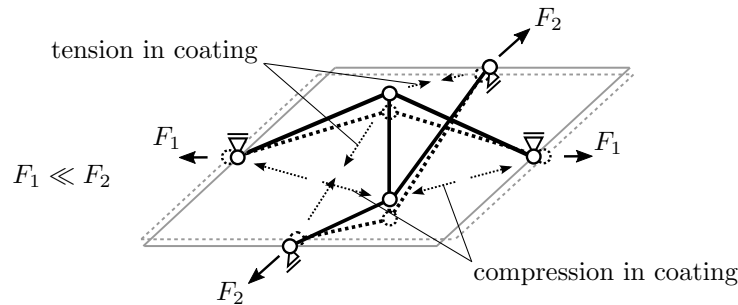


**Figure 3:** Deformation of the established model during crimp interchange

springs representing the stiffness in as well as perpendicular to the model plane. The entire model is illustrated in Figure 4. It is explained in the subsequent section. During the parameter identification process (see Chapter 6) the spring elements turned out to be the decisive elements in order to obtain results with a high accuracy in comparison with the test data.

#### 4.3 Structural analysis of the enhanced model

The enhanced model is shown in Figure 4. The blue resp. red bar elements represent the yarns, the green bar models the contact and the spring elements make consideration of the stiffness of the coating. Moreover, the geometric dimensions of the model are parametrised. The following eleven model parameters are assumed, at which the dimension  $L_1$  serves as a reference quantity of the model:

- Relative dimensions  $L_2$ ,  $H_1$  und  $H_2$  (physical unit:  $[L_1]$ );
- relative extensional stiffnesses  $k_{y,1}$ ,  $k_{y,2}$  and  $k_c$  (physical unit:  $[\text{force}]$ );

- relative spring stiffnesses  $c_{A,1}$ ,  $c_{A,2}$ ,  $c_{N,12}$  and  $c_{N,21}$  (physical unit: [force]/[ $L_1$ ]).

All parameters are posed in  $\mathbf{M}_{mic} := [L_1 \ L_2 \ H_1 \ H_2 \ k_{y,1} \ k_{y,2} \ k_c \ c_{A,1} \ c_{A,2} \ c_{N,12} \ c_{N,21}]^T$ . The index '1' corresponds to the warp direction whereas the index '2' refers to the fill direction. It is assumed, that the microstructure represents the smallest unit of the material, whose force-strain behaviour does not depend on the characteristic dimension, here  $L_1$ . Hence, there is no need to define a certain physical unit for  $L_1$ . The deformation behaviour is symmetric and is therefore determined by four displacements,  $\mathbf{u} = [u_1 \ u_2 \ u_3 \ u_4]^T$ .

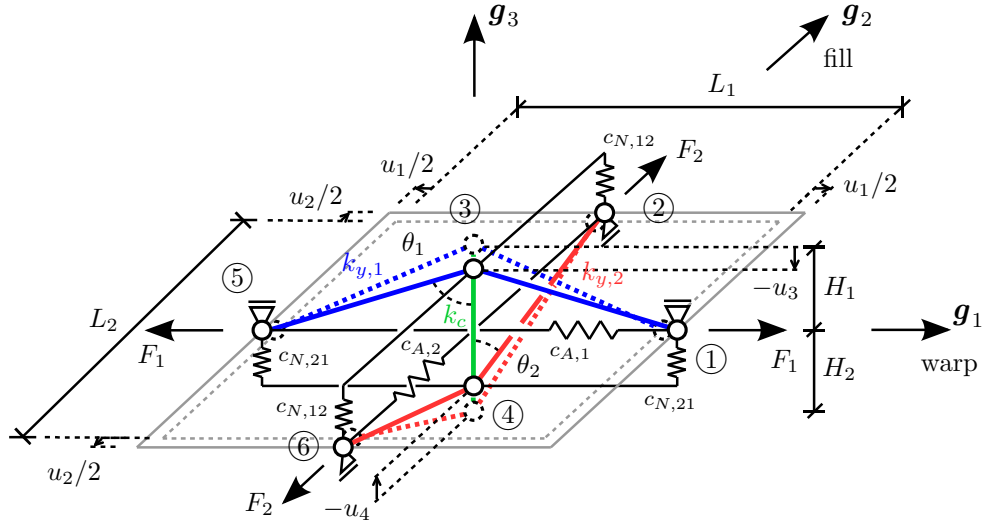


**Figure 4:** Microstructural model – undeformed and deformed configuration

**Kinematic equations** Nonlinear kinematics is applied to relate the displacements  $\mathbf{u}$  with the strains resp. elongations of the bar resp. spring elements. These equations are partially nonlinear in  $L_1$ ,  $L_2$ ,  $H_1$ ,  $H_2$  and  $\mathbf{u}$ .

**Constitutive equations** Linear equations, which plug element forces and strains resp. elongations, are assumed. Hence, the constitutive equations are linear in  $k_{y,1}$ ,  $k_{y,2}$ ,  $k_c$ ,  $c_{A,1}$ ,  $c_{A,2}$ ,  $c_{N,12}$  und  $c_{N,21}$ .

**Equilibrium** Equilibrium of forces at joints ①, ②, ③ und ④ yield four independent nonlinear equations in  $\mathbf{u}$ :

$$\mathbf{G}(\mathbf{u}) = \mathbf{F}_{\text{int}}(\mathbf{u}) - \mathbf{F}_{\text{ext}} \stackrel{!}{=} \mathbf{0}. \quad (1)$$

The residual force vector  $\mathbf{G}$  is a vector-valued, continuously differentiable nonlinear function in  $\mathbf{u}$ .  $\mathbf{F}_{\text{int}}$  means the vector of internal forces and  $\mathbf{F}_{\text{ext}}$  denotes the vector of external forces. With regard to the parameter identification the nodal forces are assumed to be  $F_1 = \bar{P}_{11,i} L_2$  resp.  $F_2 = \bar{P}_{22,i} L_1$ .

**Solution** One may solve the nonlinear system of equations (Eq. (1)) for each set of test data  $i = 1, \dots, n_V$  by using a Newton-Raphson iteration scheme (equilibrium iteration), wherein the tangential stiffness matrix  $\mathbf{K}_T = \partial \mathbf{G} / \partial \mathbf{u}$  occurs. The corresponding stretching  $\boldsymbol{\lambda}_i$  is computed as

$$\boldsymbol{\lambda}_i = [\lambda_{11,i} \ \lambda_{22,i}]^T, \quad \lambda_{dd,i} = \lambda_{dd,i}(\mathbf{u}) = \frac{u_{d,i}}{L_d} + 1, \quad d = 1, 2. \quad (2)$$

## 5 ANISOTROPIC HYPERELASTIC MODEL

In an alternative approach, a woven fabric membrane material is presumed to be anisotropic hyperelastic. HOLZAPFEL assumes a form of an energy function for an anisotropically hyperelastic material with two families of fibres to be

$$\psi = \psi(\mathbf{C}, \mathbf{M}_{(1)}, \mathbf{M}_{(2)}) = \psi(\mathbf{Q}^T \mathbf{C} \mathbf{Q}, \mathbf{Q}^T \mathbf{M}_{(1)} \mathbf{Q}, \mathbf{Q}^T \mathbf{M}_{(2)} \mathbf{Q}). \quad (3)$$

$\psi$  is an isotropic tensor function in  $(\mathbf{C}, \mathbf{M}_{(1)}, \mathbf{M}_{(2)})$ , if Eq. (3) holds for all proper orthogonal transformation tensors  $\mathbf{Q}$  [10, pp. 273ff.].  $\mathbf{C}$  is the right Cauchy-Green deformation tensor. Hence, the energy is invariant w.r.t.  $\mathbf{C}, \mathbf{M}_{(1)}$  and  $\mathbf{M}_{(2)}$ , wherein the so-called structural tensors  $\mathbf{M}_{(d)} = \mathbf{a}_{(d)} \otimes \mathbf{a}_{(d)}$  ( $d = 1, 2$ ) specify the symmetries of the material. The directions of fibres are represented by  $\mathbf{a}_{(d)}$ . Such an energy can in general be formulated in terms of nine invariants. In most woven fabric materials the two families of fibres (warp resp. fill) can be assumed to be orthogonal,  $\mathbf{a}_{(1)} \cdot \mathbf{a}_{(2)} = 0$ . The orthogonality yields  $\psi$  to be a function of only the first seven invariants:

$$\begin{aligned} \psi &= \psi(\mathbf{C}, \mathbf{M}_{(1)}, \mathbf{M}_{(2)}) = \psi(I_1, I_2, I_3, J_4^{(1)}, J_5^{(1)}, J_4^{(2)}, J_5^{(2)}), \quad d = 1, 2 \quad (4) \\ I_1 &:= \text{tr}(\mathbf{C}), \quad I_2 := \text{tr}(\text{Cof} \mathbf{C}), \quad I_3 := \det(\mathbf{C}), \quad J_4^{(d)} := \text{tr}(\mathbf{C} \mathbf{M}_{(d)}), \quad J_5^{(d)} := \text{tr}(\mathbf{C}^2 \mathbf{M}_{(d)}) \end{aligned}$$

Amongst others, [2] derives an energy function which fulfils Eq. (4):

$$\begin{aligned} \psi &= \psi_{\text{iso}} + \sum_{d=1,2} \psi_{\text{ti}}^{(d)}, \quad d = 1, 2 \quad (5) \\ \psi_{\text{iso}}(I_1, I_3) &= c_1 \left( \frac{I_1}{I_3^{1/3}} - 3 \right) + \varepsilon_1 \left( I_3^{\varepsilon_2} + \frac{1}{I_3^{\varepsilon_2}} - 2 \right), \quad c_1 > 0, \quad \varepsilon_1 > 0, \quad \varepsilon_2 > 1, \\ \psi_{\text{ti}}^{(d)}(J_4^{(d)}) &= \begin{cases} \alpha_1^{(d)} (J_4^{(d)} - 1)^{\alpha_2^{(d)}} & \text{for } J_4^{(d)} > 1 \\ 0 & \text{for } J_4^{(d)} \leq 1 \end{cases}, \quad \alpha_1^{(d)} \geq 0, \quad \alpha_2^{(d)} > 1 \end{aligned}$$

Eq. (4) is an additive decomposition in an isotropic part  $\psi_{\text{iso}}$  and two discontinuous, transversal isotropic parts  $\psi_{\text{ti}}^{(d)}$ , each of them corresponding to a certain fibre family. The decomposition is motivated by constitution of a woven fabric material, which is made of a relatively weak matrix materials and two orthogonal families of stiff fibres [3,

p. 1021]. In [2] it is proved, that this energy function is convex in all arguments (polyconvexity) and therefore stable. The meaning of each of the seven material parameters  $\mathbf{M}_{\text{hyp}} := [c_1 \ \varepsilon_1 \ \varepsilon_2 \ \alpha_1^{(1)} \ \alpha_2^{(1)} \ \alpha_1^{(2)} \ \alpha_2^{(2)}]^T$  and the case distinction in Eq. (5) is explained in [2, pp. 6058, 6064]. Based on the energy function Eq. (5) second resp. first Piola-Kirchhoff stresses  $\mathbf{S}$  resp.  $\mathbf{P}$  as well as the material tangent tensor  $\mathbb{C}$  can be computed from the deformation state, which is assumed to be characterised by right Cauchy-Green deformation tensor  $\mathbf{C}$  resp. deformation gradient  $\mathbf{F}$  resp. right stretching tensor  $\mathbf{U}$  (see [3]):

$$\mathbf{S} = 2 \frac{\partial \psi(\mathbf{C}, \mathbf{M}_{(1)}, \mathbf{M}_{(2)})}{\partial \mathbf{C}} = \sum_{j,k=1}^3 S_{jk} \mathbf{e}_j \otimes \mathbf{e}_k, \quad \mathbb{C} = 4 \frac{\partial^2 \psi}{\partial \mathbf{C} \partial \mathbf{C}} \quad (6)$$

$$\mathbf{P} = \mathbf{F} \mathbf{S} = \sum_{j,k=1}^3 P_{jk} \mathbf{e}_j \otimes \mathbf{e}_k, \quad \mathbf{C} = \mathbf{F}^T \mathbf{F} = \mathbf{U}^2, \quad \mathbf{U} = \sum_{j,k=1}^3 \lambda_{jk} \mathbf{e}_j \otimes \mathbf{e}_k \quad (7)$$

$\mathbf{S}$  and  $\mathbb{C}$  pose the expressions for the corresponding constitutive model for an anisotropic hyperelastic material with two orthogonal families of fibres. This approach has been used in several publications, e.g. [17], [16], [3].

As described so far, the constitutive model is valid for a 3d continuum. Since the assumption of a 2d plane stress state ( $P_{j3} = P_{3j} = 0$ ,  $j = 1, 2, 3$ ) is reasonable for a woven fabric material, the constitutive model has still to be condensed. While neglecting shear deformation ( $\lambda_{jk} = \lambda_{kj} = 0$ ,  $j, k = 1, 2, 3$ ,  $\beta \neq \gamma$ ) and consequently obtaining no shear stresses ( $\Rightarrow S_{\beta\gamma} = S_{\gamma\beta} = P_{\beta\gamma} = P_{\gamma\beta} = 0$ ,  $\beta, \gamma = 1, 2$ ,  $\beta \neq \gamma$ ) of the woven fabric material, the remaining three deformation quantities – namely the stretches  $\lambda_{11}, \lambda_{22}, \lambda_{33}$  – can be computed from firstly the zero-stress condition in transversal direction and secondly two conditions with regard to the imposed loads in the biaxial tension test  $\bar{P}_{11,i} = \bar{N}_{1,i}/L$  resp.  $\bar{P}_{22,i} = \bar{N}_{2,i}/L$  (w.r.t. unit thickness). These three conditions are collected in a residuum vector:

$$\mathbf{R} = \mathbf{R}(\boldsymbol{\lambda}_i, \lambda_{33}) := \begin{bmatrix} P_{33} \\ P_{11} - \bar{P}_{11,i} \\ P_{22} - \bar{P}_{22,i} \end{bmatrix} \stackrel{!}{=} \mathbf{0}, \quad \boldsymbol{\lambda}_i = [\lambda_{11,i} \ \lambda_{22,i}]^T \quad (8)$$

The stretches can be computed for each set of test data  $i = 1, \dots, n_V$  by applying a linearisation and performing a subsequent Newton-Raphson iteration scheme. Herein, the Jacobian of  $\mathbf{R}$  w.r.t. the stretches can be calculated considering the case distinction in Eq. (5).

## 6 PARAMETER IDENTIFICATION PROCESSES

In order to identify the parameters of the microstructural model, resp. the parameters of the anisotropic hyperelastic model in such a way, that they fit the load-stretch data from the biaxial tension test (see Figure 5), two different inverse problems are formulated analogously. Since the number of test data points is in general greater than the number

of identifiable model parameters, a problem of parameter identification is overdetermined and therefore is treated by methods of optimisation. Subsequently, the optimisation problem is formulated (Section 6.1), the used algorithms are mentioned briefly (Section 6.2) and the resulting model parameters are presented and discussed (Section 6.3).

## 6.1 Formulation and solution of the inverse problems

The design vector  $\mathbf{s}_{\text{mic}}$  resp.  $\mathbf{s}_{\text{hyp}}$  contain the model parameters  $\mathbf{M}_{\text{mic}}$  resp.  $\mathbf{M}_{\text{hyp}}$ , which shall be identified. The particular objective function  $f_{\text{mic}}$  resp.  $f_{\text{hyp}}$  equals the sum of squared errors and yields

$$f_{(\cdot)} = f_{(\cdot)}(\boldsymbol{\lambda}_i(\mathbf{s}_{(\cdot)}), \dots, \boldsymbol{\lambda}_{n_V}(\mathbf{s}_{(\cdot)})) = \sum_{i=1}^{n_V} \left[ w_i \underbrace{(\lambda_{11,i} - \bar{\lambda}_{11,i})^2}_{\substack{i\text{-th squared error} \\ \text{in warp direction}}} + w_i \underbrace{(\lambda_{22,i} - \bar{\lambda}_{22,i})^2}_{\substack{i\text{-th squared error} \\ \text{in fill direction}}} \right]. \quad (9)$$

$\bar{\lambda}_{dd,i}$  is the  $i$ -th measured stretch.  $\lambda_{dd,i}$  is the corresponding computed stretch (see Eq. (2) resp. Eq. (8)).  $w_i$  is the  $i$ -th weighting factor ( $w_i \in \mathbb{R}^+$ ). The particular least-squares optimisation problem yields

$$\min_{\mathbf{s}_{(\cdot)}} f_{(\cdot)}(\boldsymbol{\lambda}_i(\mathbf{s}_{(\cdot)}), \dots, \boldsymbol{\lambda}_{n_V}(\mathbf{s}_{(\cdot)})) . \quad (10)$$

## 6.2 Substantial aspects towards solution of the inverse problems

The necessary condition for stationarity of the particular problem Eq. (10) is:

$$\nabla_{\mathbf{s}_{(\cdot)}} f_{(\cdot)} \stackrel{!}{=} \mathbf{0} \Leftrightarrow \mathbf{s}_{(\cdot)} \text{ is a minimum, maximum or saddle point} \quad (11)$$

$\nabla_{\mathbf{s}_{(\cdot)}} f_{(\cdot)}$  is the particular gradient of  $f_{(\cdot)}$  w.r.t.  $\mathbf{s}_{(\cdot)}$  and therefore it contains first derivatives  $d\lambda_{dd,i}/ds_{(\cdot),j}$ . For the microstructural model, where  $\lambda_{dd,i} = \lambda_{dd,i}(\mathbf{s}_{\text{mic}}, \mathbf{u}(\mathbf{s}_{\text{mic}}))$ , the chain rule yields

$$\frac{d\lambda_{dd,i}}{ds_{\text{mic},j}} = \frac{\partial \lambda_{dd,i}}{\partial s_{\text{mic},j}} + \left( \frac{\partial \lambda_{dd,i}}{\partial \mathbf{u}} \right)^T \frac{\partial \mathbf{u}}{\partial s_{\text{mic},j}}, \quad d = 1, 2.$$

The implicit derivatives  $\partial \mathbf{u} / \partial s_{\text{mic},j}$  are computed as analytical expressions by performing a direct sensitivity analysis. The explicit derivatives result from Eq. (2) without further explanations. For the hyperelastic model, the required derivatives can be computed analogously.

The particular solution vector  $\mathbf{s}_{(\cdot)}^*$  is computed based on linearisation of Eq. (11) and subsequent application of an iteration scheme.  $\mathbf{s}_{(\cdot)}^*$  is a (local) minimum of Eq. (10), if and only if the sufficient condition for a minimum

$$\mathbf{s}_{(\cdot)}^{*T} \mathbf{H}_{f_{(\cdot)}, \mathbf{s}_{(\cdot)}, k^*} \mathbf{s}_{(\cdot)}^* > 0 \Leftrightarrow \mathbf{H}_{f_{(\cdot)}, \mathbf{s}_{(\cdot)}, k^*} \text{ positive definite}$$

is fulfilled in addition to Eq. (11). Herein,  $\mathbf{H}_{f_{(\cdot)}, \mathbf{s}_{(\cdot)}, k^*}$  means the particular Hessian matrix of  $f_{(\cdot)}$  w.r.t. to  $\mathbf{s}_{(\cdot)}$  evaluated in the  $k^*$ -th iteration step. The Hessian matrix occurs in

the linearisation of Eq. (11) as well. It contains all second derivatives of  $f_{(\cdot)}$ , which can be computed (numerically efficient) as analytical expressions analogue to the first derivatives. Moreover, the particular inverse Hessian matrix  $\mathbf{H}_{f_{(\cdot)},s_{(\cdot)},k}^{-1}$  occurs. Therefore it is necessary, however by no means trivial, to ensure a regular Hessian matrix  $\mathbf{H}_{f_{(\cdot)},s_{(\cdot)},k}$  during the entire iteration process. Amongst few strategies, a Levenberg-Marquardt algorithm is applied for parameter identification of the microstructural model. There is a close relation between the choice of design space (model parameters) and the regularity of the Hessian matrix.

For the parameter identification of the hyperelastic model, a Sequential Quadratic Programming algorithm with an Active-Set strategy (e.g. [15, Ch. 18]) is applied, in order to handle constraints in Eq. (5). Initial values are obtained by performing coarse genetic algorithm computations with slightly constrained design spaces.

### 6.3 Results of parameter identification processes

The design vector for the microstructural model is defined as

$$\mathbf{s}_{\text{mic}} = [L_2 \ H_1 \ H_2 \ k_{y,1} \ k_{y,2} \ c_{N,12} \ c_{N,21} \ c_{A,1} \ c_{A,2} \ k_c]^T.$$

The reference quantity  $L_1$  is set as  $L_1 := 1$  in order to perform a numerical computation. As argued on p. 6, there is no need to specify a certain physical unit. The design vector for the hyperelastic model is defined as

$$\mathbf{s}_{\text{hyp}} = [c_1 \ \varepsilon_1 \ \varepsilon_2 \ \alpha_1^{(1)} \ \alpha_2^{(1)} \ \alpha_1^{(2)} \ \alpha_2^{(2)}]^T.$$

The two analogous optimisation problems (Eq. (10)) are solved as described before. The identified model parameters are (rounded to five digits):

$$\mathbf{M}_{\text{mic}}^* := \begin{bmatrix} \mathbf{s}_{\text{mic}}^* \\ L_1 \end{bmatrix} = \begin{bmatrix} L_2^* \\ H_1^* \\ H_2^* \\ k_{y,1}^* \\ k_{y,2}^* \\ c_{N,12}^* \\ c_{N,21}^* \\ c_{A,1}^* \\ c_{A,2}^* \\ k_c^* \\ L_1 \end{bmatrix} = \begin{bmatrix} 0.78431 [L_1] \\ 0.10891 [L_1] \\ 0.073070 [L_1] \\ 2292.5 \text{ kN} \\ 2132.3 \text{ kN} \\ 18.259 \text{ kN}/[L_1] \\ 16.680 \text{ kN}/[L_1] \\ -115.72 \text{ kN}/[L_1] \\ -90.025 \text{ kN}/[L_1] \\ 162.43 \text{ kN} \\ 1.0 \end{bmatrix}, \quad \mathbf{M}_{\text{hyp}}^* := \begin{bmatrix} c_1^* \\ \varepsilon_1^* \\ \varepsilon_2^* \\ \alpha_1^{(1)*} \\ \alpha_2^{(1)*} \\ \alpha_1^{(2)*} \\ \alpha_2^{(2)*} \end{bmatrix} = \begin{bmatrix} 100.84 \text{ kN/m}^2 \\ 473.27 \text{ kN/m}^2 \\ 9.6713 [-] \\ 326.15 \text{ kN/m}^2 \\ 3.2936 [-] \\ 294.94 \text{ kN/m}^2 \\ 3.3357 [-] \end{bmatrix}.$$

The microstructural model with  $\mathbf{M}_{\text{mic}}^*$  is denoted by MATmic, the hyperelastic model with  $\mathbf{M}_{\text{hyp}}^*$  is denoted by MATHyp. Figure 5 shows the load- and stretch curves of the measured data in comparison with the computed results by using material models MATmic resp. MATHyp.

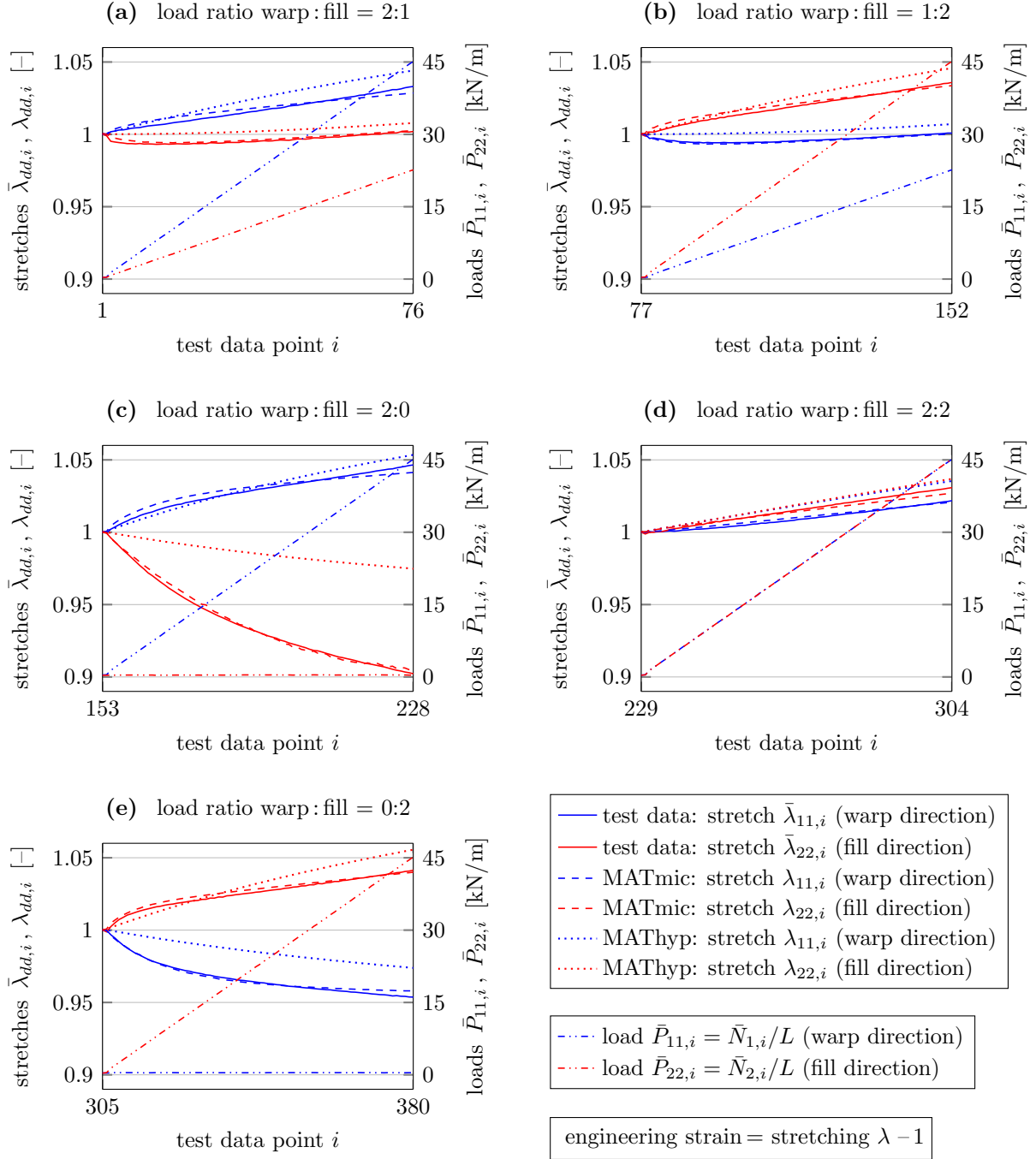


**Figure 5:** Load- and stretch curves – comparison between measured data from the biaxial tension test and computed results by using material models MATmic resp. MATHyp

## 7 DISCUSSION

Regarding  $\mathbf{M}_{\text{mic}}^*$  the dimensions  $L_2^*$ ,  $H_1^*$  and  $H_2^*$  show reasonable ratios in comparison to typical dimension ratios of woven fabrics. For example, the height of the microstructural model  $H_1^* + H_2^*$  is about a fifth of the dimension  $L_1$ . However, a direct physical interpretation of the spring stiffnesses  $c_{A,1}^*$  and  $c_{A,2}^*$  in  $\mathbf{M}_{\text{mic}}^*$  (Eq. (12)) is not given (negative values). As long as the input forces  $F_d$  are positive (tension forces) the potential of the microstructural model remains strictly convex in  $u_1, u_2, u_3, u_4$  and therefore has one unique minimum (stable equilibrium state). In order to ensure physically interpretable parameter values, one may consider constraining the design space (constrained optimisation). By means of successively leaving out one load ratio in the parameter identification, the microstructural model reveals a satisfying robustness.

Concerning  $\mathbf{M}_{\text{hyp}}^*$  the exponents of the anisotropic parts of energy function Eq. (5)  $\alpha_2^{(1)*}$  and  $\alpha_2^{(2)*}$  as well as  $c_1^*$  and  $\varepsilon_2^*$  show values, which fit well in terms of range compared to parameters given in the literature [16, 3].

Considering Figure 5, the measured and computed stretchings with MATmic match well over all considered load ratios. This is confirmed by a coefficient of determination of  $R^2 = 0.996$ . Hence, the measured data may almost completely be represented by the microstructural model. Comparing the measured and computed stretchings with MATHyp, the representation is widely satisfactory for load ratios 2:0, 2:2 and 0:2, though it is not for load ratios 2:1 and 1:2. This is reflected by a coefficient of determination of  $R^2=0.604$ .

The deviations between MATHyp and MATmic are significant. Compared to the chosen hyperelastic model the microstructural model presents a more accurate description of the elastic deformation behaviour. Considering the reasonable effort for the parameter identification the presented microstructural model is a profound and practicable modelling approach.

## Part II: An extended numerical approach for form finding and cutting patterning of membranes

### 1 INTRODUCTION

The common approach of engineering practice is to determine the cutting patterning geometry as a postprocessing step of form finding using a sequence of independent geometrical and mechanical computation steps. Therefore, an incomplete mechanical description between the unstressed cutting patterning and stressed equilibrium geometry exists. Since the equilibrium geometry of the prestressed membrane depends directly on the unstressed cutting patterning geometry, a closed mechanical approach is in demand. Such an approach is developed in the present contribution. In contrast to the approach of DIERINGER [8] the presented approach solves the form finding and cutting patterning

problem simultaneously. To this end, two topologically identical meshes are defined. One mesh represents the cutting patterning and the other one the equilibrium geometry. The mechanical behaviour is described by a Total Lagrangian finite element formulation. For the strain-stress relationship the microstructural model derived in Part I is used. The desired stress distribution does not lead to unique geometries of cutting patterning and equilibrium geometry. Defining a least-squares problem of stresses and shear strains as a weighted sum, an optimisation formulation leads to a unique solution. To keep the algorithm numerically stable, the terms that contain the shear strains have to be considerably large. Analogously to the starting point of Update Reference Strategy [4], the presented approach is from a mathematical point of view singular in the tangential plane. Internal nodes of two associated meshes can move without changing any mechanical quantities. Several strategies can be developed to overcome this issue. A robust strategy is to describe the movement of internal nodes of the cutting patterning mesh by means of movement of edge nodes of the same segment. Advantages of this approach are: Firstly, it accounts for the shear deformation of the woven fabric, which occurs during transformation of the plane cutting geometry to the doubly curved surface. Secondly, the ending of membrane fibres at inclined oriented cutting edges is considered. Moreover, it regards material nonlinearities by applying the microstructural model derived in Part I (see Part I, Chapter 4). On the other hand the definition of the seam layout at the beginning of form finding is disadvantageous.

## 2 OPTIMISATION APPROACH FOR FORM FINDING AND CUTTING PATTERNING OF MEMBRANES

The basic idea of the approach is to formulate an optimisation problem in which both the geometries of the equilibrium and cutting patterning configuration are initially unknown. The two configurations are considered as current resp. reference configuration. The design objectives are minimum deviations from prescribed stresses in warp and fill direction along with minimum shear deformation. The equilibrium equations are introduced into the optimisation problem as equality constraints. Additional design criteria can be formulated (e.g. geometry of seam lines, stress states etc.).

Equilibrium equations are used in Total Lagrange finite element formulation with 4-node membrane elements (see Figure 6). Green Lagrange strains are computed from the deformation gradient in each Gauss point. From this, the stretches of the microstructural model are calculated and a structural analysis is performed. The forces as well as the derivatives of forces of the microstructural model w.r.t. the displacements yield the constitutive equations of the material.

The optimisation problem is

$$\min_s f \quad \text{s. t.} \quad \mathbf{h}(\mathbf{s}) = \begin{bmatrix} \mathbf{R}_{CC} & \mathbf{R}_{RC} & \mathbf{G}_{CC} & \mathbf{G}_{RC} & \mathbf{F}_{CC} \end{bmatrix}^T \stackrel{!}{=} \mathbf{0}.$$

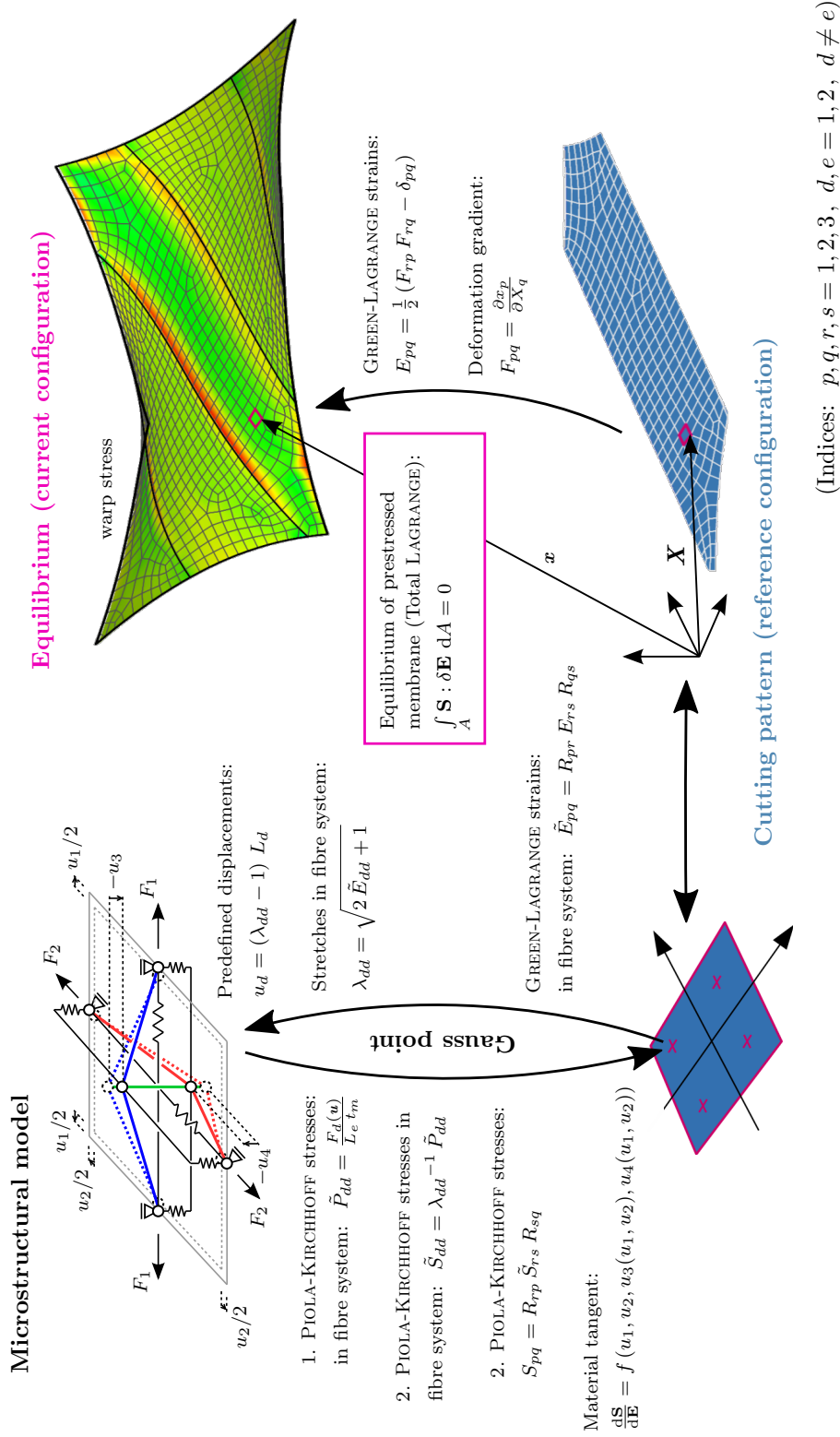


Figure 6: Embedment in finite element approach

The design vector  $\mathbf{s}$  contains the nodal coordinates of all free nodes in the current configuration as well as those coordinates in the reference configuration that are in the cutting plane. Hence, the dimension of the design space is  $\dim \mathbf{s} = 3 \cdot n_{n,CC} + 2 \cdot n_{n,RC}$ .

The objective function of the optimisation problem is:

$$f = f(\mathbf{s}) = \sum_{m=1}^{n_G} \left[ w_{11} \left( \tilde{S}_{11,m} - \bar{S}_{11,m} \right)^2 + w_{22} \left( \tilde{S}_{22,m} - \bar{S}_{22,m} \right)^2 + w_{12} \left( \tilde{\phi}_{12,m} - \bar{\phi}_{12,m} \right)^2 \right]$$

$w_{11}, w_{22}, w_{12} \in \mathbb{R}^+$ : Weighting factors

$n_{n,RC}, n_{n,CC}$ : Number of free nodes in the reference resp. current configuration

$\tilde{S}_{11,m}, \tilde{S}_{22,m}$ : Computed second Piola-Kirchhoff stresses at Gauss point  $m = 1, \dots, n_G$

$\bar{S}_{11,m}, \bar{S}_{22,m}$ : Prescribed second Piola-Kirchhoff stresses at Gauss point  $m = 1, \dots, n_G$

$\tilde{\phi}_{12,m}$ : Computed shear angle at Gauss point  $m = 1, \dots, n_G$

$\bar{\phi}_{12,m}$ : Prescribed shear angle at Gauss point  $m = 1, \dots, n_G$

In order to obtain an optimisation problem whose approximation remains regular during computation, further constraints are required along with the equilibrium equations. Amongst others, the following equality constraints  $\mathbf{h}(\mathbf{s})$  are reasonable:

- The Dirichlet boundary conditions in the current configuration;
- the fixation of the reference configuration in plane;
- the geometric position and the equilibrium of the nodes at the inner edges (seam lines) in the current or reference configuration;
- the subdivision of inner as well as free edges.

Avoiding singularities in the tangential plane is explained in the next Section in more detail.

As mentioned, the equilibrium equations are handled as equality constraints. This avoids numerically expensive implicit derivatives. Therefore, it is reasonable to plug first derivatives as well as second derivatives into the optimisation algorithm. Thus, quadratic convergence is achieved under appliance of the algorithm IPOPT [19].

### Strategies for stabilisation of cutting configuration

In order to avoid singularities in the tangential plane, several strategies can be used: Firstly, the stabilisation is possible by means of geometrical constraints that demand for elements with (nearly) quadratic shape. This approach gives rise to a multicriteria optimisation. Defining suitable weighting factors is a challenging task. Secondly, movement of inner nodes in the cutting configuration are coupled to movements of edge nodes by using shape basis vectors. This is a common technique to preserve suitable meshes in form

optimisation problems. Thirdly, the movements of the inner nodes can be controlled by formulating an additional mechanical problem. This technique is known as deformation-based shape basis vectors approach in form optimisation and leads to additional equality constraints.

Due to its robustness, the third strategy is used.

### 3 EXAMPLE

Figure 7 below shows an exemplary conic membrane structure. Due to their curvature, such membranes are characterised by relatively high stresses in warp direction. For the sake of simplicity, the problem is reduced to a quarter model and symmetric boundary conditions are considered.

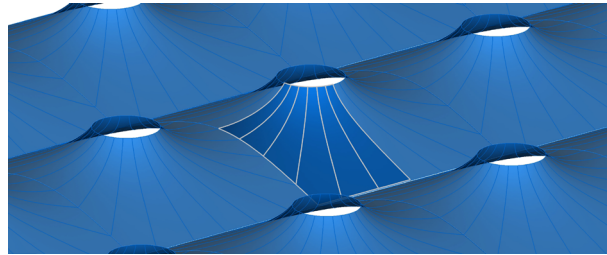


**Figure 7:** Geometry model of a conic membrane (detail)

Based on the common approach described before, the warp direction is assumed to be radial and the shear deformation is not considered. Though, the necessity of shear deformation in order to obtain a doubly curved surface from plane cutting segments is obvious. Results by using the common approach are compared to results that are obtained applying the approach presented in this contribution. Figure 8a shows the distribution of warp stress while prescribing  $\bar{S}_{11,m} = \bar{S}_{22,m} = 4.0 \text{ kN/m}^2$  in comparison. The results confirm that a homogeneously distributed stress state is not possible when considering the occurrence of shear deformation.

As additional load, a uniformly distributed snow load of  $0.85 \text{ kN/m}^2$  is imposed. Figure 8b shows the warp stresses in comparison, which reveal major deviations. In the presented approach ending of membrane fibres at the cutting edges are considered, which leads to stress concentrations nearby the cutting edges in the upper zones. In the valley zones of the cutting edges warp yarns withdraw load-carrying and therefore stresses are relatively low. This is caused by the lack of shear stiffness and a slightly destabilising effect due to fill stress.

### CONCLUSION

**Part I** Woven fabric membranes are characterised by a pronounced material and geometrically nonlinear behaviour. Part I of this contribution focuses on two different material modelling approaches. Firstly, an established microstructural model is presented

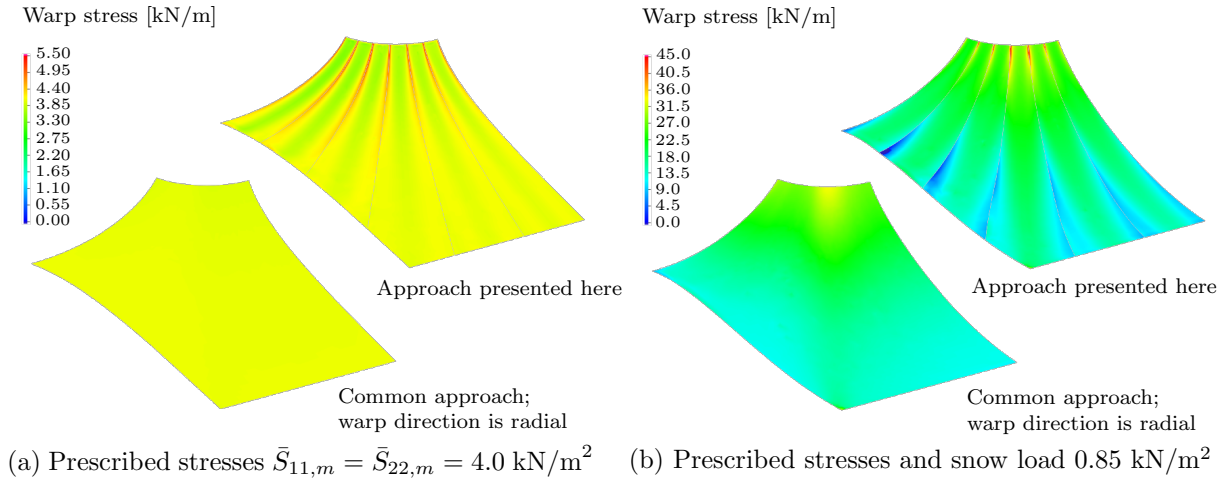


**Figure 8:** Warp stress [kN/m] – comparison of common approach to approach presented here

and enhanced by introducing transverse spring elements, considering the coating stiffness. Secondly, an established anisotropic hyperelastic model is given. The model parameters of both models are gained by inverse computations w.r.t. to measured data from a biaxial tension test using optimisation. Comparing the results of the microstructural model and the chosen anisotropic hyperelastic material model, the microstructural model is assessed as more suitable. Using a different energy function for the hyperelastic model could probably improve results of this approach. Moreover, using a larger test data set would be an interesting task in order to ensure robustness.

**Part II** In order to consider effects arising from nonlinear material behaviour, from shear deformation of the woven fabric during transformation in a doubly curved surface as well as from ending of material fibres at the cutting edges, form finding and cutting patterning has to be treated in a coupled computation. The present contribution presents an approach for consideration of the coupled problem as an optimisation problem, in which both the reference as well as the current configuration are initially unknown. In order to avoid singularity in the tangential plane of the surface, a shape basis vector technique is applied.

Based on an exemplary conic membrane structure, major deviations of the common approach in comparison to the presented approach are revealed.

## ACKNOWLEDGEMENT

The work has been partially funded by German Research Foundation (DFG) as a part of the Collaborative Research Centre (SFB) 1244 "Adaptive Envelopes and Structures for the Built Environment of the Future"/project A04 under grant number SFB 1244/1 2017. Moreover, thanks to Dipl.-Ing. Katja Bernert from Low and Bonar GmbH (former Mehler Technologies GmbH, Fulda/Germany) for providing the test data from the biaxial tension test.

## REFERENCES

- [1] Ballhause, D.: *Diskrete Modellierung des Verformungs- und Versagensverhaltens von Gewebemembranen*. Dissertation, Universität Stuttgart, 2007.
- [2] Balzani, D.; Neff, P.; Schröder, J.; Holzapfel, G. A.: *A polyconvex framework for soft biological tissues. Adjustment to experimental data*. International Journal of Solids and Structures 43(2006), pp. 6052-6070.
- [3] Balzani, D.; Gruttmann, F.; Schröder, J.: *Analysis of thin shells using anisotropic polyconvex energy densities*. Computer Methods in Applied Mechanics and Engineering 197(2008), pp. 1015-1032.
- [4] Bletzinger, K.-U.; Ramm, E.: *A general finite element approach to the form finding of tensile structures by the updated reference strategy*. International Journal of Space Structures 14, 2(1999), pp. 131–145.
- [5] Blum, R.; Bidmon, W.: *Spannungs-Dehnungs-Verhalten von Bautextilien: Theorie und Experiment*. SFB 64, Mitteilungen 74/1987, Universität Stuttgart, 1987.
- [6] Bögner, H.: *Vorgespannte Konstruktionen aus beschichteten Geweben und die Rolle des Schubverhaltens bei der Bildung von zweifach gekrümmten Flächen aus ebenen Streifen*. Dissertation, Institut für Werkstoffe im Bauwesen der Universität Stuttgart, 2004
- [7] Bridgens, B.; Gosling, P. D.: *Interpretation of results from the MSAJ 'Testing Method for Elastic Constants of Membrane Materials'*. In: Oñate, E.; Kröplin, B. (Eds.): *Proc. of et Symposium*. Sofia, 2010, pp. 49–57.
- [8] Dieringer, F. H.: *Numerical Methods for the Design and Analysis of Tensile Structures*. Dissertation, Lehrstuhl für Statik, Technische Universität München, 2014
- [9] Feyel, F.: *A multilevel finite element method ( $FE^2$ ) to describe the response of highly non-linear structures using generalized continua*. Computer Methods in Applied Mechanics and Engineering 192, 28–30(2003), pp. 3233–3244.
- [10] Holzapfel, G. A.: *Nonlinear Solid Mechanics. A Continuum Approach for Engineering*. John Wiley & Sons Ltd, Chichester, England, 2000.
- [11] Kaiser, B.; Haug, E.; Pyttel, T.; Duddeck, F.: *A generalized coupled multi-scale approach for the simulation of textile membranes*. In: Oñate, E.; Bletzinger, K.-U.; Kröplin, B. H. (Hrsg.): *VII International Conference on Textile Composites and Inflatable Structures*. Barcelona/Spain, 2015, pp. 433–444

- [12] Kawabata, S.; Niwa, M.; Kawai, H.: *The finite-deformation theory of plain-weave fabrics Part I: The biaxial-deformation theory*. The Journal of the Textile Institute 64, 1(1973), pp. 21–46.
- [13] Meffert, B.: *Mechanische Eigenschaften PVC-beschichteter Polyestergewebe*. Dissertation, Fakultät für Maschinenwesen der Rheinisch-Westfälischen Technischen Hochschule Aachen, 1978
- [14] Membrane Structures Association of Japan: *MSAJ/M-02-1995: Testing Method for Elastic Constants of Membrane Materials*. 1995.
- [15] Nocedal, J.; Wright, S. J.: *Numerical Optimization*. Springer, New York, NY, USA, 2nd edition, 2006.
- [16] Schröder, J.; Balzani, D.; Stranghöner, N.; Uhlemann, J.; Gruttmann, F.; Saxe, K.: *Membranstrukturen mit nicht-linearem anisotropem Materialverhalten - Aspekte der Materialprüfung und der numerischen Simulation*. Der Bauingenieur 86, 9(2011), pp. 381–389
- [17] Schröder, J.; Balzani, D.; Niesters, C.: *Modellierung dünner Schalen mit hyperelastischem Materialverhalten*. Essener Membranbau Symposium 2014, Essen, 2014.
- [18] Uhlemann, J.; Stranghöner, N.: *Einfluss fiktiver elastischer Konstanten von textilen Gewebemembranen in der Tragwerksanalyse von Membranstrukturen*. Stahlbau 82, 9(2013), pp. 643–651.
- [19] Wächter, A.; Biegler, L. T.: *On the Implementation of a Primal-Dual Interior Point Filter Line Search Algorithm for Large-Scale Nonlinear Programming*. Mathematical Programming 106, 1(2006), pp. 25–57.

## CHALLENGES OF THE IMPLEMENTATION OF MEMBRANE STRUCTURES INTO BIM

GREGOR GRUNWALD\*, ANDRÉ IHDE†

\* Pfeifer Seil- und Hebetchnik GmbH  
Dr.-Karl-Lenz-Str. 66, 87700 Memmingen, Germany  
E-mail: info@pfeifer.de, Internet: <http://www.pfeifer.info>

† Pfeifer Seil- und Hebetchnik GmbH Memmingen;  
Technische Universität München,  
Lehrstuhl für Tragwerksplanung Prof. Dr.-Ing. Rainer Barthel

**Key words:** BIM, Membrane Structures, IFC

**Summary.** This document presents the current situation of handling membrane structures within the BIM method, points out necessary steps to fully implement membrane structures into BIM and explains the benefit of an implementation.

### 1 INTRODUCTION TO BIM

In the age of industrialisation 4.0, dynamic processes of information and communication technology transform the work processes through computerisation. In the construction industry, this type of information-fusion is going to be implemented by the BIM method.

BIM is a communicative way of working, which makes it possible to work, plan and build together with all project participants from different disciplines and trades. The digital 3D model is at the centre of the planning process, as an anticipation of the spatial construction.

In addition to the already mentioned communicative cooperation method, the other important characteristic of the BIM idea is the phase-interrelated processing of the model, from the design to the approval phase to execution planning and construction. Even the operation phase and dismantling of the building could be taken into account. The method should enable a nearly loss-free information exchange between all involved parties <sup>1</sup>.

This article is focusing on the implementation of Membrane Structures into BIM to reach the mentioned benefits of the BIM method when planning a Membrane Structure and continues and extend the concept papers presented by Lin et al. <sup>2,3</sup>.

### 2 REPRESENTATION OF STRUCTURES IN BIM

Using the BIM method, all relevant information are linked to individual elements within the BIM model. The individual elements represent structural components of the overall

structure as 3D solid bodies, surfaces or curves.

3D solid bodies and surfaces are flexible, based on the parametric concept of the BIM method. Solids and areas can be defined by using boundary representation, Non-Uniform Rational B-Spline, polygon mesh or other modelling technics. Besides the geometry the relation between the unique geometries are implemented as references within the BIM model to allow the parametric approach as well as a common reference system. This reference can be global and local coordinate systems, individual grid lines or reference planes.

In addition to these geometrical data also alphanumeric information can be attached to each BIM element like area data, specifications, naming of elements, product data, costs, time, technical standards - in short: component and project-specific data, like the value of the door width for example. This value directly communicates with the graphical wall opening. Geometric and alphanumeric data are linked to one another. Graphical changes to the door width will automatically change the appropriate value in the database.

Using the BIM method for both geometric and alphanumeric data, a format is available, which allows collaboration via a model-based, spatial and component-related data exchange. It also allows the joint storage of data together with their relationship. ISO 16739 describes this file-based and standardised interface, the Industry Foundation Classes (IFC). IFC is a data format for the manufacturer-neutral exchange of digital building models 4. IFC defines the syntax for all data of the model. Thanks to the open accessibility of this data structure and the associated neutrality, IFC has become the basis for almost all public building projects, which BIM obligates.

### **3 CURRENT SITUATION OF HANDLING MEMBRANE STRUCTURES IN BIM**

Currently the setup of a BIM model is time-consuming, inefficient and follows these working steps: First, the geometry of the various structural elements must be generated and linked to the reference systems like coordinate systems, levels or other reference elements. This generation can be done element by element or using programming interfaces like Dynamo, Grasshopper or API-based text-based programming languages. Problems occur if geometries were generated by different software packages rather than the final BIM environment, which is mostly the case.

The IFC format currently does not include all relevant geometric description and proprietary formats like step, iges or dwg. It often shows problems referring the proper geometrical alignment and transfer into structural families of elements or the IFC-format is simply not available in the external packages. This issue must be solved by positioning and linking external element more or less manually within the final environment.

The next step is the integration of semantic information - a very time-consuming approach, especially because non-standard elements or tailored families have to be used. Non-systems internal plug-ins exist to automate the input of relevant data from external tables like Excel sheets. These plug-ins use programming interfaces like API's to include the semantic information into the BIM model.

To fully benefit from the BIM idea also information for project management coordination (time, other resources and so forth), data for the installation process as well as data for facility management purposes must be implemented and related within the BIM model of Membrane Structures.

#### **4 IMPLEMENTATION OF MEMBRANE STRUCTURES AND CABLES IN THE BIM ENVIRONMENT**

To simplify the planning process of Membrane Structures and to benefit from the advantages of the BIM method Membrane Structures need to be implemented in the BIM environment.

For the practical implementation, the description of classified component semantics is required. This description is the base on which the BIM method develops its strength and quality of interoperability during data exchange. The key to realizing this interoperability is the classification of components and its properties.

At the moment, there are various approaches around the world for the collection of structured product data. One such approach is, for example, the Construction Operations Information Exchange (COBie) format or the Product Data Templates (PDT), which provide the necessary information about products. In principle, it is important to categorize and classify the products to allow comparability of products from different manufacturers. In Germany, the DIN SPEC 91400 attempts to build an IFC-compliant component classification indirect connection to the performance specifications according to the *Standardleistungsbuch für das Bauwesen* (StLB), in which construction services for tendering, allocation and invoicing are described <sup>5,6</sup>.

For many components a classification is already developed and products have been depicted so that these elements can be used as ready-made BIM objects in the planning process. However, this does not apply to the components required for membrane structures so far. First of all, a general data concept for Membrane Structures is needed, as proposed in the following chapter.

## 5 DATA CONCEPT

Membrane Structures can be reduced to a few standard elements:

- The membrane surface, segmented into individual membrane panels with welding seams
- The border connection elements such as corner plates, clamping profiles and coupling elements
- Embedded and boundary cables

Following the BIM structure, each element has to be described by geometric and alphanumeric data.

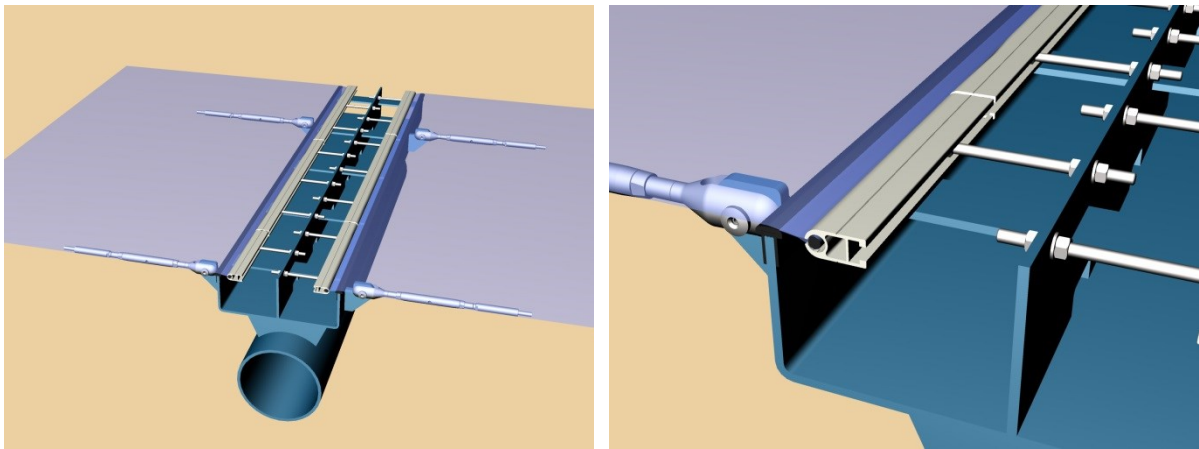


Fig. 1a,b: Membrane Construction Detail showing all mentioned standard elements such as membrane surface, profile and cable support.

### 5.1 Geometric Data

Currently, geometric data of membrane surfaces represent a simplification of the structure. No highly detailed geometries, but a simplification of the shape as a function of the level of detail (LOD) is the standard illustration for most membrane structures in BIM<sup>7</sup>. Further consideration directs towards derivation of the workshop design and more precise analyses and will require higher detailed models (up to LOD 400/500). The idea behind is that not every BIM model of a membrane structure needs the same level of detail. The level of detail reaches from LOD 100, only system lines of used structural elements, up to the highly detailed description of every connection element following the “as build” geometry of a structure (LOD 500). A model used for coordination of different trades or visualization does not necessarily need the same depth as a model used for the manufacturing process and the derivation of workshop drawings (LOD400)

Membrane structures significantly change their geometries under different permanent and variable loads which lead to discrepancies between the perfect initial geometry and the gravity

loaded and pre-tensioned structure. For most planning steps, the perfect geometry is required, but for others (i.e. installation planning) the deformed structure might be needed. Therefore different state-geometry descriptions within one model are needed.

In addition, the structure will require a flexible parametric representation of the membrane surface including local coordinate and reference systems. The reference systems would allow the linking of the all connected elements like welds, boundary cables or edge connection. State of the art is to represent membrane fields as individually inflexible polygon meshes only.

The need of a flexible parametric representation also applies for border connection elements. How this dynamic adaption to geometry changes could be implemented is shown in the Grasshopper code provided by the University Budapest<sup>8</sup>. These real-time algorithms are visualizing detail structures in Rhino such as corner plates, allowing constant alteration of the base geometry until the user wishes to freeze the model.

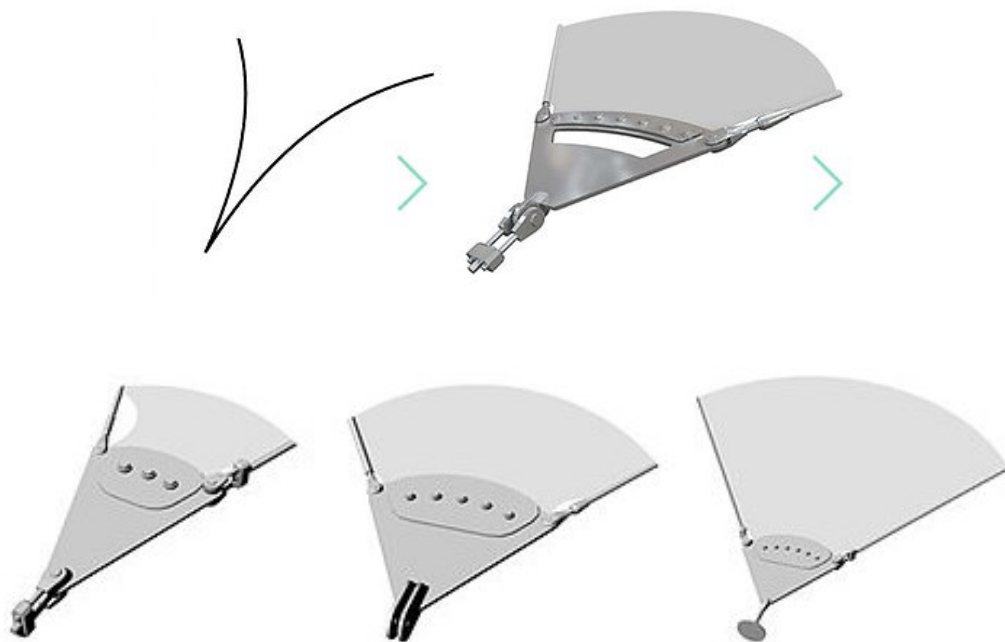


Figure 2 a-e: “Basic Corner Script” published at [www.membranedetail.com](http://www.membranedetail.com)<sup>8</sup>

The currently used representation of cables as polylines is imprecise and should be improved by using 3d splines. In general, cables follow freeform-curves as a result of forces, perpendicular to the center line of the cables. To allow connection of cable clamps and other cable attachments, a local coordinate system following the direction of the spline should be defined and implemented (Fig. 3).

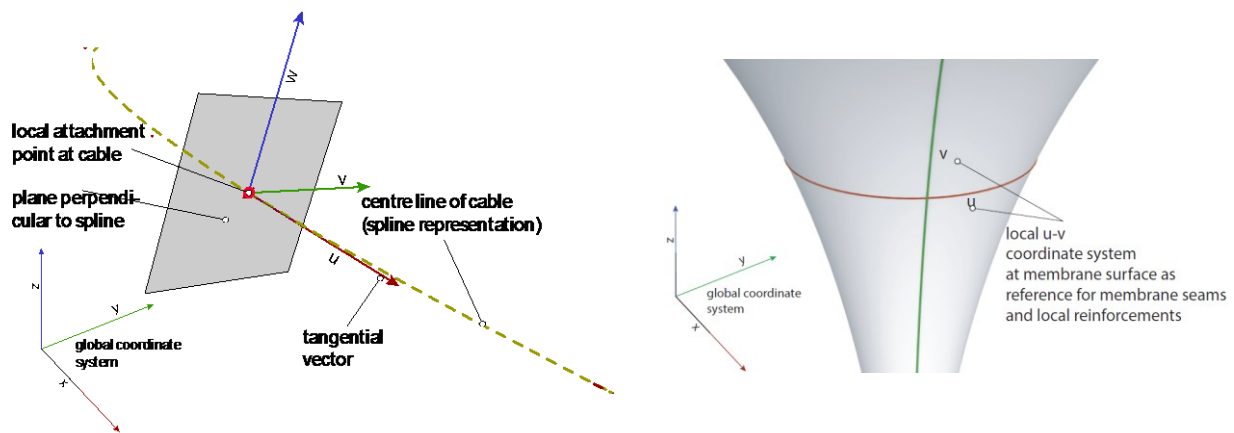


Figure 3a, b: Local reference system for cable attachments and membrane surface

## 5.2 Alphanumeric Data

In addition to geometric data relevant information can also be stored as alphanumeric data. The alphanumeric data can be divided into structured and unstructured data. Unstructured data is mostly manufacturer information, which is provided in any format (data sheets, assembly instructions, approval document). Since the format and thus the content is not determined, there is no precise definition of the unstructured data.

The following list contains aspects of information relevant for membrane surfaces:

Product data:	Type, Mesh/Solid, Base fabric material, Coating, Total Weight, Thickness, Width, Tensile strength (warp/weft), Tear resistance (warp/weft), Adhesion, Translucency, Flame retardancy, VLT, SHGC, Youngs modulus (warp/weft)
Geometric data:	Area, Curvature (Description as a NURBS-surface or poly mesh, nodes should be define further detail alignment (edge details, corner details, drainage elements) seams should be depicted as splines or polylines
Design data:	No of Edges, Edge detail, No. of Corners, Corner detail, No of Highpoints, Highpoint Detail, No of Suction Lines, Suction Detail, No of Cable support, Cable pocket detail, No. of seam lines, seam line width, keder material, keder diameter
Production data:	Producer, Production Date, Batch No., Time, Status
Fabrication data:	Fabricator, Production Date, Cutting Pattern assignment, Details, Time, Status
Installation data:	Date, Installer, Time, Status
Testing data:	Certificates, Status
Further Data:	Price, Order Date, Order No.,

The following list contains structured information relevant for Cables:

Product data:	Type, Base material, Coating, Total Weight, Diameter, Length, Youngs modulus, metallic cross-section, unstretched length, minimum breaking load, ultimate load, material safety factor, end terminals
Geometric data:	Length, Pre-Tension, Curvature, points (nodes) for further details (cable clamps), markings
Design data:	No of Terminals, Terminal detail, No. of Clamps, Clamps detail
Production data:	Producer, Production Date, Batch No., Time, Status, raw material
Fabrication data:	Fabricator, Production Date, Details, Time, Status
Installation data:	Date, Installer, Time, Status, Pre-Tension
Testing data:	Certificates, Status
Further Data:	Price, Order Date, Order No.,

Various geometric and semantic values must be stored and handled within one model to allow an efficient planning process of Membrane Structures in the BIM method.

### 5.3 Further implementation steps

If the BIM model is used for analyses, like thermal-, shading or structural verifications additional properties must be added to elements of the BIM model (i.e. properties describing the long-term behavior of the structure must be integrated to compensate time-related effects).

Membrane and cable specific form-finding processes and creation of cutting patterns are further membrane-specific planning processes for which special information is needed. The geometry of the membrane surface is usually complex and is determined using form-finding processes. The shape depends on the material properties of the membrane, the applied pre-tension, its fixation to the substructure as well as the boundary conditions of the membrane surface. It can be assumed that the surface is created with special shape-finding software and then read into the 3D BIM model. Here, a corresponding linkage of the surface parts with the relevant information of the material is required. It is desirable that the current software tools for the creation of membrane surfaces conform to the data standard and thus output the calculated geometries as a BIM object. The required developments can be categorized in four topics:

#### Geometry and form-finding generation

- Development of flexible membrane and cable families linked to the form-finding process
- Alternative form-finding processes within the BIM environment or bi-directional links to form-finding software
- Simplification of integration of external geometric properties and transformation into structural families
- Developments for more than global geometry within one model

#### Input of semantic information

- Development of tailored feeding algorithms
- Development of bidirectional links between project management software packages

#### Processing of semantic information

- Better integration of assembly sequences within the standard BIM environment by integration of enhanced grouping and filtering functions
- Standardization of bi-directional connections to external software packages like MS-project or others

#### Legal issues

Like for most other structures, different companies are involved, legal issues have to be taken into account. Currently main unsolved questions are:

- How to protect the intellectual property at high levels of detailing such as LOD 300 at specific developed construction elements and details?
- How to define the responsibilities for the geometric position of individual elements used by several planners?

Last but not least concepts of using the BIM model as a base for schedule and cost control as well as the installation process, also known as 4D (time) and 5D (costs), are possible. This approach requires the preceding input of necessary connection of corresponding information into the BIM model.

## 6 CONCLUSION

To directly derivate all information from one BIM model is currently unrealistic because of the typical decentralized planning process with many specialized planners and manufacturers using individual applications. The use of different software environments results in individual drawing formats which currently must be assembled in the final BIM model more or less manually.

The standardized IFC format could bridge these applications and would allow to bring all information into one model if once the data structure for Membrane Structures are defined. It would avoid working with different non-related models which is insufficient, ineffective, error-prone, but currently still state of the art.

The implementation of BIM into the field of membrane and cable structures has just begun. Currently, not all expected benefits of the BIM method are reached. Reasons for that lack are defined within this article. The necessity for different levels of details (LOD) related to the process requirements as well as the enrichment of the IFC-Format concerning membrane structures was discussed. Current problems using BIM for Membrane Structures were mentioned as well as necessary further developments for an easier generation, information input and information processing were given. A further progress should base on research in the described directions and implementation and evaluation within the industry.

## REFERENCES

- [1] A. Borrmann et al., “Building Information Modelling”, Springer Vieweg, 2015
- [2] E.Lin, R. Roithmayr, “Building Information Modeling: Next steps for tensile membrane architecture” VII International Conference on Textile Composites and Inflatable Structures, STRUCTURAL MEMBRANES 2015
- [3] E.Lin, R. Roithmayr, S. Chiu “A Review of BIM Maturity for Tensile Membrane Architecture” Proceedings of the International Association for Shell and Spatial Structures (IASS), Symposium 2015, Amsterdam
- [4] IFC 1.0 first time published in 1997, <http://www.buildingsmart-tech.org/specifications/ifc-releases>
- [5] STL-Bau – Dynamische BauDaten, Standardleistungsbuch für das Bauwesen – Anwenderhandbuch, aktuell unter [www.GAEB.de](http://www.GAEB.de)
- [6] K. Schiller, G. Faschingbauer, “Die BIM Anwendung der DIN SPEC 91400, Beuth Verlag, 2016
- [7] B. Füzes, D. Hegyi, [www.membranedetail.com](http://www.membranedetail.com), Budapest University of Technology and Economics, Faculty of Architecture, Department of Mechanics, Materials and Structures (<http://www.szt.bme.hu>).
- [8] LEVEL OF DEVELOPMENT SPECIFICATION October 19, 2016, <https://bimforum.org/lod/>

## FORM-FINDING OF SHELL AND MEMBRANE STRUCTURES

ROSTISLAV LANG<sup>\*</sup> AND IVAN NĚMEC<sup>†</sup>

<sup>\*,†</sup> Institute of Structural Mechanics, Faculty of Civil Engineering  
Brno University of Technology  
Veveri 331/95, 602 00 Brno, Czech Republic  
e-mail: lang.r@fce.vutbr.cz, web page: <http://www.fce.vutbr.cz/EN/>

<sup>\*,†</sup> FEM consulting, s.r.o., Veverí 331/95, CZ-602 00 Brno, Czech Republic  
web page: <http://www.fem.cz/?lang=en>

**Key words:** Form-Finding, Membrane Structure, Shell Structure, Unstable Equilibrium Position.

**Summary.** This paper deals with the form-finding process of building constructions, such as membrane, shell or cable structures. This task is an essential step in the design process of membrane or cable structures, while for shell or beam structures, it is an optional case how to prefer the axial behavior of the intended construction. As a result of the form-finding process for structures acting exclusively in tension or compression, one unique shape in equilibrium is calculated for such a requirement. In the case of combined structures, cases with more than one solution for the same form-finding definition may occur. If the form-finding process is defined as a continuum mechanics process of the energy extreme calculation, the resulting shapes can reach both stable and unstable equilibrium positions. This contribution will focus on the general behavior of the process mentioned above, particular statements will be accompanied by examples.

### 1 INTRODUCTION

Lightweight constructions are characterized by their optimal material utilization since the axial stresses are preferred to bending action. For tensile membrane structures, this is a natural way of acting because the textile or foil can virtually resist in tension only. Such a strong restriction is not required for shell structures; however, this construction optimization by minimizing bending action would provide the possibility to design slender and beautiful shapes [1]. The optimization process may also face the task of combined structures, where compressed arches are in the interaction with tensioned membranes as an example.

Shapes of the lightweight structures are interconnected with their acting and there is a need of their calculation. This problem is well-known as form-finding, where the shape is a result and internal axial forces are an input. This analysis shows some phenomena as the consequences of such an inverse process [2-6]. In the form-finding analysis, the external load and boundary conditions are the shaping parameters of the structure as well as internal forces. In order to solve this problem, certain methods have been developed to overcome or even avoid the natural singularity of such a process [2-13].

Regardless the particular method, the aim of the form-finding process is to calculate the

shape in equilibrium. The resulting shape can physically take both stable or unstable equilibrium position as both cases satisfy the extreme of the energy.

## 2 FORM-FINDING IN CONTEXT OF CONTINUUM MECHANICS

There are different ways of how to formulate the form-finding analysis, as this can be defined as a mathematical process or as a physical process. The most general methods are based on the continuum mechanics conception. The solution is derived from the energetic concept, generally from the variational formulation of the problem, where it is search for an extreme of the operator  $\Pi$  that is of an additive nature. Here, the potential energy  $\Pi = \Pi_{int} + \Pi_{ext}$  of the internal and external forces in the body is - according to the Lagrange variational principle - minimal just for the real state of the body  $(d, \varepsilon, \sigma)$  [14]. The general FEM equations can be obtained from the differentiation of  $\Pi$  with respect to the deformation  $d$  (1).

$$\frac{\partial \Pi}{\partial d} = \frac{\partial(\Pi_{int} + \Pi_{ext})}{\partial d} = \frac{\partial \Pi_{int}}{\partial d} + \frac{\partial \Pi_{ext}}{\partial d} = \mathbf{K}d - f = 0$$

The equilibrium shape is identified when the  $\partial \Pi / \partial d = 0$ , thus the integral of the internal and external energy increment over the domain  $\Omega$  has to be zero (2). Where  $\sigma$  is the Cauchy stress tensor acting in the structure,  $\delta \hat{\varepsilon}$  is a variation of the Euler-Almansi strain tensor,  $\vec{p}$  is a load, and  $\delta d$  is an increment of deformation.

$$\frac{\partial \Pi}{\partial d} = \frac{\partial \Pi_{int}}{\partial d} + \frac{\partial \Pi_{ext}}{\partial d} = \int_{\Omega} \sigma : \delta \hat{\varepsilon} d\Omega - \int_{\Omega} \vec{p} \cdot \delta d d\Omega = 0$$

Even though the spatial shape is given by the equilibrium prestress, eventually considering the load, the direct numerical solution of such a problem is not possible. This fact is described in [6] and followed by the illustration of such a singularity (Figure 1). Such a singularity has to be overcome, therefore different methods of the form-finding were proposed for such a problem [13].

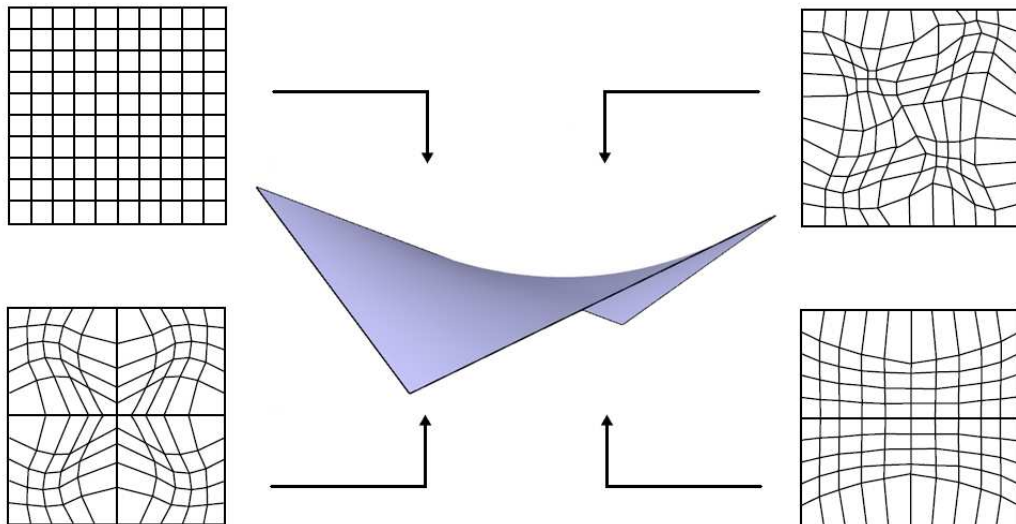


Figure 1: Arbitrarily deformed meshes for the same surface geometry ([6] with modification)

### 3 FORCE-FINDING AS A PART OF FORM-FINDING

Generally, there is one more phenomena to face in the form-finding process, which is the finding of the equilibrium prestress itself. The only homogenous prestress which can exist for surfaces with nonzero Gaussian curvature is an isotropic prestress. The homogenous orthotropic prestress is not in equilibrium for double-curved surfaces so the second task is to find the equilibrium prestress itself, which is derived from the prescribed values in warp and weft in some way. There are many methods proposed for such a stabilization; some of them are based on changing the force according to the deformation while other are derived from the restriction of the maximum allowable deformation of finite elements [5,9]. Generally, it is desirable to find as close approximation of the prescribed values as possible without objectionable concentrations.

### 4 SEARCHING FOR UNSTABLE EQUILIBRIUM POSITION OF ELEMENTS IN COMPRESSION

There is one important difference in the form-finding process of the tensioned and compressed structures or structural parts. While the tensioned elements take the stable equilibrium position in the form-finding process, the compressed elements are forced to take the unstable equilibrium position after the calculation. Such a phenomenon has to be overcome to reach the resulting equilibrium shape after the form-finding process.

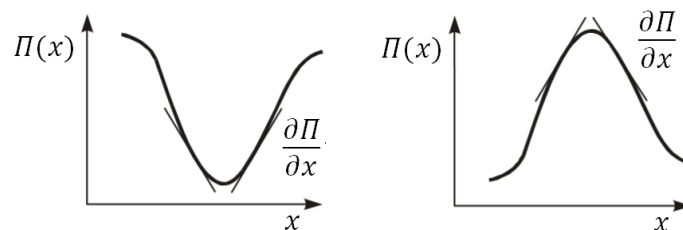


Figure 2: Stable and unstable equilibrium position

This fact can be illustrated on the example of a steel cable and a concrete arch (Figure 3). If only axial stresses are allowed in those elements, any deviation from the equilibrium position of an arbitrary node on the arch shifts the structure away from this equilibrium position.

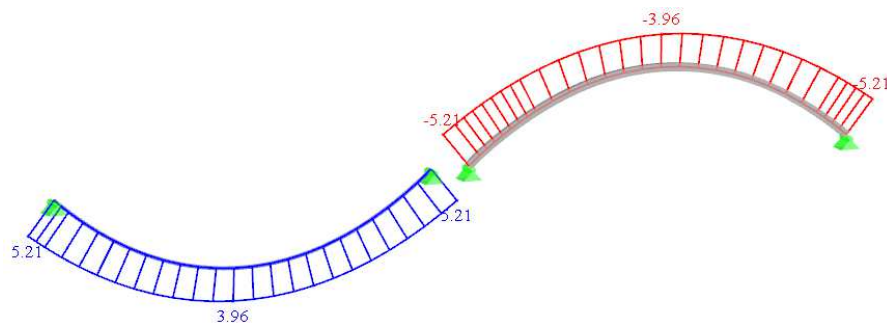


Figure 3: Equilibrium shapes of cable and arch



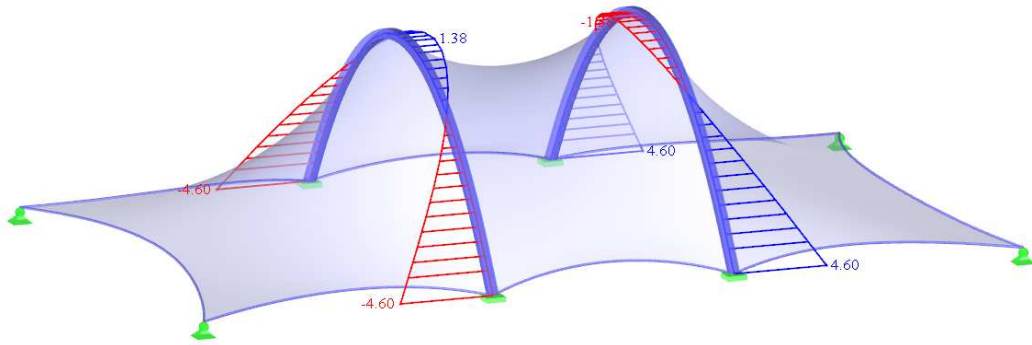


Figure 6: Equilibrium shape without beam optimization (bending moments  $M_z$  in beams)

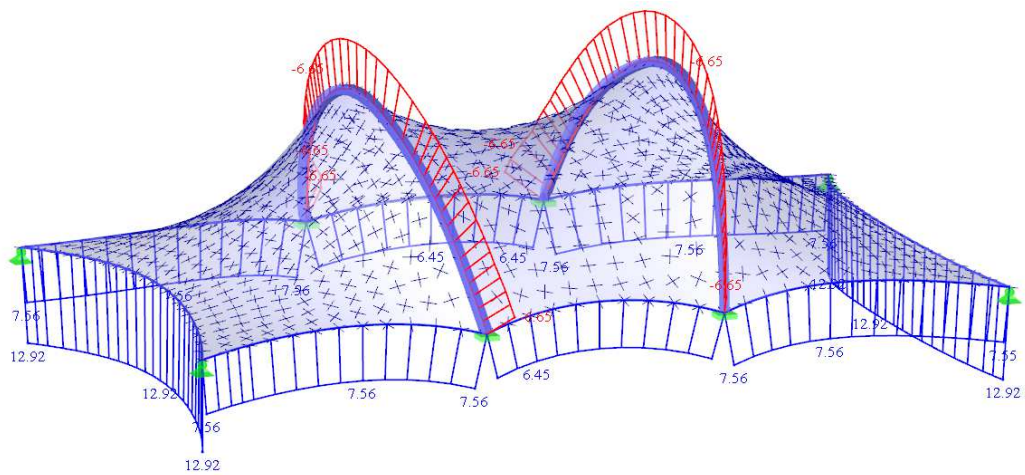


Figure 7: Equilibrium shape with beam optimization (principal forces  $n_1$  and  $n_2$  in membranes, normal forces  $N$  in beams and cables)

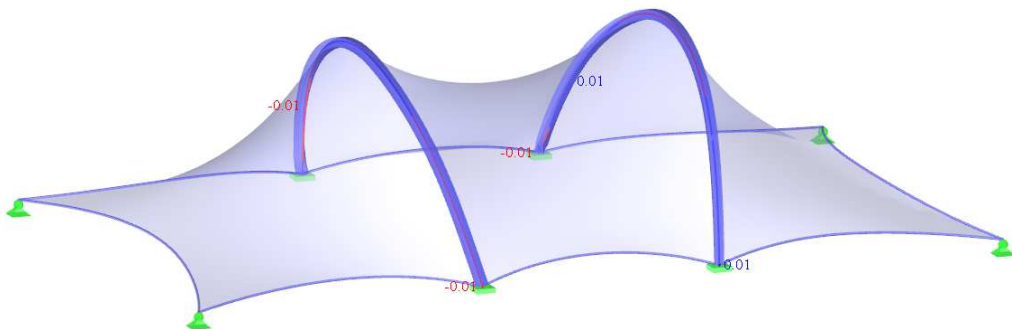


Figure 8: Equilibrium shape without beam optimization (bending moments  $M_z$  in beams)

As you can see (Figures 6 and 8), the bending moment in the second case is close to zero since the position of the arch was modified in the form-finding process. If a higher precision and a finer mesh are used, the bending moment is nearing to the limit of zero.

The form-finding process of the combined structures shows one characteristic phenomena,

that there can exist more than one right solution of the same input values (Figure 9). When the initial model is made, the shape converges to the closer equilibrium position in the form-finding analysis. That's the difference between the combined structures and the exclusively tensioned or compressed structures, since they converge to the same equilibrium position from the arbitrary initial spatial position of the model.

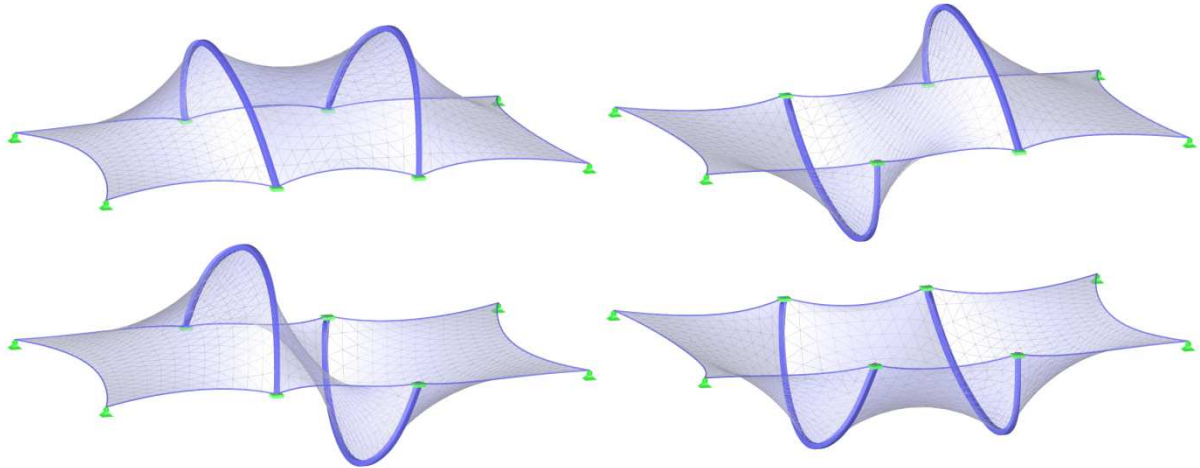


Figure 9: Existence of multiple equilibrium positions for combined structures

The last example is a concrete shell in compression supported by tensioned steel belts and with a skylight made of an ETFE cushion in the middle of this shell. Those structure components are subjected to the form-finding process and supported by concrete columns (Figures 10-11).

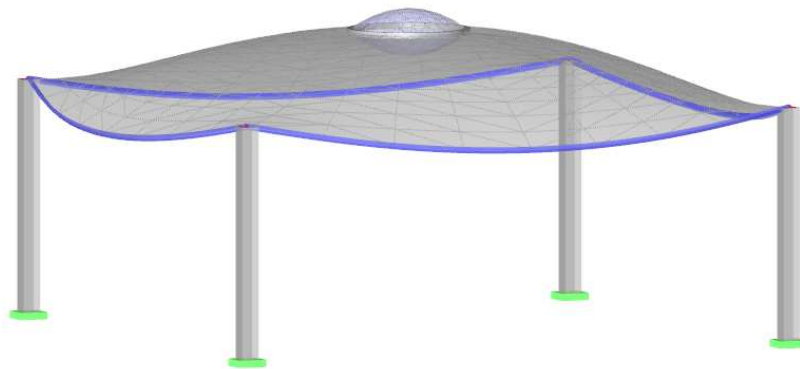


Figure 10: Equilibrium shape of a shell supported by tensioned belts on the borders with the skylight made of an ETFE cushion

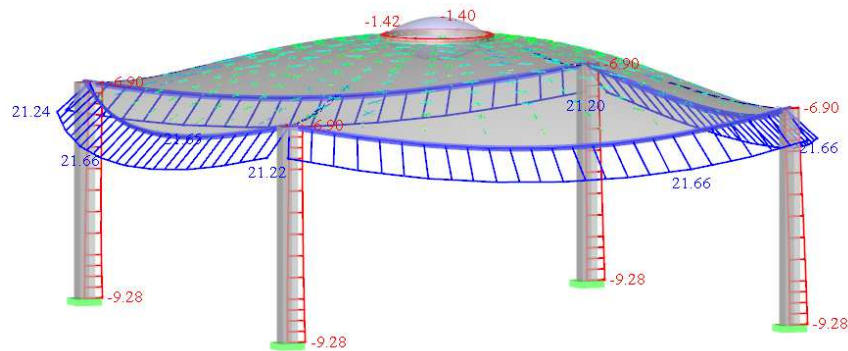


Figure 11: Compressed shell with tensioned belts and inflated cushion (principal forces  $n_1$  and  $n_2$  in shell and ETFE cushion, normal forces  $N$  in beams and cables)

## 12 CONCLUSIONS

- The paper focused on the form-finding process and the specific physical aspects and phenomena. It describes the calculation of unstable equilibrium positions of the elements in compression as well as the possibility of multiple equilibrium shapes of structures, which combine structural elements with tension and compression in the form-finding process.
- The presented examples were calculated in the RFEM software [I], where the form-finding option has been recently implemented for compressed and combined structures in cooperation of Dlubal Software and FEM consulting companies.

## REFERENCES

- [1] Otto, F., & Rasch, B. (1995). *Finding Form*. Deutscher Werkbund Bayern: A.Menges.
- [2] Bletzinger, K., & Ramm, E. (1999). A General Finite Element Approach to the Form Finding of Tensile Structures by the Updated Reference Strategy. *International Journal of Space Structures*, 14(2), 131-146.
- [3] Bletzinger, K., & Ramm, E. (2001). Structural Optimization and Form Finding of Light Weight structures. *Computers and Structures*, 79(22-25), 2053-2062.
- [4] Bletzinger, K., Wüchner, R., Daoud, F., & Camprubi, N. (2005). Computational Methods for Form Finding and Optimization of Shell and Membranes. *Computer Methods in Applied Mechanics and Engineering*, 194(30-33), 3438-3452.
- [5] Wüchner, R., & Bletzinger, K. (2005). Stress-adapted numerical form finding of pre-stressed surfaces by the updated reference strategy. *International Journal for Numerical Methods in Engineering*, 64(2), 143–166.
- [6] Bletzinger, K., Firl, M., Linhard, J., & Wüchner, R. (2010). Optimal shapes of mechanically motivated surfaces. *Computer Methods in Applied Mechanics and Engineering*, 199(5-8), 324–333.
- [7] Barnes, M. (1999). Form Finding and Analysis of Tension Structures by Dynamic Relaxation. *International Journal of Space Structures*, 14(2), 89-104.
- [8] Wakefield, D. (1999). Engineering Analysis of Tension Structures: Theory and Practice. *Engineering Structures*, 21(8), 680-690.

- [9] Schek, H. (1974). The Force Density Method for Form Finding and Computations of General Networks. *Computer Methods in Applied Mechanics and Engineering*, 3(1), 115-134.
- [10] Linkwitz, K. (1999). Formfinding by the Direct Approach and Pertinent Strategies for the Conceptual Design of Prestressed and Hanging Structures. *International Journal of Space Structures*, 14(2), 73-88.
- [11] Bletzinger, K., Linhard, J., & Wüchner, R. (2009). Extended and Integrated Numerical Form Finding and Patterning of Membrane Structures. *Journal of the international association for shell and spatial structures*, 50, 35-49.
- [12] Linhard, J., & Bletzinger, K. (2010). "Tracing" the Equilibrium - Recent Advances in Numerical Form Finding. *International Journal of Space Structures*, 25(2), 107-116.
- [13] Veenendaal, D., & Block, P. (2012). An overview and comparison of structural form finding methods for general networks. *International Journal of Space Structures*, 49(26), 3741–3753.
- [14] Němec, I. et al. (2010). *Finite element analysis of structures: Principles and Praxis*, (1<sup>st</sup> ed.). Aachen: Shaker Verlag.

#### WEB LINKS

- [I] Dlubal Software. (2017). Analysis & Design Software for Tensile Membrane Structures. Retrieved from <https://www.dlubal.com/en/solutions/industries/analysis-and-design-software-for-tensile-membrane-structures>

# ISOGEOMETRIC ANALYSIS FOR STAGED CONSTRUCTION WITHIN LIGHTWEIGHT DESIGN

ANNA M. BAUER, ROLAND WÜCHNER AND KAI-UWE  
BLETZINGER

Lehrstuhl für Statik  
Technische Universität München  
Arcisstr. 21, 80333 München, Germany  
e-mail: am.bauer@tum.de, web page: <http://www.st.bgu.tum.de>

**Key words:** Lightweight Structures, Staged Construction, Hybrid Structures, Isogeometric Analysis, Embedding, Nonlinear Kinematics

**Abstract.** Hybrid, bending-active structures constitute a challenging task for structural design due to the high dependency between shape and forces. Isogeometric analysis suggests itself in this context because of several advantages. Model conversion with concomitant corruption of the simulation results can be overcome. All stages of the construction, which are necessary for the correct simulation of such structures, can be modeled and correctly linked. Moreover, the parameter space of the NURBS description provides a perfectly suited, additional design space for embedded entities, which can be defined independently of the parametrization.

The contribution of this paper is a presentation of the basics for embedding within isogeometric analysis and reveals beneficial aspects of nested NURBS descriptions in the context of staged construction. A case study of a staged simulation is carried out and another one for the form-finding procedure of hybrid structures.

## 1 INTRODUCTION

The development of an aesthetic and robust design in lightweight design is a challenging task. Architects and engineers are required to work closely together since their decisions directly influence each other. Load bearing behavior of lightweight design is form dominated. Or to put it differently, an appropriate shape design results in a good load bearing behavior and therefore the need for less material. Lightweight design uses flexible components which form a resistant structure after forming, straining and assembling. Since the actual construction is an essential part of the resulting stiffness, it is important to also include the different stages into the simulation.

Isogeometric Analysis (IGA), as defined in [1], has several aspects, which are beneficial for lightweight design. First of all, it uses smooth Non-uniform rational B-Splines

(NURBS) as basis functions. The geometric properties are not corrupted by the polygon mesh of a classic FE-analysis. The analysis and its results can be incorporated into CAD, where several well-suited tools for the modeling of further stages, such as the derivation of a surface description from boundary curves, are available. Furthermore, NURBS patches provide a huge parameter space for the parametric design. Meshing does not subdivide the patches and the model can be modified without taking care of the meshing of interacting members. Therefore, it is very convenient to apply IGA for the definition of the interaction of single components. The parameter space can also be used for a description of embedded entities. The embedding can be realized by another NURBS description in the parameter space of the master NURBS patch. The idea stems from the trimming of CAD geometries. Here, the borders of a trimmed surface are described by curves in its parameter space. These edge curves were applied by Breitenberger et al. [2] for trimming in isogeometric B-Rep analysis (IBRA) and for coupling of multipatches as well as for edge cables by Philipp *et al.* [3]. However, such a description can also be used within the surface and be enhanced with further structural properties. The geometric description of the continuum of a one-dimensional element is then adapted to the nested NURBS description. Further derivations of structural element formulations are then analogue to the surface-independent element formulation.

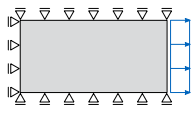
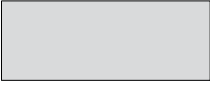
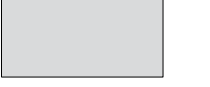
Therefore, this contribution is outlined as follows. Section 2 presents essential aspects of the simulation of staged construction. The above mentioned embedding within NURBS is explained in Section 3. A transfer to structural analysis is shown briefly for the element formulation of an embedded beam in Section 4. These two separate topics are brought together in two detailed application examples in Section 5.

## 2 STAGED CONSTRUCTION

A staged construction is still a challenge in the computer simulation. This is especially true, if some structural configurations are derived from previous results of other parts. Here, one can benefit a lot of the CAD facilities. Constructing a surface from boundary lines is for example quite effortless in CAD systems whereas it is hardly possible in a FE-kernel with a non-matching parametrization. Intermediate steps with CAD recovery are part of the classical workflow which influences the accuracy of the results, since the link between the two FE models is corrupted if the parametrization cannot be retained. In contrast, the parametrization is preserved with isogeometric analysis by retaining the basis function between CAD modeling and simulation or when needed by exactly transferring to a refined configuration.

The two usual approaches for the consideration of previous simulations are either transferring stresses on integration points (*InitStress*) or displacements of nodes (*InitDisp*). The transferred quantity is then applied as initial condition. The methods are compared for a tension test of a shell (see Fig. 1). The shell strip, modeled by a Kirchhoff-Love shell [4], is vastly stretched in two steps by increased load  $\lambda P$  and then unloaded. Note that this simulation problem is easily solved within one simulation, since the structure is not

modified. The one-simulation result serves as reference. Simulation 1 is now interrupted after solving  $\lambda = 1$  and a second simulation is started for every approach. The initial configuration ( $\lambda = 1$ ) is in equilibrium for both approaches, but a significant difference can be observed while further loading or unloading in simulation 2. The *InitStress* method differs from the reference solution for  $\lambda = 2$  and in the unloaded state ( $\lambda = 0$ ), whereas the *InitDisp* method perfectly matches. Further details can be found in the contribution of Dieringer *et al.* [5]. Only the capturing of previous simulation by initial displacement of the nodes resp. control points is suitable for statically nonlinear application, which is usually necessary for hybrid structures.

Initial Set-Up		Simulation 1	Simulation 2	
		reference	InitStress	InitDisp
 $L=10\text{m}$ $h=5\text{m}$ $t=0.1\text{m}$ $E=100\text{kN/m}^2$ $\nu=0.2$ $P=5\text{kN/m}$	$\lambda=1$			
	$\lambda=2$			
	$\lambda=0$			

**Figure 1:** Comparison of the two methods *InitStress* and *InitDisp* for simulating staged construction. Note that the computation was carried out with better refinement, *i.e.* more Gauss points and control points, than illustrated. The reference solution is added for simulation 2 with dotted lines.

### 3 EMBEDDING WITHIN NURBS GEOMETRIES

A further advantage of isogeometric analysis is the relatively huge parameter space, which is not subdivided throughout the simulation. Note that a respectively huge parameter space with “classic” low order finite elements, *i.e.* huge elements, is accompanied by a loss of accuracy. In the following, the usually used basis function, *Non-Uniform Rational B-Splines* (NURBS), of IGA are recalled briefly. NURBS provide in general a description for smooth surfaces and curves in CAD systems by a discrete number of control points  $\mathbf{P}$  with weight  $w$ , a knot vector and a polynomial degree  $p$  resp.  $q$ . The geometry description  $\mathbf{C}(\xi)$  or  $\mathbf{S}(\xi, \eta)$  is then derived by the product of the control points and their basis function  $R$ .

$$\mathbf{C}(\xi) = \sum_{i=1}^n R_{i,p}(\xi) \mathbf{P}_i \quad \mathbf{S}(\xi, \eta) = \sum_{i=1}^n \sum_{j=1}^m R_{ij,pq}(\xi, \eta) \mathbf{P}_{ij} , \quad (1)$$

The basis function  $R$  is derived by weighting the underlying B-Spline basis functions  $N$  resp.  $M$ , which in turn are defined by the knot vector and polynomial degree. Details on the computation of B-Splines and NURBS can be found in the contribution of Piegl and Tiller [6].

$$R_{i,p}(\xi) = \frac{N_{i,p}(\xi)w_i}{\sum_{j=1}^n N_{j,p}(\xi)w_j} \quad R_{ij,pq}(\xi, \eta) = \frac{\sum_{i=1}^n \sum_{j=1}^m \frac{N_{i,p}(\xi)M_{j,q}(\eta)w_{ij}}{\sum_{k=1}^n \sum_{l=1}^m N_{k,p}(\xi)M_{l,q}(\eta)w_{kl}}}{\sum_{k=1}^n \sum_{l=1}^m N_{k,p}(\xi)M_{l,q}(\eta)w_{kl}} \quad (2)$$

The parameter space spanned by a NURBS description is now taken as an additional design space. Entities which are related to a specific location on a NURBS geometry are described by a NURBS description in the respective parameter space, called the super domain. This is exemplified for a line element embedded in a surface. As a consequence, the local line is expressed by the control parameters (degrees of freedom) of the super domain. Hence, explicit coupling is avoided. All quantities which refer to the parameter space of the super domain will henceforth be denoted with  $(\bar{\bullet})$ .

$$\bar{\mathbf{C}}(\bar{\xi}) = \begin{pmatrix} \xi(\bar{\xi}) \\ \eta(\bar{\xi}) \end{pmatrix} = \sum_{\bar{i}=1}^n R_{\bar{i},\bar{p}}(\bar{\xi}) \bar{\mathbf{P}}_{\bar{i}} \quad (3)$$

The description of lines in the parameter space can be derived either manually, *i.e.* by directly defining the curve in the parameter space, or by using the CAD-implemented surface-to-surface intersection (SSI) algorithms of *e.g.* [7, 8, 9, 10] for larger and more complex tasks. Note that the precision of the mapping into the parameter space is strongly dependent on the CAD tolerances.

The embedded structural properties can be derived from the curve description in the geometry space. Every term in the embedded curve is described by the control points of the surface. If further quantities have to be described, additional control variables (DOFs) can be added to the control points of the surface, which belong to the knot spans crossed by the curve.

$$\begin{aligned} \mathbf{C}(\bar{\xi}) &= \sum_{i=1}^n \sum_{j=1}^m R_{ij,pq}(\bar{\xi}) \mathbf{P}_{ij} = \sum_{i=1}^n \sum_{j=1}^m R_{ij,pq}(\xi(\bar{\xi}), \eta(\bar{\xi})) \mathbf{P}_{ij} \\ &= \sum_{i=1}^n \sum_{j=1}^m R_{ij,pq} \left( \sum_{\bar{i}=1}^{\bar{n}} R_{\bar{i},\bar{p}}(\bar{\xi}) \bar{\mathbf{P}}_{\bar{i}} \right) \mathbf{P}_{ij} \end{aligned} \quad (4)$$

An overview of all presented geometry descriptions within the proposed workflow is given in Fig. 2.

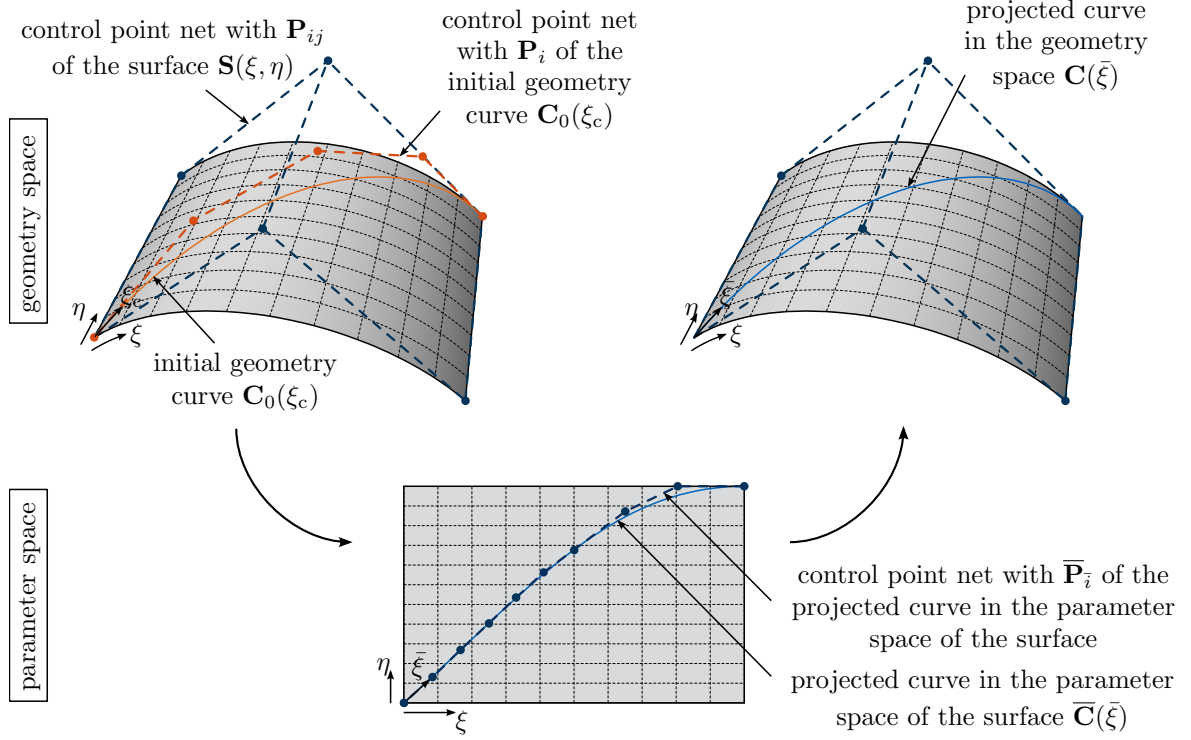


**Figure 2:** Overview of the presented geometry descriptions.

#### 4 EMBEDDED BEAM ELEMENT FORMULATION

A brief overview of the derivation of the structural element formulation of the embedded beam as proposed in [11] is presented as a template for further formulations based on the embedded curve description. The derivation is based on the *Principle of Virtual Work*. Let  $\Omega$  be the undeformed super domain and  $\partial\Omega$  be the boundary. Additional terms in the work expression are derived from the sub domain of the embedded curve  $\Omega_C$  and its respective boundary  $\partial\Omega_C$ . The second Piola-Kirchhoff (PK2) stresses are assigned by  $\mathbf{S}$  and the energetically conjugated virtual Green-Lagrange (GL) strains related to the virtual displacement  $\delta\mathbf{u}$  by  $\delta\mathbf{E}$ . The external work consists of body forces  $\mathbf{B}$  and boundary forces  $\mathbf{t}$  times their respective virtual displacement. The material density is denoted as  $\rho_0$ .

$$\begin{aligned} \delta W = -\delta W_{\text{int}} + \delta W_{\text{ext}} = & - \int_{\Omega} \mathbf{S}^S : \delta \mathbf{E}^S dx - \int_{\Omega^C} \mathbf{S}^C : \delta \mathbf{E}^C dx \\ & + \left( \int_{\partial\Omega} \mathbf{t}^S : \delta \mathbf{u}^S dx + \int_{\Omega^S} \rho_0 \mathbf{B}^S : \delta \mathbf{u}^S dx + \int_{\partial\Omega_C} \mathbf{t}^C : \delta \mathbf{u}^S dx + \int_{\Omega^C} \rho_0 \mathbf{B}^C : \delta \mathbf{u}^S dx \right) = 0 \end{aligned} \quad (5)$$

The system's solution is derived based on the fundamentals of the *Finite Element Method*. As a consequence, a discretization for describing the problem statement has to be introduced. The variation of Eq. (5) w.r.t. the discretization variables  $\delta u_r$  yields the components  $R_r$  of the residual force vector.

$$\delta W = \sum \frac{\partial W}{\partial u_r} \delta u_r = \sum R_r \delta u_r = 0 \quad (6)$$

The residual force vector is equal to zero for arbitrary variations. The resulting system of equations can be solved with linearization by the Newton-Raphson method.

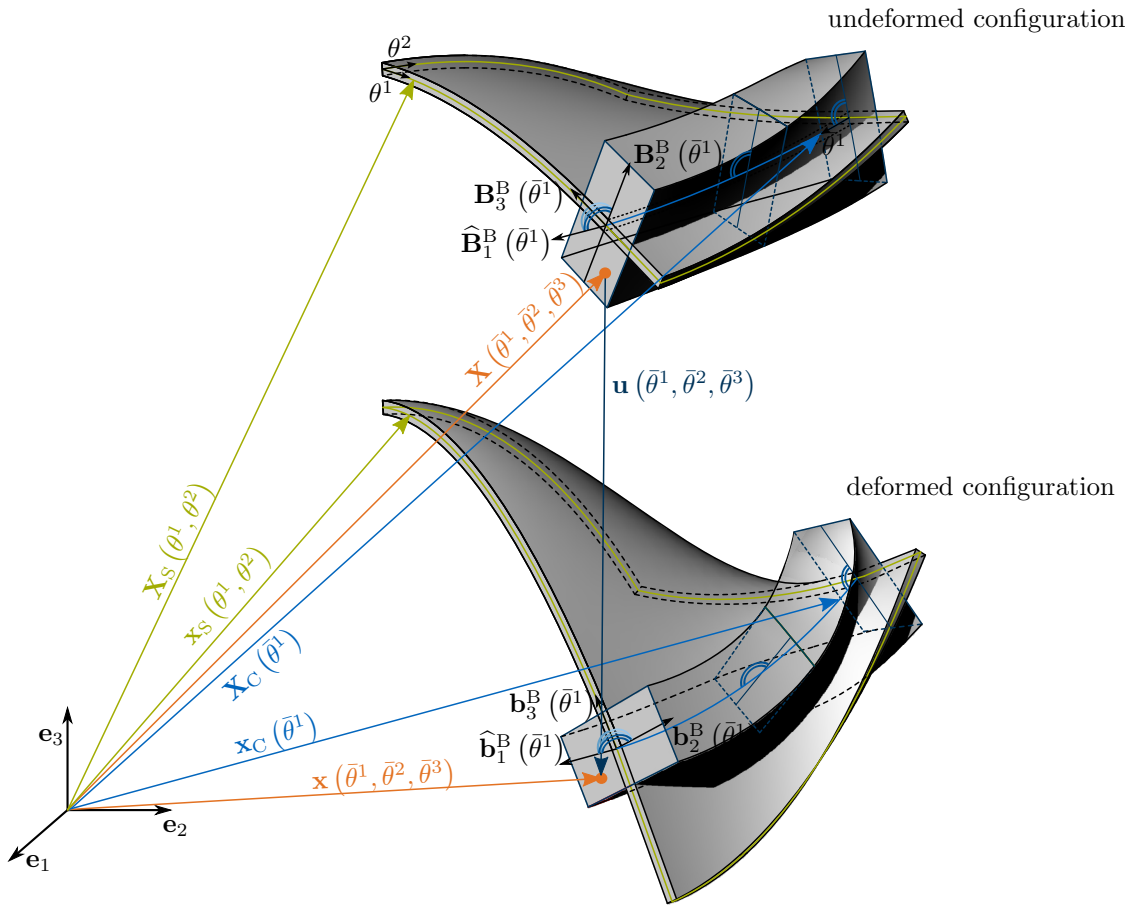


**Figure 3:** Definition of the position vectors  $\mathbf{X}$  and  $\mathbf{x}$ , the surface vectors  $\mathbf{X}_S$  and  $\mathbf{x}_S$  and the center line vectors  $\mathbf{X}_C$  and  $\mathbf{x}_C$  for the undeformed and deformed configuration with a cross section defined by  $\mathbf{B}_2^B$  and  $\mathbf{B}_3^B$ . Here illustrated for a rectangular cross section, which is aligned to the surface normal. Adapted from [11].

The element formulation is deduced from the description of the continuum of the embedded beam. The embedded curve description is used for the center line  $\mathbf{X}_C$  and the respective base vectors  $\mathbf{B}_2^B$  and  $\mathbf{B}_3^B$  for the cross section are derived from the surface

normal (*c.f.* Fig. 3). Capital letters refer in the following to the undeformed configuration whereas lower-case letters denote the deformed configuration. Bernoulli kinematics without warping are assumed.

$$\mathbf{X}(\bar{\theta}^1, \bar{\theta}^2, \bar{\theta}^3) = \mathbf{X}_C(\bar{\theta}^1) + \bar{\theta}^2 \mathbf{B}_2^B(\bar{\theta}^1) + \bar{\theta}^3 \mathbf{B}_3^B(\bar{\theta}^1) \quad (7a)$$

$$\mathbf{x}(\bar{\theta}^1, \bar{\theta}^2, \bar{\theta}^3) = \mathbf{x}_C(\bar{\theta}^1) + \bar{\theta}^2 \mathbf{b}_2^B(\bar{\theta}^1) + \bar{\theta}^3 \mathbf{b}_3^B(\bar{\theta}^1) \quad (7b)$$

The kinematics are derived straight forward from the continuum by means of fundamentals of continuum mechanics. The respective base vectors are defined as follows:

$$\mathbf{G}_i = \frac{\partial \mathbf{X}}{\partial \bar{\theta}^i} = \mathbf{X}_{,\bar{i}}, \quad \mathbf{g}_i = \frac{\partial \mathbf{x}}{\partial \bar{\theta}^i} = \mathbf{x}_{,\bar{i}} \quad (8)$$

Subsequently, the Green-Lagrange strains can be computed.

$$E_{ij} = \frac{1}{2}(g_{ij} - G_{ij}) \quad , \text{ where } i, j \in \{1, 2, 3\} \text{ and } G_{ij} = \mathbf{G}_i \cdot \mathbf{G}_j \text{ (analogously: } g_{ij}) \quad (9)$$

Stress and strain fields are linked by the constitutive law  $\mathbf{S} = \mathbf{C} : \mathbf{E}$ . A detailed specification of the resulting terms of the virtual work, as well for the boundary conditions, can be found in [11].

## 5 APPLICATION EXAMPLES

In this section, two different application examples are demonstrated. They reveal the advantages and flexibility of the proposed method in the context of architecture and structural design.

### 5.1 Membrane restrained girder

Alpermann proposed a membrane restrained girder in his PhD thesis [12]. A membrane is inserted between curved beams in order to transfer shear forces. This structural component provides a solution for lightweight and wide-span structures. Additionally, it is stated that the fabrication and transportation is facilitated by elastically bent profiles. The simulation of such structures has to consider staging. Two beams are bent into a curved form and stabilized by a inner membrane and bar spacers. Alpermann uses a circle segment as design objective. In this contribution, a bending shape is additionally examined due to the simpler construction (see Fig. 4).

In the next simulation step, the resulting shape is used for the generation of the slightly prestressed membrane and embedded bar spacers are introduced in order to keep the outer beams in position. The structure, which is in equilibrium for a fixed support on the right, is loaded in a third simulation and the right support is again released in the tangential

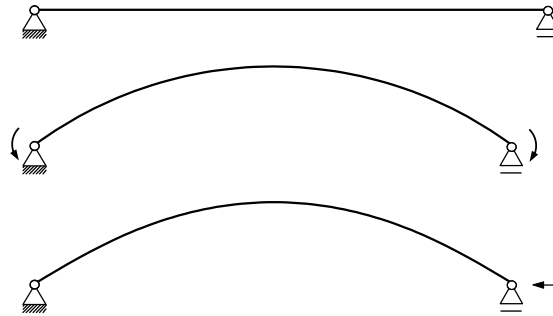


**Figure 4:** First simulation step for the membrane-restrained girder by Alpermann [12] – shaping the outer profiles.

direction. Embedding the bar spacers into the membrane has in contrast to the conventional explicit modeling the advantage that the design can be easily modified without considering the meshing and coupling of the membrane and the outer beams. Below, several exemplary configurations are examined and illustrated in Fig. 5. Additionally, type A is also computed without considering the first staging step, *i.e.* initially curved beams. This variant is marked with <sup>woR</sup>.

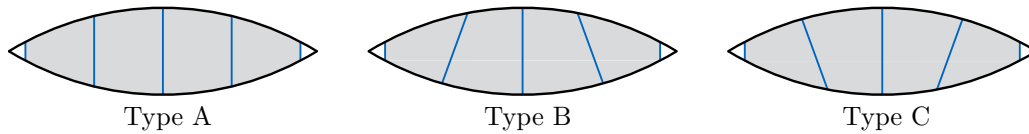


**Figure 5:** Membrane-restrained girder by Alpermann [12] with elastically bent outer profiles and varied bar spacers.

These design alternatives can be evaluated *e.g.* by the comparison of their behavior under a dead load on the lower outer beam as shown in Fig. 6. The variation study shows different structural responses and proves the benefit of a simple procedure for geometry variation during analysis.

The maximal deformation of the load study presented in Fig. 6 is shown in Fig. 7 for every variant. One observes a different behavior of deformation for the different initial shaping in the first simulation step.

## 5.2 Batsail

Another field of application within structural design can be seen in the form-finding procedure of hybrid structures. Hybrid structures in this context are prestressed membranes stiffened by elastically bent (bending-active) beams. Such systems provide high efficiency and open up new possibilities for shaping such free form geometries. However, the design procedure of hybrid structures is very complex. There is a high interdependency between form and force due to the low or even non-existing bending stiffness. A

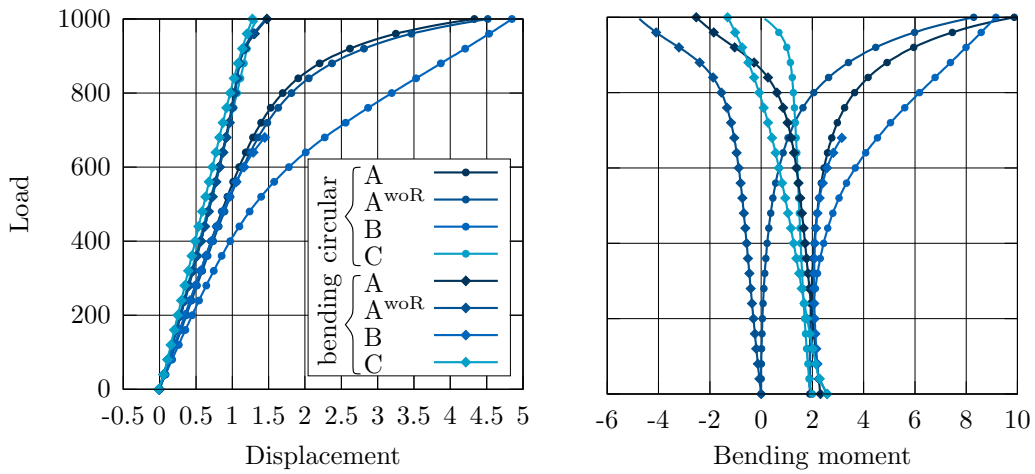


**Figure 6:** Membrane-restrained girder by Alpermann [12] with elastically bent outer profiles and varied bar spacers. Results for increasing load at the mid point of the lower outer beam for the vertical displacement and the bending moment.

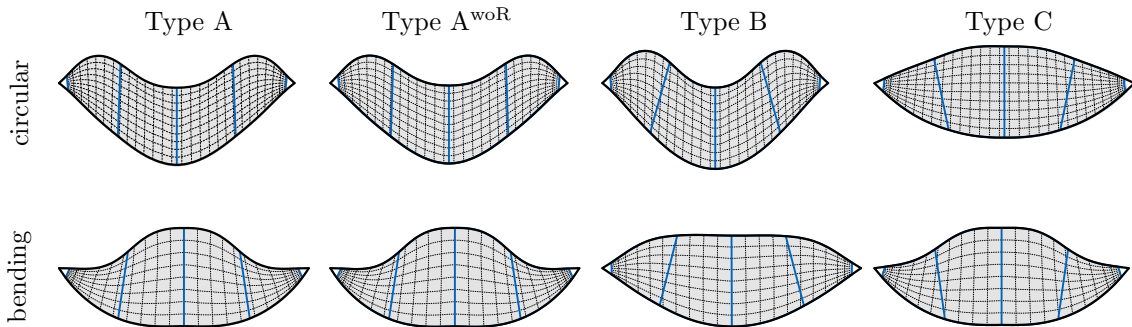


**Figure 7:** Maximal deformation of the membrane-restrained girder for every variant of the case study.

topology of membranes and cables is given in the classical approach of form-finding. The computation outputs a possible state of equilibrium under a defined force distribution and boundary conditions. The Batsail by Off [13] is chosen as demonstrator example in the following for exemplifying the extended approach. The elastic beams are embedded in the initial topology such that they have their initial length and form (see Fig. 8). Since only the topology has to be modeled for the membrane and cables, it can be modeled flat similar to the projection on the ground. Boundary conditions can be applied subsequently by fixed initial displacements (here for the high points). A deformation of the beam implies inner forces, whereas the initial geometries of the membrane and cables are updated during the form-finding analysis. Note that the initial geometry refers to the stress-free configuration in this contribution.

The initial beams are slightly curved in order to force the buckling into the desired

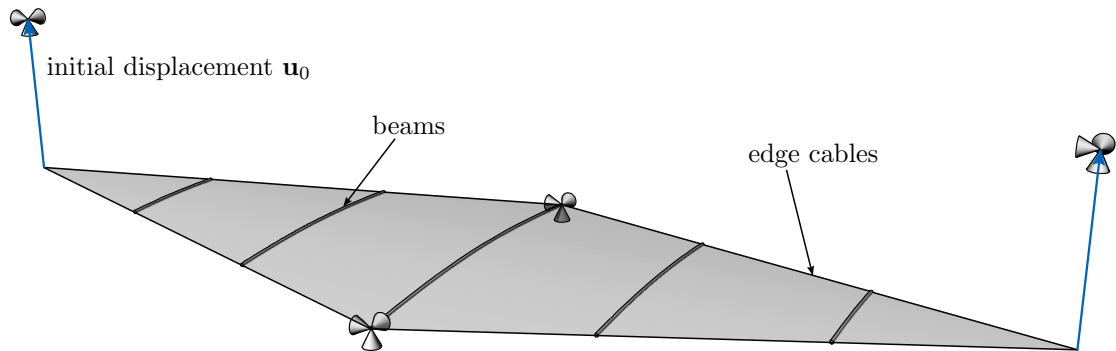


**Figure 8:** Initial topology with stress-free beams for the form-finding process of the Batsail by Off [13].

direction. Alternatively, forces can be used for controlling the buckling. The length and curvature of the beam are only varied by the forces applied through the membrane or cables. The computational form-finding analysis based on the Updated Reference Strategy (URS) by Bletzinger *et al.* [14] returns for example a solution in equilibrium as shown in Fig. 9.

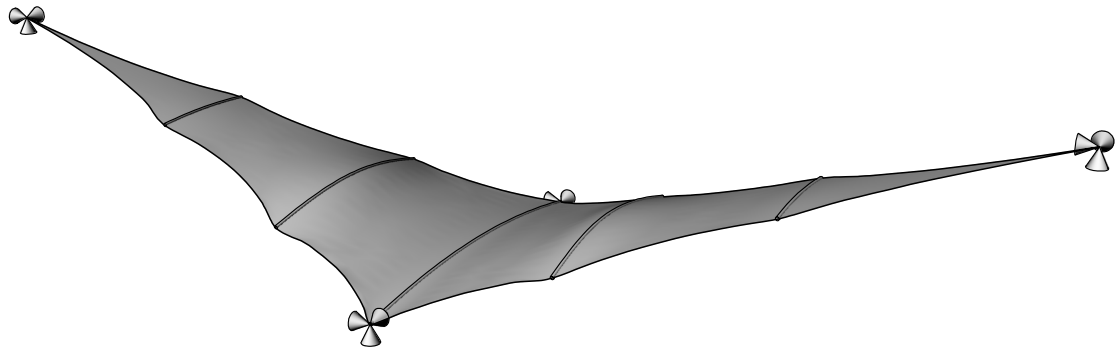


**Figure 9:** Formfound Batsail by Off [13] with elastically bent beams in equilibrium.

The advantage can be seen in the mesh independent modification of the beams. A study with several variations of the positioning of the beams with the respective parameter space and form-found structure is shown in Fig. 10.

## 6 CONCLUSIONS

The benefits of isogeometric analysis for staged construction is demonstrated. The advantages can be seen in avoiding the transfer between two frameworks and the consequent loss of result information. Furthermore, embedded entities can be defined independently of the mesh. The embedding technique within NURBS geometries is shown briefly. The application of these embedded geometries for structural analysis is explained shortly by

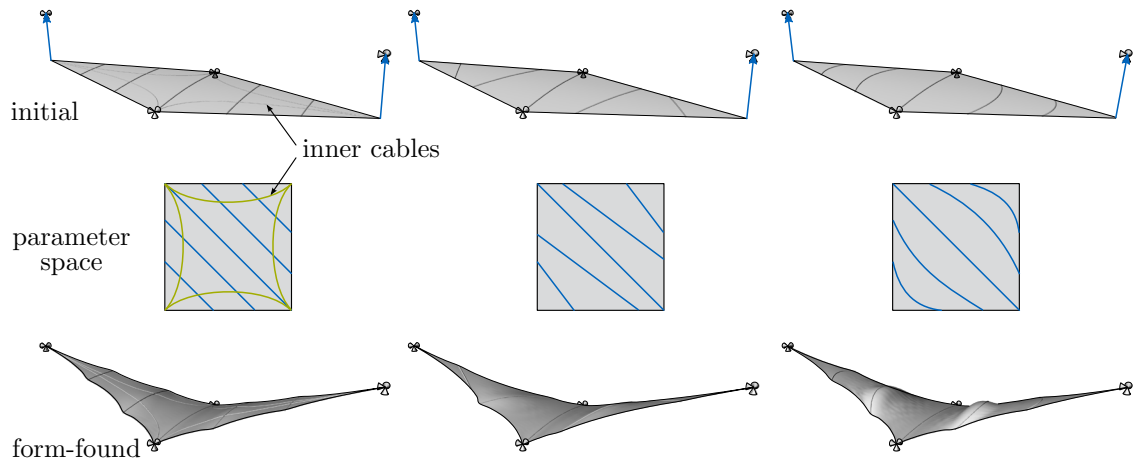


**Figure 10:** Variations of the Batsail by Off [13] with initial topology, respective parameter space and form-found solution.

using an example of a beam. Two application examples are carried out in order to prove the advantages of embedding in staged construction.

The next step will be to modify the embedding technique within NURBS such that the control points of the embedded entity are also attributed with DOFs. This enables *e.g.* the possibility of a cable that can move on a membrane while staying attached to it. It can be taken even further by nesting another NURBS curve into the parameter space of the surface-embedded curve. Such a description can represent a sliding cable in a sleeve. This would enable the simulation of prestressing during the construction by cables.

## REFERENCES

- [1] Hughes, T.J.R., Cottrell, J.A. and Bazilevs, Y., Isogeometric analysis: CAD, finite elements, NURBS, exact geometry and mesh refinement. *Comp. Meth. Appl. Mech. and Engng.* (2005) **194**:4135-4195.
- [2] Breitenberger, M., Apostolatos, A., Philipp B., Wüchner, R. and Bletzinger, K.-U., Analysis in computer aided design: Nonlinear isogeometric B-Rep analysis of shell structures. *Comp. Meth. Appl. Mech. and Engng.* (2015) **284**:401-457.
- [3] Philipp B., Breitenberger, M., D’Auria I., Wüchner, R. and Bletzinger, K.-U., Integrated design and analysis of structural membranes using the Isogeometric B-Rep Analysis. *Comp. Meth. Appl. Mech. and Engng.* (2016) **303**:312-340.
- [4] Kiendl, J., Bletzinger, K.-U., Linhard, J. and Wüchner, R., Isogeometric shell analysis with KirchhoffLove elements. *Comp. Meth. Appl. Mech. and Engng.* (2009) **198**:3902-3914.

- [5] Dieringer, F., Philipp B., Wüchner, R. and Bletzinger, K.-U., Numerical methods for the design and analysis of hybrid structures. *Int. J. Space Struct.* (2013) **28**:149-160.
- [6] Piegl, L. and Tiller, W. *The NURBS book*, in: Monographs in Visual Communication, Springer, 2nd Edition, 1997.
- [7] Choi, B.K. *Surface modeling for CAD/CAM*, in: Advances in Industrial Engineering, vol. 11, Elsevier, 1991.
- [8] Patrikalakis, N.M., Surface-to-surface intersections. *IEEE Comput. Graph. Appl.* (1993) **13**(1):89–95.
- [9] Sederberg, T.W. and Meyers, R.J., Loop detection in surface patch intersections. *Comput. Aided Geom. Des.* (1988) **5**(2):161–171.
- [10] Krishnan, S. and Manocha, D., An efficient surface intersection algorithm based on lower-dimensional formulation, *ACM Trans. Graph. (TOG)* (1997) **16**(1):74–106.
- [11] Bauer, A.M., Breitenberger, M., Philipp B., Wüchner, R. and Bletzinger, K.-U., Embedded structural entities in NURBS-based isogeometric analysis. *Comp. Meth. Appl. Mech. and Engng.* accepted for publication.
- [12] Alpermann, H. *Membranversteifte Tragwerke*. Universität der Künste Berlin, 2015.
- [13] Off, R. *New trends on membrane and shell structures - examples of batsail and cushion-belt technologies*. Structures and Architecture Cruz (Ed.), Taylor & Francis Group London, 2010.
- [14] Bletzinger, K.-U. and Ramm, E. A general finite element approach to the form-finding of tensile structures by the updated reference strategy. *Int. J. Space Struct.* (1999) **14**(2):131-145.

## Khan Shatyr Entertainment Centre cable net supply, engineering and installation

S. GEYER<sup>\*</sup>, D. LOMBARDINI<sup>\*</sup> AND S. LENK<sup>†</sup>

<sup>\*</sup> Redaelli Tecna

Via Alessandro Volta 16, 20093 Cologno monzese, Italy  
e-mail: [silvia.geyer@redaelli.com](mailto:silvia.geyer@redaelli.com), web page: <http://www.redaelli.com>

<sup>†</sup> Montageservice LB GmbH

Ismaninger Str. 98, 85399 Hallbergmoos, Germany  
Email: [info@montage-service.com](mailto:info@montage-service.com) - Web page: [www.montage-service.com](http://www.montage-service.com)

**Key words:** Cable net, Open Spiral Strand Cable, Cables Installation.

**Summary.** This paper addresses technical aspects of the Khan Shatyr Entertainment center, whose main feature is the 150-metre high mast with a tubular-steel tripod that supports a complex net of cables with a 200 x 195-metre elliptical base. The paper focuses mainly on all features related to steel cable net and cladding.

### 1 INTRODUCTION

The Khan Shatyr (“Tent of the Khan”) Entertainment Centre is a multi-purpose retail and leisure facility located in Astana, the capital of Kazakhstan. One of the largest tensile structures in the world, the building provides the city with a focal point for people to congregate for civic, cultural and social events. Foster and Partners designed the structure, in line with local traditions, as a giant transparent tent that evokes the traditional nomadic building form.

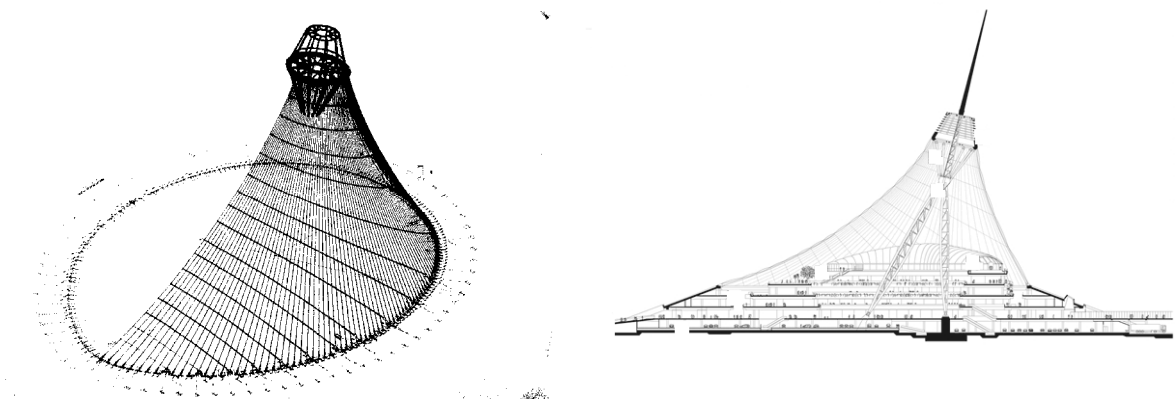


Figure 1: Khan Shatyr concept design

The tent covers an area of 100.000 square meters, sheltered from the city's drastically polar climate (temperature varies from  $-35^{\circ}\text{C}$  in the winter to  $+35^{\circ}\text{C}$  in the summer). The contribution of Redaelli and Montage Service to this giant structure embraces all aspects relating to cable net, from the production of the cables to the final on site installation.

## 2 STRUCTURE DETAILS

The single-masted cable net is the natural choice to provide such a giant, free-spanning enclosure with the minimum support: a single compression mast that lifts the cable net and creates a large volume underneath. The tensioned roof is made as a cable net, cables being extremely effective load-carrying structural elements due to the most efficient load transfer by pure tension.

Thus, the structure is designed as a tubular-steel tripod mast that rises from the 195x200-metre elliptical base and supports the cable net in a conical form. The whole mast, including its tip, is 160-metre high and it is made of about 2.500 ton of steel, the tripod consists of one 60-metre tall vertical back leg and two 70-metre long splayed front legs. Each tripod leg is a three-chord truss with a 1.000-millimetre diameter circular hollow section, which is made out of 40-millimetre thick tin. Mast's legs meet at a 7-metre high hub, constructed from a 150-millimetre thick steel plate; the hub centre line corresponds to the axis of the resultant axial force of cable net under prestress.



Figure 2: Details of the tripod mast.

Cables are connected 90-metre above the ground on a steel ring joined to the top of the tripod mast with 12 pinned struts and span to the sloped concrete perimeter that forms the base of the building. Concrete is the selected material for the structure's base due to its large thermal mass and consequent excellent insulation properties.

The top ring is articulated to allow for movements of the structure under asymmetric loads and thus reduce the peak forces in the cable net, as the entire roof is designed to move as wind and snow loads are applied. The cable net is made of 380 radial cables and 16 hoops, formed by groups of four and two cables. Radial cables are installed in pairs to provide the required strength and to facilitate the clamping between radial and circumferential cables. Hoop cables are arranged perpendicular to the ridgeline of the radials; they carry roof weight and permanent loads due to snow, restraining at the same time the roof under wind loads.



Figure 3: Cable net layout.

The cable net is clad with a three-layer envelope, which allows sunlight through and at the same time maintains an ambient microclimate all year round in a location that experiences extreme temperature variations. The cable supported fabric roof material is Ethylene Tetrafluoroethylene (ETFE), a fluorine-based plastic translucent film which combines high corrosion resistance and strength over a wide temperature range with excellent chemical, electrical and high-energy radiation resistance properties.

ETFE cladding is installed as 3.5x30-meter cushion panels tapered towards the cone and connected to the cables using a system of aluminium clamps, which are able to tolerate movements of the cables under wind and snow loads. The cushions can change shape as the cables move closer, adapting from an eye-shaped cross section to an almost cylindrical shape. In such an extreme climate, the challenge is to prevent ice forming on the inside of the cushions during winter. This is achieved by a combination of temperature control and directing warm air currents up the 19.000-square meter inner envelope surface.

### 3 CABLE SUPPLY

All radial and hoop cables are Open Spiral Strand (OSS), manufactured using helically wound hot-dip galvanized high strength steel round wires, spun in opposite directions around a central core. Redaelli supplied the entire cable system for the Khan Shatyr Entertainment Centre, the following table summarizes the entire supply, in terms of cable type, diameter, number of elements and socket types. The total length of cables supplied is about 40.000 meters.

**Table 1:** Details of cable supply

ITEM	Cable Type	Diameter (mm)	Element number	Socket 1	Socket 2
Circumferential Cables	OSS	38	16	CYL	CYL
	OSS	38	44	TBF	TBF
Radial Cables	OSS	38	332	CYR	TTF
	OSS	38	48	TTF	TBF

Fork (TTF and TBF) sockets are made of high strength cast steel, whereas cylindrical sockets (CYL and CYR), turnbuckles, threaded bars and pins are produced using machined high strength alloy steel. Cables are connected to the sockets with Polyester resin. Either the circumferential cables are fitted with cylindrical sockets in a closed arrangement or they have adjustable fork sockets to connect them to anchoring V-trusses. Hereafter some pictures illustrate the main items of cables supply.

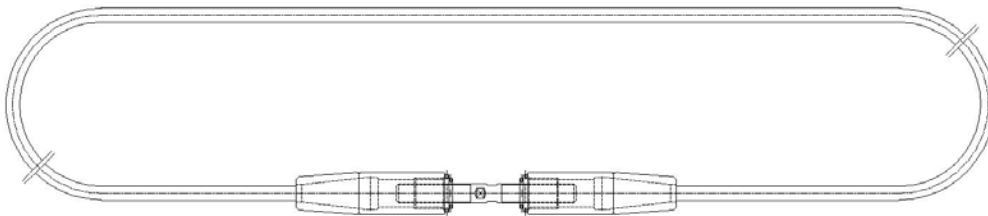


Figure 4: OSS hoop cable arrangement with CYL sockets.

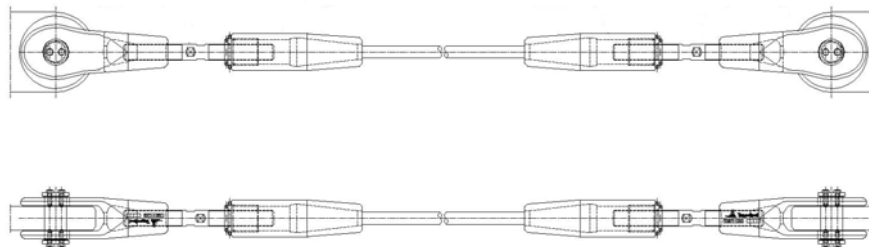


Figure 5: OSS cable arrangement with TBF sockets.



Tests are executed to verify cable modulus of elasticity and minimum breaking force and to evaluate actual clamps sliding force through a campaign of tests where actual clamps are forced to slide on a cable sample and the corresponding force is recorded. In addition to clamp slippage tests and cable tensile test, long term test is performed in order to define the actual creep coefficient and long term behaviour of the cable system.

### 3 CABLE NET INSTALLATION

Installation of such a complex cable net structure and its massive dimensions is a great challenge. Montage Service studied the engineering of cable installation and performed all related site activities, as well as the installation of ETFE cladding.

Giant dimensions of the structure, difficult accessibility to Kazakhstan's capital and small window of opportunity for site operations due to extreme climate are the main aspects that influences engineering and planning of the installation. The difficult access to site requires a careful study of transports, as all prefabricated materials are outsourced and site equipment is sent from Germany. Steel sections of tripod are prefabricated in Turkey and transported to site on trucks, ETFE cushions are made in China, numbered and labelled to be transported to site by train.

The erection of the tripod is done as a dramatic single lift process, where the mast is pivoted around pins at the base of the two front legs. In order to lift the tripod mast, a 80-meter high temporary tower is built and anchored to the structure concrete perimeter. Strand jacks running from the towers pull the tripod into position, with hub, struts and top ring already installed. As the front legs are erected, the top of the back leg is lifted on a temporary connection under the hub and its base slides on a bogie running on a rail truck. The mast top structure has a weight of 400 ton and it is supported with temporary bracing during the lift of the structure. This temporary bracing remains in position until all cable net is installed and correctly prestressed.



Figure 9: Big Lift of the tripod mast.

With the mast in its final position, cable net installation can start. Site operations are scheduled to avoid the worst of high winds that may occur during the winter. The installation sequence envisages at first radial cables lifted individually and pinned at the top anchorages. Cables are left in a slack condition, cable clamps are installed, and hoop cables are placed on top of the radials. This operation performed at height is especially difficult as two pairs of cable in orthogonal directions are involved (see Figure 10). Once all hoop cables are in place, radial cables are tensioned from the bottom adjustable socket to bring the net into shape and providing the required prestress.

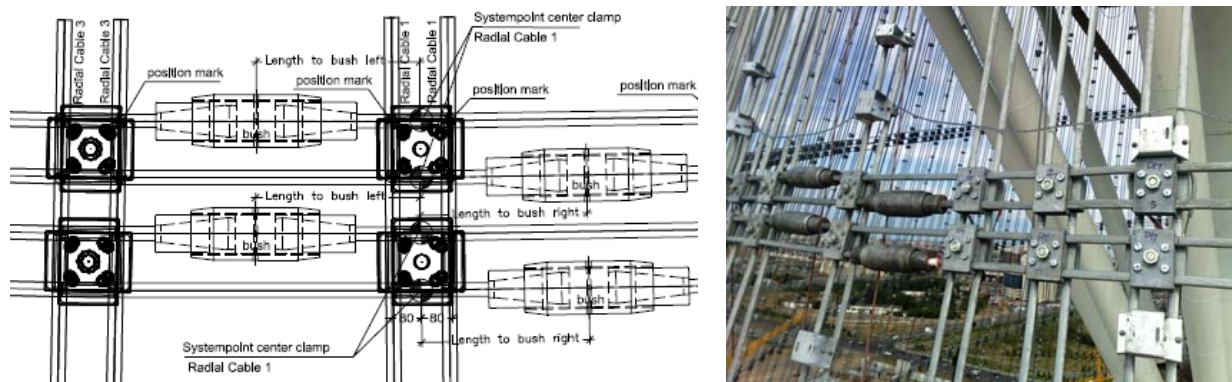


Figure 10: Crossing of radials and hoop cables.

The ETFE cushions are installed sliding into their extrusion from the base and pulled through the top. Since cushion frames are more rigid than the panels themselves, the cushions are arranged in properly studied staggered arrangement, so that the hoop frame of one panel can squeeze in on the mid point of the adjacent panel and benefit from its flexibility.



Figure 11: ETFE panels during and after installation.

#### 4 CONCLUSIONS

The Khan Shatyr Entertainment Centre spectacular design leads to numerous challenges for engineering and installation of the steel structure. All efforts put in place to succeed with these tasks results in an accurate production of cable with exact intermediate markings, careful planning of logistic to purchase the materials and deliver them on site, meticulous study of site operations to allow for all activities to be successfully completed within a time frame dictated by the extreme environment of the area.

The outstanding result is a land marking structure in one of the world most severe region, where people can significantly benefit from the comfortable microclimate created by this imaginative structural solution.



Figure 12: Khan Shatyr Entertainment Centre after completion.

## **ACOUSTIC PERFORMANCE TEST ASSESSMENT ON SOUND GENERATED BY RAINFALL ON MULTILAYER-ETFE-CUSHION SYSTEMS**

**MAURÍCIO R. P. CHIVANTE \*, SIMONE TOSO\*, KARSTEN MORITZ\***

\*Taiyo Europe GmbH  
Muehlweg 2  
82054 Sauerlach, Germany  
Email: info@taiyo-europe.com - Web page: <http://www.taiyo-europe.com>

**Key words:** ETFE cushion, Acoustic Performance, Rainfall.

**Summary.** Ethylene-tetra-fluor-ethylene (ETFE) membrane structure presents itself as an innovative construction element, taking advantage of its flexibility, lightweight, transparency and thermal insulation properties. However, for large enclosed areas, concerns exist related to the sound insulation characteristic of the system, especially related to the internal noise levels generated during rainfall conditions. Therefore, aiming to both assess the effect of rain noise on these structural elements, as well as generating a clear picture to this condition to designers and clients, Taiyo Europe promoted a measurement campaign on a predefined set of pneumatic ETFE roof elements. The set of pneumatic cushions investigated was produced from the same 250-micron thick ETFE foil. The number of layers, number of air chambers and the level of the pressure inside the cushion was variable, following a carefully predefined test plan. The elements were tested with and without an additional rain suppressor fabric mesh on top of the specimen. The tested elements were installed on a special outdoor structure designed and built for this purpose. This work will describe the tests performed, as well as an assessment of the results achieved and their impact on the design of enclosed buildings clad with ETFE pneumatic structures.

### **1 INTRODUCTION**

As an innovative construction element, it has already been extensively discussed on the literature the benefits of the multilayer-ETFE-cushion systems in comparison to other roof systems, including its aesthetic value, design flexibility, durability and lightweight. However, due to the small mass per unit area of these foil system, they mostly present a lower sound insulation than solid building materials and little reliable acoustical data (on the system) is available on the literature <sup>1</sup>.

Therefore, the current document presents the outcomes of a measurement campaign on a set of multilayer-ETFE cushions, supplied and installed by Taiyo Europe GmbH, aiming to assess the rain noise effect on these systems.

These tests were performed by the Textiles Hub Laboratory at Politecnico di Milano from July 18<sup>th</sup> to 22<sup>nd</sup>, 2016, at their own premises (31 Ponzio St., Milan, Italy).

## 2 TEST ARRANGEMENT AND PROCEDURE

The tested cushion samples were manufactured with the same geometry (3,2m x 3,4m) and using the same 250 micron clear ETFE foil. However, the number of layers, number of air chambers and inner pressure within the chambers were variable (**Table 1**).

Moreover, samples with and without the installation of an outer fabric mesh rain suppressor were also assessed. Covering a film with a mesh aims to reduce the rain noise from ETFE system, once the rain accumulates inside the mesh and forms a layer of water, which will weaken the strikes of the rain drop and also damps the vibration of the roof <sup>1</sup>.

**Table 1:** List of Tests Performed

Test Code	Description of the tested specimen				
	Number of layers	Inner Chamber pressure		Rain type	Rain suppressor
		Middle [Pa]	Outer [Pa]		
L4_P300_HR_O	4	400	300	Heavy	
L4_P600_HR_O	4	700	600	Heavy	
L4_P900_HR_O	4	1000	900	Heavy	
L3_P300_HR_O	3	400	300	Heavy	
L3_P300_HR_R	3	400	300	Heavy	Yes
L3_P300_IR_O	3	400	300	Intense	
L3_P300_IR_R	3	400	300	Intense	Yes
L3_P600_HR_O	3	700	600	Heavy	
L3_P900_HR_O	3	1000	900	Heavy	
L2_P300_HR_O	2	-	300	Heavy	
L2_P600_HR_O	2	-	600	Heavy	
L2_P900_HR_O	2	-	900	Heavy	

The following standards were considered on performing these test:

- International Standards Organization, “Acoustics - Measurement of sound insulation in buildings and of building elements - Part 18: Laboratory measurement of sound generated by rainfall on building elements (ISO 140-18:2006)”. International Standard DIN EN ISO 140-18:2007-02.

- International Standards Organization, “Acoustics - Laboratory measurement of sound insulation of building elements - Part 1: Application rules for specific products”. International Standard DIN EN ISO 10140-1:2016-12.
- International Standards Organization, “Acoustics – Measurement of sound insulation in buildings and of building elements using sound intensity – Part 1: Laboratory measurements”. International Standard ISO 15186-1, 2000-03.

## 2.1 Test Hut

A special insulated outdoor hut was built at POLIMI labs, in order to arrange the ETFE system specimens to be tested. This hut is shaped as a 3,5m x4,5m box, with variable height (from 2,5m to 3,5m), in order to create an inclined roofing surface (roughly 20°) as recommended by the followed standards. It was fabricated using steel structure and insulated lightweight drywalls (**Figure 1**).

The whole inside surface was treated with sound-proof materials, using both mineral wool, polyester non-woven mattresses and melamine foam modules, aiming to reducing the internal reverberation components and allowing a better use of intensimetry method.



Figure 1 (left): External View of the Test Hut;  
Figure 2 (right): Detail of the Steel Tank Perforated Base Used for Simulating Intense and Heavy Rain Scenarios.

## 2.2 Apparatus for rainfall simulation

For artificial raindrop production, a movable tank with a perforated base (area of 1,60m<sup>2</sup>) was installed over the hut, following the specifications defined on DIN EN ISO 140-18:2007-02 (Table A.1 of Annex A). This allowed the simulation of two different conditions: INTENSE and HEAVY rain (**Figure 2**).

The heavy rain scenario was achieved by producing a rainfall rate of 40 mm/h from the base

suspended 3,5m over the test specimen. The intense rain scenario was achieved by producing a rainfall rate of 14 mm/h from the base suspended 1m over the test specimen (see **Figure 3**).

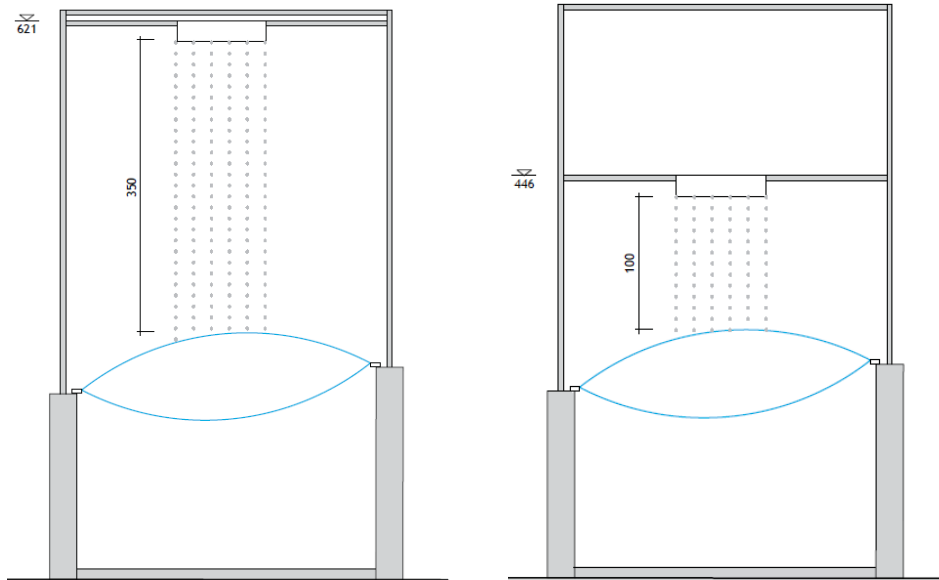


Figure 3: Schematic Section of The Test Unit, With the Configuration for Heavy (Left) and Intense (Right) Rain.

### 2.3 Rainfall Measurement

The rainfall measurement area was arranged in a grid subdivided in 24 (6x4) sub-areas. A microphone was positioned at the center of each of those 24 sub-areas.

The time of measurement was of at least 20 seconds of each 24 points, from which the spectra of results were built on a frequency range corresponding to one-third octave, from 100Hz to over 5000Hz.

The measurement frequency range was organized in ranges of one-third octave and one octave (from 100Hz to 5000Hz). Sound intensity level was then calculated for each cushion configuration. Furthermore, the Global A-weighted sound intensity level was calculated by adding A-frequency weighting to the measured results of the whole ranges.

### 2.4 Possible interferences during the tests

In order to assess possible interferences during the tests, the surrounding acoustic level was measured to validate both the sound intensity and sound pressure measurements. The following sound sources were registered as the main components of the background sound level during the test campaign: blowing machine sound, water pump noise, anthropic noise and traffic noise.

The background sound was measured on every day of the test campaign. The result was always 10db lower than the registered measurements. Therefore all the tests results were not influenced by the background sound.

### 3 RESULTS

The following graphics present the result of the tests described on Table 1.

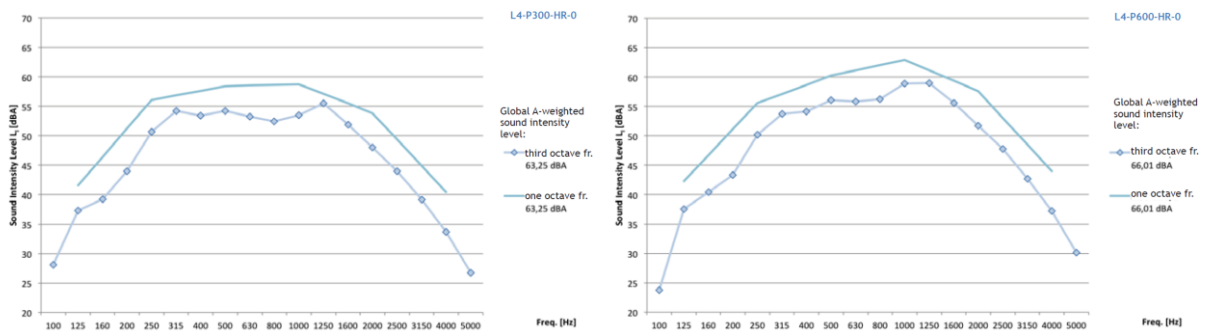


Figure 4 (left): Test Result L4\_P300\_HR\_O; Figure 5 (right): Test Result L4\_P600\_HR\_O.

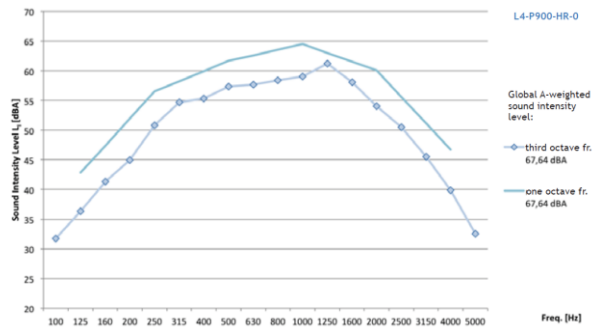


Figure 6: Test Result L4\_P900\_HR\_O.

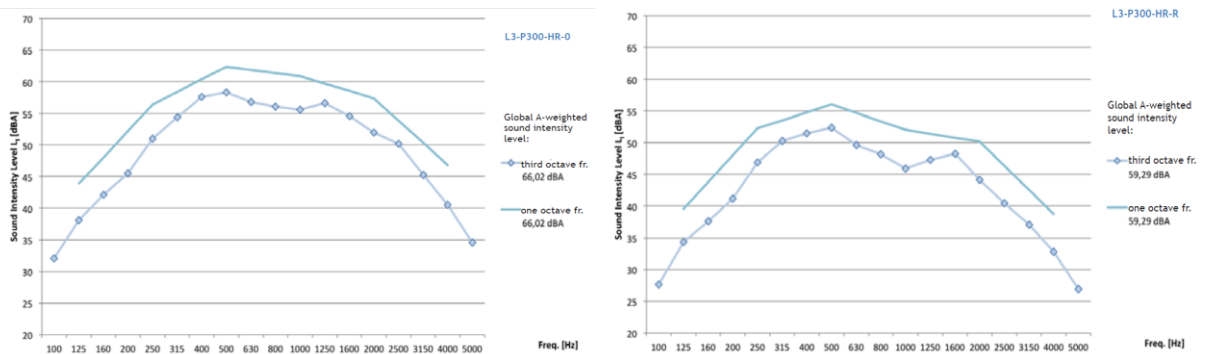


Figure 7 (left): Test Result L3\_P300\_HR\_O; Figure 8 (right): Test Result L3\_P300\_HR\_R.

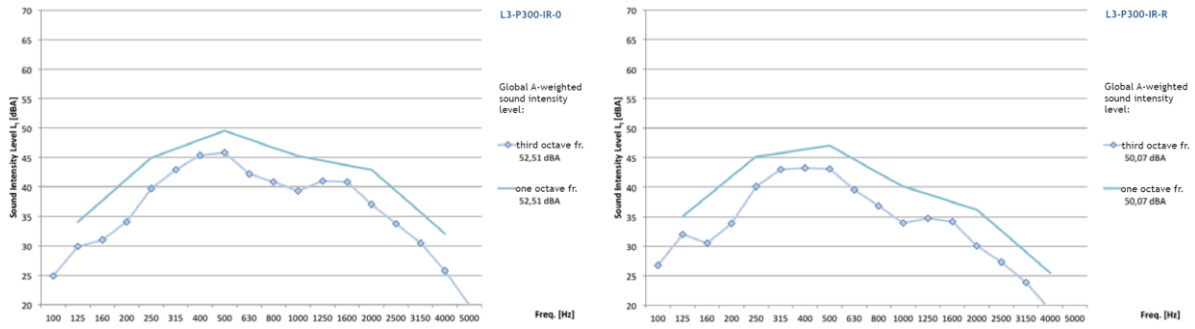


Figure 9 (left): Test Result L3\_P300\_IR\_O; Figure 10 (right): Test Result L3\_P300\_IR\_R.

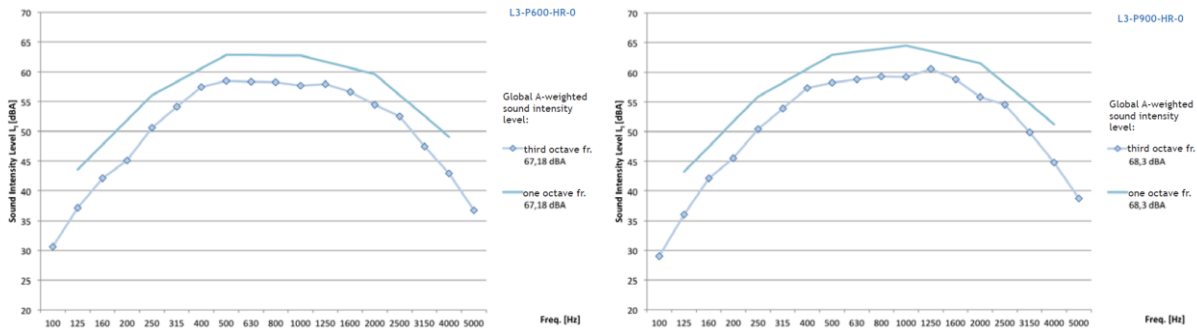


Figure 11 (left): Test Result L3\_P600\_HR\_O; Figure 12 (right): Test Result L3\_P900\_HR\_O.

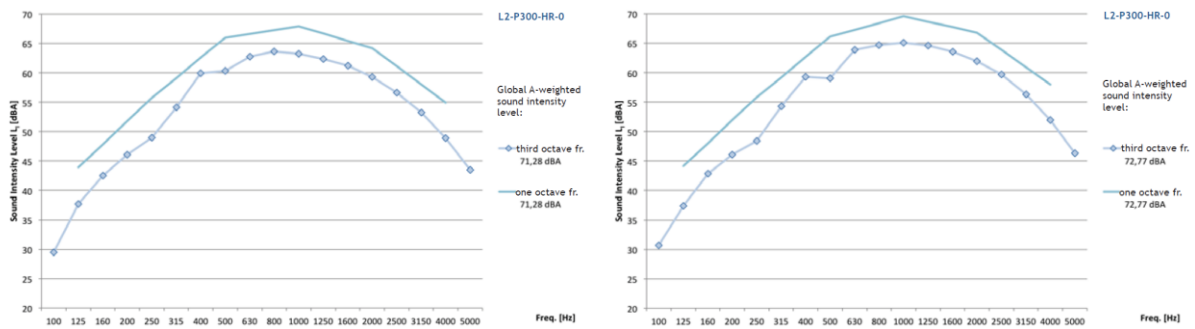


Figure 13 (left): Test Result L2\_P300\_HR\_O; Figure 14 (right): Test Result L2\_P600\_HR\_O.

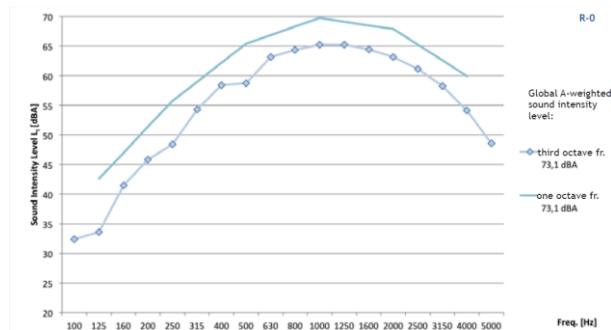


Figure 15: Test Result L2\_P900\_HR\_O.

## 4 DISCUSSION

A comparative evaluation of the test results indicate (as expected) that the quantity of layers (and air chambers) affect the rain noise perceived under the ETFE cushion. The more layers the system have, the lower the rain noise levels under it.

Following a comparison between samples with the same configuration of the ETFE layers but with variation on the inner pressure, it is observable that the intensity of the rain noise increases following an increase of the internal air chamber pressure. However, in the range of the lower frequencies (under 1kHz) the different inner pressure levels seem not to affect the rain noise perception.

A comparison between samples with the same configuration of the ETFE layers, with and without adding an external rain suppressor layer show that the rain suppressor contributes more during an intense rain than a heavy rain. During the Intense Rain set-up, the maximum difference between the specimen's configuration with and without rain suppressor is 6,68 dB. During the Heavy Rain set-up, the maximum difference is 5,23 dB. Furthermore, the results show that the rain suppressor seems not to give a significant contribution for frequencies under 1kHz – region where we found the rain noise intensity peak.

## 5 CONCLUSIONS

This work presents an assessment of the noise derived from heavy and intense rain on multilayer-ETFE-cushion systems. It also brings a clear picture to this condition to researchers, designers and clients.

The generation of rain noise was experimentally investigated on a number of different ETFE cushions configurations. It concludes that the quantity of layers and the inner system pressure affects the rain noise.

It also indicates that the application of a rain suppressor fabric mesh over the system does not to give a significant contribution for frequencies under 1kHz – region where we found the rain noise intensity peak. Therefore, the decision for the application of this element should be assessed along with other project related specificities, such as: Additional implementation costs; visual obstruction (reducing the translucency of the system); and additional maintenance costs (once the mesh will accumulate airborne suspension, affecting not only its aesthetical appearance but also reducing the system's light transmittance).

## REFERENCES

- [1] L. Weber, S. R. Mehra, "Sound Insulation of Foils and Membranes", Fraunhofer Institute of Building Physics (IBP), Stuttgart (2002)
- [2] M. Toyoda, D. Takahashi, "Reduction of Rain Noise from Ethylene/TetrafluoroEthylene Membrane Structures", Vol. 74, pp. 1309-1314, (2013)

## ENGINEERING AND FABRICATION OF THE “OFF THE CUFF” PAVILION, FUORISALONE 2017, MILAN

P. BECCARELLI\* AND R. MAFFEI†

\* Department of Architecture & Built Environment  
University of Nottingham  
University Park, Nottingham NG7 2RD, United Kingdom  
e-mail: paolo.beccarelli@nottingham.ac.uk, web page: <https://www.nottingham.ac.uk>

† Maco Technology srl  
Via U. La Malfa 86/88, 25050 Provaglio d’Iseo (BS), Italy  
Email: [design@macotechnology.com](mailto:design@macotechnology.com), web page: <http://www.macotechnology.com/>

**Key words:** Off The Cuff, DS+R, Diller Scofidio + Renfro, Salone del Mobile, 2017, Milan, Linking Minds.

**Summary.** The paper presents the engineering and fabrication of the “Off The Cuff” pavilion designed by Diller Scofidio + Renfro for the exhibition “A Matter of Perception: LINKING MINDS” organised by DAMN° and Mosca Partners at Palazzo Litta for the FuoriSalone2017.

The roof canopy is composed of 300 pairs of jeans. DS+R deploys the jeans as ready-mades, intentionally misusing and translating them from the context of the human body into an architectural module.

The design exploits the implicit structural logic of the jeans connecting them waist-to-waist and cuff-to-cuff to create a tensile, catenary diagrid that spans the open space of the courtyard. The net gives the impression of a body imprinted in space, but one also defamiliarised by repetition.

As an architectural figure, the net springs across the courtyard, describing a collective ethos; as a series of modular parts, the jeans point to the individual human dimension. A contemporary folly in the bracketed context of monumental classicism, the canopy stitches together two vital scales of urban life.

The authors, with Maco Technology srl as main contractor and the University of Nottingham as structural consultant, worked as project managers for the pavilion supporting DS+R from the progressive development of the initial idea to the fabrication and installation of the pavilion. The activity here presented included the refining the preliminary engineering design done by Thornton Tomasetti and the selection of the suppliers.

### 1 INTRODUCTION

Every year the “Salone del Mobile” represents one of the main international events for Milan with more than 343.600 attendees in 6 days from 165 countries. During the same days the city becomes the international capital of design with hundreds of events and exhibitions organized around the City.

The pavilion “Off the Cuff” is the main installation of the third edition of the ‘A Matter of Perception’ exhibition which explored the theme of LINKING MINDS. The exhibition, organized by Mosca Partners and DAMN°, was hosted by Palazzo Litta which is itself a fascinating example of Lombard Baroque architecture in the city and an expression of the connection between Milanese culture and the French and English Enlightenment (fig. 1).

The pavilion was designed by Diller Scofidio + Renfro, an interdisciplinary design studio based in New York City that integrates architecture, the visual arts, and the performing arts. According to Liz Diller, the initial concept was based on the idea of “using ready-made modules – actually misusing them – for architectural purposes. In the back of our minds – and this might sound very peculiar – we have always wanted to use actual trousers as a module”<sup>1</sup>.

Maco Technology and the University of Nottingham were contacted in January 2017 in order to provide the support for the final engineering, manufacturing and installation of the pavilion by the 3<sup>rd</sup> of April 2017.



Figure 1: View of Palazzo Litta, location of the exhibition ‘A Matter of Perception: LINKING MINDS 2017’. The palace is placed in in the 5VIE design district.

### 3 THE TECHNICAL SOLUTIONS ADOPTED

The project has been challenging under several aspects such as the extremely tight time schedule, the constraints imposed by the Monuments and Fine Arts Department, the building materials used and the complex 3D modelling of the structure.

The reduced time available for the project, 12 weeks in total, imposed the development of a final version of the initial idea in less than 6 weeks in order to start the manufacturing of the

components (4 weeks), the preassembly of the units (1 week) and the final installation (1 week).

The canopy (fig. 2) is a jean fabric grid stretched between cable-stay posts. Structural stability is ensured through a balance of form-finding and the base structure which resolves the system without the need for heavy ballast under the ties. Material testing was performed to verify the structural integrity of the denim and connections with transmitted forces of up to 2kN. Thin Kevlar rope was introduced as an erection aid and remains to provide supplementary support to the system. A PVC foil sits above the denim and kevlar mesh.

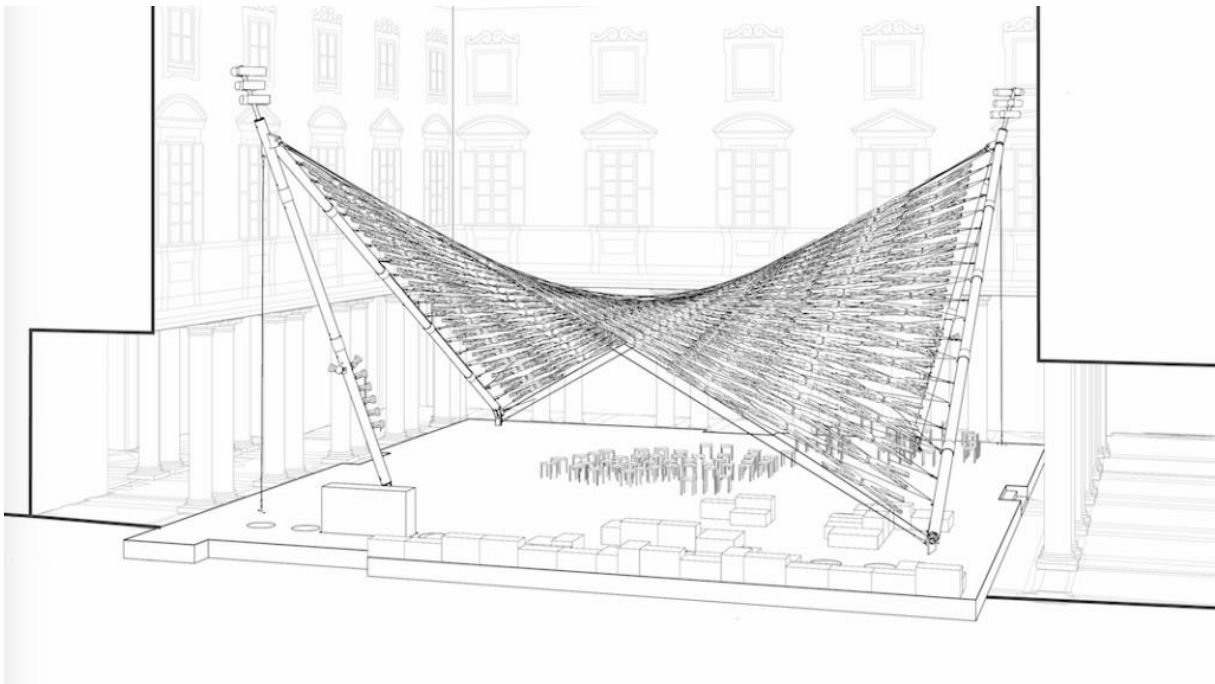


Figure 2: 3D view of the pavilion by Diller Scofidio + Renfro<sup>2</sup>

The main challenge was to optimize the shape of the pairs of trousers which had to fit the mesh selected by the architect and the size of the inflatable mannequins available on the market (Fig. 3). Thanks to a form finding algorithm it has been possible to adjust the geometry of the surface in order to have only one module and, consequently, only one size of trousers to be produced. The required strength of the trousers has been achieved by increasing the number and size of the belt loops and by inserting a metal ring in correspondence of the cuffs.

The elongation of the denim under load and in presence of different levels of humidity has been addressed through adjustable connections (cable ties) in correspondence of the cuffs and the waist of each unit and adding a set of adjustable Kevlar ropes between the steel frame and the mesh in order to introduce the required level of pretension into the tensile structure. The length of the Kevlar rope was controlled by means of a GI-GI plate, a multiuse belay plate commonly used for climbing.

The mesh was supported by a rigid steel structure designed to avoid the transfer of additional loads to the existing building apart from the gravity loads. The final structural

solutions did not require permanent foundations, anchoring points or heavy ballasts. The vertical loads have been distributed on the ground through thick timber boards.

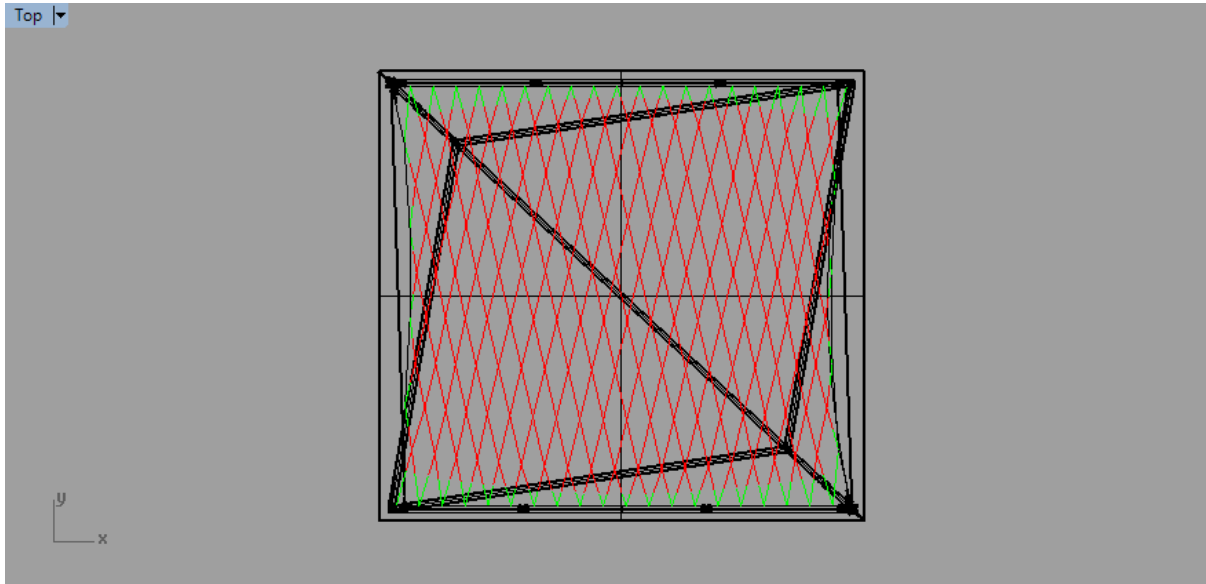


Figure 3: Top view of the mesh with the units with a fixed length (in red) and the adjustable Kevlar ropes (in green)

In order to facilitate the installation of the steel structure, the two main posts have been designed with pinned joints able to allow the rotation from the initial horizontal plane, used for the connection of the components at ground level, to the vertical plane required by the final geometry of the pavilion. Each post was stabilized by two cables (Full Locked Coil by Redaelli Tecna) connected to the basement.

#### 4 DESIGNED AND MANUFACTURING OF THE TROUSERS

The final design implemented several solutions designed to optimize the manufacturing and installation of the pavilion. One key aspects was the manufacturing of the 360 pairs of trousers which had to be manufactured for the final mock-up and for the pavilion. Thanks to the optimization of the diamond mesh it has been possible to produce only one single model of trousers able to fit into all the units of the mesh.

The trousers (fig. 4) has been sponsored and manufactured by Trussardi Spa according to the specification developed considering the sized of the mesh, the dimension and shape of the connection, the required strength of the fabric and the aesthetic requirements. The main features included a set of eight reinforced belt loops, a total length equal to 96.5cm and a bespoke cuff able to host the metal ring used to distribute the tensile load into the full section of the trousers.

Once ready, the trousers were filled with inflatable mannequins, used to improve the shape and the structural stiffness, and pre-assembled in units of two connecting the belt loops with black cable ties and inserting the metal rings in correspondence of the cuffs. The cable ties provided the required strength and allowed the re-tensioning necessary to compensate the

progressive elongation of the jeans fabric and to adjust potential inaccuracies in the manufacturing and installation of the 304 pairs of jeans. Once completed, the units have been treated with a fire retardant liquid and transported onsite ready for the installation.

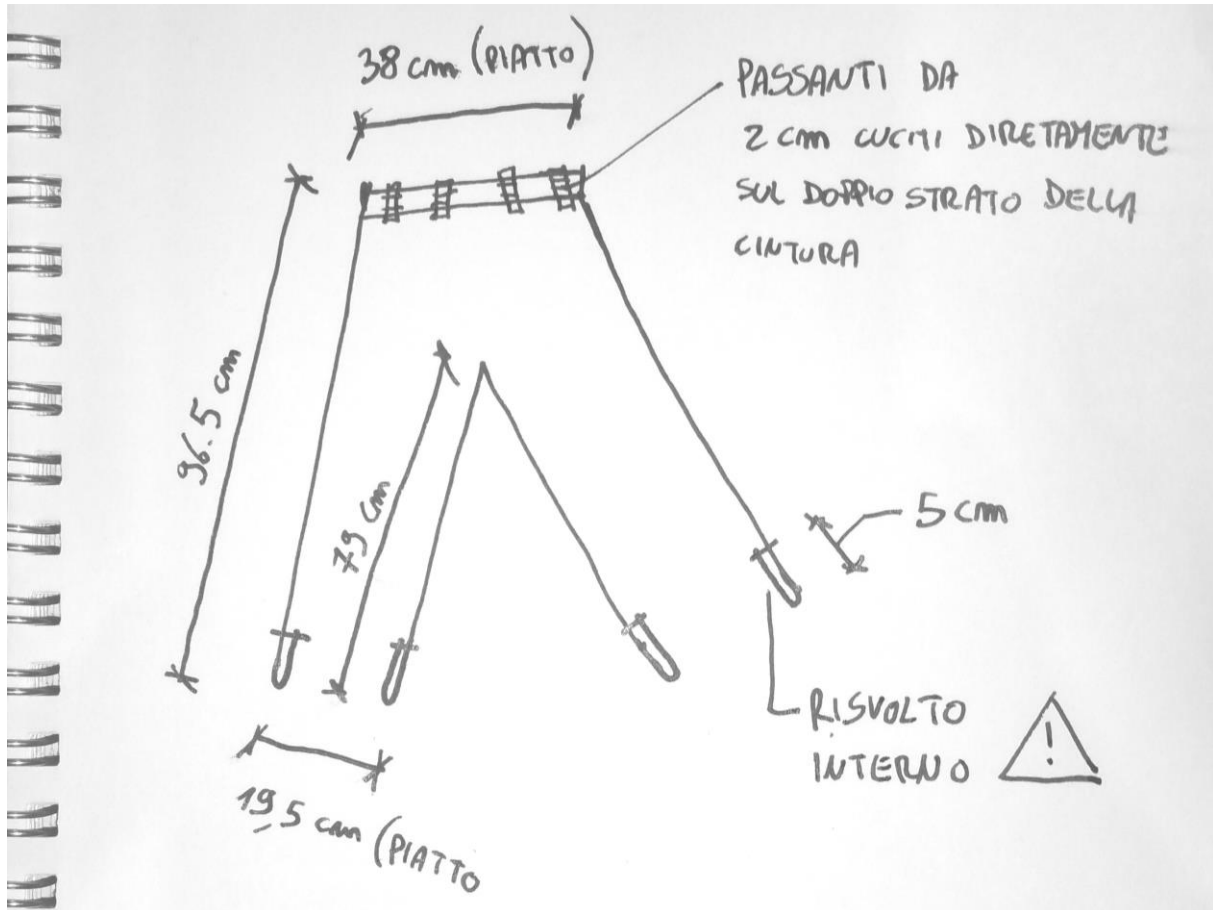


Figure 4: Copy of the sketch used for the production of the trousers.

## 5 INSTALLATION OF THE PAVILION

The installation of the pavilion was mainly driven by the limited access to the site which was located in one of the busiest areas of the historic centre of Milan. Due to the small size of the main gate and because of the reduced space available inside the courtyard, which was almost entirely occupied by the pavilion, the pavilion had to be subdivided in small components which could be easily moved and assembled by a team of 6 people with the support of the hydraulic crane installed on the truck used to deliver the components onsite.

In addition, the courtyard of the palace was available only for eight working days with a very tight programme that limited to a maximum of five days the time available for the erection of the structure of the pavilion.

The installation started with the assembly of the basement made by a rigid steel frame obtained by welding and bolting a set of hollow square sections 400x200x5mm (diagonals) and 260x260x4mm (perimeter). Timber beams were used to level the steel basement and to

spread the load in order to reduce the risk of damages to the ancient floor made of pebbles stones.



Figure 5: Installation of the steel structure. Detail of the Lifting of the steel posts<sup>3</sup>.

Once completed the basement, the team of workers installed the lateral beams and posts which, thanks to the special pinned joints, were initially installed in the horizontal plane and then lifted by means of the hydraulic crane installed on the truck. A set of two cables were designed to stop the rotation of the steel structure once reached the correct position. The task was extremely challenging due to the limited space available and the risk of damaging the columns and the facades of the building.

The following step was the assembly of the mesh of safety Kevlar ropes designed to support the mesh of trousers during the installation and to provide an emergency support in case of failure of one, or more, of the units. Finally, the surface was completed with the installation of 304 pairs of trousers which were partially covered by a strip of PVC Crystal designed to protect the central part of the pavilion from the rain.

The installation included a bespoke lighting provided by Zumtobel and a timber floor used to cover the grid of beams used for the foundations.



Figure 6: Final adjustments of the level of pretension introduced in the mesh.



Figure 7: Detail of the structural connection between the thousers



Figure 8: View of the clear PCV foil applied on top of the pavilion



Figure 9: View of the mesh for underneath.



Figure 9: View of the pavilion at night (photo: Ruy Teixeira)

## CONCLUSIONS

The paper describes the design and manufacturing process of the “Off the Cuff” pavilion designed by Diller Scofidio + Renfro for the exhibition ‘A Matter of Perception: LINKING MINDS 2017’ presented during the Milan Design Week.

The description includes the technical solutions adopted during the structural design, the detailing, the manufacturing and installation.

## ACKNOWLEDGMENTS

The authors would like to thank the team of companies involved in the project: Mosca Partners, DAMN°, Diller Scofidio + Renfro, Thornton Tomasetti, Maco Technology, L’observatoire International, Emeco, Eterno Ivica, Gaggenau, Living Divani, Trussardi, Zumtobel, Redaelli Tecna, F.Lli Giovanardi

## REFERENCES

- [1] <http://www.moscapartners.it>.
- [2] <http://www.dsrfny.com/>
- [3] <http://www.macotechnology.com/>

## ETFE FOIL CUSHION TECHNOLOGY FOR CRUISE LINERS

**Gabriele Müller\*, Florian Goecke\*, Karsten Moritz**

\*seele cover GmbH  
Bahnhofstraße 28  
83119 Obing, Germany  
E-mail: info.cover@seele.com - Web page: www.seele.com

**Key words:** ETFE cushion, cruise liner, membrane architecture, ETFE roof, movable roof

### Summary

*AIDA Cruises, the German-Italian subsidiary of the American shipping company Carnival Corporation, has one of the world's most modern and most environmentally friendly fleets of cruise liners. The name AIDA suggests visits to other cities and countries, dream holidays, relaxation and experiencing nature on the very highest level.*

*The AIDAprima and its sister ship the AIDAprera are two new Hyperion Class cruise liners that have now entered service. Both ships were built at the Mitsubishi Heavy Industries Ltd. (MHI) shipyard in Nagasaki, Japan.*

*The total area of the ETFE roofs on both ships is about 4,000 sqm. Three-layer, transparent ETFE foil cushions span over the pool and leisure areas of the activity decks with their "4 Elements" and "Beach Club" centrepieces. Movable roof sections enable the areas of the "4 Elements" to be opened to the sky.*

*Vibrations from the ship's engines, acceleration forces due to the motion of the ship, high wind loads some 50 m above sea level, the marine climate with its corresponding salt concentrations plus the different climate zones place tough demands on the materials and combinations thereof as well as the structural design and the detailing. ETFE foil roofs in ship-building are new, which is why the necessary engineering solutions represent a huge challenge.*

## 1. INTRODUCTION

For the first time on cruise liners, two large upper deck areas have been roofed over with transparent ETFE foil domes (Fig. 1). A total of 82 three-layer, transparent foil cushions with printed areas cover the steel frames of the “Four Elements” (Fig. 2) and “Beach Club” (Fig. 4) domes – a roof area of almost 2000 m<sup>2</sup> per ship. Beneath the foil domes there are extensive pool and leisure areas with bars, waterslide and climbing course.



Fig. 1: The upper decks of the AIDA Prima with the two foil domes “Four Elements” and “Beach Club”; 3D computer image, copyright: AIDA CRUISES, Rostock, PSD, Hamburg

The “Four Elements” dome is composed of two movable halves so that – depending on weather conditions – it can be opened to allow crew and passengers to enjoy the fresh sea air or closed to protect against wind and rain while enjoying the pool facilities (Figs. 2 and 3).

Following extensive studies and investigations, the designers at Hamburg-based PartnerShipDesign (PSD) and the AIDA Cruises shipping company in Rostock opted to use ETFE as the roof covering – a new material on cruise liners – because it offers a number of advantages compared with the designs in laminated safety glass used up until now:

- lower weight per unit area
- larger support spacing (lower self-weight, greater transparency)
- lower system stiffness
- higher UV transmission

The weight per unit area of the three-layer ETFE foil cushions (with thicknesses of 250, 200 and 250  $\mu\text{m}$ ) is less than  $1.5 \text{ kg/m}^2$ . A corresponding laminated safety glass roof would weigh at least 20 times this figure.

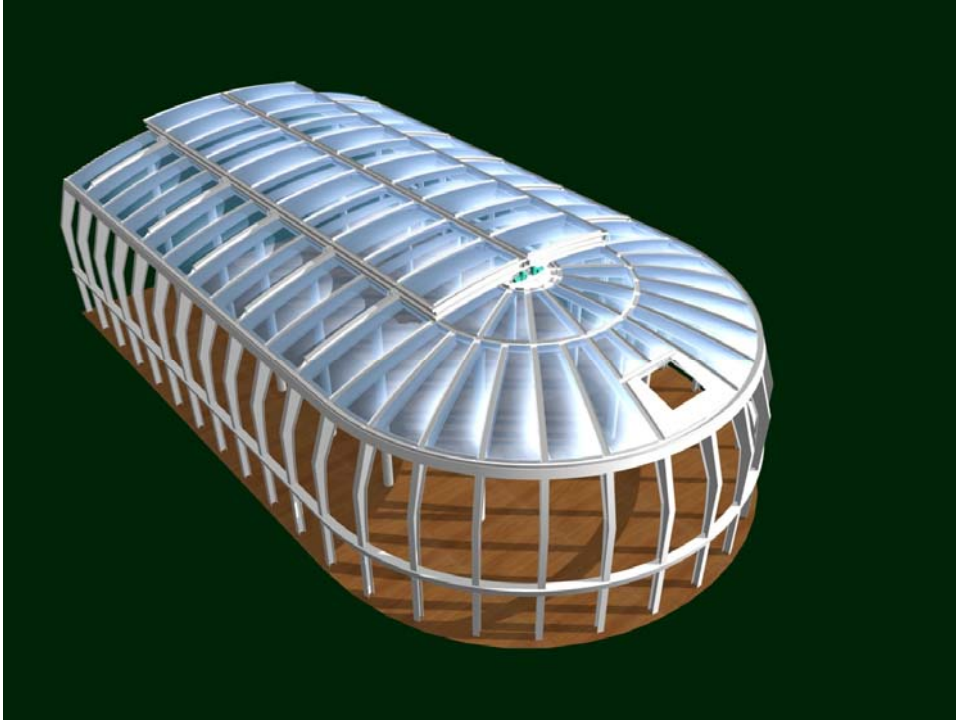


Fig. 2: The “Four Elements” foil dome when closed; 3D computer image, draft design, seele cover



Fig. 3: The “Four Elements” foil dome when open; 3D computer image, draft design, seele cover

The span of the ETFE foil cushions achieved here is, on average, about 2.5 m between the curved members of the steel frame. The longest ETFE cushions on the “Beach Club” roof are about 33 m long. Linear support to panes of laminated safety glass would require a steel member every 1.2 m. So compared with glass, ETFE is an advantage when it comes to transparency and weight of the structure. Moreover, the low system stiffness of the ETFE foil cushions turned out to be another benefit. They are forgiving when it comes to larger deformations of the structure which result from the motion of the ship (hogging, sagging, etc.) and temperature fluctuations. Finally, on the “Beach Club” structure the shipbuilders managed to avoid load bearing members parallel with the longitudinal axis of the ship, so the uniform appearance of the soffit is not interrupted by any longitudinal members (Fig. 4). Another aspect in favour of ETFE foil is its high UV transmission. An ETFE roof favours the growth of plants underneath – an important criterion for leisure areas with natural flora (and fauna).

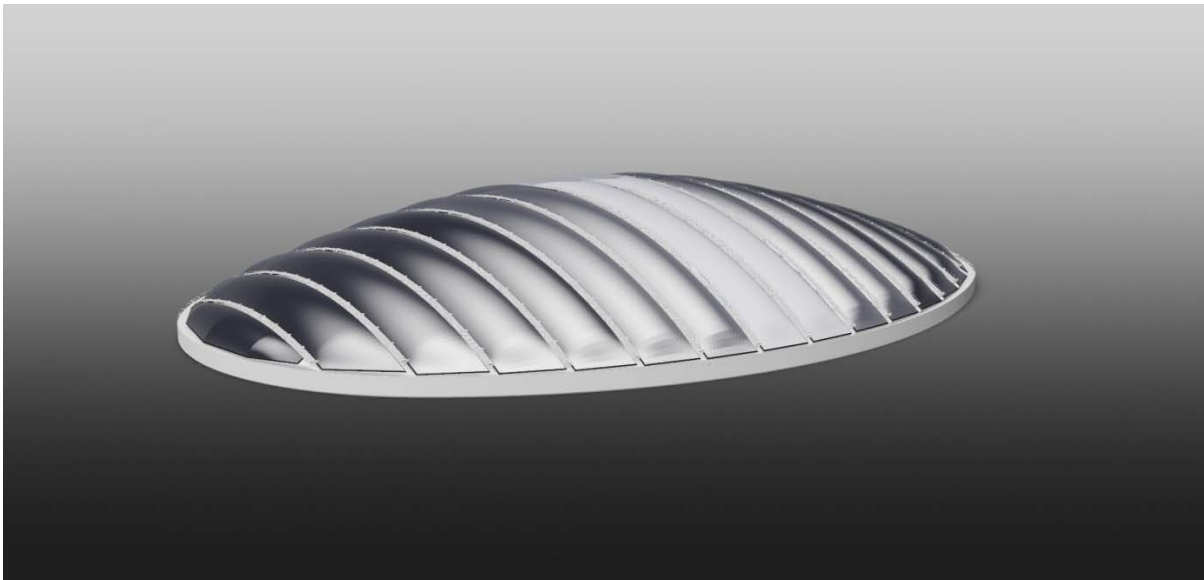


Fig. 4: The “Beach Club” foil dome; 3D computer image, draft design, seele cover

## 2. DESIGN

seele cover was appointed by the Mitsubishi Heavy Industries (MHI) shipyard in 2013 to carry out a design and build contract for a total of four ETFE foil roofs on the two cruise liners. The contract included very different types of work:

- ETFE foil cushions with clamping plates and temporary protection measures during construction.
- Air supply systems, including fan units, supply lines, power chains and pressure instrumentation.
- Gutter systems with foam glass insulation and waterproofing-sealing of the surfaces.
- A ventilation element in the “Beach Club” dome and movable roof segments in the “Four Elements” dome, including the necessary electrical installation, sensors, control system, remote controls, geared motors, belt drives, lip and pneumatic seals and pneumatic locking devices.

- Mobile maintenance bridge
- Mock-ups in Japan and Germany
- Design concept for GFRP open-grid flooring for maintenance walkways, with steel supports
- Design concept for external washing systems for both domes
- Design concept for fall protection systems with fixings
- Design concept for primary load bearing structure in steel (Figs. 5 and 6)

The upper decks of cruise liners represents a new application for ETFE foil cushions and this led to special requirements that do not normally have to be considered for structures on land.

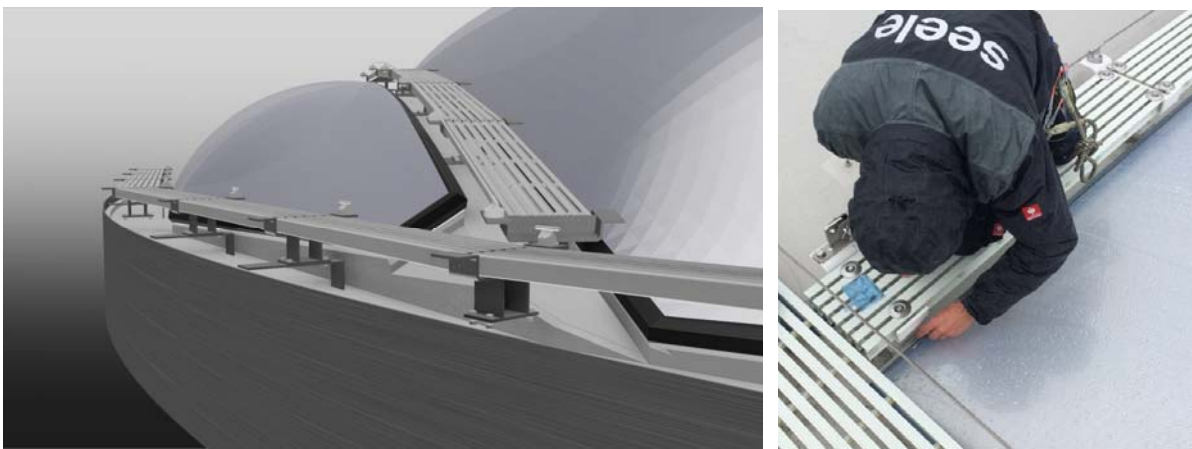


Fig. 5: “Beach Club” foil dome, isometric view showing GFRP walkway and ETFE cushion connection; 3D computer image, draft design, and picture from the installation process, seele cover

## 2.1 Shipbuilding specifications

The directives and codes of practice applicable in shipbuilding are in some instances very different to those that apply to buildings. For obvious reasons, on ships there are very stringent requirements covering fire protection, emissions of hazardous substances and potential noise and vibrations and their possible effects (sound transmission, fatigue strength and fixing of components).

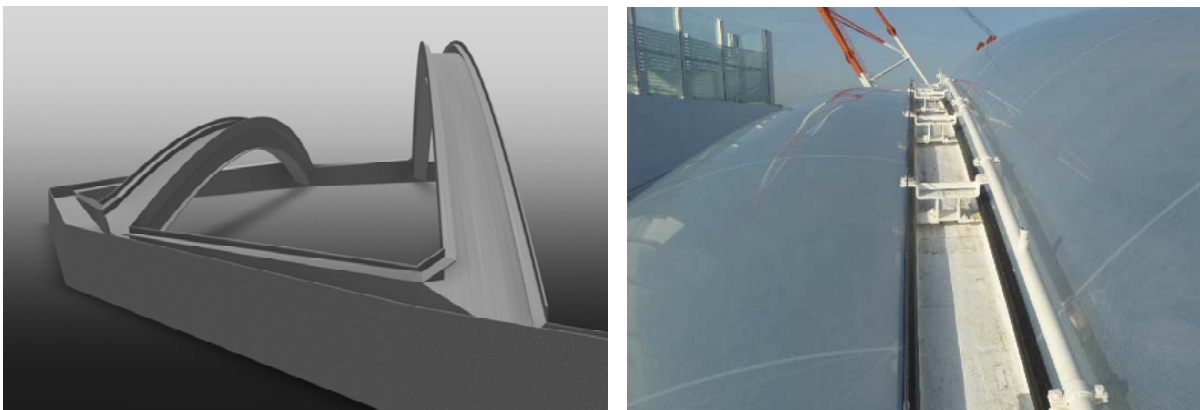


Fig. 6: “Beach Club” foil dome, detail of steelwork connections; 3D computer image, draft design, and picture from the installation process, seele cover

Load assumptions and structural safety concepts are especially important in shipbuilding. The design code normally used for buildings in Europe, Eurocode (EC) 0, Basis of structural design, is not generally applied in shipbuilding, likewise the (semi-)probabilistic safety concept of partial safety factors for actions and resistances associated with this standard.

## 2.2 Corrosion protection

The salt-laden marine climate places high demands on the corrosion resistance of metal components and their connections. However, the requirements are known from building in corrosive environments on land (coastal areas, swimming pools, saltwater baths). In this respect, the classification company (e.g. DNV GL) offers comprehensive and helpful rules and specifications in its directives.

Retaining members in the form of clamping plates made from aluminium are normally used along all the edges of the textile or foil membranes of membrane structures. Such clamping plates are usually connected to the primary structure, e.g. in steel, by means of (stainless steel) screws or bolts.

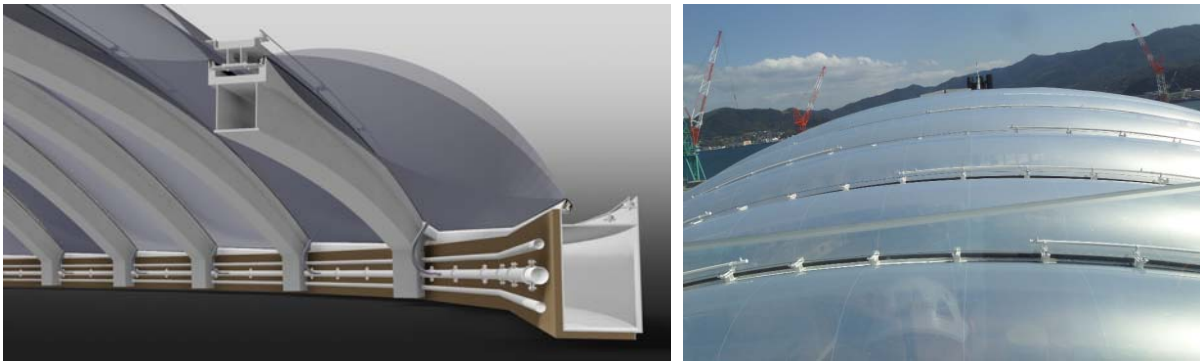


Fig. 7: “Beach Club” foil dome, steel sections with thermal insulation and services; 3D computer image, draft design, and picture from the installation process, seele cover

Such connections consist of three different metals: steel, aluminium, stainless steel. If the different metals are not kept apart by separating membranes, there is a great risk of galvanic corrosion. seele cover has therefore developed a clamping plate specifically for use in corrosive environments. The patented aluminium section does not need any screws because it clips onto the painted mild steel of the primary structure. A separating layer made from EPDM prevents galvanic corrosion between the anodised aluminium and the painted mild steel (Fig. 8).

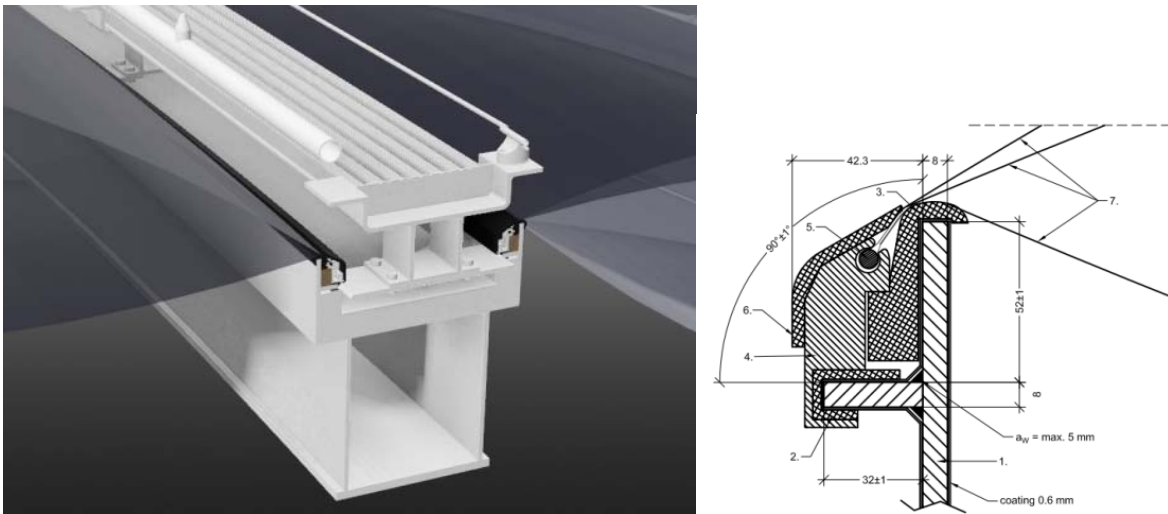


Fig. 8: “Beach Club” foil dome, gutter cross-section with thermal insulation; 3D computer image and detail drawing, draft design, seele cover

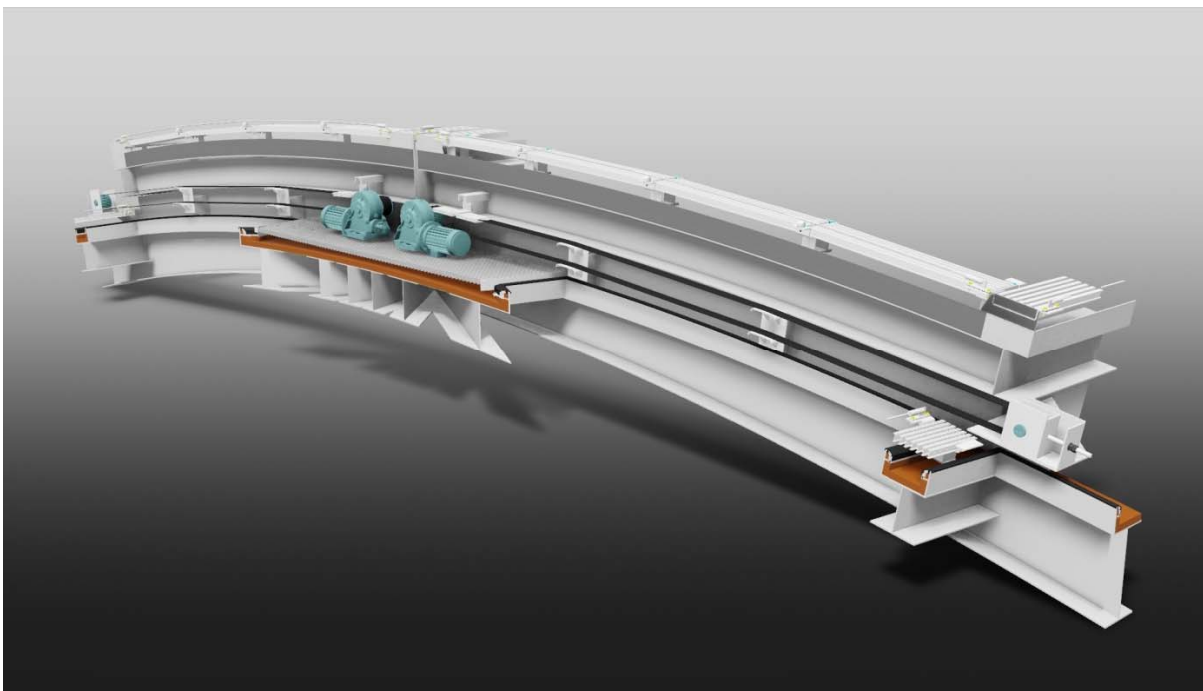


Fig. 9: “Four Elements” foil dome, drive mechanism for movable roof segment; 3D computer image, draft design, seele cover

### 2.3 Vibrations, noise

Minimising vibrations is not only a vital criterion for comfort on board a cruise liner. In extreme cases, even safety can be affected.

Of course, on the one hand, noise or vibrations should not have any unnecessary or unacceptable effects on passenger operations. On the other, a ship is a means of transport, which

obviously involves adverse effects due to its motion and engines. On ships, vibrations and noise can be caused by, for example:

- ship's engines
- waves
- motion of the ship
- deformations of the ship
- equipment (drive mechanisms, motors, fans, air conditioning, etc.)
- flow noises from air ducts

Specific measures must be employed to deal with the above:

- avoiding natural frequencies and brittle failure of important or load bearing components (fatigue strength).
- use of vibration-cushioned fixings for components.
- acoustic insulation and suitable supports for installations, equipment, fans and drive mechanisms (Figs. 9 and 10).
- adequate sizing of air ducts and fans.

seele cover, for example, has fitted the acoustic-insulated fans with damped bearings, increased the sizes of air supply lines beyond the actual flow requirements and installed low-vibration fixings for components.

## 2.4 Temperature and humidity fluctuations

The transparent domes of the upper decks on both cruise liners have been fitted with thermal insulation for the first time. However, the members of the project team agreed that owing to the many openings and seals (windows, doors, movable roof segments), avoiding all local thermal bridges would result in excessive costs. Furthermore, as the geographic location of the ship changes constantly and not all the cruise routes could be defined exactly beforehand, the actual temperature differences (inside/outside) that would actually occur could only be specified roughly in advance.

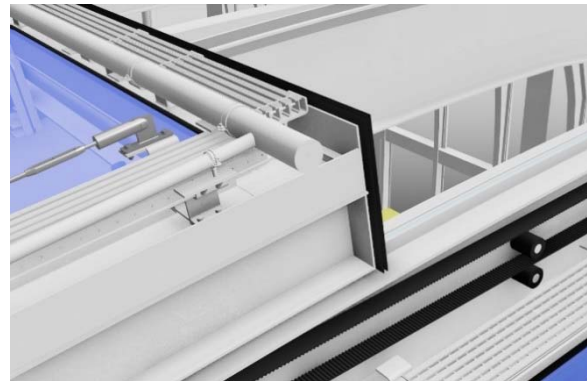


Fig. 10: "Four Elements" foil dome, movable roof segment sealed with pneumatic seal plus additional lip seals; 3D computer image, draft design, seele cover

With such boundary conditions, in certain climatic conditions (temperature gradient and humidity) there is still a certain risk with regard to local and temporary condensation, especially on the steel components. Any condensation that does occur can be minimised or even totally avoided by temporarily increasing the flow velocity of the circulating interior air. The distribution of the air in the two domes by the air-conditioning system (which is required anyway) should achieve the desired effect.

## 2.5 Loading assumptions

As mentioned above, the geographical location of the ship changes and so – unlike for buildings on land – the load assumptions cannot be defined according to the location. Instead, they must be prescribed on the basis of the empirical figures of the ship's owner and the recommendations of the classification company (in this case Germanischer Lloyd, now DNV GL). The load cases for the (quasi-)static design of the ETFE foil domes are made up of the following actions:

- dead loads
- wind loads
- snow loads
- vibrations
- acceleration forces (motion of the ship)
- restraint forces (ship deformations, temperature)

### 2.5.1 Dead loads

The weight of the structure plays a major role for ships. In particular, the weight of components that are located high above the waterline, e.g. steel domes on upper decks, should be kept as low as possible.

As rigid frames are frequently used on ships, the self-weight of the steel structure converted into a weight per unit area is about 60–80 kg/m<sup>2</sup>, depending on the loads to be considered and the type of structure (planar or curved, space frame, etc.). This also roughly matches the weight of conventional dome structures in steel which are glazed with laminated safety glass.

However, the self-weight of ETFE foil cushions, including their clamping plates, is less than 5 kg/m<sup>2</sup>. That is only about 10% of the weight per unit area of overhead glazing in laminated safety glass, with the associated shorter spans of the glass panes between the steel members of the primary structure. So the use of ETFE foil cushions considerably reduces the dead loads on the upper decks.

Besides the self-weight of the structure, the loads of items fixed to the structure, which can amount to 30 kg/m<sup>2</sup> or more, must also be considered; e. g. loudspeakers, lighting, stage equipment, water-filled sprinkler pipes, waterslides, climbing courses, fall protection systems or also roof and façade washing installations.

### 2.5.2 Wind loads

The MHI shipyard appointed Rostock-based engineers Motoren- und Energietechnik (MET) GmbH to determine the wind loads on the foil roofs.

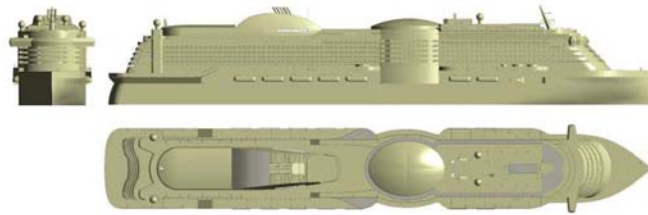


Fig. 11: 3D model of ship for CFD simulations; MET on behalf of MHI

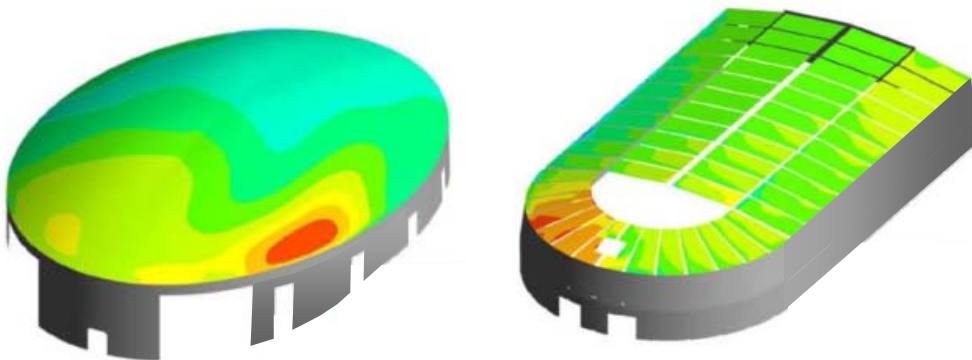


Fig. 12: CFD simulations of wind loads on both foil domes; MET on behalf of MHI

The CFD simulations (CFD = computational fluid dynamics) carried out by MET were based on a design wind speed of 56 m/s, which corresponds to 201.6 km/h. In the computer this wind speed was applied to the 3D model of the ship in 45° steps over its full height (Figs. 11 and 12). The results show that the foil domes at a height of about 50 m above sea level are primarily subjected to symmetrical wind suction actions.

The fact that only low wind pressures and hardly any asymmetrical wind loads occur on the upper decks is obviously due to the high and dominant hull of the ship, which rises above the waterline like a wall, and the relatively shallow form of the ETFE foil domes. In order to be able to check the stability of the load bearing structure for non-uniform wind loads as well, the wind suction loads determined were applied not only symmetrically (all sides), but also asymmetrically (one-sided).

### 2.5.3 Snow loads

Of course, quite different snow loads can occur depending on whether the ship is cruising through the Caribbean or in polar regions. Taking into account the recommendations of the classification company (in this case Germanischer Lloyd, now DNV GL), a design snow load of 1.5 kN/m<sup>2</sup> was assumed for the ETFE foil roofs on these ships. Assuming a snow density of 300 kg/m<sup>3</sup>, this would correspond to a constant snow depth of 50 cm over the entire roof.

### 2.5.4 Acceleration forces

The motion of the ship can lead to acceleration forces that act on the structure, items fixed to the structure and any snow loads on the roof. Acceleration forces can be reduced to three translational and three rotational ship movements:

### *translational motion*

- surging (motion along the longitudinal axis)
- swaying (motion along the transverse axis)
- heaving (motion along the vertical axis)

### *rotational motion*

- rolling (motion about the longitudinal axis)
- pitching (motion about the transverse axis)
- yawing (motion about the vertical axis)

The acceleration forces result from the specification of the ship, which was drawn up by the owner taking into account the guidelines and recommendations of the classification company (in this case Germanischer Lloyd, now DNV GL).

#### **2.5.5 Restraint forces**

The load bearing structure of the foil domes can be subjected to restraint forces caused by deformations of the ship or temperature fluctuations.

Restraint forces due to deformations of the ship can occur when the ship's hull bends upwards on the crest of a wave (hogging) or, correspondingly, bends downwards in the trough of a wave (sagging). The magnitude of the forces acting on a component depends on various factors, e.g. the stiffness of the hull, the distribution of stiffness and hence also the location of the component on the ship.

Temperature fluctuations impose restraint forces on a component when its expansion is hindered. This is especially the case for structures with multiple degrees of static indeterminacy (with fixity and rigid connections), which are frequently used in shipbuilding.

The ship deformations to be assumed in the calculations and the temperature ranges to be considered likewise arise out of the specification for the ship.

#### **2.5.6 Vibrations**

A modal analysis is carried out to assess whether the load bearing structure of the respective dome is susceptible to vibration. This analysis is initially based on masses estimated as accurately as possible, but on calculations of the masses in later phases of the design.

The modal analysis includes the numerical characterisation of the dynamic behaviour of load bearing structures with the help of vibration figures, i.e. the modal parameters natural frequency, modal form, modal mass and modal damping. Defined frequency ranges for structural vibrations must be avoided in order to avoid resonances with the excitation frequencies (first and second order) of the ship's propellers.

It can be seen that the weight of the structure must be ascertained as quickly and accurately as possible because all design steps and calculations depend on the masses and the distribution

of those masses over the ship. Those masses in turn depend on the external loads (wind, snow, etc.). The significance of the loading assumptions for the structure, and hence the weight of the structure and the costs, is frequently underestimated – in shipbuilding just as much as for buildings on land. That also applies to the work involved in determining the loading assumptions as carefully as possible.

## 2.6 Installation

Installing ETFE foil cushions on board a ship can be very different to conventional erection work for a similar assembly on land. Some of those aspects are:

- parallel working on several levels (suspended scaffolds, safety nets, fall protection); safety nets may not be permitted (Japan).
- narrow access to working areas, confined working spaces, limited crane times and restrictions on storage and floor space on board.
- possibly interim storage of materials and tools in the shipyard.
- more stringent demands regarding fire protection (also during erection).
- different tolerances in shipbuilding (structural steelwork).
- follow shipbuilding and shipyard rules and regulations.
- necessary particular protective measures for any subsequent painting and welding work required on site (steel and aluminium structures).
- corrosive environment (marine climate, salt-laden air), possibly corrosive mists in the air (paints, solvents, filler metals).
- possible downtimes due to poor weather (“typhoon season”, work outdoors).



Fig. 13: ETFE foil cushions being installed on board the AIDAprima, MHI shipyard; seele cover 2015

## 2.7 Design and documentation

In a design and build contract the many different types of work involved (steelwork, ETFE cushions, fan units, air supply lines, sensors, power chains, safety system, washing installation, drive mechanisms, maintenance walkways, motors, controls, pneumatic seals, etc.) must be coordinated with each other in terms of materials, architecture, construction and structural analysis in order to achieve a coherent and functioning overall concept. This represents a great challenge and entails a great deal of planning work.

In this project the draft, detailed and fabrication planning work was carried out internally in three planning phases. The approval work was carried out by the institutions of the respective classification company (class) and country of registration (flag). The approvals of further institutions involved (US Coast Guard etc.) were obtained by the shipyard during the planning process. As ETFE foil cushions are being used on a cruise liner for the very first time, the planning work represented a new departure in membrane construction which has enhanced the range of experience of seele cover.

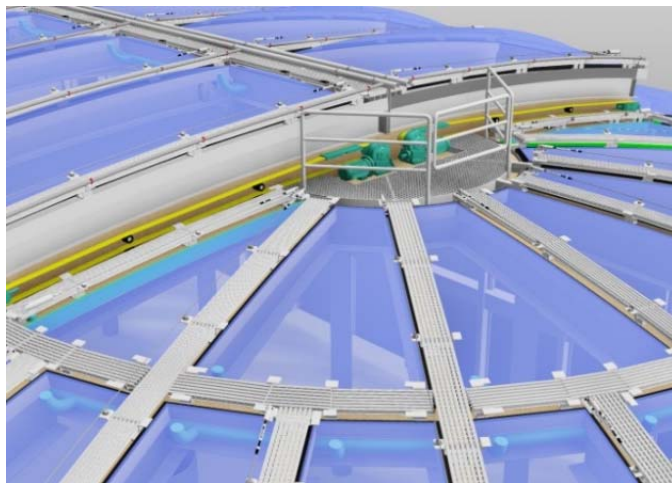


Fig. 14: Isometric view “Four Elements” foil dome; draft design, seele cover 2013

If a problem occurs, the ship is somewhere at sea, and so it should be possible for the crew to rectify the problem themselves if at all possible. As a result, the accuracy and succinctness of the operating instructions are crucial factors. Therefore, if possible, the designers should consider in advance which defects could possibly occur and how the crew could deal with these. Some work can, should or may only be performed by trained specialists or only by the company that carried out the work in the first place. It is also vital to carry out maintenance of the structure regularly in order to prevent problems and potential secondary damage. It was important to consider which inspection and maintenance measures could be carried out by the crew and which only by the company responsible. This is regulated by a detailed checklist with information on the respective inspection and maintenance intervals.

Some contractors might already be dreaming of a two-week maintenance or erection contract on the AIDAprima when it is anchored somewhere in the Caribbean!

## 3. RÉSUMÉ

With the international make-up of the project team, the long distances between design and building locations and also the complex works involved with the need to coordinate the many interfaces, the AIDA project placed great demands on all those involved. seele cover and its planning team were happy to rise to this challenge.

## AERODYNAMIC DAMPING OF MEMBRANES IN STILL AIR

MARTIN ZASCHKE AND JÜRGEN WACKER

Wacker Ingenieure - Wind Engineering Consultants  
Gewerbestr. 2  
75217 Birkenfeld, Germany  
e-mail: m.zaschke@wacker-ingenieure.de

**Key words:** Aerodynamic Damping, Added Mass, Vortex Dynamics

**Summary.** The aerodynamic mechanisms modifying the dynamic response of membrane structures oscillating in still air are discussed. Emphasis is placed on aerodynamic damping and its connection to vortex shedding from the membrane edges. A simplified vortex-particle method for the prediction of aerodynamic damping and added mass for two-dimensional configurations is implemented and tested. It appears to be valuable for preliminary assessments of the corresponding parameters.

### 1 INTRODUCTION

Under atmospheric conditions, no matter if windy or not, oscillations of membrane structures are necessarily accompanied by air movements. With increasing lightness of the structures and oscillation amplitudes, these movements may result in considerable forces that strongly modify the dynamic response of the structure. An unfavourable consequence of this interaction may be the effective load increase due to the inertial forces caused by the added air mass that moves with the membrane. This load-increasing effect is on the other hand counteracted by the transfer of vibration energy from the oscillating structure to the surrounding air taking the form of an additional aerodynamic damping. Certainly, the most accurate way to cover these effects numerically or experimentally is to perform full FSI (fluid-structure-interaction) simulations or to do wind tunnel tests with exactly scaled aero-elastic models. However, both techniques are often far too expensive or even technically infeasible. This is especially true with regard to the majority of projects that require quick solutions and do not budget for highly advanced research efforts. Therefore, it is necessary to formulate and assess simplified procedures to model the complexities of real fluid structure interactions without disregarding too much of the underlying physics.

A first step towards this direction is the restriction to a limited number of modes and the introduction of linearized relations between deformation and deformation-induced forces. Such an approach is frequently applied in bridge aerodynamics where the stability characteristics of bridge sections at a specified reduced frequency are derived from the aerodynamic derivatives. The aerodynamic derivatives are measures quantifying the change rate of aerodynamic forces (lift, drag and torsional moment coefficients) due to modal displacements, velocities and accelerations of the section and can be obtained from section wind tunnel tests or numerical (CFD) computations carried out in two or three dimensions. Details about the theory can be found in numerous publications and textbooks (e.g. [1] and

references therein).

Despite the evident differences between membrane structures and bridges, a similar approach can be used for membranes. If only one mode of vibration is considered and restriction is made to the still-air case, which is usually not of interest in bridge aerodynamics, the set of aerodynamic derivatives effectively collapses to just two parameters describing the air influence on the dynamical characteristics: added mass and aerodynamic damping.

The term “added mass” refers to the effect of air that is accelerated and decelerated with every oscillation cycle and therefore leaves an additional pressure footprint on the membrane in phase with the motions. Understanding and modelling of added mass effects have advanced relatively far. An extensive review is provided in AlSofi *et al.* [2]. For the still-air situation, the added mass effect is well represented when the flow induced by the modal movements is regarded as irrotational except at the boundaries where a time-varying thin vortex-sheet is assumed. A corresponding analytical solution had been suggested by Minami [3] and was confirmed experimentally [4]. Due to the predominantly irrotational nature of the flow induced by the membrane movements, the problem of added-mass computation is well-suited for boundary element methods which do not require any spatial discretization of the entire flow domain but just a discretization of the surfaces [5]. The scaling of the added mass in still air is only related to the geometry of the setup; the added mass ratio is independent of the oscillation frequency. For the range of amplitudes of practical interest with  $a_0/L \ll 1$ , where  $a_0$  is the maximum oscillation amplitude and  $L$  is a representative length scale of the structure, the added mass is also amplitude-independent.

The potential flow approach that proves to be useful for the modelling of added mass, however, implies that there is no energy flux from the oscillating structure into the fluid where it would be finally dissipated. In reality, viscous friction at the boundaries and separation of the vortex sheet at the membrane edges are unavoidable and will be perceived by the membrane as aerodynamic damping. It is very important, however, to distinguish between the still-air case (which we are focussing on) and a situation with oncoming wind where negative damping cannot be excluded.

An overview over the current state of research on aerodynamic damping of membranes is provided by AlSofi *et al.* [2] together with a presentation of results obtained from FSI simulations. Moreover, a concept is proposed on how to combine wind-tunnel time series from rigid model tests and simplified FSI computations in order to obtain realistic results. As the computed results show, the dependencies of aerodynamic damping on the considered parameters, especially on the ratio  $a_0/L$  between oscillation amplitude and length scale of the structure, are more intricate than for added mass and not fully understood yet.

The scope of this paper is not to offer a ready-to-use method to quantify aerodynamic damping but rather to explore the underlying mechanism and to check for the appropriateness of vortex methods for its modelling. As outlined above, the added mass effect in still air can be relatively well captured by potential flow theory. Therefore, our initial assumption is that the flow field around an oscillating membrane is in fact well-represented by potential flow theory but becomes perturbed by vorticity released into the flow domain at the membrane edges. The presence of a large irrotational region and some smaller areas of highly concentrated vorticity suggests the use of vortex particle (or vortex filament) methods. In order to concentrate on the very essentials of the underlying mechanisms we restrict ourselves

to two dimensional geometries (1d membrane within a 2d flow domain) and only consider the still air case.

This paper is organized as follows: First (chapter 2), the generalized equation of motion for a 1d-membran surrounded by a two-dimensional fluid is stated and the generalized damping and mass parameters are introduced. This is followed by an illustration of a possible mechanism leading to aerodynamic damping (chapter 3) and a brief introduction to the vortex-particle method (chapter 4). In chapter 5, the method is applied in order to compute the added mass and aerodynamic damping for an example documented in [2] and finally (chapter 6), a short outlook is given.

## 2 EQUATION OF MOTION

Starting point for our analysis is a 1d-membrane with a constant mass distribution surrounded by an infinite two-dimensional flow domain. We consider only the first mode of vibration which we assume to be known and not to be modified by added-air impacts.

The generalized equation of motion for the first mode equals the equation of motion for a 1-DOF oscillator:

$$m_{gen}\ddot{q} + c_{gen}\dot{q} + k_{gen}q = F_{gen}(t) \quad (1)$$

where  $m_{gen}$ ,  $c_{gen}$ ,  $k_{gen}$  are the generalized mass, damping and stiffness, respectively, and  $F_{gen}$  is the generalized external force.

For the sake of simplicity, we consider the case of a free oscillation after an initial modal displacement. It is assumed that external forces acting on the membrane depend exclusively on its current motion velocity and acceleration:

$$F_{gen}(t) = F_{gen,mot}(t) = f(\dot{q}, \ddot{q}) \quad (2)$$

As outlined above, we consider only the still-air case. Strictly speaking, this would imply that fluid motions that were induced during previous oscillation cycles are still moving around in the vicinity of the membrane and may influence the surface pressure at later instants. However, the influence of this flow field evolution is neglected in equation (2) - possible consequences will be addressed in chapter 5.

Linearization of equation (2) in the range of small amplitudes may be expressed as:

$$F_{gen,mot}(q, \dot{q}, \ddot{q}) \approx \frac{dF_{gen}}{d\dot{q}} \dot{q} + \frac{dF_{gen}}{d\ddot{q}} \ddot{q} . \quad (3)$$

Inserting (3) into the equation of motion (1) results in the equation of motion including the added quantities:

$$(m_{gen} + m_{gen,air})\ddot{q} + (c_{gen} + c_{gen,air})\dot{q} + k_{gen}q = 0 \quad (4)$$

where the added mass and added damping are:

$$c_{gen,air} = -\frac{dF_{gen}}{d\dot{q}} \quad (5)$$

$$m_{gen,air} = -\frac{dF_{gen}}{d\ddot{q}} \quad (6)$$

Thus, the added mass and damping parameters of a specific mode (here the lowest mode of vibration) describe the dependence of the additional generalized air forces on the velocity and acceleration of the modal displacement. Assuming the validity of equation (2), it should be possible to determine these parameters from the surface pressure timeseries obtained from experimental or numerical tests with membrane sections undergoing forced motions. Considering, for example, a sinusoidal motion  $q(t) = q_0 \cdot \sin(2\pi f \cdot t)$ , the added mass can be derived from the sinusoidal part of the pressure reaction while the aerodynamic damping is related to the cosine component.

Thus, modelling the added quantities is basically equivalent to modelling the flow and pressure patterns resulting from the air displacements around an oscillating structure. These flow patterns shall be briefly discussed in the following chapter.

### 3 A QUALITATIVE PICTURE OF AERODYNAMIC DAMPING

As outlined in the introduction, added mass effects are well represented assuming a vortex sheet at the current position of the membrane and an otherwise irrotational flow field. Figure 1 shows an image taken from Minami [3] which illustrates the flow pattern outside the ends of a vibrating membrane. The corresponding potential flow solution exhibits singularities at the membrane ends so that the tangential flow velocities as well as the surface suction locally grow to infinity. In the instant of maximum velocity, i.e. when  $\dot{q} = \max$  and  $q=0$ , the pressure distributions on the upper and lower surface of the membrane would cancel out and not produce any net force leading to damping.

Under real conditions, the vortex sheet will neither remain infinitely thin nor attached to the membrane surfaces. Due to viscosity, it will diffuse from the boundaries into the flow domain. In the high Reynolds number limit, the flow will immediately separate at the membrane edges and the separated vortex sheet will roll up into a spiral vortex (Figure 2). This spiral vortex grows and its further dynamics depends on the subsequent motions of the

membrane as will be shown in chapter 5.

Despite possible Reynolds-number dependencies of the flow dynamics caused by a moving membrane, it appears reasonable to assume the Reynolds number to be high enough so that viscosity has no further influence except that it enforces the formation of the vortex sheet and its separation at the edges. In this case, the viscous vorticity diffusion from the membrane surface into the flow domain along the boundaries does not need to be considered and all vorticity entering the flow domain may be assumed to be released from the edges. Thus, the flow in the domain around the oscillating membrane may be regarded as an initially irrotational, temporally varying flow field which is continuously contaminated by vorticity released from the membrane edges. The corresponding vortical disturbances result in pressure perturbations causing the damping of the oscillation.

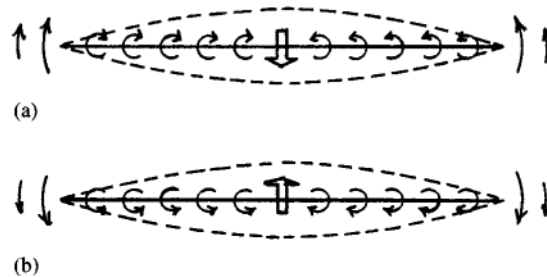


Figure 1: Schematic patterns of flow around the outside ends of the vibrating membrane (image taken from [3])

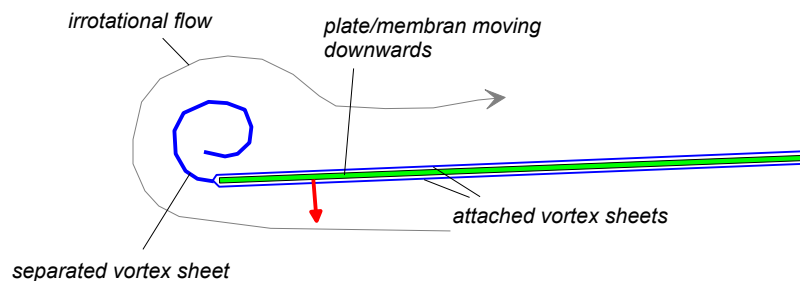


Figure 2: Formation of the spiral vortex immediately after the onset of downward motion of the object (symbolized by the red arrow)

#### 4 VORTEX-PARTICLE METHOD

The basics of Vortex Particle Methods (VPM) are extensively described in numerous articles and textbooks, e.g. Walther, Larsen [6]. Vortex particle methods make use of the fact that the vorticity  $\omega$  is conserved along the trajectories of the flow as long as viscous diffusion of vorticity is not directly accounted for:

$$\frac{D\omega}{Dt} = 0 \quad (7)$$

The vorticity field at a particular instant is represented by  $N$  vortex particles with circulation  $\Gamma_i$  ( $i=1\dots N$ ) and position  $\mathbf{x}_i$ :

$$\omega(\mathbf{x}) = \sum_{i=1\dots N} \zeta_\varepsilon(\mathbf{x}_i - \mathbf{x}) \Gamma_i \quad (8)$$

The function  $\zeta_\varepsilon$  is a smooth approximate to the Dirac function (see, e.g., [7]) which is applied in order to avoid the infinite velocity that would be caused by a singular vortex if  $(\mathbf{x}_i - \mathbf{x}) \rightarrow 0$ .

Since the circulation of each vortex particle is conserved, the dynamics of the flow field depends on the velocity on each one of these particles induced by the other particles. The velocity field is linked to the vorticity field via the Poisson equation

$$\Delta\psi = -\omega \quad (9)$$

where  $\psi$  is the stream function so that:

$$\mathbf{u} = \begin{bmatrix} u \\ v \end{bmatrix} = \begin{bmatrix} \psi_z \\ -\psi_x \end{bmatrix} \quad (10)$$

An explicit time scheme is applied in order to compute the evolution of the flow field. The membrane is discretized using boundary elements assigned with a specific circulation which are calculated for each time step in dependence of the current flow field and the current membrane position such that there is no vortex-induced flow through the membrane surface and such that the overall circulation of all elements and particles is zero. Usually, vortex-particle methods seek to approximate the effect of vorticity diffusion by a random walk which is superimposed to the particle convection [6]. This is omitted in our method because, as outlined above, the effect of vorticity release at the membrane edge is regarded as dominant and the random walk would quickly populate the vicinity of the membrane surfaces with vortex particles and thus increase the computational effort. However, an a-priori definition of the separation points is necessary.

Given a flow field with  $N$  vortex elements, the computational effort increases with  $N^2$  if all particle interactions are accounted for. This would render the method very inefficient for many practical cases. There are several numerical recipes to overcome this drawback. Nevertheless, it turned out that a fairly low number of particles already delivers valuable results for the simple test case documented in the following chapter. At this moment, no further attention has been paid to the question of accelerating the numerical procedure.

## 5 EVALUATION OF A SELECTED CASE

FSI simulations of differently configured one-dimensional and two-dimensional membranes are documented in [2]. We will focus on the test case of a membrane spanning 10 meters with a uniform mass distribution of  $2 \text{ kg/m}^2$ . The 1d case represents an infinitely wide membrane while the membrane of the 2d case is 20 meters wide and geometrically fixed at the lateral edges. The evaluation of aerodynamic damping has been done for the two-dimensional case at different initial amplitudes so that the results are not strictly comparable to our 1d run. However, an inspection of the graphically represented displacements for the 1d membrane suggests that the differences in aerodynamic damping between the 1d and the 2d case should be around 20% so the results should be comparable.

The vortex method was applied to a membrane undergoing a forced oscillation at different amplitudes ( $a_0/L=0.005, 0.015, 0.02$  and  $0.03$  in analogy to [2] and the added mass and aerodynamic damping parameters were obtained in the way described in the second chapter. An example for a timeseries of the generalized air force acting on the membrane induced by the forced oscillation is given in Figure 3. In the upper image it is sketched how to obtain the generalized added mass while the detail in the lower image illustrates the phase shift between motion and force which is linked to the damping. The time step size of the vortex particle method has been reduced until the phase shift was found to converge to a fixed value. As suggested above, the air pressures acting on the moving membrane are not purely dependent on its current velocities and accelerations as implied in equation (2) but are somewhat distorted by the remaining vortical structures from previous motions. This leads to differences in the phase shift between the subsequent cycles. The aerodynamic damping decrement was therefore derived from the first oscillation cycle only.

The obtained results for the reduced frequencies  $f_a$  (due to the added mass effect) and the aerodynamic damping ratios for the different investigated amplitudes are stated in Table 1. They can be interpreted as follows:

- The reduced frequency due to added mass corresponds almost exactly to the value obtained in [2] for the 1d-case. The deviation between the value for the 1d configuration and the 2d configuration is due to the different geometry. However, as the results in [2] and other work suggest, the added mass effect is almost independent on the amplitude (at least if  $a_0/L \ll 1$ ) and there are only slight variations of the reduced frequency with increasing amplitude.
- The aerodynamic damping is about 30% below the value of AlSofi *et al.* [2] at the lowest investigated amplitude ( $a_0/L=0.005$ ) but grows stronger with increasing amplitude reaching a value of about 20% above the FSI value for  $a_0/L=0.03$ . At the moment, it is unclear in how far these differences stem from the different dimensionality of the domains. However, from an engineering point of view, the obtained aerodynamic damping decrements are within the same range so that the vortex particle method could readily serve as a quick tool for a rough prediction of aerodynamic damping for simple configurations.

Apart from the usability of the obtained results, the time-dependent vorticity distributions obtained from the VPM give some insight into the basic flow patterns induced by the oscillation of the membrane. A series of flow field snapshots at time steps of quarter cycles is displayed in Figure 4. The vorticity distributions around the single vortex particles were somewhat smoothed in order to allow for a better graphical display. The oscillation timeseries which starts with an initial displacement of the membrane and a definition of the plot position

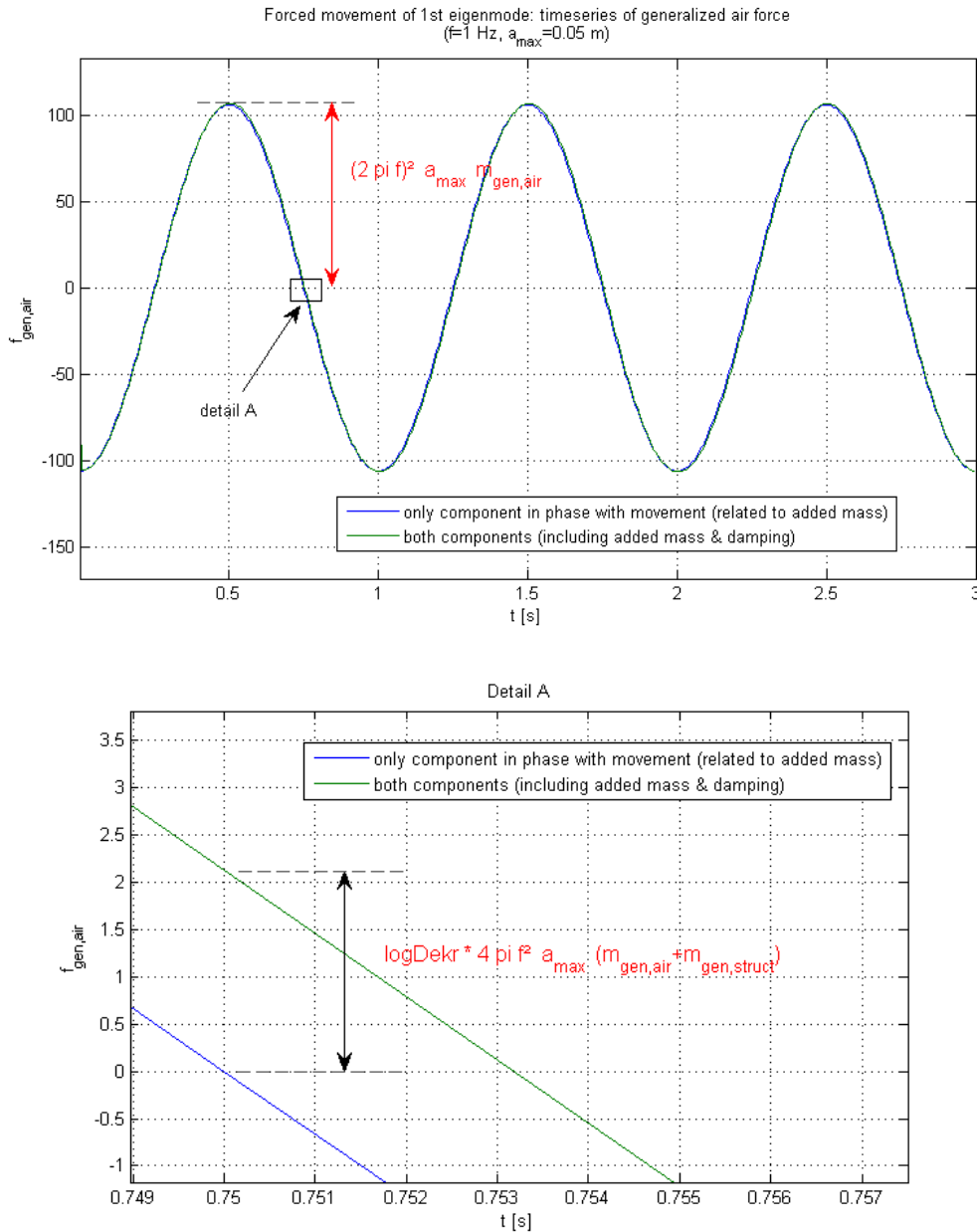


Figure 3 : Time series of the reaction force obtained from a forced-oscillation simulation of the 1d-membrane example and geometrical interpretation of the target parameters  $m_{gen,air}$  and  $\delta_{air}$ . As shown in the detail (lower image), the phase of the overall generalized force (green line) is somewhat shifted from the membrane motion.

are sketched in Figure 5. Image 1 (in Figure 4) shows the vorticity shortly after the onset of motion which is concentrated in the vicinity of the membrane edge. When the membrane passes its rest position (image 2), the spiral vortex composed of negative vorticity from the lower surface of the membrane has clearly developed. The growing spiral vortex induces counteracting positive vorticity which is shed from the upper surface of the membrane. This is already clearly visible after half a cycle (image 3), i.e. when the membrane changes its direction of motion. Now, the background potential flow turns around and transports the initial spiral vortex downwards around the edge, where it separates and develops into a dipole vortex together with the counteracting vorticity field resulting from the vortex sheet that separates from the upper surface (image 4). It appears that the dipole moves away due to its self-induced velocity and finally detaches from the membrane. As images 5 and 6 show, the process is repeated in a similar way after one entire oscillation cycle has past. However, the detached dipole vortices are still left in the domain and it is unclear in how far they influence the further development of the flow field or become decorrelated or dissipated after some time.

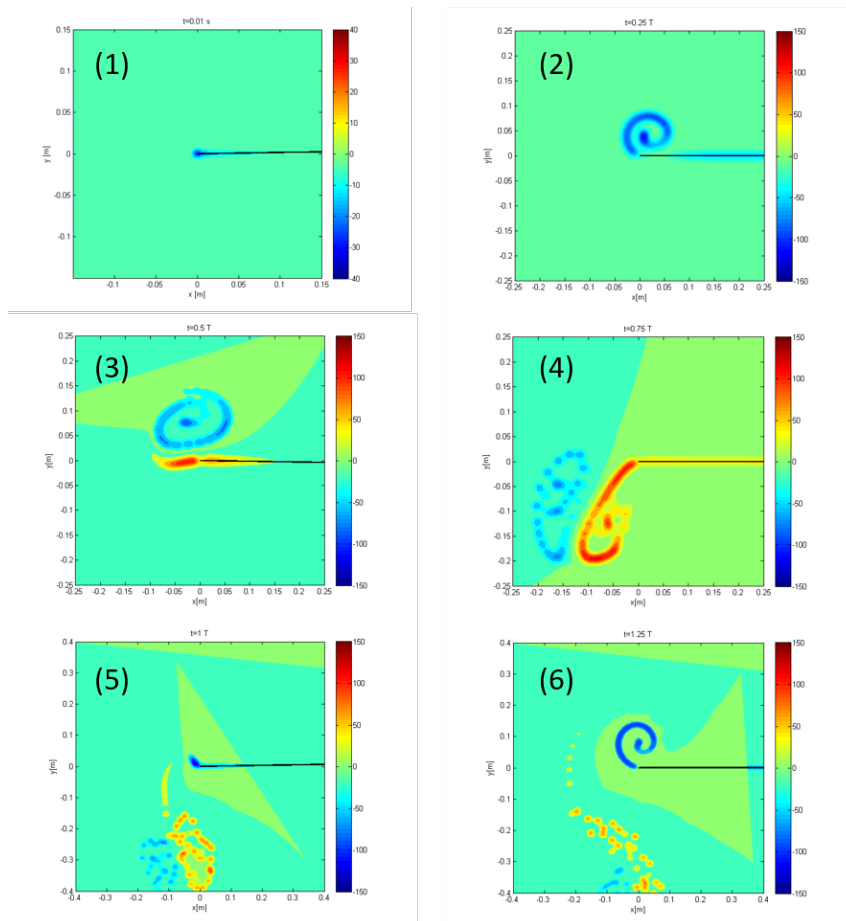


Figure 4: Snapshots of the vorticity field at time  $t=0.01T$  (1),  $t=0.25T$  (2),  $t=0.50T$  (3),  $t=0.75T$  (4),  $t=1.00T$  (5),  $t=1.25T$  (6) obtained from a forced-oscillation simulation of the 1d-membrane example ( $a_0/L=0.005$ ).  $T$  is the entire oscillation period. The visible frame represents a small area in the vicinity of the left edge (see Figure 5). The membrane and the time series of its prescribed motion are displayed in Fig. 5.

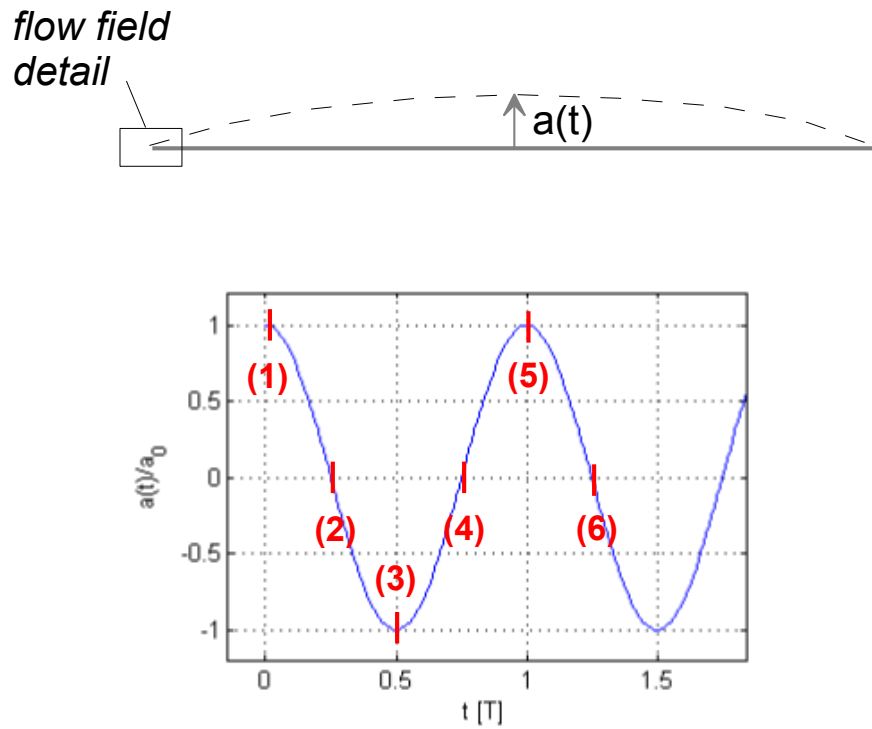


Figure 5: Sketch of the test case (1d-membrane with sinusoidal eigenmode) with indication of the detail frame shown in Figure 4 (upper image) and display of the membrane motion time series including indication of the snapshot times of images 1 to 6 in Figure 4 (lower image).

**Table 1:** Reduced frequencies due to added mass and aerodynamic damping decrements for the test case at different amplitudes  $a_0$ . The values obtained in [2] are displayed for comparison. Index “1d” refers to the output of the 1d-membrane tests (2d fluid domain) and index “2d” to the 2d-membrane tests (3d fluid domain). All values are based on the vacuum eigenfrequency  $f_s$  stated in the second column.

$a_0/L$	$f_s$ [Hz]	Free oscillation test using FSI (from AlSofi et al., 2015)			Forced oscillation test using vortex particle method	
		$f_{a1,1d}$ [Hz]	$f_{a1,2d}$ [Hz]	$\delta_{a1,2d}$	$f_{a1,1d}$ [Hz]	$\delta_{a1,1d}$
0.005	0.820	0.322	0.372	0.054	0.325	0.041
0.015	1.022	-	0.453	0.080	0.404	0.089
0.020	1.170	-	0.511	0.089	0.462	0.107
0.030	1.510	-	0.645	0.118	0.594	0.137

## 6 CONCLUSION AND OUTLOOK

A first attempt was made in order to explain and model the aerodynamic damping of membranes in still air in terms of vortex dynamics. This approach may be regarded as an extension to already existing potential flow models for the determination of added air mass. The obtained results and insights are of preliminary character and further testing and verifying are necessary. An essential fact is that vorticity is concentrated in the vicinity of the membrane edges for realistic vibration amplitudes while large parts of the flow domain remain irrotational. This definitely suggests the use of vortex methods which may be capable of capturing the flow field dynamics with a relatively little number of vortex particles and do not require extensive numerical efforts. We have restricted ourselves to the two-dimensional case, where vortices are modelled as particles. This does not reflect real-life conditions in the engineering of membrane structures. However, an extension of the model to three-dimensions (vortex filament method) might be promising.

## REFERENCES

- [1] E.N. Strømmen, *Theory of Bridge Aerodynamics*, Springer, 2006.
- [2] H. AlSofi, R. Wüchner, K.-U. Bletzinger, Evaluation of added mass modeling approaches for the design of membrane structures by fully coupled FSI simulations. *Proc. VII International Conference on Textile Composites and Inflatable Structures STRUCTURAL MEMBRANES 2015*, E. Oñate, K.-U. Bletzinger and B. Kröplin (Eds.)
- [3] H. Minami, Added mass of a membrane vibrating at finite amplitude. *J. Fluid Struct.* (1998) **12**: 919-932
- [4] Y. Li, L. Wang, Z. Shen, Y. Tamura, Added-mass estimation of flat membranes vibrating in still air. *J. Wind Eng. Ind. Aerodyn.* (2011) **206**(99): 815-824
- [5] Y. Zhou, Y. Li, Z. Shen, L. Wang, Y. Tamura, Numerical analysis of added mass for open flat membrane vibrating in still air using the boundary element method. *J. Wind Eng. Ind. Aerodyn.* (2014) **131**: 100-111
- [6] J.H. Walther, A. Larsen, Two-dimensional discrete vortex method for application to bluff bod aerodynamics. *J. Wind Eng. Ind. Aerodyn.* (1997) **67&68**: 183-193
- [7] J.T. Rasmussen, M.M. Hejlesen, A. Larsen, J.H. Walther, Discrete vortex simulations of the aerodynamic admittance in bridge aerodynamics, *J. Wind Eng. Ind. Aerodyn.* (2010) **98**: 754-766

## AN INTEGRATED FRAMEWORK FOR THE RELIABILITY AND VALIDITY ASSESSMENT OF NUMERICAL WIND ENGINEERING SIMULATIONS

AHMED ABODONYA\*, JORDI COTELS†, ROLAND WÜCHNER\* AND  
KAI-UWE BLETZINGER\*

\* Chair of Structural Analysis  
Technical University of Munich  
Arcisstr. 21, D-80333 München  
e-mail: ahmed.abodonya@tum.de - Web page: <http://www.st.bgu.tum.de>

† CIMNE - Centre Internacional de Metodes Numerics en Enginyeria  
Universitat Politècnica de Catalunya  
Campus Norte UPC, 08034 Barcelona, Spain  
e-mail: [jcotela@cimne.upc.edu](mailto:jcotela@cimne.upc.edu), web page: <http://www.cimne.com/>

**Key words:** Simulation Reliability, Code Verification, CWE, KRATOSMultiphysics

**Abstract.** Towards complex architecture and light-weight structures, conventional wind load estimation techniques fail. Hence, Computational Wind Engineering (CWE) plays a crucial role. CWE can be a very helpful tool in all design stages from schematic to detailed design stage. With the current advances in CWE, numerical wind tunnel simulations has a great potential towards improving the structural design quality through better understanding of the wind loads on structures. However, the quality of simulations is still questionable. Despite the increasing attention given to the quantification of error and uncertainty in CFD, the techniques that have been developed for general fluid engineering problems to assess the quality of CFD simulations are still marginally used in CWE (Jrg Franke, 2010). This paper is part of a project aiming at defining a framework to assess the predictive capability of wind load computation using CWE with error estimation. The framework consists of three main work packages: Code Verification, Solution Verification, and Validation. Overall, the generic definition of the framework is stepwise exemplified with the open-source code KRATOSMultiphysics. In this paper, Code Verification is the main concern. The Method of Manufactured solutions is used to verify the Variational Multiscale (VMS) element in KratosCFD incompressible Navier-Stokes solver. Taylor-Green vortex is the basis for the verification test. The Taylor-Green vortex is a well-studied test problem for large eddy simulation (LES) subgrid scale models. Moreover, Taylor-Green vortex is modified to have more extensive testing for the code. Finally, a second order convergence rate is observed which verifies the tested code functionality, then numerical errors are to be quantified.

## 1 INTRODUCTION

In today's world, societal needs have led to the wide spread of tall buildings and large span light weight structures. Limited spaces and modern architectural features are imposing challenges to designers of tall and super-tall buildings. Consequently, emphasis is added on safety, human comfort and serviceability under wind loading. These considerations together with geometrically complex shapes have led to two main challenges for the designers. Firstly, the wind loading assessment on such structures is very complex using experimental approaches which raises the attention towards computational analysis. Secondly, the high aerodynamic loads acting on the structures lead to the usage of more materials. Consequently, both the computational wind loading assessment on structures and the reduction of aerodynamic loads are of crucial impact on having optimal building design. Furthermore, information on the wind loads can be obtained through the physical modelling of Fluid-Structure Interactions (FSI). Recently, FSI in Computational Wind Engineering (CWE) is gaining confidence and is widely used in aerospace and mechanical engineering applications. From [3] and [4], it was concluded that the accuracy of both wind tunnel testing and CWE is questionable. Therefore, it can be safely said that both methods need some error indicators to increase their reliability. Consequently, the need for a quality assessment approach in CWE is raised and is the subject of this project. This project aims at developing an integrated methodology that is used in the assessment of simulation predictive quality. The development will be robust and software independent. These tools are envisaged as fundamental contributions for the development of an integrated framework for a reliable wind loads prediction.

## 2 ASSESSMENT FRAMEWORK

The proposed framework shown in figure 1 is a sequential evaluation for the simulation quality. Code verification, solution verification and validation are the main building blocks for the assessment procedures.

### 2.1 Code verification

This part of the process is essential to the process of having a reliable simulation. Code verification is defined in [5] as "The process of determining that the numerical algorithms are correctly implemented in the computer code and of identifying errors in the software". In the context of this paper, code verification is performed using the method of exact solution (MES) as a base, then more sophisticated approach is developed using the method of manufactured solution (MMS). The flowchart in figure 1 shows the important steps to follow in order to have a meaningful code verification campaign. Moreover, section 3 shows a detailed case study for the proposed code verification approach.

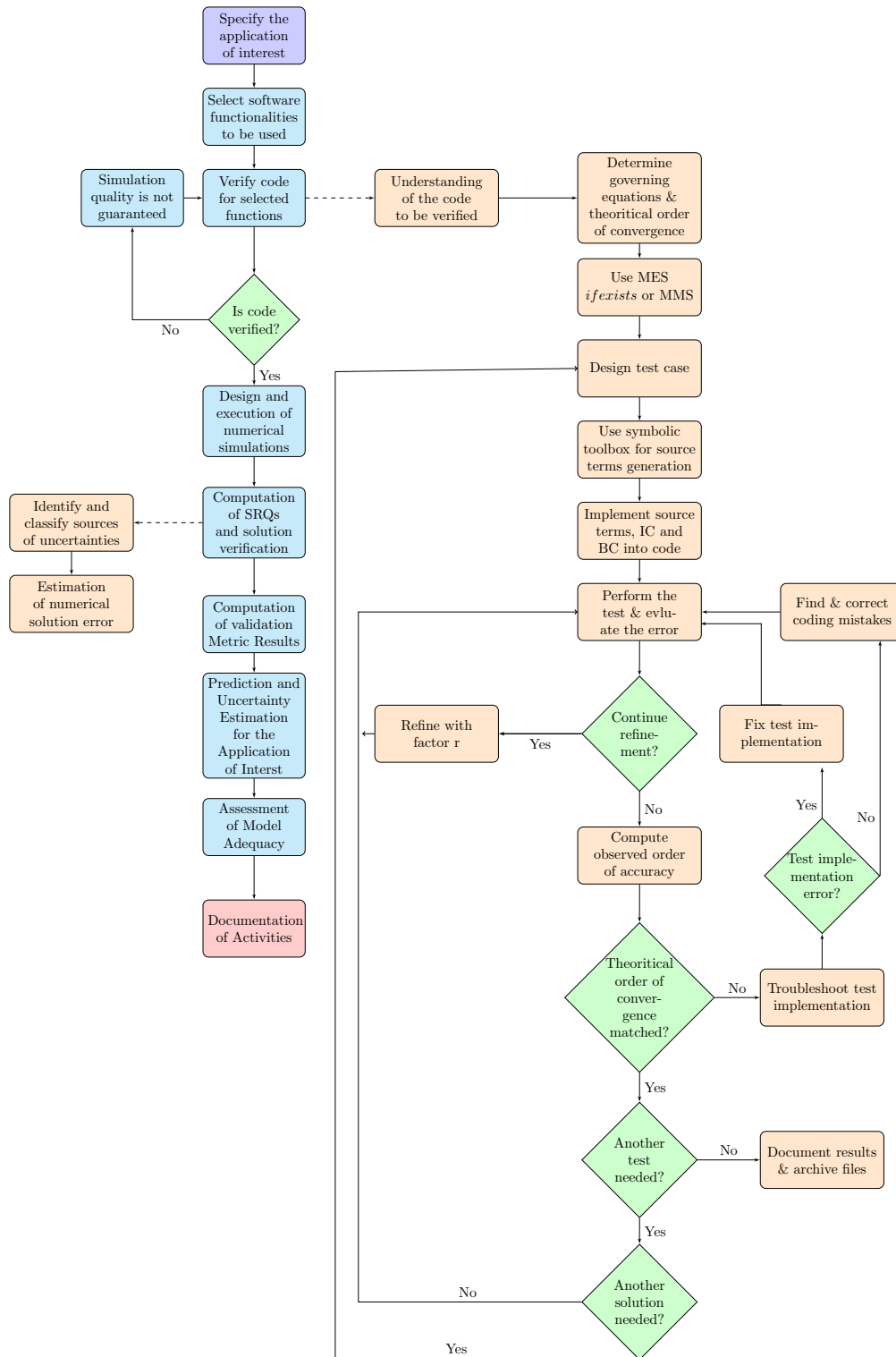


Figure 1: Flowchart for the integrated procedure for V&V adapted from [6], [8], [7]

## 2.2 Solution verification

Solution verification is defined in [5] as "The process of determining the correctness of the input data, the numerical accuracy of the solution obtained, and the correctness of the output data for a particular simulation". It addresses the quantification of error originating from human intervention and numerical errors. In the scope of this paper, this part of the process is under development where it will be designed to deal with unsteadiness in the flow field.

## 2.3 Computation of validation metric results

Graphical comparisons between simulations and experiments are not considered sufficient to judge the quality of CWE simulations. For a sufficient validation process, code correctness must be checked as of code verification. Moreover, simulation error is to be quantified as of solution verification. Then, the validation process can be completed as described in [1] and [2].

## 3 PROBLEM SETUP FOR KratosCFD CODE VERIFICATION

In this section, code verification activities are presented for KratosCFD [9] open source code. The formulation for tested functionalities and code implementation can be found in [10] and [11]. The code verification activities performed are based on the Taylor-Green Vortex. In the context of this work only 2D Navier-Stokes equations for an incompressible Newtonian fluid is considered. The testing activities have an increasing complexity starting from an equal contribution of all the terms in the Navier-Stokes equations to a term dominating solution. The following benchmark series is developed based on the Taylor-Green Vortex to test each term in the Navier-Stokes Equations. This is done for the purpose of exploring which term is affecting the code order of convergence and needs more investigation in case of unclear convergence. The approach is through giving the term of interest very high weight compared to others in the N-S in which the error generated from this term will be the dominating error.

### 3.1 Taylor-Green Vortex (TGV)

The Taylor-Green vortex is an exact closed form solution of the incompressible N-S equations. It is an unsteady flow of a decaying vortex. The solution is a periodic array of vortices that repeats itself in two Cartesian dimensions. Detailed description of the TGV can be found in [12] and [13]. The general form of the Taylor-Green Vortex is defined as following:

$$u_x = u_0 f(t) \sin(kx) \cos(ky) \quad (1)$$

$$v_y = -u_0 f(t) \cos(kx) \sin(ky) \quad (2)$$

$$Pr = \frac{\rho u_0^2}{4} f(t)^2 (\cos(2kx) + \sin(2ky)) \quad (3)$$

Where:

$$f(t) = e^{-2\nu k^2 t}; \nu \rightarrow \text{kinematic viscosity} \quad (4)$$

$$k = \frac{2\pi}{L}; L \rightarrow \text{Periodic Length}; \rho \rightarrow \text{Density} \quad (5)$$

$$\text{Reynolds number: } Re = \frac{Lu_0}{\nu} \quad \text{Courant number: } CFL = \frac{u_0 \Delta t}{\Delta x} \quad (6)$$

### 3.2 Overview for KratosCFD Tested Functionalities

In the course of this work KratosMULTIPHYSICS FEM based solver, developed at CIMNE, is to be verified. The code is claimed to have a second order convergence in space and time. The actual order of convergence of the following functionalities is to be verified:

Finite Element Method Steady State Unsteady using WBZ- $\alpha$ (Bossak) Incompressible Fluid VMS Monolithic Solver Orthogonal Subscales Stabilization
---

### 3.3 Calculation of the error and order of convergence

The numerical solution consists of values of the dependent variables on some set of discrete locations. To compute the discretization error, two error norms are used. Error norms can be used to determine the global error of a field  $\mathbf{b}$  in its spatial domain  $K$ . An  $E_2$  error norm for the variable  $\mathbf{x}$  compared to the exact solution  $\hat{\mathbf{x}}$  in the domain  $\mathbf{K}$  can be seen in equation 7.

$$E_2 = \|\mathbf{x} - \hat{\mathbf{x}}\|^2 = \sqrt{\frac{1}{K} \int_K (\mathbf{x} - \hat{\mathbf{x}})^2 dK} \quad (7)$$

Moreover, the infinity (inf) norm returns the maximum absolute error over the entire domain given by equation 8. Therefore, it is the most sensitive error measure. It is very proper to detect local discontinuities or singularities.

$$E_i = \max |x_n - \hat{x}_n|, \quad n \in [1, N] \quad (8)$$

After error evaluation and simulating over several meshes, the information is used to estimate the observed order-of-convergence. The observed order-of-convergence is estimated using the expression shown in equation 9.

$$p = \frac{\log \left( \frac{E(h_{coarse})}{E(h_{fine})} \right)}{\log(r)} \quad (9)$$

### 3.4 Simulation setup

1. Spatial and temporal resolutions:

Kratos uses triangular elements in which meshes can be designed in three ways:

- Unidirectional Structured Mesh
- Alternate Diagonal Structured Mesh
- Unstructured Mesh

In the scope of the results presented below, unidirectional structured mesh is considered. The extension to unstructured mesh is the most crucial because it is the most commonly used mesh type in Kratos. Consequently, the behavior of the code for unstructured meshes is of high interest. Both Reynolds number and Courant number are considered while deciding on the spatial and temporal resolution. CFL number is kept below one for all the simulations. The refinement ratio in both space and time is 2 which complies with the code’s theoretical order of convergence.

2. Dirichlet boundary condition is used for both velocity and pressure terms in all the boundaries, because our target is the verification of the interior equations.
3. The discretization error should be isolated from the total numerical error. Therefore, the used software is using a double precision accuracy to minimize the round-off error. To keep the IICE as small as possible, the solution tolerance in a non-normalized version of the  $E_2$  norm of velocity and pressure fields is set to  $10^{-10}$ .
4. A direct solver is used for solving the linear system of equations.
5. The basic setup for the simulations is declared in table 1.

**Table 1:** Basic simulation setup declaration

<b>Mesh Type:</b>	Unidirectional Structured Mesh
<b>Element:</b>	VMS Monolithic Solver
<b>Linear System Solver:</b>	Super LU "Direct Solver"
<b>Domain size:</b>	$X_1 = x \in [0, 2\pi], X_2 = y \in [0, 2\pi], t \in [0, 10]$
<b>Space Refinement (SR):</b>	Space (cells/direction): $2^{\frac{\text{increment } 1}{\rightarrow} 8}$ , $\Delta t = 0.001$
<b>Time Refinement (TR):</b>	Space (cells/direction): $2^8$ , $\Delta t = 2^{\frac{\text{increment } 1}{\rightarrow} 7} 10^{-3}$
<b>Space-Time Refinement (STR):</b>	Space (cells/direction): $2^{\frac{\text{increment } 1}{\rightarrow} 8}$ , $\Delta t = 2^{\frac{\text{decrement } 1}{\rightarrow} 7} 10^{-3}$

## 4 BENCHMARKS

In this section all the benchmarks will be defined in tables 2 and 3.

**Table 2:** Base Benchmark

Test Case	Fields	Material	Source Terms	Discretization
TGV1	Using the general form of the Taylor-Green Vortex with parameters: $k = 1.0$ , $u_0 = 1.0$	$\nu = 0.2$	NO	SR
TGV2		$\rho = 1.0$		TR
TGV3				STR

**Table 3:** Developed Benchmarks

Test Case	Fields	Material	Source Terms	Discretization
IN1	$u_x = \sin(t)$	$\nu = 0.1$ $\rho = 1.0$	Yes	SR
IN2	$v_y = -\sin(t)$			TR
IN3	$Pr = \sin(t)$			STR
IN4	$u_x = \sin(2t) \cos(y)$	$\nu = 0.1$ $\rho = 1.0$	Yes	SR
IN5	$v_y = -\sin(2t) \cos(x)$ $Pr = \sin(2t)(\cos(2x) + \cos(2y))$			STR
PRES	$u_x = e^{-0.2t} \sin(x) \cos(y)$ $v_y = -e^{-0.2t} \cos(x) \sin(y)$ $Pr = e^{-0.4t}(\cos(2x) + \cos(2y))$	$\nu = 0.1$ $\rho = 1.0$	Yes	SR
CON	$u_x = e^{-0.1t} \sin(x) \cos(y)$ $v_y = -e^{-0.1t} \cos(x) \sin(y)$ $Pr = \frac{3}{80}e^{-0.2t}(\cos(2x) + \cos(2y))$	$\nu = 0.05$ $\rho = 1.5$	Yes	SR
VIS	$u_x = e^{-t} \sin(x) \cos(y)$ $v_y = -e^{-t} \cos(x) \sin(y)$ $Pr = \frac{3}{40}e^{-2t}(\cos(2x) + \cos(2y))$	$\nu = 0.5$ $\rho = 0.3$	Yes	SR

## 5 RESULTS

### 5.1 Taylor Green Vortex (TGV)

In this benchmark, all the terms in the N-S equations are having equal weights. TGV constitutes the simplest flow for which a turbulent energy cascade can be observed numerically.

The rationale for choosing TGV as an initial test case for KratosCFD VMS monolithic solver was two-fold: Firstly, the TGV is a well-established reference in the literature. Secondly, the physics of the flow field and the ease of BC constitute and excellent benchmark

for VMS implementations. Three simulations were performed using TGV for different refinement approaches as listed in table 2 (TGV1, TGV2 and TGV3). For TGV1, spatial refinement was performed having a very fine time step. The reason was to minimize the time discretization error and test the spatial discretization. For TGV2, temporal refinement was performed having a very fine mesh to minimize space discretization error and test the temporal discretization.

Finally TGV3, both space and time were refined sequentially to check the discretization in space and time. The third approach, TGV3, was used because both time and space discretization have a theoretical second order convergence. In this case of having equal orders, convergence studies can be performed for space and time simultaneously.

The results produced by KratosCFD for the presented test cases are shown in figure 2. The figure shows the observed order of accuracy ( $p$ ) versus refinement. As can be seen from the figure, a second order of accuracy is observed which complies with the theoretical order of accuracy.

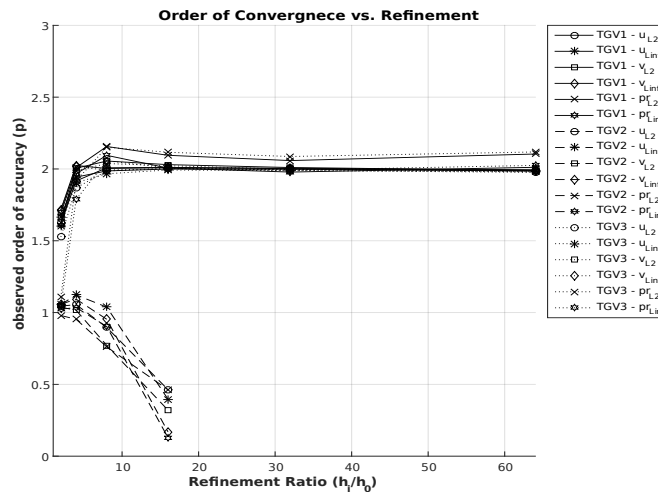


Figure 2: Observed order of accuracy for Taylor-Green Vortex (TGV Benchmark)

## 5.2 Inertia dominated flow (IN)

From the first test case, it can be concluded that the code performance is acceptable. But TGV2 showed a deviation from the expected performance. For time refinement only, the code performance is unexpected. Consequently, this case study was designed to only test the inertial term in the N-S equations. The case study presented shows two different approaches: Firstly, the manufactured solution fields are only time dependent functions as in cases IN1, IN2 and IN3. Secondly, the manufactured solution fields have time and

space dependency as in cases IN4, IN5. In both cases, the time derivative term of the unsteady N-S equations is dominating. Contributions from all other terms are zero in the first case and negligible in the second case.

The code's performance for a time dependent solution is evaluated in test cases IN1 to IN5. Figure 3 shows a reasonable results for a spaces only refinement (IN1) in a time driven solution where there is no clear convergence behavior.

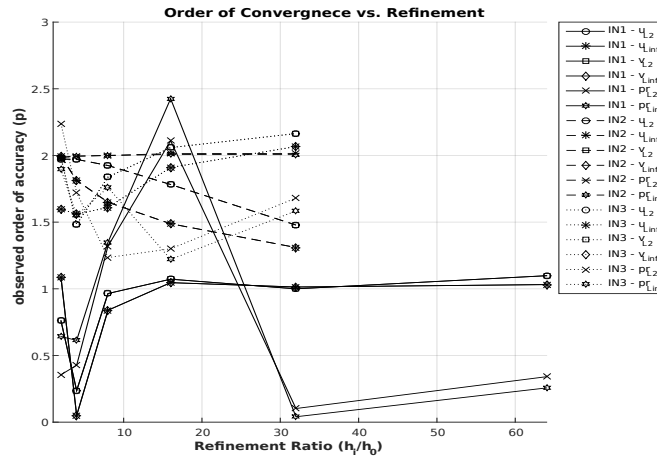


Figure 3: Observed order of accuracy for Inertia dominated flow (IN Benchmark)

Consequently, case IN2 was performed, where the simulation was performed with a time refinement at the finest mesh. Figure 3 shows that a second order of accuracy is observed for the pressure field (IN2). Whereas for the velocity field, the observed order of accuracy is between 1.5 and 2 for some simulations. The performance of the code is not as expected for a time-only dependent solution. Consequently, IN3 is performed having a space-time refinement. Figure 3 shows a second order of accuracy for the velocity field, but an order between 1.5 and 2 for the pressure field (IN3). From cases IN1, IN2 and IN3, it can be concluded that there is some sort of instability in Kratos VMS formulation for cases of only time-dependent solutions.

This observation is investigated more by cases IN4 and IN5. In this approach the time derivative of the N-S equations is high compared to the minor contribution from the space derivative. Figure 4 show an order of convergence slightly below 2 for all the fields. Consequently, it can be safely said that the code has a second order of accuracy for time derivatives.

### 5.3 Pressure dominated flow (PRES)

The purpose of this simulation is to numerically check the code's accuracy if the pressure term in the N-S equations is dominating the flow. From previous cases, it can be

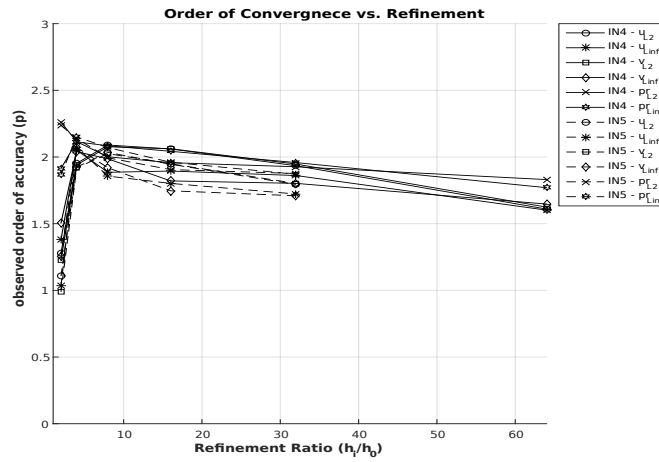


**Figure 4:** Observed order of accuracy for Modified Inertia dominated flow (IN4 and IN5 Benchmark)

concluded that for the Kratos code, spatial and temporal discretization are correlated in some sense and solution accuracy is more sensitive for mesh refinement than for time refinement. Consequently, only mesh refinement simulations were performed for this case.

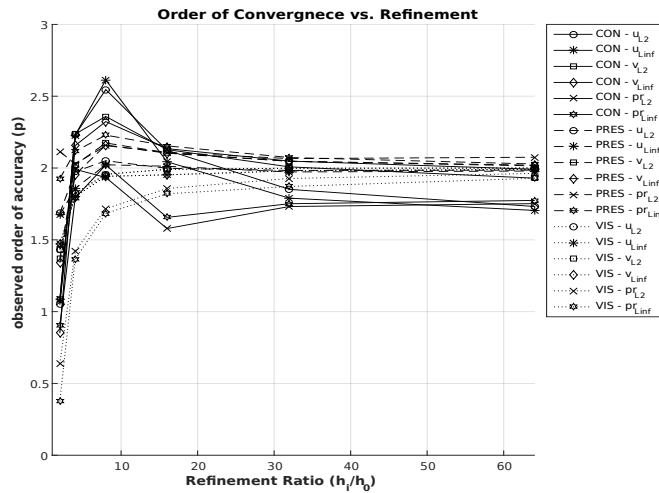


**Figure 5:** Observed order of accuracy for pressure, convection and viscous dominated flows (PRES, CON and VIS Benchmark)

PRES simulation is performed with spatial refinement. From figure 5, it can be concluded that the observed order of accuracy in both cases is almost second order.

#### 5.4 Convection dominated flow (CON)

The purpose of this simulation is to numerically check the code's accuracy if the Convection term in the N-S equations is dominating the flow. It can be concluded that the observed order of accuracy is approaching second order as shown in figure 5.

#### 5.5 Viscous dominated flow (VIS)

The purpose of this simulation is to numerically check the code's accuracy if the Viscous term in the N-S equations is dominating the flow. Only mesh refinement simulations are performed for this case. It can be concluded that the observed order of accuracy is near second order as shown in figure 5.

### 6 CONCLUSIONS

The presented test cases are not meant to test the physical efficiency of the code but the numerics. The development of the test cases is code dependent. For example, a code that performs as expected from the first test case (TGV) can be considered verified. Whereas, verifying Kratos has required more than the base test. While performing the TGV2 simulation, the code performance was completely unexpected. Therefore, more rigorous tests were required. Four test cases are developed to examine the code performance under different numerical testing by numerical exploit the effect of each of the four terms in the N-S equations. From the inertia dominated terms, it can be safely concluded that there is a time-space correlation in the discretized space. In other words, time-dependent only solutions such as IN1 cannot be handled by the code. This is not a disadvantage of the code but it is part of the formulation used for the VMS element. All test cases showed an observed second order accuracy. Therefore, the observed order of accuracy matches the theoretical order of accuracy. Finally, it can be safely said that the VMS monolithic solver is verified in KratosCFD.

### REFERENCES

- [1] J. Franke, A review of verification and validation in relation to CWE. *The Fifth International Symposium on Computational Wind Engineering (CWE2010)*. North Carolina, USA, 2010.
- [2] R. Jauregui and F. Silva, Numerical Validation Methods, Numerical Analysis - Theory and Application. *n, Prof. Jan Awrejcewicz (Ed.), ISBN: 978-953-307-389-7, In-Tech*. Available from: <http://www.intechopen.com/books/numerical-analysis-theory-and-application/numerical-validation-methods>.
- [3] A. Abodonya, Validation of Wind-Structure Interaction Simulations for Pneumatic Inflatable Structures. *Master Thesis, Technical University of Munich*. Germany, 2014.

- [4] A. Abodonya, H. Alsofi, R. Wüchner and K. Bletzinger, From Experimental Wind Tunnel to Wind-Structure Interaction Simulations of a Shell Structure. *Resilient Infrastructure (CSCE2016)*. London, Ontario, Canada, 2016.
- [5] R. Fisch, Code verification of partitioned FSI environments for lightweight structures. *PhD Thesis, Technical University of Munich*. Germany, 2014.
- [6] W. L. Oberkampf and C. J. Roy, Verification and Validation in Scientific Computing. *Cambridge University Press*. 2010.
- [7] P. Knupp and K. Salari, Verification of Computer Codes in Computational Science and Engineering. *CHAPMAN & HALL/CRC*. 2003.
- [8] P. J. Roache, Verification and Validation in Computational Science and Engineering. *hermosa publishers*. 1998.
- [9] KRATOSMulti-physics, GitHub repository, <https://github.com/KratosMultiphysics/Kratos>. 2017.
- [10] R. Codina, Stabilized finite element approximation of transient incompressible flows using orthogonal subscales. *Computer methods in applied mechanics and engineering*. 2002.
- [11] J. Cotella, Applications of turbulence modeling in civil engineering. *PhD Thesis, Universitat Politècnica de Catalunya*. Spain, 2016.
- [12] G. I. Taylor and A. E. Green, Mechanism of the Production of Small Eddies from Large Ones. *Proceedings of the Royal Society of London. Series A, Mathematical and Physical Sciences*. Vol. 158, No. 895, pp. 499-521, 1937.
- [13] A. J. Chorin, Numerical solution of the NavierStokes equations. *Math. Comp.*, 22, 745762, 1968.

## NUMERICAL SIMULATION OF AN AIR-SUPPORTED STRUCTURE IN THE AIR FLOW

Nikolay A. Mokin<sup>\*</sup>, Alexey A. Kustov<sup>†</sup> and Sergey I. Trushin<sup>††</sup>

<sup>\*</sup> Department of Structural and Theoretical Mechanics  
Moscow State University of Civil Engineering (National Research University)  
Yaroslavskoye shosse, 26, 129337 Moscow, Russian Federation  
e-mail: mokiavelli@mail.ru, web page: <http://www.mgsu.ru>

<sup>†</sup> Department of Metal and Timber Structures  
Moscow State University of Civil Engineering (National Research University)  
Yaroslavskoye shosse, 26, 129337 Moscow, Russian Federation  
e-mail: alexeykustov@outlook.com, web page: <http://www.mgsu.ru>

<sup>††</sup> Department of Structural and Theoretical Mechanics  
Moscow State University of Civil Engineering (National Research University)  
Yaroslavskoye shosse, 26, 129337 Moscow, Russian Federation  
e-mail: trushin2006@yandex.ru, web page: <http://www.mgsu.ru>

**Key words:** air-supported structures, fluid-structure interaction, aeroelasticity, computational fluid dynamics, finite element method, ANSYS.

**Summary.** Wind load is often the critical load for air-supported structures. For example, high wind demolished an air-supported tennis court roof in Zhulebino district of Moscow on May 29, 2017. Aerodynamic instability (buffeting, flutter, etc.) can produce excessive slack regions and extremely large deflections. That is why the coupled analysis should be carried out to understanding aeroelastic behavior of air-supported structures under wind loads. The technique of the nonlinear numerical analysis of air-supported structures including fluid-structural interaction (FSI) has been described in the present paper. Numerical simulation of the tunnel test of large-scale air-supported model has been carried out as an example of using this technique. Wind tunnel study is described in the papers<sup>1, 2</sup>. Experimental deformed shape, pressure coefficients and aerodynamic forces were compared with the results of presented numerical simulation. Computations were carried out with using of commercial code ANSYS 15.0. Some difficulties appeared during simulation process are discussed. An applicability of the proposed technique to the considered problem was confirmed by a good agreement of the experimental and numerical results. Both methods showed that surface wind loads can increase due to deformation of a structure. These conclusions emphasize the importance of researches on wind interaction with air-supported structures.

### 1 INTRODUCTION

Air-supported structure – a membrane structure that encloses an occupied space and has a shape that is maintained by air pressure acting within the occupied space. Great opportunities of air-supported and inflatable structures were demonstrated at world's fair Expo '70 in Suita,

Osaka, Japan. A lot of scientists worked on the problems of the air-supported structures. Most part of national standards has been developed. For example, in Russian Federation temporally instructions were written in 1977, and, unfortunately, have been used up to now without any changes.

Wind, especially in the form of an uplift, is regularly the critical load case for membrane and cable stresses in light-weight membrane structures<sup>3</sup>.

High winds produce movement of the structure and deflections that may be quite significant. Large deflections are undesirable from structural and functional considerations and can be partially controlled by internal pressure of the structure.

Since for most air-structure shapes, the wind pressure is negative over the majority of the surface, the wind pressure plus maximum operating pressure in an appropriate load combination must not exceed the available resistance. The calculated forces in membrane and cables or webs should remain in tension so as to avoid structural instability and excessive motions, insofar as possible without violating the above in some other area of the structure.

There are some recommendations about determination of wind load in the Standard<sup>4</sup>: in case no reliable documentation pertaining to wind effects is available in the literature, experimental procedures are recommended for ascertaining wind loads. So, physical experimental approach is considered as basic research method of wind-structure interaction. Thus, a lot of tunnel tests on the air-supported structures have been carried out during the 1970-80th<sup>1, 2, 5, 6, 7</sup>. Experiments show that wind load on air supported structures is higher than on traditional rigid constructions of the same shape<sup>1</sup>.

Tunnel tests with aeroelastic behavior of model are very sophisticated, and conditions of similarity can be met only partially. Amount of coupled multi-physical problems, which allowed to successfully solving, has been highly grown in last years. The reason is fast development of the computer technologies and software. Numerical simulation of strong coupled fluid-structure interaction (FSI) becomes "usual" nowadays. One can find a lot of test cases (benchmarks) in the paper<sup>8</sup> and its references.

There are some research works on the coupled numerical simulation of membrane structures under wind loads<sup>3, 9</sup>, but not so much addressed to air-supported structures.

In this paper it is proposed to use commercial code ANSYS 15.0 for the numerical simulation of aeroelastic behavior of air-supported structure in the air flow. Results of fully coupled FSI numerical simulations can be used for improvement for design and load-analysis standards addressed to the air-supported structures.

For the treatment of nonlinear multi-physics problems, two general approaches can be identified<sup>3</sup>:

1) **Simultaneous** analysis (also referred to as monolithic analysis): the entire multiphysics problem, with all physical fields involved, is summarized in one set of equations, discretized, and solved as one.

2) **Partitioned** analysis: the physical fields are solved independently. The term 'partitioned' refers to a spatial decomposition, which in the case of fluid-structure interaction means the decomposition into a structural and a fluid domain. The coupling of the individual fields is realized by the exchange of boundary conditions.

In present work we use the second strategy - partitioned analysis. ANSYS Fluent solves fluid dynamics, ANSYS Mechanical performs transient structural analysis, and the

Workbench System Coupling organizes data transfers between these solvers.

There are two general types of FSI simulation:

1-way FSI (“import load”). The results from solution of computational fluid dynamics (CFD) are transferred as pressure load to the transient structural analysis. Deformations of model doesn’t influence on CFD solution.

2-way FSI (bidirectional). The solution of two-way fluid-structure interaction requires co-simulation between computational fluid dynamics and structural mechanics. There are two (or more) data transfers. Exchanging data is performed after every coupling iteration during time step. In our case, deformations of the air-supported shell from ANSYS Mechanical are imported to the ANSYS Fluent as a dynamic mesh motion (solution often need to include remeshing of the fluid domain to the process). Then CFD part of problem is solved on the new mesh and resulting pressure distribution forms new load case for the transient structural analysis.

2-way FSI simulation is more accurate, but, of course, more expensive (in point of view of solution setup, computer resources and calculation time) and less stable.

## 2 EXPERIMENTAL INVESTIGATION

This work is based on the experiment data obtained by V.P. Polyakov et al in 1970th. Wind tunnel study is described in the papers <sup>1, 2</sup>. It was a tunnel test of an air-supported 3/4 spherical shell with diameter of  $D = 4.2$  m and height of  $H = 3.36$  m. One can see that the sizes of an experimental model are comparable to the sizes of real constructions.

Wind tunnel T-101 (TsAGI, Zhukovsky, Moscow Region) is a subsonic continuous-operation, closed-layout wind tunnel with two reverse channels and an open test section. Area of its elliptical cross section is  $264 \text{ m}^2$ .

Experiments were conducted at several tunnel speeds from 12 to 45 m/s, which comparable with real wind speed during storms and hurricanes. Value of the Reynolds number based on the tunnel flow speed  $V = 40$  m/s and the initial diameter of the structure  $D = 4.2$  m was  $Re = VD/\nu = 1.15 \cdot 10^7$ .

Besides the great sizes of model, it should be noted the fact that the data set for comparison is presented rather fully: flow speed  $V$  and internal pressure  $p$  in different combinations, deformed shape of the structure, which was measured by stereophotogrammetry method and surface distribution of pressure coefficient  $C_p$ .

There were data of two series of tests:

1) Internal pressure was constant  $p = 1000$  Pa, flow speed  $V$  was changed in such range: 12; 20; 30; 40; 45 m/s.

2) Flow speed pressure was constant  $V = 40$  m/s, internal pressure was changed in range: 500; 1000; 1500; 2000 Pa.

In present work, we consider the first case of constant pressure  $p = 1000$  Pa.

We enter the designation (1):

$$\psi = \frac{p}{q} \quad (1)$$

where  $q$ , Pa, is dynamic pressure of air flow, calculating by formula (2):

$$q = \frac{\rho V^2}{2} \quad (2)$$

where  $\rho$  is air density at 15°C,  $\rho = 1.225 \text{ kg/m}^3$ .

The value of parameter  $\psi$  influences significantly on a membrane shape in the air flow. When  $\psi < 1.0$  the dent is formed in front of shell. This case corresponds to the greatest distortion of an initial form of a shell, and formation of the dent can be referred to local loss of stability. This scenario presents the greatest difficulties for numerical modeling, that's why we focused on the value of  $\psi \approx 1.0$ . It can be observed when internal pressure  $p = 1000 \text{ Pa}$ , and air speed  $V = 40 \text{ m/s}$  ( $q = 980 \text{ Pa}$ ). For this case, there are two experimental curves for  $C_p$  along main meridian from two series of experiments (see Figure 4).

The material of membrane is rubber-coated kapron fabric (art. 51-060) 0.6 mm thick. As known, coated fabric has nonlinear mechanical properties. Unfortunately, only two moduli of elasticity were presented in the paper<sup>1</sup> – in warp and fill direction. There is no information about level of stress corresponded to this values. Also, there is no information about shear modulus and Poisson's coefficients. That's why mechanical properties, used in simulation, were adjusted during trial numerical calculations so that the deformed shape of numerical model membrane was close to the experimental one.

The air-supported model was mounted on the horizontal round plate. But, we have no geometrical parameters (height from floor, diameter, and thickness) of the plate. The lack of the specified information results in additional errors in results of numerical modeling.

### 3 NUMERICAL SIMULATION

#### 3.1 On the simulation of fluid-structure interaction (ANSYS System Coupling)

The Workbench System Coupling component system is an easy-to-use, all-purpose infrastructure that facilitates comprehensive multidisciplinary simulations between coupling participants.

In this paper we have been carried out calculation using ANSYS Workbench platform. Project Schematic of the 2-way FSI analysis is shown on Figure 1. One can see different modules used in analysis and data links between them.

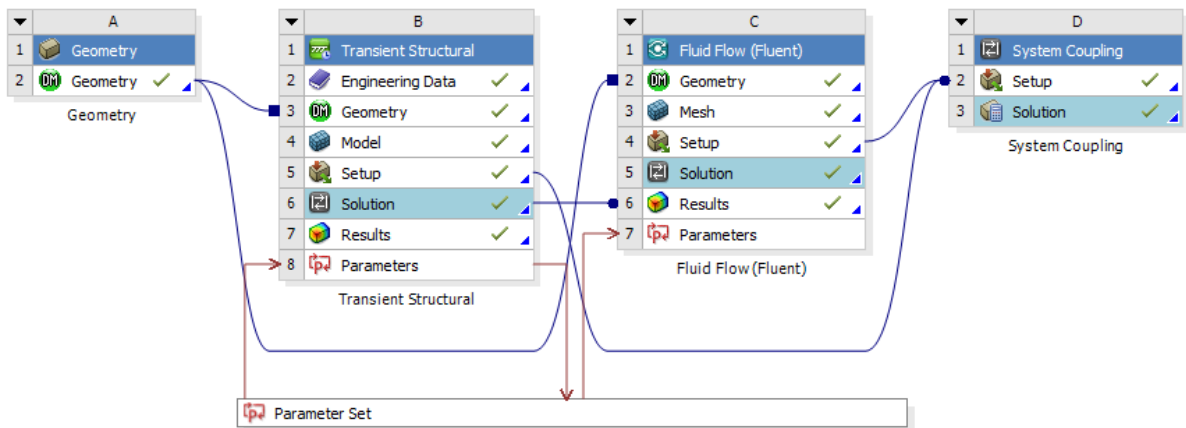


Figure 1: Project Schematic of the 2-way FSI analysis

### 3.2 Fluid model (ANSYS Fluent)

The fluid solver software used in this work is ANSYS Fluent based on the finite-volume method (FVM). In the finite volume method, volume integrals in a partial differential equation that contain a divergence term are converted to surface integrals, using the divergence theorem. Shell deformations results in need of the transient solution. The second order implicit transient formulation was used in this work. “Coupled” pressure-velocity coupling scheme were selected.

The carried-out calculations were directed to approbation and verification of a calculation procedure. Present results have been obtained on the rough unstructured tetrahedral mesh with rather small number of nodes (about 400000). This mesh was created by automatic procedures of ANSYS Meshing. Fluid domain has been a rectangular box with following dimensions: length –  $25D$ , width –  $10D$ , height –  $8D$  (where  $D = 4.2$  m is diameter of shell).

We have used diffusion-based smoothing and dynamic remeshing after every coupling step. These actions have prevented emergence of errors.

Turbulent intensity has been adopted as 1%, because it is usually low in tunnel tests. Air velocity at the inlet has been adopted constant. Gauge pressure at the outlet has been retained equal to the default value of 0 Pa. Top and lateral sides of fluid domain has been accepted as symmetry boundary conditions. Shell surface has been accepted as no-slip wall with 1 mm uniform roughness.

The boundary layer near the shell has been meshed into prismatic cells (Figure 2, a). Hexahedral structured has been already created, but it will be used in future work.

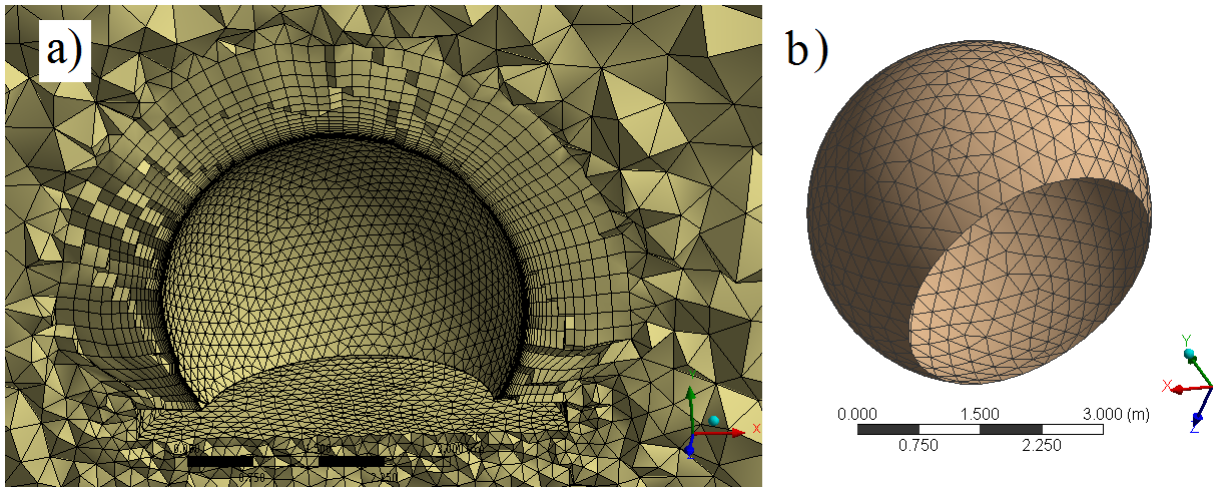


Figure 2: Computational models used in different modules:  
ANSYS Fluent (a), ANSYS Mechanical (b)

We have decided to find out what model of turbulence within RANS approach<sup>10</sup> will provide the best coincidence of numerical and experimental results. Such approach the most economic from the point of view of requirements to mesh and time discretization and also to the computer resources.

Three RANS-based eddy-viscosity turbulence models have been considered in the fluid simulations:

- 1) One-equation The Spalart–Allmaras model<sup>11</sup>
- 2) Two-equation  $k$ - $\varepsilon$  turbulence model<sup>12</sup>
- 3) Two-equation  $k$ - $\omega$  SST (Menter’s Shear Stress Transport) turbulence model<sup>13</sup>

The last one model combines the  $k$ - $\omega$  turbulence model and  $k$ - $\varepsilon$  turbulence model such that the  $k$ - $\omega$  is used in the inner region of the boundary layer and switches to the  $k$ - $\varepsilon$  in the free shear flow. Thus advantages of both models are used in the respective regions.

### 3.3 Structural Model (ANSYS Mechanical)

ANSYS Mechanical is based on finite-element method (FEM). The structural dynamic solution has been got by Newton-Raphson method with taking into account large deflections (geometrical nonlinearity). Internal pressure has been simulated as a constant follower distributed force, changing of its value in the experiment has been neglected.

In this paper, we use Shell181 element type for the structural analysis. Shell181 is a three- or four-nodes element with six degrees of freedom at each node: translations in the x, y, and z directions, and rotations about the x, y, and z-axes (if the membrane option is used, the element has translational degrees of freedom only). Shell181 accounts for follower (load stiffness) effects of distributed pressures. The triangle form is generally more robust when using the membrane option with large deflections<sup>14</sup>. Finite element mesh is shown on the Figure 2, b. Mesh size has been accepted as 0.3 m.

Shell181 has been chosen, because it has a “membrane” option. Elements with this option activated allow deformation in the plane of the surface only (that is, stresses do not vary

through the thickness and all stress components with respect to the thickness direction are zero). Only membrane stiffness is accounted for. Shell bending and transverse shear stiffness are excluded; therefore, only translational degrees of freedom are retained<sup>14</sup>.

During the modeling process we had to apply pressure load onto inner face of shell and assign fluid-solid interface to the outer face. In ANSYS Mechanical there is no difference between outer and inner faces of surface. That's why pressure load is applied to the fluid-solid interface. But all loads applied onto the fluid-solid interface are ignored (it is restriction of using the Workbench System Coupling). We had to separate membrane into two parts of half thickness (0.3 mm, see Table 1). Linear bonded contact (MPC formulation) has been applied on these membranes.

For the numerical model, a simple linear orthotropic plane stress material model is used. This simple approach is allowed<sup>15</sup>, because real behavior of fabric is very sophisticated, but information about material used in the experiment, was scanty. That's why we had to perform several trial simulations that helped to determine the mechanical properties of fabric. Besides, the simple material model reduces time of carrying out calculation.

The formula (3) describes the stress-strain relationship:

$$\begin{bmatrix} \varepsilon_w \\ \varepsilon_f \\ 2\gamma_{wf} \end{bmatrix} = \begin{bmatrix} \frac{1}{E_w} & \frac{-\nu_{fw}}{E_f} & 0 \\ \frac{-\nu_{wf}}{E_f} & \frac{1}{E_f} & 0 \\ 0 & 0 & \frac{1}{G_{wf}} \end{bmatrix} \cdot \begin{bmatrix} \sigma_w \\ \sigma_f \\ \tau_{wf} \end{bmatrix} \quad (3)$$

where  $E_w$  and  $E_f$  are elastic moduli in respectively warp and fill (weft) direction, MPa;

$\nu_{wf}$  and  $\nu_{fw}$  are the Poisson's coefficients;

$G_{wf}$  is the shear stiffness, MPa;

$\varepsilon_w$  and  $\varepsilon_f$  are the normal strains;

$\sigma_w$  and  $\sigma_f$  are the normal stresses, MPa.

A local spherical coordinate system has been used to orient the local axes of elements for the correct modeling of the meridian patterning.

As the stiffness matrix (eq.(3)) is symmetric, the membrane properties have to comply with the following reciprocal relationship:

$$\frac{\nu_{wf}}{E_w} = \frac{\nu_{fw}}{E_f} \quad (4)$$

Table 1 contains material properties, which were used in the calculations.

**Table 1:** Used reference material parameters

$E_w$ , MPa	$E_f$ , MPa	$\nu_{wf}$	$\nu_{fw}$	$G_{wf}$ , MPa	$t$ , mm
200	185	0.1	0.0925	0.1	0.6 (0.3+0.3)

#### 4 RESULTS & DISCUSSION

On the Figure 3 one can see the contours of the pressure coefficient  $C_p$  in the plane of main meridian as results of 1-way FSI analysis (a) and 2-way FSI analysis (b). The minimum values of  $C_p$  (-1.45 and -1.22) differ significantly. Thus wind load (depending on pressure coefficient) is higher in case of 2-way FSI.

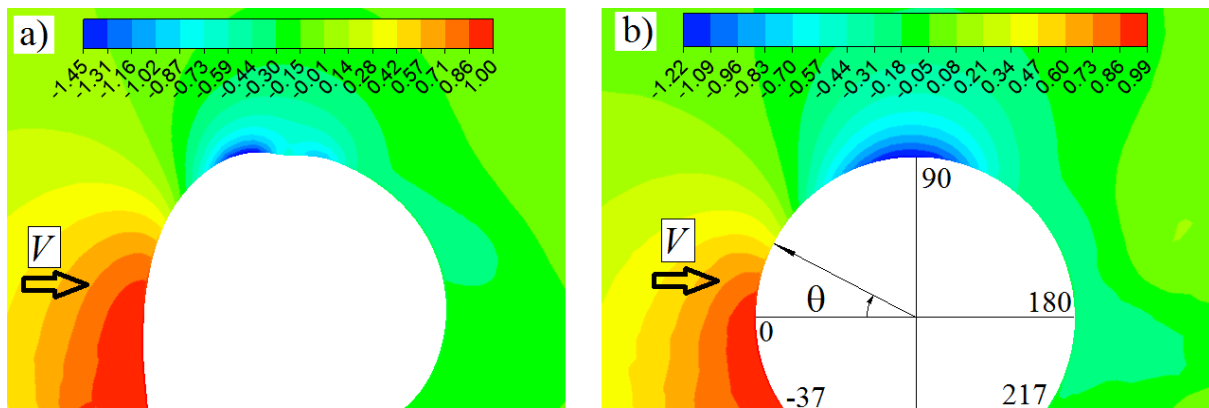


Figure 3: The distributions of pressure coefficient  $C_p$  in the main meridian plane: 2-way coupled FSI analysis (left) and 1-way FSI analysis (right). In both cases  $V = 40$  m/s

Charts of pressure coefficient  $C_p$  for different turbulent models are shown on the Figure 4 and Figure 5. X-axis is the latitude angle  $\theta$  (reference direction is shown on the Figure 3, b). There are two minimum peaks on the Figure 5. The second one arises because of emergence of deepening on the top of shell.

The  $k-\omega$  SST turbulence model demonstrates better agreement of the experimental and numerical results than other turbulence models used in this work ( $k-\epsilon$  and Spalart–Allmaras). It should be noted, that there are two curves (similar, but not identical) for the experimental results from two series of tests (in case of  $V = 40$  m/s).

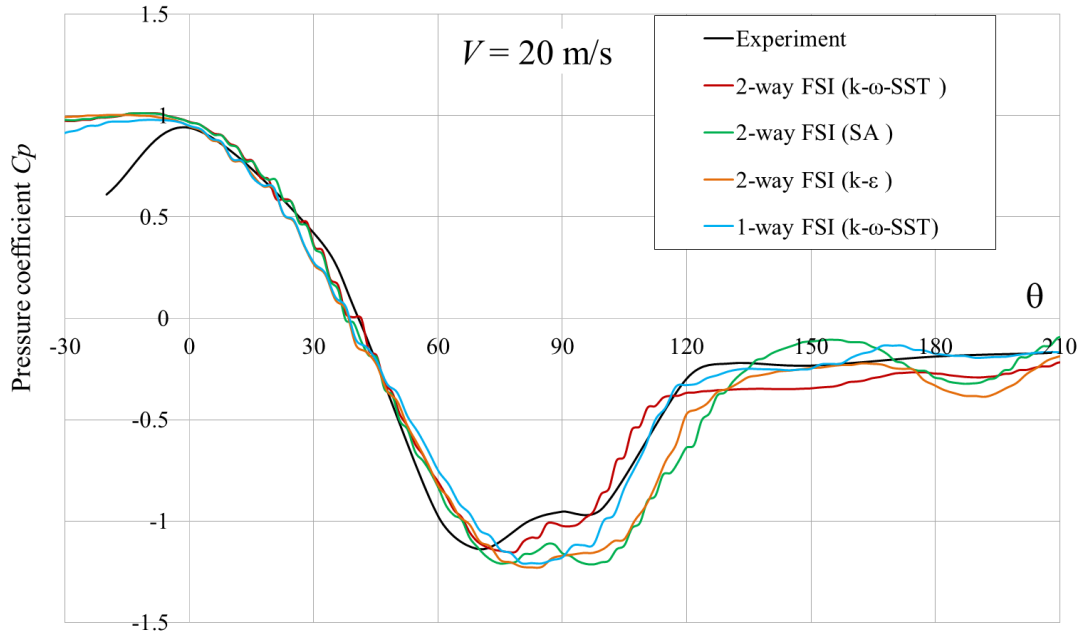


Figure 4: Results of experiments and numerical calculations of pressure coefficient  $C_p$  for different turbulent models on the line of main meridian. Internal pressure  $p = 1000$  Pa, air speed  $V = 20$  m/s,  $\psi = 4.08$

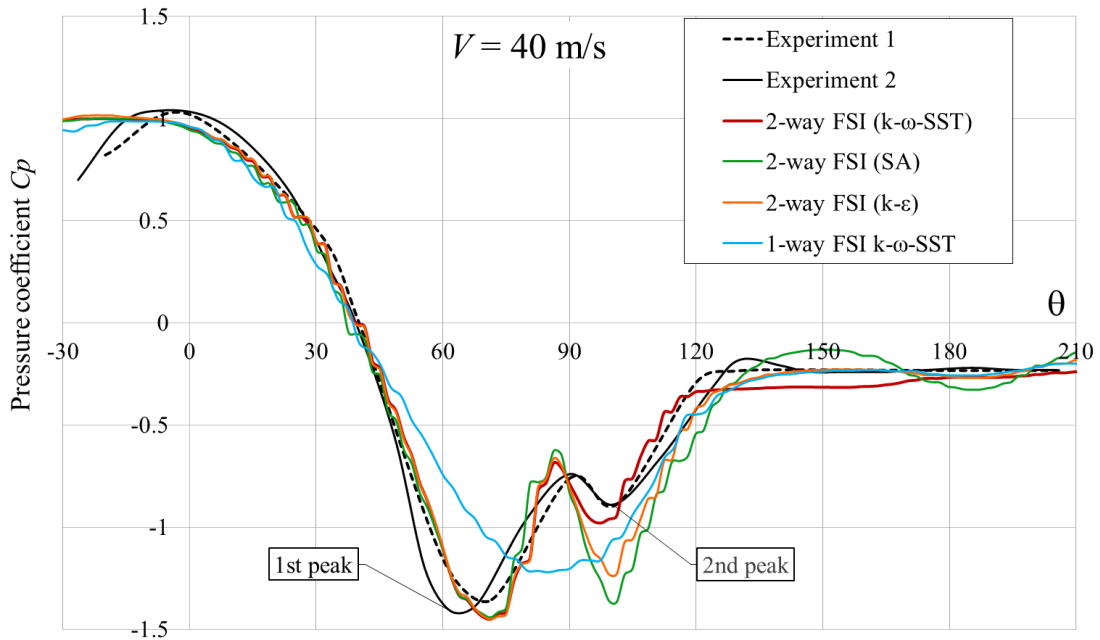


Figure 5: Results of experiments and numerical calculations of pressure coefficient  $C_p$  for different turbulent models on the line of main meridian. Internal pressure  $p = 1000$  Pa, air speed  $V = 40$  m/s,  $\psi = 1.02$

The deformations of the shell are shown in the real scale on the Figure 3, and on the Figure 6. One can notice small deepening on the top of the shell. This deepening is appeared only when orthotropic material model with higher meridian modulus is used.

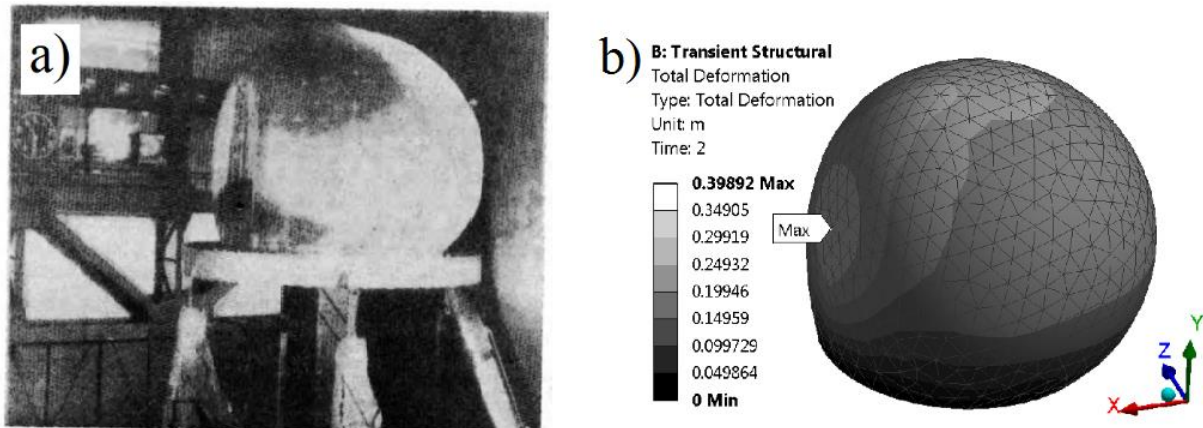


Figure 6: The deformed shape of the air-supported structure in the air flow. Photo of experiment (a), numerical results (b). Internal pressure  $p = 1000$  Pa, air speed  $V = 40$  m/s,  $\psi = 1.02$

## 5 CONCLUSIONS

The fully coupled FSI simulation of air-supported structure in the air-flow is presented and discussed in this work. The comparison of the numerical and experimental results allows drawing the following conclusions.

Experimental and numerical methods showed that surface wind loads can increase due to deformation of a structure. These conclusions emphasize the importance of researches on wind interaction with air-supported structures.

An applicability of the proposed technique to the considered problem was confirmed by a good agreement of the experimental and numerical results.

The  $k-\omega$  SST turbulence model demonstrates the best agreement of the experimental and numerical results than other turbulence models used in this work ( $k-\varepsilon$  and Spalart–Allmaras). That's why the  $k-\omega$  SST model is planned to be used in further calculations.

When values of parameter  $\psi$  are near or less than 1.0, the initial spherical shape of the membrane becomes highly distorted. Therefore, location of the flow separation point is easier to define. It explains good coincidence of results at high speeds of a stream even using coarse mesh.

The orthotropic mechanical properties of membrane material significantly influence to the deformed shape. It is shown, that deformations, in turn, affects to the distribution and values of pressure coefficient  $C_p$  (the second peak doesn't appear and the first is smaller).

Using of the linear orthotropic model for the membrane material is reasonable compromise of accuracy and speed.

Periodic separation of vortices (like described at paper<sup>16</sup>) wasn't observed, because of using the coarse tetrahedral mesh and RANS approach. Hexahedral detailed mesh combined with using of DES approach solves this problem.

Received results are the basis for future work. The following steps are planned:

- correct simulation of transient response of vibrating air-supported structure including vortex shedding (by using detached eddy simulation approach and detailed hexahedral mesh);
- damping factors need to be clarified;

- fully coupled FSI numerical simulation of the real scale air-supported structure in the more natural turbulent wind flow.

## 6 REFERENCES

- [1] D.A. Beylin, V.P. Polyakov, V.N. Shmyreva, V.A. Yakovlev, “Using of stereophotogrammetry for the investigation of the stress-strain state of soft spherical envelope in the air-flow” (Russian) *Uchenye zapiski TsAGI [TsAGI Science Journal]*. (1982) **6**:66-76. Available: <https://cyberleninka.ru/article/n/ispolzovanie-stereofotogrammetricheskogo-metoda-dlya-issledovaniya-napryazhenno-deformirovannogo-sostoyaniya-myagkoy-obolochki>
- [2] V.P. Polyakov, D.A. Beylin. An experimental study of the wind pressure on the soft orthotropic spherical shell. (Russian) *Soobshcheniya DVVIMU po sudovym myagkim obolochkam [DVVIMU reports on the ship soft shells]*. (1977) **35**:215-227.
- [3] A.M. Kupzok, *Modeling the interaction of wind and membrane structures by numerical simulation* (Dr.-Ing. Thesis), Technical University of Munich, 2009
- [4] ASCE 17-96, *Air-supported structures*, American Society of Civil Engineers, 1997
- [5] Newman, B.G., and Goland, D. Two-dimensional inflated buildings in a cross wind. *Journal of Fluid Mechanics* (1982) **117**:507-530.
- [6] Newman, B.G., Ganguli, U. and Shrivastava S.C. Flow over spherical inflated buildings. *Journal of wind engineering and industrial aerodynamics* (1984) **17.3**:305-327.
- [7] Kawamura, S. and Tatsuhiko, K. An experimental study of a one-membrane type pneumatic structure - wind load and response. *Journal of Wind Engineering and Industrial Aerodynamics* (1986) **23**:127-140.
- [8] Bathe, K.-J. and Ledezma, G.A. Benchmark problems for incompressible fluid flows with structural interactions. *Computers & structures* (2007) **85.11**:628-644.
- [9] Michalski, A., Kermel, P.D., Haug, E., Löhner, R., Wüchner, R., and Bletzinger, K.U. Validation of the computational fluid-structure interaction simulation at real-scale tests of a flexible 29m umbrella in natural wind flow. *Journal of Wind Engineering and Industrial Aerodynamics* (2011) **99.4**:400-413.
- [10] D.C. Wilcox, *Turbulence Modeling for CFD*, DCW Industries, Inc., 3<sup>rd</sup> edition, 2006
- [11] Spalart, P.R. and Allmaras, S.R. A one-equation turbulence model for aerodynamic flows. *AIAA Journal* (1992) **94**:5-21.
- [12] Launder, B.E., Spalding, D.B. The numerical computation of turbulent flows, *Computer Methods in Applied Mechanics and Engineering*, 1974, **3.2**:269-289.
- [13] Menter, F.R. Two-equation eddy-viscosity turbulence models for engineering applications. *AIAA journal* (1994) **32.8**:1598-1605.
- [14] *ANSYS Mechanical APDL Element Reference. Release 15.0*, SAS IP, Inc., 2013
- [15] ASCE/SEI 55-10, *Tensile membrane structures*, American Society of Civil Engineers, 2010
- [16] Taneda, S. Visual observations of the flow past a sphere at Reynolds numbers between  $10^4$  and  $10^6$  *Journal of Fluid Mechanics* (1978) **85.1**:187-192.

RESEARCH ON WIND PRESSURE AND WIND-INDUCED VIBRATION  
CHARACTERISTICS OF EXPO AXIS CABLE-MEMBRANE STRUCTURE BY FIELD  
MEASUREMENT

**STRUCTURAL MEMBRANES 2017**

**QILIN ZHANG<sup>\*</sup>, ZHAOYANG LI<sup>†</sup>**

<sup>\*</sup> College of Civil Engineering  
Tongji University  
200092 Shanghai, China.  
E-mail: zhangqilin@tongji.edu.cn

<sup>†</sup> College of Civil Engineering  
Tongji University  
200092 Shanghai, China.  
E-mail: lizhaoyangzh@163.com

**Key words:** Cable-Membrane Structure, Field Measurement Research, Wind Pressure Characteristics, Wind-Induced Response, Damping Ratio.

**Summary.** In order to deeply investigate the wind pressure characteristics and the wind-induced vibration characteristics of cable-membrane structure, a monitoring study on the Expo Axis cable-membrane structure was carried out. The wind speed, wind pressure and wind-induced response were measured simultaneously. The wind pressure characteristics, the structure's dynamic characteristics and the damping ratio were analyzed based on the monitoring data. The probability density distribution of wind pressure has some non-Gauss property. With the change of wind direction wind pressure coefficient by field measurement and wind tunnel test has the same trend. The acceleration RMS and power spectral density vary with the wind direction. The acceleration RMS increases with the increase of mean wind speed. Damping ratio decreases with the increase of natural frequency.

## 1 INTRODUCTION

Cable-membrane structure is a new type of structure developed in recent decades. It has been widely used in large span spatial structures. It has the advantages of novel appearance, excellent mechanical property, better flexibility and unique aesthetic compared to traditional structures. Also it has the characteristics of light weight, small stiffness, low and dense natural frequency. It belongs to the wind-induced sensitivity structure, and wind load is the control load<sup>[1, 2]</sup>. The damping ratio of cable-membrane structures is always a difficult parameter to determine.

The research methods of the wind resistance of cable membrane structures are mainly focused on numerical wind tunnel method, random vibration analysis method and wind tunnel test method. Field measurement is the most direct and reliable method to study the characteristics of wind load and wind-induced response on structures. However, field

measurement has the characteristics of long cycle, high difficulty and high cost, the lack of field measurement research has become an important factor in the study of wind resistance.

Some scholars, such as Li<sup>[3, 4]</sup> have carried out a series of field measurement research on low rise buildings and high-rise buildings. However, there are few studies on the wind pressure characteristics of cable-membrane structures. Kim<sup>[5]</sup> carried out a long term monitoring study on the dynamic response of the membrane structure of the World Cup Stadium in Jeju Island.

Expo Axis' roof in Expo 2010 Shanghai China is composed of two parts, the cable-membrane structure and Sun Valleys. The cable-membrane structure is open structure with a total length of about 840m, the maximum span of 97m, the maximum height of 38m, an area of about 64000 m<sup>2</sup>. The cable-membrane structure roof comprises two parts of the supporting system and the membrane surface system. PTFE membrane material was used as membrane surface. It locates in Shanghai Pudong New Area in China and adjacent to Huangpu River, wind speed is large all year round, and in the summer and autumn it is easily affected by the typhoon. It is necessary to study wind pressure characteristics and dynamic characteristics of such structures.

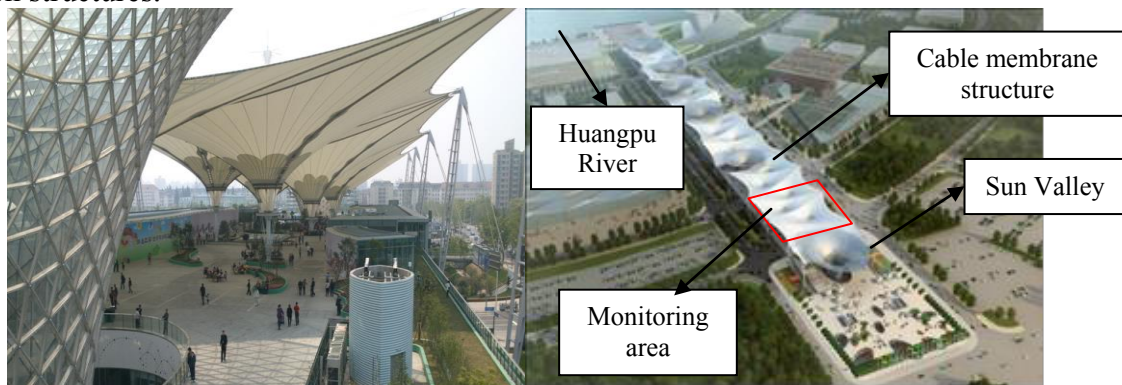


Figure 1: Expo Axis' roof in Expo 2010 Shanghai China

## 2 MONITORING SYSTEM

A long term monitoring system of Expo Axis' roof in Expo 2010 Shanghai China which consists of 5 main parts: the sensor system, the automatic collection system, the central database subsystem, the structural health warning assessment system and IoT monitoring system was built.

A 3-axis ultrasonic anemometers of Model 81000 produced by R.M. YOUNG COMPANY was used to measure the wind speed and the wind direction. For wind speed, its range is from 0 to 40m/s, the resolution is 0.01m/s and the accuracy is  $\pm 1\%$  rms  $\pm 0.05$  m/s (0 to 30 m/s) or  $\pm 3\%$  rms (30 to 40 m/s). For wind direction, its range is from  $0^\circ$  to  $359.9^\circ$ , the resolution is  $0.1^\circ$  and the accuracy is  $\pm 2^\circ$  (1 to 30 m/s) or  $\pm 5^\circ$  (30 to 40 m/s). It was arranged at the top of the mast in the main measuring area.

22 micro differential pressure sensors were placed on membrane surface and for each measuring point there were two sensors arranged symmetrically top and bottom membrane surface. The measuring range is 0 ~ 1000Pa and the precision is  $\pm 1\%$ .

8 acceleration sensors were placed on membrane surface to monitor the wind effect. The acceleration ranges from 0 to 0.5g ( $1g=9.8m/s^2$ ) and the sampling frequency ranges from 0.05 to 300Hz, the voltage sensitivity is 10V/g.

The collection and processing system was specifically designed and developed according to the characteristics of the project. 5 dynamic acquisition instruments of 8 channels were used and were connected to the master station in main control room through optical fiber. The data was transferred to a proprietary database by internet.

Table 1: Measuring points of sensors

Point location	Main measuring area								Secondary measuring area		
	1	2	3	4	5	6	7	8	9	10	11
Pressure sensors (top)	1	2	3	4	5	6	7	8	9	10	11
Pressure sensors (bottom)	12	13	14	15	16	17	18	19	20	21	22
Acceleration sensors	1	2	3	4	5	6	7	8			

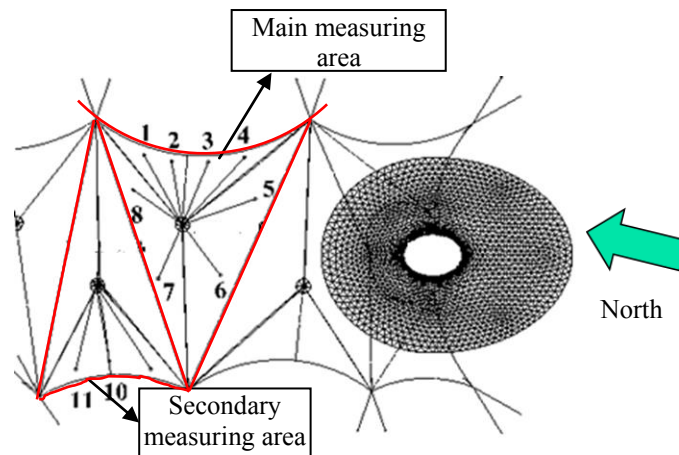


Figure 2: Measuring point layout

### 3 WIND PRESSURE CHARACTERISTICS

Similar to the probability density distribution of wind speed, the probability density distribution of wind pressure is analyzed by using higher order statistics analysis method. Table 2 shows the Mean values of skewness and kurtosis of fluctuating wind pressure of Measuring point 4, 9 and 15. Skewness is larger than 0 and kurtosis is larger than 3. It indicates that fluctuating wind pressure has some non-Gaussian characteristics. It is thought that the reason should be that wind pressure characteristics is not only affected by oncoming

flow, but also by the signature turbulence of the structure. What's more the vibration of the structure can also affect the wind pressure characteristics.

Table 2: Mean values of skewness and kurtosis of fluctuating wind pressure

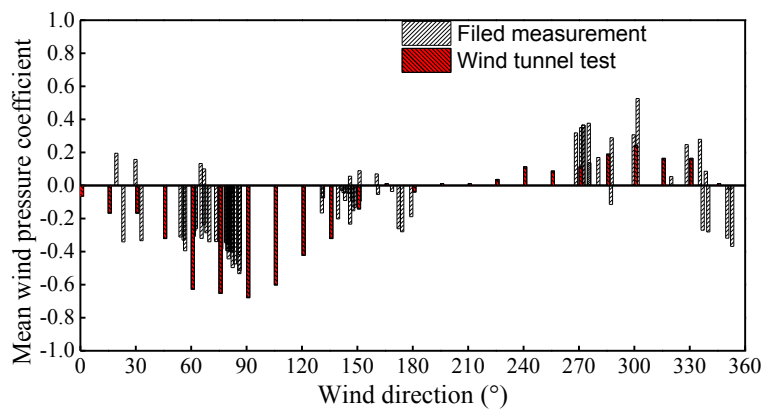
Measuring point	4	9	15
skewness	0.502	0.577	0.355
kurtosis	3.378	4.615	5.058

Mean wind pressure coefficient  $C_{P_{mean}}$ , Maximum wind pressure coefficient  $C_{P_{max}}$ , Minimum wind pressure coefficient  $C_{P_{min}}$  can be calculated as:

$$C_{P_{mean}} = \frac{P_{mean}}{\frac{1}{2}\rho U^2} \quad C_{P_{max}} = \frac{P_{max}}{\frac{1}{2}\rho U^2} \quad C_{P_{min}} = \frac{P_{min}}{\frac{1}{2}\rho U^2} \quad (1)$$

In Formula (2),  $P_{mean}$ ,  $P_{max}$ ,  $P_{min}$  are the mean value, maximum value, minimum value of wind pressure in 10 minutes, for membrane, wind pressure can be obtained by making the difference between pressure measured by the wind pressure sensors top and bottom membrane surface at the same place.  $U$  is the 10min mean wind speed, for comparison, it is chosen as the gradient wind speed, which can be calculated according to the measured mean wind speed.

Some wind tunnel tests of rigid model of Expo Axis' roof have been conducted. Figure 3 shows the mean, maximum and minimum wind pressure coefficient of Measuring point 1 by field measurement and wind tunnel test. The results show that with the change of wind direction, wind pressure coefficient by field measurement and wind tunnel test has the same trend. however maximum and minimum wind pressure coefficient by field measurement is greater. the difference may be due to the difference of wind filed simulation and the neglect of structural vibration in wind tunnel tests.



a) Mean wind pressure coefficient

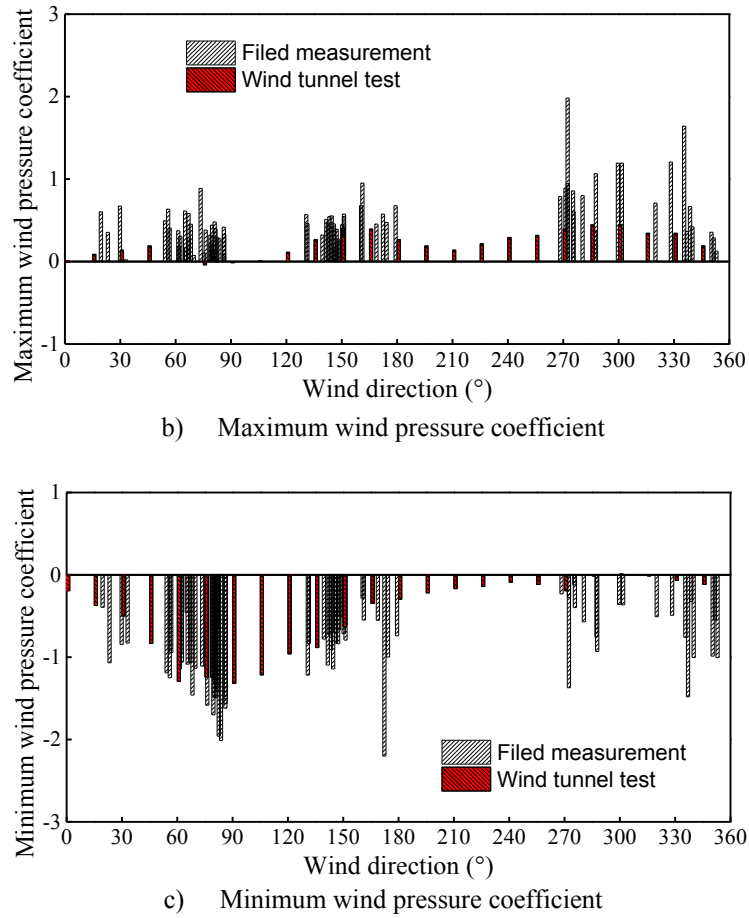


Figure 3: Comparison of Wind pressure coefficients of Measuring point 1 obtained by field measurement and wind tunnel test

#### 4 WIND-INDUCED VIBRATION

Vibration strength of the structure can be represented by the root mean square of acceleration. The mean wind speed of 8 m/s was chosen, the acceleration RMS values changing with wind direction were shown in Figure 4. The root mean square value of acceleration response varies regularly with the direction of the wind, when the mean wind direction angle is near  $0^\circ$  and  $90^\circ$ , the acceleration RMS is larger, and the RMS is smaller when the mean wind direction angle is near  $45^\circ$ .

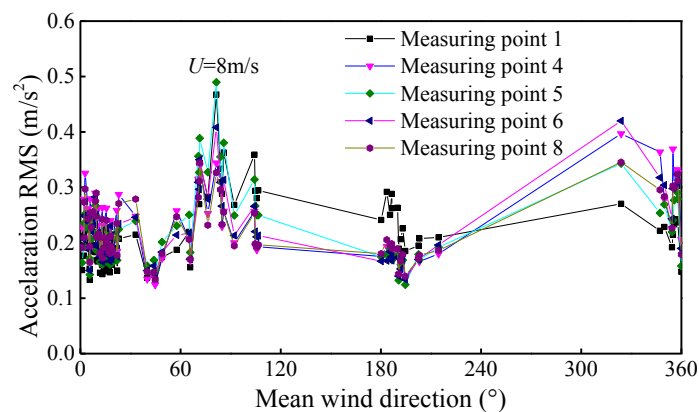


Figure 4: Acceleration rms versus wind direction

Figure 5 shows the power spectral density of measuring point 1 with mean wind speed of 8 m/s changing with wind direction. From the graph, when the wind direction angle is  $2^\circ$ ,  $23^\circ$  and  $45^\circ$ , the power spectral density is small, especially at  $45^\circ$ , while at  $65^\circ$ ,  $81^\circ$  and  $106^\circ$ , the power spectral is relatively large.

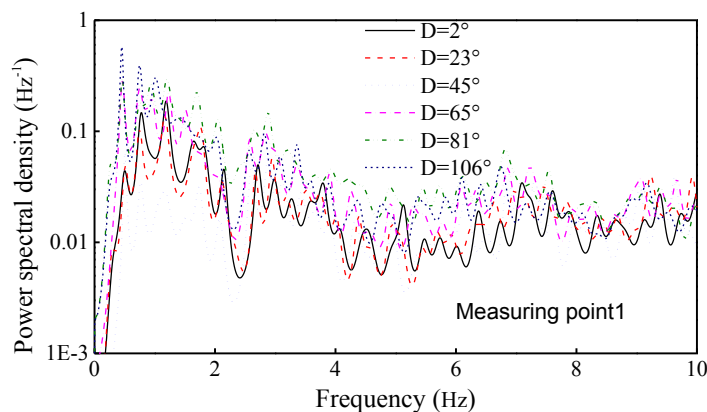


Figure 5: Power spectral density of Measuring point 1 versus wind direction

Figure 6 shows the relationship between acceleration RMS and mean wind speed, the acceleration RMS increases with the increase of mean wind speed, and the increase rate and the dispersion are also increasing.

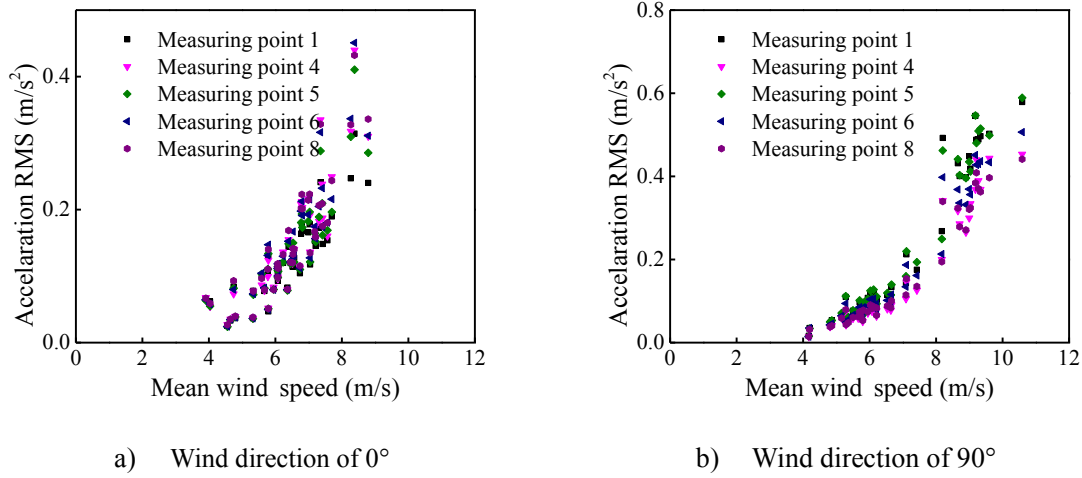


Figure 6: Acceleration RMS versus mean wind speed

### 5 NATURAL FREQUENCY AND DAMPING RATIO

Measuring point 1, 5 and 6 were chosen to analyze the structural natural frequency and the damping ratio. Peak picking method (PP), Hilbert-Huang Transform method (HHT) and Stochastic Subspace Identification method (SSI) were adopted.

Table 3 shows the natural frequency results calculated by PP, HHT and SSI. The results were mean values by several measurements. It is easy to see the first order frequencies were very close.

Table 3: Natural frequencies calculated by PP, HHT and SSI

Frequency (Hz)	Method		
	PP	HHT	SSI
1st order	2.86	2.85	2.70
2nd order	13.08	14.66	12.17
3rd order	24.72	24.50	15.15
4th order			18.94
5th order			25.12

Some pieces of 10 minutes data were selected at different time to analyze the damping ratio. Figure 7 shows the damping ratio results calculated by SSI using different data. It indicates that damping ratio decreases with the increase of frequency.

The damping form of the cable-membrane structure is assumed to conform to Rayleigh damping. The damping ratio formation of  $i$ -th order can be described as:

$$\xi_i = \frac{\alpha}{2\omega_i} + \frac{\beta}{2}\omega_i \tag{2}$$

where  $\alpha$ ,  $\beta$  are fitting parameters,  $\omega_i$  is the  $i$ -th order frequency.  $\alpha = 0.4084$ ,  $\beta = 0.0007$ , based on least square method. Figure 8 shows the mean value of damping ratio by SSI and the fitting curve based on Formula (2).

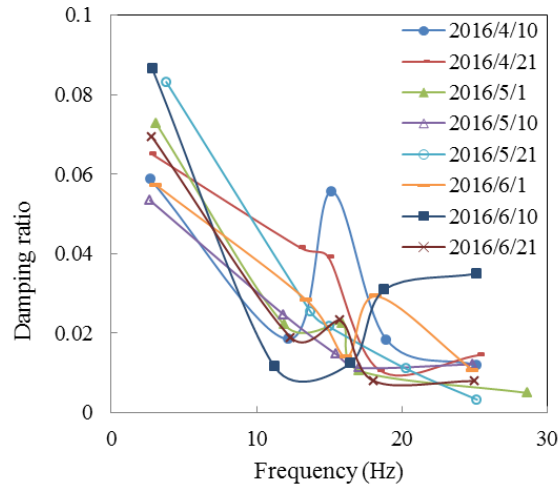


Figure 7: Damping ratio calculated by SSI

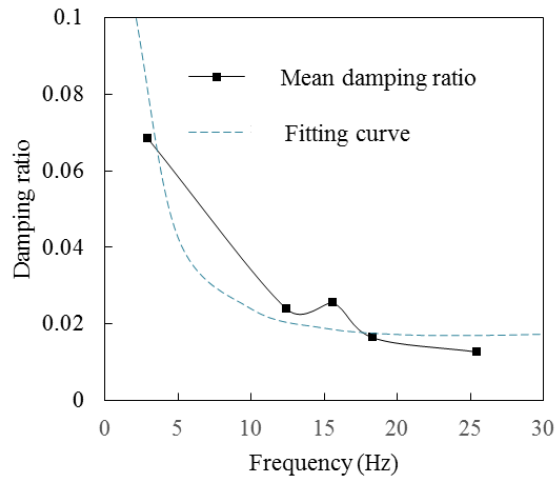


Figure 8: Mean value of damping ratio calculated by SSI and the fitting curve based on Formula (2)

## 6 CONCLUSIONS

This paper introduces the field measurement of Expo Axis' roof in Expo 2010 Shanghai China and shows wind pressure and the wind-induced vibration characteristics of the cable-membrane structure. The main conclusions are as follows:

- Obtaining the wind field, wind pressure and the structure's wind-induced response by field measurement is the most effective means to study the wind effects of cable-membrane structure.
- Fluctuating wind pressure has some non-Gaussian characteristics. With the change of wind direction wind pressure coefficient by field measurement and wind tunnel test has the same trend.

- The acceleration RMS and power spectral density vary with the wind direction. The acceleration RMS increases with the increase of mean wind speed and the increase rate and the dispersion are also increasing.
- Damping ratio decreases with the increase of natural frequency and it can be fitted in the Rayleigh damping form in this case.

## REFERENCES

- [1] Gu M., Lu H. F., Wind loads and wind-induced vibration of membrane structures: State of the art. *Journal of Vibration and Shock*, 2006; **25**; 25-28+43.
- [2] Shen S. Z., Wu Y., Overview of wind-induced response for large-span tension structures. *Journal of Tongji University*, 2002; **30**; 533-538.
- [3] Li Q. S., Hu S. Y., Dai Y. M., Li Z. N., Analysis of the field measured suction peak pressure coefficients on the flat roof of a low-rise building. *Journal of Hunan University Natural Sciences*, 2010; **37**; 11-16.
- [4] Li Q. S., Xiao Y. Q., Fu J. Y., et al. Full-scale measurements of wind effects on the Jin Mao building. *Journal of Wind Engineering and Industrial Aerodynamics*. 2007; **95**; 445-466.
- [5] Kim J. Y., Yu E., Kim D. Y., et al. Long-term monitoring of wind-induced responses of a large-span roof structure. *Journal of Wind Engineering & Industrial Aerodynamics*. 2011; **99**; 955- 963.

# THE EFFECT OF GRAVITY IN TRANSIENT FLUID-STRUCTURE INTERACTION SIMULATIONS OF A LARGE WIND TURBINE WITH COMPOSITE BLADES

G. SANTO<sup>\*</sup>, M. PEETERS<sup>†</sup>, W. VAN PAEPEGEM<sup>†</sup> AND J. DEGROOTE<sup>\*</sup>

<sup>\*</sup> Department of Flow, Heat and Combustion Mechanics, Ghent University  
Sint-Pietersnieuwstraat 41 – 9000 Ghent, Belgium  
{gilberto.santo; joris.degroote}@ugent.be

<sup>†</sup> Department of Materials, Textiles and Chemical Engineering, Ghent University  
Technologiepark-Zwijnaarde 907 – 9052 Zwijnaarde, Belgium  
{mathijs.peeters; wim.vanpaepegem}@ugent.be

**Key words:** Fluid-Structure Interaction, Composite Materials, Wind Turbine, Atmospheric Boundary Layer.

**Summary.** In this work the effect of the gravity force on the fluid-structure interaction (FSI) simulation of a large horizontal axis wind turbine (HAWT) is analyzed in detail. FSI simulations with and without gravity are carried out and compared in order to highlight the effect of gravity force on the loads and performance of the analyzed HAWT.

## 1 INTRODUCTION

The increasing size of the horizontal axis wind turbine's rotor<sup>1</sup> in order to maximize the captured energy, and the resulting higher slenderness of their blades, have led to the need of investigating the mutual interaction of wind flow and structural response of the blades. It has already been shown in previous research that the axial deflection of the blade tips can reach 10-15% of the total blade span during the normal operation of wind turbines<sup>2, 3</sup>. The deforming motion of the blades influences the wind flow around them and, in turn, the wind loads are also modified. This results in a fully coupled fluid-structure interaction (FSI) problem, which is important to be accounted for in many processes such as design and maintenance estimation of modern horizontal axis wind turbines (HAWTs)<sup>4</sup>.

Both the aerodynamic and the structural sides of the FSI problem involve a large number of complexities when it comes to numerical simulation. On the aerodynamic side, the high Reynolds number of the flow (up to  $10^8$ ) and the consequent high turbulence levels are challenging to simulate. Furthermore, wind turbines are immersed in the atmospheric boundary layer (ABL)<sup>5, 6</sup>, i.e. an increasing wind speed with height, such that the complete rotor has to be simulated with the loads on each blade fluctuating in time. On the structural side, HAWT blades are normally made of anisotropic composite materials built up of several plies<sup>7, 8</sup>. The presence of inner structures (shear webs and shear caps) and adhesive joints makes the modelling even more challenging. The gravity load also plays a major role on the structural response of the blades and will be the focus of this paper.

The present work aims at simulating the fully coupled FSI problem on a full scale HAWT employing accurate flow and structural models, leading to a fully coupled FSI model. The ABL is taken into account in detail as opposed to what is normally done in literature. The gravity load is considered in the structural model and its effect is highlighted by comparison with analogous results obtained neglecting this load. The oscillating loads and stresses on each blade are analysed in detail. On the structural side, a complete and accurate model reproducing the complex composite nature of each blade is built and employed. The implicit coupling between the flow and the structural models is guaranteed by the in-house code Tango, resulting in a segregated approach<sup>9</sup>.

## 2 METHODOLOGY

Both the computational fluid dynamics (CFD) and computational structural mechanics (CSM) models are now described. Afterwards, the details of the coupling will be given.

### 2.1 The CFD model

In terms of modelling, the inclusion of the ABL implies that the entire rotor needs to be analyzed and the reduction to one single blade with periodic boundary conditions is not possible. Furthermore, different reference frames are necessary: a stationary and a rotating domain are adopted. The layout of the complete mesh is shown in fig. 1.

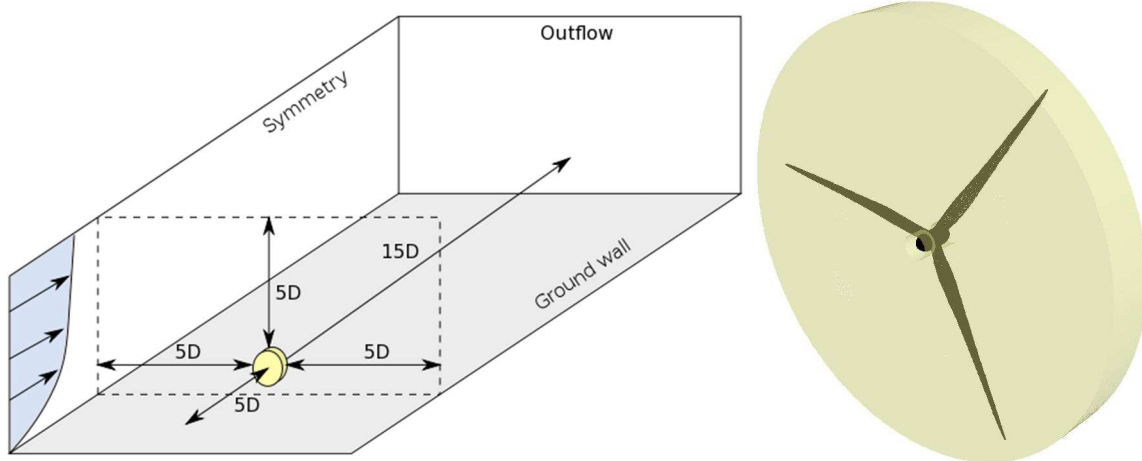


Figure 1: (left) layout of the HAWT simulations and (right) detail of the rotating domain.

The rotor, whose radius  $R$  is 50m, is embedded in the rotating cylindrically-shaped domain (marked in yellow in fig. 1), which has a length of 12 m and a radius of 52 m. The rotating and stationary domains are separated by sliding interfaces where all the information is passed through by interpolation. The distance of the rotor from the symmetry sides and top surface is chosen equal to 5 rotor diameters in order to avoid artificial acceleration of the flow. The inflow and the outflow are respectively 5 and 15 rotor diameters away from the rotor. These distances

are chosen sufficiently large to avoid any influence of the boundaries on the flow around the turbine.

The case is considered to be incompressible, given the low Mach numbers typical of the HAWTs. The turbulence model is chosen to be the *k-epsilon* (unsteady RANS) model. The ABL inlet conditions first proposed by Richard and Hoxey<sup>5</sup> are employed for the velocity  $u$ , the turbulent kinetic energy  $k$  and the dissipation rate  $\varepsilon$  in order to replicate the neutral ABL (no heat flux) conditions in the numerical domain, with  $z$  the height, thus the distance from the ground wall.

$$\begin{aligned} u(z) &= \frac{u_*}{K} \ln\left(\frac{z+z_0}{z_0}\right) \\ k &= \frac{u_*^2}{\sqrt{C_\mu}} \\ \varepsilon(z) &= \frac{u_*^3}{K(z+z_0)} \end{aligned}$$

In these equations,  $u_*$  is the friction velocity, an index of the global wind intensity, and  $z_0$  is the aerodynamic roughness length which provides a measure of how rough the ground wall is. These two parameters fully define the ABL characteristics.  $K$  is the von Karman constant (0.4187) while  $C_\mu$  is a constant of the *k-epsilon* model (0.09).

To guarantee that the profiles imposed as inlet conditions are preserved throughout an empty domain, a new formulation of the wall functions for the ground wall is required. Thus, the aerodynamic roughness length is explicitly included in the wall functions, following the formulation proposed by Parente et al.<sup>6</sup>, leading to a modified non-dimensional wall distance  $z^+$  and a modified wall function constant  $E$ .

$$\begin{aligned} z_{mod}^+ &= \frac{(z+z_0)u_*\rho}{\mu} \\ E_{mod} &= \frac{\mu}{\rho z_0 u_*} \end{aligned}$$

On the inlet surface, the previously defined inlet ABL profiles are prescribed with  $u_* = 0.791959$  m/s and  $z_0 = 0.5$  m. The standard wall functions are employed on the rotor walls, while the modified ones are employed on the ground wall. The mesh is fully structured and composed of 13M cells in total, 3M for the rotating domain and 10M for the stationary one. The mesh in the rotating domain (highlighted in yellow in fig. 1) is obtained by means of a multi-block strategy. Only one blade and the 120° sector around it are explicitly meshed, while the complete rotor mesh is obtained taking advantage of the geometrical periodic condition, thus repeating the one sector mesh two more times. Two sections of the mesh around one single blade are shown in fig. 2, with one of them taken close to the blade root and the other close to the blade tip.

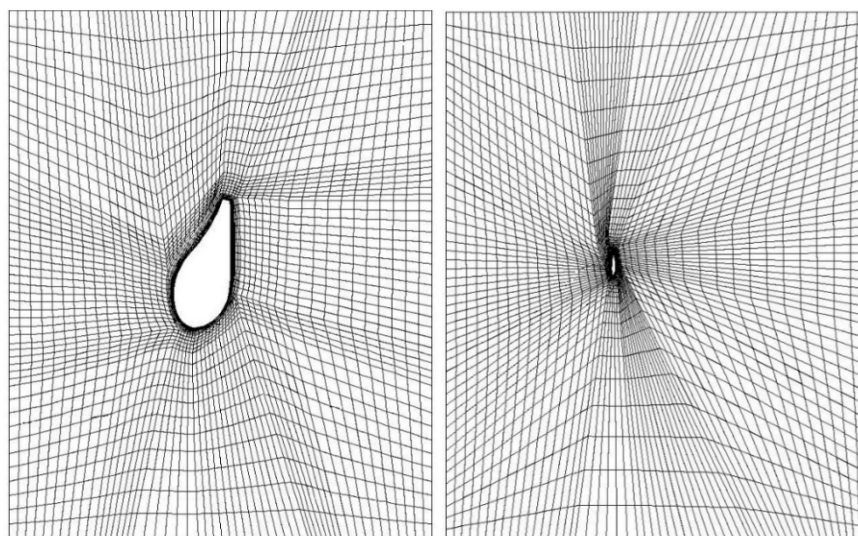


Fig. 2 – Sections of the mesh around one blade: (left) close to the root at  $r/R = 20\%$  and (right) close to the tip at  $r/R = 99\%$ .

The momentum equations and pressure-based continuity equation are solved together with implicit coupling. 2<sup>nd</sup> order upwind discretization for momentum is applied and a 2<sup>nd</sup> order implicit scheme is used for time discretization.

## 2.2 The CSM model

The analyzed blade is entirely made of composite material, with a total weight exceeding 9 tons. Several airfoils are lofted throughout its 50 m span. Inside the structure itself, three shear webs cover a large portion of the total span and provide additional stiffness to the blade.

Only shell elements with reduced integration are employed and composite layups are defined to reproduce the composite layering. The elements are positioned on the outer mold layer (OML) with material offset towards the inside, mimicking the blade's manufacturing process and maintaining the correct outer blade shape. Different layups are assigned to different regions of the structure, modelling its real composition. A local reference frame is discretely defined in every element in order to fix the global orientation of the layup. Every layup is then composed of a varying number of plies ranging from 1 to 127. For each ply, a material and a thickness are assigned, together with a relative orientation in the form of a rotation angle with respect to the global layup orientation. This relative orientation is necessary to fully define the characteristics of layers made of anisotropic materials. In every element, the stresses are computed in each ply. The shear webs and the shear caps are modelled using the same strategy. The adhesive joints are also included in the model by the introduction of layers of adhesive material. The mesh is created according to the process outlined and discussed in ref.<sup>7</sup>. Following this procedure, a mesh composed of 64000 three-dimensional shell elements is obtained, as shown in fig. 3.

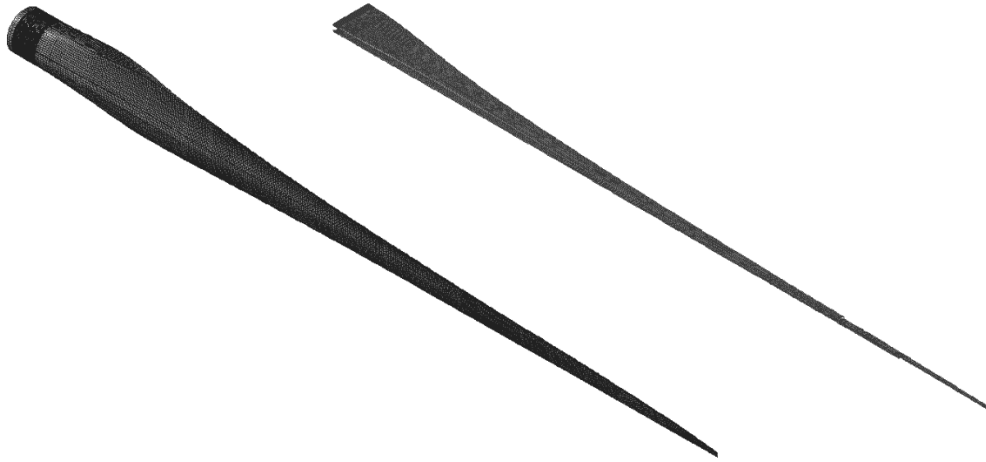


Figure 3: (left) overview of the structural mesh and (right) inner structures.

In order to validate the structural model, the eigenfrequencies of the blade are computed, pinning its root. The manufacturer provides only ranges for the first flap-wise and chord-wise modes as benchmarks. The results of the modal analysis are reported in Table 1.

**Table 1:** Experimental/numerical comparison of the eigenfrequencies of the blade.

	Manufacturer	Modal analysis
First flap-wise mode	0.74 Hz – 0.91 Hz	0.644 Hz
First chord-wise mode	1.01 Hz – 1.35 Hz	1.162 Hz

In the FSI simulations, the rotational speed is fixed at the root of the blade, where any other degree of freedom is constrained.

Two distinct dynamic simulations are carried out and analyzed. The coupled simulation with no gravity in the structural model will be, in the remainder, addressed as “FSI”. In contrast with it, the simulation where the gravity force is accounted for on the blade structures will be called “FSIg”. The results of these two cases will be compared in order to clearly highlight the effect of the gravity load on the blade operation.

## 2.2 FSI coupling

The CFD and CSM models are coupled by an in-house code, named Tango<sup>9</sup>. Within every time step, the information is exchanged as outlined in fig. 4.

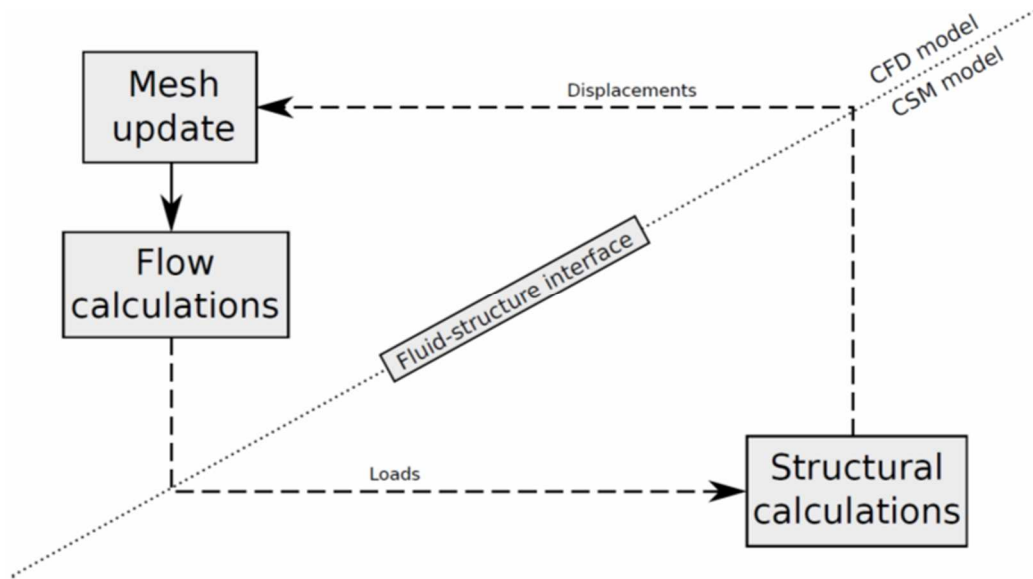


Figure 4: FSI coupling scheme (Gauss-Seidel).

This strategy corresponds to the Gauss-Seidel coupling algorithm. Given the non-conformal meshes, interpolation is required when any information (loads or displacements) is passed from one side of the fluid-structure interface to the other. A 2nd order spatial interpolation is therefore applied in both directions.

The displacements are applied on the blades according to the output of the structural solver at the beginning of every coupling iteration. In the first coupling iteration of every time step, no mesh update in addition to rigid rotation is performed since there is still no structural data available for the current time step. An arbitrary Lagrangian Eulerian (ALE) formulation is employed for the mesh update. Only the mesh in the rotating domain is deformed by means of the diffusion method with diffusivity based on boundary distance. Once the deformation of the blades is read in, the mesh velocity  $\vec{w}$  in the rotating domain is obtained by solving the equation  $\nabla \cdot (\gamma \nabla \vec{w}) = 0$  with  $d$  the distance from the blade wall and with the diffusivity  $\gamma$  defined as  $\gamma = 1/d^a$ . The diffusion factor  $a$  is chosen to be 1 in the case without gravity and 1.2 in the case with gravity. The boundary conditions for the diffusion equation are the prescribed motion of the blades and the need to preserve the shape of the sliding interfaces.

In this work, the rotational speed of the turbine is chosen to be 1.3 rad/s. Combined with a wind speed of 10 m/s (at the hub height), this leads to a tip speed ratio  $\lambda$  approximately equal to 6.5. 120 time steps are required to complete a full revolution. The loop shown in fig. 4 is repeated 3 times within every time step, leading to fluid-structure interface displacement absolute residual to drop below 5 cm.

### 3 RESULTS AND DISCUSSION

In this section, the results of the FSI and FSIg calculations will be presented. Both the simulations are transient and are started from the results of a steady state one. In the remainder, the logics illustrated in fig. 5 will be followed when defining the azimuth angle of each blade

and the sign of the radial and tangential forces and velocities.

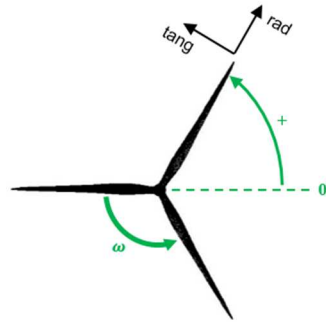


Figure 5: Definitions of blade azimuth angle and components of forces and velocities.

Furthermore, the torque  $T$  acting on the blades is made non-dimensional by means of the following formula:

$$c_T = \frac{T}{\frac{1}{2}\rho v^2 AR}$$

where  $\rho$  is the air density,  $A$  the frontal area of the rotor and  $R$  its radius. The velocity  $v$  of the undisturbed flow is chosen to be the wind free stream velocity at the hub height, namely 10 m/s. Starting from a steady FSI simulation, one full revolution of the rotor is necessary to reach regime in time. Fig. 6 illustrates the contours of velocity magnitude in a section of the computational domain, showing the velocity distribution typical of the neutral ABL.

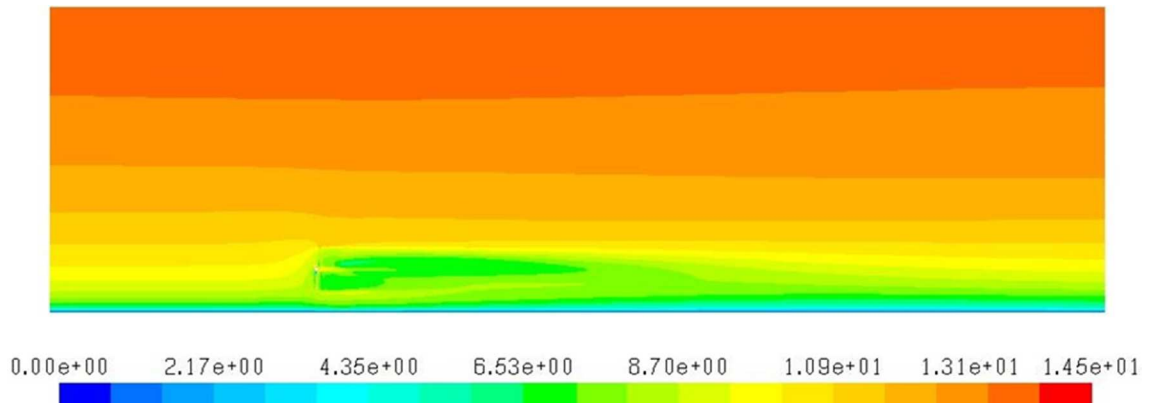


Figure 6: contours of velocity magnitude [m/s] across the computational domain.

For an azimuth angle between 0 and 180 *deg* (i.e. when the blade points upwards), the wind velocity is higher, leading to higher angle of attacks and higher relative incoming velocity throughout the entire blade span (fig. 7).

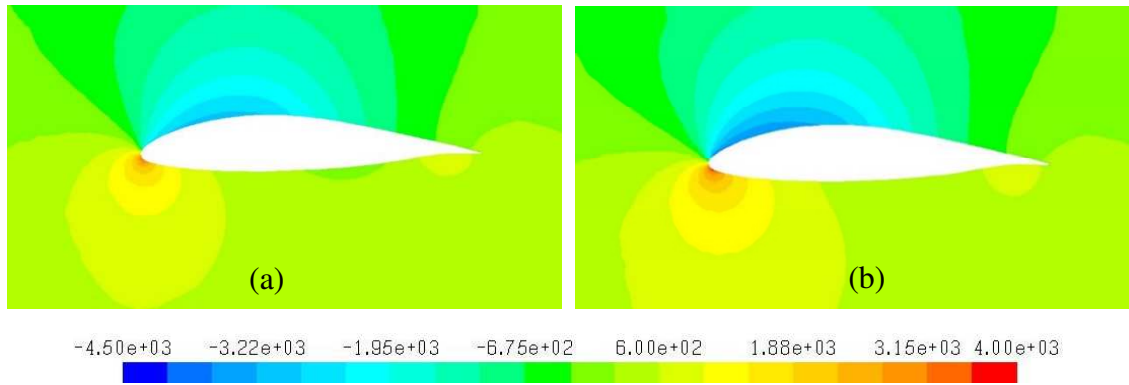


Figure 7: Pressure contours [Pa] around blade tip section at azimuth angles of (a)  $-90^\circ$  and (b)  $+90^\circ$ .

As a direct consequence, also the bending moment on the blade varies. Additionally, the gravity force tends to increase the bending moment when the blade point upwards, while it tends to decrease it when the blade point downwards, as illustrated by fig. 8.

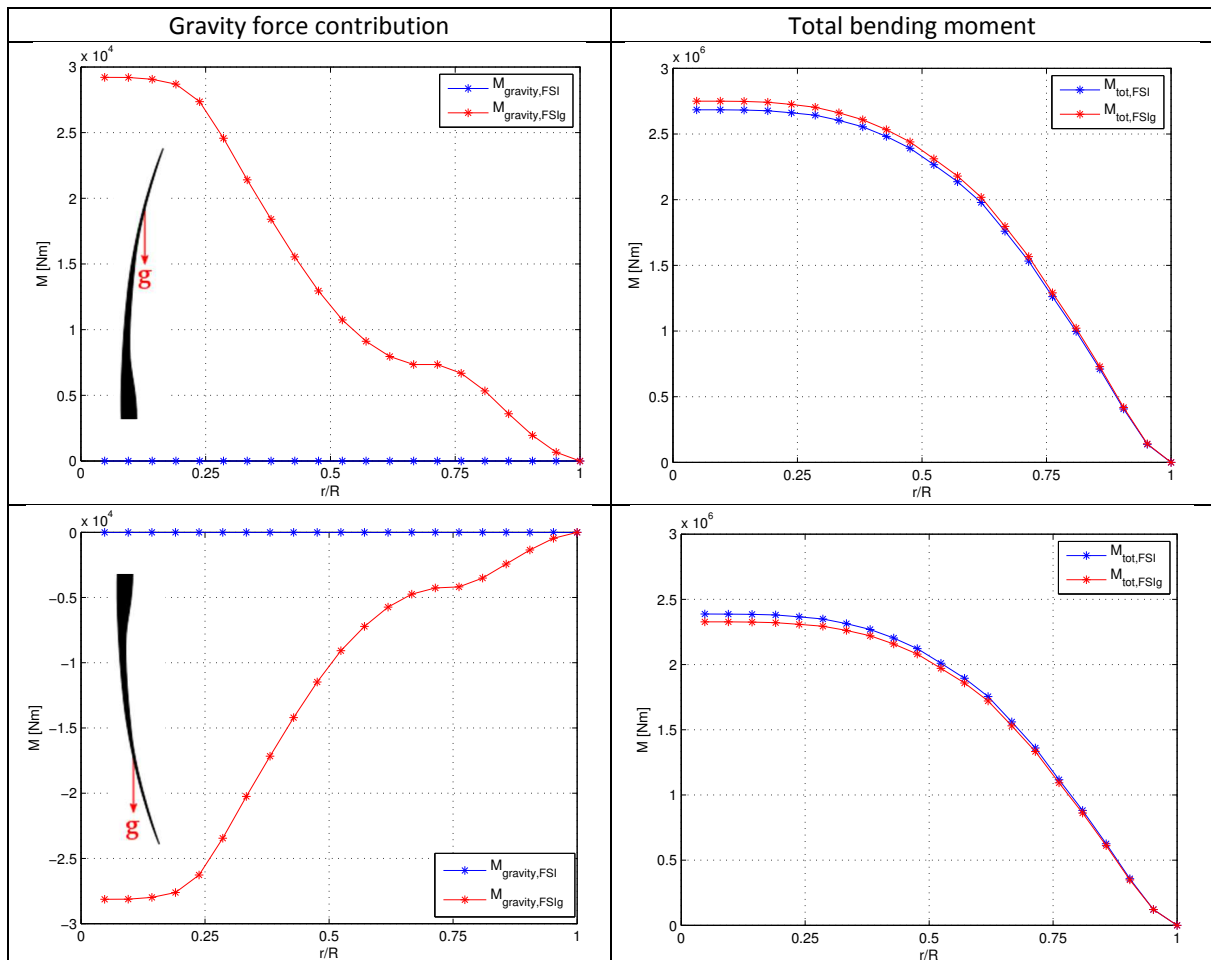


Figure 8: Flapwise bending moment diagrams: bending moment as a function of the radial position along the blade for azimuth angles of (up)  $+90^\circ$  (blade vertically up) and (down)  $-90^\circ$  (blade vertically down).

The varying gravity contribution to the bending moment translates directly into an increased amplitude of the tip axial displacement oscillation in the FSIg case with respect to the FSI case. Fig. 10 compares the tip axial displacement and the tip axial velocity in both cases.

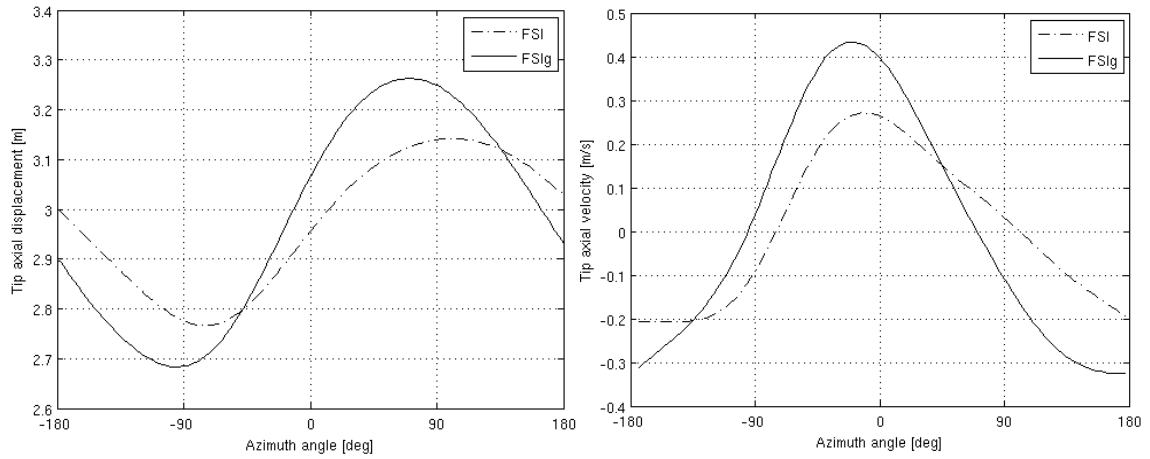


Figure 10: (left) Tip axial displacement and (right) tip axial velocity.

Similarly, also the tip tangential displacement and the consequent tangential velocity are sensibly affected by the gravity force, as shown by fig. 11.

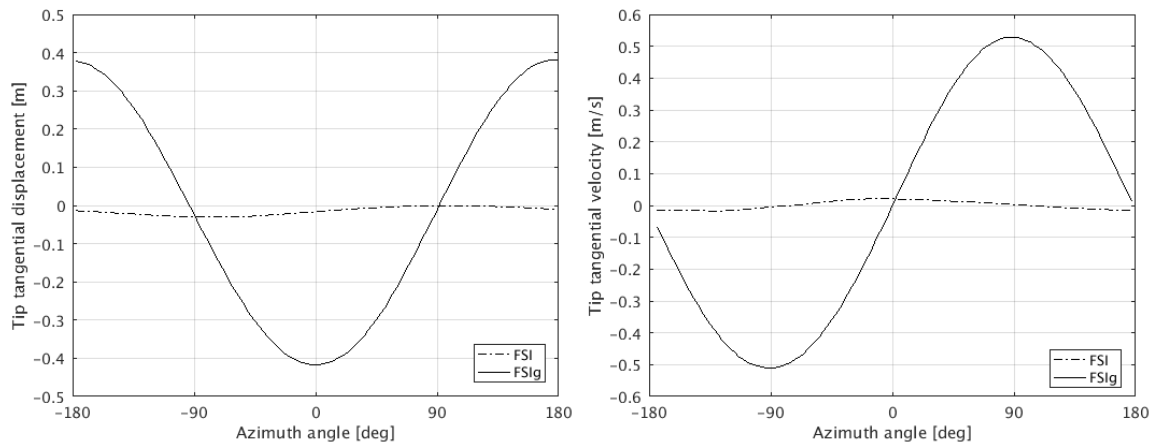


Figure 11: (left) Tip tangential displacement and (right) tip tangential velocity.

The gravity tends to tangentially deflect the blade when it is horizontally positioned, namely for 0 and  $\pm 180$  deg azimuth angles. The blade deflection will also modify the blade speed, modifying the velocity triangles throughout the revolution.

Despite the constancy of the total torque coefficient (0.0291 for both FSI and FSIg), the single blade contribution varies throughout the revolution as shown in fig. 12. The oscillation of the torque provided by each blade is a direct consequence of the velocity gradient induced by the ABL.

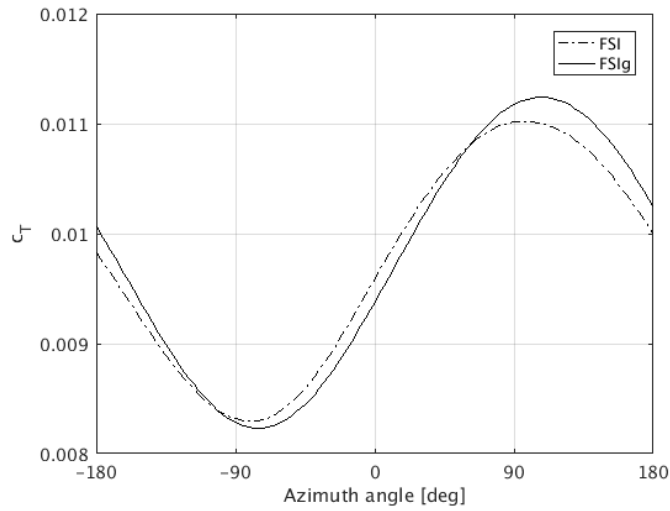


Figure 12: Single blade contribution to the torque.

Moreover, a delay in the peak of the torque contribution of each blade is observed in the FSIg case with respect to the FSI case. This difference is linked to the different magnitude and direction of the tip velocity. When the blade tip undergoes a negative axial velocity (i.e. displaces towards the incoming flow and its displacement decreases in magnitude) a beneficial effect is expected on the blade tip performance: the apparent wind speed (purely axial) is increased by the negative axial velocity of the tip, which leads to higher angles of attack and higher relative velocity magnitude. On the other hand, the same reasoning can be reversed for positive tip axial velocity. Similarly, an increase in the tip tangential speed leads on the one hand to an increase in the relative velocity magnitude, but on the other hand to a decrease in the angle of attack. The two effects counteract each other and it is not straightforward to assess which one dominates on the other during the blade motion. The blade axial and tangential velocities can be used to correct the blade speed and reconstruct the evolution of the angle of attack at the tip of the blade. Fig. 13 shows the difference in the tip angle of attack between FSIg and FSI case and compares it with the difference in torque between the same cases.

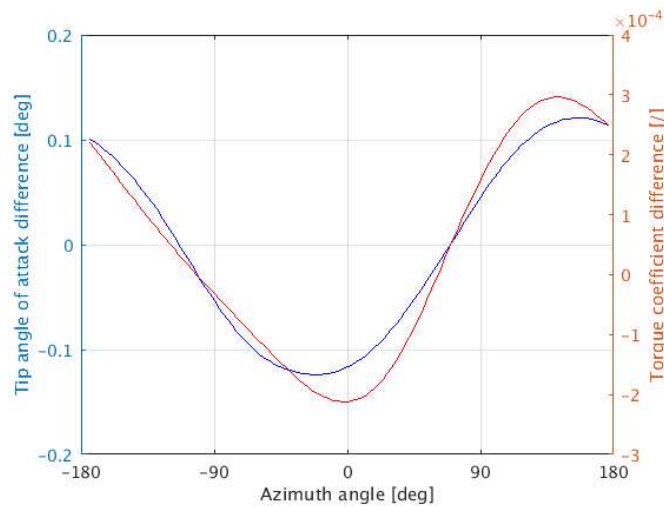


Figure 13: Tip angle of attack difference and torque coefficient difference between FSIg and FSI cases.

The qualitative similarity of these two differences is a strong indication that the tip velocity induced by its deflection has an effect on the local angle of attack and thus on the local performance of the blade and this effect can be seen in the torque coefficient evolution as well.

In terms of internal stresses, the inner structures (shear webs) of the blade are responsible for most of its structural response. Fig. 14 shows the pattern of the bending solicitation acting on them. Furthermore, fig. 15 shows the magnitude of the maximum (traction) and minimum (compression) stress in the blade shear webs.

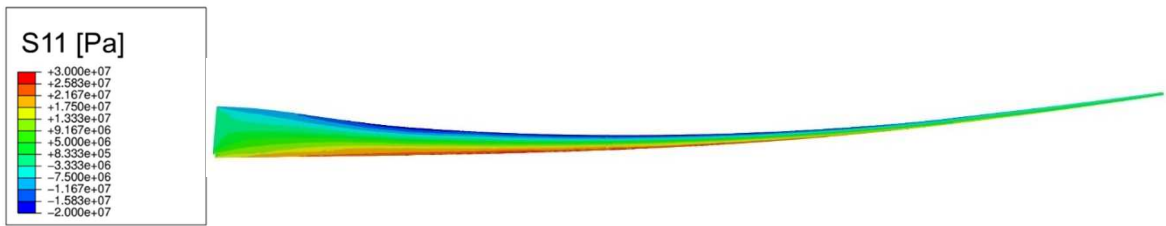


Figure 14: Longitudinal stresses in the shear webs at +90 deg azimuth angle (FSIg case)

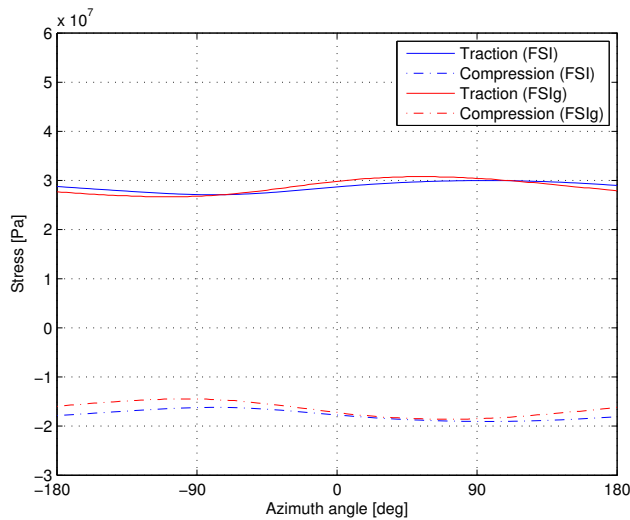


Figure 15: Stress evolution in the maximal traction and compression points of the shear webs.

## 4 CONCLUSIONS

A coupled FSI model was employed to investigate the effect of the gravity load on the structural response of the composite blades of a large HAWT. The gravity has a clear effect on the bending solicitation acting on the blades and sensibly modifies their deformation both in axial and tangential directions. However, the overall performance level of the machine is not affected by the gravity load: changes in the peak positions of the torque are monitored with a negligible effect on the global performance level of each blade.

## REFERENCES

- [1] M. Caduff, M.A.J. Huijbregts, H.J. Althaus, A. Koehler, S. Hellweg. Wind power electricity: the bigger the turbine, the greener the electricity? *Environmental Science & Technology* 2012. DOI: 10.1021/es204108n
- [2] Y. Bazilevs, M.C. Hsu, I. Akkerman, S. Wright, K. Takizawa, B. Henicke, T. Spielman, T.E. Tezduyar. 3D simulation of wind turbine rotors at full scale. Part I: Geometry modeling and Aerodynamics. *International journal for numerical methods in fluids* 2010. DOI: 10.1002/flid.2400
- [3] Y. Bazilevs, M.C. Hsu, I. Akkerman, S. Wright, K. Takizawa, B. Henicke, T. Spielman, T.E. Tezduyar. 3D simulation of wind turbine rotors at full scale. Part II: Fluid–structure interaction modeling with composite blades. *International journal for numerical methods in fluids* 2010. DOI: 10.1002/flid.2400
- [4] E. Hau. “Wind Turbines: fundamentals, Technologies, Application, Economics” (2nd Edition). Springer: Berlin, 2006
- [5] P.J. Richards, R.P. Hoxey. Appropriate boundary conditions for computational wind engineering models using the k- $\epsilon$  turbulence model. *Journal of Wind Engineering and Industrial Aerodynamics* 1993, 46 & 47, 145-153.
- [6] A. Parente, C. Górlé, J. van Beeck, C. Benocci. A Comprehensive Modelling Approach for the Neutral Atmospheric Boundary Layer: Consistent Inflow Conditions, Wall Function and Turbulence Model. *Boundary Layer Meteorology* 2011. DOI 10.1007/s10546-011-9621-5
- [7] M. Peeters , W. Van Paepegem. “Development of automated high fidelity finite element models for large wind turbine blades”. 16th European Conference on Composite Materials, Seville, Spain, 22-26 June 2014
- [8] YJ Lee, YT Jhan, CH Chung. Fluid–structure interaction of FRP wind turbine blades under aerodynamic effect. *Composites Part B: Engineering* 2012. ISSN 1359-8368
- [9] J. Degroote. Partitioned simulation of fluid-structure interaction: Coupling black-box solvers with quasi-Newton techniques. *Archives of Computational Methods in Engineering*, 20(3):185–238, 2013. DOI: 10.1007/s11831-013-9085-5

## TANGENT DEVELOPABLE SURFACES ELEMENTS IN THIN-WALLED STRUCTURES

Zoya V. Belyaeva, Svetlana A. Berestova, Evgeny A. Mityushov

Ural Federal University named after the first President of Russia B. N. Yeltsin,  
620049 Yekaterinburg, Russia  
e-mail: belyaeva-zv@yandex.ru, web page: <http://urfu.ru>

**Key words:** tangent developable surface, surface development, analytical algorithm.

**Summary.** This report demonstrates the capabilities of an advanced research area of the applied mathematics, i.e., computational geometry to be applied for shaping dimensional structures. Vector-matrix models are provided to purpose of piecewise-smooth structures modelling by surface elements with zero Gaussian curvature (elements of developable surfaces). The elements of tangent developable surfaces can be built on the directing curves pieces located arbitrarily in space.

The paper presents an analytical algorithm for drawing a cutting for the tangent developable surface element with two specified directing curves and the edge of regression known. An analytic algorithm for the curve on tangent developable surface development via the parametric equations of the edge of regression and the curve itself is obtained based on the tangent developable surface edge of regression development algorithm.

### 1 INTRODUCTION

Developable surfaces can be used as structure elements and find wide application in construction, engineering and textile industries [1, 2]. Developable surfaces are especially in demand in tent and plate structures, as they provide the possibility of making structures from flat pieces with subsequent connections along the cut lines.

Using of developable surface elements in the design and manufacture of sheet and textile structures one can apply analytical algorithms for modeling surface features and their developments.

The use of analytical algorithms for the elements of cylindrical and conical surfaces development in the design of tent structures is demonstrated in [3]. Tangent developable surfaces are deployable surfaces as well and can be used in the design of the tent and metal sheet structures along with cylindrical and conical surfaces, and in some cases can provide wider choice of surfaces forms.

### 2 METHODS OF TANGENT DEVELOPADLE SURFACE ELEMENTS MODELLING

One of the ruled surfaces, which can be used in geometric modeling, is tangent developable surfaces – the surface of tangents to an arbitrary smooth space curve. The tangent developable surface at every point has zero Gaussian curvature, and according to the differential geometry methods is a developable ruled surface, which means that an element of such surface can be unfolded into a plane without stretching or tearing. In the fabrication of

different plate, tent and others structures this property allows to use materials which are not amenable to stretching.

The general equation of the tangent developable surface, based on its definition as a surface of tangents to a space curve, can be written in the form:

$$\hat{r}(u, v) = \hat{r}_d(u) + v\hat{\tau}(u), \quad (1)$$

where  $\hat{r}_d(u)$  = a directive curve,  $\hat{\tau}$  = unit tangent vector to the directive curve defined by the relationship

$$\hat{\tau}(u) = \frac{\frac{d\hat{r}_d}{du}}{\left| \frac{d\hat{r}_d}{du} \right|}. \quad (2)$$

Using relation (2) the general equation of the tangent developable surface can be written in the form<sup>^</sup>

$$\hat{r}(u, v) = \hat{r}_d(u) + v \frac{d\hat{r}_d/du}{\left| d\hat{r}_d/du \right|}. \quad (3)$$

The examples of tangent developable surface elements created with this method are presented in Figures 1 and 2.

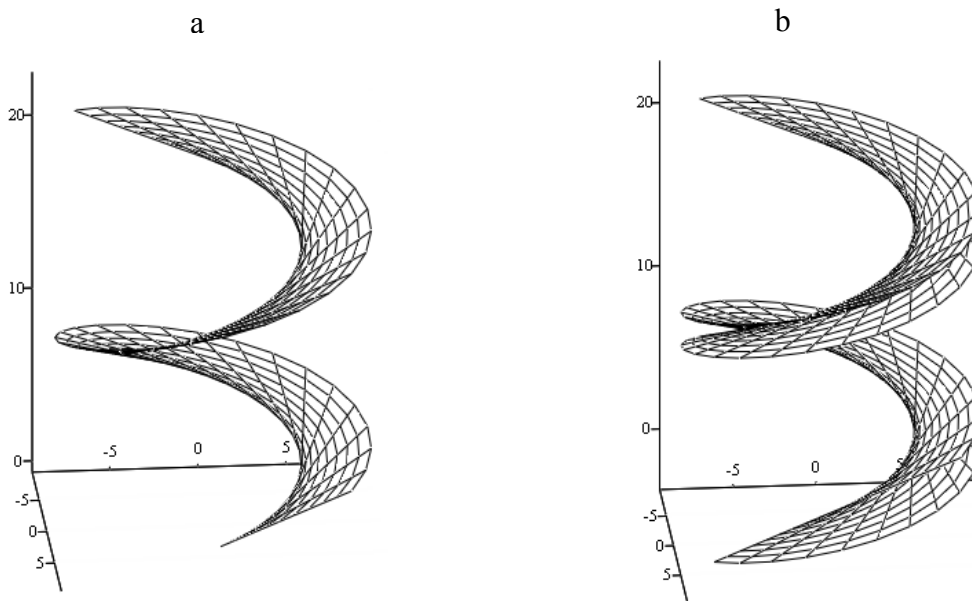


Figure 1. Tangent developable surface with directive curve in form of the circular helix

$$\vec{r}_d(u) = \{5 \cos u, 5 \sin u, u\}, \quad 0 \leq u \leq 3\pi:$$

a – with  $0 \leq v \leq 8$ ; b – with  $-8 \leq v \leq 8$

Figure 1a shows the tangent developable surface with the directive curve in the form of circular helix when parameter ranging  $0 \leq v \leq 8$ . This surface is referred to as the Archimedes screw and was used in ancient times in the simplest hydraulic structures. Figure 1b shows the same tangent developable surface with parameter ranging  $-8 \leq v \leq 8$ , and this illustrates the directive curve to be the edge of regression of tangent developable surface and that the surface itself consists of two cavities. The tangent developable surface with the directive curve in form of helical spiral is shown in the Figure 2.

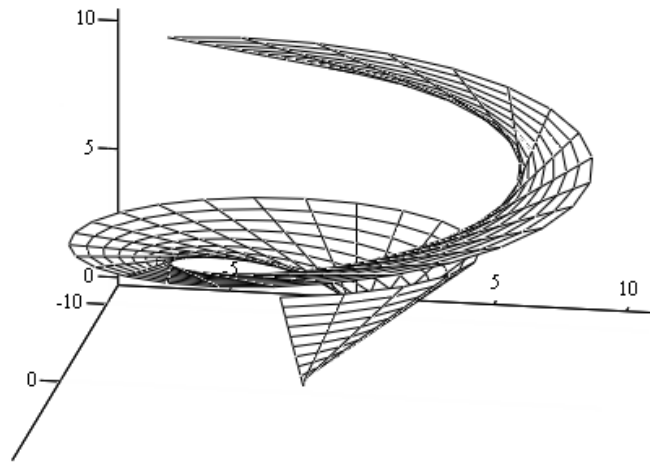


Figure 2. Tangent developable surface with directive curve in form of the helical spiral

$$\vec{r}_d(u) = \{u \cos u; u \sin u; u\}, \quad 0 \leq u \leq 3\pi, \quad 0 \leq v \leq 7$$

Another method of tangent developable surface modeling is to build surface elements on the segments of the directive curves located arbitrarily in space. A large number of options for modelling of tangent developable surface elements with different directive curves are given in the *Encyclopedia of analytical surfaces*<sup>4</sup>. Using one of the algorithms suggested in *Encyclopedia of analytical surfaces*<sup>4</sup>, we can make a model of a tangent developable surface element on the ellipse and the parabola, which are located in parallel planes.

Let us define the ellipse by the matrix equation

$$\hat{r}_1(u) = \begin{pmatrix} a \cos u \\ 0 \\ b \sin u \end{pmatrix}, \quad u_1 \leq u \leq u_2, \quad (4)$$

and the parabola by the matrix equation

$$\hat{r}_2(v) = \begin{pmatrix} 2cv \\ l \\ (b - cv^2) \end{pmatrix}, \quad v_1 \leq v \leq v_2. \quad (5)$$

Under the uniqueness of the tangent developable surface containing an ellipse and a parabola located in parallel planes, it is possible to find the relation between the parameters of directive curves  $v = (b/a) \tan u$ . Then, the equation of the tangent developable surface element will be described by the formula:

$$\hat{r}(u, k) = k \begin{pmatrix} a \sin u \\ 0 \\ b \cos u \end{pmatrix} + (1 - k) \begin{pmatrix} 2c \frac{b}{a} \tan u \\ l \\ \left( b - c \left( \frac{b}{a} \tan u \right)^2 \right) \end{pmatrix}, \quad u_1 \leq u \leq u_2, \quad 0 \leq k \leq 1. \quad (6)$$

This tangent developable surface element with parameters  $a = 2$ ,  $b = 3$ ,  $c = 0.4$ ,  $l = 4$ ,  $-1 \leq u \leq 1$ ,  $0 \leq k \leq 1$  is shown in Figure 3.

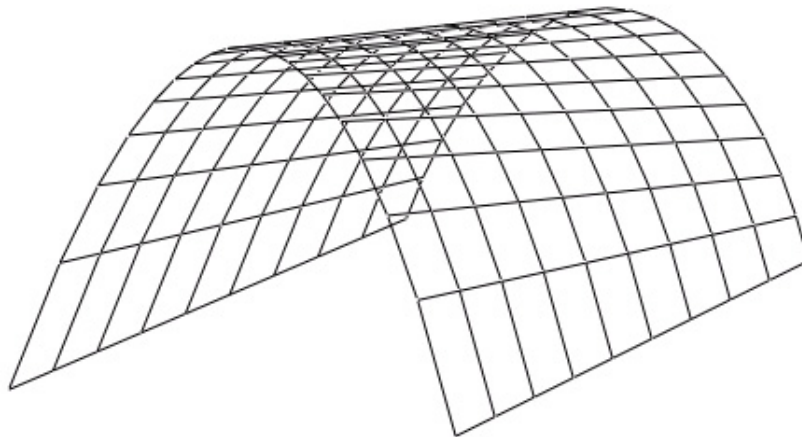


Figure 3. Tangent developable surface with ellipse and parabolic curve for directive lines and parameters within ranges  $-1 \leq u \leq 1$ ,  $0 \leq k \leq 1$

Another example is the tangent developable surface element formed on both the circumference and the parabola which are located in parallel planes and set by the corresponding equations:

$$\hat{r}_1(u) = \begin{pmatrix} -\sqrt{R^2 - u^2} \\ 0 \\ u \end{pmatrix}, \quad u_1 \leq u \leq u_2 \quad \text{and} \quad \hat{r}_2(v) = \begin{pmatrix} \frac{v^2}{2p} \\ l \\ v \end{pmatrix}, \quad v_1 \leq v \leq v_2. \quad (7)$$

In this case, the equation of the tangent developable surface element takes the following form<sup>4</sup>:

$$\hat{r}(\lambda, \beta) = \begin{pmatrix} (\lambda - 1)\sqrt{R^2 - \beta^2} + \frac{\lambda p \beta^2}{2(R^2 - \beta^2)} \\ \lambda l \\ \beta \left( 1 - \lambda + \frac{p\lambda}{\sqrt{R^2 - \beta^2}} \right) \end{pmatrix}, \quad 0 \leq \lambda \leq 1, \quad (8)$$

and the equation of the edge of regression to this surface can be written as

$$\hat{r}_a(\beta) = \begin{pmatrix} \frac{h}{1 - \frac{pR^2}{(R^2 - \beta^2)^{\frac{3}{2}}}} \\ \frac{p}{2} \sqrt{R^2 - \beta^2} \left[ \frac{\beta^2 + 2R^2}{(R^2 - \beta^2)^{\frac{3}{2}} - pR^2} \right] \\ - \frac{p\beta^3}{(R^2 - \beta^2)^{\frac{3}{2}} - pR^2} \end{pmatrix}. \quad (9)$$

The tangent developable surface element with parameters  $R = 4$ ,  $p = 2$ ,  $l = 6$ ,  $-3.5 \leq u \leq 3.5$ ,  $-3.5 \leq v \leq 3.5$  is presented in Figure 4.

Another way to model a tangent developable surface element is to write the equation of the ruled surface with two directive curves in the following form:

$$\hat{r}(u, v) = v\hat{r}_a(u) + (1 - v)\hat{r}_1(u), \quad 0 \leq v \leq 1, \quad u_1 \leq u \leq u_2, \quad (10)$$

provided that the first guiding line is the edge of regression for the considered tangent developable surface and the second guiding line is expressed through the edge of regression:

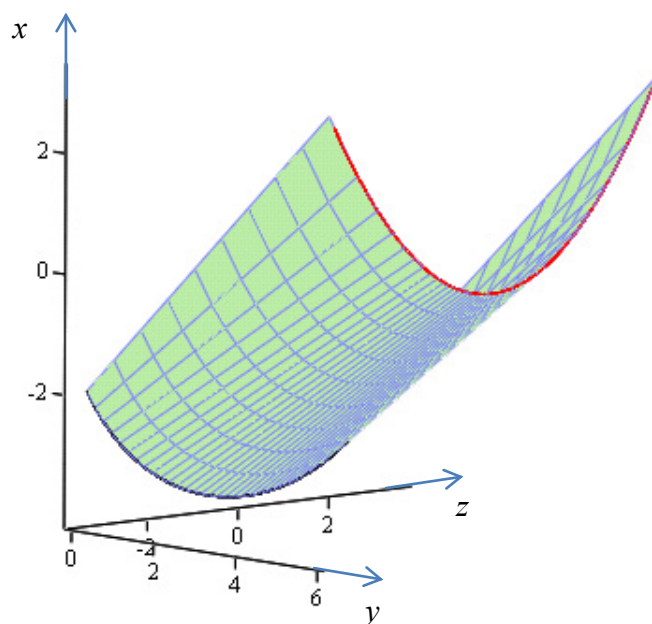


Figure 4. Tangent developable surface with directive lines in the form of circle and parabolic curves, parameters within ranges  $-3.5 \leq u \leq 3.5$ ,  $-3.5 \leq v \leq 3.5$

$$\hat{r}_1(u) = \hat{r}_d(u) + v(u)\hat{\tau}(u). \quad (11)$$

Here  $\hat{\tau}$  is the unit tangent vector to the edge of regression  $\hat{r}_d(u)$ .

If we set the edge of regression and the second guiding line by the following equations

$$\hat{r}_d(u) = \begin{pmatrix} \cos u \\ \sin u \\ u \end{pmatrix}, \quad u_1 \leq u \leq u_2, \quad (12)$$

$$\hat{r}_1(u) = \hat{r}_d(u) + \sqrt{2}\hat{\tau}, \quad u_1 \leq u \leq u_2 \quad (13)$$

and perform the necessary transformations, the equation of the tangent developable surface element (Figure 5) takes the form:

$$\hat{r}(u, v) = v\hat{r}_d(u) + (1-v)\hat{r}_1(u) = v \begin{pmatrix} \cos u \\ \sin u \\ u \end{pmatrix} + (1-v) \begin{pmatrix} \cos u - \sin u \\ \sin u + \cos u \\ u + 1 \end{pmatrix}, \quad (14)$$

$$0 \leq v \leq 1, \quad u_1 \leq u \leq u_2.$$

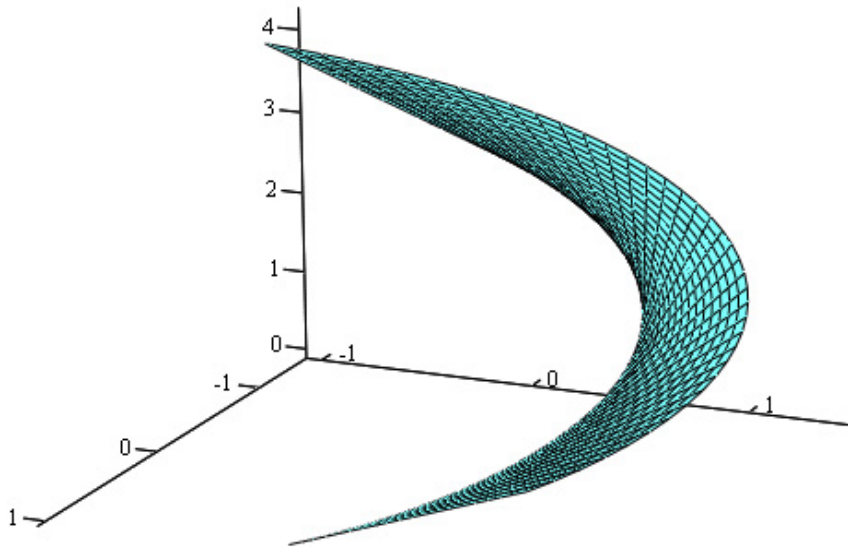


Figure 5. Tangent developable surface with directing lines  $\hat{r}_d(u) = \begin{pmatrix} \cos u \\ \sin u \\ u \end{pmatrix}$  and

$$\hat{r}_1(u) = \hat{r}_d(u) + \sqrt{2}\hat{\tau} \quad \text{and parameter } 0 \leq u \leq \pi$$

### 3 ANALYTICAL DEVELOPING METHODS OF THE CURVE LINES BELONGING TO TANGENT DEVELOPABLE SURFACES

Based on the condition of the lengths of the arcs  $ds$  and the curvature  $k$  for the edge of regression and its development line in all corresponding points coincide the development of the edge of regression  $\vec{r}_d(u)$  of a tangent developable surface can be found. Using the definitions of the planar and spatial curves curvature

$$k = \frac{d\phi}{ds} = \frac{|\dot{\vec{r}}_d(u) \times \ddot{\vec{r}}_d(u)|}{|\dot{\vec{r}}_d(u)|^3} \quad (15)$$

we can find the increment of the angle  $\phi$  when moving a point at a distance  $ds$  along a planar curve on the plain of development:

$$d\phi = \frac{|\dot{\vec{r}}_d(u) \times \ddot{\vec{r}}_d(u)|}{|\dot{\vec{r}}_d(u)|^3} ds = \frac{|\dot{\vec{r}}_d(u) \times \ddot{\vec{r}}_d(u)|}{|\dot{\vec{r}}_d(u)|^2} du . \quad (16)$$

If we select the plane of development  $O\xi\eta$ , in which the axis  $O\xi$  is directed along a tangent to the directive curve in its initial point, the equation of the development curve for the edge of regression takes the following form<sup>5</sup>:

$$\begin{cases} \xi = \int_{u_1}^u |\dot{\vec{r}}_d(t)| \cos \left( \int_{u_1}^t \frac{|\dot{\vec{r}}_d(u) \times \ddot{\vec{r}}_d(u)|}{|\dot{\vec{r}}_d(u)|^2} du \right) dt, \\ \eta = \int_{u_1}^u |\dot{\vec{r}}_d(t)| \sin \left( \int_{u_1}^t \frac{|\dot{\vec{r}}_d(u) \times \ddot{\vec{r}}_d(u)|}{|\dot{\vec{r}}_d(u)|^2} du \right) dt, \end{cases} \quad u_1 \leq u \leq u_2 . \quad (17)$$

As an example, let us build the development curve for the edge of regression which is defined by the equation (12) and shown in Figure 6.

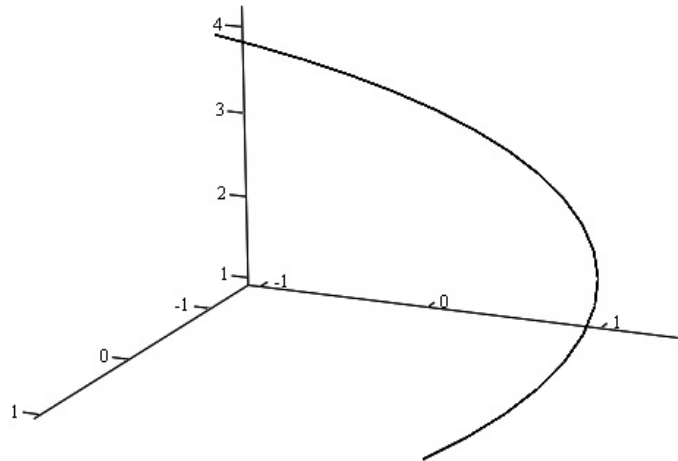


Figure 6. The edge of regression  $\hat{\vec{r}}_d(u) = \begin{pmatrix} \cos u \\ \sin u \\ u \end{pmatrix}$  with parameter  $0 \leq u \leq \pi$

Let us perform the intermediate calculations for finding the development curve equations:

$$\frac{d\hat{r}_d(u)}{du} = \begin{pmatrix} -\sin u \\ \cos u \\ 1 \end{pmatrix}, \quad \frac{d^2\hat{r}_d(u)}{du^2} = \begin{pmatrix} -\cos u \\ -\sin u \\ 0 \end{pmatrix}, \quad \frac{d\hat{r}_d(u)}{du} \times \frac{d^2\hat{r}_d(u)}{du^2} = \begin{pmatrix} \sin u \\ -\cos u \\ 1 \end{pmatrix},$$

$$\left| \frac{d\hat{r}_d(u)}{du} \times \frac{d^2\hat{r}_d(u)}{du^2} \right| = \sqrt{2}, \quad \left| \frac{d\hat{r}_d(u)}{du} \right|^2 = 2, \quad \frac{\left| \frac{d\hat{r}_d(u)}{du} \times \frac{d^2\hat{r}_d(u)}{du^2} \right|}{\left| \frac{d\hat{r}_d(u)}{du} \right|^2} = \frac{\sqrt{2}}{2}.$$
(18)

The calculation of the required integrals in this case is possible to perform analytically:

$$\int_{u_1}^t \frac{\left| \frac{d\hat{r}_d(u)}{du} \times \frac{d^2\hat{r}_d(u)}{du^2} \right|}{\left| \frac{d\hat{r}_d(u)}{du} \right|^2} du = \int_{u_1}^t \frac{\sqrt{2}}{2} du = \frac{\sqrt{2}}{2}(t - u_1),$$

$$\xi = \int_{u_1}^u \left[ \sqrt{2} \cos \frac{\sqrt{2}}{2}(t - u_1) \right] dt = 2 \left[ \sin \frac{\sqrt{2}}{2}(u - u_1) \right],$$

$$\eta = \int_{u_1}^u \left[ \sqrt{2} \sin \frac{\sqrt{2}}{2}(t - u_1) \right] dt = 2 \left[ 1 - \cos \frac{\sqrt{2}}{2}(u - u_1) \right],$$
(19)

and we can finally the obtained equations of the development curve for the edge of regression  $\hat{r}_d(u)$  in the parametric form

$$\begin{cases} \xi = 2 \left[ \sin \frac{\sqrt{2}}{2}(u - u_1) \right], \\ \eta = 2 \left[ 1 - \cos \frac{\sqrt{2}}{2}(u - u_1) \right], \end{cases} \quad u_1 \leq u \leq u_2 \dots$$
(20)

The development curve for the edge of regression, obtained according to equations (20) is shown in Figure 7.

The development of the curve, which lies on a tangent developable surface and is expressed through the edge of regression of this surface, can be obtained using the equations of development curve for the edge of regression. If the line can be written by the equation (11), the equations of its development in the edge of regression development plane will take the form of

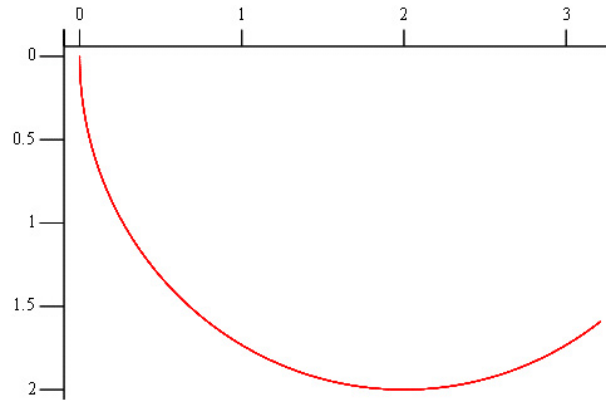


Figure 7. Development curve for edge of regression  $\hat{r}_d(u) = \begin{pmatrix} \cos u \\ \sin u \\ u \end{pmatrix}$  with parameter  $0 \leq u \leq \pi$

$$\begin{cases} \xi_1 = \xi + |\hat{r}_d(u) - \hat{r}_1(u)| \cdot \cos \alpha, \\ \eta_1 = \eta + |\hat{r}_d(u) - \hat{r}_1(u)| \cdot \sin \alpha, \end{cases} \quad u_1 \leq u \leq u_2, \quad (21)$$

where

$$\cos \alpha = \frac{d\xi/du}{\sqrt{\left(\frac{d\xi}{du}\right)^2 + \left(\frac{d\eta}{du}\right)^2}}, \quad \sin \alpha = \frac{d\eta/du}{\sqrt{\left(\frac{d\xi}{du}\right)^2 + \left(\frac{d\eta}{du}\right)^2}}. \quad (22)$$

Using the proposed method it is possible to build the development for the tangent developable surface element defined by the equation (14). We will need to find the equations of the development curve for the directive curve of this surface element, while the equations of the development curve for the edge of regression were found above.

Taking into account the formulas (13) and (2) the guiding curve equation can be written in the following form:

$$\hat{r}_1(u) = \hat{r}_d(u) + \sqrt{2}\hat{\tau} = \begin{pmatrix} \cos u - \sin u \\ \sin u + \cos u \\ u + 1 \end{pmatrix}, \quad u_1 \leq u \leq u_2. \quad (23)$$

Then we can get

$$\begin{cases} \xi_1 = \xi + \sqrt{2} \cdot \cos \alpha, \\ \eta_1 = \eta + \sqrt{2} \cdot \sin \alpha. \end{cases}, u_1 \leq u \leq u_2. \quad (24)$$

Let's perform the required calculations:

$$\begin{aligned} \frac{d\xi}{du} &= \sqrt{2} \left[ \cos \frac{\sqrt{2}}{2} (u - u_1) \right], \quad \frac{d\eta}{du} = \sqrt{2} \left[ \sin \frac{\sqrt{2}}{2} (u - u_1) \right], \\ \sqrt{\left(\frac{d\xi}{du}\right)^2 + \left(\frac{d\eta}{du}\right)^2} &= \sqrt{2 \left[ \cos^2 \frac{\sqrt{2}}{2} (u - u_1) \right] + 2 \left[ \sin^2 \frac{\sqrt{2}}{2} (u - u_1) \right]} = \sqrt{2}, \\ \cos \alpha &= \cos \frac{\sqrt{2}}{2} (u - u_1), \quad \sin \alpha = \sin \frac{\sqrt{2}}{2} (u - u_1), \end{aligned} \quad (25)$$

and finally obtain the equations of the curve  $\hat{r}_1(u)$  development in the parametric form:

$$\begin{cases} \xi_1 = 2 \left[ \sin \frac{\sqrt{2}}{2} (u - u_1) \right] + \sqrt{2} \cdot \cos \frac{\sqrt{2}}{2} (u - u_1), \\ \eta_1 = 2 \left[ 1 - \cos \frac{\sqrt{2}}{2} (u - u_1) \right] + \sqrt{2} \cdot \sin \frac{\sqrt{2}}{2} (u - u_1), \end{cases} \quad u_1 \leq u \leq u_2.. \quad (26)$$

The development of the tangent developable surface element, obtained according the to equations (20) and (26) is shown in Figure 8.

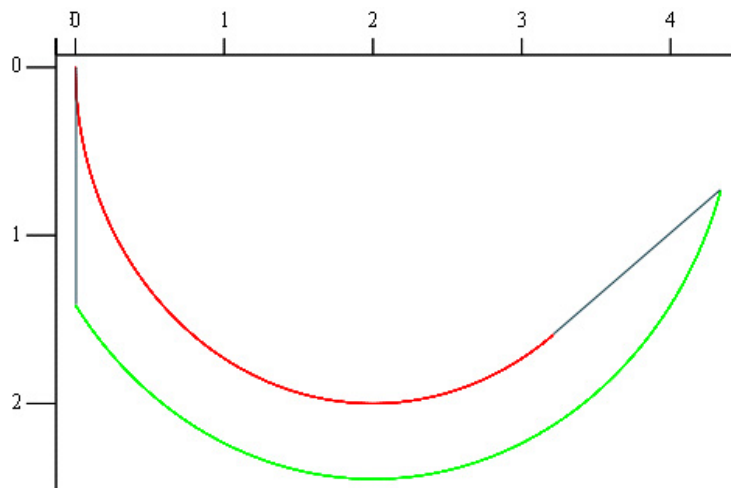


Figure 8. Development of the tangent developable surface element

## CONCLUSION

Tangent developable surface along with a conical and cylindrical surfaces provide ample opportunity for solving problems in various fields of technology. Described modeling methods of the tangent developable surfaces and their developments can be applied in the design and manufacturing of plate and tent structures with various materials. The need for the unfolding curve expressing through the edge of regression of the tangent developable surfaces limits the algorithm application ability; therefore, the authors aim is to get developing algorithm for arbitrary tangent developable surface element.

## REFERENCES

- [1] Myskova O. V. *Tentovye sooruzheniia v sovremennoi arhitekture*. Promyshlennoe i grazhdanskoe stroitel'stvo. 2003. No.7. P. 41-42. (*Tent structures in modern architecture*. Industrial and civil construction. 2003. No.7. P. 41-42. In Russ.)
- [2] Ito Miori, Imaoka Haruki. *A method of predicting sewn shapes and a possibility of sewing by the theory of de-velopable surfaces*. Journal of the Japan Research Association for Textile End-Uses. 2007. Vol. 48. No.1. P. 42-51.
- [3] Belyaeva Z. V., Berestova S. A., Misura N. E., Mityushov E. A. *Invariant algorithms of spatial constructions elements forming and cutting*. STRUCTURAL MEMBRANES 2015: VII International Conference on TextileComposites and Inflatable Structures. 19-21 October 2015, Barcelona, Spain. P. 401-412.
- [4] Krivoschapko S.N., Ivanov V.N. *Encyclopedia of analytical surfaces*. Switzerland, Springer International Publishing, 2015. 752 p.
- [5] Mityushov E. A., Belyaeva Z. V. *Geometricheskoe modelirovanie prostranstvennyh konstruksii. Matematicheskie modeli i vizuilizatsia*. LAMBERT Academic Publishing, 2011. 134 p. (*Geometric modeling of spatial structures. Mathematical models and visualization*. LAMBERT Academic Publishing, 2011. 134 p. In Russ.)

## BENDING-ACTIVE DOME-SHAPED STRUCTURE

A.V. CHESNOKOV<sup>\*</sup>, V.V. MIKHAYLOV<sup>∨</sup>, I.V. DOLMATOV<sup>♦</sup>

<sup>\*</sup> The Faculty of Civil Engineering  
Lipetsk State Technical University  
Moskovskaya street 30, 398600 Lipetsk, Russian Federation  
e-mail: [andreychess742@gmail.com](mailto:andreychess742@gmail.com), web page: <http://ixserv.stu.lipetsk.ru/>

<sup>∨</sup> The Faculty of Civil Engineering  
Lipetsk State Technical University  
Moskovskaya street 30, 398600 Lipetsk, Russian Federation  
e-mail: [mmvv46@rambler.ru](mailto:mmvv46@rambler.ru), web page: <http://ixserv.stu.lipetsk.ru/>

<sup>♦</sup> The Faculty of Civil Engineering  
Lipetsk State Technical University  
Moskovskaya street 30, 398600 Lipetsk, Russian Federation  
e-mail: [dolmivv@gmail.com](mailto:dolmivv@gmail.com), web page: <http://ixserv.stu.lipetsk.ru/>

**Key words:** Bending-Active Structures, Dome, Flexible Membrane

**Summary.** *The structure, proposed in the present work, belongs to, so-called, “bending-active” systems. It comprises high-strength low-modulus initially straight beams. The beams, arranged in the radial direction, are supported by spreaders and steel cables underneath. Tensioning of cables results in substantial shape modification of the beams and turning the structure into a convex dome. The frame of the structure is investigated by means of the special computer program EASY. Uniform and non-uniform external loads are taken into account. Influence of flexible fabric membrane, attached to the upper chord of the frame, is analyzed.*

### 1 INTRODUCTION

Bending-active structures comprise initially straight beams, which are shaped into curved arch-like elements by means of elastic deformation<sup>1</sup>. The primary aim is to facilitate the process of production, transportation and installation of the construction. Complex procedure of curved beam fabrication gives way to relatively easy operations, which are performed on a construction site<sup>2</sup>.

Flexible fabric membrane is often a constituent part of a bending-active structure<sup>3</sup>. The membrane provides the cladding and stabilizes curved arch-like members by means of prevention them from buckling. On the other hand, the membrane with bending elements included<sup>4,5</sup> becomes much more practical and cost-effective in comparison to ordinary fabric structures (e.g. saddle roofs), which often provide insufficient shading area. In addition, bending elements and flexible membrane equilibrate each other minimizing horizontal thrust. They result in effective engineering solutions due to reduction of expenditures required for foundations or supporting structures<sup>6</sup>.

Bending-active structures are more flexible in comparison to usual systems and should include appropriate means for shape stabilization under various external loads. They are also to be made of materials allowing substantial deformations without overstress. The ratio of flexural strength (MPa) to young's modulus<sup>2</sup> (GPa) must not be less than 2.5. Fiber reinforced polymers<sup>2,7</sup> with the ratio in the range from 4.5 to 17.0, are far superior to the conventional structural steel. They, however, significantly lose their mechanical properties over time<sup>8</sup> and should preferably be used in temporary structures.

## 2 DESCRIPTION OF THE STRUCTURE

Dome-shaped structure, proposed in the present work, consists of a frame and a covering (figure 1). Although the covering may be of stiff plates or shells, flexible fabric membrane is much more appropriate due to its low weight, light translucence and possibility to withstand substantial deformations.

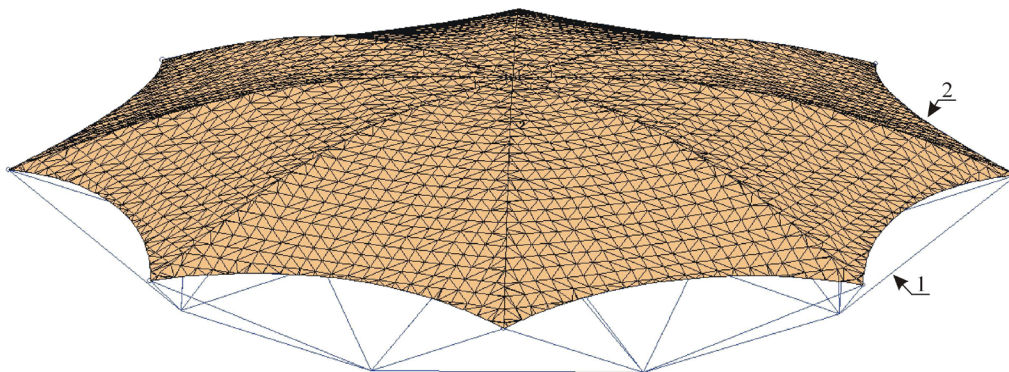


Figure 1: Dome-shaped structure, considered in the research. 1 – frame; 2 - flexible fabric membrane

The frame consists of high-strength low-modulus beams 1, supported with struts and steel cables underneath (figure 2). The beams, forming the upper chord of the frame, are initially straight. They are situated in the horizontal plane and arranged in the radial direction. The beams are made of pultruded glass-fiber reinforced polymer<sup>7</sup>, having the modulus of elasticity  $2.4 \cdot 10^4$  MPa and strength 185 MPa.

The bottom chord of the frame consists of bearer diagonal 2 and circular cables 3, outer and inner hinged struts (4 and 5) and ties. The outer struts are inclined to vertical planes of the beams. It ensures stability of the beams in so-called “out-of-plane” direction<sup>9</sup>, especially in the event of non equal external loadings.

Tensioning of circular cables results in deformation of the upper chord of the frame and shaping the beams into curved arch-like elements. In accordance with growth of beam camber, the span of the structure diminishes, but arising bending moments ensure structural equilibrium (figure 2, b).

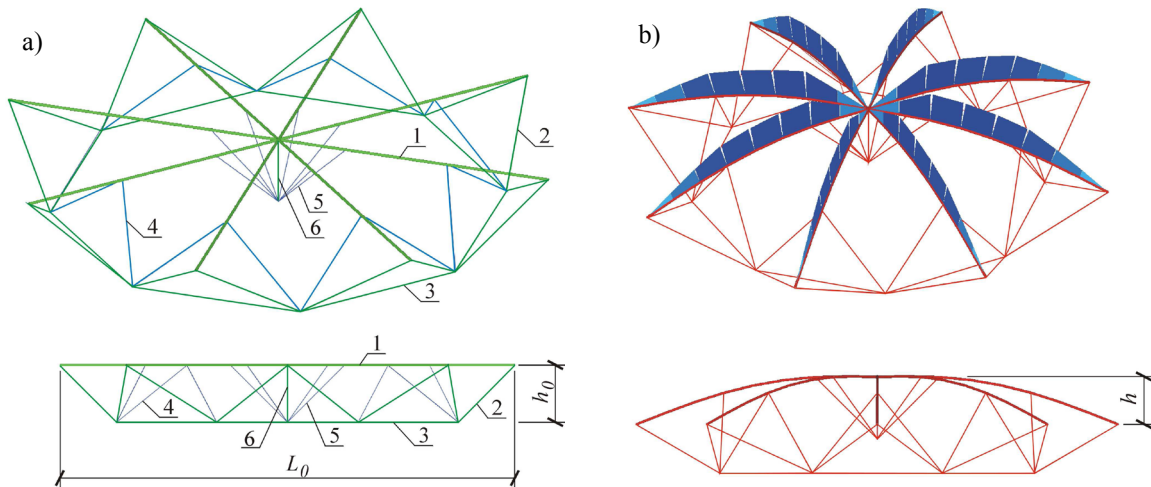


Figure 2: The frame of the structure. a – initial configuration; b – pre-stressed configuration, ready to bear external loads; 1 – beam of the upper chord; 2 – diagonal cable; 3 - circular cable; 4, 5 – outer and inner hinged struts; 6 – central tie

### 3 STRUCTURAL BEHAVIOR OF THE FRAME

The initial span and the height of the frame are assumed the following:  $L_0 = 12$  m and  $h_0 = 1.5$  m, respectively (figure 2, a). When the tensioning of circular cables is completed the upper chord of the frame takes on dome-like shape with the height in the center  $h = 1.15$  m.

The upper beams are made of glass-fiber reinforced polymer tubes with the outer diameter 99 mm and the wall thickness 5 mm. The limit bending moment sustained by the beams is  $M_{lim} = 6$  kN·m. The beams are connected to each other in the center of the frame by means of pin joints.

The diameter of steel cables of the bottom chord is 10.1 mm. According to the catalogue<sup>10</sup> the limit tension is  $N_{lim} = 44$  kN. The struts are made of steel tubes. Their outer diameter is 45mm and the wall thickness is 3.5 mm.

External loads, influencing the frame, can be classified into installation and operational. The first ones arise during the process of frame mounting. Their values are substantially confined because the frame hasn't reached its final shape yet and the preliminary stresses have not been provided in all the elements. It has been found that the frame can sustain uniformly distributed load  $0.1$  kN/m<sup>2</sup> before the beginning of tensioning of the bottom chord.

Excessive installation loads may result in permanent downward camber of the upper chord of the frame. Thus, the structure will become not serviceable (figure 3).

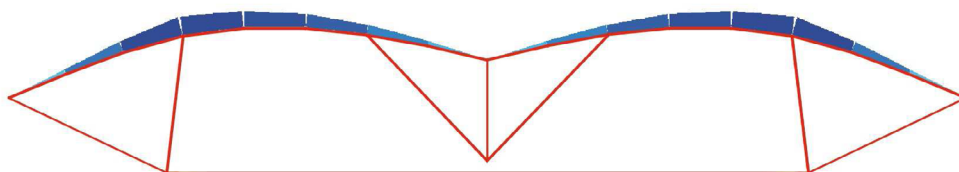


Figure 3: Influence of the vertical external load  $0.3$  kN/m<sup>2</sup> before the process of tensioning of the bottom chord is completed

Structural behavior of the frame is analyzed in two stages: pre-stress of the frame and, so-called, operational mode. Operational loads are applied after the first stage is finished. The shape of the frame and forces in its elements are to be updated before the implementation of structural analysis of the second stage. It includes the following steps:

- modification of initial coordinates  $\vec{X}_0$  of all joints in accordance with their displacements  $\vec{\Delta X}$  during the tensioning of the circular cables:

$$\vec{X}_1 = \vec{X}_0 + \vec{\Delta X} \quad (1)$$

- updating the initial lengths  $L_0$  of all structural elements in accordance with values, assumed in the first stage;
- implementation of angular deformations of all beams in accordance with their bending moments (figure 4) and flexural rigidity  $EI$ :

$$\Delta\psi_s = \frac{l_0}{6 \cdot EI} \cdot (2 \cdot M_s - M_e) \quad (2)$$

$$\Delta\psi_e = \frac{l_0}{6 \cdot EI} \cdot (2 \cdot M_e - M_s) \quad (3)$$

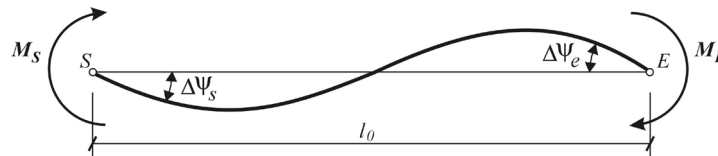


Figure 4: Angular deformations  $\Delta\psi$  of a beam, influenced by bending moments  $M$  - index “ $S$ ” corresponds to the starting point of the beam, and index “ $E$ ” corresponds to the end point

The behavior of the frame is investigated by means of the special computer program EASY. The following load-cases are taken into account:

- $LC_1$ : uniform load distributed on the entire surface;
- $LC_2$ : uniform load distributed on a half of the span only;
- $LC_3$ : wind load.

Loads  $LC_1$  and  $LC_2$  are directed from top to bottom, while the load  $LC_3$  acts outwards the building. Due to the radial arrangement of the upper beams, uniform loads are transformed into, so-called, triangular ones (figure 5).

Load-case  $LC_1$  results in relatively small deformations of the structure. The graph of axial force  $N$  in cables of the bottom chord is approximately linear (figure 6, a), while the curve of vertical displacements  $\Delta Z$  of the central joint has slight downward camber. Bending moment in the top chord  $M$  tends to decrease until the load reaches  $0.5 \text{ kN/m}^2$  and linearly increases afterwards (figure 6, b). Maximum load value  $1.75 \text{ kN/m}^2$  may be derived from the graphs in accordance to the strength properties of structural elements.

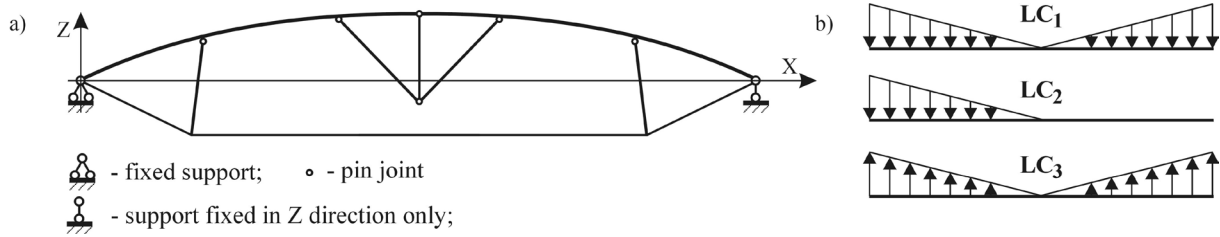


Figure 5: Plane model of the structure – a, and schematic load distribution - b

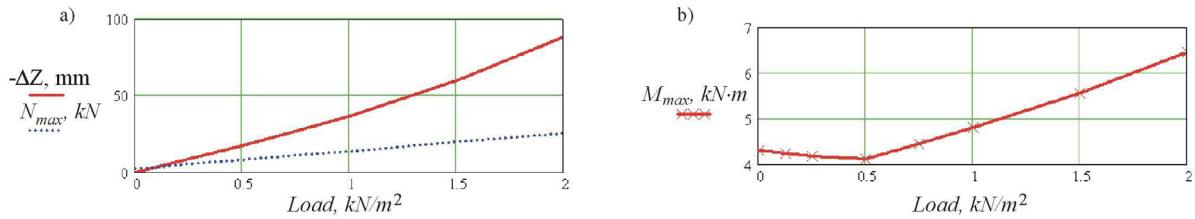


Figure 6: Graphs for the uniform load  $LC_1$ .

a - vertical displacement of the central joint ( $\Delta Z$ , mm) and axial forces in the bottom chord ( $N_{max}$ , kN);  
 b - bending moments ( $M_{max}$ , kN·m) in the top chord

Load-case  $LC_2$ , acting on a half of the span only, results in much more substantial moments and deformations in comparison to loading of the entire span (figures 7, a and 7, b). Maximum load value  $0.4 \text{ kN/m}^2$  may be applied on the structure without overstress of its elements. Even in this case, vertical displacements can reach 200 mm in a quarter of the span, which may be unacceptable from the operational point of view.

Additional ties, embedded in the bottom chord of the frame, result in substantial favorable effect. The ties connect the joints of the bottom chord with each other (figure 7, c). They should preferably be installed in the preliminary stressed structure (figure 2, b). If embedded into the initially undeformed frame (figure 2, a) the ties should be additionally tensioned after the structure has reached its final arch-like shape. Additional ties substantially diminish moments and displacements brought about by non-uniform loads. They ensure the behavior of the frame approximately linear (figure 8).

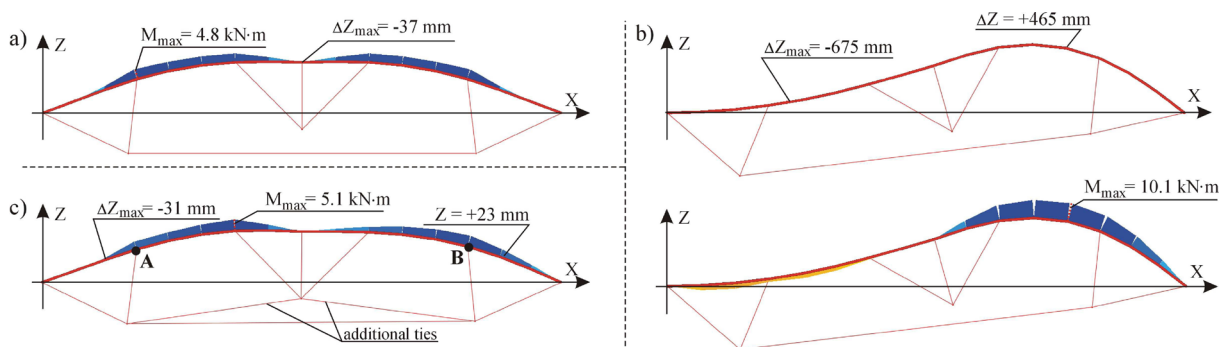


Figure 7: Deformations of the frame and diagrams of moments.

a - vertical load ( $1.0 \text{ kN/m}^2$ ) is distributed on the entire span;  
 b, c - vertical load ( $1.0 \text{ kN/m}^2$ ) is distributed on the left side only

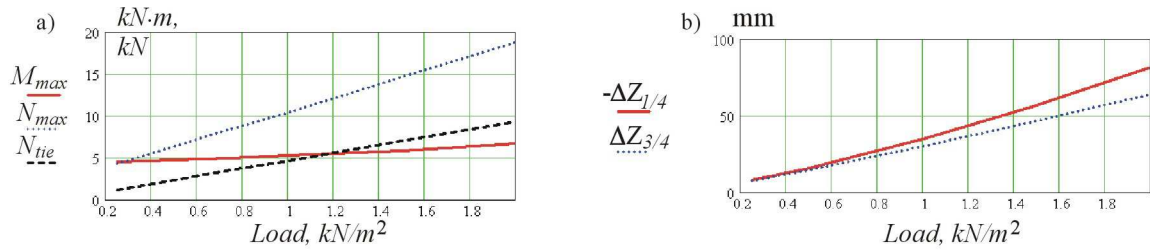


Figure 8: Graphs for the load  $LC_2$  (additional ties are installed).

a – bending moments ( $M_{max}$ , kN·m) in the top chord and axial forces ( $N_{max}$  and  $N_{tie}$ , kN) in the bottom chord and in the additional ties; b - vertical displacement ( $\Delta Z_{1/4}$  and  $\Delta Z_{3/4}$ , mm) in quarters of the span (points A and B in figure 7, c)

So called ‘top to bottom’ loads of load-cases  $LC_1$  and  $LC_2$  don’t result in the emergence of the horizontal thrust because reactions of upper beams and bottom cables equilibrate each other. Thus, the frame needs vertical supports only. On the other hand, loads acting in the opposite direction, e.g. wind, bring about very substantial deformations of the structure (figure 9, a). In addition, the wind load results in sagging of bottom chord cables. Excessive moments and deformations arise after the complete cable slackening (figures 9,b – 9,d). So, the maximum wind load, permissible for the frame, is approximately  $0.2 \text{ kN/m}^2$ . It is usually inappropriate for most sites due to climatic conditions and regulations.

Installation of an additional horizontal support in point A (the point is marked in figure 9,a) helps to fix the problem. In case if the wind load is equal to  $0.5 \text{ kN/m}^2$  the vertical displacement in the center of the frame is 11 mm and the moment in the upper beam is 4kN·m. These values are substantially smaller in comparison to the ones obtained without the support (figure 9). Thus, the horizontal support makes the frame functionally operative for the most conditions.

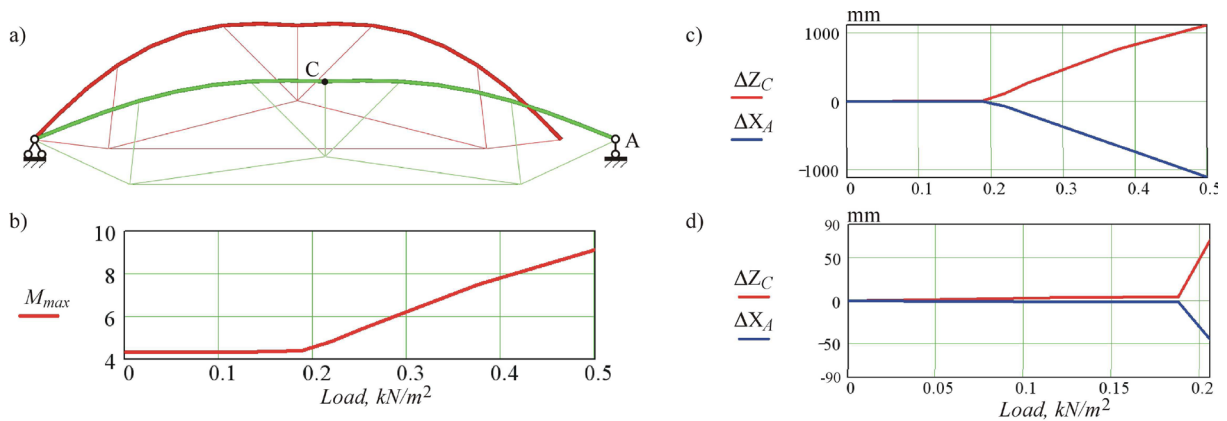


Figure 9: Behavior of the frame under load-case  $LC_3$  (wind load). a – the frame without horizontal support in its right side; b – graph of bending moments ( $M_{max}$ , kN·m) in the top chord; c – graphs of vertical displacements  $\Delta Z_C$  of joint C and horizontal displacements  $\Delta X_A$  of joint A (mm); d – enlarged view of graphs in figure c

The additional horizontal supports should be installed at least in three ribs of a spatial frame. The ribs are to be arranged in different vertical planes (figure 10). Preferably they should be spaced approximately 120 degrees apart.

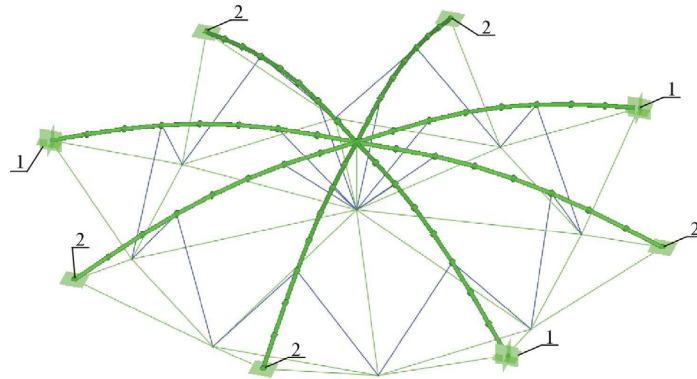


Figure 10: Spatial frame improved to sustain the wind load.  
1 – fixed support; 2 – support fixed in the vertical direction only

#### 4 FLEXIBLE FABRIC MEMBRANE

Hanging the membrane should be fulfilled after the frame has been completely installed and transformed from the initial, so called “flat”, configuration (figure 2, a) into an operational one (figure 2, b). Otherwise the membrane will sag on the entire surface.

The frame, covered with membrane, is much less susceptible to adverse effect of non-uniform loads. So-called “out-of-plane moments”  $M_w$ , which arise in the upper beams of the frame, are illustrated by diagrams (figure 11). Additional ties (shown in figure 7, c) diminish the deformations of the frame and contribute to the reduction of stresses in its beams (figure 12). They facilitate the favorable effect of inclined outer struts (shown in figure 2, a), causing negative moment (shown with the arrow in figure 11, a).

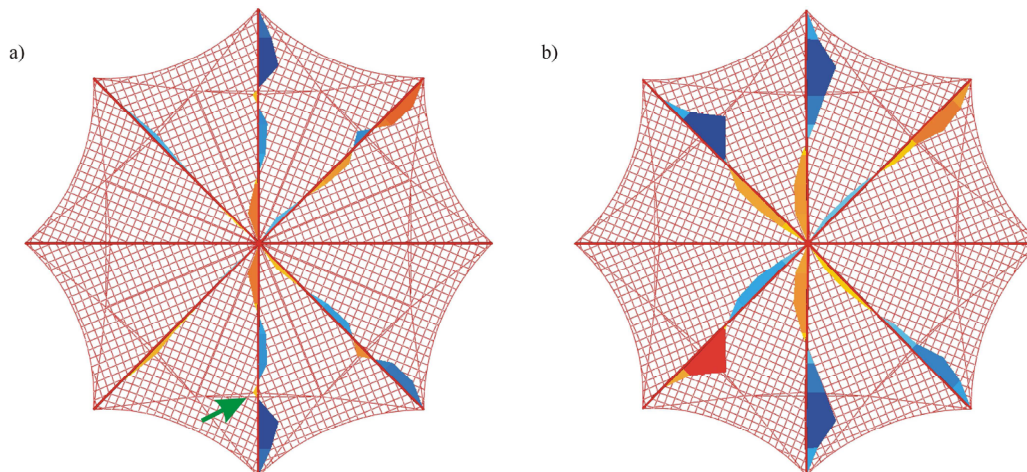


Figure 11: Diagram of out-of-plane moments,  $M_w$ .  
a – the frame with additional ties (figure 7,c); b – the frame without the ties

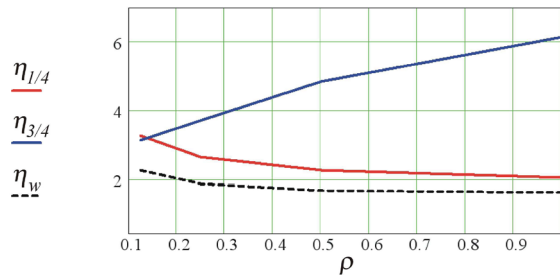


Figure 12: Ratios of displacements and moments  $\eta$  in relation to the fabric relative stiffness  $\rho$

Labels in figure 12 are the following:  $\eta_{1/4} = \Delta Z_{1/4} / \Delta Z_{1/4}^{tie}$ ,  $\eta_{3/4} = \Delta Z_{3/4} / \Delta Z_{3/4}^{tie}$ ,  $\eta_w = M_w / M_w^{tie}$ , where  $\Delta Z_{1/4}$  and  $\Delta Z_{3/4}$ , are displacements in quarters of the span (points A and B in figure 7, c), index “tie” means that the additional ties are installed. Fabric stiffness in the warp and fill directions are assumed the following:  $E_{warp} = 1200 \cdot \rho$  and  $E_{fill} = 800 \cdot \rho$ , kN/m. Coefficient  $\rho$  varies in the range: 0.15 ... 1.0.

On the other hand, improving the frame behavior under load, the ties, however, are not inevitable in contrast to the frame without a flexible covering. Whether the ties are installed or not, the out-of-plane moments  $M_w$  in the beams (figure 13, a) are substantially smaller in comparison to so-called “in-plane of the rib moment”  $M_v$ , which is close to the value 5.7 kN·m for the same load. Judging by the relative displacements (figure 13, b), the frame, covered with the flexible fabric membrane, is a sufficiently stiff structure.

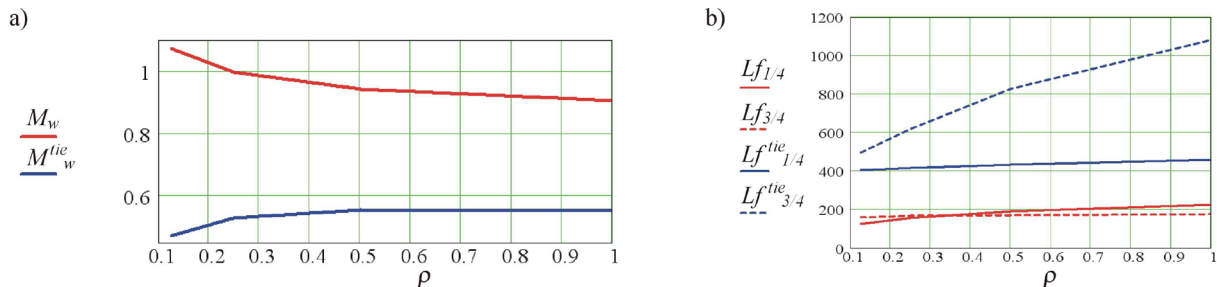


Figure 13: Behavior of the frame, covered with the membrane, under the load-case  $LC_2$  (1.0 kN/m<sup>2</sup> distributed on a half of the span only).

a – graphs of moments  $M_w$ ; b –graphs of relative displacements  $Lf$

Labels in figure 13,b are the following:  $Lf_{1/4} = -L / \Delta Z_{1/4}$ ,  $Lf_{1/4}^{tie} = -L / \Delta Z_{1/4}^{tie}$ ,  $Lf_{3/4} = L / \Delta Z_{3/4}$ ,  $Lf_{3/4}^{tie} = L / \Delta Z_{3/4}^{tie}$ , where  $Lf$  is relative displacement,  $L$  is the span of the frame.

## 5 CONCLUSIONS

Dome-shaped structure, proposed in the present work, comprises high-strength low-modulus beams, supported with spreaders and steel cables underneath. The beams, forming the upper chord of the dome, are initially straight, but substantial shape modification arises by means of cable tensioning.

The research is carried out with the help of the special computer program EASY. Non-uniform snow and wind loads result in substantial unfavorable effect on the frame of the structure. Installation of ties and horizontal supports is proposed in order to ensure serviceability of the frame. In addition, flexible fabric membrane, attached to the upper chord of the frame, substantially improves its structural behavior by reducing bending moments and deformations.

Bending-active dome-shaped structure, proposed in the present paper, is intended to be used for temporary covering of spaces of social occasions, entertaining events, points of retail, bus stations, etc. The structure may be installed and dismantled in a short period of time with comparatively small labor input.

## REFERENCES

- [1] J. Knippers, J. Cremers, M. Gabler, J. Lienhard, *Construction Manual for Polymers + Membranes*. Institut fur internationale Architektur-Dokumentation. Munchen, 2011, 296 p.
- [2] J. Lienhard, H. Alpermann, C. Gengnagel, J. Knippers, "Active Bending, a Review on Structures where Bending is used as a Self-Formation Process", *International Journal of Space Structures*, Vol. **28**, No. **3 & 4**, pp. 187-196, (2013).
- [3] J. Lienhard, "Bending-active membrane structure", *Tensinews*, No. **22**, pp. 9, (2012).
- [4] R. Off and H. Runne, "IMS Research Project "Batsail", *Tensinews*, No. **18**, pp. 14-15, (2010).
- [5] R. Off, "IMS Research Project "Bat-wing sail. A new Approach to Membrane Structures", *Fabric Architecture*, pp. 24-25, (January-February, 2010).
- [6] S. Ahlquist, J. Lienhard, "Textile Hybrid M1", *Tensinews*, No. **24**, pp. 6-9, (2013).
- [7] *Composite materials SMC/BMC. Pultrusion*. LLC "Tatneft-Presscomposite". Online: <http://www.tnpc.ru/rus/produkcija/pultruziya/> - (19 June 2017).
- [8] N. Kotelnikova-Weiler, C. Douthe, E.L. Hernandez, O. Baverel, C. Gengnagel and J.-F. Caron, "Materials for Actively-Bent Structures", *International Journal of Space Structures*, Vol. **28**, No. **3 & 4**, pp. 229-240, (2013).
- [9] A.V. Chesnokov, V.V. Mikhaylov and I.V. Dolmatov, "Development of the Hybrid Dome and Research of its Behaviour under Load", *Proc. of the VII International Conference on Textile Composites and Inflatable Structures. Structural Membranes 2015*, pp. 469-476. 19-21 October 2015, Barcelona, Spain.
- [10] *PFEIFER Tension Members*. PFEIFER seil- und hebetechnik GMBH, 2017, 76 p. Online: <http://www.pfeifer.de/en/cable-structures/download/brochures/?dlid=4586> - (19 June 2017).

## CABLE ROOF STRUCTURE WITH FLEXIBLE FABRIC COVERING

V.V. MIKHAYLOV<sup>Y</sup>, A.V. CHESNOKOV<sup>\*</sup>

<sup>Y</sup> The Faculty of Civil Engineering  
Lipetsk State Technical University  
Moskovskaya street 30, 398600 Lipetsk, Russian Federation  
e-mail: [mmvv46@rambler.ru](mailto:mmvv46@rambler.ru), web page: <http://ixserv.stu.lipetsk.ru/>

<sup>\*</sup> The Faculty of Civil Engineering  
Lipetsk State Technical University  
Moskovskaya street 30, 398600 Lipetsk, Russian Federation  
e-mail: [andreychess742@gmail.com](mailto:andreychess742@gmail.com), web page: <http://ixserv.stu.lipetsk.ru/>

**Key words:** Cable Roof, Fabric, Flexible Membrane, Tensegrity

**Summary.** *The proposed roof structure consists of a frame covered with a flexible fabric membrane. The frame comprises steel cable members linked together by struts and ties. Calculation formulas, needed for static analysis of the proposed roof structure, are given. The technique for estimation of its basic parameters is offered. The proposed roof structure is intended to be used for public and industrial buildings having large column spacing. Its primary advantages are reduced overall height and possibility to tension the entire structure by means of small number of cables.*

### 1 INTRODUCTION

Cable roof, covered with a flexible fabric membrane, is a low-weight translucent structure. Unlike conventional constructions, comprising steel and concrete elements, fabric covering is set into place in form of large-scale sheets. It reduces amount of site joints and results in diminishing of labor input of the project<sup>1</sup>.

On the other hand, fabric membrane must be preliminary tensioned in order to bear external loads without wrinkles. Appropriate supporting members, e.g. single cables or cable trusses, should be provided so as to confine sagging of the membrane and to ensure its structural ability.

Flexible fabric covering is generally used in buildings having significant overall height of the roof. It is suitable for improving architectural appearance but sometimes results in excessive internal space of the construction<sup>2</sup>. An approximately flat roof is often much more appropriate for a lot of public and industrial buildings, than the roof having substantial difference between elevations of its ridge and valley. Under this condition the distance between supporting members of the roof becomes comparatively small in order to ensure required curvature of the membrane. It results in reduction of column spacing and may be unacceptable for buildings, which require large free spans.

In order to overcome this problem, the fabric covering is proposed to be supported with, so called “ordinary” members. They are arranged comparatively closely to each other and lean

on “primary” members which are, in turn, connected to columns of the building. The primary and ordinary members, united with struts and ties, form the frame of the proposed roof structure<sup>3,4</sup> (figure 1). Thus, the flexible membrane, covering the frame, can be properly tensioned so as to bear external loads without excessive sagging.

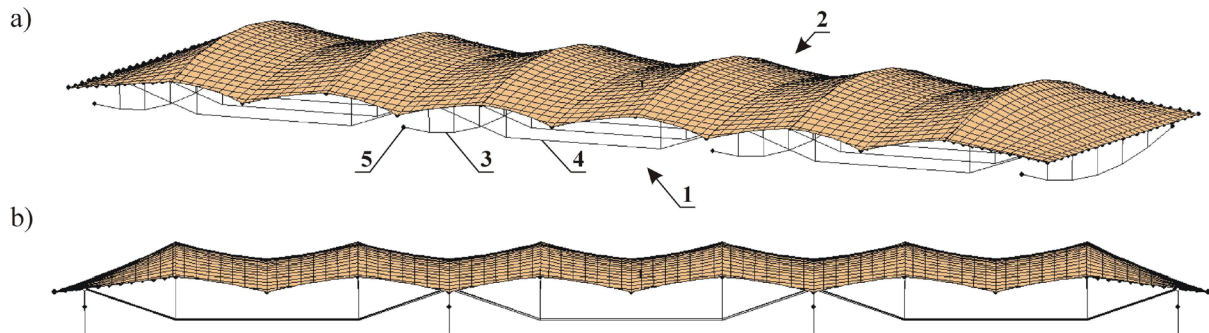


Figure 1: The proposed roof structure<sup>3,4</sup>. a - axonometric view; b - front view; 1 – the frame of the structure; 2 – flexible covering (membrane); 3 - primary member; 4 - ordinary member; 5 – fixed support (e.g. column of the building)

## 2 THE FRAME OF THE PROPOSED ROOF STRUCTURE

The frame of the proposed roof structure belongs to, so-called, “tensegrity” systems<sup>5,6</sup> of class 1. It consists of continuous cables and multitude of discontinuous struts, which are not directly coupled. The frame comprises a number of sections (figure 2). The sections are connected with each other successively. Longitudinal thrust, brought about by a section, is either equilibrated by an adjacent one, or transmits to horizontal supports provided in the ends of the frame.

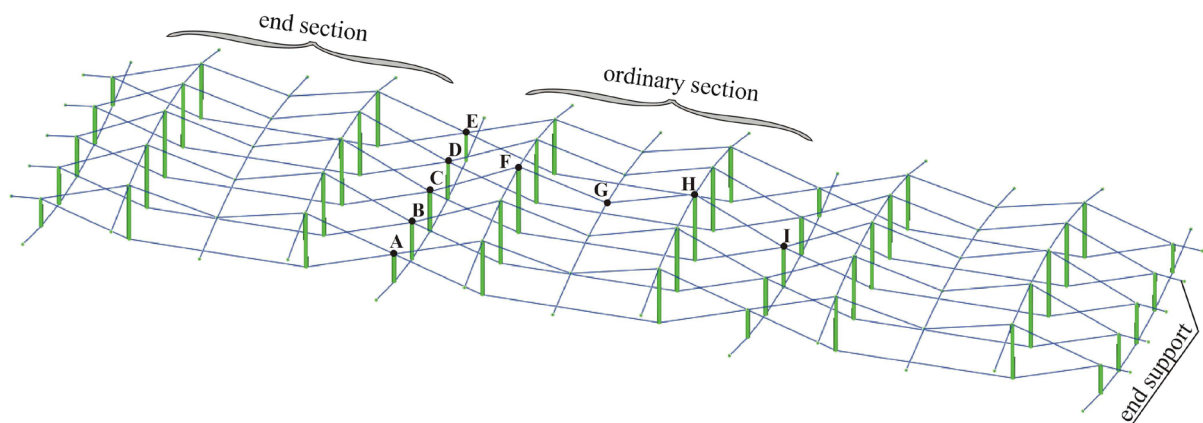


Figure 2: The frame of the roof structure

A section of the frame (figure 3) consists of preliminary stressed cables 1, 2 and 4. The cables are arranged in vertical planes. They are linked together by means of struts 5 and 6. The cables are subdivided into bearer and backstay ones. Backstay cables 2, to which the

flexible fabric covering is attached, are convex upwards. Together with flexible ties 3, 7 and 8 they form the upper chord of the frame. Bearer cables 1 and 4 are convex downwards. They are arranged in mutually-perpendicular directions and may be classified into primary and ordinary ones.

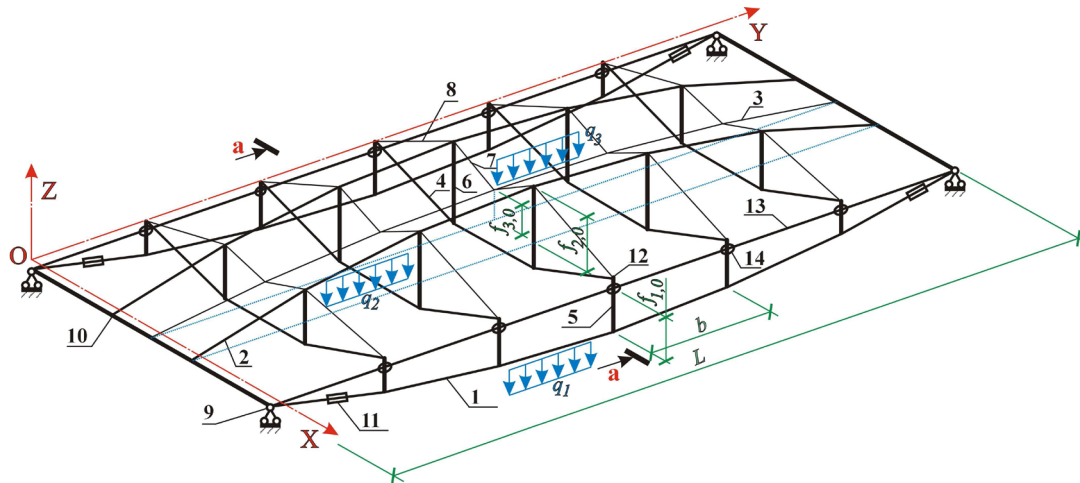


Figure 3: Axonometric view of a section of the frame

Primary bearer cables 1, equipped with tensioning appliances 11, are connected to columns of the building at points 9. Ordinary cables 4 are supported by primary ones by means of struts. The struts 5 are fixed in the direction along the Y-axis by means of ties 13 (figure 3). The ties are equipped with special connections 14, allowing the struts to freely pass in the longitudinal direction only.

The connections 12 of cables 4 to struts 5 are proposed to be arranged in a horizontal plane<sup>4</sup> (XOY) which is situated above the supports 9. The plane also should be arranged between upper and lower joints of the struts 6. It ensures the bearer cables 1 and 4 to keep their vertical position due to the emergence of stabilizing forces.

Backstay cables 2 are attached fixedly to supports 10. The thrust, brought about by cables 2, is much smaller in comparison to the thrust of bearer cables 1. It allows simplifying the construction of supports 10 in contrast to supports 9, which should be capable to sustain substantial forces.

### 3 ANALYSIS OF THE FRAME

In the assumption, that the roof structure is influenced by uniformly distributed external loads, calculation formulas, needed for its static analysis, are derived as follows.

Model of structure is shown in figures 3 and 4. It is assumed, that external loads ( $q_1$ ,  $q_2$  and  $q_3$ ) are uniformly distributed along the spans of the cables 1, 2 and 3. Positive directions of displacements and loads are indicated in the figures.

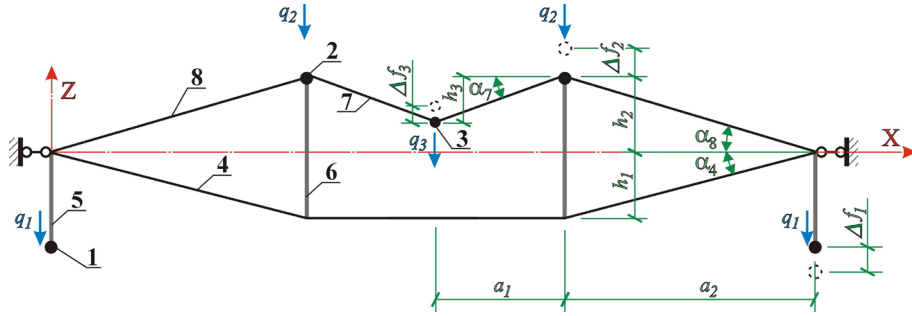


Figure 4: View of the frame along the line a-a in figure 3

Cables 1, 2 and 3, situated along the span of the frame, are loaded with approximately uniformly distributed vertical forces  $p_1$ ,  $p_2$  and  $p_3$ . The forces are the sums of external loads  $q$  and vertical reactions of struts 5 and 6, ordinary bearer cables 4 and ties 7 and 8.

The equilibrium of a uniformly loaded cable  $i$ , where  $i = 1, 2$  and  $3$ , may be written as follows:

$$\frac{f_{i,0} + \Delta f_i}{p_i} = \frac{\rho_i}{Lc_i - Lc_{i,0}} \quad (1)$$

where  $f_{i,0}$  is the initial sag of the cable  $i$  in the middle of its span  $L$ ;  $\Delta f_i$  is the deflection of the cable  $i$ ;  $p_i$  is the resulting load, influencing the cable;  $Lc_i$  and  $Lc_{i,0}$  are the lengths of the cable in deformed and initial states, respectively;  $\rho_i$  is the coefficient:

$$\rho_i = \frac{L^2 \cdot Lc_{i,0}}{8 \cdot EA_i} \quad (2)$$

where  $EA_i$  is the stiffness of the cable  $i$ , equal to the product of the modulus of elasticity by its cross section area.

The length of the cable is calculated according to the expression:

$$L_{cab} = \Psi_2 \cdot f^2 + L \quad (3)$$

where  $\Psi_2$  is the coefficient:  $\Psi_2 = 8/(3 \cdot L)$ .

The initial length of the cable is calculated as follows:

$$Lc_{i,0} = Lc_{i,0,0} - \Delta L_{p,i} \quad (4)$$

where  $Lc_{i,0,0}$  is, so called, geometrical length, calculated from (3) for the initial sag  $f_{i,0}$ ;  $\Delta L_{p,i}$  is tensioning of the cable by means of a turnbuckle or another appropriate equipment in order to ensure required pre-stress.

The length of the cable in deformed state  $Lc_i$  is derived from (3) as a function of the deflection  $Lc(\Delta f_i)$  using the following expression:  $f = f_{i,0} + \Delta f_i$ . Substituting the function into (1) yields the cubic equation:

$$f_{i,0} + \Delta f_i = \frac{\rho_i \cdot p_i}{Lc(\Delta f_i) - Lc_{i,0}} \quad (1')$$

In order to convert it into the linear one, the simplification is proposed by the Taylor series:

$$\Delta f^r \approx r \cdot \Delta f_a^{(r-1)} \cdot \Delta f + (1-r) \cdot \Delta f_a^r \quad (5)$$

where  $\Delta f_a$  is an approximation to the value  $\Delta f$ .

Substituting (5) into (1') for each cable  $i$  yields a set of three simultaneous equations from which unknown cable deflections are to be calculated:

$$\Delta f_i \cdot \mu_i + \lambda_i = p_i(\Delta f_1, \Delta f_2, \Delta f_3) \quad (6)$$

where  $\mu_i, \lambda_i$  are the following coefficients:

$$\mu_i = \frac{\Delta L_{p,i} + \Psi_2 \cdot [3 \cdot (\Delta f_{a,i} + f_{i,0})^2 - (f_{i,0})^2]}{\rho_i} \quad (7, a)$$

$$\lambda_i = \frac{\Delta L_{p,i} \cdot f_{i,0} - \Psi_2 \cdot (\Delta f_{a,i})^2 \cdot (2 \cdot \Delta f_{a,i} + 3 \cdot f_{i,0})}{\rho_i} \quad (7, b)$$

and  $p_i$  is a linear approximation to the load, written as follows:

$$p_i(\Delta f_1, \Delta f_2, \Delta f_3) = \Omega_{i,0} + \Omega_{i,1} \cdot \Delta f_1 + \Omega_{i,2} \cdot \Delta f_2 + \Omega_{i,3} \cdot \Delta f_3 \quad (8)$$

where coefficients  $\Omega$  are calculated as follows:

$$\Omega_{3,0} = -q_3 \quad (9, a)$$

$$\Omega_{3,1} = \frac{\sin(2 \cdot \alpha_8) \cdot \cos(\alpha_7)}{2 \cdot \tau_3} \quad (9, b)$$

$$\Omega_{3,2} = \frac{\sin(\alpha_7 + \alpha_8) \cdot \cos(\alpha_8)}{\tau_3} \quad (9, c)$$

$$\Omega_{3,3} = \frac{-\sin(\alpha_7) \cdot \cos(\alpha_8)^2}{\tau_3} \quad (9, d)$$

and

$$\Omega_{2,0} = -q_2 \quad (10, a)$$

$$\Omega_{2,1} = \tau_1 \cdot \Omega_{3,1} + \tau_2 \quad (10, b)$$

$$\Omega_{2,2} = \tau_1 \cdot \Omega_{3,2} + \tau_2 \quad (10, c)$$

$$\Omega_{2,3} = \tau_l \cdot \Omega_{3,3} \quad (10, d)$$

and

$$\Omega_{1,0} = q_1 \quad (11, a)$$

$$\Omega_{1,1} = \chi \cdot (\Omega_{2,1} + 0.5 \cdot \Omega_{3,1}) \quad (11, b)$$

$$\Omega_{1,2} = \chi \cdot (\Omega_{2,2} + 0.5 \cdot \Omega_{3,2}) \quad (11, c)$$

$$\Omega_{1,3} = \chi \cdot (\Omega_{2,3} + 0.5 \cdot \Omega_{3,3}) \quad (11, d)$$

where  $\chi$  is the coefficient equal to 1.0 if the primary bearer cable 1 is situated at the end of the frame and  $\chi = 2.0$  if the cable 1 is situated between two adjacent sections of the frame; and  $\tau_i$  ( $i = 1, 2$  and  $3$ ) are the following coefficients:

$$\tau_1 = \frac{-\sin(\alpha_7 + \alpha_8)}{2 \cdot \sin(\alpha_7) \cdot \cos(\alpha_8)} \quad (12, a)$$

$$\tau_2 = \frac{-1}{b} \cdot \frac{EA_4 \cdot \sin(\alpha_4)^2}{L_4 + a_1 \cdot \cos(\alpha_4)^2} \quad (12, b)$$

$$\tau_3 = \frac{1}{2} \cdot \frac{b}{\sin(\alpha_7)} \cdot \left( \frac{L_7}{EA_7} \cdot \cos(\alpha_8)^2 + \frac{L_8}{EA_8} \cdot \cos(\alpha_7)^2 \right) \quad (12, c)$$

where  $a_1, b, \alpha_4, \alpha_7, \alpha_8$  are initial dimensions and angles, designated in figures 3 and 4;  $L_4, L_7, L_8$  are initial lengths of the cables;  $EA_4, EA_7, EA_8$  are stiffness of the cables.

Solution of (6) is derived as follows:

$$\vec{\Delta f} = [M]^{-1} \cdot \vec{V} \quad (13)$$

where

$$\vec{\Delta f} = \begin{pmatrix} \Delta f_1 \\ \Delta f_2 \\ \Delta f_3 \end{pmatrix}, \quad M = \begin{pmatrix} \Omega_{1,1} - \mu_1 & \Omega_{1,2} & \Omega_{1,3} \\ \Omega_{2,1} & \Omega_{2,2} - \mu_2 & \Omega_{2,3} \\ \Omega_{3,1} & \Omega_{3,2} & \Omega_{3,3} - \mu_3 \end{pmatrix}, \quad \text{and} \quad \vec{V} = \begin{pmatrix} \lambda_1 - \Omega_{1,0} \\ \lambda_2 - \Omega_{2,0} \\ \lambda_3 - \Omega_{3,0} \end{pmatrix}.$$

Loads  $p_i$  are obtained from (8), and forces in frame members are calculated as follows:

– cables  $i = 1, 2, 3$ , situated along the span:

$$N_i = \frac{p_i \cdot L^2}{8 \cdot (f_{i,0} + \Delta f_i)} \quad (14, a)$$

– cables, arranged in transverse direction:

$$N_4 = \left[ (q_2 + p_2) - (q_3 + p_3) \cdot \tau_1 \right] \cdot \frac{b}{\sin(\alpha_4)} \quad (14, b)$$

$$N_7 = \frac{b}{2 \cdot \sin(\alpha_7)} \cdot (q_3 + p_3) \quad (14, c)$$

$$N_8 = N_7 \cdot \frac{\cos(\alpha_7)}{\cos(\alpha_8)} \quad (14, d)$$

Analysis of the roof structure is proposed to be implemented in two stages. In the first stage, approximations  $\Delta f_{a,i}$  (see expression (5)) to the deflections  $\Delta f_i$  are equal to zero for all three cables ( $i = 1, 2$  and  $3$ ). The second stage uses results  $\Delta f_i$ , found in the previous stage, as initial approximation  $\Delta f_{a,i} = \Delta f_i$ , in order to improve tolerance of the solution.

#### 4 ESTIMATION OF THE FRAME PARAMETERS

The frame of the roof structure exhibits complex behavior under load. Cables, which constitute the top and bottom chords, should be in tension. Otherwise they sag and the frame will become unstable. It may substantially complicate computer simulation of the proposed roof due to divergence of the iteration process. In contrast to ordinary constructions, the main parameters of the frame of the proposed roof should be estimated before implementation of the static analysis. The parameters include geometrical dimensions, strength properties, pre-stresses and stiffness values of structural elements.

Expressions (14) allow estimating structural parameters by means of the following conditions:

$$\Theta > 0.1 \quad (15, a)$$

$$\Theta < 1.0 \quad (15, b)$$

$$\Theta = N_{cab} / (A \cdot R) \quad (16)$$

where  $N_{cab}$  is the force in the cable;  $A$  – is the cable cross section area;  $R$  is the cable strength.

Let's consider the frame with the following dimensions (figures 3 and 4) expressed in meters:

$$L = 12 \quad b = 2 \quad a_1 = a_2 = 3 \quad h_1 = 1 \quad h_2 = 1.5 \quad h_3 = 0.8 \quad f_{1,0} = f_{2,0} = 1 \quad f_{3,0} = 0.7$$

Cable mechanical properties are adopted from the catalogue<sup>7</sup>:  $E = 1.3 \cdot 10^8$  kN/m<sup>2</sup> and  $R = 7 \cdot 10^5$  kN/m<sup>2</sup>. Uniformly distributed external load acts on the roof. The load is equal to 1.8 kN/m<sup>2</sup>. In the assumption, that the membrane is attached to the backstay cables 2, the area load is converted into the line distributed one:  $q_2 = 10.8$  kN/m, and  $q_1 = q_3 = 0$ . Pre-stress of the frame is implemented by means of tensioning  $\Delta L_{p,1}$  of the bottom chord only. Thus, elongations of cables 2 and 3 are equal to zero:  $\Delta L_{p,2} = \Delta L_{p,3} = 0$ .

Estimation of cross section areas of frame members and the value  $\Delta L_{p,1}$  is proposed to be executed in the step by step manner. Having started from an initial approximation, the parameters to be determined are being modified in order to fulfill conditions (15).

So-called, targeted search is performed by using graphs of impact (figure 5). The graphs are plotted according to the expression (16). They illustrate the influence of frame parameter variation on values  $\Theta$ . Cross section areas of bearer cables ( $A_1$  and  $A_4$ ), main backstay cables ( $A_2$ ) and also elongation  $\Delta L_{p,1}$  of the bottom chord are chosen due to their greatest influence on (16).

Indexes, shown in figure 5, correspond to element numbers (see figures 3 and 4). Each curve is obtained as a result of two calculations of the frame: without external loads (pre-stress only) -  $Value_0$  and with loads -  $Value_1$ . The maximum of these values is used for every curve, except  $\Theta_3$ , for which the minimum value is chosen. Every graph (figure 5) allows specifying permissible sub-range of parameter variation according to conditions (15).

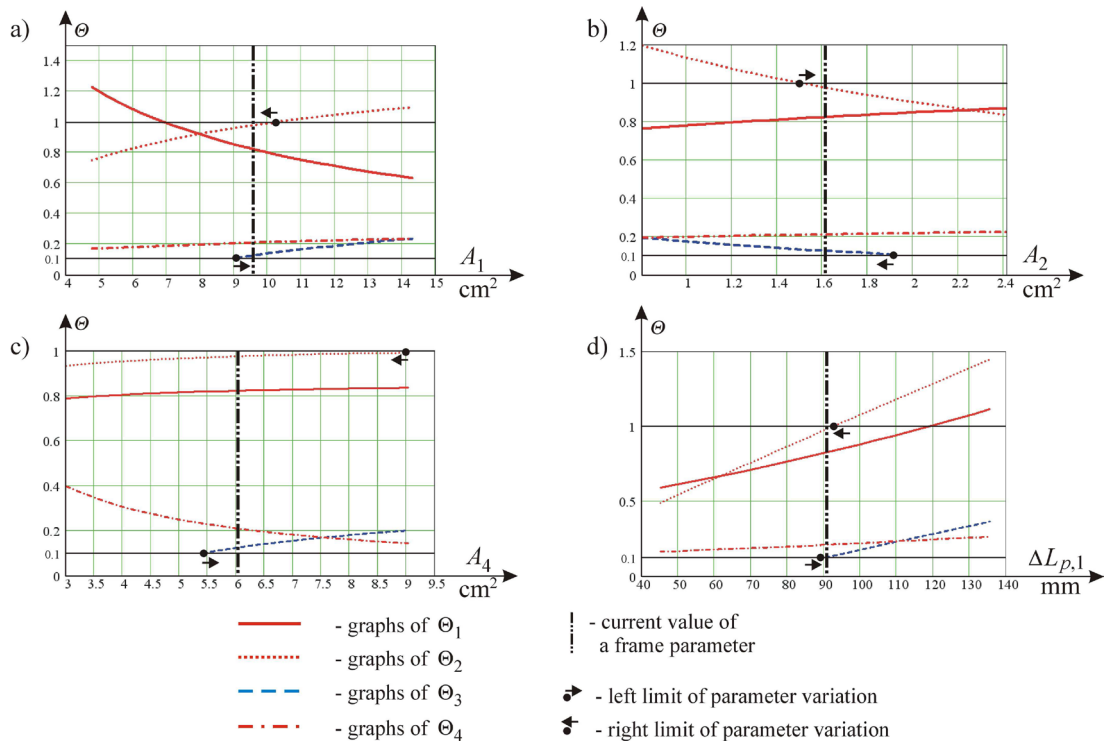


Figure 5: Graphs of impact of frame parameters

According to the catalogue<sup>7</sup> the following cables are chosen: primary bearer cable 1 is made of two strands  $d_s = 28.6$  mm with total cross section area  $A_1 = 9.54$  cm<sup>2</sup>, ordinary cable 4 is made of a strand  $d_s = 32.1$  mm with cross section area  $A_4 = 6.02$  cm<sup>2</sup>, backstay cable 2 is made of a strand  $d_s = 16.6$  mm with cross section area  $A_2 = 1.61$  cm<sup>2</sup>. Flexible ties 3, 7 and 8 are made of the smallest strand in the catalogue<sup>7</sup> -  $d_s = 6.1$  mm with cross section area  $A_2 = 0.22$  cm<sup>2</sup>.

Comparison of results, obtained by the proposed formulations (index “p”) and by means of the special computer program Easy (index “e”), are in tables 1 and 2. Discrepancies  $\varpi$  are indicated beneath the corresponding data.

**Table 1:** Deflections of the roof structure

Load-case	Deflections, mm					
	$\Delta f_{1,p}$	$\Delta f_{1,e}$	$\Delta f_{2,p}$	$\Delta f_{2,e}$	$\Delta f_{3,p}$	$\Delta f_{3,e}$
Pre-stress only: $q_1 = q_2 = q_3 = 0$	-147	-154	136	144	102	115
	$\varpi = 4.4 \%$		$\varpi = 5.5 \%$		$\varpi = 11.8 \%$	
Pre-stress and vertical load: $q_2 = 10.8,$ $q_1 = q_3 = 0$	-87	-91	66	67	24	20
	$\varpi = 5.0 \%$		$\varpi = 1.8 \%$		$\varpi = 18.2 \%$	

**Table 2:** Forces in elements of the structure

Load-case	Forces, kN							
	$N_{1,p}$	$N_{1,e}$	$N_{2,p}$	$N_{2,e}$	$N_{3,p}$	$N_{3,e}$	$N_{4,p}$	$N_{4,e}$
Pre-stress only: $q_1 = q_2 = q_3 = 0$	302.5	298.2	110.7	108.0	8.0	7.9	47.2	46.5
	$\varpi = 1.4 \%$		$\varpi = 2.4 \%$		$\varpi = 2.2 \%$		$\varpi = 1.5 \%$	
Pre-stress and vertical load: $q_2 = 10.8,$ $q_1 = q_3 = 0$	547.7	536.0	51.7	47.0	1.8	1.8	88.3	84.5
	$\varpi = 2.2 \%$		$\varpi = 9.4 \%$		$\varpi = 0 \%$		$\varpi = 4.3 \%$	

Tables 1 and 2 show that formulas, proposed for static analysis of the frame, well simulate its structural behaviour. Discrepancies of forces  $N_2$  and deflections  $\Delta f_3$  may be explained by divergence of backstay cables 2 and ties 3 from their initial parabolic shape. These inaccuracies negligibly affect estimation of frame parameters, and the proposed formulas may successfully be used for structural behaviour investigation.

## 5 THE FLEXIBLE FABRIC MEMBRANE

Flexible fabric membrane is supported by the upper chord of the frame. It is also attached to catenary cables, restrained by backstay cables and connected to the ends of the roof structure (figure 6).

The membrane should be preliminary stressed not less than 1.3% of the average tensile strength<sup>2</sup> in order to be able to sustain external loads. The following ways of its tensioning are considered: by means of special additional equipment, and with the help of appliances already used for pre-stressing the frame of the roof structure.

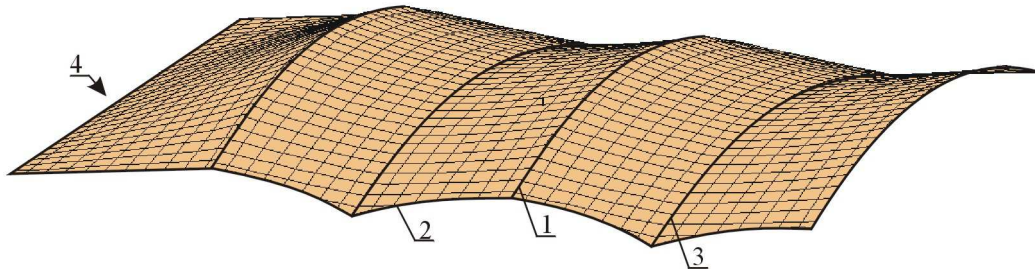


Figure 6: A fragment of the membrane.

1 - upper chord of the frame; 2 - catenary cable; 3 - backstay cable; 4 – end of the roof

In the first case the frame is assumed to be fully completed before hanging the membrane. Catenary and backstay cables are tensioned by means of turnbuckles, while membrane edges are connected to ends of the roof using lashing strap systems<sup>1</sup>. This method results in approximately uniform stress distribution in the membrane due to the possibility of adjusting any inaccuracies.

On the other hand, tensioning the frame and the membrane by appliances embedded in the bottom chord of the roof structure (elements 11 shown in figure 3) allows substantial reducing of labor input of the project. The frame should have been tensioned halfway in order to be able to sustain loads brought about by the membrane. Then, the membrane is attached to supports and the process continues simultaneously. Resulting stress distribution is substantially uneven in comparison to the previous tensioning technique (figure 7).

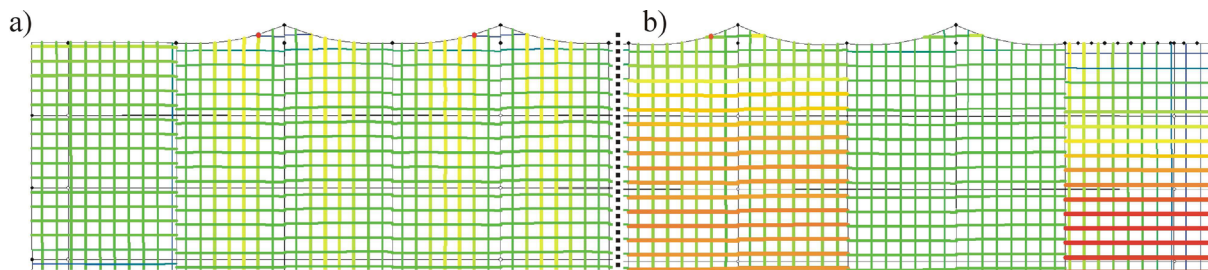


Figure 7: Diagrams of stresses in the flexible fabric membrane.

a – the membrane is tensioned by means of additional appliances after the completion of the frame; b – the membrane is tensioned together with the frame

The roof structure is analyzed with the help of computer program EASY. The following loads are taken into account: vertical load  $S_1 = 1.5 \text{ kN/m}^2$ , acting on area “1” of the roof structure and load  $S_2 = S_1 \cdot \vartheta$ , acting on area “2”. Layout of the areas is in figure 8. Load  $1.5 \text{ kN/m}^2$  is adopted in the assumption, that vertical reaction of the fabric membrane is approximately  $0.3 \text{ kN/m}^2$ . Resultant load, equal to  $1.8 \text{ kN/m}^2$ , corresponds to the value, for which parameters of the frame are determined. Coefficient  $\vartheta$  varies in the range  $\vartheta = 0..1$ . It allows simulating non-uniform impacts. Vertical deflections of the roof structure are shown in figure 9.

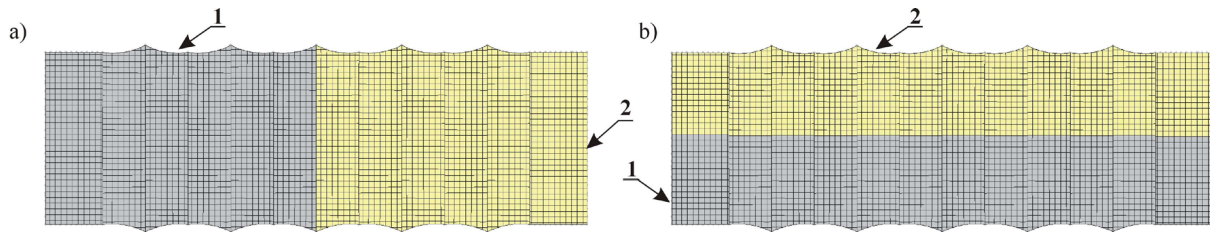


Figure 8: Variants of load distribution. 1, 2 – number of area

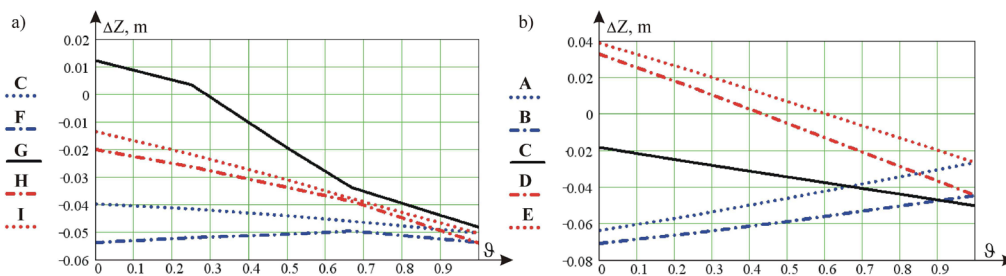


Figure 9: Graphs of deflections of the roof structure, influenced by non-uniform external loads. a, b - variants of load distribution according to figure 8; A ... I are points, marked in figure 2

Figure 9 shows that deflections of the roof structure under non-uniform external loads are approximately linear, except point G, which belongs to tie 3. This non-linear behaviour may be explained by, so-called, “kinematic” movements of the tie and by horizontal displacements of joints F and H. On the other hand, the proposed roof structure behaves stable. It may successfully withstand external effects in real conditions.

## 6 CONCLUSIONS

The proposed cable roof structure is intended to be used for public and industrial buildings with enlarged column spacing. It consists of the frame covered with the flexible fabric membrane.

The frame comprises so called “primary” and “ordinary” members, made of steel cables. The cables are linked together by struts and ties. The ordinary members, arranged comparatively closely to each other, support the fabric membrane. They lean on the primary ones, connected to columns of a building. The roof has substantially lower overall height in comparison to usual membrane structures of the same span. Resulting in diminishing of unused internal space of the building, it is more attractive from an economic point of view.

Calculation formulas for static analysis of the roof structure are proposed. They are verified by comparison with results provided by the computer program EASY. The technique for estimation of basic parameter of the proposed roof structure is offered.

The roof structure well behaves in case of potential external loads, including non-uniformly distributed effects.

## REFERENCES

- [1] M. Seidel, *Tensile Surface Structures: A Practical Guide to Cable and Membrane Construction*. Ernst & Sohn, 2009, 229 p.
- [2] B. Forster, M. Mollaert, *European design guide for tensile surface structures*. TensiNet, 2004, 354 p.
- [3] Patent for Invention RU 2567588. *Cable roof* / A.V. Chesnokov, V.V. Mikhaylov.
- [4] Utility Model Patent RU 169612. *Cable roof structure* / A.V. Chesnokov, V.V. Mikhaylov.
- [5] Snelson, K. "The Art of Tensegrity", *International Journal of Space Structures*, Vol. 27, № 2-3 (2012), pp. 71-80.
- [6] R.E. Skelton and M.C. de Oliveira, *Tensegrity Systems*. Springer, 2009, 216 p.
- [7] *PFEIFER Tension Members*. PFEIFER seil- und hebetechnik GMBH, 2017, 76 p. Online: <http://www.pfeifer.de/en/cable-structures/download/brochures/?dlid=4586> - (19 June 2017).

## DESIGN OF A COST EFFECTIVE SMALL SPAN TENSILE ROOF

IBRAHIM ALI H. <sup>\*</sup>, BECCARELLI P. <sup>\*</sup>, REED V. <sup>†</sup> AND CARPENTER R. <sup>†</sup>

<sup>\*</sup> Department of Architecture and Built Environment  
The University of Nottingham  
University Park, NG72RD Nottingham, UK  
Hend.ibrahimali@nottingham.ac.uk  
Paolo.beccarelli@nottingham.ac.uk

<sup>†</sup> I2O ltd  
Fenstanton, Cambridgeshire, PE28 9HU, UK  
vanessa@i2old.co.uk  
Robert.Carpenter@inside2outside.co.uk

**Key words:** Tensile Roof, tree-like structures, form-finding, membrane structure, coated fabric, KTP, Innovate UK.

### Summary:

Tensile Structures offer a wide variety of membrane forms however, due to the interdependence of form and structural behaviour, only few forms have so far been built. The increasing need for building new tensile forms and investigating innovative solutions for manufacturing and detailing is pushing the lightweight structures market, a strategy adopted by a UK based company, I2O ltd who design and manufacture bespoke innovative tensile structures.

The company held a competition for an innovative, scalable design to complement their product range. The competition was open to all schools, students, sports clubs, restaurants, golf clubs and theme parks and resulted in many entries designed by both school children and adults. The winning design is from Priory Park Infant School in St Neots, UK. The so-called tree-like design is inspired by the school tree emblem and its forest school status. The structure will replace the loss of the school's horse chestnut tree providing shaded creative space for outdoor learning activities. The design challenges for this project derives from two main aspects: I: Transforming the free organic form of trees found in nature into a form that follows a geometric order proven to be structurally stable under different loading conditions whilst maintaining the visual perception of the inspired design. II. Cost-effective solutions for manufacture and detailing of the structure for market development.

The project is designed by Inside2Outside Ltd in the UK, as part of an Innovate UK funded knowledge Transfer partnership with Nottingham University. The project will be manufactured and installed by I2O Ltd who plan to add the structure to its standard products for sale.

## 1 INTRODUCTION

This project is the result of the ongoing research collaboration between the University of Nottingham and I2O Ltd supported by Innovate UK through the Knowledge Transfer Partnership – KTP9912 funded to develop novel tensile membrane structures.

The Knowledge Transfer Partnerships is a UK-wide programme conceived to improve the competitiveness of British businesses through the better use of knowledge, technology and skills that reside within the British Universities. The research project aims to meet a core strategic need and to identify innovative solutions to help that business grow with the consequent increase of the overall profitability for the company involved<sup>1</sup>.

This paper describes one of the new structures developed during the KTP project. The design is the result of a competition open to all schools, students, sports clubs, restaurants, golf clubs and theme parks. The winner is the project submitted by the Priory Park Infant School (Cambridgeshire, UK) which designed a structure that could replace the loss of the school's Horse Chestnut tree providing a shaded creative space for outdoor learning activities.

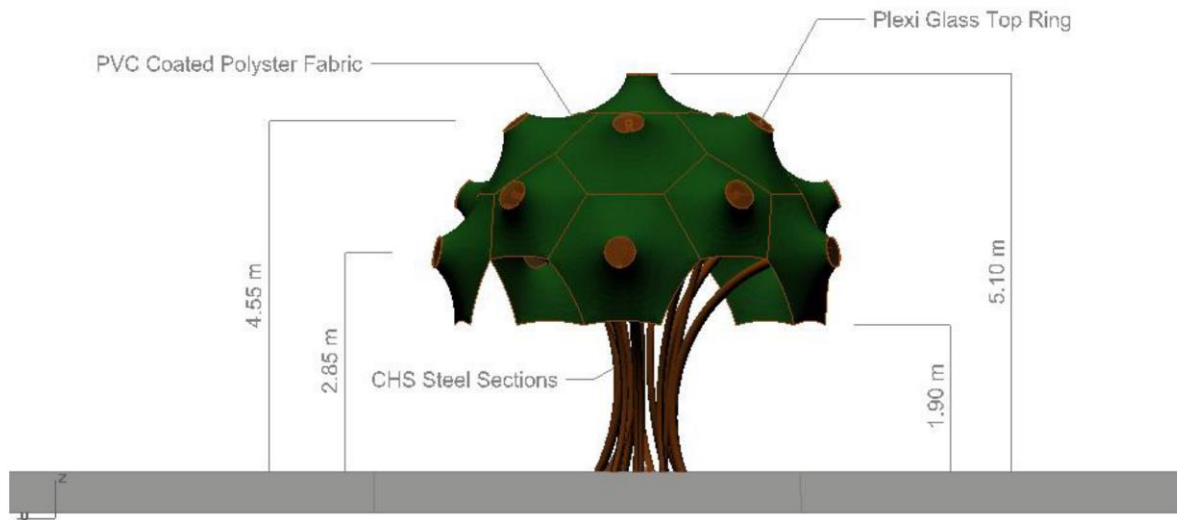


Fig.1. Front elevation of the initial architectural concept.

For the team of researchers from the University of Nottingham, this case study represents an interesting opportunity to test the advanced 3D digital modeling techniques currently available and investigate the correspondence between the digital model and the as-built structure. The comparison includes the match between the final geometry and the surface obtained through the form-finding software, the discrepancy between the results of the finite element structural analysis and the actual structural performance, the inaccuracies due to the flatterness of the surface and the subsequent manufacturing of the connections.

I2O Ltd will use the pilot project to investigate the feasibility of bespoke products based on complex geometries and manufacturing techniques characterized by a certain level of unpredictability and challenges which, however, could open new profitable markets for the business.

## 2 TREE-LIKE STRUCTURES IN ARCHITECTURE

The shape of trees and has always fascinated architects, builders and engineers due to their intrinsic elegance and the interesting structural performance. The impact of this this long-term relationship between nature and architecture has been studied and documented by several researches<sup>2,3</sup> which identified and classified examples of structures inspired by nature form 1400 BC until nowadays. The early examples include columns and capitals used in ancient Egyptian, Greek, Roman, Indian, Chinese and Byzantines palaces and religious buildings. The level of complexity and sophistication reached unprecedented levels during the Gothic period with pointed-arches and vaults designed to mimic the nature using a series of tree-like columns which becomes ribs in correspondence of the vaults (Fig.2).



Fig.2. Columns and capitals inspired by nature in: a) Corinthian column capital, temple of Zeus Olympian, Athens; b) Lincoln Cathedral Chapter House, UK; c) Dougong, Forbidden City, Beijing, China.

The level of accuracy in the structural design and optimization evolved from the graphic static, extensively used by Antony Gaudi, to the most recent finite element methods through several approximated analytical methods. A key step in the structural optimization is the work carried out at the Institute for Lightweight Structures (ILEK) at the University of Stuttgart between 1964 and 1990 under the supervision of Frei Otto who investigated and tested new form-finding techniques inspired by nature.

One of the most relevant studies for this type of structures is the design for the Stuttgart Airport Terminal by Von Gerkan, Marg+Partner (1991). The project (Fig.3b) is based on innovative form-finding techniques (Fig.3a) which has been proven to be extremely effective in the optimization of the structure<sup>5</sup>.

The success of tree-like structures continued in the last decades with several iconic projects, from the concrete structure designed by Pier luigi Nervi for the Palazzo del Lavoro in Turin (1961) to the Tree of Life for the Expo 2015 in Milan, from the Centre Pompidou in Metz by Shigeru Ban and Jean de Gastines to the Tote Banqueting Hall designed by Serie Architects in Mumbai. The combination of a tree-like rigid structure and a membrane cladding lead to a new generation of lightweight structures characterized by the efficient use of the materials and cost-effective manufacturing techniques. Like the examples shown in Fig. 4, given the rigid boundaries and the level of pretention of the membrane, the double curved surface can be easily obtained through form-finding techniques and manufactured with reasonably simple cutting pattern.



Fig. 3. Stuttgart Airport Terminal: a) Frei Otto's hanging models of branching systems<sup>4</sup>; b) Internal view of the Stuttgart Airport Terminal.



Fig. 4. Tree-Like Fractal Structures: a) Tensile umbrella in Delhi, India; b) Inverted cone for the shopping mall "Parc des Vergers de la Plaine", Chambourcy, France; c) Folding Umbrellas, SL-Rash; d) Centre for Nature Interpretation in Melilla, North Africa

## 2 THE DESIGN OF A SMALL SPAN TENSILE ROOF FOR THE PRIORY PARK INFANT SCHOOL IN ST NEOTS, UK

The structure has been designed to replace the loss of the school's horse chestnut tree providing shaded creative space for outdoor learning activities. The tree was the symbol of Priory Park Infant School in St Neots and the team of designers decided to create a tensile roof able to mimic the size and the shape of the original tree and, at the same time, to provide a modern and functional structure which could become the new emblem of the school and promote its image of forest school status.

The shape of the tree crown (Fig. 5a) has been obtained starting from the geometry of a truncated icosahedron (Fig. 5c), an Archimedean solid with 12 regular pentagonal faces, 20 regular hexagonal faces, 60 vertices and 90 edges (Fig. 5b).

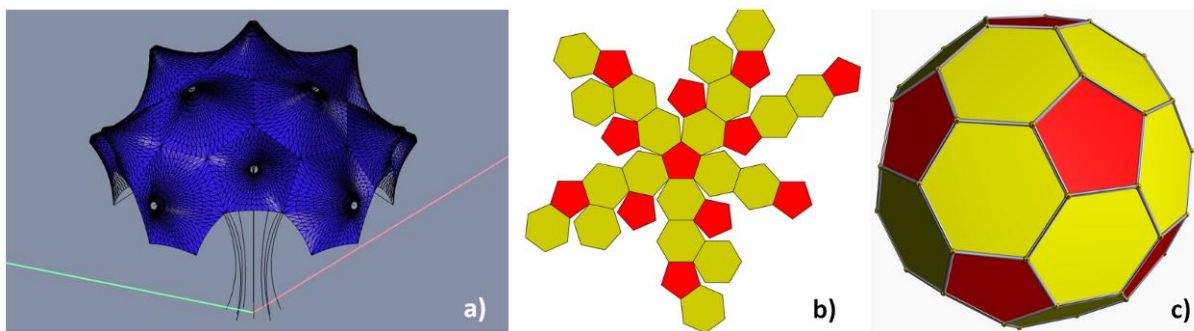


Fig.5. Geometrical model of the tensile roof: a) 3D model in Rhino; b) Net of a truncated icosahedron<sup>6</sup>; c) Colored faces of a truncated icosahedron<sup>6</sup>;

### 2.1. Steel frame

The steel frame is made of a set of independent curved circular hollow sections which are fixed to the concrete foundation and grouped together to mimic the shape of the tree and to improve the overall stability of the structure. Each tube ends with a circular support for each module of the membrane and provide the anchoring point for the cables used for the tensioning of the surface. The details (Fig. 6) have been modeled in 3D with Rhino.

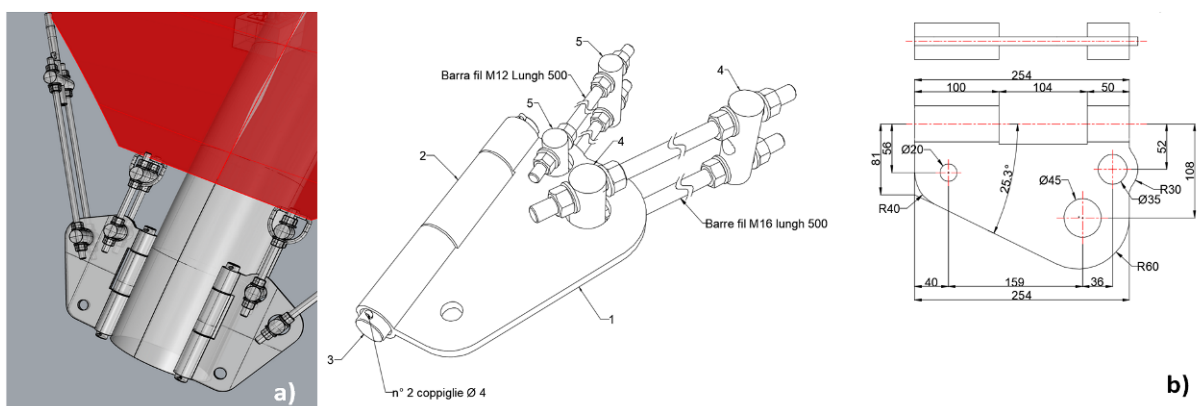


Fig.6. Digital model of the structural connections: a) 3D view; b) Blueprints generated from the digital model

## 2.2. Membrane

The membrane roof will be manufactured with a PVC coated Polyester fabric which is one of the most used textile membranes in the building industry due to the good compromise of price and performance<sup>7</sup>.

The 3D geometry has been generated using the form-finding module of ixCube 4-10 which is based on the force density method. The overall target is to have a level of pre-stress between 1kN/m and 1.5kN/m with the only exception of the extremity of the cones. The stability of the membrane roof has been also investigated under the expected wind and snow loads.

The cutting pattern will follow the modular geometry of the faces of the truncated icosahedron. Each pentagon (or hexagon) will be subdivided in five (or six) triangles which will be subsequently welded together to obtain the final 3D geometry.

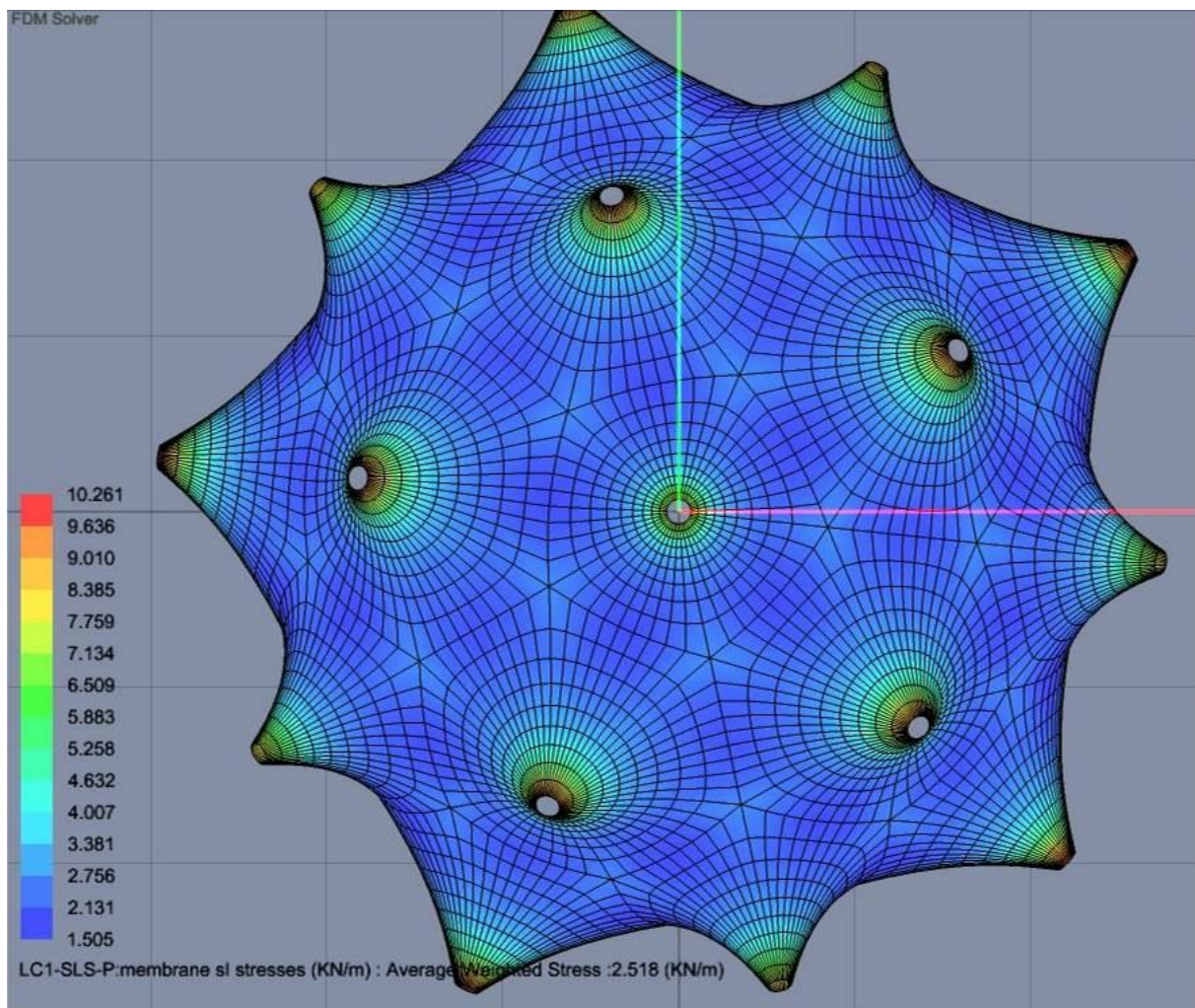


Fig.7. Digital model of the membrane structure with color mapping for a visual depiction of the expected stress distribution in the membrane after the initial installation and pre-stress.

### 2.3. Installation

The tensile roof is designed to be permanent structure. The design has been optimized in order to minimize the need of large lifting equipment. The components of the structure will be transported on site with a truck equipped with a hydraulic crane able to lift the steel components. The curved tubes will be bolted to a reinforced concrete platform and connected in order to improve the lateral stability. Once the steel frame is installed, the membrane will be lifted and connected in correspondence of the circular supports placed at the end of each tube. Finally, the membrane will be tensioned through the adjustment of the length of the cables in correspondence of the edges the vertex of the truncated icosahedron.

## 4 CONCLUSION

The paper describes the design of a tensile roof for an infant school designed to mimic and replace the original horse chestnut tree emblem of the school. The project is the result of a KTP research project funded by Innovate UK in order to develop new membranes structures based on advanced digital modelling and manufacturing techniques. The structure will be manufactured and installed by Insde2Outside Ltd which aims to open a new market for bespoke membrane structures.

## 5 ACKNOWLEDGMENTS

The project is designed by Insde2Outside Ltd in the UK, as part of an Innovate UK funded Knowledge Transfer partnership (KTP9912) with Nottingham University. The software used for the structural design of the tensioned membrane, ixCube 4-10, has been kindly provided by IxRay ltd and the Master of Membrane Structures at Anhalt University of Applied Sciences, Dessau, Germany.

## REFERENCES

- [1] <http://ktp.innovateuk.org/>
- [2] I.M. Rian, M. Sassone, *Tree-inspired dendriforms and fractal-like branching structures in architecture: A brief historical overview*, *Frontiers of Architectural Research* (2014) **3**: 298–323
- [3] J. Sánchez-Sánchez, F.E. Pallarés, M. T. Rodríguez-León, *Reciprocal Tree-Like Fractal Structures*, *Nexus Netw J* (2014) **16**:135–150.
- [4] W. Nerdinger, *Frei Otto Complete Works: Lightweight Construction Natural Design*. (2005) Birkhäuser, Basel; Boston; Berlin.
- [5] Flamur Ahmeti (2007), *Efficiency of Lightweight Structural Forms: The Case of Treelike Structures - A comparative Structural Analysis*. MSc Program "Building Science & Technology", TU Vienna.
- [6] [https://en.wikipedia.org/wiki/Truncated\\_icosahedron](https://en.wikipedia.org/wiki/Truncated_icosahedron).
- [7] P. Beccarelli, *Biaxial tests and procedures for fabrics and foils*, Springer Briefs in Applied Sciences and Technology, (2015), Springer, New York.

## ANALYSIS OF CABLE STRUCTURES BY MEANS OF TRIGONOMETRIC SERIES

A.V. CHESNOKOV<sup>\*</sup>, V.V. MIKHAYLOV<sup>Y</sup>

<sup>\*</sup> The Faculty of Civil Engineering  
Lipetsk State Technical University  
Moskovskaya street 30, 398600 Lipetsk, Russian Federation  
e-mail: [andreychess742@gmail.com](mailto:andreychess742@gmail.com), web page: <http://ixserv.stu.lipetsk.ru/>

<sup>Y</sup> The Faculty of Civil Engineering  
Lipetsk State Technical University  
Moskovskaya street 30, 398600 Lipetsk, Russian Federation  
e-mail: [mmvv46@rambler.ru](mailto:mmvv46@rambler.ru), web page: <http://ixserv.stu.lipetsk.ru/>

**Key words:** Cable, Analysis, Trigonometric Series

**Summary.** *Cable structures are light-weight, expressive from an architectural point of view and allow covering large spans without intermediate supports. They are far superior to the conventional bearer systems of buildings and constructions. On the other hand, cables are very deformable and possess complex non-linear behavior under load. In spite of availability of special computer programs, designed for iteration analysis of cable systems, the problems of optimization require elaboration of analytical structural models. In the present paper, the behavior of flexible cables is analyzed by means of trigonometric series. This technique may be used for simulation of complex structures, comprising several tiers or flexible chords. It extends the scope of analytical approach on cables, influenced by substantially non-uniform loads. The present work also contributes to the analysis of flexible membrane systems, which are often simulated by a number of cables, arranged in mutual-perpendicular directions.*

### 1 INTRODUCTION

Cable structures are applied in buildings of various types and assignments. They substantially reduce assembly expenditures and amount of steel needed for the construction. In contrast to beams, girders and trusses, cables can span large areas without installation of intermediate supports.

Light-weight cable structures are intended to be covered with flexible high-strength polymer membranes or architectural fabrics, allowing the roof to be light-translucent. In addition, structural behavior of membranes is usually simulated by means of a number of flexible cables, arranged in mutual - perpendicular directions<sup>1,2</sup>.

On the other hand, cables are very deformable and can sustain tensile forces only. They exhibit complex non-linear behavior under load. For a given set of parameters, such as sag and curvature of cables, values of preliminary stresses, cross section areas etc., structural analysis is performed by means of iteration techniques, with the help of specialized computer programs. These parameters are not usually known in advance, especially when the problem of optimization arises and the designer is to elaborate a cost-effective construction. This

complex task may be solved by analytical investigation of the structure in order to get appropriate results directly or to substantially confine number of unknown structural parameters and their possible combinations. In addition, analytical approach is required to determine the influence of structural parameters on structural behavior. It allows checking numerical results, obtained by iteration techniques<sup>2</sup>.

In the present paper, flexible cables are analyzed by means of trigonometric series<sup>3,4</sup>. Coefficients of load distribution are calculated in accordance to the formulations of Fourier's theory<sup>5,6</sup>. The cable shape function is represented by means of a multitude of coefficients. They depend on each other and may be expressed in terms of one coefficient. The technique for obtaining the coefficient is given. It is based on the differential equation of equilibrium of a flexible cable.

## 2 A FLEXIBLE CABLE UNDER LOAD

A flexible cable, influenced by non-uniform external load  $q(x)$ , is illustrated in figure 1. The present study concerns so-called shallow cables, with sag-to-span ratio ( $f/L$ ) less than  $1/8$ . In the assumption that the cable is perfectly flexible its shape is entirely determined by the load distribution. The horizontal support reactions  $H$ , called thrust, arise on both sides of the cable.

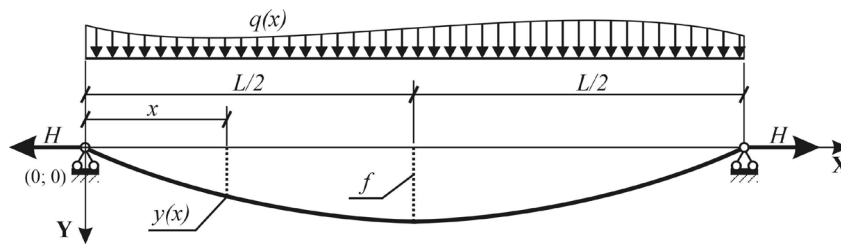


Figure 1: A cable under load

Cable shape, determined by a function  $y(x)$ , as well as external load  $q(x)$  (figure 1) may be represented with the trigonometric sine-series as follows:

$$y(x) = S(x, \vec{kY}) \quad (1)$$

$$q(x) = S(x, \vec{kq}) \quad (2)$$

where  $\vec{kY}$  and  $\vec{kq}$  are the coefficients of the series<sup>3,4</sup>:

$$S(x, \vec{k}) = \sum_{m=1}^{nM} k_m \cdot \sin\left(\frac{m \cdot \pi \cdot x}{L}\right) \quad (3)$$

where  $m$  is a number of a term of the series;  $nM$  is the quantity of considered series terms;  $L$  is the span of the cable.

The expression (1) satisfies the boundary conditions of the cable:  $y(0) = y(L) = 0$  due to the numbers  $m$  are integer. In accordance to (2) load values also should be zero at  $x=0$  and

$x = L$ . However, the more the terms of the series are considered the smaller the discrepancy to the given load distribution arises. It is additionally diminished by reduction of influence of the load near the supports of the cable.

Coefficients  $\vec{kq}$  are calculated by means of the theory of Fourier series<sup>5,6</sup>:

$$kq_m = \frac{2}{L} \cdot \int_0^L \left( q(x) \cdot \sin\left(\frac{m \cdot \pi \cdot x}{L}\right) \right) dx \quad (4)$$

The differential equation of the cable, influenced by an external load  $q(x)$ , is written as follows<sup>3</sup>:

$$\frac{d^2}{dx^2} y(x) = \frac{-q(x)}{H} \quad (5)$$

where  $H$  is the thrust. It depends on the axial force  $N$  in the cable and the angle  $\gamma$  between the tangent to it and  $X$ -axis:

$$H = N(x) \cdot \cos[\gamma(x)] \quad (6)$$

Variation of the force  $N$  along the span of a shallow cable is negligible. It may be considered approximately constant and equal to the thrust  $H$ :

$$N(x) \approx H. \quad (7)$$

Thus, the force  $N$  is obtained from the Hook's law:

$$N = N(\vec{kY}) = EA \cdot \frac{L_{c,1}(\vec{kY}) - L_{c,0}}{L_{c,0}} \quad (8)$$

where  $EA$  is the tensile stiffness of the cable;  $L_{c,0}$ ,  $L_{c,1}$  are total lengths of the cable in initial state and under external load  $q$ , respectively.

Substituting (1) and (2) into (5), considering (7), yields the set of  $nM$  equations:

$$m^2 \cdot \frac{kY_m}{kq_m} = \frac{1}{N(\vec{kY})} \cdot \left(\frac{L}{\pi}\right)^2 \quad (9)$$

where  $m = 1 \dots nM$ .

The right-hand side of every equation (9) is constant for a given vector of coefficients  $\vec{kY}$ . Consequently, the dependence for different indexes  $m$  and  $j$  may be written as follows:

$$m^2 \cdot \frac{kY_m}{kq_m} = j^2 \cdot \frac{kY_j}{kq_j} \quad (10)$$

It results in the following relationships between the coefficients  $\vec{kY}$  of the series (1):

$$kY_m = \left(\frac{j}{m}\right)^2 \cdot kmj_m \cdot kY_j \quad (11)$$

where

$$kmj_m = kq_m / kq_j \quad (12)$$

The ratios  $kmj_m$  depend only on the type of the load, for example equal or inverse-symmetric one, and do not depend on particular load values.

The equation (11) means, that all coefficients  $\vec{kY}$  of the series (1) depend on each other and may be expressed in terms of one coefficient  $kY_j$ . The index  $j$  must be selected according to the condition:  $kq_j \neq 0$ . In most cases it is advisable to apply  $j=1$ , however for inverse-symmetric load it should be  $j=2$ .

Substituting (11) into (9) yields the following equation in one unknown  $kY_j$ :

$$kY_j = \frac{kq_j}{N(kY_j)} \cdot \left(\frac{L}{j \cdot \pi}\right)^2 \quad (13)$$

In order to solve (13), cable length  $L_c$ , involved in (8), should be expressed in terms of the coefficient  $kY_j$ .

### 3 DERIVATION OF THE LENGTH OF THE CABLE

Cable length may be found from the simplified expression, valid for shallow cables only<sup>7</sup>:

$$L_c = \int_0^L \left[ 1 + \frac{1}{2} \cdot \left(\frac{d}{dx} y(x)\right)^2 - \frac{1}{8} \cdot \left(\frac{d}{dx} y(x)\right)^4 \right] dx \quad (14)$$

Substituting (1) into (14), considering (11), yields the following expression:

$$L_c = L + k_2 \cdot (kY_j)^2 - k_4 \cdot (kY_j)^4 \quad (15)$$

where  $k_2$  and  $k_4$  are the coefficients:

$$k_2 = \frac{\pi^2}{4 \cdot L} \cdot j^4 \cdot \sum_{m=1}^{nM} (\xi_m)^2 \quad (16)$$

$$k_4 = \frac{\pi^4 \cdot j^8}{8 \cdot L^3} \cdot \sum_{i=1}^5 k_{4,i} \quad (17)$$

where

$$\xi_m = kmj_m / m \quad (18)$$

and

$$k_{4,1} = \frac{3}{8} \cdot \sum_{m=1}^{nM} (\xi_m)^4 \quad (19, a)$$

$$k_{4,2} = 1.5 \cdot \sum_{m_1=1}^{nM-1} \sum_{m_2=m_1+1}^{nM} (\xi_{m_1} \cdot \xi_{m_2})^2 \quad (19, b)$$

$$k_{4,3} = \frac{1}{2} \cdot \sum_{m_1=1}^{nM} \sum_{m_2=1}^{nM-1} (\xi_{m_1})^2 \cdot \xi_{m_2} \cdot \xi_{m_3} \quad (19, c)$$

where  $m_3 = 2 \cdot m_1 \pm m_2$ , under the condition:  $m_3 \in [(m_2 + 1); nM]$ ;

$$k_{4,4} = \sum_{m_1=1}^{nM-2} \sum_{m_2=m_1+1}^{nM} \sum_{m_3=m_1+1}^{nM-1} \xi_{m_1} \cdot \xi_{m_2} \cdot \xi_{m_3} \cdot \xi_{m_4} \quad (19, d)$$

where  $m_4 = \pm m_1 + m_2 \pm m_3$ , under the condition:  $m_4 \in [(m_3 + 1); nM]$ ;

$$k_{4,5} = \sum_{m_1=1}^{nM-2} \sum_{m_2=m_1+1}^{nM-1} (\xi_{m_1})^2 \cdot \xi_{m_2} \cdot \xi_{m_3} \quad (19, e)$$

where  $m_3 = 2 \cdot m_1 + m_2$ , under the condition:  $m_3 \in [(m_2 + 1); nM]$ .

Coefficients  $k_2$  and  $k_4$  depend on the type of the load, but not on its particular values.

The coefficient  $kY_j$  in (15) may be replaced with a cable ordinate  $f = y(X)$  at a given point  $X \in (0..L)$  along the span:

$$kY_j = \frac{f}{\Psi} \quad (20)$$

The coefficient  $\Psi$  is derived from (1) and (11):

$$\Psi = f^2 \cdot \sum_{m=1}^{nM} \mu_m \cdot \sin\left(\frac{m \cdot \pi \cdot X}{L}\right) \quad (21)$$

where

$$\mu_m = kmj_m / m^2 \quad (22)$$

Consequently, the equilibrium shape of the cable is uniquely defined by the type of the external load and one point between supports.

Expression (21) may be written for three main points on the cable, situated in  $1/4$ ,  $1/2$  and  $3/4$  along length of the span:

$$\Psi = j^2 \cdot \sum_{n=1}^{nN} \sum_{t=1}^3 \sin\left(t \cdot \frac{\beta \cdot \pi}{4}\right) \cdot \left[ \mu_{i_1(n,t)} - (2 - |\beta - 2|) \cdot \mu_{i_2(n,t)} \right] \quad (23)$$

where  $\beta = 1, 2$  or  $3$  for  $X = 1/4 \cdot L$ ,  $1/2 \cdot L$  and  $3/4 \cdot L$ , respectively;  $nN$  is an integer number, which obeys the condition:  $nN \leq (nM + 1)/8$ ;  $i_1$  and  $i_2$  are the following indexes:

$$i_1(n,t) = 4 \cdot n - t + 4 \cdot (n - 1) \cdot |\beta - 2| \quad (24, a)$$

$$i_2(n,t) = 4 \cdot n - t + 4 \cdot n \cdot |\beta - 2| \quad (24, b)$$

Substituting (20) into (15) results in the expression, from which the length of the cable may be found:

$$L_c(f) = \Psi_4 \cdot f^4 + \Psi_2 \cdot f^2 + L \quad (25)$$

where

$$\Psi_2 = k_2 / \Psi^2 \quad \text{and} \quad \Psi_4 = -k_4 / \Psi^4. \quad (26)$$

#### 4 DEFLECTION OF THE CABLE UNDER LOAD

Substituting (8) and (20) into (13), considering (25), yields a quintic equation in one unknown  $f$ :

$$f = \frac{\rho}{L_c(f) - L_{c,0}} \quad (27)$$

where

$$\rho = \left( \frac{L}{j \cdot \pi} \right)^2 \cdot \frac{L_{c,0}}{EA} \cdot \Psi \cdot kq_j \quad (28)$$

Cable ordinate  $f$  may be found from (27) by a diagram. On the other hand, graphical solution of the equation is a universal but inconvenient technique. In order to solve it analytically it is proposed to replace the ordinate  $f$  with cable deflection  $\Delta f$ , namely:  $f = f_0 + \Delta f$ . Terms of the equation, having degree higher than the second one, are omitted because the deflection is substantially smaller, than cable span and sag. Thus, the deflection is obtained as follows:

$$\Delta f = \frac{-A_1 + \sqrt{(A_1)^2 + 4 \cdot A_2 \cdot (\rho - A_0 \cdot f_0)}}{2 \cdot A_2} \quad (29)$$

where  $f_0$  is the given ordinate of the cable in the initial state;  $A_0, A_1$  and  $A_2$  are the following coefficients:

$$A_0 = \Psi_4 \cdot (f_0)^4 + \Psi_2 \cdot (f_0)^2 + L - L_{c,0}, \quad A_1 = A_0 + 2 \cdot (f_0)^2 \cdot [2 \cdot \Psi_4 \cdot (f_0)^2 + \Psi_2], \quad A_2 = f_0 \cdot [10 \cdot \Psi_4 \cdot (f_0)^2 + 3 \cdot \Psi_2].$$

### 5 ANALYSIS OF TWO-CHORD PRETENSIONED CABLE TRUSS

Pretensioned cable truss<sup>8</sup>, made of two flexible chords connected with ties (figure 2) is considered.

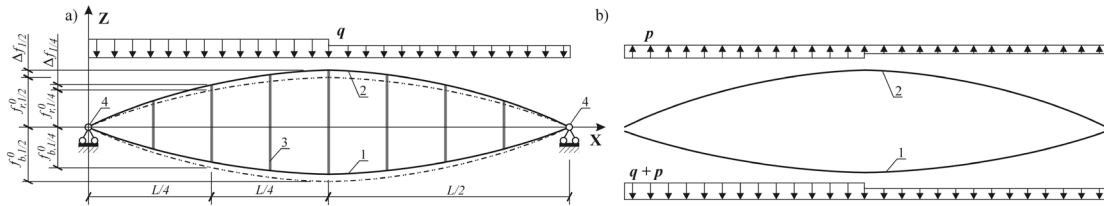


Figure 2: Two-chord cable truss. a – model of the structure; b – loads, acting on the chords; 1 – pre-stressed bearer chord; 2 – restraining chord; 3 – tie (spreader); 4 – fixed support

Loads, acting on the chords of the truss are the following: bearer chord -  $Load_b = q(x) + p(x)$  and restraining chord -  $Load_r = p(x)$ , where  $q(x)$  is an external load assumed to influence from top to bottom;  $p(x)$  is, so-called, “link load”, transmitting from a chord to the other one by means of ties; hereinafter index “b” refers to the bearer chord, and index “r” – to the restraining chord.

It is assumed that loads  $p$  and  $q$  may be split into uniformly distributed (index ‘Eq’) and inverse-symmetric (index ‘Inv’) parts (figure 3):

$$x = 0.. \frac{L}{2} \quad q(x) = q_{Eq} + q_{Inv} \quad p(x) = p_{Eq} + p_{Inv} \quad (30, a)$$

$$x = \frac{L}{2}.. L \quad q(x) = q_{Eq} - q_{Inv} \quad p(x) = p_{Eq} - p_{Inv} \quad (30, b)$$

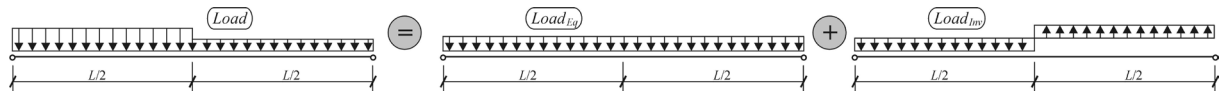


Figure 3: Decomposition of the load into uniformly distributed and inverse-symmetric parts

Loads, acting on the chords, may be represented by a similar way:

$$Load_{b,Eq} = q_{Eq} + p_{Eq} \quad \text{and} \quad Load_{b,Inv} = q_{Inv} + p_{Inv}, \quad (31, a)$$

$$Load_{r,Eq} = p_{Eq} \quad \text{and} \quad Load_{r,Inv} = p_{Inv}. \quad (31, b)$$

The ratios  $kmj_m$ , defined by (12), may be written for uniformly distributed and inverse-symmetric loads as follows:

$$eq_{\tau_i} = \frac{j}{\tau_i}, \quad eq_{(m \neq \tau_i)} = 0 \quad (32, a)$$

$$inv_{2\tau_i} = \eta \cdot eq_{\tau_i}, \quad inv_{(m \neq 2\tau_i)} = 0 \quad (32, b)$$

where  $\tau_i = 2 \cdot i - 1$  is the number of non-zero ratio;  $i$  is an integer number 1, 2, etc.;  $\eta$  is the ratio of inverse-symmetric load to the uniformly distributed part:

$$\eta = Load_{inv} / Load_{Eq}. \quad (33)$$

Expression (33), written for the bearer and restraining chords according to (31, a) and (31,b), results in the dependence between load coefficients  $\eta_b$  and  $\eta_r$  of the chords:

$$\eta_b = \frac{q_{Inv} + \eta_r \cdot p_{Eq}}{q_{Eq} + p_{Eq}} \quad (34)$$

Structural analysis of two-chord cable truss, influenced by non-uniformly distributed external loads, requires at least two points  $X_1$  and  $X_2$  to control deflections of upper and lower cables. According to (20), the relationship between ordinates  $f_{1/4}, f_{1/2}$  and the coefficients  $\Psi_{1/4}$  and  $\Psi_{1/2}$  at points  $X_1 = L/4$  and  $X_2 = L/2$  is written as follows:

$$\frac{\Psi_{1/2}}{\Psi_{1/4}} = \frac{f_{1/2}}{f_{1/4}} = k_f \quad (35)$$

where  $\Psi_{1/4}$  and  $\Psi_{1/2}$  are obtained from (23), using  $\beta = 1$  and  $\beta = 2$ , respectively.

The ordinates in the middle and in the quarter of the span ( $f_{1/2}, f_{1/4}$ ) may be written for bearer and restraining chords as follows:

$$f_{b,1/2} = f_{b,1/2}^0 - \Delta f_{1/2} \quad \text{and} \quad f_{b,1/4} = f_{b,1/4}^0 - \Delta f_{1/4}, \quad (36, a)$$

$$f_{r,1/2} = f_{r,1/2}^0 + \Delta f_{1/2} \quad \text{and} \quad f_{r,1/4} = f_{r,1/4}^0 + \Delta f_{1/4}, \quad (36, b)$$

where  $f_{1/4}^0$  and  $f_{1/2}^0$  are initial ordinates of the bearer or restraining chord, which are usually given in advance;  $\Delta f_{1/4}$  and  $\Delta f_{1/2}$  are deflections of the cable truss, which are to be found.

Having substituted (23), written for  $\beta = 1$  and  $\beta = 2$ , into (35), and taking into account (32), the expression for the coefficient  $k_f$  is derived as follows:

$$k_f = \frac{4}{\eta - \Theta} \quad (37)$$

where  $\Theta$  is the coefficient:

$$\Theta = 2 \cdot \sqrt{2} \cdot \frac{\sum_{n=1}^{nN} \left[ \frac{1}{(8 \cdot n - 3)^3} + \frac{1}{(8 \cdot n - 1)^3} - \frac{1}{(8 \cdot n - 7)^3} - \frac{1}{(8 \cdot n - 5)^3} \right]}{\sum_{n=1}^{nN} \left[ \frac{1}{(4 \cdot n - 3)^3} - \frac{1}{(4 \cdot n - 1)^3} \right]}$$

It is obvious, that the coefficient  $\Theta$  is constant for  $nN \rightarrow \infty$ , namely  $\Theta = -3.0$ . Therefore, the expression (37) is written as follows:

$$k_f = \frac{4}{\eta + 3.0} \quad (37')$$

Substituting (37') into (35) yields the following dependence between load ratio  $\eta$  and the ratio of ordinates of the cable:

$$\eta = 4 \cdot f_{1/4} / f_{1/2} - 3 \quad (38)$$

Coefficient  $kq_j$ , required for the equilibrium equation (27), may be written according to (31) as follows:

$$kq_{b,j} = (q_{Eq} + p_{Eq}) \cdot kEq_{1,j} + (q_{Inv} + p_{Inv}) \cdot kInv_{1,j} \quad (39, a)$$

$$kq_{r,j} = p_{Eq} \cdot kEq_{1,j} + p_{Inv} \cdot kInv_{1,j} \quad (39, b)$$

where  $kEq_{1,j}$  and  $kInv_{1,j}$  are the coefficients of unit loads expansion (uniformly distributed and inverse-symmetric, respectively), defined by (4).

Either  $kEq_{1,j}$  or  $kInv_{1,j}$  is equal to zero for the same  $j$ . Hereinafter index  $j$  is omitted (it is adopted  $j = 1$ ) and expressions (39) is simplified as follows:

$$kq_b = (q_{Eq} + p_{Eq}) \cdot kEq_1 \quad (39', a)$$

$$kq_r = p_{Eq} \cdot kEq_1 \quad (39', b)$$

where  $kEq_1 = 4 / \pi$ .

Thus, equation (27) may be written for the chords as follows:

$$\frac{f_{b,1/2}}{q_{Eq} + p_{Eq}} = \frac{\rho_b}{\Delta L^b} \quad (40, a)$$

$$\frac{f_{r,1/2}}{p_{Eq}} = \frac{\rho_r}{\Delta L^r} \quad (40, b)$$

where  $\rho_b$  and  $\rho_r$  are the coefficients, calculated for the chords according to (28), using the following values  $kq_j = kEq_1$  and  $\Psi = \Psi_{1/2} = 1 - 1/3^3 + 1/5^3 - 1/7^3 \dots \approx 0.96894$ ;  $\Delta L^b$  and  $\Delta L^r$  are elongations of the chords:

$$\Delta L = L_c - L_{c,0} \quad (41)$$

where  $L_c$  is the length of the chord under load;  $L_{c,0} = L_{c,0}^0 - \Delta L_p$  is the initial length of the chord, where  $L_{c,0}^0$  is, so called, geometrical chord length in unloaded state and  $\Delta L_p$  is tensioning of the chord by means of a turnbuckle or another appropriate equipment in order to ensure required pre-stress of the truss.

Geometrical chord lengths  $L_c$  and  $L_{c,0}^0$  are found from (25), using chord ordinates in the middle of the span. Coefficients  $\Psi_2$  and  $\Psi_4$ , given by (26), may be approximated as follows:

$$\Psi_2(\eta) = \frac{\eta^2 + 4}{1.5 \cdot L} \quad (42, a)$$

$$\Psi_4(\eta) = -\frac{\eta^4 + 16 \cdot (\eta^2 + 1)}{2.5 \cdot L^3} \quad (42, b)$$

The coefficient  $\eta=0$  should be applied in expressions (42) to get cable length  $L_{c,0}^0$ . For the length of the cable under load  $L_c$ , the coefficient  $\eta$  is defined by (38).

According to (25), (36), (38), (41) and (42), elongations of the chords  $\Delta L^b$ ,  $\Delta L^r$  and load ratios  $\eta_b$ ,  $\eta_r$  are the functions of the deflections:  $\Delta f_{1/4}$  and  $\Delta f_{1/2}$ . Thus, there are three simultaneous equations: (34), (40, a) and (40, b). They allow deriving uniformly distributed part of the “link load”  $p_{Eq}$  and deflections ( $\Delta f_{1/4}$ ,  $\Delta f_{1/2}$ ) of the truss in the quarter and in the middle of the span.

Inverse-symmetric part of the “link load”  $p_{Inv}$  is obtained from (31, b) and (33), written for the restraining chord:

$$p_{Inv} = p_{Eq} \cdot \eta_r \quad (43)$$

## 6 EXAMPLES

### 6.1 Single cable

The cable is illustrated in figures 1 and 4. Its span is  $L=12$  m. In the assumption, that the shape of the cable obeys parabola, the initial ordinates are the following:  $f_{1/2}^0 = 1.5$  m – in the center of the span and  $f_{1/4}^0 = 1.125$  m – in quarters of the span. Modulus of elasticity of the cable is  $E = 1.3 \cdot 10^4$  kN/cm<sup>2</sup>. Cross section area is 3 cm<sup>2</sup>.

The following load-cases are considered (figure 4): uniformly distributed load on the entire span –  $Ld_1$ , load on a half of the span –  $Ld_2$  and triangular load -  $Ld_3$ . The magnitude of load is  $q = 10$  kN/m.

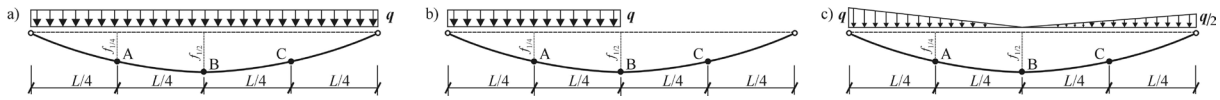


Figure 4: Flexible cable under load. a – load-case Ld<sub>1</sub>, b – load-case Ld<sub>2</sub>, c – load-case Ld<sub>3</sub>

Comparison of results, obtained by the proposed formulations (index “p”) and by means of the special computer program Easy (index “e”), is in the table 1. Indexes “A”, “B” and “C” relate to the points, marked in figure 4. The force is shown in the middle of the span. Discrepancies  $\varpi$  are indicated beneath the corresponding data.

Table 1: Comparison of results for the single cable

Load-case	Deflections, mm						Force, kN	
	$\Delta f_{A,p}$	$\Delta f_{A,e}$	$\Delta f_{B,p}$	$\Delta f_{B,e}$	$\Delta f_{C,p}$	$\Delta f_{C,e}$	$N^p$	$N^e$
Ld <sub>1</sub>	44.3	44.3	61.3	60.7	44.3	44.3	115.4	115.3
	$\varpi = 0 \%$		$\varpi = 0.9 \%$		$\varpi = 0 \%$		$\varpi = 0.1 \%$	
Ld <sub>2</sub>	232.8	236.7	-105.8	-113.3	-402.3	-412.9	64.7	64.2
	$\varpi = 1.7 \%$		$\varpi = 6.9 \%$		$\varpi = 2.6 \%$		$\varpi = 0.8 \%$	
Ld <sub>3</sub>	158.8	150.8	-198.1	-207.9	-143.5	-141.9	33.8	34.1
	$\varpi = 5.2 \%$		$\varpi = 4.8 \%$		$\varpi = 1.1 \%$		$\varpi = 0.9 \%$	

### 6.2 Two-chord cable truss

Model of structure is shown in figure 2. The span of the truss is  $L = 12$  m. Initial ordinates of the chords of the truss are the following:  $f^0_{b,1/2} = 1.5$  m,  $f^0_{b,1/4} = 1.125$  m,  $f^0_{r,1/2} = 1.0$  m,  $f^0_{r,1/4} = 0.75$  m. The chords are made of steel cables. Modulus of elasticity is  $E = 1.3 \cdot 10^4$  kN/cm<sup>2</sup>. Cross section areas are the following: bearer cable  $A_b = 3$  cm<sup>2</sup> and restraining cable  $A_r = 1$  cm<sup>2</sup>. The bearer cable is preliminary tensioned in order to ensure pre-stress in the truss:  $\Delta L^b_p = 0.1$  m.

The following load-cases are considered (figure 5): uniformly distributed load on the entire span – Ld<sub>1</sub>, load on a half of the span – Ld<sub>2</sub> and quasi inverse-symmetric load - Ld<sub>3</sub>. The magnitude of load is  $q = 10$  kN/m.

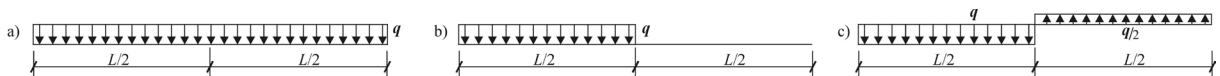


Figure 5: Loads on two-chord cable truss, considered in the example.  
a – load-case Ld<sub>1</sub>, b – load-case Ld<sub>2</sub>, c – load-case Ld<sub>3</sub>

Comparison of results, obtained by the proposed formulations (index “p”) and by means of the special computer program Easy (index “e”), is in the table 2. The forces are shown in the middle of the span of the bearer ( $N_b$ ) and restraining ( $N_r$ ) chords.

**Table 2:** Comparison of results for the two-chord cable truss

Load-case	Deflections, mm				Forces, kN			
	$\Delta f^{p_{1/2}}$	$\Delta f^{e_{1/2}}$	$\Delta f^{p_{1/4}}$	$\Delta f^{e_{1/4}}$	$N^p_b$	$N^e_b$	$N^p_r$	$N^e_r$
Ld <sub>1</sub>	83.0	80.2	62.3	58.9	157.5	155.3	39.4	37.0
	$\varpi = 3.5 \%$		$\varpi = 5.8 \%$		$\varpi = 1.4 \%$		$\varpi = 6.5 \%$	
Ld <sub>2</sub>	120.7	119.0	-26.5	-27.3	122.1	119.8	70.1	68.4
	$\varpi = 1.4 \%$		$\varpi = 2.8 \%$		$\varpi = 1.9 \%$		$\varpi = 2.5 \%$	
Ld <sub>3</sub>	144.0	143.3	-54.7	-55.1	111.6	110.2	93.0	93.6
	$\varpi = 0.5 \%$		$\varpi = 0.6 \%$		$\varpi = 1.3 \%$		$\varpi = 0.6 \%$	

## 7 CONCLUSIONS

The present work contributes to the structural analysis of cable systems. Trigonometric sine-series is used to deal with the differential equation of equilibrium. Cable shape function is represented by a multitude of coefficients. It is shown that they depend on each other and on the type of load. The technique for finding these coefficients and deflections of the cable is given. This approach may be used for analysis of single cables and cable structures, influenced by substantially non-uniform external loads. It allows to gain precise analytical results, proved by the comparison with data, provided by special computer program EASY.

The present work also contributes to the structural analysis of flexible membrane systems, simulated by a number of cables, arranged in mutual-perpendicular directions.

The proposed results are intended to be used for purposes of structural optimization. They facilitate elaboration of analytical models in order to estimate system parameter values. The paper allows additional tools for verification of numerical results, obtained by computer systems of static analysis.

The technique considered in the present work is able to be extended on complex cable structures, comprising several tiers or chords. It can, also, be generalized to non-shallow cables, having the sag comparable to the span.

## REFERENCES

- [1] R. Wagner, *Bauen mit seilen und membranen*. Beuth Verlag GmbH, 2016, 517 p.
- [2] Wagner, R. "Simplified Design Tools for Single/Double Curved Membranes and Inflated Cushions", *International Journal of Space Structures*, Vol. **23**, No. 4 (2008), pp. 233-241.
- [3] Erzen, C.Z. "Analysis of suspension bridges by the minimum energy principle", *IABSE publications*, Vol. **15**, pp. 51-68, (1955). <http://www.e-periodica.ch>.
- [4] D.A. Morelli, *Some contributions to the theory of the stiffened suspension bridge*. Thesis in partial fulfilment of the requirements for the degree of doctor of philosophy. California institute of technology, 1946.
- [5] G.P. Tolstov, *Fourier Series*. Translated by R.A. Silverman. Dover Publications, 2012, 352 p.
- [6] N.J. Hoff, *The Analysis of Structures based on the Minimal Principles and the Principle of Virtual Displacements*. John Wiley and Sons, 1956, 493 p.
- [7] E.I. Belenya, N.N. Streletski, G.S. Vedenikov, *Metal constructions: Special Course*. Stroiizdat, 1991, 687 p.
- [8] G. Tibert, *Numerical Analyses of Cable Roof Structures*. Licentiate Thesis. Royal institute of technology, Department of Structural Engineering. Stockholm, Sweden, 1999, 183 p.

# HIGH SPEED DESIGN AND ANALYSIS OF CABLE-MEMBRANE STRUCTURES ON GRAPHICS CARDS

PÉTER IVÁNYI

Faculty of Engineering and Information Technology  
University of Pécs  
Boszorkány str 2, Pécs, H-7624, Hungary  
e-mail: ivanyi.peter@mik.pte.hu, web page: <http://english.mik.pte.hu>

**Key words:** Dynamic relaxation, Parallel implementation, NVIDIA, CUDA

**Abstract.** This paper discusses a new parallelization approach of the dynamic relaxation method, which is programmed with the NVIDIA CUDA API and executed on the graphics cards (GPU) of a computer. The main advantage of a GPU card is that it has a very large number of computing cores and a separate memory from the computer and they may reside inside a normal desktop computer. However due to architectural simplifications of the GPU systems, synchronization of cores is rather limited. This has a major effect on the parallelization, since the contribution of calculated values at the boundary nodes would require some form of synchronization. This limitation resulted in the new parallelization approach, where the nodes of the finite element mesh are distributed between the cores of the GPU and the elements are “duplicated”. The paper discusses the implementation details of this new parallel approach and some performance measurements of the new parallel dynamic relaxation method on GPU systems are also presented.

## 1 INTRODUCTION

The method of dynamic relaxation, initially invented by A. Day [1] is applicable for different engineering problems, however probably most often it is used for the design and analysis of cable-membrane structures. The method has several advantages compared to other methods. For example there is no need to assemble a global stiffness matrix, as the results are always expressed in terms of the current coordinates. It also means that it can handle geometrically non-linear cases when there are large displacements. The method is iterative therefore one way to speed up the analysis was to parallelize the algorithm. Topping and Khan [2, 3], Topping and Iványi [4] researched the parallelization of the dynamic relaxation method. In these references the approach is mainly using the MPI [5] environment and geometric parallelism.

In the past years significant interest has been generated by the use of the GPU architecture for parallel computing due to their power and wide spread availability. At the same time the special architecture of GPU should be considered when a numerical code is parallelised. For example the GPU has a separate memory, therefore the programmer should consider the distributed programming paradigm. At the same time the GPU itself has many core and generally a shared memory. Despite the shared memory the synchronization of parallel threads is difficult and requires special attention when the parallel algorithm is designed.

An earlier work [6] has already presented a parallel procedure of the dynamic relaxation method for the GPU architecture, however in this paper the method is completely reorganised to take advantage of the architecture. In the proposed parallel implementation the calculation will be based on nodes and not on elements as in the case of the MPI environment.

The paper is organised in the following way. Section 2 introduces the dynamic relaxation method. Section 3 discusses the parallelisation of the dynamic relaxation method with the MPI environment. Section 4 presents the new parallelisation scheme for the GPU architecture. Results and performances of the implementation are presented in Section 5.

## 2 DYNAMIC RELAXATION

The dynamic relaxation method calculates the dynamic behaviour of a structure by direct application of Newton's second law which states that "*the rate of change of momentum of a body is proportional to the applied force and takes place in the direction of the applied force*".

$$F = M \cdot a = M \cdot \dot{v} \quad , \quad (1)$$

where  $F$  denotes the force,  $M$  denotes the mass and  $a$  or  $\dot{v}$  denotes the acceleration. Although the method determines the static solution of a problem, however it traces the fictitious movement of a structure. Since this movement should follow a path, which converges to the final solution as quickly as possible, therefore in this fictitious analysis the masses are also fictitious. Furthermore the mass of the structure is assumed to be concentrated at the joints and an additional viscous damping term which is proportional to the velocity of the joint is included in the formulation. Considering these assumptions at any given time  $t$  the out of balance or residual force in the  $x$  coordinate direction at joint  $i$  may be expressed as follows:

$$R_{ix}^t = M_{ix} \cdot \dot{v}_{ix}^t + C_{ix} \cdot v_{ix}^t \quad , \quad (2)$$

where  $R_{ix}^t$  is the residual force at time  $t$  in the  $x$  direction at joint  $i$ ,  $M_{ix}$  is the fictitious mass at joint  $i$  in the  $x$  direction,  $C_{ix}$  is the viscous damping factor for joint  $i$  in the  $x$  direction and  $v_{ix}^t, \dot{v}_{ix}^t$  are the velocity and acceleration at time  $t$  in the  $x$  direction at joint  $i$ .

The analysis traces the behaviour of the structure at a series of points in time  $t$ ,  $t + \Delta t$ ,  $t + 2\Delta t$ . Over a time step the velocity is assumed to vary linearly with time, hence the velocity can be expressed

$$v_{ix}^t = \left( v_{ix}^{(t+\Delta t/2)} + v_{ix}^{(t-\Delta t/2)} \right) / 2 \quad , \quad (3)$$

and the acceleration is assumed constant over the time step hence:

$$\dot{v}_{ix}^t = \left( v_{ix}^{(t+\Delta t/2)} - v_{ix}^{(t-\Delta t/2)} \right) / \Delta t \quad . \quad (4)$$

Substituting these equations into Equation 2 the result is:

$$R_{ix}^t = \frac{M_{ix}}{\Delta t} \left( v_{ix}^{(t+\Delta t/2)} - v_{ix}^{(t-\Delta t/2)} \right) + \frac{C_{ix}}{2} \left( v_{ix}^{(t+\Delta t/2)} + v_{ix}^{(t-\Delta t/2)} \right) \quad . \quad (5)$$

This equation can be rearranged to calculate the velocity at the new time step  $(t + \Delta t/2)$  from the velocity of the previous time step  $(t - \Delta t/2)$ :

$$v_{ix}^{(t+\Delta t/2)} = v_{ix}^{(t-\Delta t/2)} \left( \frac{M_{ix}/\Delta t - C_{ix}/2}{M_{ix}/\Delta t + C_{ix}/2} \right) + R_{ix}^t \left( \frac{1}{M_{ix}/\Delta t + C_{ix}/2} \right) \quad . \quad (6)$$

Using Equation 6 the displacement of joint  $i$  in the  $x$  direction during time interval from  $t$  to  $(t + \Delta t)$  is given by:

$$\Delta x_i^{(t+\Delta t)} = \Delta t \cdot v_{ix}^{(t+\Delta t/2)} \quad , \quad (7)$$

and the current coordinates may be expressed as

$$x_i^{(t+\Delta t)} = x_i^t + \Delta t \cdot v_{ix}^{(t+\Delta t/2)} \quad . \quad (8)$$

Similar equations can be written for the  $y$  and  $z$  coordinate directions. In Equation 6 the residual forces can be calculated from the contribution of each element connected to joint  $i$  as:

$$R_{ix}^{(t+\Delta t)} = F_{ix} + \sum_m T_{ixm}^{(t+\Delta t)} \quad , \quad (9)$$

where  $m$  represent the indices of all elements connected to joint  $i$ ,  $F_i$  is the applied loading and  $T_i$  is the internal forces.

## 2.1 The general iteration of the dynamic relaxation method

The general iteration of the dynamic relaxation method contains the following steps:

- Calculation of the out of balance force (residuals) at each node of the structure using Equation 9;
- Calculation of the nodal velocities using Equation 6;

- Calculation of the coordinates of the nodes using Equation 8; and
- Check convergence, for example the kinetic energy is smaller than a threshold ( $U_k \leq U_\varepsilon$ ).

The kinetic energy can be calculated as:

$$U_k = \sum_i^n \sum_j^m M_{ij} v_{ij}^2, \quad (10)$$

where  $n$  is the number of nodes and  $m$  is the number of dimensions.

## 2.2 Control of the method

To ensure the initial conditions ( $v_{ix}^0 = 0$  and  $R_{ix}^0 = F_{ix}$ ) the velocity at time  $\Delta t/2$  must be given by:

$$v_{ix}^{(\Delta t/2)} = \frac{\Delta t}{2M_{ix}} F_{ix}, \quad (11)$$

where  $F_{ix}$  is the initial external force at joint  $i$  in the  $x$  coordinate direction. The controlling parameters for the stability of the method are:

- the nodal mass components which may be fictitious;
- the damping factor; and
- the time interval.

Further details about this parameters can be found in [4].

Kinetic damping is an alternative to viscous damping and the kinetic energy of the complete structure is traced as the undamped oscillations proceed and all current nodal velocities are reset to zero whenever an energy peak is detected [4].

## 3 PARALLEL DYNAMIC RELAXATION WITH MPI

The parallel implementation of the dynamic relaxation algorithm has been investigated in the past [2, 3, 4]. These papers have concluded that geometric parallelism offers the best opportunity for parallelization of the method. Geometric parallelism takes advantage of solving subregions of the structure on a distributed array of processors. Figure 1 shows a partial view of the partitioning of a finite element mesh. The figure shows that the elements are distributed between the partitions, while the nodes on the boundary are duplicated in the partitions. Values at these nodes must be communicated between the partitions, which is also marked in the figure. The parallel algorithm of the dynamic relaxation is organized in such a way, that only the partial contribution of the sum of the forces at the boundary nodes are exchanged. Once the total forces at every node in every

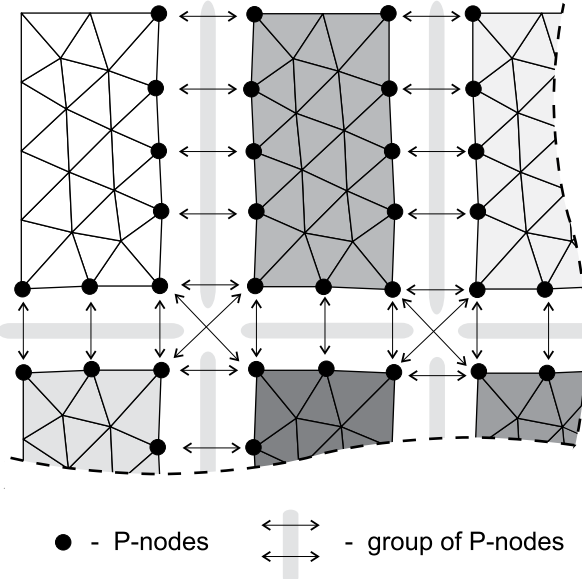


**Figure 1:** Element based partitioning of a finite element mesh and the required communications between partitions.

partition are known then all other values can be calculated in the partition independently according to Equations 6 and 8. Another communication is also required when the total kinetic energy of the structure must be determined. The iteration for parallel computation with the communication steps can be seen in Figure 2a.

#### 4 PARALLEL DYNAMIC RELAXATION WITH GPU

Rek and Němec [6] have presented a parallel implementation for the GPU architecture. In their implementation they still use the element based partitioning, but they had to pay attention to the synchronization between the block of threads on the GPU. They have created two kernels for the GPU. The first kernel calculates the internal and external forces while the second kernel calculates the equation of motion. The division of the kernels is due to the same reason as it was discussed in Section 3, where after the calculation of the residuals they are communicated between the processes. In the case of a GPU the main synchronization possibility between the threads is to quit the kernel, execute some code on the CPU and start the new kernel to calculate the velocities and coordinates with the already known residuals.

This paper presents a different approach. To explain the reason behind this different approach Listing 1 shows a code snippet from the dynamic relaxation method. In the code the loop iterates over all cable elements and their internal force is added to the residual vector. From the code it can be seen that at lines 28 and 29 there would be a

race condition on a shared memory architecture system, since all elements connecting to node  $n1$  and  $n2$  would add its contribution to the residual vector and it is not possible to determine in what order the threads will do the adding. Theoretically this can be solved by introducing a critical section around this part of the code, however a critical section requires synchronization between the threads. Unfortunately on the GPU architecture synchronization is only possible between a block of threads or by quitting the GPU kernel and then restarting another kernel.

**Listing 1:** Calculation of residuals for every cable element

```

1  for(i = 0; i < nelems; i++)
2  {
3      /* node numbers of the cable element */
4      n1 = nodes[i][0]-1;
5      n2 = nodes[i][1]-1;
6
7      /* determine current length and length components */
8      link_length = 0.0;
9      for(k = 0; k < dimension; k++)
10     {
11         dl[k] = (coords[n2][k] - coords[n1][k]);
12         link_length += dl[k] * dl[k];
13     }
14     link_length = sqrt(link_length);
15
16     young = material[i]->YMod;    /* Young's modulus*/
17     area = material[i]->dParam1; /* area of cross section */
18     deltal = link_length - init_length[i];
19     /* determine internal force */
20     force = deltal * young * area / init_length[i];
21
22     for(k = 0; k < dimension; k++)
23     {
24         /* determine force components in directions X, Y and Z */
25         dr = dl[k] * force / link_length;
26
27         /* add component forces to both nodes of the element */
28         residual[n1][k] += dr;
29         residual[n2][k] -= dr;
30     }
31 }

```

To avoid this synchronization problem, in the proposed approach of this paper a similar loop would iterate through all nodes. Listing 2 shows the code snippet of this node oriented loop, which should be compared to Listing 1. On the GPU architecture this loop would translate to the situation where one thread handles one iteration of the loop, specifically one node of the finite element mesh. In this case there is no race condition since at lines 35 and 36 the force contribution is added only to the current node ( $j$ ) and no other thread is

writing to the same position in the residual vector. This approach allows to have a single GPU kernel which calculates the residuals, velocities and coordinates together.

It is important, that in this case the internal forces of the elements are calculated as many times as the number of nodes of the element, which means recalculation of certain values on different threads. For example in the case of a cable element node 11 belongs to thread 157 and node 24 belongs to thread 231, then both threads (157 and 231) will read material data of the element and calculate the stiffness of the element and determine the internal force of the cable element. Thread 157 will update the residual vector for node 11 and thread 231 will update the residual vector for node 24 respectively. Although it seems very inefficient, but theoretically this double calculation should not be a problem since the GPU architecture is designed for throughput-oriented calculation, where calculation is cheaper than accessing the memory or synchronize.

**Listing 2:** Calculation of residuals for all nodes considering only cable elements

```

1  for(j = 0; j < nnode; j++)
2  {
3      /* number of elements connected to node j */
4      ne = n_node_elem[j];
5      /* go thorough all elements connected to node j */
6      for(ie = 0; ie < ne; ie++)
7      {
8          /* element index connected to node j */
9          i = node_elem[j][ie];
10
11         /* node numbers of cable element i */
12         n1 = nodes[i][0]-1;
13         n2 = nodes[i][1]-1;
14
15         /* determine current length and components */
16         ...
17
18         /* determine internal force */
19         ...
20
21         for(k = 0; k < dimension; k++)
22         {
23             /* determine force components in X, Y and Z direction */
24             dr = dl[k] * force / link_length;
25
26             /* add component forces only to node j */
27             if(j == n1) residual[n1][k] += dr;
28             if(j == n2) residual[n2][k] -= dr;
29         }
30     }
31 }

```

#### 4.1 Summation of kinetic energy on GPU

Once the residual forces, the velocities and the new coordinates of all points have been calculated then the total kinetic energy must be determined. One approach would be to copy the mass and velocity of all nodes back to the memory of the CPU, however this communication would reduce the efficiency of the algorithm. Another approach would be to perform the summation of the kinetic energy on the GPU since all data is available in the memory of the GPU. A highly optimised implementation of the parallel reduction on GPUs is available [7], therefore this very efficient version of the reduction is used in this research.

#### 4.2 General iteration of dynamic relaxation on GPU

Figure 2b shows the general iteration of the parallel dynamic relaxation method for the GPU architecture. In the figure the shaded boxes denote kernel functions executed on the GPU and all other operations are executed on the CPU. The `kernel_step` function performs the residual, velocity and coordinate calculations at one node of the finite element mesh on the GPU. When the kernel exits, there is a barrier, therefore all threads will finish their calculation together. The `kernel_reduction` function sums up the total kinetic energy on the GPU. At the end of this kernel a single floating point value must be copied back from the GPU to the CPU. This energy value will be used to determine whether the method has reached an energy peak or convergence.

### 5 PERFORMANCE OF THE METHOD

The previously presented new implementations of the dynamic relaxation method have been tested on a PC (with Intel Core2 Quad CPU, 2.83GHz, 4GB RAM) with an NVIDIA GeForce GTX 780 graphics card (Compute Capability: 3.5). The operating system is a 64 bit Windows 10 with an NVIDIA driver version 353.62. All programs were compiled with double precision. Unfortunately this is a requirement, since the method does not converge with single precision.

To measure the performance of the implementations a mesh of a cable net is considered in this paper. Figure 3 shows the geometry of this cable net. Further parameters are shown in Table 1, for example the number of vertical and horizontal lines and the total number of cable elements in the mesh. The table shows the sequential execution time of 10000 iterations that is executed on the PC with a single a processor core. The synchronous execution in the table corresponds to the iteration shown in Figure 2b. The table also shows the speedup calculated from the sequential and the synchronous parallel execution time.

### 6 CONCLUSION

This paper has presented a new parallel implementation of the dynamic relaxation method for the GPU architecture. The results are very promising, since even in the case

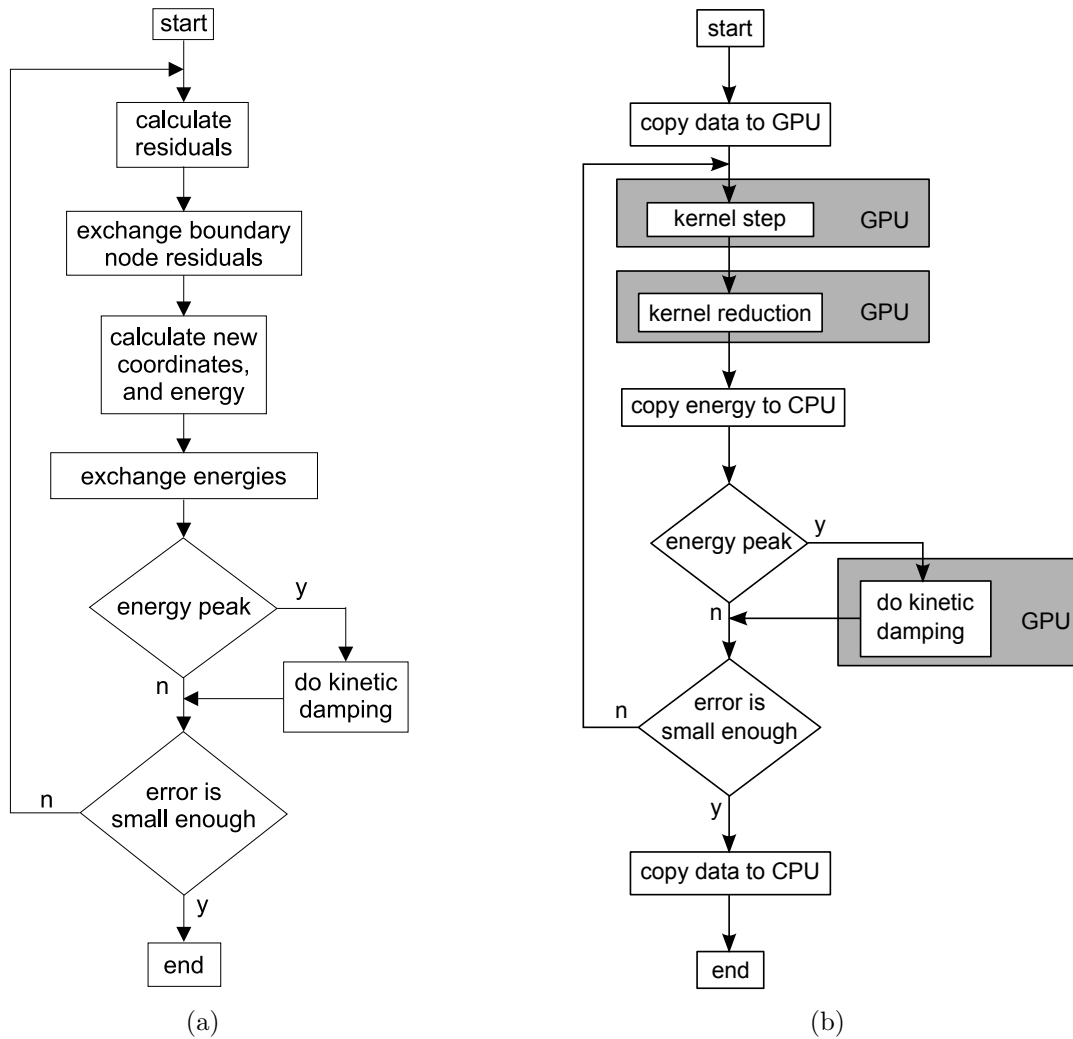


**Figure 2:** (a) Parallel implementation of the dynamic relaxation with the communication steps. (b) Parallel implementation of the dynamic relaxation with GPU.

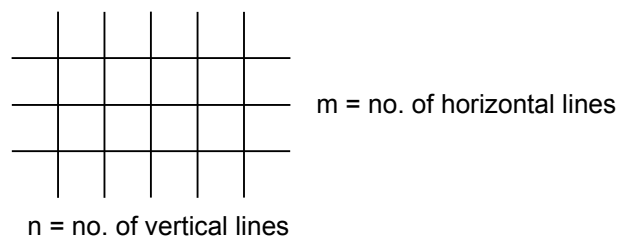


**Figure 3:** The geometry of the example cable grid.

Mesh n x m	No of elements	Sequential execution time	Synchronous execution time	Speedup for synchronous execution [sec]
		[sec]	[sec]	
100x100	19 404	13.65	2.98	4.58
200x200	78 804	62.73	5.38	11.66
300x300	178 204	167.77	9.27	18.10
400x400	317 604	313.02	14.47	21.63
500x500	497 004	491.27	21.54	22.81
600x600	716 404	708.33	30.20	23.45
700x700	975 804	962.69	40.89	23.54
800x800	1 275 204	1254.30	53.68	23.37
900x900	1 614 604	1583.02	68.58	23.08
1000x1000	1 994 004	1946.06	85.58	22.74

**Table 1:** Parameters of the example meshes and the sequential and parallel execution times on the GPU

of two million cable elements the solution can be obtained in approximately 85 seconds on a GPU, instead of running the program for half an hour sequentially.

In the current implementation the CPU is idle. This is very inefficient, therefore one approach for future improvement can be, that the calculation of nodes in one iteration is divided up between the CPU and the GPU. Although it is a promising approach, however in this case more data must be transmitted between the CPU and the GPU and this may reduce the efficiency. This will be a future direction of the research.

Another possibility for the optimization of the method, as usually suggested in the literature, would be the use of the shared memory of the GPU during the calculation, however it will make the code more complex.

## ACKNOWLEDGEMENT

The support of the NVIDIA Corporation for the donation of graphics cards used for this research is gratefully acknowledged. The support of the SmartDiag Research project (PTE Excellence Center) is also acknowledged.

## REFERENCES

- [1] A.S. Day, “An introduction to dynamic relaxation”, *The Engineer*, January, 1965.
- [2] B.H.V. Topping, A.I. Khan, “Parallel computation schemes for dynamic relaxation”, *Engineering Computations*, 11(6): 513–548, 1994.
- [3] B.H.V. Topping, A.I. Khan, *Parallel Finite Element Computations*, Saxe-Coburg Publications, Edinburgh, 1996.

- [4] B.H.V. Topping, P. Iványi, *Computer Aided Design of Cable-Membrane Structures*, Saxe-Coburg Publications, Stirling, 2007.
- [5] Message Passing Interface Forum, “MPI: A Message-Passing Interface Standard”, *International Journal of Supercomputer Applications*, 8(3/4), 1994.
- [6] V. Rek, I. Němec, “Parallel Computing Procedure for Dynamic Relaxation Method on GPU Using NVIDIA’s CUDA”, in *21st International Conference ENGINEERING MECHANICS 2015*, pages 254–255, May 2015.
- [7] M. Harris, “Optimizing Parallel Reduction in CUDA”, Technical report, NVIDIA Developer Technology, 2007.

## MEMBRANE ROOF STRUCTURES

CARSTEN CORTE

Baustatik – Baudynamik – Numerische Modellierung  
Thrasoltstraße 12, D-10585 Berlin, Tel. / Fax +49-(0)30-347 871 78 / 80

**Key words:** elastic structural membranes, in-plane force equilibrium, static force equilibrium, dynamic force equilibrium, fluid-structure interaction, viscous fluid flow, membrane roof structures.

**Summary.** The governing equations for static structural membrane force equilibrium, for dynamic structural membrane force equilibrium and for transient strongly coupled fluid-structure interaction force equilibrium between structural membranes and viscous (laminar) fluids are presented. The approach for static and dynamic membrane force equilibrium is applied to a square Hypar membrane of 5 m edge length and  $\pm 0.0625$  m vertical corner elevation. Furthermore, a steel cable net roof structure that spans over a museum building of  $88 \text{ m} \times 52.8 \text{ m}$  ground section is computationally represented by a membrane that satisfies stiffness as well as mass conservation in comparison with the steel cable net structure. To obtain sufficient curvature throughout the saddle shaped roof structure two Gaussian bell curves as well as two additional Hyparforms are considered for the overall shape of the cable net, i.e. the computational membrane. The roof structure is exposed to eigenload as well as to external load. Displacement results are shown for the different considered cases. To obtain a more detailed statement on external load due to surrounding flow viscous (laminar) fluid flow around the museum building and across its roof structure is computationally modeled. The procedure to interpolate fluid load onto the structural membrane and vice versa to interpolate structural membrane load onto the adjacent fluid is given.

### 1 INTRODUCTION

Frei [24], [25], [26], [27], [35] invented the membrane state of force equilibrium for the application of roof structures with comparatively small eigenmass per square meter of roof structure. Computational methods to model structural membranes force equilibrium were developed by Weitgespannte Flächentragwerke [38], [21], Zerning [42], Bubner [9], Weitgespannte Flächentragwerke [39], Bubner et al. [10], Brinkmann [7]. Reviews on structural membrane structures are given by Drew [22], [23], Hoppe [30], Berger [3], Schock [36], Renner [34], Apelman et al. [1], Göppert [28], Cremers et al. [20], Seel et al. [37]. Neuhäuser et al. [33] show adaptive lightweight structures. Sophisticated numerical methods are developed by Trostel [26], Linkwitz et al. [32], Bufler [11], Bletzinger et al. [5], [6], [4], Wüchner et al. [40] with form finding of membrane structures by Wüchner [41], Linhard [31]. Corte et al. [12], [13] and Corte [14] show mutual force equilibrium based on weak [12] and strong [13], [14] coupling of fluid-structure interaction between elastic structures and viscous fluids. Corte [15], [16], [17] shows a consistent approach on fluid-structure interaction for large deformation with evaluation [15], [16] and application to a 3D elastic sail structure [17].

Corte [18], [19] shows a consistent computational approach for static and dynamic structural force equilibrium of elastic membrane structures.

As membrane roof structures generally possess curved shape it is difficult to define realistic dynamic load distribution due to surrounding fluid flow. The aim is to perform static membrane force equilibrium computations as well as dynamic membrane force equilibrium computations and to show the respective performance. With the next level of model complexity, surrounding viscous fluid flow around a considered structure is taken into account. Viscous fluid flow computations allow access to local fluid load onto the membrane roof structure and thus access to assessment of overall (transient) fluid load onto the considered membrane structure for design purpose.

## 2 COMPUTATIONAL APPROACH

### 2.1 Structural membrane force equilibrium

The computational model for the structural membrane approach applied here is explained in Corte [18], [19]. Along a spatial parameter coordinate system of  $\xi$  and  $\eta$  the undeformed stress-free shape of a considered membrane surface is defined by cartesian coordinates  $[{}^0x(\xi,\eta), {}^0y(\xi,\eta), {}^0z(\xi,\eta)]$  together with its three-dimensional cartesian displacement  $[{}^{t+\Delta t}u_{Sx}(\xi,\eta), {}^{t+\Delta t}u_{Sy}(\xi,\eta), {}^{t+\Delta t}u_{Sz}(\xi,\eta)]$  at a considered state  $t+\Delta t$ . The tensile force equilibrium within the membrane can be expressed with reference to the undeformed state 0 of the membrane (2<sup>nd</sup> Piola-Kirchhoff stress, Green-Langrange strain) or with reference to the deformed stress-carrying state  $t+\Delta t$  (Cauchy stress, Euler-Almansi strain), Bletzinger [4]; see Bathe [2] for detailed expressions on the definitions of the different stress and strain measures. The dynamic force equilibrium for structural membranes is here given in its form of virtual work expression as

$$\begin{aligned} & \iint [S_{\xi\xi}(\xi,\eta); S_{\eta\eta}(\xi,\eta); S_{\xi\eta}(\xi,\eta)] \bullet [\delta\varepsilon_{\xi\xi}(\xi,\eta); \delta\varepsilon_{\eta\eta}(\xi,\eta); \delta\varepsilon_{\xi\eta}(\xi,\eta)]^T dA(\xi,\eta) dx_{\text{normal}}(\xi,\eta) \\ = & \iint \{ \rho_S \cdot [\ddot{u}_{Sx}(\xi,\eta); \ddot{u}_{Sy}(\xi,\eta); \ddot{u}_{Sz}(\xi,\eta)] \bullet [\delta u_x(\xi,\eta); \delta u_y(\xi,\eta); \delta u_z(\xi,\eta)]^T \\ & + [f_{Sx}^{\text{ext}}(\xi,\eta); f_{Sy}^{\text{ext}}(\xi,\eta); f_{Sz}^{\text{ext}}(\xi,\eta)] \bullet [\delta u_x(\xi,\eta); \delta u_y(\xi,\eta); \delta u_z(\xi,\eta)]^T \} dA(\xi,\eta) dx_{\text{normal}}(\xi,\eta) \end{aligned} \quad (1)$$

where nonlinear membrane stresses are defined as

$$\begin{aligned} S_{\xi\xi}(\xi,\eta); & \quad [[C_{1111}; C_{1122}; C_{1112}]; \quad [\varepsilon_{\xi\xi}(\xi,\eta); \\ S_{\eta\eta}(\xi,\eta); & \quad [C_{2211}; C_{2222}; C_{2212}]; \quad \bullet \quad \varepsilon_{\eta\eta}(\xi,\eta); \\ S_{\xi\eta}(\xi,\eta)] & \quad [C_{1211}; C_{1222}; C_{1212}]] \quad \varepsilon_{\eta\xi}(\xi,\eta) \end{aligned} \quad (2)$$

with  $[[C_{1111}; C_{1122}; C_{1112}]; [C_{2211}; C_{2222}; C_{2212}]; [C_{1211}; C_{1222}; C_{1212}]]$  constant elasticity tensor for linear elastic material and nonlinear strain defined as

$$\begin{aligned} \varepsilon_{\xi\xi}(\xi,\eta); & \quad [[\partial u_\xi(\xi,\eta)/\partial x_\xi(\xi,\eta) + 1/2 \{ \partial u_\xi(\xi,\eta)/\partial x_\xi(\xi,\eta) \}^2 + 1/2 \{ \partial u_\eta(\xi,\eta)/\partial x_\xi(\xi,\eta) \}^2; \\ \varepsilon_{\eta\eta}(\xi,\eta); & \quad [\partial u_\eta(\xi,\eta)/\partial x_\eta(\xi,\eta) + 1/2 \{ \partial u_\xi(\xi,\eta)/\partial x_\eta(\xi,\eta) \}^2 + 1/2 \{ \partial u_\eta(\xi,\eta)/\partial x_\eta(\xi,\eta) \}^2; \\ \varepsilon_{\xi\eta}(\xi,\eta)] & \quad \{ \partial u_\xi(\xi,\eta)/\partial x_\eta(\xi,\eta) + \partial u_\eta(\xi,\eta)/\partial x_\xi(\xi,\eta) \\ & \quad + \partial u_\xi(\xi,\eta)/\partial x_\xi(\xi,\eta) + \partial u_\xi(\xi,\eta)/\partial x_\eta(\xi,\eta) \\ & \quad + \partial u_\eta(\xi,\eta)/\partial x_\xi(\xi,\eta) + \partial u_\eta(\xi,\eta)/\partial x_\eta(\xi,\eta) \} \end{aligned} \quad (3)$$

( $\rho_s$ : structural density). Tangential vectors of the membrane surface along the spatial membrane parameter coordinates  $\xi$  and  $\eta$  are defined as  ${}^0g_\xi(\xi,\eta)=\partial[{}^0x(\xi,\eta), {}^0y(\xi,\eta), {}^0z(\xi,\eta)]/\partial\xi$  and  ${}^0g_\eta(\xi,\eta)=\partial[{}^0x(\xi,\eta), {}^0y(\xi,\eta), {}^0z(\xi,\eta)]/\partial\eta$  both with respect to the undeformed state 0 of the membrane or as  ${}^{t+\Delta t}g_\xi(\xi,\eta)=\partial[{}^{t+\Delta t}x(\xi,\eta), {}^{t+\Delta t}y(\xi,\eta), {}^{t+\Delta t}z(\xi,\eta)]/\partial\xi$  and  ${}^{t+\Delta t}g_\eta(\xi,\eta)=\partial[{}^{t+\Delta t}x(\xi,\eta), {}^{t+\Delta t}y(\xi,\eta), {}^{t+\Delta t}z(\xi,\eta)]/\partial\eta$  both with respect to the deformed state  $t+\Delta t$  of the membrane. Appropriately the respective normal vector onto the membrane surface is defined as  ${}^0g_{\text{normal}}(\xi,\eta)={}^0g_\xi(\xi,\eta)\times{}^0g_\eta(\xi,\eta)$  with respect to the undeformed state 0 of the membrane or as  ${}^{t+\Delta t}g_{\text{normal}}(\xi,\eta)={}^{t+\Delta t}g_\xi(\xi,\eta)\times{}^{t+\Delta t}g_\eta(\xi,\eta)$  with respect to the deformed state  $t+\Delta t$  of the membrane. With the above definitions displacement in local  $\xi$  and local  $\eta$  membrane direction is defined as  ${}^{t+\Delta t}{}_0u_\xi(\xi,\eta)=[{}^{t+\Delta t}u_{s_x}(\xi,\eta), {}^{t+\Delta t}u_{s_y}(\xi,\eta), {}^{t+\Delta t}u_{s_z}(\xi,\eta)]\bullet{}^0g_\xi(\xi,\eta)$  and  ${}^{t+\Delta t}{}_0u_\eta(\xi,\eta)=[{}^{t+\Delta t}u_{s_x}(\xi,\eta), {}^{t+\Delta t}u_{s_y}(\xi,\eta), {}^{t+\Delta t}u_{s_z}(\xi,\eta)]\bullet{}^0g_\eta(\xi,\eta)$  with respect to the undeformed state 0 as well as  ${}^{t+\Delta t}{}_{t+\Delta t}u_\xi(\xi,\eta)=[{}^{t+\Delta t}u_{s_x}(\xi,\eta), {}^{t+\Delta t}u_{s_y}(\xi,\eta), {}^{t+\Delta t}u_{s_z}(\xi,\eta)]\bullet{}^{t+\Delta t}g_\xi(\xi,\eta)$  and  ${}^{t+\Delta t}{}_{t+\Delta t}u_\eta(\xi,\eta)=[{}^{t+\Delta t}u_{s_x}(\xi,\eta), {}^{t+\Delta t}u_{s_y}(\xi,\eta), {}^{t+\Delta t}u_{s_z}(\xi,\eta)]\bullet{}^{t+\Delta t}g_\eta(\xi,\eta)$  with respect to the deformed state  $t+\Delta t$ , respectively. Within equation (1) the *virtual* strain expressions are assumed to be the linear part of strain defined in equation (3); so equation (1) becomes unique in unknowns  $[{}^{t+\Delta t}u_{s_x}(\xi,\eta), {}^{t+\Delta t}u_{s_y}(\xi,\eta), {}^{t+\Delta t}u_{s_z}(\xi,\eta)]$  at a considered state  $t+\Delta t$ . The analytic expression for the membrane area differential is  $d^0A(\xi,\eta)={}^0g_\xi(\xi,\eta)\times{}^0g_\eta(\xi,\eta)d\xi d\eta$  and  $d{}^{t+\Delta t}A(\xi,\eta)={}^{t+\Delta t}g_\xi(\xi,\eta)\times{}^{t+\Delta t}g_\eta(\xi,\eta)d\xi d\eta$ , respectively.  ${}^0x_{\text{normal}}(\xi,\eta)$  and  ${}^{t+\Delta t}x_{\text{normal}}(\xi,\eta)$ , respectively, is membrane thickness at state 0 and state  $t+\Delta t$ , respectively.

Equation (1) describes the general dynamic membrane force equilibrium. In case the mass (inertia) term  $\int\int\rho_s\cdot[\ddot{u}_{s_x}(\xi,\eta); \ddot{u}_{s_y}(\xi,\eta); \ddot{u}_{s_z}(\xi,\eta)]\bullet[\delta u_x(\xi,\eta); \delta u_y(\xi,\eta); \delta u_z(\xi,\eta)]^T dA(\xi,\eta)x_{\text{normal}}(\xi,\eta)$  in equation (1) is neglected then the general static membrane force equilibrium is described. For the applied finite element approach the considered continuous membrane domain is spatially discretized by discrete 3D nodes with nodal 3D displacement  $[u_{s_x}, u_{s_y}, u_{s_z}]$  and by 9-node-4-corner finite elements with interpolation functions that have quadratic polynomials in  $\xi$  and quadratic polynomials in  $\eta$ , Corte [18], [19]. In time direction discretization is performed by the HHT- $\alpha$  method (Hilber et al. [29]), Corte [18], [19].

## 2.2 Viscous laminar fluid force equilibrium and fluid incompressibility

To obtain access to action of the surrounding flow around the considered structure and in particular across the considered membrane roof structure (here laminar) viscous fluid flow is described by the incompressible Navier-Stokes equation that is expressed as

$$\begin{aligned} &[\rho_F\partial u_x/\partial t+\rho_F u_x\partial u_x/\partial x+\rho_F u_y\partial u_x/\partial y+\rho_F u_z\partial u_x/\partial z-\mu_F(\partial^2 u_x/\partial x^2+\partial^2 u_x/\partial y^2+\partial^2 u_x/\partial z^2)+\partial p_F/\partial x; \\ &\rho_F\partial u_y/\partial t+\rho_F u_x\partial u_y/\partial x+\rho_F u_y\partial u_y/\partial y+\rho_F u_z\partial u_y/\partial z-\mu_F(\partial^2 u_y/\partial x^2+\partial^2 u_y/\partial y^2+\partial^2 u_y/\partial z^2)+\partial p_F/\partial y; \\ &\rho_F\partial u_z/\partial t+\rho_F u_x\partial u_z/\partial x+\rho_F u_y\partial u_z/\partial y+\rho_F u_z\partial u_z/\partial z-\mu_F(\partial^2 u_z/\partial x^2+\partial^2 u_z/\partial y^2+\partial^2 u_z/\partial z^2)+\partial p_F/\partial z] \mathbf{f}_{Fz}^{\text{ext}} \end{aligned} \quad (4)$$

with the incompressibility demand

$$\partial u_x/\partial x+\partial u_y/\partial y+\partial u_z/\partial z=0 \quad (5)$$

( $[u_x, u_y, u_z]$ : fluid velocity,  $\rho_F$ : fluid density,  $\mu_F$ : fluid (dynamic) viscosity).

Equations (4) and (5) are both discretized in space direction with discrete 3D fluid node and  $[u_x, u_y, u_z, p_F]$  as nodal unknowns fluid velocity cartesian components and fluid pressure and 8-node hexahedra elements with linear interpolation functions in each elementwise local coordinate  $\xi$ ,  $\eta$  and  $\zeta$  direction. In equation (4) for time discretization the Euler backwards (one-step) method is applied. For consideration of the flow direction that becomes of importance in the convective terms of equation (4) appropriate artificial diffusion is introduced within the convective terms of equation (4). The artificial diffusion is considered componentwise in x-, in y- and in z-direction following the componentwise 1D analytic expression  $[u_x h_x / 2 \cdot \coth(u_x h_x / (2\mu_F)); u_y h_y / 2 \cdot \coth(u_y h_y / (2\mu_F)); u_z h_z / 2 \cdot \coth(u_z h_z / (2\mu_F))]$ ,  $h_x: \max |x_i - x_j|$ ,  $h_y: \max |y_i - y_j|$ ,  $h_z: \max |z_i - z_j|$ ,  $i \neq j$ ,  $i, j = 1 \dots 8$ : element's local nodes' indices, that is shown in Brooks and Hughes [8]. Equation (4) is solved componentwise for fluid velocity components  $[u_x, u_y, u_z]$  at the new timestep of a considered discrete time interval, assuming an up-to-then known pressure distribution within the fluid domain. With the incompressibility demand in equation (5) that is inserted into equation (4) the resulting equation [(5) in (4)] is then solved for the pressure at the new timestep of the considered discrete time interval, using the already-computed fluid velocity field  $[u_x, u_y, u_z]$  that was obtained from solving equation (4). By computing the pressure at the new timestep from equation [(5) in (4)] the before-assumed pressure distribution for solving equation (4) is corrected in that particular way that the computed-by-equation (4) fluid velocity for the new timestep is incompressible regarding the computed-by-equation [(5) in (4)] pressure distribution at the new timestep. Within a considered discrete time interval there are iterations performed on the sequence of solving equation (4) for the fluid velocity at the new timestep and then solving equation [(5) in (4)] for the fluid pressure at the new timestep. It is remarked here that by using equation [(5) in (4)] to obtain the appropriate fluid pressure distribution at the new timestep the full incompressibility demand is kept. No weakening of the incompressibility demand equation (5) is introduced into the computational approach during discretization.

### **2.3 Fluid-structure interaction between elastic structural membrane and viscous laminar fluid with fluid incompressibility**

The fluid-structure interaction between elastic structural membranes and viscous (here laminar) fluids with fluid incompressibility is achieved by strong segregated coupling of fluid forces onto the structure and structural forces onto the fluid across the common fluid-structure interface that both elastic membrane structure and viscous fluid share with each other. In the application that is treated here the common fluid-structure interface consists of the considered structural membrane and the fluid boundary that is adjacent to the structural membrane. Due to the curved shape of the respective structural membrane and due to the wide-range fluid environment around the considered structure for the membrane spatial finite element discretization and the fluid domain spatial finite element discretization on the fluid-structure interface two different non-matching node distributions are used for the structural membrane on the one hand side and the fluid domain on the other hand side.

The equation that describes the dynamic structural membrane force equilibrium is extended to consider fluid load in addition to other external load onto the structure, i.e. equation (1) is extended to

$$\begin{aligned}
 & \iint [S_{\xi\xi}(\xi,\eta); S_{\eta\eta}(\xi,\eta); S_{\xi\eta}(\xi,\eta)] \bullet [\delta\varepsilon_{\xi\xi}(\xi,\eta); \delta\varepsilon_{\eta\eta}(\xi,\eta); \delta\varepsilon_{\xi\eta}(\xi,\eta)]^T dA(\xi,\eta) dx_{\text{normal}}(\xi,\eta) \\
 = & \iint \{ \rho_S \cdot [\ddot{u}_{Sx}(\xi,\eta); \ddot{u}_{Sy}(\xi,\eta); \ddot{u}_{Sz}(\xi,\eta)] \bullet [\delta u_x(\xi,\eta); \delta u_y(\xi,\eta); \delta u_z(\xi,\eta)]^T \\
 & + [f_{Sx}^{\text{ext}}(\xi,\eta); f_{Sy}^{\text{ext}}(\xi,\eta); f_{Sz}^{\text{ext}}(\xi,\eta)] \bullet [\delta u_x(\xi,\eta); \delta u_y(\xi,\eta); \delta u_z(\xi,\eta)]^T \} dA(\xi,\eta) dx_{\text{normal}}(\xi,\eta) \\
 - & \{ \iiint \\
 & [\rho_F \partial u_x / \partial t + \rho_F u_x \partial u_x / \partial x + \rho_F u_y \partial u_x / \partial y + \rho_F u_z \partial u_x / \partial z - \mu_F (\partial^2 u_x / \partial x^2 + \partial^2 u_x / \partial y^2 + \partial^2 u_x / \partial z^2) + \partial p_F / \partial x; [w_x; \\
 & \rho_F \partial u_y / \partial t + \rho_F u_x \partial u_y / \partial x + \rho_F u_y \partial u_y / \partial y + \rho_F u_z \partial u_y / \partial z - \mu_F (\partial^2 u_y / \partial x^2 + \partial^2 u_y / \partial y^2 + \partial^2 u_y / \partial z^2) + \partial p_F / \partial y; \bullet w_y; \\
 & \rho_F \partial u_z / \partial t + \rho_F u_x \partial u_z / \partial x + \rho_F u_y \partial u_z / \partial y + \rho_F u_z \partial u_z / \partial z - \mu_F (\partial^2 u_z / \partial x^2 + \partial^2 u_z / \partial y^2 + \partial^2 u_z / \partial z^2) + \partial p_F / \partial z] w_z] \\
 & - [f_{Fx}^{\text{ext}}; [w_x; \\
 & f_{Fy}^{\text{ext}}; \bullet w_y; \\
 & f_{Fz}^{\text{ext}}] w_z] \\
 & \} dx(\xi,\eta,\zeta) dy(\xi,\eta,\zeta) dz(\xi,\eta,\zeta)
 \end{aligned} \tag{6}$$

on the shared common fluid-structure interface ( $w_x, w_y, w_z$ : weighing functions for x-, y- and z-fluid forces).

On the other hand the equation that describes the fluid force equilibrium is extended to consider structural load in addition to other external load onto the fluid, i.e. equation (4) is extended to (weighed weak integral form here)

$$\begin{aligned}
 & \{ \iiint \\
 & [\rho_F \partial u_x / \partial t + \rho_F u_x \partial u_x / \partial x + \rho_F u_y \partial u_x / \partial y + \rho_F u_z \partial u_x / \partial z - \mu_F (\partial^2 u_x / \partial x^2 + \partial^2 u_x / \partial y^2 + \partial^2 u_x / \partial z^2) + \partial p_F / \partial x; [w_x; \\
 & \rho_F \partial u_y / \partial t + \rho_F u_x \partial u_y / \partial x + \rho_F u_y \partial u_y / \partial y + \rho_F u_z \partial u_y / \partial z - \mu_F (\partial^2 u_y / \partial x^2 + \partial^2 u_y / \partial y^2 + \partial^2 u_y / \partial z^2) + \partial p_F / \partial y; \bullet w_y; \\
 & \rho_F \partial u_z / \partial t + \rho_F u_x \partial u_z / \partial x + \rho_F u_y \partial u_z / \partial y + \rho_F u_z \partial u_z / \partial z - \mu_F (\partial^2 u_z / \partial x^2 + \partial^2 u_z / \partial y^2 + \partial^2 u_z / \partial z^2) + \partial p_F / \partial z] w_z] \\
 & - [f_{Fx}^{\text{ext}}; [w_x; \\
 & f_{Fy}^{\text{ext}}; \bullet w_y; \\
 & f_{Fz}^{\text{ext}}] w_z] \\
 & \} dx(\xi,\eta,\zeta) dy(\xi,\eta,\zeta) dz(\xi,\eta,\zeta) \\
 - & \{ \\
 & \iint [S_{\xi\xi}(\xi,\eta); S_{\eta\eta}(\xi,\eta); S_{\xi\eta}(\xi,\eta)] \bullet [\delta\varepsilon_{\xi\xi}(\xi,\eta); \delta\varepsilon_{\eta\eta}(\xi,\eta); \delta\varepsilon_{\xi\eta}(\xi,\eta)]^T dA(\xi,\eta) dx_{\text{normal}}(\xi,\eta) \\
 - & \iint \{ \rho_S \cdot [\ddot{u}_{Sx}(\xi,\eta); \ddot{u}_{Sy}(\xi,\eta); \ddot{u}_{Sz}(\xi,\eta)] \bullet [\delta u_x(\xi,\eta); \delta u_y(\xi,\eta); \delta u_z(\xi,\eta)]^T \\
 & + [f_{Sx}^{\text{ext}}(\xi,\eta); f_{Sy}^{\text{ext}}(\xi,\eta); f_{Sz}^{\text{ext}}(\xi,\eta)] \bullet [\delta u_x(\xi,\eta); \delta u_y(\xi,\eta); \delta u_z(\xi,\eta)]^T \} dA(\xi,\eta) dx_{\text{normal}}(\xi,\eta) \\
 & \} = [0;0;0]^T
 \end{aligned} \tag{7}$$

on the shared common fluid-structure interface, where the fluid incompressibility demand equation (5) in its analytic form stays the same, i.e. stays

$$\partial u_x / \partial x + \partial u_y / \partial y + \partial u_z / \partial z = 0 \tag{8}$$

on the shared common fluid-structure interface.

Because of – as mentioned above – the non-matching two different meshes for the structural side and the fluid side an interpolation procedure becomes necessary to interpolate fluid force data onto positions of structural nodes and vice versa to interpolate structural force data onto positions of fluid nodes. The two directions (fluid  $\rightarrow$  structure; structure  $\rightarrow$  fluid) of interpolation procedure involve determination of intrinsic local coordinates  $\xi$  and  $\eta$  and thus solving (nonlinear) equation systems for the purpose of exact load transfer from the fluid onto the structure and from the structure onto the fluid. The solution to obtain exact intrinsic local coordinates  $\xi$  and  $\eta$  is satisfied by the two interpolation procedures

Find  $(\xi_F, \eta_F)$ :

$$\{F_F(\xi_F, \eta_F) = | [p_x^{\text{Structure}}, p_y^{\text{Structure}}, p_z^{\text{Structure}}] - \sum_{i=1...4} [p_{i,x}^{\text{Fluid}}, p_{i,y}^{\text{Fluid}}, p_{i,z}^{\text{Fluid}}] \cdot N_i^{\text{Fluid}}(\xi_F, \eta_F) | \\ = \text{minimum}\} \wedge \{\xi_F \in [-1;1]\} \wedge \{\eta_F \in [-1;1]\}.$$

$([p_x^{\text{Structure}}, p_y^{\text{Structure}}, p_z^{\text{Structure}}])$ : considered structural node,  $[p_{i,x}^{\text{Fluid}}, p_{i,y}^{\text{Fluid}}, p_{i,z}^{\text{Fluid}}]$ ,  $i=1...4$ : fluid element's surface nodes,  $N_i^{\text{Fluid}}(\xi_F, \eta_F)$ ,  $i=1...4$ : bilinear fluid nodes' interpolation functions on appropriate fluid element's surface) for to interpolate fluid force data onto the considered structural mesh node and

Find  $(\xi_S, \eta_S)$ :

$$\{F_S(\xi_S, \eta_S) = | [p_x^{\text{Fluid}}, p_y^{\text{Fluid}}, p_z^{\text{Fluid}}] - \sum_{i=1...9} [p_{i,x}^{\text{Structure}}, p_{i,y}^{\text{Structure}}, p_{i,z}^{\text{Structure}}] \cdot N_i^{\text{Structure}}(\xi_S, \eta_S) | \\ = \text{minimum}\} \wedge \{\xi_S \in [-1;1]\} \wedge \{\eta_S \in [-1;1]\}.$$

$([p_x^{\text{Fluid}}, p_y^{\text{Fluid}}, p_z^{\text{Fluid}}])$ : considered fluid node,  $[p_{i,x}^{\text{Structure}}, p_{i,y}^{\text{Structure}}, p_{i,z}^{\text{Structure}}]$ ,  $i=1...9$ : structural element's nodes,  $N_i^{\text{Structure}}(\xi_S, \eta_S)$ ,  $i=1...9$ : binonlinear structural nodes' interpolation functions) for to interpolate structural force data onto the considered fluid mesh node. The interpolation procedure of fluid force data onto the structural mesh is linear in  $(\xi_F, \eta_F)$  (8-node hexahedra fluid elements, linear interpolation functions) whereas the interpolation procedure of structural data onto the fluid mesh is nonlinear in  $(\xi_S, \eta_S)$  (9-node-4-corner structural membrane elements, quadratic interpolation functions, Corte [18], [19]).  $\partial F_F(\xi_F, \eta_F)/\partial \xi_F = 0$  and  $\partial F_F(\xi_F, \eta_F)/\partial \eta_F = 0$  appropriately deliver  $(\xi_F, \eta_F)$ ,  $\partial F_S(\xi_S, \eta_S)/\partial \xi_S = 0$  and  $\partial F_S(\xi_S, \eta_S)/\partial \eta_S = 0$  appropriately deliver  $(\xi_S, \eta_S)$ .

### 3 HYPARFORM (L=5 M)

A membrane with initial stress-free (displacement and strain equal zero) Hypar shape of 5 m edge length (ground view) and  $\pm 0.0625$  m vertical corner elevation is considered. The membrane is discretized with  $15 \times 15 = 225$  nodes and  $7 \times 7 = 49$  9-node-4-corner finite elements of quadratic interpolation functions.

#### 3.1 Hyparform (L=5 m): Static force equilibrium

The membrane has material properties modulus of elasticity  $E=2.5e7$  N/m<sup>2</sup>, Poisson's ratio  $\nu=0.25$ , density  $\rho=1000$  kg/m<sup>3</sup> and membrane thickness of 0.001 m. Gravity is assumed with 10 m/s<sup>2</sup>. The membrane is exposed to 100 times of its eigenload, i.e. to  $100 \cdot 10$  m/s<sup>2</sup> · 1000 kg/m<sup>3</sup> · 0.001 m = 1000 N/m<sup>2</sup> in (vertical) gravity direction. Boundary conditions define completely fixed displacement ( $u_x=0$ ,  $u_y=0$ ,  $u_z=0$ ) on the four edges of the membrane. In the inner part of the membrane surface, excluding the four boundary edges, case i) horizontal displacement is fixed ( $u_x=0$ ,  $u_y=0$ ) and vertical displacement is free ( $u_z$ : free), case ii) horizontal displacement is free ( $u_x$ : free,  $u_y$ : free) and vertical displacement is free ( $u_z$ : free). For case i) 200 equilibrium iterations, for case ii) 10000 equilibrium iterations are performed. For both case i) and ii) the size of the displacement increment within an equilibrium iteration is limited to 0.01 m as the maximum for one single displacement component ( $u_x$ ,  $u_y$  or  $u_z$ ) of one single node within the all-nodes-covering displacement increment vector. For case i) a

strictly monotonic increase of the vertical displacement at the membrane center (uz of node 201, degree of freedom 603) appears that reaches a value of  $uz=0.16$  m after 200 equilibrium iterations. For case ii) a vertical displacement at the membrane center (uz of node 201, degree of freedom 603) reaches 0.25 m after less than 1000 equilibrium iterations and then stays around 0.25 m for until 10000 equilibrium iterations. The iterative solutions for case i) and ii) and the appropriate membrane undisplaced and displaced shape for case i) and ii) are shown in figure 1.

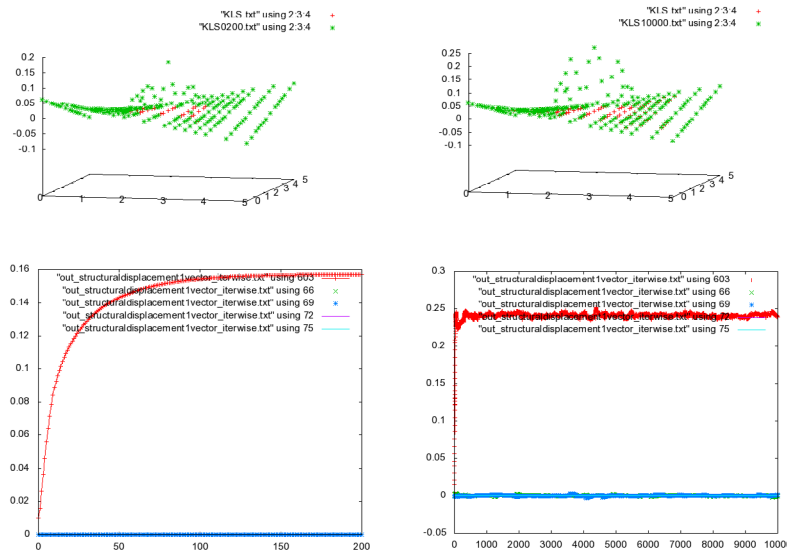


Figure 1: square Hypar membrane ( $L=5$  m),  $\pm 0.0625$  m vertical corner elevation: undeformed and deformed membrane shape (top row) [in m] and membrane center vertical displacement [in m] over cumulated equilibrium iteration index (bottom row) for case i) field displacement [ $u_x=0$ ,  $u_y=0$ ,  $u_z$ : free] within the inner part of the membrane (left column) and for case ii) field displacement [ $u_x$ : free,  $u_y$ : free,  $u_z$ : free] within the inner part of the membrane (right column) (vertical displacement in load direction is plotted upward here (in this figure))

### 3.2 Hyparform ( $L=5$ m): Dynamic force equilibrium

For the three cases iii), iv) and v) transient external load is applied to the membrane in time domain.

For case iii) membrane material properties are  $E=2.5e7$  N/m<sup>2</sup>,  $\nu=0.25$ ,  $\rho=1000$  kg/m<sup>3</sup> and membrane thickness is 0.001 m. Transient harmonic external load ranges from 100 times to 300 times of its eigenload and follows the time-t-dependent function  $[2+\cos(2\pi \cdot 0.1\text{Hz} \cdot t)] \cdot 100 \cdot 10$  m/s<sup>2</sup>  $\cdot 1000$  kg/m<sup>3</sup>  $\cdot 0.001$  m =  $[2+\cos(2\pi \cdot 0.1\text{Hz} \cdot t)] \cdot 1000$  N/m<sup>2</sup> in (vertical) gravity direction with 0.1 Hz oscillation frequency. Time integration is performed for 20 time intervals of 0.5 s constant time interval size with 10 s total time. Within each considered time interval 1000 equilibrium iterations are performed. The HHT- $\alpha$  parameter is selected as  $\alpha_{\text{HHT}}=-0.1$ . The size of the displacement increment is limited to 0.01 m as the maximum for one single displacement component ( $u_x$ ,  $u_y$  or  $u_z$ ) of one single node within the all-nodes-covering displacement increment vector.

For case iv) and v) membrane material properties  $E$ ,  $\nu$  and  $\rho$  are selected to represent a cable-net structure that consists of crosswise orthogonal steel cables of 5 mm=0.005 m diameter (cross-section area  $\pi \cdot (0.0025 \text{ m})^2 \approx 0.00002 \text{ m}^2$ ) of 0.357 m distance from each other. For steel it is set  $E_{\text{Steel}}=2.1 \text{e}11 \text{ N/m}^2$ ,  $\nu_{\text{Steel}}=0.3$ ,  $\rho_{\text{Steel}}=7860 \text{ kg/m}^3$ . So for one square meter of the membrane the membrane mass shall represent one square meter of the steel cable net, and for one meter width of the membrane the membrane stiffness shall represent one meter width of the steel cable net. The computational membrane material parameters  $E$ ,  $\nu$  and  $\rho$  and the membrane thickness  $d$  are derived as follows ( $A$  in  $\text{m}^2/(\text{width in m})$ ,  $A_{\text{Steel}}$  in  $\text{m}^2/(\text{width in m})$ ):

$$EA=E \cdot 1 \text{ m} \cdot d/(1 \text{ m})=E_{\text{Steel}} A_{\text{steel}}$$

$$\nu=\nu_{\text{Steel}}$$

$$\rho_{\text{Steel}}(A_{\text{Steel}} \cdot 1 \text{ m}) \cdot 1 \text{ m} + \rho_{\text{Steel}}(A_{\text{Steel}} \cdot 1 \text{ m}) \cdot 1 \text{ m} = \rho \cdot 1 \text{ m} \cdot 1 \text{ m} \cdot d$$

(longitudinal)                      (orthogonal)                      (1 m<sup>2</sup> membrane)

$$EA=E \cdot 1 \text{ m} \cdot d/(1 \text{ m})=E_{\text{Steel}} A_{\text{steel}}$$

The computational membrane thickness  $d$  is selected here as  $d=1 \text{ mm}=0.001 \text{ m}$ .

$$EA=E \cdot 1 \text{ m} \cdot 0.001 \text{ m}/(1 \text{ m}) \approx 2.1 \text{e}11 \text{ N/m}^2 \cdot 0.00002 \text{ m}^2/(0.357 \text{ m})$$

$$\underline{E \approx [2.1 \text{e}11 \text{ N/m}^2 \cdot 0.00002 \text{ m}^2/(0.357 \text{ m})]/[1 \text{ m} \cdot 0.001 \text{ m}/(1 \text{ m})] \approx 1.175 \text{e}10 \text{ N/m}^2}$$

$$\underline{\nu = \nu_{\text{Steel}} = 0.3}$$

$$\rho \approx [7860 \text{ kg/m}^3 \cdot (0.00002 \text{ m}^2/(0.357 \text{ m}) \cdot 1 \text{ m}) \cdot 1 \text{ m} + 7860 \text{ kg/m}^3 \cdot (0.00002 \text{ m}^2/(0.357 \text{ m}) \cdot 1 \text{ m}) \cdot 1 \text{ m}]/[1 \text{ m} \cdot 1 \text{ m} \cdot d]$$

$$\underline{\rho \approx 2 \cdot [7860 \text{ kg/m}^3 \cdot 0.00002 \text{ m}^2/(0.357 \text{ m}) \cdot 1 \text{ m}^2]/[1 \text{ m}^2 \cdot 0.001 \text{ m}] \approx 880 \text{ kg/m}^3}$$

As a simplification it is assumed here that for case iv) and v) the steel cable net is computationally represented by a membrane that has isotropic material properties ( $E$ ,  $\nu$ ). For cases iii), iv) and v) boundary conditions define completely fixed displacement ( $u_x=0$ ,  $u_y=0$ ,  $u_z=0$ ) on the four edges of the membrane, whereas in the inner part of the membrane surface, excluding the four boundary edges, horizontal displacement is free ( $u_x$ : free,  $u_y$ : free) and vertical displacement is free ( $u_z$ : free). Time integration is performed, case iii) and iv), for 20 time intervals of constant time interval size 0.5 s, 10 s total time, case v) for 235 time intervals of 0.1 s constant time interval size, 23.5 s total time. Within each considered time interval for case iii) 100 equilibrium iterations, for case iv) and v) 1000 equilibrium iterations are performed. The HHT- $\alpha$  parameter is selected as  $\alpha_{\text{HHT}}=-0.1$ . The size of the displacement increment is limited to 0.01 m for case iii) and limited to 0.0001 m for case iv) and v) as the maximum for one single displacement component ( $u_x$ ,  $u_y$  or  $u_z$ ) of one single node within the all-nodes-covering displacement increment vector. Figure 2 shows the transient evolution of the vertical displacement of the membrane center ( $u_z$  of node 201, degree of freedom 603) and the undeformed and timestep-selected deformed shape of the membrane for cases iii), iv) and v). For material properties  $E=2.5 \text{e}7 \text{ N/m}^2$ ,  $\rho=1000 \text{ kg/m}^3$ , case iii), vertical displacement of the membrane center ranges between 0.25 m and 0.30 m, for material properties  $E \approx 1.175 \text{e}10 \text{ N/m}^2$ ,  $\rho \approx 880 \text{ kg/m}^3$ , case iv) and v), vertical displacement of the membrane center ranges between 0.04 m and 0.06 m.

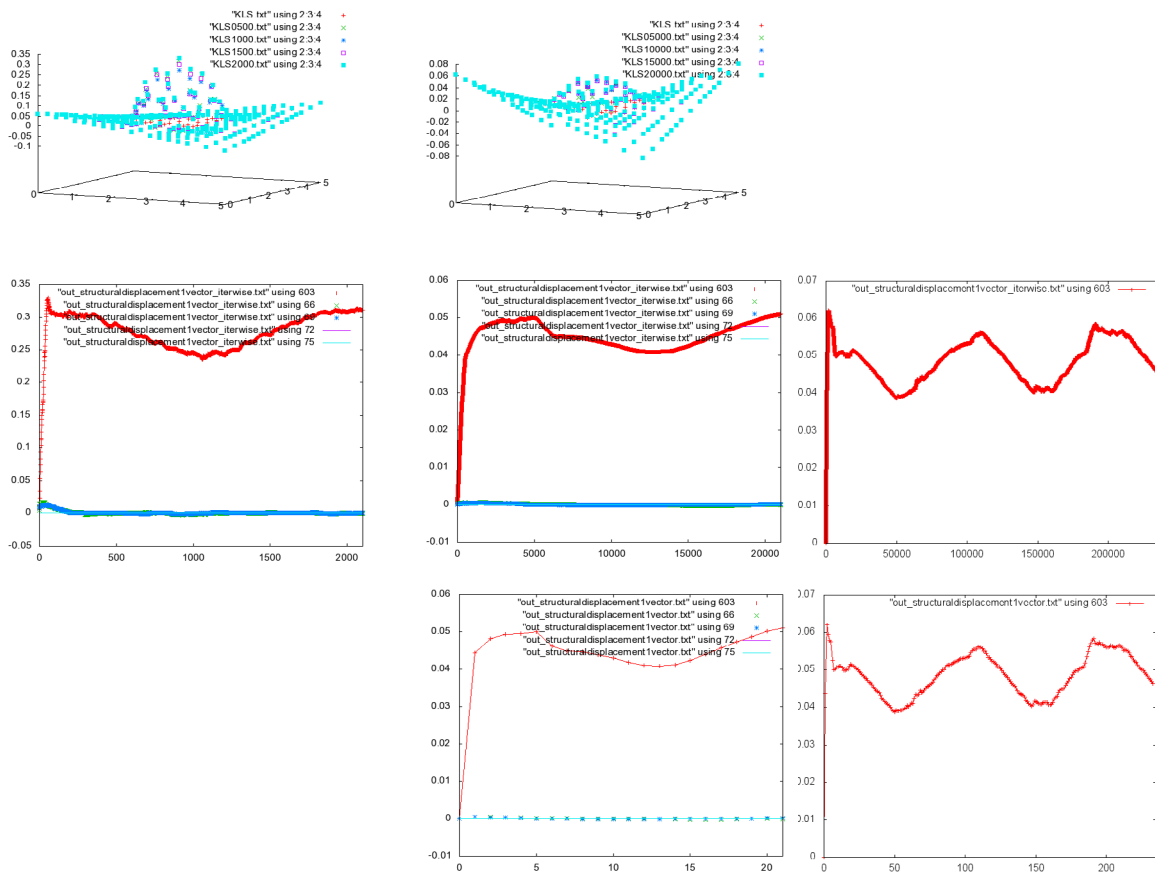


Figure 2: square Hypar membrane (L=5 m), ±0.0625 m vertical corner elevation: undeformed and deformed membrane shape (top row) [in m] and membrane center vertical displacement [in m] over cumulated equilibrium iteration index (center row) and over timestep index (bottom row) for case iii)  $\Delta t=0.5$  s, 100 equilibrium iterations per time interval (left column), case iv)  $\Delta t=0.5$  s, 1000 equilibrium iterations per time interval (center column), case v)  $\Delta t=0.1$  s, 1000 equilibrium iterations per time interval (right column); case iii), iv) and v) field displacement [ux: free, uy: free, uz: free] within the inner part of the membrane (vertical displacement in load direction is plotted upward here (in this figure))

#### 4 ROOF STRUCTURE (L=88 M, B=52.8 M)

A saddle-shaped roof structure of 88 m × 52.8 m ground section for a museum building of 13 m height above ground in the design process shall be analyzed. The ground view horizontal coordinates for the roof reach from (x=0, y=0) to (x=88 m, y=52.8 m). The museum of lower level, base level and first floor carries a steel cable net roof (→ computationally represented by an elastic membrane roof) above with central roof ridge of 5.28 m relative height at horizontal coordinate y=26.4 m. The roof consists of crosswise orthogonal steel cables of 20 mm=0.02 m diameter (cross-section area  $\pi \cdot (0.01$

m)<sup>2</sup>≈0.00031415 m<sup>2</sup>) of 0.50 m distance from each other. The steel cable net is represented by an elastic membrane with isotropic material properties that consider mass conservation as well as stiffness conservation from the steel cable net geometry to the computational elastic membrane. The membrane roof is supported along the circumventing (here rigid) beam structure at the gutter, along the roof ridge, along four intermediate girders from gutter to roof ridge and along the zero-curvature-rings of two radial Gaussian bell curve shaped roof shapes, each of which is located individually on each of the two sides of the roof ridge and one of which has a maximum vertical elevation of 5.28 m and the other one of which has a maximum vertical elevation of 3.28 m each at their respective radial center. During the design process, the curvature of the membrane shape is analyzed analytically, and as static displacement computations show large displacement where Gaussian bell curve curvature becomes very small, two Hypar shapes of ±1.20 m vertical corner elevation and two Hypar shapes of ±0.35 m vertical corner elevation, respectively, are added to increase the membrane system stiffness where Gaussian bell curve curvature becomes very small. The eventually found final Gaussian bell curve and Hypar shaped membrane roof is exposed to static external load (10 times of its eigenload; 1 time of its eigenload). In a more complex model, the geometry of the museum building is surrounded by viscous fluid flow, and fluid-structure interaction (FSI) is intended between the elastic membrane roof structure and the adjacent viscous fluid flow in time domain. The fluid-structure interaction approach is based on the mutual force equilibrium of viscous fluid forces and elastic structural forces on the shared common geometric fluid-structure interface. The membrane roof of 88 m × 52.8 m ground section is discretized by 33×29=957 nodes and 16×14=224 9-node-4-corner finite elements. The geometric distribution of the finite element nodes that represent the membrane roof shape is illustrated in figure 3.

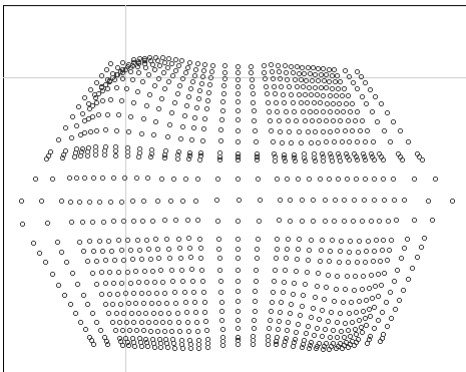


Figure 3: topview onto structural membrane nodes: Gaussian bell curves and Hypar ±0.35 m (x here from left to right, y here (in this plot) from top to bottom (!))

The shape of the membrane roof is given here more in detail. For structural computations the membrane roof structure is rigidly fixed in all three cartesian components of nodal displacement at planes  $x=0$ ,  $x=35$  m,  $x=53$  m,  $x=88$  m,  $y=0$ ,  $y=26.4$  m,  $y=52.8$  m and at the two (x,y)-curves for which the curvature of the two Gaussian bell curves is zero. The two Gaussian bell curves have their respective radial centers at  $(x_A, y_A)=(17$  m, 12 m) (Gaussian bell curve height  $z_A=5.28$  m at  $(x_A, y_A)$  with radius  $R_A=8$  m and at  $(x_B, y_B)=(71$  m, 42.8 m)

(Gaussian bell curve height  $z_B=3.28$  m at  $(x_B, y_B)$  with radius  $R_B=8$  m. Radius  $R_A$  and  $R_B$  label the radial distance from the radial center of the Gaussian bell curve to where the curvature of the Gaussian bell curve is zero. Each of the two Gaussian bell curves holds on one of the two sides of the roof ridge. The two Gaussian bell curves follow the function

$$z(x,y) = z_m \cdot e^{-\lambda^2[(x-x_m)^2+(y-y_m)^2]} = z(r(x,y)) = z_m \cdot e^{-\lambda^2[r(x,y)^2]}$$

where  $r(x,y)=\sqrt{[(x-x_m)^2+(y-y_m)^2]}$ ,  $z_m=z_A$ ,  $x_m=x_A$ ,  $y_m=y_A$  and  $z_m=z_B$ ,  $x_m=x_B$ ,  $y_m=y_B$  for the two different Gaussian bell curves. First radial derivative (radial slope) and second radial derivative (approximation for radial curvature) of the Gaussian bell curves are

$$\begin{aligned} \partial z(x,y)/\partial r(x,y) &= -2 \cdot r(x,y) \cdot \lambda^2 \cdot z_m \cdot e^{-\lambda^2[r(x,y)^2]}, \\ \partial^2 z(x,y)/\partial [r(x,y)]^2 &= (-2+4 \cdot [r(x,y)]^2 \cdot \lambda^2) \cdot \lambda^2 \cdot z_m \cdot e^{-\lambda^2[r(x,y)^2]} \end{aligned}$$

. Demanding for the approximation of the curvature that  $\partial^2 z(x,y)/\partial [r(x,y)]^2=0$  it follows

$$\begin{aligned} r(x,y) &= 1/[\sqrt{2}] \cdot \lambda \quad ] \text{ at } \partial^2 z(x,y)/\partial [r(x,y)]^2=0, \\ \lambda &= 1/[\sqrt{2}] \cdot r(x,y) \quad ] \text{ at } \partial^2 z(x,y)/\partial [r(x,y)]^2=0. \end{aligned}$$

The radial distance where the Gaussian bells curves shall have zero curvature is here selected to be  $r(x,y)=R_m=R_A$  and  $r(x,y)=R_m=R_B$ , respectively. The appropriate value of  $\lambda$  follows as (here  $R_m=R_A=8$  m,  $R_m=R_B=8$  m)

$$\lambda = 1/[\sqrt{2}] \cdot 8 \text{ m} \approx 0.088388 \text{ 1/m for } \partial^2 z(x,y)/\partial [r(x,y)]^2=0 \text{ at } r(x,y)=R_m$$

. For the selected values  $R_m=R_A=8$  m and  $R_m=R_B=8$  m the height ( $R_m=R_A=8$  m,  $z_A=5.28$  m), the slope and the (approximation of) curvature are computed ( $0 \cdot R_m=0$ ,  $1 \cdot R_m=8$  m,  $2 \cdot R_m=16$  m,  $3 \cdot R_m=24$  m) as

[ $z(x,y)$	]( $r(x,y)=0 \cdot R_m$ ) = 5.28 m	(for $R_m=R_A=8$ m, $z_A=5.28$ m)
[ $z(x,y)$	]( $r(x,y)=1 \cdot R_m$ ) $\approx$ 3.20 m	(for $R_m=R_A=8$ m, $z_A=5.28$ m)
[ $z(x,y)$	]( $r(x,y)=2 \cdot R_m$ ) $\approx$ 0.71 m	(for $R_m=R_A=8$ m, $z_A=5.28$ m)
[ $z(x,y)$	]( $r(x,y)=3 \cdot R_m$ ) $\approx$ 0.058 m	(for $R_m=R_A=8$ m, $z_A=5.28$ m)

[ $\partial z(x,y)/\partial r(x,y)$	]( $r(x,y)=0 \cdot R_m$ ) = 0	m/m (slope $0^\circ$ , $R_m=R_A=8$ m, $z_A=5.28$ m)
[ $\partial z(x,y)/\partial r(x,y)$	]( $r(x,y)=1 \cdot R_m$ ) $\approx$ -0.40030	m/m (slope $-21.81^\circ$ , $R_m=R_A=8$ m, $z_A=5.28$ m)
[ $\partial z(x,y)/\partial r(x,y)$	]( $r(x,y)=2 \cdot R_m$ ) $\approx$ -0.17864	m/m (slope $-10.12^\circ$ , $R_m=R_A=8$ m, $z_A=5.28$ m)
[ $\partial z(x,y)/\partial r(x,y)$	]( $r(x,y)=3 \cdot R_m$ ) $\approx$ -0.02199	m/m (slope $-1.26^\circ$ , $R_m=R_A=8$ m, $z_A=5.28$ m)

[ $\partial^2 z(x,y)/\partial [r(x,y)]^2$	]( $r(x,y)=0 \cdot R_m$ ) $\approx$ -0.0825	1/m (curvature radius -12.12 m, $z_A=5.28$ m)
[ $\partial^2 z(x,y)/\partial [r(x,y)]^2$	]( $r(x,y)=1 \cdot R_m$ ) = 0	1/m (curvature radius undefined, $z_A=5.28$ m)
[ $\partial^2 z(x,y)/\partial [r(x,y)]^2$	]( $r(x,y)=2 \cdot R_m$ ) $\approx$ 0.03349	1/m (curvature radius 29.85 m, $z_A=5.28$ m)
[ $\partial^2 z(x,y)/\partial [r(x,y)]^2$	]( $r(x,y)=3 \cdot R_m$ ) $\approx$ 0.00733	1/m (curvature radius 136.37 m, $z_A=5.28$ m)

Regarding that the membrane roof has a roof ridge and so two saddle shaped sides with inclination the overall shape function of each side is given here as

$$z(x,y)=z_m \cdot e^{-\lambda^2[(x-x_m)^2+(y-y_m)^2]}+c_y \cdot (y-y_0)=z(r(x,y))=z_m \cdot e^{-\lambda^2[r(x,y)^2]}+c_y \cdot (y-y_0)$$

( $c_y=5.28 \text{ m}/26.4 \text{ m}=0.2$ ,  $y_0=0$  for roof saddle shape side with Gaussian bell curve radial center at  $(x_A, y_A)$ ;  $c_y=-5.28 \text{ m}/26.4 \text{ m}=-0.2$ ,  $y_0=52.8 \text{ m}$  for roof saddle shape side with Gaussian bell curve radial center at  $(x_B, y_B)$ ).

For the above geometric configuration of the steel cable net the corresponding computational membrane material properties are determined as follows (A in  $\text{m}^2/(\text{width in m})$ ,  $A_{\text{Steel}}$  in  $\text{m}^2/(\text{width in m})$ ):

$$EA=E \cdot 1 \text{ m} \cdot d=E_{\text{Steel}} A_{\text{steel}}$$

$$v=v_{\text{Steel}}$$

$$\rho_{\text{Steel}}(A_{\text{Steel}} \cdot 1 \text{ m}) \cdot 1 \text{ m} + \rho_{\text{Steel}}(A_{\text{Steel}} \cdot 1 \text{ m}) \cdot 1 \text{ m} = \rho \cdot 1 \text{ m} \cdot 1 \text{ m} \cdot d$$

(longitudinal)                      (orthogonal)                      (1  $\text{m}^2$  membrane)

$$EA=E \cdot 1 \text{ m} \cdot d/(1 \text{ m})=E_{\text{Steel}} A_{\text{steel}}$$

The computational membrane thickness d is selected here as  $d=1 \text{ cm}=0.010 \text{ m}$ .

$$EA=E \cdot 1 \text{ m} \cdot 0.010 \text{ m}/(1 \text{ m}) \approx 2.1 \text{e}11 \text{ N/m}^2 \cdot 0.00031415 \text{ m}^2/(0.50 \text{ m})$$

$$E \approx [2.1 \text{e}11 \text{ N/m}^2 \cdot 0.00031415 \text{ m}^2/(0.50 \text{ m})]/[1 \text{ m} \cdot 0.010 \text{ m}/(1 \text{ m})] \approx \underline{1.319 \text{e}10 \text{ N/m}^2}$$

$$v=v_{\text{Steel}}=\underline{0.3}$$

$$\rho \approx [7860 \text{ kg/m}^3 \cdot (0.00031415 \text{ m}^2/(0.50 \text{ m}) \cdot 1 \text{ m}) \cdot 1 \text{ m} + 7860 \text{ kg/m}^3 \cdot (0.00031415 \text{ m}^2/(0.50 \text{ m}) \cdot 1 \text{ m}) \cdot 1 \text{ m}]/[1 \text{ m} \cdot 1 \text{ m} \cdot d]$$

$$\rho \approx 2 \cdot [7860 \text{ kg/m}^3 \cdot 0.00031415 \text{ m}^2/(0.50 \text{ m}) \cdot 1 \text{ m}^2]/[1 \text{ m}^2 \cdot 0.010 \text{ m}] \approx \underline{987.7 \text{ kg/m}^3}$$

Furthermore, for to have a more flexible material for comparative reasons with potentially better convergence behaviour, a second set of computational membrane material properties is applied with  $E=2.5 \text{e}9 \text{ N/m}^2$ ,  $v=0.3$ ,  $\rho \approx 987.7 \text{ kg/m}^3$ .

Gravity is assumed to be  $10 \text{ m/s}^2$  in downward vertical z-direction; so gravity-induced vertical z-displacement is negative.

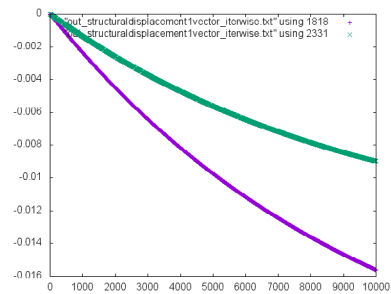
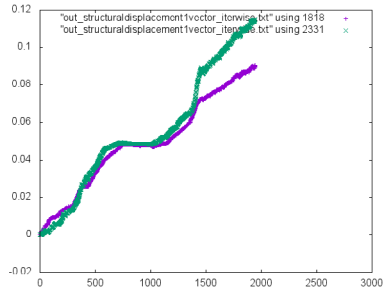
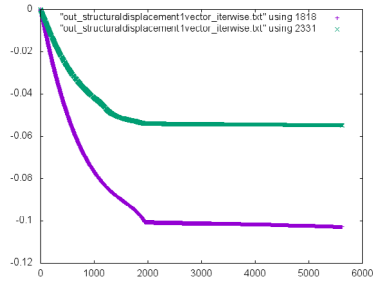
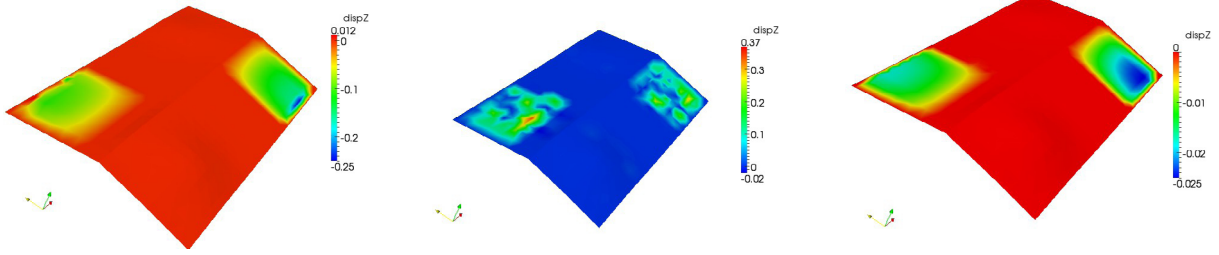
#### 4.1 Gaussian bell curves (L=88 m, B=52.8 m): Static force equilibrium

For the structural membrane roof with pure Gaussian bell curve shape three cases are considered: Case i) material properties  $E=2.5 \text{e}9 \text{ N/m}^2$ ,  $v=0.3$ ,  $\rho \approx 987.7 \text{ kg/m}^3$ , field displacement [ $u_x=0$ ,  $u_y=0$ ,  $u_z$ : free] within the inner part of the membrane, excluding rigid edges with boundary conditions [ $u_x=0$ ,  $u_y=0$ ,  $u_z=0$ ], maximum nodal  $u_x$ -,  $u_y$ -, or  $u_z$ -displacement increment is 0.001 m per equilibrium iteration, external load 10 times of its eigenload= $10 \cdot 98.77 \text{ N/m}^2=987.7 \text{ N/m}^2$ , 5700 equilibrium iterations; case ii) material properties  $E=2.5 \text{e}9 \text{ N/m}^2$ ,  $v=0.3$ ,  $\rho \approx 987.7 \text{ kg/m}^3$ , field displacement [ $u_x$ : free,  $u_y$ : free,  $u_z$ : free] within the inner part of the membrane, excluding rigid edges with boundary conditions [ $u_x=0$ ,  $u_y=0$ ,  $u_z=0$ ], maximum nodal  $u_x$ -,  $u_y$ -, or  $u_z$ - displacement increment is 0.001 m per equilibrium iteration, external load 10 times of its eigenload= $10 \cdot 98.77 \text{ N/m}^2=987.7 \text{ N/m}^2$ ,

2000 equilibrium iterations; case iii) material properties  $E \approx 1.319 \times 10^{10} \text{ N/m}^2$ ,  $\nu = 0.3$ ,  $\rho \approx 987.7 \text{ kg/m}^3$ , field displacement [ $u_x=0$ ,  $u_y=0$ ,  $u_z$ : free] within the inner part of the membrane, excluding rigid edges with boundary conditions [ $u_x=0$ ,  $u_y=0$ ,  $u_z=0$ ], maximum nodal  $u_x$ -,  $u_y$ -, or  $u_z$ - displacement increment is 0.001 m per equilibrium iteration, external load 10 times of its eigenload  $= 10 \cdot 98.77 \text{ N/m}^2 = 987.7 \text{ N/m}^2$ , 10000 equilibrium iterations.

Evaluated is the vertical displacement at node 606 (degree of freedom 1818) at  $x=67.0 \text{ m}$ ,  $y=14.0 \text{ m}$ ,  $z \approx 2.777 \text{ m}$ , where the curvature of the Gaussian bell curve with maximum vertical elevation of ( $x_A, y_A, z_A=5.28 \text{ m}$ ) becomes very small, and at node 777 (degree of freedom 2331) at  $x=21.0 \text{ m}$ ,  $y=38.8 \text{ m}$ ,  $z \approx 2.777 \text{ m}$ , where the curvature of the Gaussian bell curve with maximum vertical elevation of ( $x_B, y_B, z_B=3.28 \text{ m}$ ) becomes very small. Computational results for case i), ii) and iii) are shown in figure 4.

In figure 4 (very bottom left plot) the position of the two centers of the two Gaussian bell curves (position front right: maximum vertical elevation 5.28 m, position rear left: maximum vertical elevation 3.28 m) within the shape of the roof structure can be located. From figure 4 it can be found that after 5700 equilibrium iterations vertical field displacement [ $u_x=0$ ,  $u_y=0$ ,  $u_z$ : free] reaches a large maximum value of 0.25 m near the gutter for case i). Case ii) (field displacement [ $u_x$ : free,  $u_y$ : free,  $u_z$ : free]) does not show convergence at all. For case iii) (field displacement [ $u_x=0$ ,  $u_y=0$ ,  $u_z$ : free]) after 10000 equilibrium iterations vertical field displacement reaches a maximum value of 0.025 m near the gutter and still is not converged yet. For case iii) after 3950 equilibrium iterations membrane stress evaluation shows maximum tensile stress level of  $\sigma_{\xi\xi}^{\text{max,membrane}} = 2 \times 10^6 \text{ N/m}^2 = 0.2 \text{ kN/cm}^2$  and  $\sigma_{\eta\eta}^{\text{max,membrane}} = 3 \times 10^6 \text{ N/m}^2 = 0.3 \text{ kN/cm}^2$  in the two quadrants of the membrane roof structure where the curvature of the two respective Gaussian bell curves is very small; detailed plots of  $\sigma_{\xi\xi}^{\text{membrane}}$  and  $\sigma_{\eta\eta}^{\text{membrane}}$  show that around the two Gaussian bell curves tensile stress of lower order of magnitude appears, whereas towards the fixed edges of the membrane roof structure along the gutter (corner regions, where fixed nodes due to zero-displacement boundary conditions hinder the membrane to establish membrane tensile stress state) computational compressive stress appears. It is now mentioned that the computational membrane representation of the steel cable net structure experiences the same strain as the real cable net structure. So steel cable net structure stresses differ from the computational membrane stresses by the factor of  $E_{\text{Steel}}/E_{\text{computational membrane}}$ . Thus, referring to the above maximum computational membrane stresses of  $\sigma_{\xi\xi}^{\text{max,membrane}} = 2 \times 10^6 \text{ N/m}^2 = 0.2 \text{ kN/cm}^2$  and  $\sigma_{\eta\eta}^{\text{max,membrane}} = 3 \times 10^6 \text{ N/m}^2 = 0.3 \text{ kN/cm}^2$ , the appropriate maximum steel cable net structure stresses result as  $\sigma_{\xi\xi}^{\text{max,steel cable net}} = E_{\text{Steel}}/E_{\text{computational membrane}} \cdot \sigma_{\xi\xi}^{\text{max,membrane}} \approx 2.100 \times 10^{11} / 1.319 \times 10^{10} \cdot 2 \times 10^6 \text{ N/m}^2 \approx 3.2 \text{ kN/cm}^2$  and  $\sigma_{\eta\eta}^{\text{max,steel cable net}} = E_{\text{Steel}}/E_{\text{computational membrane}} \cdot \sigma_{\eta\eta}^{\text{max,membrane}} \approx 2.100 \times 10^{11} / 1.319 \times 10^{10} \cdot 3 \times 10^6 \text{ N/m}^2 \approx 4.8 \text{ kN/cm}^2$  at equilibrium iteration 3950. Vertical displacement is as well the largest in the two quadrants where the curvature of the two Gaussian bell curves is very small. A detailed plot of the vertical displacement shows the vertical displacement around the two Gaussian bell curves. Altogether, considering for case iii) ( $E \approx 1.319 \times 10^{10} \text{ N/m}^2$ ,  $\nu = 0.3$ ,  $\rho \approx 987.7 \text{ kg/m}^3$ , computational membrane representation for steel cable net) the vertical displacement distribution and the equilibrium iteration evolution of the vertical displacement after 10000 iterations (not converged yet) it is concluded that the two Gaussian bell curves within the shape of the roof structure do not deliver sufficient system stiffness throughout the whole roof structure to



case i) iter 5700

case ii) iter 2000

case iii) iter 10000

case iii)  $\sigma_{\xi\xi}^{\text{membrane}}$  [N/m<sup>2</sup>] iter 3950 case iii)  $\sigma_{\eta\eta}^{\text{membrane}}$  [N/m<sup>2</sup>] iter 3950 case iii) iter 3950

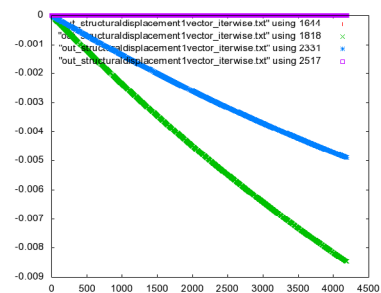
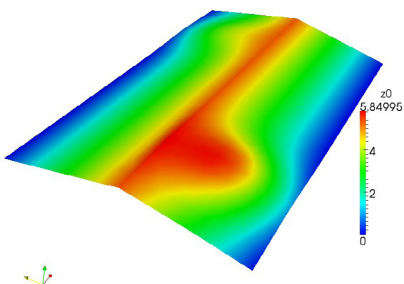
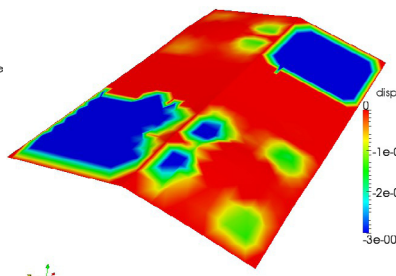
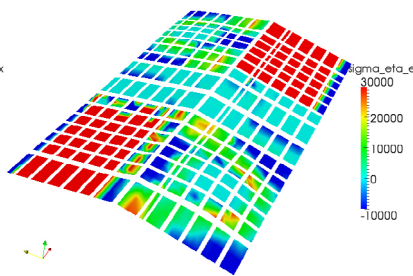
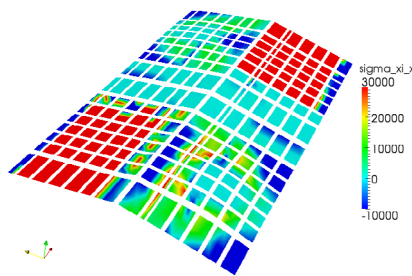
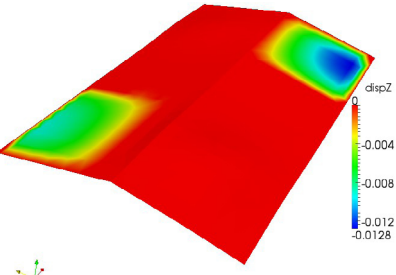
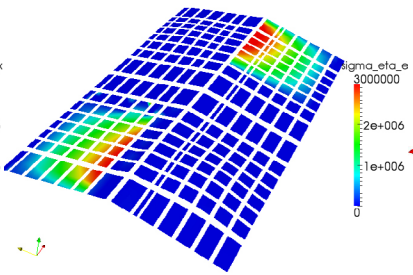
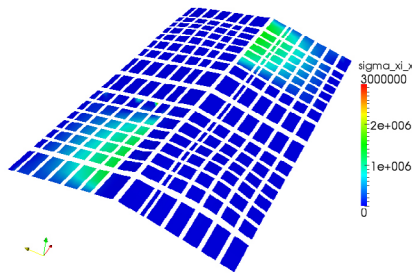


Figure 4: roof structure Gaussian bell curves (L=88 m, B=52.8 m): case i) (top left), case ii) (top center), case iii) (top right) vertical displacement [in m] and membrane nodes 606 and 777 vertical displacement [in m] over cumulated equilibrium iteration index, case iii) (bottom row) membrane stress  $\sigma_{\xi\xi}^{\text{membrane}}$  [in N/m<sup>2</sup>] in x-direction and roof structure elevation [in m] (bottom left), membrane stress  $\sigma_{\eta\eta}^{\text{membrane}}$  [in N/m<sup>2</sup>] in y-direction (bottom center), vertical displacement [in m] and membrane nodes 606 and 777 vertical displacement [in m] over cumulated equilibrium iteration index (bottom right)

guarantee a limited maximum vertical displacement of the roof structure within an acceptable range of displacement. So, as a consequence, in the two quadrants of the roof structure, where the two Gaussian bell curves have very small curvature, appropriately case a) two Hyparforms of  $\pm 1.20$  m vertical corner elevation and case b) two Hyparforms of  $\pm 0.35$  m vertical corner elevation are added to the roof structure shape to give the total shape of the roof structure. The appropriate Hyparforms have their respective centers at  $(x_c=70.5 \text{ m}, y_c=13.2 \text{ m}, z_c=0)$  and  $(x_D=17.5 \text{ m}, y_D=39.6 \text{ m}, z_D=0)$ .

#### 4.2 Gaussian bell curves and Hypar $\pm 1.20\text{m}$ (L=88m,B=52.8m): Static force equilibrium

For the structural membrane roof with Gaussian bell curve shape and additional Hyparform of  $\pm 1.20$  m vertical corner elevation four cases are considered:

- case i)  $E=2.5e9 \text{ N/m}^2$ ,  $\nu=0.3$ ,  $\rho \approx 987.7 \text{ kg/m}^3$ , field displacement [ux=0, uy=0, uz:free],
- case ii)  $E=2.5e9 \text{ N/m}^2$ ,  $\nu=0.3$ ,  $\rho \approx 987.7 \text{ kg/m}^3$ , field displacement [ux:free, uy:free, uz:free],
- case iii)  $E \approx 1.319e10 \text{ N/m}^2$ ,  $\nu=0.3$ ,  $\rho \approx 987.7 \text{ kg/m}^3$ , field displacement [ux=0, uy=0, uz:free],
- case iv)  $E \approx 1.319e10 \text{ N/m}^2$ ,  $\nu=0.3$ ,  $\rho \approx 987.7 \text{ kg/m}^3$ , field displacement [ux:free, uy:free, uz:free].

For all cases i), ii), iii), iv) external load is 10 times the eigenload of the membrane, i.e.  $10 \cdot 98.77 \text{ N/m}^2 = 987.7 \text{ N/m}^2$ , maximum nodewise ux-, uy- and uz-displacement increment is limited to 0.001 m per equilibrium iteration, 10000 equilibrium iterations are performed. In figure 5 vertical displacement after 10000 equilibrium iterations and the evolution of vertical displacement for node 606 (degree of freedom 1818) and node 777 (degree of freedom 2331) over the cumulated iteration index are shown for case i), ii), iii), iv).

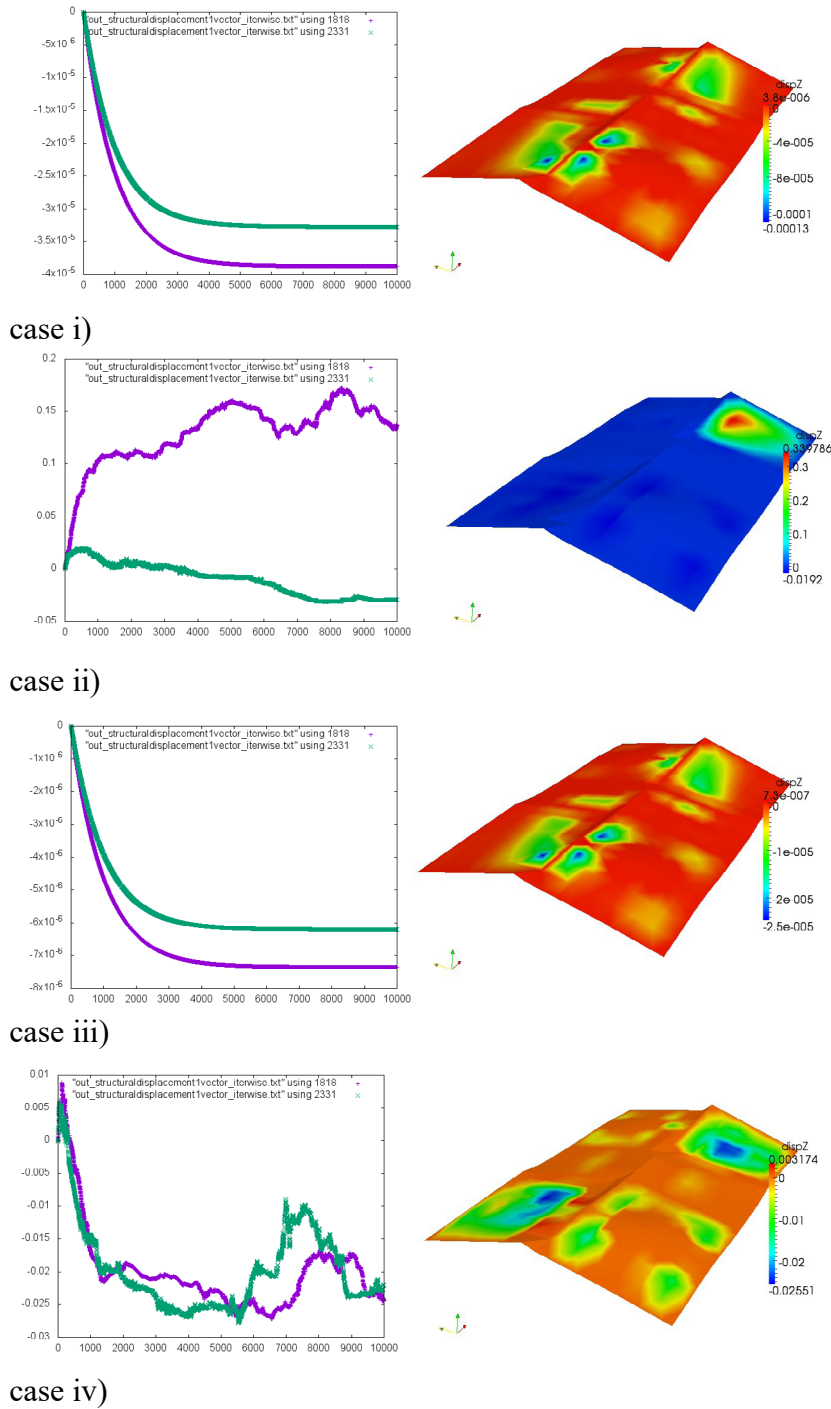


Figure 5: roof structure Gaussian bell curves and Hypar  $\pm 1.20$  m (L=88 m, B=52.8 m): membrane nodes 606 and 777 vertical displacement [in m] over cumulated equilibrium iteration index (left) and vertical displacement [in m] (right) for case i, ii, iii, iv)

Case i) and iii) (both field displacement [ux=0, uy=0, uz: free]) show strictly monotonic evolution in vertical displacement and convergence with very small maximum downward vertical displacement of 0.00013 m (case i)) and 2.5e-5 m (case iii)); the vertical displacement distribution plots indicate the regions of maximum downward vertical displacement. Case ii) (E=2.5e9 N/m<sup>2</sup>, field displacement [ux: free, uy: free, uz: free]) does not show any convergence in vertical displacement after 10000 equilibrium iterations. Case iv) (E≈1.319e10 N/m<sup>2</sup>, field displacement [ux: free, uy: free, uz: free], computational membrane representation of steel cable net) shows continuous evolution with the equilibrium iterations until vertical downward displacement of 0.025 m (node 603, d.o.f 1818) and 0.025 m (node 777, d.o.f. 2331) is reached (approx. eq. iter. 5500), after which a change in vertical displacement appears (approx. eq. iter. 7000) that again leads to a vertical downward displacement of 0.025 m (node 603, d.o.f 1818) and 0.025 m (node 777, d.o.f. 2331) (approx. eq. iter. 10000); so the equilibrium iterations twice lead to the same vertical displacement of 0.025 m (node 603, d.o.f 1818) and 0.025 m (node 777, d.o.f. 2331). The vertical displacement distribution plot indicates the regions of maximum downward displacement (in the two quadrants where the curvature of the two Gaussian bell curves is very small and so the two Hypar shapes are added).

#### 4.3 Gaussian bell curves and Hypar ±0.35m (L=88m,B=52.8m): Static force equilibrium

For the structural membrane roof with Gaussian bell curve shape and additional Hyperform of ±0.35 m vertical corner elevation four cases are considered:

- case i) E=2.5e9 N/m<sup>2</sup>, ν=0.3, ρ≈987.7 kg/m<sup>3</sup>, field displacement [ux=0, uy=0, uz:free],
- case ii) E=2.5e9 N/m<sup>2</sup>, ν=0.3, ρ≈987.7 kg/m<sup>3</sup>, field displacement [ux:free, uy:free, uz:free],
- case iii) E≈1.319e10 N/m<sup>2</sup>, ν=0.3, ρ≈987.7 kg/m<sup>3</sup>, field displacement [ux=0, uy=0, uz:free],
- case iv) E≈1.319e10 N/m<sup>2</sup>, ν=0.3, ρ≈987.7 kg/m<sup>3</sup>, field displacement[ux:free,uy:free,uz:free].

For all cases i), ii), iii), iv) external load is 10 times the eigenload of the membrane, i.e. 10·98.77 N/m<sup>2</sup>=987.7 N/m<sup>2</sup>, maximum nodewise ux-, uy- and uz-displacement increment is limited to 0.001 m per equilibrium iteration, 10000 equilibrium iterations are performed. In figure 6 vertical displacement after 10000 equilibrium iterations and the evolution of vertical displacement for node 606 (degree of freedom 1818) and node 777 (degree of freedom 2331) over the cumulated iteration index are shown for case i), ii), iii), iv).

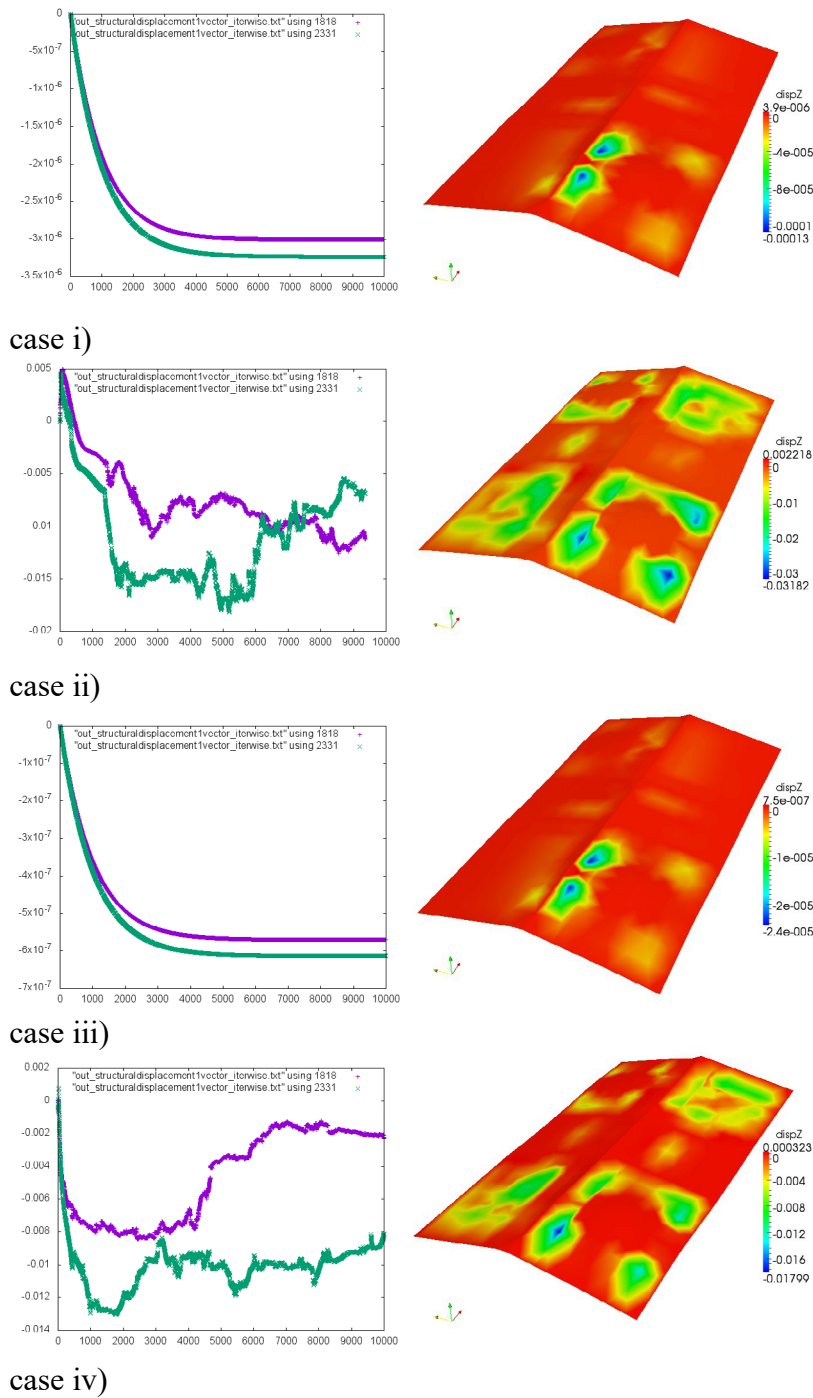


Figure 6: roof structure Gaussian bell curves and Hypar  $\pm 0.35$  m (L=88 m, B=52.8 m): membrane nodes 606 and 777 vertical displacement [in m] over cumulated equilibrium iteration index (left) and vertical displacement [in m] (right) for case i), ii), iii), iv)

Case i) and iii) (both field displacement [ $u_x=0$ ,  $u_y=0$ ,  $u_z$ : free]) show strictly monotonic evolution in vertical displacement and convergence with very small maximum downward vertical displacement of 0.00013 m (case i)) and  $2.4e-5$  m (case iii)); the vertical displacement distribution plots indicate the regions of maximum downward vertical displacement (maximum vertical downward displacement for case i) and iii) has the same order of magnitude as for case i) and iii) with Gaussian bell curves and Hypar  $\pm 1.20$  m (see above)). Case ii) ( $E=2.5e9$  N/m<sup>2</sup>, field displacement [ $u_x$ : free,  $u_y$ : free,  $u_z$ : free]) shows a constant range for vertical downward displacement of node 603 (d.o.f. 1818) around 0.01 m (eq. iter. 3000 to 10000), whereas for node 777 (d.o.f. 2331) vertical downward displacement reaches a constant range of 0.015 m (eq. iter. 2000 to 6000) and then experiences a change to around 0.01 m (eq. iter. 6500 to 10000); the vertical displacement distribution plot indicates the regions of maximum downward vertical displacement of 0.032 m. Case iv) ( $E \approx 1.319e10$  N/m<sup>2</sup>, field displacement [ $u_x$ : free,  $u_y$ : free,  $u_z$ : free], computational membrane representation of steel cable net) shows a constant range of vertical displacement for node 777 (d.o.f. 2331) around 0.01 m, whereas for node 603 (d.o.f. 1818) vertical downward displacement reaches 0.008 m (eq. iter. 1000 to 4500) and then changes to a constant range around 0.002 m (eq. iter. 6500 to 10000); the vertical displacement distribution plot indicates the regions of maximum downward vertical displacement of 0.018 m. Altogether displacement distributions due to external load (10 times of the membrane's eigenload= $10 \cdot 98.77$  N/m<sup>2</sup>= $987.7$  N/m<sup>2</sup>) onto the membrane show representative displacement distributions for cases ii) and iv) (both field displacement [ $u_x$ : free,  $u_y$ : free,  $u_z$ : free]) and also acceptable maximum downward displacement of 0.032 m (case ii),  $E=2.5e9$  N/m<sup>2</sup>) and particularly 0.018 m (case iv),  $E \approx 1.319e10$  N/m<sup>2</sup>, computational membrane representation of steel cable net) with the roof structure of two Gaussian bell curves and additional two Hypar  $\pm 0.35$  m. Thus the structural roof shape that is designed with two Gaussian bell curves and additional two Hypar  $\pm 0.35$  m is assessed as favourable to be selected as a structural roof shape of sufficient system stiffness against external vertical downward load in the range of 1 kN/m<sup>2</sup>.

#### 4.4 Gaussian bell curves and Hypar $\pm 0.35$ m (L=88 m, B=52.8 m): Exposure to eigenload

For the analyzed-above structural membrane roof with Gaussian bell curve shape and additional Hyparform of  $\pm 0.35$  m vertical corner elevation the case

$$E \approx 1.319e10 \text{ N/m}^2, \nu=0.3, \rho \approx 987.7 \text{ kg/m}^3, \text{ field displacement } [u_x:\text{free}, u_y:\text{free}, u_z:\text{free}]$$

is considered for vertical eigenload of the membrane, i.e. 98.77 N/m<sup>2</sup> (distributed eigenmass of the steel cable net and so its computational membrane representation is  $987.7 \text{ kg/m}^3 \cdot 0.01 \text{ m} = 9.877 \text{ kg/m}^2 \approx 10 \text{ kg/m}^2$ ). This case represents the considered steel cable net when potentially in addition dynamic load e.g. due to wind (uprising forces) might appear. Maximum nodewise  $u_x$ -,  $u_y$ - and  $u_z$ -displacement increment is limited to 0.001 m per equilibrium iteration, 10000 equilibrium iterations are performed. In figure 7 vertical displacement after 10000 equilibrium iterations and the evolution of vertical displacement as well as horizontal displacement for node 606 (degree of freedom 1818) and node 777 (degree of freedom 2331) over the cumulated iteration index are shown.

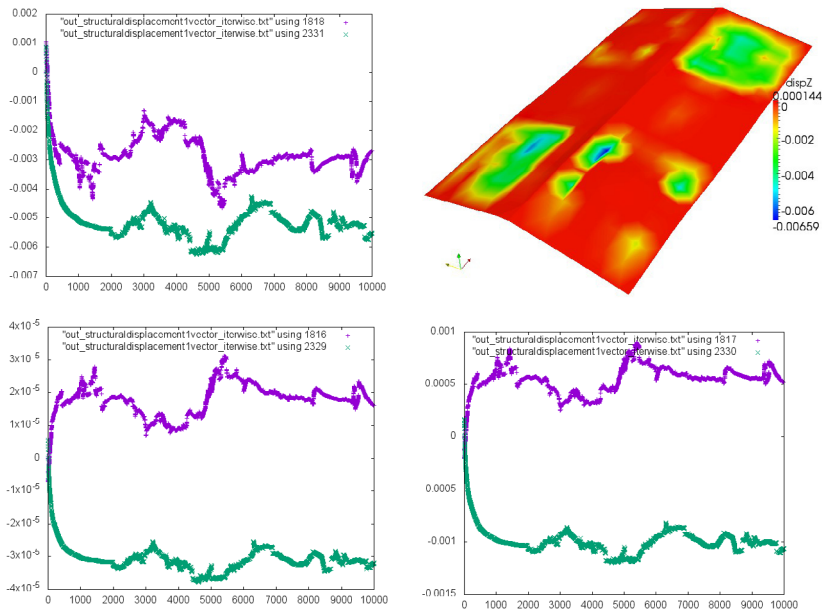


Figure 7: roof structure Gaussian bell curves and Hypar  $\pm 0.35$  m ( $L=88$  m,  $B=52.8$  m): membrane nodes 606 and 777 vertical displacement [in m] over cumulated equilibrium iteration index (top left) and vertical displacement [in m] (top right) for exposure to eigenload ( $98.77$  N/m<sup>2</sup>), membrane node 606 and 777 horizontal x-displacement [in m] (bottom left) and horizontal y-displacement [in m] (bottom right) over cumulated equilibrium iteration index

The equilibrium iteration evolution shows a range of vertical downward displacement of  $0.003$  m for node 603 (d.o.f. 1818) (eq. iter. 1500 to 10000 with an intermediate variation from eq. iter. 3000 to 5500) and  $0.005$  m for node 777 (d.o.f. 2331) (eq. iter. 1000 to 10000). The vertical displacement distribution plot indicates the region with maximum downward vertical displacement of  $0.0066$  m  $\approx 0.007$  m. Horizontal x-displacement reaches a range of  $+2e-5$  m (node 603, d.o.f. 1816) and  $-3e-5$  m (node 777, d.o.f. 2329), horizontal y-displacement reaches a range of  $+0.0005$  m (node 603, d.o.f. 1817) and  $-0.001$  m (node 777, d.o.f. 2330).

#### 4.5 Gaussian bell curves and Hypar $\pm 0.35$ m ( $L=88$ m, $B=52.8$ m): Surround. visc. fluid flow

The computational membrane roof structure with two Gaussian bell curves and additional Hypar  $\pm 0.35$  m ( $L=88$  m,  $B=52.8$  m) with its museum building underneath is surrounded by viscous fluid flow (eventually to model transient air flow along the elastic structural membrane roof structure). Therefore the surrounding viscous fluid flow is modeled by the Navier-Stokes equations for laminar viscous fluid flow. The computational fluid domain stretches horizontally from  $x=-176$  m to  $x=264$  m and from  $y=-105.6$  m to  $y=158.4$  m and stretches vertically from  $-8$  m to  $10$  m, where at the center of the fluid domain with dimensions of the museum domain a void is located within the fluid domain. Flow direction is case a) considered in horizontal x-direction and case b) considered in horizontal y-direction. For both case a) and case b) the fluid domain is discretized with 8-node hexahedra elements

with linear interpolation functions. For both case a) and case b) the fluid domain is horizontally discretized with 30 element layers upstream of the museum structure, with 30 element layers along the museum structure and with 30 element layers downstream of the museum structure all in flow direction and is horizontally discretized with 10 element layers left of the museum structure, with 30 element layers along the museum structure and with 10 element layers right of the museum structure all transversal to the flow direction. In vertical direction the fluid domain is discretized with altogether 36 element layers, 14 of which are located from soil to below bottom of the roof structure, 14 of which are located from below bottom of the roof structure to above top of the roof structure and 8 of which are located from above top of the roof structure to about 5 m above top of the roof structure. Fluid elements' edge lengths range from 0.5 m to a few meters. In the vicinity of the museum structure fluid element lengths are about 0.5 m. As the regions directly upstream and directly downstream of the museum structure are discretized with higher refinement of the mesh than the regions laterally left and right of the museum structure for case a) (flow in x-direction) and case b) (flow in y-direction) two different fluid meshes, but both with the same number of fluid nodes and same number of fluid elements, namely 159943 fluid nodes and 149400 fluid elements, are used. The two different computational fluid domains for case a) (flow in x-direction) and case b) (flow in y-direction) are illustrated in figure 8. The fluid mesh discretization is nonsymmetric.

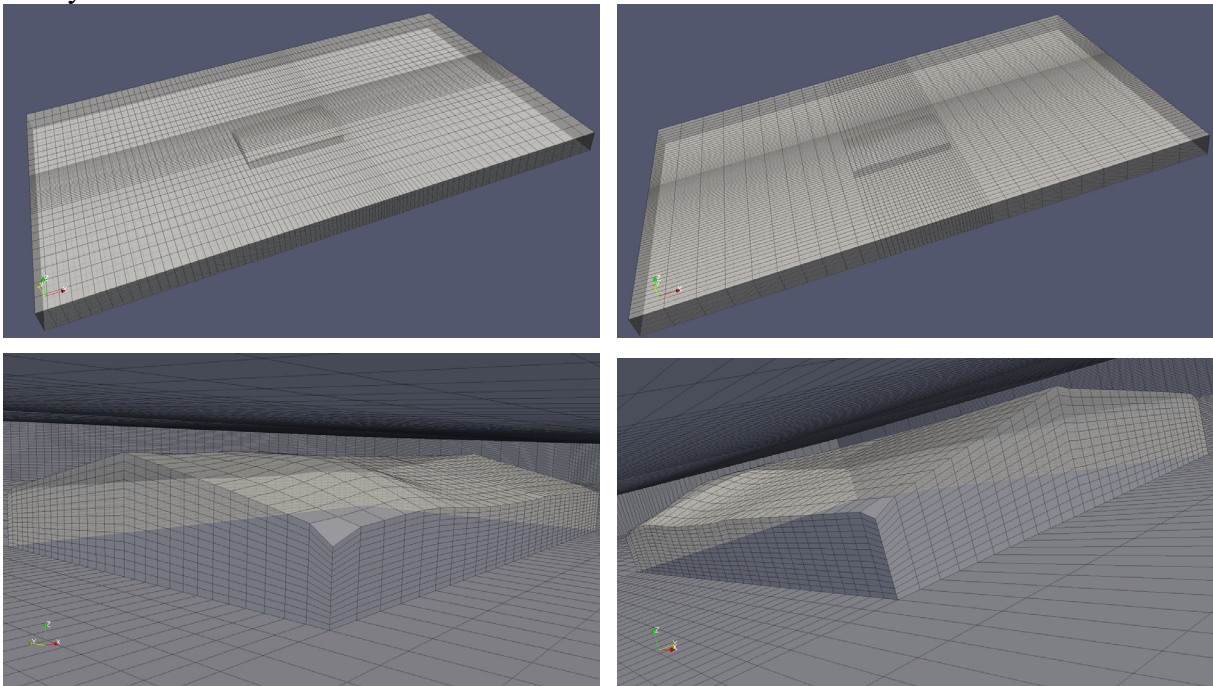
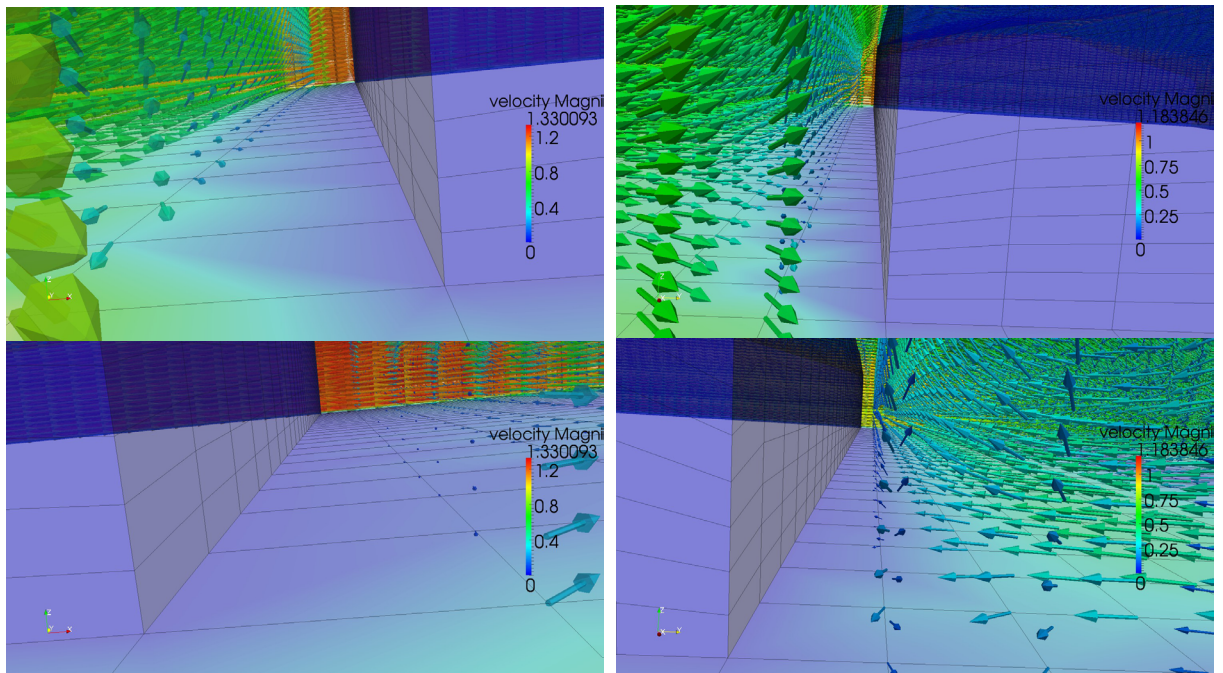
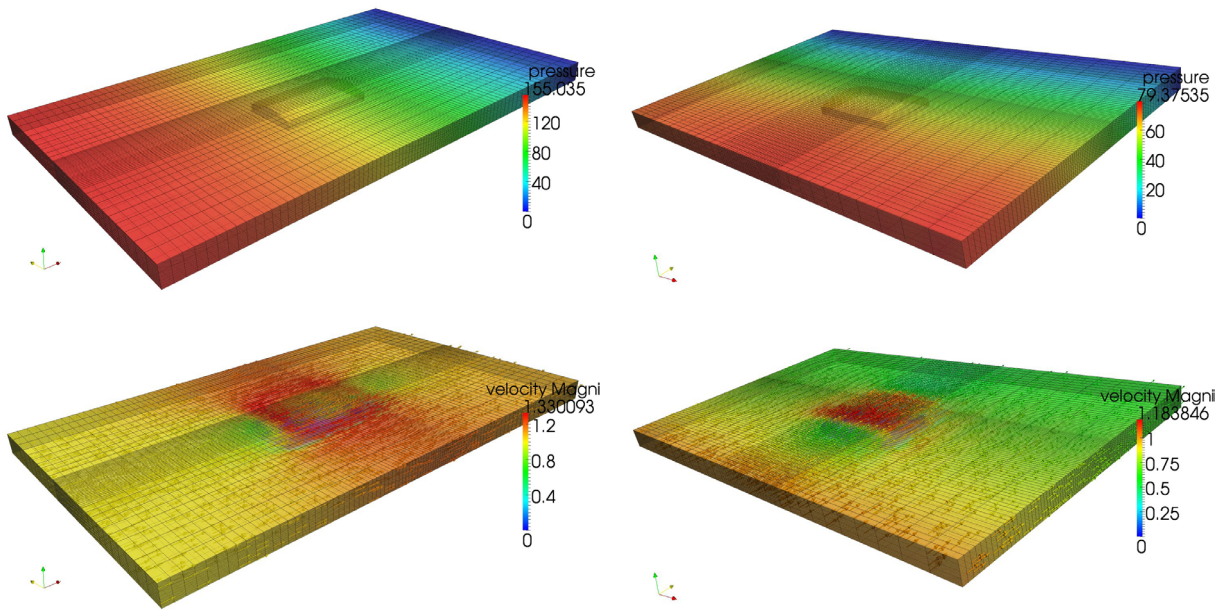


Figure 8: computational fluid domain for flow in x-direction (left), flow in y-direction (right)

At the beginning of computations for case a) and case b) the fluid within the computational fluid domain is completely at rest, i.e fluid velocity vector and fluid pressure are completely zero throughout the whole fluid domain. Boundary conditions define zero normal velocity at left, right, bottom and top boundary of the fluid domain. On the upstream boundary, inflow



case a) (flow in x-direction at  $t=38.7$  s)

case b) (flow in y-direction at  $t=23.6$  s)

Figure 9: fluid state for case a) flow in x-direction (left) and case b) flow in y-direction (right): fluid pressure field (top), fluid velocity field (second top), fluid velocity upstream of structure (second bottom) with upward velocity direction, fluid velocity downstream of structure (bottom) with reversing upstream velocity direction near bottom within vortex downstream of structure

velocity of 1.0 m/s is defined. On the downstream boundary, outflow pressure of zero is defined. On all boundaries of the structural museum domain, i.e. upstream and downstream museum surface and left and right lateral museum surface and top museum roof surface (with two Gaussian bell curves and additional two Hypar  $\pm 0.35\text{m}$ ), fluid velocity vector is defined as the zero vector. Time domain computations are performed with 0.1 s constant time interval size and 3 equilibrium iterations within the fluid equation solution scheme for each considered time interval. Fluid material properties are (dynamic) viscosity  $\mu_F=0.5 \text{ kg}/(\text{m}\cdot\text{s})$  and density  $\rho_F=1.0 \text{ kg}/\text{m}^3$ . Time integration is performed for case a) as well as for case b) using a constant time interval size of 0.1 s for a total of 400 time intervals. Fluid pressure distribution and fluid velocity distribution for case a) timestep 387 (38.7 s) and for case b) timestep 263 (26.3 s) are shown in figure 9.

Figure 9 shows the fluid pressure field where upstream pressure is high and downstream pressure is zero at the outflow boundary. The fluid velocity field shows higher velocity magnitude above the structure. At the upstream end of the museum structure the velocity field is directed vertically upward, at the downstream end of the museum structure an at the bottom upstream directed vortex flow is found.

## 5 CONCLUSIONS

Membrane roof structures of continuously opposite curvature (so-called negative curvature) are considered. Structural membrane force equilibrium due to static and dynamic external load without pretension of the membrane is obtained by a constant range of displacement after about 100 to 1000 to 10000 equilibrium iterations where nodewise componentwise displacement increment is limited to between 0.01 m and 0.0001 m per equilibrium iteration. Boundary conditions that fix the horizontal movement of membrane field finite element nodes to reduce the number of degrees of freedom lead to very small vertical membrane displacement. In contrast, boundary conditions that allow completely free horizontal as well as vertical displacement for membrane nodes apart from boundary edges lead to finite vertical displacement of a few centimeters that reaches the order of approximately 1/100 and 1/300 of the respective span-width of the membrane roof, which seems acceptable for the considered steel cable net structures that are computationally represented by membrane roof structures, here a Hyparform ( $L=5 \text{ m}$ ) and a museum building with saddle shaped roof structure ( $L=88 \text{ m}$ ,  $B=52.8 \text{ m}$ ) with two Gaussian bell curves (and additional Hypar), for the latter of which analytic assessment of curvature distribution is taken into account. The distributed eigenmass of the roof structures is of order  $10 \text{ kg}/\text{m}^2$ . Surrounding viscous fluid flow around the considered museum structure shows typical vortex patterns in the leeward zone downstream of the museum building (obstacle) within the fluid domain. A strongly coupled segregated approach for fluid-structure interaction between structural membranes and viscous (laminar) fluid flow is presented together with an altogether (nonlinear) interpolation procedure to interpolate viscous fluid load onto the membrane structure and to interpolate structural membrane load onto the adjacent viscous fluid for pairs of non-matching structural membrane mesh and viscous fluid meshes.

**REFERENCES**

- [1] H. Apelmann, C. Gengnagel. Interaktion von Membranen und biegesteifen Bogentragwerken. *Stahlbau* 72, Heft 10, 702-707, 2003
- [2] K.-J. Bathe. *Finite-Elemente-Methoden*. Springer-Verlag Berlin, 2002
- [3] H. Berger. *Light structures – structures of light*. Birkhäuser, Basel/Boston/Berlin, 1996
- [4] K.-U. Bletzinger. Formfindung von leichten Tragwerken. in *Baustatik-Baupraxis* (Hrsg. D. Dinkler), 99-110, Institut für Statik, Technische Universität Braunschweig, 2002
- [5] K.-U. Bletzinger, E. Ramm. Structural optimization and form finding of light weight structures. *Computers and Structures* 79, 2053-2962, 2001
- [6] K.-U. Bletzinger, R. Ziegler. Theoretische Grundlagen der numerischen Formfindung von Membrantragwerken und Minimalflächen. *Beton-Kalender BK2*, 2000, 441-456, Ernst & Sohn, Berlin, 2000
- [7] G. Brinkmann (Hrsg.). *Weitgespannte Flächentragwerke*. Zusammenfassender Bericht, SFB 64, Universität Stuttgart, 1990
- [8] A. Brooks and T.J.R. Hughes. Streamline upwind/Petrov-Galerkin formulations for convection dominated flows with particular emphasis on the incompressible Navier-Stokes equations, *Computer methods in applied mechanics and engineering*, 32, 199-259, 1982.
- [9] E. Bubner et al. *Minimalkonstruktionen*. Symposium Universität Essen Gesamthochschule, 1977
- [10] E. Bubner et al. *Membrankonstruktionen*, Teil 1, Teil 2, Teil 3, Teil 4. Haus der Technik Essen / Universität Essen Gesamthochschule, 1979-1982
- [11] H. Buefler. Pressure loaded structures under large deformations. *Zeitschrift für Angewandte Mathematik und Mechanik* 64, Heft 7, 287-295, 1984
- [12] C. Corte, J. Garcia, E. Oñate. Three-dimensional flow around rigid and elastic cylindrical structures. 32 pages, CIMNE Barcelona, 2007
- [13] C. Corte, J. Garcia, E. Oñate. A strongly-coupled segregated approach for finite element modeling of fluid-structure interaction. 17 pages, CIMNE Barcelona, 2008
- [14] C. Corte. A segregated approach for strong coupling of finite element solvers to model fluid-structure interaction. 30 pages, CIMNE Barcelona, 2008
- [15] C. Corte. A 3D approach for finite element modeling of viscous fluid flow. 24 pages, Dr. C. Corte, *Baustatik – Baudynamik – Numerische Modellierung*, Berlin, Tel./Fax +49(0)30-347871 78/80, 2010
- [16] C. Corte. A 3D approach for finite element modeling of fluid-structure interaction between incompressible viscous fluids and elastic structures. 64 pages, Dr. C. Corte, *Baustatik – Baudynamik – Numerische Modellierung*, Berlin, Tel./Fax +49-(0)30-347871 78/80, 2011
- [17] C. Corte. Finite element modeling of fluid-structure interaction for an elastic 2D flag in harmonic viscous fluid flow and an elastic 3D sail structure in stationary viscous fluid flow. 39 pages, Dr. C. Corte, *Baustatik – Baudynamik – Numerische Modellierung*, Berlin, Tel./Fax +49-(0)30-347871 78/80, 2012
- [18] C. Corte. *3D-Membrantheorie*. *Stahlbau* 83, Heft 5, 343-358, Ernst und Sohn Verlag, 2014.

- 
- [19] C. Corte. 3D membrane theory. 11<sup>th</sup> World Congress on Computational Mechanics, 268-292, Barcelona/Spain, 2014
- [20] J. Cremers, G. Grunwald. Innovative Membran-Stadiondächer in Kiew, Warschau und Vancouver. Stahlbau 80, Heft 9, 678-686, 2011
- [21] H. Dirlewanger et al. Ausgewählte Flächentragwerke. Internationales Symposium Weitgespannte Flächentragwerke, SFB 64, Universität Stuttgart, 1976
- [22] P. Drew. Tensile structures. Granada publishing London, 1979
- [23] P. Drew. New tent architecture. Thames and Hudson, 2007
- [24] O. Frei, Das hängende Dach, Technische Universität Berlin, 1954
- [25] O. Frei et al. Mitteilungen der Entwicklungsstelle für den Leichtbau in Berlin. Nr. 7, Nr. 8, Nr. 9. Entwicklungsstelle für den Leichtbau in Berlin, 1961-1963
- [26] O. Frei, R. Trostel. Zugbeanspruchte Konstruktionen, Band 1. Ullstein Fachverlag Berlin/Frankfurt, 1962
- [27] O. Frei, F.-K. Schleyer. Zugbeanspruchte Konstruktionen, Band 2. Ullstein Fachverlag Berlin/Frankfurt, 1966
- [28] K. Göppert. Membrankonstruktionen – Form und Detail. Stahlbau 73, Heft 12, 990-1000, 2004
- [29] H. M. Hilber, T. J. R. Hughes, R. L. Taylor. Improved numerical dissipation for time integration algorithms in structural dynamics. Earthquake engineering and structural dynamics, vol. 5, 283-292, 1977
- [30] D. Hoppe. Textile Membrankonstruktionen. Böhlau Verlag Wien/Köln/Weimar, 2007
- [31] J. Linhard. Numerisch-mechanische Betrachtung des Entwurfsprozesses von Membrantragwerken. TU München, 2009
- [32] K. Linkwitz, H.-J. Schek. Einige Bemerkungen zur Berechnung von vorgespannten Seilnetzkonstruktionen. Ingenieur-Archiv 40, 145-158, 1971
- [33] S. Neuhäuser et al. Adaptive Tragwerke – Aktuelle Forschung im Ultraleichtbau. Stahlbau 82, Heft 6, 428-437, 2013
- [34] W. Renner. Membrantragwerke – Konzepte, Bemessung, Ausführung. Stahlbau 69, Heft 7, 2000
- [35] C. Roland. Frei Otto – Spannweiten. Ullstein Fachverlag Berlin/Frankfurt, 1965
- [36] H.-J. Schock. Segel, Folien und Membranen. Birkhäuser, Basel/Boston/Berlin, 1997
- [37] M. Seel, G. Siebert. Analytische Lösungen für Kreis- und Kreisringplatten unter symmetrischer und antisymmetrischer Einwirkung. Stahlbau 81, Heft 9, 711-718, 2012
- [38] Weitgespannte Flächentragwerke, Band 1 bis 3. Internationales Symposium Weitgespannte Flächentragwerke, SFB 64, Universität Stuttgart, 1976
- [39] Weitgespannte Flächentragwerke. Band 1 und 2. Internationales Symposium Weitgespannte Flächentragwerke, SFB 64, Universität Stuttgart, 1979
- [40] R. Wüchner, K.-U. Bletzinger. Stress-adapted numerical form finding of pre-stressed surfaces by updated reference strategy. International Journal for Numerical Methods in Engineering 64, 143-166, 2005
- [41] R. Wüchner. Mechanik und Numerik der Formfindung und Fluid-Struktur-Interaktion von Membrantragwerken. TU München, 2006
- [42] J. Zerning. Design guide to anticlastic structures in plastic. Polytec of London, 1975

## AUTHORS INDEX

Abodonya, A. ....	371	Ibrahim Ali, H. ....	141, 448
Arnim, V. ....	241	Ihde, A. ....	294
Asadi, H. ....	217	Iványi, P. ....	467
Balzani, D. ....	229	Kato, S. ....	253
Barthel, R. ....	178	Kemmler, R. ....	275
Bauer, A. M. ....	311	Kunze, A. ....	241
Beccarelli, P. ....	141, 338, 448	Kustov, A. ....	100, 383
Bellmann, J. ....	265	Lang, R. ....	303
Belyaeva, Z. ....	514	Lenk, S. ....	323
Berestova, S. ....	514	Li, Y.T. ....	125
Bernert, K. ....	51	Li, Z.Y. ....	394
Bischoff, M. ....	275	Lin, G.C. ....	198
Bletzinger, K-U. ....	311, 371	Lombardini, D. ....	323
Carpenter, J. ....	57	Luo, X.L. ....	198
Carpenter, R. ....	448	Maffei, R. ....	338
Chen, J. W. ....	112	Marx, H. ....	133
Chen, W. ....	93	Mikhaylov, V.V. ....	427, 436, 455
Chen, W. J. ....	112	Mityushov, E. ....	514
Cherunov, P. ....	210	Mokin, N. ....	100, 383
Cherunova, I. ....	210	Moritz, K. ....	190, 331, 347
Chesnokov, A.V. ....	427, 436, 455	Motevalli, M. ....	229
Chivante, M. ....	190, 331	Müller, G. ....	347
Corte, C. ....	478	Němec, I. ....	303
Cotela, J. ....	371	Peeters, M. ....	403
Cremers, J. ....	133	Reed, V. ....	448
De Llorens, J.I. ....	69	Roberts, M. ....	29
Degroote, J. ....	403	Santo, G. ....	403
Dolmatov, I.V. ....	427	Schickore, J. ....	178
Ewert, B. ....	241	Schling, E. ....	178
Gade, J. ....	275	Shi, T. ....	93
Gao, C. ....	93	Simiu, E. ....	17
Geyer, S. ....	323	Stegmaier, T. ....	217, 241
Goecke, F. ....	347	Stenkina, M. ....	210
Gresser, G. ....	241	Stimpfle, B. ....	81
Grunwald, G. ....	294	Stranghöner, N. ....	217, 229
Hitrec, D. ....	178	Tan, H. ....	41
Hu, J. ....	93	Tan, H.F. ....	198
Hu, JH. ....	112	Teixeira, A. ....	241
Huntington, C. ....	57	Toso, S. ....	190, 331
Ibragimov, A. ....	100	Trushin, S. ....	383

Uhlemann, J. ....	217, 229
Van Paepegem, W. ....	403
von Arnim, V. ....	217
Wacker, J. ....	360
Wang, M. Y. ....	112
Wei, J. ....	41
Weininger, F. ....	241
Weller, F. ....	147
Wüchner, R. ....	311, 371
Yao, B. ....	112
Yoshino, T. ....	253
Yu, J. ....	41
Yu, L. ....	41
Zaschke, M. ....	360
Zhang, Q.L. ....	125, 394
Zhao, B. ....	93, 112
Zhou, H. ....	112

